TESIS DE LA UNIVERSIDAD DE ZARAGOZA
2023
28

Elisa Laita Florián

Caracterización mineral y química de arcillas alumínicas (Cretácico Inferior, NE Península Ibérica): implicaciones paleoclimáticas e industriales

Director/es
Bauluz Lázaro, Blanca
Yuste Oliete, Alfonso

ISSN 2254-7606

Prensas de la Universidad
Universidad Zaragoza

ISSN 2254-7606

Universidad Zaragoza
1542

Tesis Doctoral

CARACTERIZACIÓN MINERAL Y QUÍMICA DE ARCILLAS ALUMÍNICAS (CRETÁCICO INFERIOR, NE PENÍNSULA IBÉRICA): IMPLICACIONES PALEOCLIMÁTICAS E INDUSTRIALES

Autor

Elisa Laita Florián

Director/es

Bauluz Lázaro, Blanca
Yuste Oliete, Alfonso

UNIVERSIDAD DE ZARAGOZA
Escuela de Doctorado

Programa de Doctorado en Geología

2022

TESIS DOCTORAL

CARACTERIZACIÓN MINERAL Y QUÍMICA DE ARCILLAS ALUMÍNICAS (CRETÁCICO INFERIOR, NE PENÍNSULA IBÉRICA): IMPLICACIONES PALEOCLIMÁTICAS E INDUSTRIALES

Elisa Laita Florián
Universidad de Zaragoza, 2022

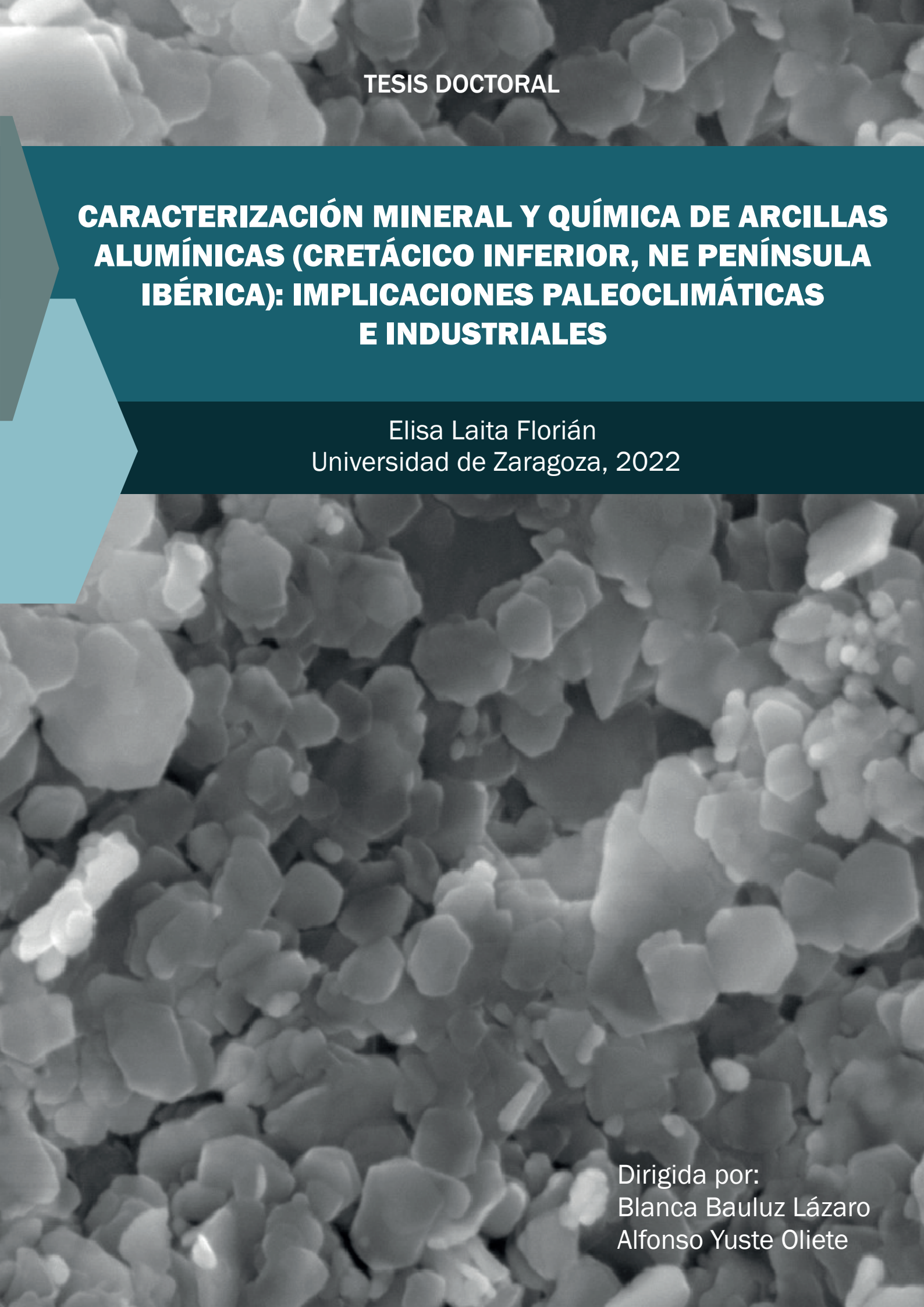

Dirigida por:
Blanca Bauluz Lázaro
Alfonso Yuste Oliete

Tesis Doctoral

CARACTERIZACIÓN MINERAL Y QUÍMICA DE ARCILLAS ALUMÍNICAS (CRETÁCICO INFERIOR, NE PENÍNSULA IBÉRICA): IMPLICACIONES PALEOCLIMÁTICAS E INDUSTRIALES.

Elisa Laita Florián

Facultad de Ciencias

Departamento de Ciencias de la Tierra

Directores

Blanca Bauluz Lázaro

Alfonso Yuste Oliete

Zaragoza, 2022

Departamento de Ciencias de la Tierra
Universidad Zaragoza

Instituto Universitario de Investigación en Ciencias Ambientales de Aragón
Universidad Zaragoza

Facultad de Ciencias
Universidad Zaragoza

Grupo aragosaurus

Universidad Zaragoza

Portada: Cristales pseudohexagonales de caolinita vistos con microscopía electrónica de barrido en una muestra de paleosuelos de la Fm. Blesa (Cretácico Inferior).

This PhD thesis is presented as a compendium of scientific papers and is composed of the following scientific works:

- **Laita, E.**, Bauluz, B., Yuste, A., 2019. High-Temperature Mineral Phases Generated in Natural Clinkers by Spontaneous Combustion of Coal. Minerals 9(4), 213. https://doi.org/10.3390/min9040213
- **Laita, E.,** Bauluz, B., Aurell, M., Bádenas, B., Canudo, J. I., Yuste, A., 2020. A change from warm/humid to cold/dry climate conditions recorded in lower Barremian clay-dominated continental successions from the SE Iberian Chain (NE Spain). Sedimentary Geology 403, 105673. https://doi.org/10.1016/j.sedgeo.2020.105673
- **Laita, E.,** Bauluz, B., Mayayo, M. J., Yuste, A., 2021. Mineral and textural transformations in mixtures of Al-rich and Al–K-rich clays with firing: Refractory potential of the fired products. Ceramics International 47(10), 14527–14539. https://doi.org/10.1016/j.ceramint.2021.02.032
- **Laita, E.,** Bauluz, B., Aurell, M., Bádenas, B., Yuste, A., 2022. Weathering events recorded in uppermost Hauterivian–lower Barremian clay-dominated continental successions from the NW Iberian Range: climatic vs. tectonic controls. Journal of Iberian Geology 48, 45–63. https://doi.org/10.1007/s41513-021-00181-0
- **Laita, E.,** Subirana, M.A., Schaumlöffel, D., Yuste, A., Bauluz, B., 2022. NanoSIMS as an analytical tool for measuring oxygen and hydrogen isotopes in clay minerals from palaeosols: procedure and first results. *Under review.*

The author also collaborated in the following scientific papers, which are related with the thematic of the thesis but are not included in the compendium:

- **Laita, E.,** Bauluz, B., 2018. Mineral and textural transformations in aluminium-rich clays during ceramic firing. Applied Clay Science 152, 284–294. https://doi.org/10.1016/j.clay.2017.11.025
- Yuste, A., Camacho, I., Bauluz, B., Mayayo, M.J., **Laita, E.,** 2020. Palaeoweathering events recorded on siliciclastic continental deposits (Albian, Lower Cretaceous) in NE Spain. Applied Clay Science 190, 105598. https://doi.org/10.1016/j.clay.2020.105598
- Brlek, M., Gaynor, S. P., Mongelli, G., Bauluz, B., Sinisi, R., Brčić, V., Peytcheva, I., Mišur, I., Tapster, S., Trinajstić, N., **Laita, E.,** Yuste, A. Šuica, S., Grizelj, A., Kukoč, D., Schaltegger, U., 2021. Karst bauxite formation during Miocene Climatic Optimum (central Dalmatia, Croatia): mineralogical, compositional and

geochronological perspectives. International Journal of Earth Sciences 110, 2899–2922. https://doi.org/10.1007/s00531-021-02091-z

- Aurell, M., Bádenas, B., Castanera, D., Gasca, J. M., Canudo, J. I., **Laita, E.,** Liesa, C. L., 2021. Latest Jurassic–Early Cretaceous synrift evolution of the Torrelapaja Subbasin (Cameros Basin): implications for Northeast Iberia palaeogeography. Cretaceous Research 128, 104997. https://doi.org/10.1016/j.cretres.2021.104997
- Bauluz, B., Mayayo, M. J., **Laita, E.,** Yuste, A., 2021. Micro- and Nanotexture and Genesis of Ball Clays in the Lower Cretaceous (SE Iberian Range, NE Spain). Minerals 11(12), 1339. https://doi.org/10.3390/min11121339

In addition, the author published a didactic paper related to minerals, as well as a scientific dissemination work related to the thematic of the thesis:

- **Laita, E.,** Mateo, E., Mazas, B., Bravo, B., Lucha, P., 2018. ¿Cómo se abordan los minerales en la enseñanza obligatoria? Análisis del modelo de mineral implícito en el currículo y en los libros de texto en España. Enseñanza de las Ciencias de la Tierra 26(3), 256–256.
- Bauluz, B., **Laita, E.,** 2022. Escrito en las rocas. conCIENCIAS 28, 57–67.

A Víctor Laita

Agradecimientos

Esta tesis no habría sido posible sin la ayuda de diferentes entidades financiadoras. La estudiante de doctorado ha sido beneficiaria de un contrato predoctoral de la Diputación General de Aragón y el trabajo desarrollado a lo largo de esta tesis doctoral forma parte de los Proyectos del Ministerio de Ciencia, Innovación y Universidades (RTI2018-093419-B-I00 y PID2021-123127OB-I00) y del Gobierno de Aragón (Grupo Aragosaurus: Recursos geológicos y paleoambientes, E18_20R). También se ha contado con el apoyo del Instituto Universitario de Ciencias Ambientales de Aragón (IUCA), de la Sociedad Española de Mineralogía (SEM) y de la Sociedad Española de Arcillas (SEA), que han contribuido con diversas ayudas para la asistencia a congresos científicos. La estudiante de doctorado se ha beneficiado, además, de una ayuda del Programa CAI-Ibercaja de Estancias de Investigación para la realización de una estancia en el IPREM (Institut des Sciences Analytiques et de Physico-Chimie pour l'Environnement et les Matériaux) de la Université de Pau et des Pays de L´Adour (Francia).

En el plano más personal, me gustaría comenzar dando las gracias, y no puede ser de otra forma, a mis dos directores, Blanca Bauluz y Alfonso Yuste, por aceptarme en su equipo y permitirme llevar a cabo esta tesis. No solo estoy orgullosa de decir que sois mis directores de tesis, sino que os habéis convertido en mucho más para mí. Habéis inculcado en mí el afán por la ciencia y la investigación. Vuestro enfoque y conocimientos, junto con el apoyo y compresión que me habéis brindado, han sido vitales a la hora de embarcarme en esta aventura científica que en ocasiones ha estado llena de dudas y frustraciones, pero también de muchos momentos gratificantes y apasionantes que nunca voy a olvidar.

Blanca, confiaste en mí allá por 2015 cuando era una recién graduada, para hacer un Trabajo Fin de Máster sobre cerámicas refractarias que nunca me habría imaginado que se transformaría en mi primera publicación científica. Me "engañaste" para ir a aquella reunión de la SEA en Madrid en 2016 o al ICC de Granada en 2017 y lo más importante, me animaste a iniciar este viaje, durante el cual, no solo me has guiado, sino también escuchado y animado cuando lo he necesitado. Mil gracias, Blanca.

Por otro lado, que habría hecho yo sin tu carácter y actitud, Alfonso, que han sido esenciales durante todo este recorrido. Estuviste conmigo cuando recibí mi primer premio (y lo que te reíste) y desde entonces me has guiado y ayudado en todos los aspectos. Tu positivismo y tus "pálpitos" me han salvado en muchos momentos de crisis. Mil gracias, Alfonso.

Con vuestra ayuda me he hecho "mayor" como científica y quedan para siempre en mi memoria todos esos buenos momentos que hemos pasado juntos en los congresos, en el campo o en el laboratorio.

También quiero dar las gracias a Marcos Aurell y a Beatriz Bádenas por involucrarse con tanto entusiasmo en el estudio de los paleosuelos, por acompañarme al campo y enseñarme tanto sobre las Fms. Blesa y Torrelapaja. Vuestra ayuda a la hora de caracterizar las muestras desde un punto de vista sedimentológico ha enriquecido enormemente esta tesis.

María José Mayayo, no solo ha colaborado en algunos de los trabajos de esta tesis, sino que ha estado siempre dispuesta a echarme una mano en todo momento durante el desarrollo de la misma. Muchas gracias, Pepa, por tu ayuda y tus ánimos.

Dirk Schaumlöffel y Maria Àngels Subirana me permitieron realizar una estancia de investigación en el IPREM. Gracias a ambos por acogerme con tanta amabilidad en vuestro laboratorio de NanoSIMS y por facilitarme, no solo el aprendizaje sobre esta técnica, sino también sobre el sincrotrón tanto en Grenoble como en Barcelona. Muchas gracias también por vuestra ayuda a la hora de tratar los datos isotópicos y escribir el manuscrito.

Gran parte de los análisis que se presentan en esta tesis se realizaron en el Servicio General de Apoyo a la Investigación-SAI. Quiero dar las gracias al personal de este servicio, especialmente al del servicio de preparación de rocas, Felipe y Manolo, que se han encargado de preparar todas las láminas delgadas y probetas. Por otro lado, a Cristina Gallego, técnico del servicio de microscopía electrónica de materiales, quiero agradecerle especialmente su ayuda y consejos durante todas las sesiones de FESEM que he realizado con ella a lo largo de la tesis (que no han sido pocas).

También me gustaría agradecer a la Sociedad Española de Mineralogía y la Sociedad Española de arcillas el haberme otorgado el Premio Jóvenes Investigadores en 2019 (SEA) y en 2020 (SEM) por dos de los trabajos que se presentan en esta tesis.

Finalmente, gracias a las Dras. Margarita Do Campo y Martine Buatier por haber realizado los informes de expertos que avalan la tesis, así como a los revisores y editores de las revistas en las que se encuentra publicados los artículos.

Sin embargo, esta dedicatoria no puede terminar aquí, ya que hay muchas personas fuera del plano académico que han contribuido en otros muchos aspectos que también se relacionan de algún modo con esta tesis.

En primer lugar, quiero dar las gracias a mi familia, especialmente a mi madre, a mi hermano y a mis tías (Mª Carmen y Toña) por escucharme siempre y apoyarme durante todo el transcurso de mi formación académica. Me habéis animado a embarcarme en esta Tesis Doctoral que espero que solo sea el principio de mi camino en la Ciencia.

Muchas gracias a todos mis compañeros del Departamento de Ciencias de la Tierra, tanto del grupo Aragosaurus como de otros grupos. Ha sido una suerte poder compartir todo este tiempo con vosotros. Gracias a todos los que habéis acogido a esta loca solitaria de las arcillas, aunque no estudie dinosaurios. Gracias por esas sesiones psicoterapéuticas durante el café y por esos vermuts

que de vez en cuando se han alargado y han acabo en la Z (malditos liantes). Sinceramente, yo todo esto lo he considerado terapia de grupo.

No puedo olvidarme tampoco de mi querida #FrikiCave que ha sido mi compañera durante el Grado, Máster y Doctorado. Gracias, Ana, no solo por confiar a la #FrikiClay el estudio de las arcillas de tu cueva mallorquina, sino por escuchar mis lloros y darme ánimos durante toda la tesis.

No podría imaginar que durante mi estancia de investigación me iba a encontrar a una persona que se convirtiese a la vez en profesora, compañera de laboratorio y amiga. Muchísimas gracias, Maria Àngels, por explicarme todo acerca del NanoSIMS y ayudarme a sacar adelante el trabajo con este equipo, por acogerme en tu casa y por presentarme a todas esas personas del grupo "beach" que ahora, junto a ti, considero mis amigos. ¡Nos vemos en Pau!

Tengo que darles las gracias también a mis amigos no geólogos, especialmente a alguien a quien considero mi hermana y que para mí siempre será "la niña", Alicia, que ha aguantado incansablemente todos mis dramitas y ha estado ahí para apoyarme. A ti Alicia, junto con Ana (las Karens, madres de michis, A2E) quiero daros las gracias por todos vuestros consejos, por darme siempre ánimos, por escuchar mis audios infinitos (aunque sea en x2) y por cuidar y amar a Moko y Mica como yo cuido y amo a Bucky, Xena, Rowina y Sarabi.

A Moko y Mica debo darles igualmente las gracias ya que han sido, y siempre serán, mis pechochos, mis bolitas pruprú antiestrés y los pobres han escuchado los ensayos de mis presentaciones más veces de las que desearían.

Muchas gracias a mis "Brasimaños" Flávio y Diego por ayudarme a reírme de los problemas. Gracias Diego por todos los viajes juntos y los días de juegos viendo "el cosmus". A Flávio quiero agradecerle especialmente todas las tardes de cerveceo (o cervecenas), muchas de las cuales han terminado en masterclass sobre química analítica. Gracias y saúde!

Por último, he dejado para el final a la persona que considero el pilar más importante de mi vida. Él es la química de esta tesis. Gracias, Raúl, por estar siempre conmigo en los buenos momentos y aguantarme también en los malos, pese a lo insoportable que puedo llegar a ser. Gracias por confiar siempre en mí y hacerme ver que valgo para esto. Te quiero.

Elisa

INDEX

FORMAL STRUCTURE OF THE PHD THESIS

The volume of this PhD thesis is composed of an abstract, nine chapters and four annexes. Chapter 1 (in Spanish) includes the general introduction to the PhD thesis. The objectives and the justification of the scientific papers that compose the compendium are presented in Chapter 2. Chapters 3, 4, 6 and 7 are transcriptions of the published scientific papers, whereas Chapter 5 includes unpublished data, which are currently under review in the journal Chemical Geology. Chapter 8 (in Spanish) presents the general discussion of the PhD thesis, and Chapter 9 comprises the main conclusions. Annex I (in Spanish) presents the impact factor and the thematic areas of the scientific journals in which the papers that form this thesis are published, as well as the contribution of the author in each work, since they are co-authored works. Finally, Annexes II–V present the scientific papers of the compendium in their respective journal format.

Chapter 1: Introducción general

This chapter contains a general introduction to the thematic of the PhD thesis through a review of the most relevant scientific literature. Clay and clay mineral terms are defined, and a brief description of the structure and classification of clay minerals is provided, together with the conditions of their formation. This chapter highlights the interest of clay minerals as palaeoclimatic indicators and their industrial usefulness due to their ceramic and refractory properties.

Chapter 2: Objectives and thematic unit

This chapter presents the objectives of the PhD thesis and establishes the thematic unity of the scientific papers that form the compendium of publications.

Chapter 3: Palaeoclimatic data recorded in Lower Cretaceous palaeosols from the SE Iberian Chain (NE Spain)

This chapter corresponds to the paper published in 2020 in Sedimentary Geology, which is included in Annex II. A combined facies and clay mineralogy analysis of lower Barremian palaeosols located in the SE of the Iberian Chain is presented. The results obtained regarding the palaeoclimatic and palaeoenvironmental conditions under which these palaeosols were generated are discussed.

Chapter 4: Palaeoclimatic data recorded in Lower Cretaceous palaeosols from the NW Iberian Chain (NE Spain)

This chapter corresponds to the paper published in 2022 in the Journal of Iberian Geology, which is included in Annex III. A combined facies and clay mineralogy analysis

of upper Hauterivian–lower Barremian palaeosols located in the NW of the Iberian Chain is presented. The results obtained regarding the palaeoclimatic and palaeoenvironmental conditions under which these palaeosols were generated are discussed. The data are compared with the data obtained from the palaeosols located in the SE of the Iberian Chain, which are the focus of the previous chapter.

Chapter 5: NanoSIMS: a new technique for analysing oxygen and hydrogen isotopes in clay minerals from palaeosols

This chapter corresponds to an unpublished manuscript, which is currently under review in Chemical Geology. In this chapter the results of oxygen and hydrogen isotopic analyses of the clay minerals from the palaeosols previously described in Chapter 3 are presented. The usefulness of NanoSIMS (nanoscale secondary ion mass spectrometry) in this kind of research is evaluated, and the first palaeoclimatic and palaeotemperature results obtained from the isotopic data are discussed.

Chapter 6: The effect of mixing Al-rich and Al–K-rich clays on the refractory potential of fired products

This chapter corresponds to the paper published in 2021 in Ceramics International, which is included in Annex IV. An evaluation of the refractory potential of refractory ceramics made up of mixtures composed of different aluminium-rich clays is included in this chapter. The mineral and textural transformations that take place in ceramics with firing and their influence on the physical properties of the final products are discussed.

Chapter 7: High-temperature mineral phases in natural clinkers: a natural analogy to refractory materials

This chapter corresponds to the paper published in 2019 in Minerals, which is included in Annex V. This chapter presents the results of a mineralogical and textural study of naturally calcined clays generated by spontaneous coal combustion (natural clinkers). The mineralogical and textural changes that take place in the natural clinkers are discussed and compared with other natural and ceramic processes.

Chapter 8: Discusión general

The main results obtained in this PhD thesis are discussed in this chapter. The contributions to the Lower Cretaceous palaeoclimatic record of the NE of the Iberian Peninsula based on clay minerals are examined. The usefulness of NanoSIMS as an analytical technique for the isotopic analysis of clay minerals is assessed. The mineralogy

of natural clinkers and refractory cylinders is compared, and the refractory potential of the latter is discussed.

Chapter 9: General conclusions

This chapter presents the main conclusions obtained in this PhD thesis.

Annex I. Impact factor, thematic areas of the papers and contribution of the author in each work.

Annex II. Paper published in Sedimentary Geology.

Annex III. Paper published in the Journal of Iberian Geology.

Annex IV. Paper published in Ceramics International.

Annex V. Paper published in Minerals.

ABSTRACT

The study of aluminium-rich clays from a geological and industrial point of view has permitted the overall characterization of these materials. Aluminium-rich clays are abundant in certain areas and constitute an important mineral resource from scientific and economic point of view.

The application of a combination of different techniques such as facies analysis, clay mineralogy (X-ray diffraction), textural and compositional characterization (optical and electron microscopy), and stable isotope analysis (NanoSIMS) to the characterization of palaeosols that developed in the continental successions of the Blesa and Torrelapaja Fms. (late Hauterivian–early Barremian, NE Spain) allows us to infer the palaeoclimatic and palaeoenvironmental conditions under which these palaeosols were generated. The applicability of NanoSIMS in palaeoclimatic studies using oxygen and hydrogen isotope ratios in nanometre-sized clay minerals is also demonstrated. The mineralogical association found in the palaeosols, characterized by authigenic kaolinite, smectite, hematite, goethite, rutile, anatase, ilmenite and diaspore and the presence of ferruginous pisoids, is characteristic of oxisols, which develop under warm and humid climatic conditions. The decrease in the authigenic kaolinite and the hematite and goethite content from the bottom to the top of all the studied profiles, along with the increase in detrital quartz and illitic phases content and the presence of authigenic smectite, indicates a decrease in the intensity of chemical weathering. The oxygen and hydrogen isotope compositions of kaolinite and smectite are consistent with the formation in a weathering environment, but the decrease in the $^{18}O/^{16}O$ and D/H ratios from the bottom to the top of the profiles also reflects a change towards colder conditions. All this suggests a change from warm/humid to colder/dryer conditions in the studied area, which is also supported by a decrease in the crystallization temperature from the kaolinite at the bottom of the palaeosols (21–22 ºC) to that of the smectite in the upper levels (16–17 ºC).

Analysis by X-ray diffraction, X-ray fluorescence, and optical and electron microscopy of natural clinkers and fired clay cylinders (1000–1270 ºC) manufactured from mixtures of bauxite and illite- and kaolinite-rich clay makes it possible to describe and compare the mineralogical and textural transformations produced by firing in these materials. The influence of the mineralogical transformations in the physical properties of the cylinders also permit us to evaluate their refractory potential by comparing them with commercial materials.

Mineralogical and textural changes take place in natural clinkers and cylinders during the coal combustion and ceramic processes, respectively. These changes include the

destabilization of the initial phases and the formation of an Al- and Si-rich vitreous phase. From this phase, new phases such as mullite, corundum, cristobalite, hercynite and ceramic pyroxenes crystallize. The new minerals are not stoichiometric, due to the dynamics of the ceramic and coal combustion processes, and their genesis depends on the composition of the raw materials. The mullite and hercynite formed in the natural clinkers are similar to those in the cylinders fired at 1000–1200 ºC, so the coal combustion probably reached this range of temperatures. The increase in density and linear shrinkage of the cylinders is related to the vitreous phase and mullite formation and correlates well with the decrease in porosity, water absorption and thermal conductivity. The changes in the colour of the samples are a consequence of the hematite and clay content at each temperature, whereas the point load resistance is greater with higher corundum content. Both the firing temperature and the clay content influence the refractory potential of the cylinders, since those mixed with illite- and kaolinite-rich clay have a higher density and lower porosity at lower firing temperatures than other refractory ceramics fired at 1200–1540 ºC. Those cylinders fired at 1200 ºC have similar properties to the fired commercial bauxites.

Introducción general

1

Clay minerals are phyllosilicates that are present in soils, sediments, and numerous sedimentary rocks on the surface of the Earth. The genesis of clays takes place very predominantly in those environments where chemical weathering and edaphic processes occur. Both processes are strongly controlled by climate (temperature and precipitation), so the clay minerals formed in soils by weathering processes are indicative of specific climatic and environmental conditions. On the other hand, clays are used as a raw material in the manufacture of various products, such as paper, absorbent materials, and ceramic materials, among many others. Therefore, the interest of clays is twofold, since they can be used as palaeoclimatic and palaeoenvironmental indicators, but they also have numerous applications in a range of industries.

1 GENERALIDADES DE LOS MINERALES DE LA ARCILLA

1.1 Definición, estructura y tipos de minerales de la arcilla

El término "arcilla" fue definido por primera vez por Agricola en 1546. La nomenclatura de los comités de la *Association Internationale Pour L'Etude des Argiles* (AIPEA) y de la Clay Minerals Society indica que es un material natural compuesto principalmente por minerales de grano fino, que es plástico cuando se añade un contenido apropiado de agua y se endurece tras el secado o cocción (Guggenheim y Martin, 1995).

Las arcillas están formadas principalmente por minerales de la arcilla junto con algunos minerales asociados como cuarzo, calcita, dolomita, feldespatos, óxidos e hidróxidos de hierro o zeolitas. Además, pueden contener también fases no minerales como materia orgánica, sílice coloidal o geles de hidróxidos de hierro.

Los minerales de la arcilla son minerales de tamaño inferior a 2 μm que confieren a la arcilla las propiedades de plasticidad y endurecimiento tras el secado o cocción. Se trata de silicatos hidratados que constituyen una gran parte de la subclase de los filosilicatos y que están compuestos por diversos cationes: Si^{4+}, Al^{3+}, Fe^{3+}, Mg^{2+}, Fe^{2+}, Ca^{2+}, Na^{+}, y K^{+}, entre otros, y aniones como O^{2-} y OH^{-} (Chamley, 1989; Barton y Karathanasis, 2002).

Su estructura se basa en el apilamiento de capas tetraédricas y octaédricas. Las capas tetraédricas tienen una composición general T_2O_5, donde T es el catión tetraédrico (principalmente Si, que puede estar sustituido por Al). Las capas octaédricas contienen cationes de tamaño medio (normalmente Al, Mg, Fe^{2+} y Fe^{3+}) y oxígenos o grupos OH^{-} en los seis extremos de los octaedros. Si el catión que hay en el centro del octaedro es divalente (Mg, Fe^{2+}), todos los octaedros están ocupados y la capa se denomina de tipo brucita o capa trioctaédrica. Por el contrario, si el catión del centro es trivalente (Al, Fe^{3+}), solamente 2/3 partes de los octaedros están ocupados y se denomina de tipo gibbsita o capa dioctaédrica (Brindley y Pedro, 1976; Chamley, 1989; Velde, 1995).

Los tetraedros se unen lateralmente entre ellos compartiendo tres vértices (los tres oxígenos basales), formando anillos hexagonales en los que los oxígenos apicales apuntan siempre hacia el mismo sentido. Los octaedros se unen entre ellos lateralmente y comparten oxígenos con los tetraedros, a los que se unen verticalmente. El plano de unión entre las capas tetraédricas y octaédricas son los oxígenos apicales de los tetraedros que son compartidos con los octaedros, junto con grupos OH^{-} de octaedros que quedan sin compartir y que se sitúan en el centro de los anillos hexagonales a la misma altura que los oxígenos apicales (Chamley, 1989) (Fig. 1.1).

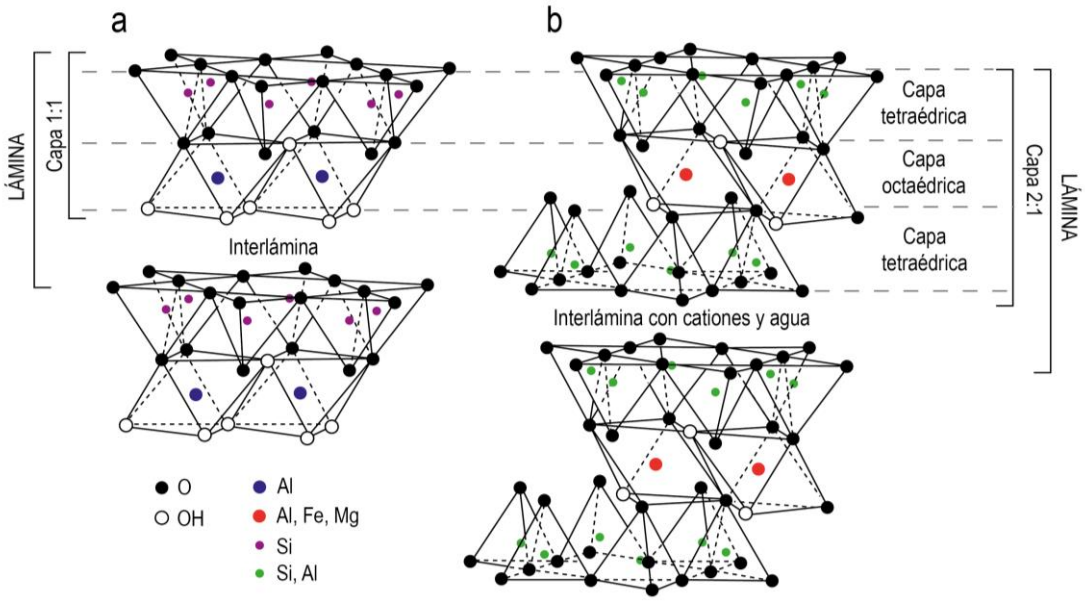

Fig. 1.1. Esquema tridimensional de la estructura de caolinita **(a)** y esmectita **(b)** (modificado de Grim, 1968).

La unión de distintas capas tetraédricas y octaédricas forma una lámina. Dependiendo de cómo se produce el apilamiento de las capas tetraédricas (T) y octaédricas (O), se diferencian tres grandes grupos de filosilicatos (Chamley, 1989; Velde, 1992; Velde, 1995): Filosilicatos 1:1 (TO), filosilicatos 2:1 (TOT) y filosilicatos 2:1:1 (TOTO).

Los filosilicatos 1:1 están formados por láminas con una capa tetraédrica y otra octaédrica y esta estructura es típica de minerales como la caolinita (Fig. 1.1a). En los filosilicatos 2:1, las láminas se componen de dos capas tetraédricas en los extremos y una capa octaédrica entre ellas. Las capas tetraédricas están invertidas una respecto a otra, de manera que todos sus oxígenos apicales apuntan hacia la capa octaédrica y pueden ser compartidos. Esta estructura es típica de minerales como las esmectitas y las micas (Fig. 1.1b). Por último, las láminas de los filosilicatos 2:1:1 son similares a las de los filosilicatos 2:1 pero con una capa octaédrica extra, siendo esta estructura típica de las cloritas.

El espacio situado entre dos láminas se denomina interlámina (Fig. 1.1). Si la unidad estructural es eléctricamente neutra, la interlámina no contendrá elementos químicos. Si embargo, debido a sustituciones catiónicas, muchos minerales de la arcilla tienen un exceso de carga negativa en la unidad estructural, que se neutraliza con la entrada de cationes (principalmente K, Na, Mg o Ca) y, en ocasiones, H_2O en la interlámina.

Según el apilamiento de las capas tetraédricas y octaédricas, el tipo de lámina octaédrica (dioctaédrica o triocaédrica) y si existe o no déficit de carga, se diferencian tres grandes grupos de filosilicatos (Tabla 1.1) (Chamley, 1989; Velde, 1995).

Tabla 1.1. Clasificación de los filosilicatos con relación a los minerales de la arcilla (Modificado de Bailey, 1980). *X*=carga de capa por fórmula unidad $O_{10}(OH)_2$. *Di*=dioctaédrica; *Tri*=trioctaédrcia.

Grupo	Carácter de la capa octaédrica	Ejemplos de especies
Filosilicatos 1:1		
Caolinita-serpentina (X~0)	Di	Caolinita, dickita, nacrita
	Tri	Crisotilo, lizardita, antigorita
Filosilicatos 2:1		
Pirofilita-talco (X~0)	Di	Pirofilita
	Tri	Talco
Esmectita (X~0.2-0.6)	Di	Montmorillonita, beidellita
	Tri	Saponita, hectorita,
Vermiculita (X~0.2-0.9)	Di	Vermiculitas dioctaédricas
	Tri	Vermiculitas trioctaédricas
Micas (X~1.0)	Di	Illita, moscovita
	Tri	Flogopita, biotita
Micas frágiles (X~2.0)	Di	Margarita
	Tri	Clintonita
Palygorskita-sepiolita (minerales fibrosos) (X~variable)	Di	Palygorskita
	Tri	Sepiolita
Filosilicatos 2:1:1		
Cloritas (X~variable)	Di	Donbasita
	Tri	Clinocloro, chamosita
	Di, tri	Cookeita, sudoita

1.2 Condiciones de formación de los minerales de la arcilla

Los minerales de la arcilla se forman como resultado de la interacción de soluciones acuosas de baja temperatura (inferiores a 200 ºC) con rocas en procesos que tienen lugar en o cerca de la superficie de la Tierra. Estos procesos dependen de la temperatura y del tiempo (Fig. 1.2). Cuando se produce la interacción agua-roca tiene lugar un proceso de disolución que aumentará cuanto mayor sea la tasa de renovación del agua (por lluvia o por circulación de fluidos). Si la proporción agua/roca es muy alta, los procesos de disolución de los componentes son más efectivos, y la cantidad y composición del agua frente a la de roca con la que interactúa determina el tipo de

reacción química que tiene lugar y, por tanto, el tipo de mineral de la arcilla que se forme (Chamley, 1989; Velde, 1992, 1995; White y Brantley, 2003; Galán, 2006).

Dependiendo del tipo de ambiente, temperatura, cantidad relativa de agua disponible y tipo de roca con la que interactúa, existen distintos procesos geológicos que dan lugar a la formación de arcillas (Fig. 1.2a).

Un proceso importante que da lugar a la formación de arcillas es la meteorización, que puede tener carácter físico o químico, dependiendo del clima y el relieve. La meteorización química es el fenómeno más extendido a partir del cual se forman arcillas y se produce por la interacción del agua de lluvia con las rocas (Chamley, 1989). Durante este proceso, los silicatos que componen la roca madre se disuelven parcial o completamente y cristalizan fases nuevas, como los minerales de la arcilla. (Chamley, 1989; Velde, 1992, Righi y Meunier, 1995).

Los minerales de la arcilla formados por meteorización pueden posteriormente ser sometidos a erosión, transportados (generalmente por suspensión en sistemas fluviales) y depositados en otra zona. Por ello, normalmente los minerales de la arcilla presentes en un ambiente sedimentario tienen un origen detrítico (es decir, heredado de otro ambiente), aunque también puede ocurrir que en ocasiones se formen *in-situ*. Estos minerales de la arcilla autigénicos se suelen formar principalmente por precipitación directa a partir de una solución, por la cristalización de fases amorfas o por la transformación de un mineral previo (Velde, 1992; Hillier, 1995).

Posteriormente, los sedimentos arcillosos pueden sufrir progresivamente procesos de enterramiento y de compactación. Estos procesos favorecen que se elimine el agua libre y se produzca un paulatino aumento de la temperatura, según el gradiente geotérmico, llegando a la diagénesis y/o metamorfismo de muy bajo grado que desestabiliza los minerales de la arcilla previos y genera la formación de nuevos minerales de la arcilla (Velde, 1992, 1995; Galán, 2006).

Por último, otro proceso por el que se forman minerales de la arcilla es la alteración hidrotermal. En los ambientes hidrotermales circulan fluidos derivados de intrusiones magmáticas o de aguas meteóricas que pueden interactuar con las rocas formando nuevos minerales. Cuando los fluidos hidrotermales son de baja temperatura (<200 ºC) se forman minerales de arcilla por precipitación directa del fluido o por transformación de minerales previos (Velde, 1992; Inoue, 1995).

De todos estos procesos, la mayor parte de los minerales de la arcilla se forman por meteorización química, que también es la responsable de la formación de suelos. Este proceso tiene lugar como resultado de la interacción entre la litosfera, la atmósfera, la hidrosfera y la biosfera y está controlado por el tipo de roca, el clima (temperatura y

precipitación), la topografía (que influye en el drenaje) y el tiempo (Chamley 1989; Weaver, 1989; Velde, 1992, Righi y Meunier, 1995; Tabor et al., 2017).

Entre las reacciones que se producen en el ambiente sedimentario durante la meteorización química, posiblemente la más relevante y que da lugar a la formación de los minerales de la arcilla, es la hidrólisis. Cuando las aguas de lluvia ligeramente ácidas interactúan con rocas de la corteza terrestre, se produce una de las reacciones de hidrólisis más habituales como es la del feldespato potásico, que da lugar a la formación de caolinita (Chamley, 1989; Righi y Meunier, 1995):

$$2KAlSi_3O_8 + 9H_2O + 2H^+ \rightarrow Al_2Si_2O_5(OH)_4 + 4H_4SiO_4 + 2K^+$$

En general, mediante las reacciones de hidrólisis, los silicatos presentes en la roca original (ej. piroxenos, anfíboles, feldespatos o micas), que constituyen sales de ácidos débiles, reaccionan con el agua formando ácido silícico disuelto y diversas bases, junto con minerales secundarios, como los minerales de la arcilla (Chamley, 1989; Velde, 1992; Righi y Meunier, 1995; Galán, 2006). Estos nuevos minerales tendrán agua cristalina en su estructura en forma de grupos OH.

Durante la hidrólisis se liberan progresivamente iones de los diferentes minerales de la roca madre (Fig. 1.2b). Primero se liberan los iones más móviles, como Na, K, Ca, Mg o Sr, después los elementos de transición como Mn, Ni, Cu, Co o Fe, y por último Si y Al (Chamley, 1989; Righi y Meunier, 1995). Por tanto, un aumento de la intensidad de la hidrólisis durante la meteorización dará lugar a la formación de minerales secundarios empobrecidos en cationes móviles. De este modo, cuando la hidrólisis sea muy intensa, como ocurre por ejemplo bajo condiciones climáticas cálidas y húmedas, se pueden formar suelos ferruginosos (ej. lateritas) en los que las fases dominantes son la caolinita junto con óxidos y oxihidróxidos de hierro. Por otro lado, si bajo condiciones de hidrólisis intensa el pH es más alto (entre 5 y 9), el Al es completamente inmóvil, dando lugar a la formación de bauxitas en las que dominan los hidróxidos y oxihidróxidos de Al (Schellmann, 1994).

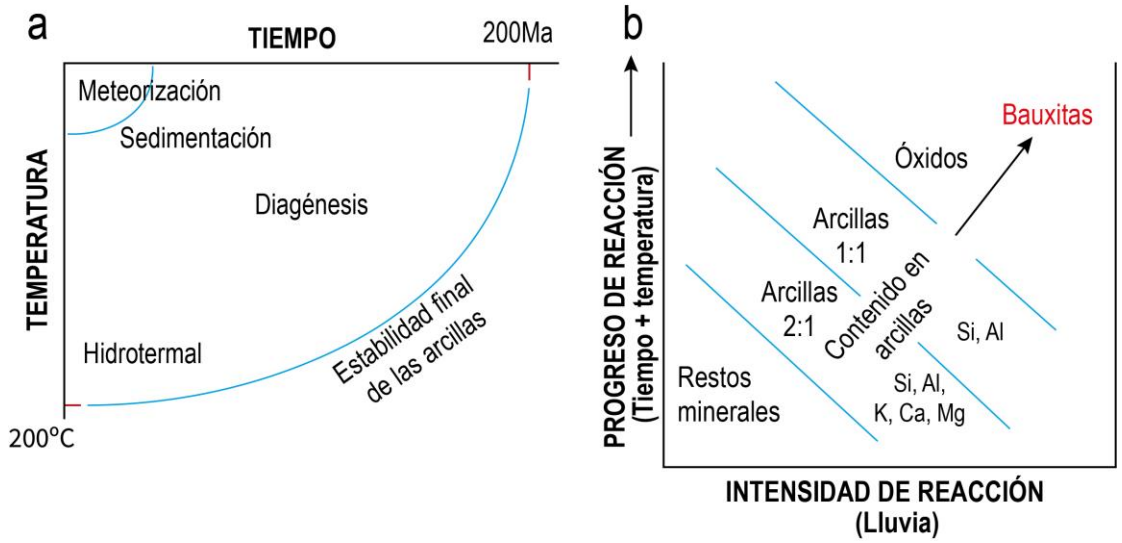

Fig. 1.2. a) Rango de estabilidad de las arcillas según temperatura y tiempo bajo condiciones de meteorización, sedimentación, diagénesis y alteración hidrotermal; **b)** tipos de minerales de la arcilla que se forman conforme avanza el proceso de hidrólisis (modificado de Velde, 1992, 1995).

2 INTERÉS PALEOCLIMÁTICO DE LAS ARCILLAS

El interés en la sociedad sobre el cambio climático que está afectando a la Tierra ha ido creciendo notablemente en los últimos años, por lo que comprender como ha sido el clima y que procesos han producido cambios climáticos en el pasado tiene cada vez más relevancia (Hugget y Cuadros, 2005). Aunque muchas de las reconstrucciones paleoclimáticas continentales se basan en registros paleontológicos y sedimentológicos (ej. Utescher et al., 2000; Mosbrugger et al., 2005; Wang et al., 2013), los minerales de la arcilla presentes en suelos del pasado (es decir, paleosuelos) también constituyen importantes herramientas paleoclimáticas.

Esto se debe a que el tipo de minerales de la arcilla autigénicos que se formen en una roca meteorizada o en un suelo dependerá de la intensidad de la meteorización que, como ya se ha comentado, está influenciada por la litología de la roca madre, el clima, el tiempo y la topografía. Por tanto, estos minerales dan información directa sobre el clima y el ambiente bajo el que se formaron (Chamley, 1989; Velde, 1992; Righi y Meunier, 1995; Thiry, 2000; Mack et al., 1993; Tabor et al., 2017).

Por ello, en la literatura se encuentran numerosos estudios sobre reconstrucciones paleoclimáticas y paleoambientales que se basan en los minerales de la arcilla autigénicos incluidos en paleosuelos.

Al sur de la Patagonia argentina se han descrito durante el Cretácico Superior (Cenomaniense) procesos de meteorización que dieron lugar a la formación de suelos ricos en caolinita característicos de climas tropicales durante el Mesozoico (Varela et al.,

2018). Además, en secuencias continentales del Paleoceno–Eoceno, también se registra la presencia de paleosuelos al noroeste de Argentina y al oeste del Estado de Minas Gerais (suroeste de Brasil), en los que el contenido en caolinita, esmectita y micas indica un clima cálido con alternancias de periodos húmedos y más secos (ej. Do Campo et al., 2018; Coelho et al., 2019; Do Campo et al., 2021).

Otros trabajos que también utilizan minerales de la arcilla como indicadores paleoclimáticos han identificado paleosuelos al noroeste de Wyoming (oeste de Estados Unidos) y al noroeste de China (ej. Wang et al., 2017; Won et al., 2018) similares a los descritos por Do Campo et al., 2018, Coelho et al., 2019 y Do Campo et al., 2021 en Argentina y Brasil.

En Europa se ha documentado un amplio registro de paleosuelos al suroeste de Francia, este de Suiza, noroeste de Cerdeña (Italia) y noreste de España durante el Cretácico Inferior (Hauteriviense–Aptiense), en los que las asociaciones de minerales de la arcilla (principalmente caolinita) evidencian unas condiciones de meteorización intensas típicas de climas cálidos y húmedos (ej. Ruffell et al., 2002; Bauluz et al., 2008; Godet et al., 2008; Bauluz et al., 2014; Yuste et al., 2015; Chanvry et al., 2020; Mameli et al., 2020).

Además, no solo las abundancias relativas de determinados minerales de la arcilla en un paleosuelo o roca meteorizada son indicativas de las condiciones climáticas y ambientales, sino que también lo es su composición isotópica. Esto es debido a que, durante los procesos de meteorización, los minerales de la arcilla se forman en equilibrio químico con el agua a partir de la que cristalizan. Por ello, los valores isotópicos de oxígeno e hidrógenos de los minerales de la arcilla autigénicos presentes en paleosuelos han sido también ampliamente utilizados en reconstrucciones paleoclimáticas y paleoambientales, ya que aportan información sobre su temperatura de formación (Delgado y Reyes, 1996; Savin y Hsieh., 1998; Giral-kacmarcík et al., 1998; Tabor et al., 2002; Sheldon y Tabor, 2009; Tabor y Myers., 2015; Kuligiewicz et al., 2021).

Sin embargo, muchos paleosuelos contienen, no solo minerales autigénicos formados por meteorización química, sino también otros que pueden tener distinto origen (detrítico o diagenético). Esto debe tenerse en cuenta al utilizar los minerales de la arcilla como indicadores paleoclimáticos y paleoambientales, ya que los minerales detríticos son heredados y reflejarán, por tanto, los procesos de meteorización desarrollados en las correspondientes áreas fuente y los procesos diagenéticos pueden modificar las asociaciones de minerales de la arcilla, transformándolos en nuevas fases diagenéticas e invalidar su uso como indicador paleoclimático y paleoambiental (Wilson, 1999; Galán, 2006; Dera et al., 2009; Bauluz et al., 2014).

Si bien la metodología más común para determinar el tipo de mineral de la arcilla que se encuentra en un paleosuelo es la difracción de rayos X, para evaluar si su origen es autigénico es necesario llevar a cabo estudios microtexturales a través de técnicas microscópicas de alta resolución. Los agregados vermiculares o "en libro" que forman comúnmente los cristales de caolinita que se han generado *in-situ* son demasiado delicados para soportar ningún tipo de transporte y también se verían afectados al sufrir alteraciones diagenéticas (Dera et al., 2009; Bauluz et al., 2014), por lo que un buen estudio microtextural es clave a la hora de determinar el origen de los minerales de la arcilla. Sin embargo, aunque en la mayoría de los trabajos mencionados anteriormente se utiliza algún tipo de microscopía electrónica para determinar la posible génesis de los minerales de la arcilla, otros estudios se basan en la combinación de la difracción de rayos X con análisis químicos, pero no realizan análisis microtexturales detallados.

Por otra parte, como ya se ha comentado anteriormente, los paleosuelos pueden contener minerales de origen detrítico y diagenético que, por tanto, no estarían en equilibrio isotópico con las arcillas formadas durante la meteorización. Esto, junto con el pequeño tamaño que suelen presentar los minerales de la arcilla (micrométrico o nanométrico) en la mayoría de los paleosuelos, puede generar problemas a la hora de llevar a cabo estudios isotópicos por espectrometría de masas, ya que durante los análisis se podrían obtener resultados que procedieran de mezclas de diferentes fases (Tabor et al., 2002; Kuligiewicz et al., 2021).

En numerosos estudios isotópicos cuyas determinaciones de oxígeno e hidrógeno se han hecho en muestras en polvo, este aspecto se ha resuelto aplicando diversos tratamientos químicos en las muestras para separar el mineral de interés del resto de las fases (ej. Delgado y Reyes, 1996; Giral-Kacmarcík et al., 1998; Gilg et al., 2003; Gilg et al., 2004). Otro procedimiento bastante utilizado se basa en hacer disoluciones selectivas a partir de las cuales, conociendo la fracción molar de todos los elementos que componen la muestra, se puede calcular el valor isotópico de una fase determinada mediante la siguiente ecuación (Tabor, 2007):

$$\delta^{18}O_{Mezcla} = X(O)_{Fase1}\,\delta^{18}O_{Fase1} + X(O)_{Fase2}\,\delta^{18}O_{Fase2} + \ldots + X(O)_{FaseN}\,\delta^{18}O_{FaseN}$$

Donde $\delta^{18}O$ es la composición isotópica y X(O) es la fracción molar del oxígeno de las distintas fases que forman la mezcla.

Si bien estos tratamientos reducen significativamente el problema de analizar la señal isotópica de varias fases mezcladas, hoy en día existen técnicas más avanzadas como puede ser el NanoSIMS (*nanoscale secondary ion mass spectrometry*). La alta resolución espacial y sensibilidad de esta técnica permite realizar imágenes composicionales en una muestra con una resolución de hasta 50 nm y, de este modo,

identificar zonas enriquecidas en el mineral de la arcilla de interés y llevar a cabo análisis isotópicos de oxígeno e hidrógeno puntuales en zonas de 1 x 1 μm^2. Por ello, el NanoSIMS es una técnica con gran potencial para el análisis isotópico de arcillas en muestras de paleosuelos de manera efectiva y sin tener que realizar tratamientos previos.

3 INTERÉS INDUSTRIAL DE LAS ARCILLAS

Las arcillas son materiales de gran interés industrial y económico. En la actualidad, se utilizan en muchos tipos de industrias, ya que constituyen componentes importantes de la fabricación de muchos productos como plásticos, papel, cemento, lodos de perforación, materiales absorbentes, materiales cerámicos y refractarios, piensos para animales, medicamentos, detergentes, pinturas, cosméticos, entre otras muchas aplicaciones (Velde, 1992; Manning, 1995; Chang, 2002; Galán, 2003; Christidis, 2013).

Dentro del campo de la industria, una línea importante es la fabricación de refractarios, donde las materias primas más utilizadas son arcillas alumínicas como las arcillas caoliníferas y las bauxitas (Velde, 1992; Manning, 1995; Bartolomé, 1997; Chang, 2002; Díaz Rodríguez y Torrecillas, 2002; Galán, 2003).

3.1 Materiales cerámicos y refractarios

Las arcillas caoliníferas son rocas de origen sedimentario formadas por un porcentaje variable de minerales de la arcilla pertenecientes al grupo de la caolinita junto con minerales detríticos como cuarzo, micas, feldespatos u óxidos de hierro (Manning, 1995; Bartolomé, 1997; Díaz Rodríguez y Torrecillas, 2002).

Estas arcillas son materiales plásticos y dispersables en agua, lo que permite moldearlos fácilmente. Estas propiedades, junto con su resistencia mecánica y la baja contracción que sufren durante la cocción, hacen que sean materias primas de interés en la industria cerámica. Además, dependiendo de su contenido en aluminio, poseen carácter refractario y pueden fundir a temperaturas superiores a los 1800 ºC (Bartolomé, 1997; Murray, 1991; 1999; 2006).

La plasticidad y resistencia mecánica de las arcillas caoliníferas está directamente relacionada con su granulometría. La forma y el tamaño de las partículas regula la viscosidad de las suspensiones acuosas y la resistencia mecánica de las pastas cerámicas por lo que cuanto más fina sea la granulometría, mayor será la plasticidad y resistencia mecánica del material (Bartolomé, 1997). Las arcillas caoliníferas presentan una granulometría fina que no permite separar las diferentes fases y se destinan a la industria cerámica y refractaria sin tratamientos previos (Manning, 1995; Bartolomé, 1997; Díaz Rodríguez y Torrecillas, 2002).

Existen depósitos de caolines y arcillas caoliníferas en diversos países como Estados Unidos, Reino Unido, Brasil, Ucrania o China, entre otros (Chang, 2002; Galán, 2003; McCuistion y Wilson, 2003; Harvey et al., 2003). En España, se encuentran importantes depósitos de arcillas caoliníferas en la formación Escucha (Cretácico Inferior), cuyos afloramientos se extienden desde Asturias hasta Murcia (Doval Montoya et al., 1991). Una de las mayores explotaciones de arcillas caoliníferas se encuentra en la Cordillera Ibérica (NE de España), donde existen numerosos depósitos arcillosos illítico-caoliníferos pertenecientes a las formaciones Escucha y Utrillas (Cretácico Inferior) que están siendo actualmente explotados para la industria cerámica y refractaria (Bauluz et al., 2008; Rodríguez-López et al., 2009; Jordán, 2020; Bauluz et al., 2021).

Debido a su alto contenido en aluminio, otra materia prima que también se utiliza con frecuencia en la industria refractaria es la bauxita. Las bauxitas representan el extremo alumínico de la serie aluminio-ferrosa de las lateritas y se forman, por tanto, bajo condiciones de hidrólisis intensa. Están compuestas principalmente por hidróxidos y oxihidróxidos de aluminio (gibbsita, boehmita y diásporo), junto con minerales del grupo del caolín (caolinita, haloisita), cuarzo, óxidos e hidróxidos de hierro (hematites, goethita) y óxidos de titanio (rutilo, anatasa) (Bárdossy, 1982; Chang, 2002).

Al igual que ocurre con los caolines y las arcillas caoliníferas, existen numerosos yacimientos de bauxitas localizados en diversas áreas de distintos continentes de todo el mundo (Harben y Bates, 1990), si bien los países más enriquecidos en este tipo de depósitos son Australia, Guinea y Camerún (Ordóñez, 1991; Chang, 2002).

En España se localizan cuatro regiones principales con depósitos bauxíticos: 1) Zona Subbética (Cordilleras Béticas); 2) Zona de enlace entre la cordillera Costero-Catalana y la Cordillera Ibérica; 3) Cordillera Costero-Catalana y 4) Zona Sur-Pirenaica (Molina, 1991; Molina y Salas, 1993; Salas et al., 2004; Yuste et al., 2015). En esta última, se encuentran numerosos yacimientos de bauxitas que fueron explotados a cielo abierto en la década de los 90 (Molina et al 1994).

Aunque la bauxita que se explota en muchos de los yacimientos del mundo se destina principalmente a la producción de aluminio, un 15% se utiliza como materia prima en otras industrias, entre ellas la refractaria (Chang, 2002; Plunkert, 2005). Las bauxitas pueden diferenciarse de las arcillas por su contenido en aluminio de la siguiente manera (Bárdossy, 1982):

- Bauxita: Al_2O_3 = 70–100%
- Bauxita arcillosa: Al_2O_3 = 50–70%
- Arcilla bauxítica: Al_2O_3 = 20–50%
- Arcilla: Al_2O_3 <20%

En general, en la industria refractaria es necesario que el material de partida tenga cierto contenido en aluminio. Si bien los caolines y arcillas caoliníferas cumplen este requisito, para obtener un producto final que requiera un contenido en aluminio superior al 45–50%, se debe utilizar bauxita como materia prima (Chang, 2002).

3.2 Caracterización de arcillas cerámicas y refractarias

Durante el proceso de cocción de las arcillas y las bauxitas, se producen una serie de transformaciones mineralógicas y texturales que estarán influenciadas por la composición mineralógica de la materia prima, su granulometría, la temperatura y el tiempo de cocción y las condiciones atmosféricas del horno. Además, estas transformaciones controlarán las propiedades físicas de los productos cocidos (González-García et al., 1990; Jordán et al., 1999, 2001; Pardo et al., 2011).

Conforme aumenta la temperatura, los minerales de la arcilla empiezan a desestabilizarse, dando lugar a la formación de una fase vítrea y a la cristalización de nuevas fases (Fig. 1.3). Esto ocurre (dependiendo de la composición del material de partida) a partir de los 700–1000 ºC (ej. Jordán et al., 1999; Bauluz et al., 2003; Bauluz et al., 2004; Lee et al., 2008; Pardo et al., 2011; Jordán, 2020).

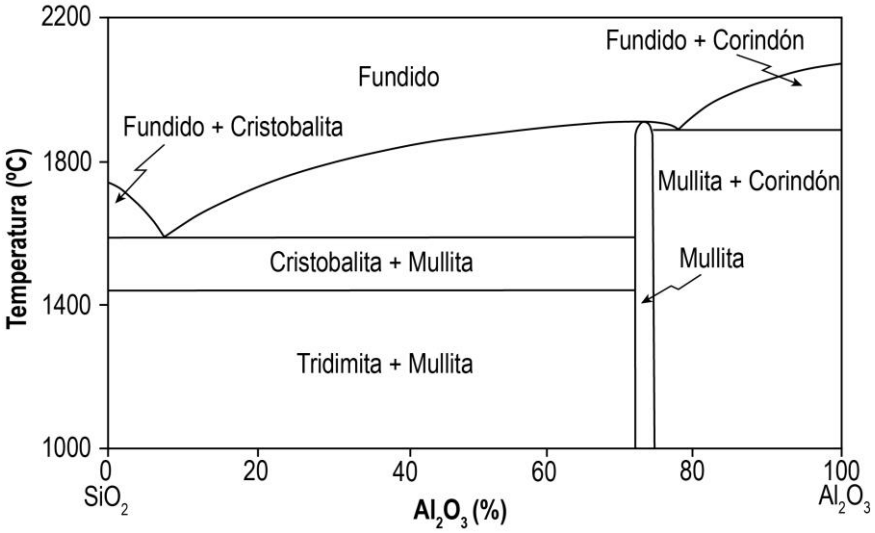

Fig. 1.3. Relación de fases en el sistema binario Al_2O_3—SiO_2 a una atmósfera de presión (modificado de Manning, 1995).

Dos de las fases más comunes que se forman durante la cocción de arcillas y bauxitas son mullita y corindón (Fig. 1.3) y su génesis tiene efectos sobre las propiedades físicas de los productos cerámicos.

La génesis de mullita afecta especialmente a las propiedades mecánicas (Lee et al., 2008; Zawrah y Khalil, 2001; Pardo et al., 2011). Algunos estudios han puesto de

manifiesto que su presencia influye en determinadas propiedades de los productos cerámicos como la densidad, porosidad, la contracción o la resistencia a la compresión (ej. Dong et al., 2008; Andrews et al., 2013; Zake-Tiluga et al., 2014; Jordán, 2020). La resistencia a la compresión también depende del contenido en corindón, el cual además influye en otros parámetros como puede ser el módulo de Young o el coeficiente de expansión térmica (Altun, 2001; Medvedovski, 2001; Kim et al., 2021).

Para comprender como evoluciona el proceso cerámico, es importante profundizar en el conocimiento de los cambios mineralógicos, composicionales y texturales que se producen en los materiales con el incremento de la temperatura a escala micro y nanométrica (Maggetti, 1982; Bauluz et al., 2004; Kakroudi et al., 2008; Jordán et al., 2020). Por otro lado, es importante también determinar la influencia de estos cambios en las propiedades físicas de los productos finales para poder caracterizarlos y deducir su potencial cerámico o refractario (Altun, 2001; Gavshina et al., 2019; Jordán, 2020).

En la literatura, numerosos estudios describen los cambios mineralógicos y texturales en materiales cerámicos y refractarios (ej. Jordán et al., 1999, 2001; Bauluz et al., 2004; Trindade et al., 2009; Pardo et al., 2011; Laita y Bauluz, 2018; Jordán, 2020) y algunos hacen referencia a las propiedades físicas de los materiales (ej. Bauluz et al., 2003; Kakroudi et al., 2008; Iglesias et al., 2011; Andrews et al., 2013; Boussen et al., 2016; Semiz y Çelik, 2020). Sin embargo, no hay casi estudios que expliquen en detalle estas transformaciones en bauxitas, ni la relación entre los distintos cambios mineralógicos que se producen a diferentes temperaturas y cómo afectan a las propiedades físicas de estos materiales.

Por último, cabe destacar, además, que las fases minerales que se forman durante los procesos de cocción han sido también descritas en procesos ígneos y metamórficos (ej. Worden et al., 1992; Török, 2002; Schneider et al., 2008) y en arcillas calcinadas de manera natural por procesos de autocombustión de carbón, conocidas como clinkers naturales (ej. Sokol et al., 1998; Estrada et al., 2009). En el caso particular de los clinkers naturales, determinar en detalle las características mineralógicas y texturales de estos materiales puede ser de gran interés para poder, no solo entender cómo tiene lugar el proceso de autocombustión, sino para poder también compararlo con los procesos cerámicos y geológicos de alta temperatura.

Objectives and thematic unity

2

Two main lines of research have been followed in the present PhD thesis. One is related to the interest of clay minerals as palaeoclimatic indicators, and the other is focused on the usefulness of clay minerals as raw materials in the ceramic and refractory industry. For this reason, this PhD thesis has two main objectives: on the one hand, to deduce the climatic conditions in the NE sector of the Iberian Peninsula during the Lower Cretaceous and, on the other hand, to evaluate the refractory potential of several mixtures of different Lower Cretaceous clayey materials from mineral deposits in the NE of Spain. Some of the results obtained from this PhD thesis have been published in scientific journals, and thus the PhD is presented as a compendium of publications. This chapter elucidates the objectives of the PhD thesis and establishes the thematic unity of the scientific papers that constitute the compendium of publications.

1. OBJECTIVES OF THE PHD THESIS

The study of aluminium-rich clays is approached from two different points of view in this PhD thesis. On the one hand, geological aspects are addressed, involving palaeoclimatic reconstructions based on clay mineral assemblages present in the palaeosols that developed in the continental sequences of the Lower Cretaceous of the Iberian Cordillera (NE Spain). On the other hand, the refractory potential of ceramics manufactured from different aluminium-rich clays from the Iberian Chain and the southern Pyrenean mountains is evaluated.

Therefore, two main lines of research have been followed in this PhD thesis. One is related to the interest of clay minerals as palaeoclimatic indicators, and the other focuses on them as raw materials in the ceramic and refractory industry. Consequently, this PhD thesis has two main aims, from which the following specific objectives are derived:

1. To deduce the climatic conditions and possible variations in the NE of the Iberian Peninsula during the Lower Cretaceous from sedimentological, mineralogical, and geochemical analyses of palaeosol outcrops located in the SE and NW of the Iberian Chain. In achieving this aim, the specific objectives are:
   - To determine whether the origin of the clay minerals present in palaeosols is authigenic, detrital or diagenetic.
   - To analyse the vertical and lateral variations in authigenic clay minerals assemblages present in palaeosols and their relationship with the palaeoenvironmental and palaeoclimatic conditions.
   - To evaluate the usefulness of NanoSIMS (nanoscale secondary ion mass spectrometry) in isotopic studies involving micro- and nanometre-sized clay minerals included in palaeosols, as well as carrying out oxygen and hydrogen isotopic analyses of these clay minerals to obtain data about their formation temperatures and conditions.
2. To analyse the behaviour of different mixtures of clayey materials (illite- and kaolinite-rich clays and bauxites) from Lower Cretaceous deposits in NE Spain during firing. In achieving this aim, the specific objectives are:
   - To determine in detail the mineralogical and textural changes that take place during firing at different temperatures in cylinders made up of mixtures composed of different proportions of illite- and kaolinite-rich clays and bauxites.

- To evaluate the influence of these changes on relevant physical properties of the final products such as: density, lineal shrinkage, porosity, colour, water absorption, thermal conductivity and point load resistance.
- To compare these data with the mineralogy and properties of fired commercial bauxites to deduce the refractory potential of the studied mixtures.
- To understand the dynamic of the ceramic process and compare it with other natural processes, exemplified by the calcined clays generated by the spontaneous combustion of coal.

2. THEMATIC UNITY OF THE PHD THESIS

In order to achieve the aforementioned aims, clay mineral assemblages present in palaeosol levels included in Lower Cretaceous continental sequences located in different areas of the Iberian Chain have been studied. Specifically, two different studies have been carried out on palaeosols located in the SE and NW Iberian Chain, in the provinces of Teruel and Zaragoza. These studies are particularly relevant since they add greater detail to the palaeoclimatic record of the Lower Cretaceous of NE Spain. The results of these studies have been published in two journals indexed in the JCR (Journal Citation Reports). The first paper focuses on palaeosols from the SE Iberian Chain and is published in Sedimentary Geology. The second paper is a study of palaeosols from the NW Iberian Chain and is published in the Journal of Iberian Geology:

- Laita, E., Bauluz, B., Aurell, M., Bádenas, B., Canudo, J. I., Yuste, A., 2020. A change from warm/humid to cold/dry climate conditions recorded in lower Barremian clay-dominated continental successions from the SE Iberian Chain (NE Spain). Sedimentary Geology 403, 105673.
- Laita, E., Bauluz, B., Aurell, M., Bádenas, B., Yuste, A., 2022. Weathering events recorded in uppermost Hauterivian–lower Barremian clay-dominated continental successions from the NW Iberian Range: climatic vs. tectonic controls. Journal of Iberian Geology 48, 45–63.

The isotopic composition (oxygen and hydrogen) of clay minerals present in soils also indicates the climatic and environmental conditions under which they were generated. However, authigenic clay minerals included in most palaeosols are generally small-sized (micrometre to nanometre-seized), generating difficulties in isotope analyses by conventional geochemical techniques. The PhD student therefore spent three months at the IPREM (Institut des sciences analytiques et de physico-chimie pour l'environnement et les matériaux) in Pau, France, in order to use NanoSIMS (nanoscale

secondary ion mass spectrometry). The purpose of using this technique was to analyse the isotopic composition (oxygen and hydrogen) of different authigenic clay minerals included in some of the palaeosols previously studied. This study has made it possible to evaluate the usefulness of NanoSIMS in isotopic studies involving clay minerals, since to date there have been no investigations into this topic. This research has provided significant information about the formation temperature of the analysed clays. The results of the study are currently under review in Chemical Geology.

Regarding the industrial applications of aluminium-rich clays, the refractory potential of cylinders manufactured using mixtures of different proportions of bauxites and illite- and kaolinite-rich clays has been evaluated. The bauxites are from Cretaceous bauxite deposits located in the southern Pyrenean mountains (NE Spain), which were opencast-mined during the 1990s. The illite- and kaolinite-rich clays belong to the Lower Cretaceous Escucha Formation, which is located in the Iberian Range and currently mined by the ceramic and refractory industries. The novelty of this work is that both the mineralogical and textural transformations that take place in the cylinders at different firing temperatures and the influence of these changes on the physical properties of the final products have been evaluated. Since there are not many investigations describing in detail how different mixtures can affect the properties of the final product, this research is of great relevance to the industrial applications of this kind of materials. This study showed that when mixing bauxite and illite- and kaolinite-rich clays, it is not necessary to reach such high temperatures as those of the commercial materials to achieve proper refractory materials. The results of this study are published in Ceramics International (indexed in the JRC):

- **Laita, E.,** Bauluz, B., Mayayo, M. J., Yuste, A., 2021. Mineral and textural transformations in mixtures of Al-rich and Al–K-rich clays with firing: Refractory potential of the fired products. Ceramics International 47(10), 14527–14539.

On the other hand, not only currently mined illite- and kaolinite-rich clays are found in the Escucha Formation, but also coal layers. These coal layers were mined from the 1980s until 2016. During these years, spontaneous combustion of coal took place, naturally calcining the clays, giving rise to the genesis of natural clinkers. Some of the mineral phases generated during the ceramic process have also been described in naturally calcined clays generated by spontaneous coal combustion. For this reason, it was considered of interest to conduct a detailed mineral and textural study of the new phases generated in the natural clinkers included in the Escucha Formation. The study of these mineral phases shed light on the spontaneous combustion process, as well as

establishing similarities and differences between this process and the ceramic processes. The results of this study are published in Minerals (indexed in the JRC):

- **Laita, E.**, Bauluz, B., Yuste, A., 2019. High-Temperature Mineral Phases Generated in Natural Clinkers by Spontaneous Combustion of Coal. Minerals 9(4), 213.

All the results and discussions included in this PhD thesis are contributions of the author.

3 Palaeoclimatic data recorded in Lower Cretaceous palaeosols from the SE Iberian Chain (NE Spain)

A combined facies and clay mineralogy analysis of the continental succession recorded in the lower part of the Blesa Formation (early Barremian, Oliete subbasin, NE Spain) allowed us to specify the palaeoclimatic and palaeoenvironmental conditions under which this sedimentary record originated. Six outcrops including clays, clays/marls and dm-thick interbedded palustrine-lacustrine limestone levels were logged and sampled for X-ray diffraction and optical and electron microscopy analysis. The lower levels consist of red clays with abundant ferruginous pisoids (1–5 mm in size) and macropisoids (>5 mm), whereas the intermediate and upper levels are ochre and violet clays/marls with few or no pisoids. The pisoids normally consist of a nucleus and a cortex made up of several layers. Some pisoids have a fragment of a previous pisoid acting as a nucleus, indicating local re-working processes. Both the nucleus and the cortex are formed by hematite, goethite, variable contents of kaolinite, and minor proportions of ilmenite. Their texture and mineralogy show an *in-situ* growth. Interbedded limestone beds within the clay- and clay/marl-dominated levels are formed by micrite, microsparite and sparite. These limestones are cemented by kaolinite and they also have pisoids, indicating the occurrence of edaphic processes. The red clays have the lowest calcite content and the highest hematite, anatase, diaspore, goethite and kaolinite content. By contrast, the ochre and violet clays/marls have higher illite content. Smectite is only detected in the ochre clays/marls. This mineral association is characteristic of lateritic palaeosols, formed under warm and humid conditions. Kaolinite and smectite textures indicate that they are authigenic, whereas illite may be of detrital origin. The upward decrease in kaolinite, hematite, anatase, diaspore and goethite content, along with the increase in quartz content and the presence of smectite and illite, reflect a change from warm and humid conditions to drier and colder conditions during the early Barremian in the studied area.

1 INTRODUCTION

The study of both facies and clay mineralogy in sedimentary successions is of great interest in allowing palaeoclimatic and palaeoenvironmental conditions to be inferred (Chamley, 1989; Velde, 1995; Thiry, 2000). In Mesozoic and Cenozoic sequences of continental materials, which include palaeosol developments, the variations in clay mineral assemblages have been widely used as palaeoclimatic and palaeoenvironmental proxies (e.g. Ehrmann et al., 2005; Raucskik and Varga, 2008; Do Campo et al., 2010; Bauluz et al., 2014; Do Campo et al., 2018 and references therein). Notably, palaeosols are formed in direct contact with the atmosphere, and thus clay minerals formed during their development can be correlated with climatic and palaeoenvironmental factors such as temperature, water availability during pedogenesis and vegetation cover, which control chemical weathering (Sheldon and Tabor, 2009; Varela et al., 2018).

Physical weathering processes predominate in dry and cold climates, and palaeosols that form under these conditions contain mineral assemblages dominated by illite and/or chlorite (Chamley, 1989). In contrast, intense hydrolysis processes take place under humid subtropical to tropical climates, giving rise to the formation of laterites, lateritic clays, and bauxites, where kaolinite is the main clay mineral (Chamley, 1989; Righi and Meunier, 1995). On the other hand, chemical weathering is less intense under warm climates with alternating humid and dry seasons, and in these cases smectite is formed (Buurman et al., 1988; Güven, 1988; Chamley, 1989; Murakami et al., 1996).

In NW Europe, a warm and humid climate was recorded during the early Barremian (Wright et al., 2000), which is also evidenced by the presence of ferruginous palaeosols and bauxites (Bárdossy, 1982). By contrast, an alternation of wet and dry seasons has been described during this period in the west of Europe (Haywood et al., 2004).

In the Iberian Range (NE Spain), a seasonal subtropical climate has been described during the Lower Cretaceous (Buscalioni and Fregenal-Martínez, 2010). Previous researchers pointed out the presence of Barremian kaolinite-rich clays, bauxite deposits and lateritic clays in this area (Combes, 1969; Molina and Salas, 1993; Bauluz et al., 2014; Yuste et al., 2015; Yuste et al., 2017), which is also consistent with relatively warm and humid conditions.

The link of clay mineral assemblages with the palaeoclimate-palaeoenvironment is not always straightforward. Clay-rich rocks and palaeosols frequently include not only authigenic clay minerals, but also others that formed during diagenetic processes. These processes could transform the clay minerals initially formed and therefore alter the palaeoclimatic-palaeoenvironmental signal (Dera et al., 2009; Bauluz et al., 2014). For

this reason, it is necessary to conduct textural studies to assess possible diagenetic modifications in clay minerals before using them as palaeoclimatic indicators.

In this work, the use of X-ray diffraction and optical and electron microscopy to undertake a sedimentological, mineralogical and textural characterization of clay-rich outcrops present in the early Barremian (Lower Cretaceous) continental successions of the Oliete subbasin (Maestrazgo Basin; NE Spain) allowed us: 1) to characterize sedimentary (*in-situ* vs. detrital) and diagenetic minerals; 2) to establish the variation in *in-situ* clay mineral assemblages and the palaeoenvironmental conditions under which they were formed; 3) to link the vertical trends of *in-situ* clay mineral assemblages with variations in the formation conditions, in particular temperature/humidity.

2 GEOLOGICAL SETTING

The opening of the Atlantic Ocean along with the westward spread of the Tethys Ocean during the Late Jurassic–Early Cretaceous generated rifting processes in the eastern part of the Iberian Plate. During this active rifting period, extensional fault activity resulted in the progressive structural compartmentalization of the wide marine carbonate platforms that had previously developed during the Jurassic. All this resulted in the generation of independent subsiding rift-related sedimentary basins and subbasins, such as the Maestrazgo Basin in the eastern part of the Iberian Plate (e.g., Van Wees et al., 1998; Salas et al., 2001; Aurell et al., 2019).

The subbasin under study, the Oliete subbasin, is located in the northwestern marginal area of the Maestrazgo Basin (Fig. 3.1). The lower synrift sedimentary unit of the Oliete subbasin is the Blesa Formation, which reaches a thickness of up to 150 m (Canérot et al., 1982). This formation is divided into three genetic stratigraphic sequences: the lower Blesa (LBS), middle Blesa (MBS) and upper Blesa (UBS) sequences (Aurell et al., 2018). These authors describe the LBS as consisting of distal alluvial to palustrine marls/clays and palustrine-lacustrine limestones upwards and including clay-rich materials in its lowermost part; these are the materials studied in the present work. The MBS is formed by oyster-rich limestones and marls grading upwards and landwards to distal alluvial and palustrine-lacustrine marls/clays and limestones. Finally, the UBS contains distal alluvial red clays in its lowermost part and palustrine and lacustrine carbonates and marls/clays towards the top (Aurell et al., 2018). The Barremian age of the Blesa Formation is well-constrained by the presence of charophytes in the palustrine-lacustrine marly and limestone facies found in the LBS and UPS (Canudo et al., 2010; Moreno-Azanza et al., 2014).

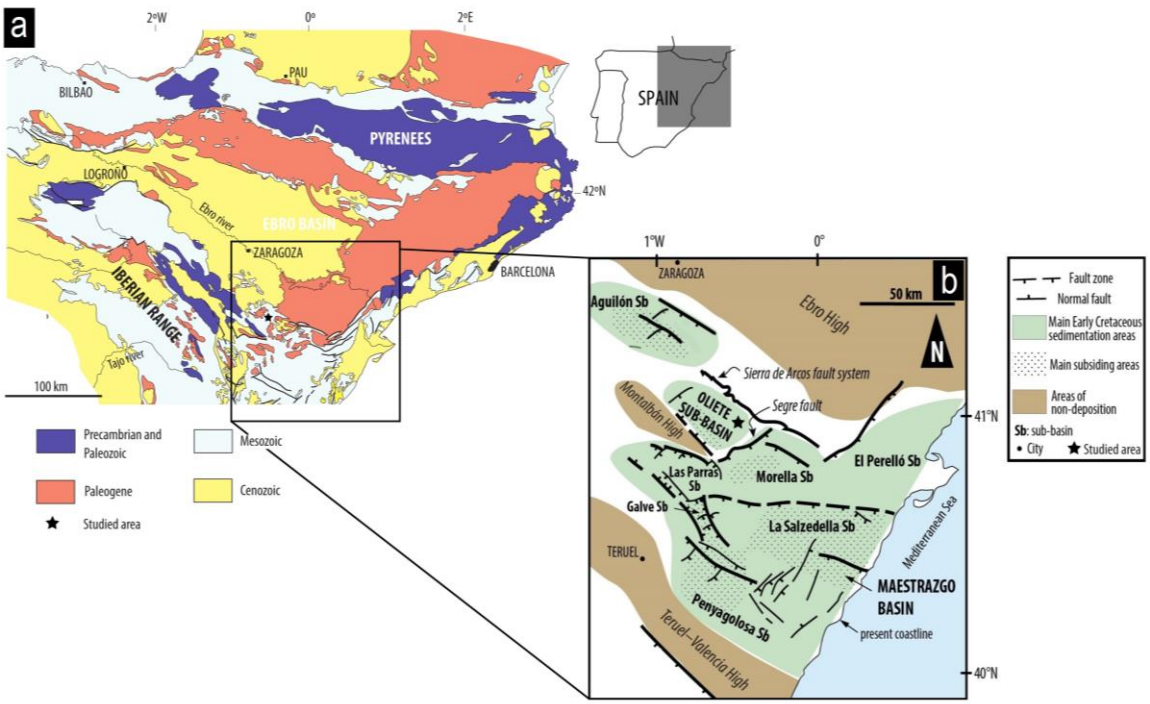

Fig. 3.1. a) Simplified geological map of the NE Iberian Peninsula; **b)** palaeogeographical reconstruction of the main Early Cretaceous sedimentation areas in NE Iberia, including the studied Oliete subbasin within the Maestrazgo Basin (from Aurell et al., 2018).

The lower part of the LBS studied here contains red to ochre and violet-ochre marls/clays of very variable thickness (0–60 m thick) at subbasin scale and local intercalations of carbonate-rich beds with root traces, charophytes and vertebrate fossils (Aurell et al., 2018 and references therein). Of particular interest for this work is the presence of dominant red clays in the lowermost part of the LBS, including ferruginous pisoids, thus indicating soil development at the onset of the sedimentation of the Blesa Formation. The tectono-sedimentary evolution at this initial development stage of the Oliete subbasin has been documented in Aurell et al. (2018). According to these authors, there was a period of subaerial exposure and erosion after the Jurassic marine carbonate sedimentation, which encompassed most of the Tithonian–Hauterivian, and normal faulting involved the overall tilting of the Jurassic limestones, which resulted in higher uplift and erosion of the areas located to the SW. In these areas only the lowermost Jurassic units are preserved from erosion (see the Montalbán Anticline in Fig. 3.2a), whereas a more complete Upper Jurassic succession is preserved in the NE domains (see the Alacón area in Fig. 3.2a). The angular erosive unconformity (Fig. 3.2c–e) over the tilted Jurassic limestones is linked to a palaeokarst surface, which includes dissolution–precipitation meteoric features. The clay/marl dominated succession of the lower part of the LBS studied here covers this palaeokarst (Fig. 3.2c, e). The main areas of clay-rich deposits with ferruginous pisoids within the Oliete subbasin are located in the northern

(around Alacón) and southern regions (between the villages of Josa and Estercuel) (Fig. 3.2a). Further tectonic reactivation during the early Barremian gave rise to the development of an orthogonal system of NW–SE and NE–SW trending normal faults (Fig. 3.2b), which enabled the spreading of the distal alluvial and palustrine-shallow lacustrine sedimentation that characterizes most of the LBS (Aurell et al., 2018).

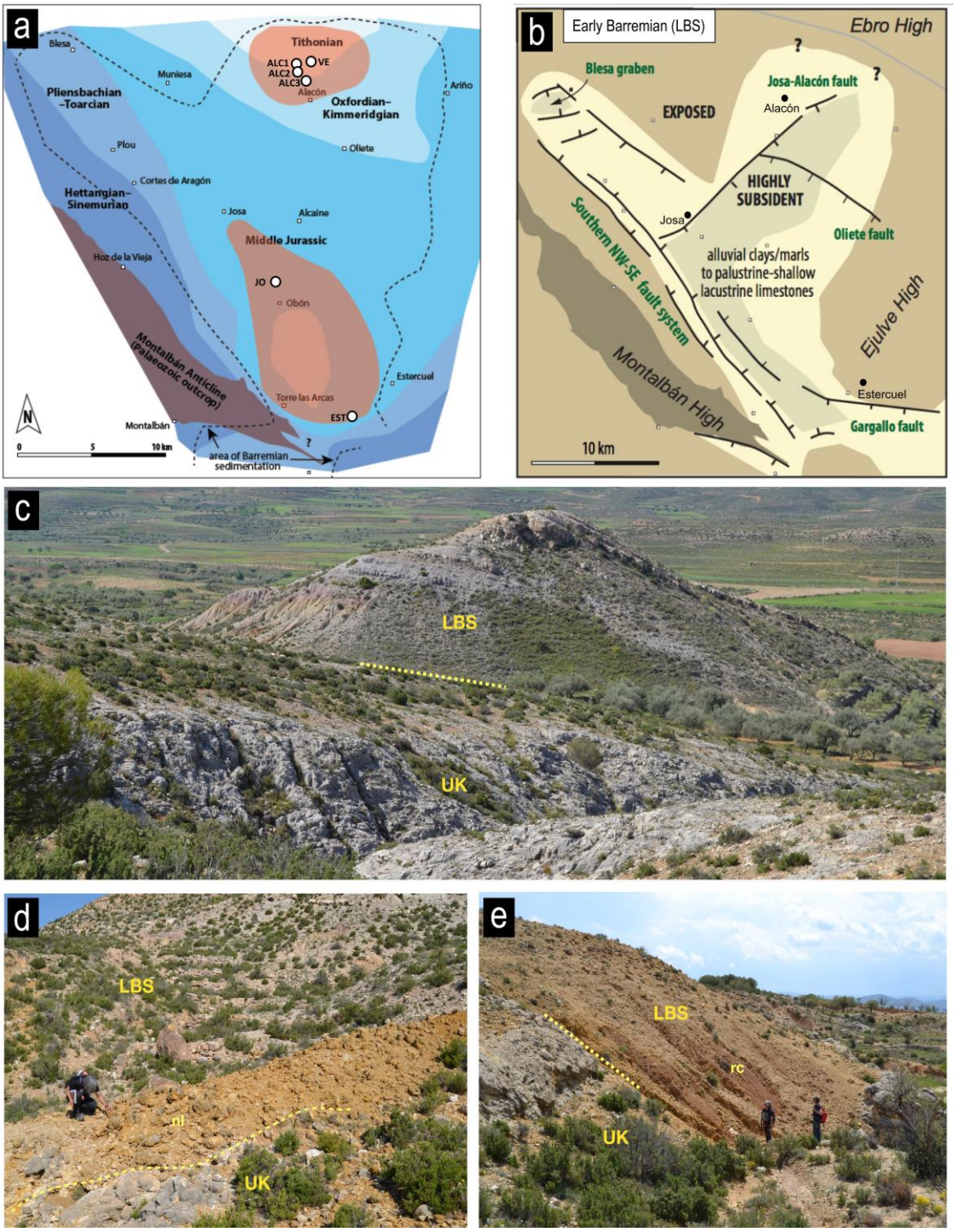

Fig. 3.2. a) Palaeogeological map of the Oliete subbasin showing the age of the youngest marine units preserved below the unconformity between the Jurassic and the Barremian Blesa Formation (modified from Aurell et al., 2018). The areas where the lowermost Blesa Formation (i.e. lower Blesa Sequence: LBS) includes frequent clays with pisoids are indicated in orange. The six outcrops of the lower part of the LSB logged and sampled in the present work are located near the villages of Alacón, Josa and Estercuel (see white circles); **b)** palaeogeography of the Oliete subbasin during the sedimentation of the LBS (modified from Aurell et al., 2018); **c)** field view around the ALC2 log showing the upper Kimmeridgian (UK) shallow marine carbonates overlain by the clays and limestones of the LBS; **d)** close view near the ALC2 log showing the irregular palaeokarstic surface (yellow dashed line) that developed at the boundary between the UK and the LBS, and overlain by a nodular level (nl) formed by abundant fibrous-radial calcite nodules; **e)** field view of the lowermost part of the LBS at the ALC3 log showing the red clays (rc) overlying the UK.

3 METHODS

3.1 Logging and sampling

Six outcrops of the lower part of the LBS in the northern and southern areas of the Oliete subbasin were selected for logging and sampling (Fig. 3.2a). Logs ALC1, ALC2, ALC3 and VE are located to the north of the locality of Alacón, whereas logs JO and EST are found to the south of the towns of Josa and Estercuel, respectively.

The logged sections include different levels of red clays with pisoids, ochre or violet clays/marls with few or no pisoids, and a few intercalated palustrine-lacustrine limestone beds. Thickness, lithology, colour, texture and stratification were studied bed-by-bed, and a total of 47 samples of clays and clays/marls, palustrine-lacustrine limestones and ferruginous pisoids were taken for further analyses of texture and mineralogical composition in the laboratory (Table 3.1).

3.2 X-ray diffraction

The mineralogical composition of 47 samples was determined by X-ray diffraction (XRD). The <2 μm fractions of clay and clay/marl samples (n = 33) were also analysed (Table 3.1). These fractions were concentrated by centrifugation and analysed on both air-dried and ethyleneglycol-treated oriented aggregates, following the procedure described by Bauluz et al. (2014). The diffraction patterns were obtained using a Philips 1710 diffractometer at the University of Zaragoza (Zaragoza, Spain), with 40 kV voltage, 30 mA current, CuKα radiation, automatic slit, and a graphite monochromator. The XRD patterns were acquired from 3 to 60° 2θ and 3 to 30° 2θ for whole samples and <2 μm fractions, respectively. The analyses were performed using the XPowderX software (Martin, 2017).

After determining the mineralogy of the samples, relative proportions of the mineral phases were acquired using Reference Intensity Ratio (RIR) values from Schultz (1964), Biscaye (1965) and Smith and Johnson Jr. (2000). The RIR values were calculated according to Hillier (2003). In addition, the full width at half maximum (FWHM) of the 001 reflections of kaolinite in both air-dried and ethylene-glycoltreated oriented aggregates was measured in order to determine kaolinite crystallinity.

3.3 Optical and electron microscopy

Twenty-one thin sections of clays and clays/marls, palustrine-lacustrine limestones and ferruginous pisoids (coated with a thin layer of epoxy resin) were studied by both transmitted and reflected light microscopy in order to identify transparent and opaque minerals as well as to characterize their texture (Table 3.1). The description of the ferruginous particles was made following the terms given by Bárdossy (1982): macropisoids (>5 mm), pisoids (1–5 mm), ooids (100 mm–1000 μm) and micro-ooids (<100 μm).

Seventeen thin sections were studied using a Carl Zeiss Merlin field emission scanning electron microscope (FESEM) equipped with an Oxford energy-dispersive X-ray (EDS) detector at the University of Zaragoza (Zaragoza, Spain) (Table 3.1). For this, the thin sections were previously carbon-coated. Compositional images of the samples were obtained using two types of backscattered electron detectors: angular selective (AsB) and energy selective (EsB). The accelerating voltage used for the former and for the EDS was 15 kV with a beam current of 400 pA. For the latter, the accelerating voltage was 4 kV with a beam current of 2.0 nA. In addition, morphological images were obtained from fragments of the rocks using a secondary electron detector (Inlens). In this case, the accelerating voltage was 5 kVwith a beamcurrent of 800 pA.

Semi-quantitative analyses were carried out using the EDS detector, which has a detection limit of 0.1%. From these analyses, clay mineral formulas were calculated in order to compare them with the theoretical compositions. The kaolinite formula was calculated on the basis of $O_5(OH)_4$, and the smectite and illite-type-phase formulas were calculated on the basis of $O_{10}(OH)_2$.

Table 3.1. Summary of sample analyses at the laboratory (n= number of samples/analyses).

Field samples (**n=47**)	**X-ray diffraction** (Mineralogical composition)		**Optical and electron microscopy** (Texture & mineral identification)	
	whole rock (**n=47**)	<2 μm fraction of clays & clays/marls (**n=33**)	Optical microscopy (**n=21**)	Electron microscopy-FESEM/EDS (**n=17**)
Red clays- **24**	**24**	**24**	**9**	**7**
Ocher clays/marls- **7**	**7**	**7**	**2**	**2**
Violet clays/marls- **2**	**2**	**2**	**1**	**1**
Ferruginous pisoids- **6**	**6**	**-**	**5**	**3**
Limestones- **8**	**8**	**-**	**4**	**4**
	-Relative proportions of the mineral phases -Kaolinite crystallinity		-Textures -Identification of opaque and transparent minerals	-Micro- and nanotextures -Chemical composition of the phases
	Derived data			

4 RESULTS

4.1 Stratigraphy and facies distribution

4.1.1 Northern area

In the Alacón area (logs ALC1, ALC2, ALC3 and VE), the lower part of the LBS has a very variable thickness ranging from 3 to 23 m (Fig. 3.3a–c). Within individual logs there is a vertical distribution of facies from red clays with variable pisoid content to ochre clays/marls with few pisoids, and to violet clays/marls without pisoids. In addition, a dm- to m-thick fibrous-radial nodular calcite bed and limestone beds are also recognized in the lower part of the successions, intercalated in the red clays.

Log correlation indicates that the number and thickness of clayey and limestone levels vary among the outcrops studied around Alacón (Fig. 3.3a). The first deposits of the LBS overlying the palaeokarstified Jurassic limestones correspond to a lowermost, 3-m-thick red clay level with fibrous-radial calcite nodules (5–12 cm in diameter) and pisoids, which is only recorded in log ALC2. This level pinches out laterally due to the irregular topography of the underlying palaeokarstified Jurassic limestones. A lower

nodular limestone level (0.5 to 2 m thick) with fibrous-radial calcite nodules (5–10 cm in diameter) and some ferruginous pisoids overlies the basal red clay level in ALC2 and the palaeokarstic surface in ALC1, ALC3 and VE.

Upwards, red clay levels with abundant pisoids and intercalated palustrine-lacustrine limestone beds are recognized (Fig. 3.3a–d). Log correlation indicates variation in the number and thickness of red clay levels. In particular, there are three red clay levels (~1.5 m thick) in logs ALC1 and VE (levels 1 to 3 in Fig. 3.3a), whereas there is only one level (up to 5 m thick) in log ALC3. The intercalated limestone beds are 0.6 to 2 m in thickness and contain ferruginous pisoids but no fibrous-radial calcite nodules.

Overlying the red clays with interbedded limestones, there is an ochre clay/marl level (4 to 5 m thick) that contains few ferruginous pisoids (level 4 in Fig. 3.3a), which in turn is overlain by a topmost 1.5 to 2 m-thick violet clay/marl level without pisoids (level 5 in Fig. 3.3a).

4.1.2 Southern area

The overall thickness of the lower part of the LBS is variable in the southern outcrops logged near Josa (JO, 9 m thick; Fig. 3.4a) and Estercuel (EST, 36 m thick; Fig. 3.4b). Successive red clay levels (3 to 6 m thick) overlie the palaeokarstic surface that developed over the Jurassic limestones. These levels contain abundant ferruginous pisoids (with the exception of the last level of red clays of EST). Limestone beds intercalated in these red clays are very scarce. In the EST log, a 0.3-m-thick limestone bed with fibrous-radial calcite nodules and pisoids, similar to that observed in ALC2 and VE, is interbedded between the two red clay levels with abundant pisoids. In the JO log, on top of the red clay there is a 0.3-m-thick palustrine-lacustrine limestone bed with micrite intraclasts and pisoids, but without fibrous-radial calcite nodules.

The successions end with an ochre clay/marl level (2 m thick in JO, 10 m thick in EST) and a 10-m-thick violet clay/marl level in the EST log. Neither the ochre nor the violet levels contain ferruginous pisoids.

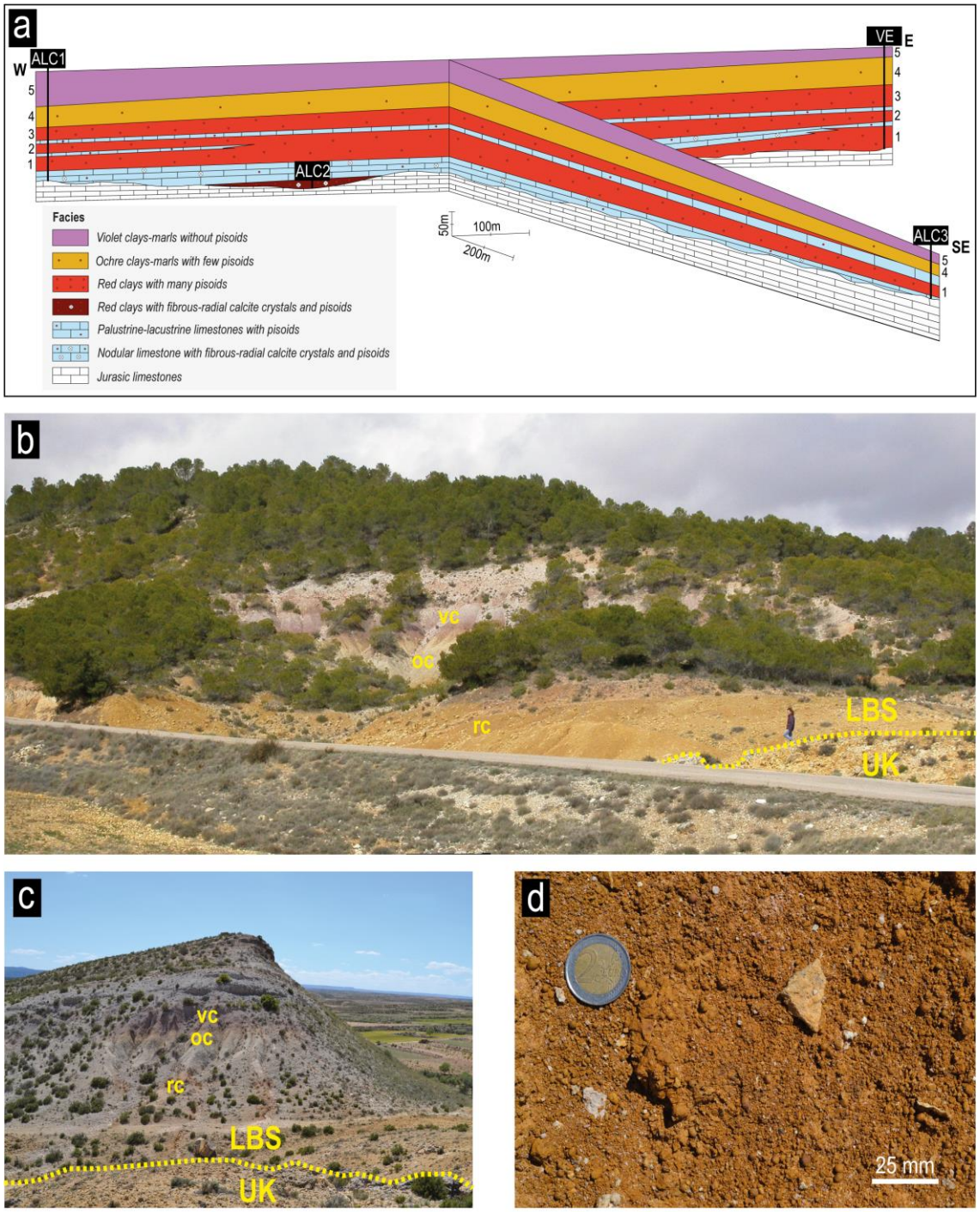

Fig. 3.3. a) Stratigraphic correlation between the four stratigraphic logs from the Alacón area (their geographical coordinates are ALC1: N41°2′42.0″ W0°42′47.6″; ALC2: N41°2′29.1″ W0°42′42.4″; ALC3: N41°2′3.3″ W0°42′10.9″; and VE: N41°02′46.5″ W0°42′07″). The proposed correlation is based on the observation of lateral continuity at outcrop scale in continuous outcrops; **b)** and **c)** field views around the VE and ALC1 logs, respectively, showing the upper Kimmeridgian (UK) shallow marine limestones, overlain successively by red clays (rc), ochre clays/marls (oc) and violet clays/marls (vc); **d)** detail of ferruginous pisoids and macropisoids (up to several mm in diameter) found in the red clays.

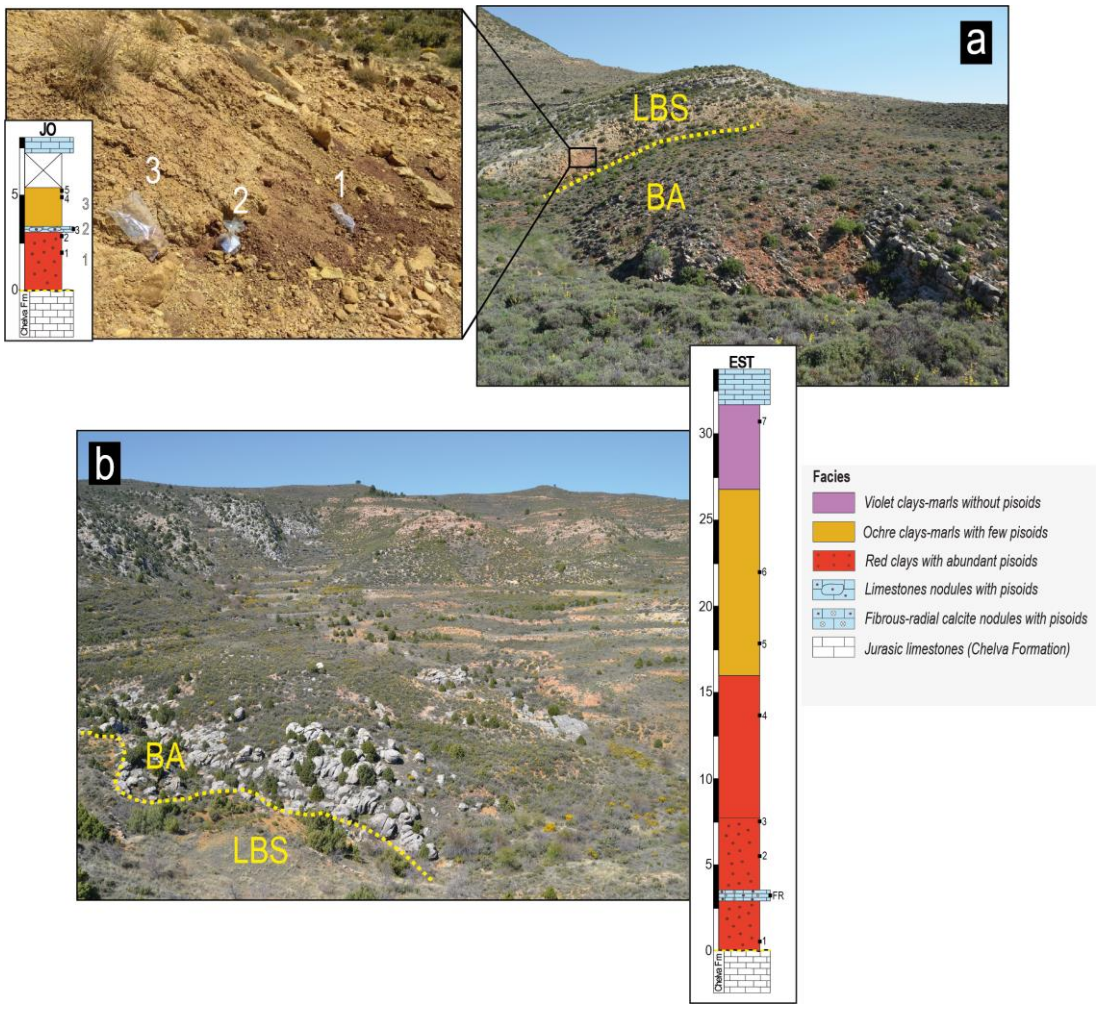

Fig. 3.4. a) Field view of the Josa (JO) outcrop (at N40°55′20.64″ W0°44′33.18″) showing the Bajocian-Bathonian (BA) shallow marine limestones, overlain by the red LBS succession. The stratigraphic log shows the red and ochre clays/marls found in this area; **b)** field view of the Estercuel (EST) outcrop (at N40°50′22.58″ W0°39′36.53″) showing the lowermost red clays over the upper Bajocian-Bathonian limestones (BA). The stratigraphic log shows the red clays, and ochre and violet clay/marls dominant in this section.

4.2 Optical microscopy results

The fine-grained matrix of red clays and ochre and violet clays/marls are formed by clay minerals and oxides that cannot be identified at the resolution of the optical microscope. Occasionally, quartz fragments (10–600 μm) and micron-sized oxides can be recognized (Fig. 3.5a). Carbonate is observed as micritic nodules (Fig. 3.5b) or as sparitic crystals cementing the matrix (Fig. 3.5c). Microsparite carbonate cement is also observed in some samples.

The ferruginous pisoids found in the red clays and ochre clays/marls encompass macropisoids, pisoids and ooids/micro-ooids, following the classification proposed by Bárdossy (1982).

Macropisoids are spherical to ellipsoidal and have a nucleus formed by pisoids (Fig. 3.6a), ooids and micro-ooids coated by goethite and hematite with botryoidal textures (Fig. 3.6b, c, d and e), sometimes forming a sequence of alternate layers (25 to 700 μm thick) of both phases (Fig. 3.6b, d and e). Occasionally, an up to 1–3 mm-thick outer cortex formed by several concentric layers is observed over the nucleus of some macropisoids (Fig. 3.6d). The concentric layers consist of goethite, as deduced by optical properties under reflected light. Occasional quartz fragments and small rutile crystals are included among the cortex layers.

The pisoids display spherical and occasionally ellipsoidal morphologies. Using the classification of Guerrak (1987), they can be categorized as simple or fragmented. Simple pisoids show a massive nucleus and a cortex with several concentric layers (Fig. 3.5d), both formed by a mixture of iron oxides and clay minerals with occasional quartz fragments and rutile crystals. Fragmented pisoids have a nucleus formed by a fragment of a pisoid and a cortex with concentric layers similar to that of the simple pisoids (Fig. 3.5d). Some pisoids (both simple and fragmented) are fractured and partly replaced by sparitic carbonate (Fig. 3.5c). Broken pisoids are also observed. In addition, scour-and-fill textures, similar to those described by Taylor et al. (2008), are found in the cortex in some pisoids (Fig. 3.5e).

Ooids and micro-ooids (sensu Bárdossy, 1982) are also observed in some clayey levels. The size ranges from 200 to 400 μm for the ooids and from 20 to 100 μm for the micro-ooids. Like the simple pisoids, they present spherical morphologies with a massive nucleus and a cortex with concentric layers and are formed by hematite and goethite (Fig. 3.5f).

The palustrine-lacustrine limestones are formed mainly by micrite, locally with microsparite and sparite crystals, and they also contain some micritic nodules and intraclasts (1–4 mm in size; Fig. 3.5h), spherical ferruginous pisoids (1–4 mm) and ferruginous ooids (200–400 μm). Fe-rich pisoids are simple,with a massive nucleus and concentric layers; most of them are fractured and others are partly replaced by micritic and sparitic carbonate (Fig. 3.5g). Some limestones also contain fossil remains such as disarticulated bivalve shells (Fig. 3.5h).

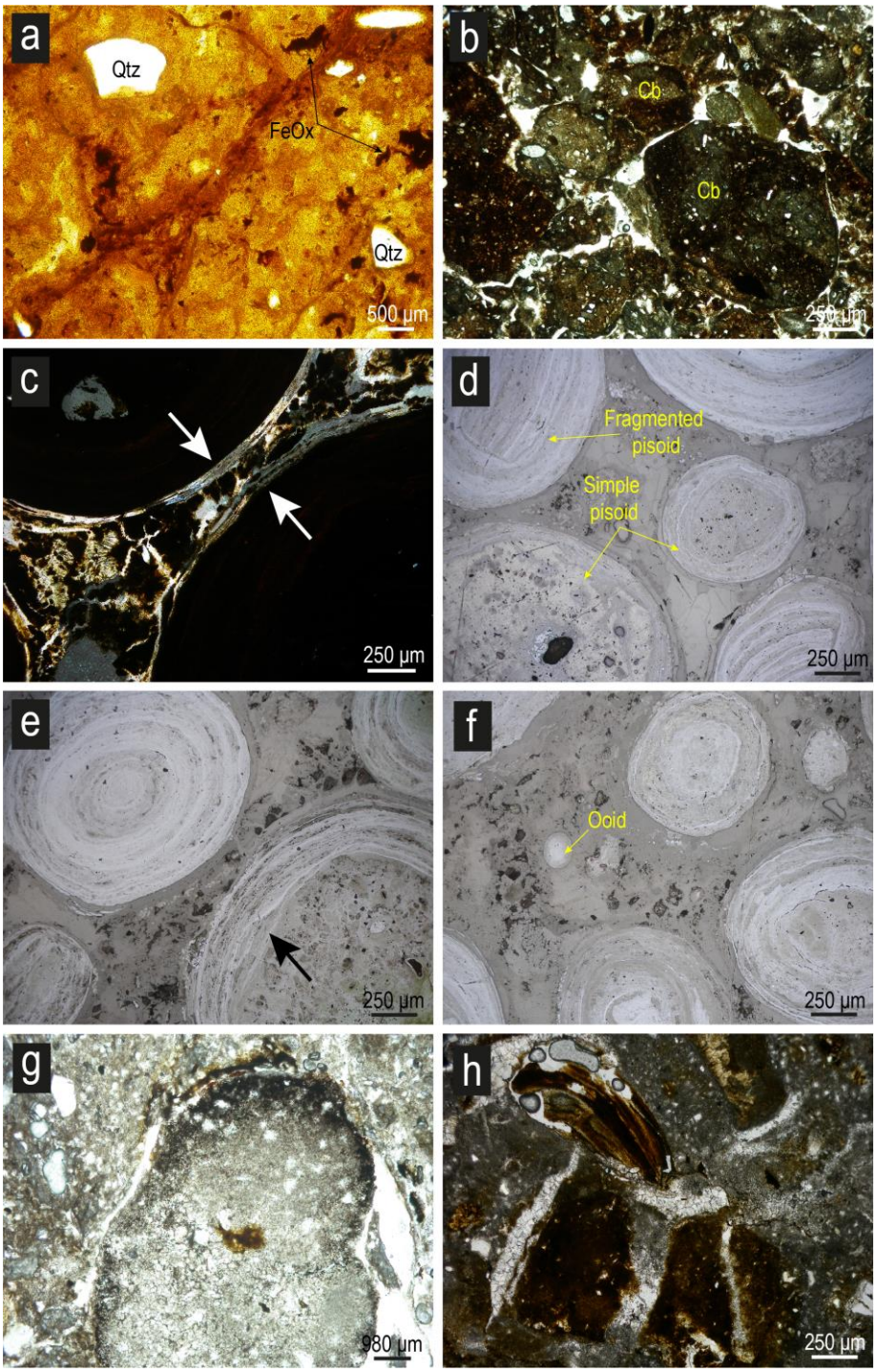

Fig. 3.5. Transmitted and reflected light optical microscopy images of the samples. **a)** Clays and clays/marls including occasional quartz grains and Fe oxides; **b)** micritic carbonate nodules in violet clays/marls; **c)** sparitic carbonate cementing the matrix and replacing the external concentric layers of pisoids in the red clays (see arrows); **d)** simple and fragmented pisoids in the red clays; **e)** scour-and-fill texture in the cortex of a simple pisoid; **f)** ferruginous pisoids and ooids in the red clays (see arrow); **g)** pisoid partly replaced by carbonate in the ochre marls/clays; **h)** micritic intraclasts and disarticulated bivalve shell in a palustrine-lacustrine limestone sample. *FeOx*=Fe oxides, *Qtz*=quartz, *Cb*=carbonate.

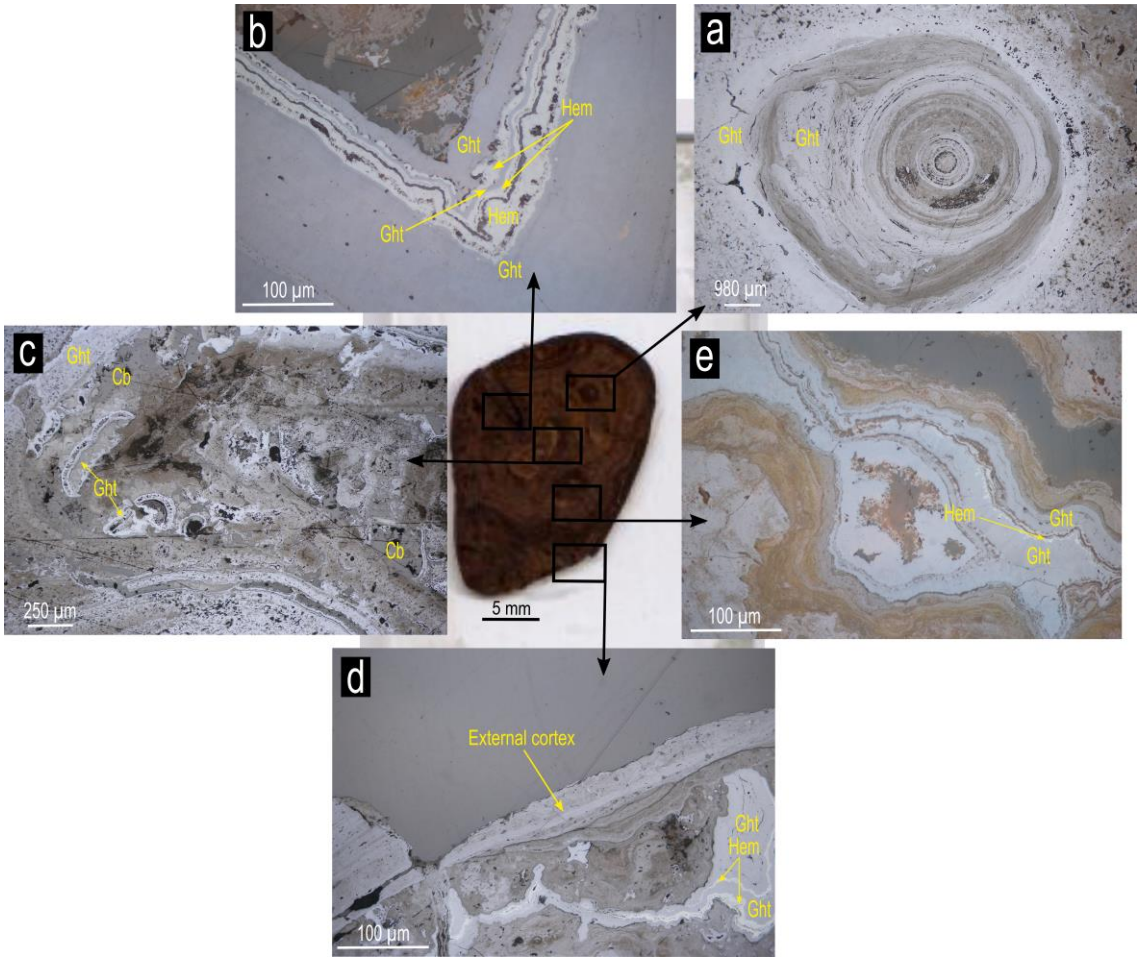

Fig. 3.6. Reflected light optical microscopy images of different parts of a macropisoid showing: **a)** a pisoid in the nucleus of the macropisoid; **b), c), d)** and **e)** goethite and hematite with botryoidal textures and/or forming a sequence of alternate layers; **d)** the external cortex formed by concentric layers. *Hem*=hematite, *Ght*=goethite, *Cb*=carbonate.

4.3 XRD results

XRD patterns of samples of the clays and clays/marls of the ALC1 and EST logs are shown in Fig. 3.7. The same mineral phases were detected in the samples taken in the rest of the outcrops. The XRD results show that the clays and clays/marls are formed mainly by calcite, quartz, and clay minerals, with minor quantities of orthoclase, hematite, goethite, anatase, rutile, ilmenite and diaspore. In the <2 µm fraction, abundant kaolinite with illite, smectite and mixed-layers of illite/smectite (I/S) and chlorite/smectite (C/S) are identified as clay minerals.

The red clays have the lowest calcite content but they present the highest hematite, anatase, diaspore, goethite and kaolinite content. By contrast, the ochre and violet clays/marls have higher illite content, and smectite is only detected in the ochre clays/marls.

Using the classification of Allix et al. (2011), the studied samples of clays and clays/marls show hybrid compositions including argillaceous mudstones, argillaceous marlstones, siliceous marlstones and calcareous mudstones. These variations in lithology are a consequence of the variable proportions of carbonates and silicates. Specifically, the red clays correspond to argillaceous mudstones and argillaceous marlstones, whereas the ochre and violet clays/marls are formed by siliceous marlstones and calcareous mudstones. Palustrine-lacustrine limestones are classified as calcareous mudstones.

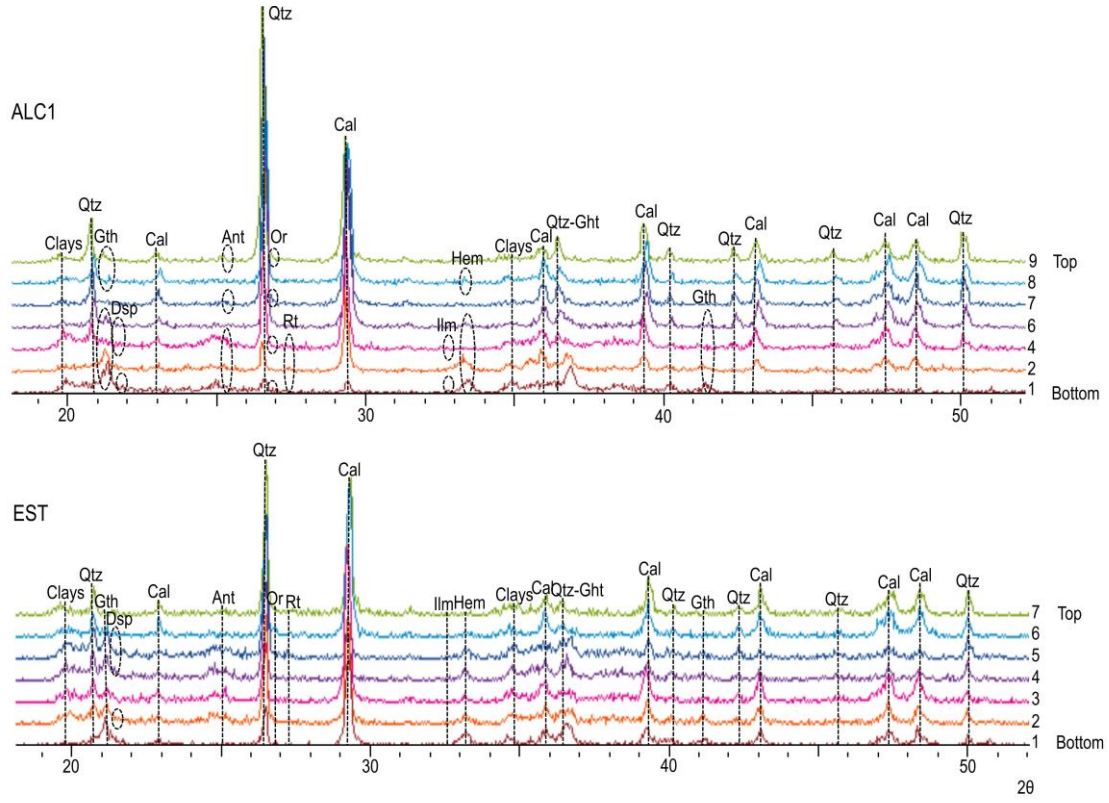

Fig. 3.7. XRD patterns obtained from clay and clay/marl samples in the ALC1 log (samples 1–9) and EST log (samples 1–7). *Clays*=clay minerals, *Qtz*=quartz, *Cal*=calcite, *Ght*=goethite, *Dsp*=diaspore, *Ant*=anatase, *Or*=orthoclase, *Rt*=rutile, *Ilm*=ilmenite, *Hem*=hematite.

The relative proportions of mineral phases in the thickest outcrops (the ALC1, VE, JO and EST logs) are shown in Fig. 3.8. Calcite detected by XRD is not represented, because, as will be explained below, a large part of it did not form coetaneously with the clays and clays/marls. Proportions of mineral phases vary from bottom to top. Quartz content increases upwards whereas hematite, goethite, anatase, rutile, ilmenite and diaspore content decrease. Furthermore, kaolinite is the only clay mineral in the lower red clays reaching >50%. Its content decreases upwards coeval with an increase in the variety of clay minerals, where illite, smectite and mixed-layers of I/S and C/S are detected along with the kaolinite. This change almost coincides with the change from

red clays to ochre clays/marls. Finally, in the violet clays/marls at the top, the dominant clay mineral is illite.

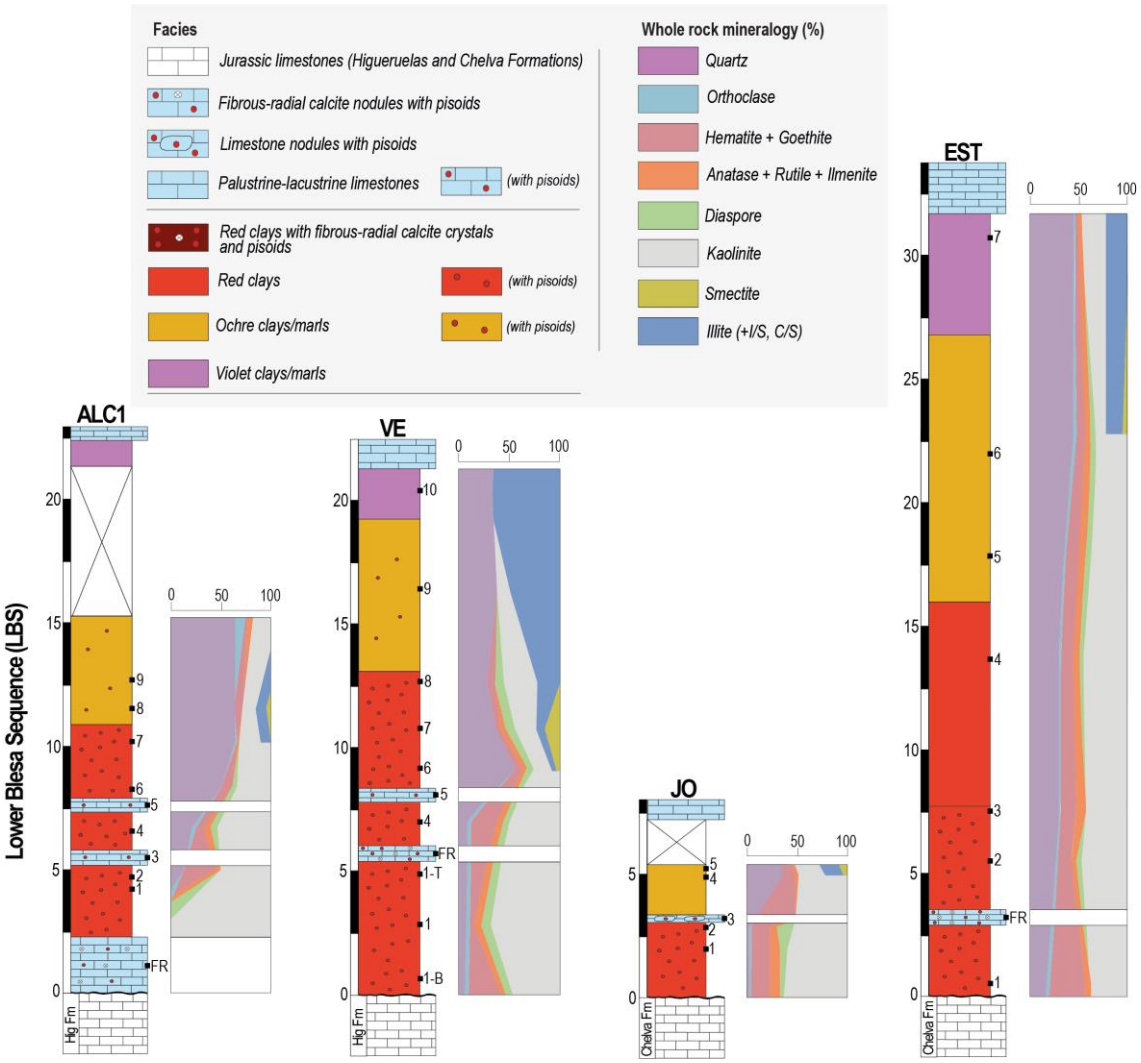

Fig. 3.8. Variations in mineral content of clays and clays/marls in the ALC1, VE, JO and EST logs. The Jurassic marine carbonate rocks are represented either by the latest Kimmeridgian Higueruelas Formation (Hig. Fm) or by the Bajocian-Bathonian Chelva Formation.

Table 3.2 shows kaolinite crystallinity values, which are in general >0.4 and thus indicate low crystallinity. Overall, comparison of the values measured in air-dried and ethylene-glycol-treated samples shows that there are no significant differences, except in some cases where the difference between the two values could be indicative of the presence of expandable components such as smectit

Table 3.2. Kaolinite crystallinity values of the samples of clays and clays/marls from the different outcrops measured in air-dried (AD) and ethylene-glycol-treated (EG) samples. *Am*=argillaceous mudstone, *Amr*=argillaceous marlstone, *Smr*=siliceous marlstone, *Cm*=calcareous marlstone.

Alacón						Josa and Estercuel					
				KC						KC	
Log	Sample number	Sample description	Facies	AD (001)	EG (001)	Log	Sample number	Sample description	Facies	AD (001)	EG (001)
ALC 1	1	Am	red clays	0.5	0.5	JO	1	Am	red clays	0.5	0.4
	2	Amr	red clays	0.7	0.4		2	Am	red clays	0.4	0.4
	4	Am	red clays	0.5	0.6		4	Amr	ocher clays/marls	0.4	0.4
	6	Smr	red clays	0.6	0.4		5	Amr	ocher clays/marls	0.3	0.4
	7	Smr	red clays	0.5	0.4	EST	1	Am	red clays	0.3	0.3
	8	Smr	ocher clays/marls	0.3	0.5		2	Amr	red clays	0.4	0.5
	9	Smr	ocher clays/marls	0.4	0.3		3	Amr	red clays	0.4	0.4
ALC 2	2M	Am	red clays	0.6	0.5		4	Am	red clays	0.4	0.6
	2V	Am	red clays	0.5	0.6		5	Am	ocher clays/marls	0.5	0.6
	3	Am	red clays	0.6	0.6		6	Amr	ocher clays/marls	0.2	0.6
ALC 3	1	Amr	red clays	0.5	0.5		7	Am	violet clays/marls	0.3	0.3
	2M	Am	red clays	0.6	0.6						
	2V	Am	red clays	0.6	0.6						
VE	1-B	Am	red clays	0.6	0.6						
	1	Am	red clays	0.6	0.7						
	1-T	Am	red clays	0.5	0.6						
	4	Am	red clays	0.4	0.4						
	6	Smr	red clays	0.5	0.5						
	7	Amr	red clays	0.5	0.5						
	8	Amr	red clays	0.5	0.4						
	9	Cm	ocher clays/marls	0.6	0.5						

As far as macropisoids are concerned, XRD patterns show that they contain quartz, calcite, clay minerals (kaolinite, as deduced from the FESEM study), hematite, goethite, ferrihydrite and ilmenite. The relative proportions of these minerals in four macropisoids from the first and second red clay levels in the ALC1 and VE logs are shown in Fig. 3.9 as an example. In particular, macropisoids are mainly formed by Fe oxyhydroxides (hematite, goethite and ferrihydrite), kaolinite, and occasionally lower proportions of ilmenite. Calcite was not included, for the same reason as in the case of the clays and clays/marls.

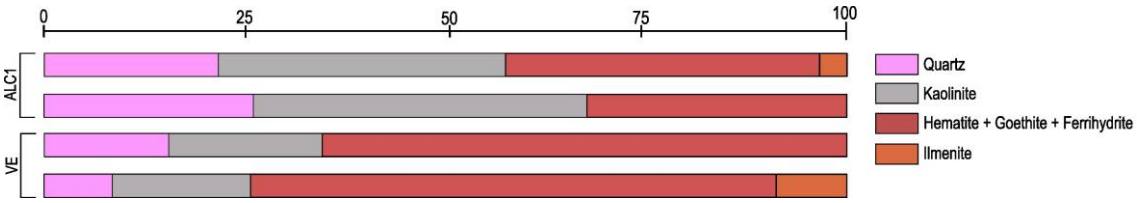

Fig. 3.9. Relative proportions of mineral phases in macropisoids from the first and second red clay levels of the ALC1 and VE logs.

4.4 FESEM results

4.4.1 Backscattered and secondary electron images

Backscattered and secondary electron images of clay and clay/marl samples (Fig. 3.10) show that the matrix of red clays is formed by kaolinite, hematite, goethite, anatase/rutile and ilmenite. Quartz fragments and orthoclase with anhedral morphologies are occasionally observed.

Kaolinite appears mainly as subhedral to euhedral nanometric plates, commonly showing pseudohexagonal outlines (Fig. 3.10a and b) and less frequently forming booklets (Fig. 3.10c and d). In the ochre and violet clays/marls, Fe and Ti oxides are less abundant or are even absent. In these cases, smectite (in the ochre samples) with flake morphologies and illite with wavy shapes (Fig. 3.10e and f) are observed.

Pisoids and macropisoids are mainly composed of hematite and goethite, with different proportions of kaolinite and minor proportions of ilmenite and calcite. Oxides in the nucleus are occasionally observed to be acicular whereas those in the cortex are anhedral (Fig. 3.11a). Kaolinite in the pisoids, in both the nucleus and the cortex, shows the same morphologies as those observed in the matrix, occurring with platy shapes and random orientation (Fig. 3.11b) or, alternatively, forming booklet aggregates (Fig. 3.11c). Booklets are also observed filling the internal cavities of the pisoids. These booklets are larger in size compared with those found in the matrix of the clays and the clays/marls and the nucleus of the pisoids. They reach up to 1 μm in diameter and >2 μm of

longitudinal development in the direction of the c crystallographic axis (Fig. 3.11d). On the other hand, the concentric layers of the cortex show different proportions of kaolinite and Fe oxides, allowing one layer to be distinguished from another. Fe oxides also appear among the matrix of the clays and clays/marls (Figs. 3.11b and c).

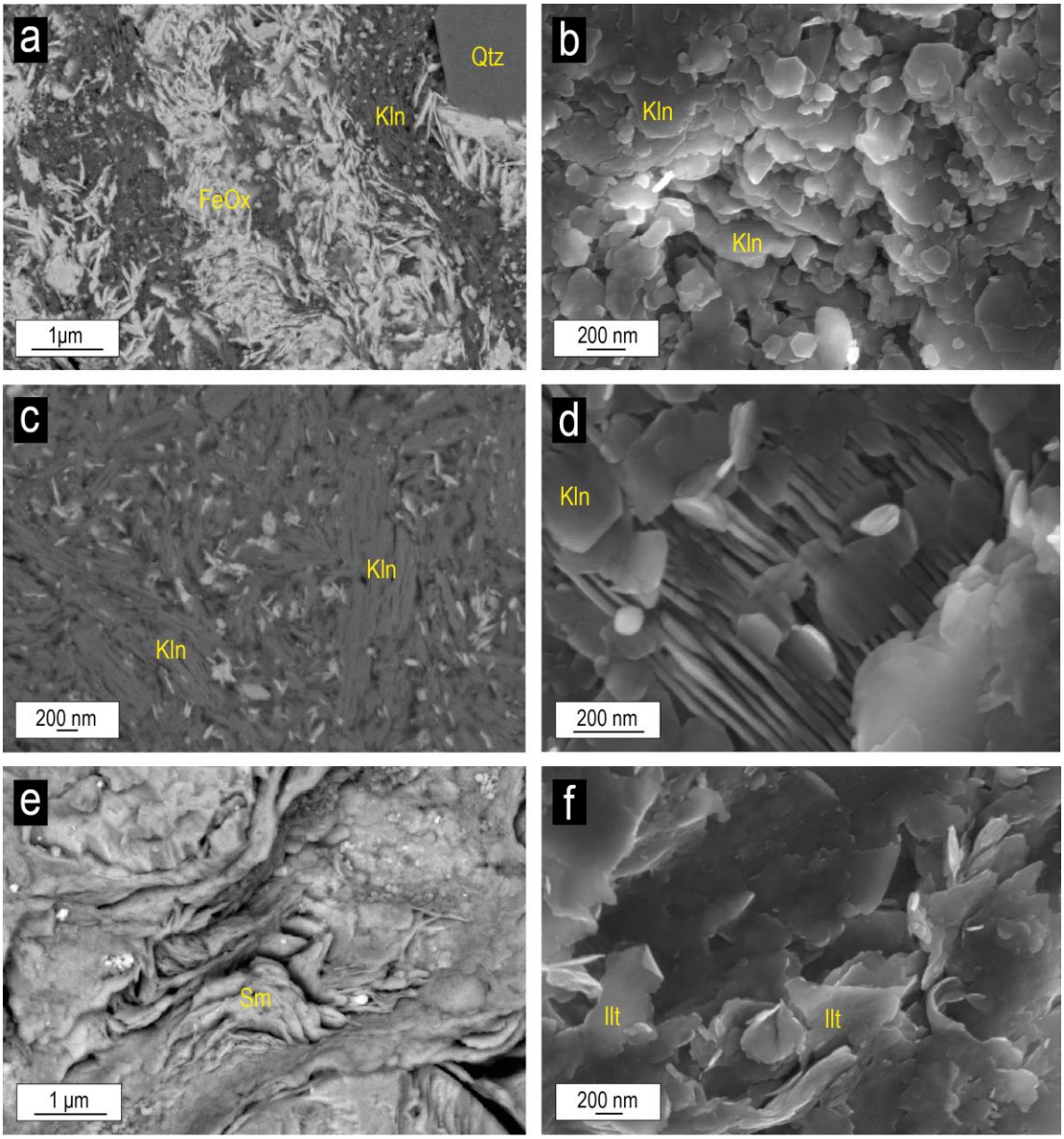

Fig. 3.10. FESEM images of samples of red clays, ochre clays/marls and violet clays/marls. **a)** Matrix of the red clays; **b)** pseudohexagonal kaolinite crystals in red clays; **c)** and **d)** kaolinite booklets in red clays; **e)** smectite with flake morphologies in ochre clays/marls; **f)** illite-type morphologies in violet clays/marls. *Kln*=kaolinite, *FeOx*=Fe oxides, *Qtz*=quartz, *Sm*=smectite and *Ilt*=illite.

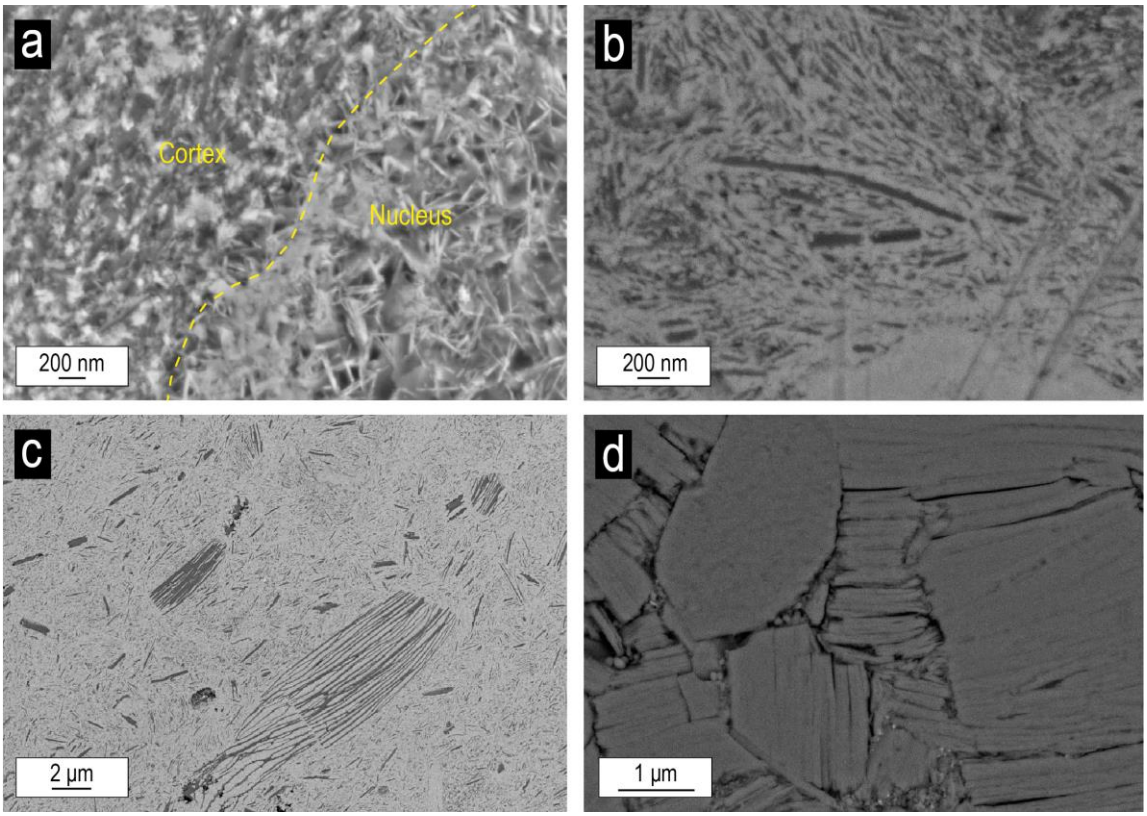

Fig. 3.11. FESEM images of ferruginous pisoids showing: **a)** nucleus and cortex contact with acicular (in the nucleus) and anhedral (in the cortex) oxide crystals; **b)** platy kaolinites in the nucleus of pisoids together with abundant Fe oxides; **c)** kaolinite booklets in the nucleus of pisoids; **d)** kaolinite booklets filling cavities observed within some pisoids.

Carbonate intraclasts found in the violet and ochre clays and clays/ marls are formed by sparite and/or microsparite, whose EDS analyses show homogeneous calcite compositions (Fig. 3.12a). Partly dissolved, reworked calcite fragments cemented by kaolinite from the matrix are observed in the ochre and violet clays and clays/marls (Fig. 3.12b). The palustrine-lacustrine limestones are also locally cemented by kaolinite (Fig. 3.12c). On the other hand, the replacement of some fractured pisoids and partially of the clay matrix by sparitic calcite (Fig. 3.12d) is better observed with the FESEM images than by optical microscopy.

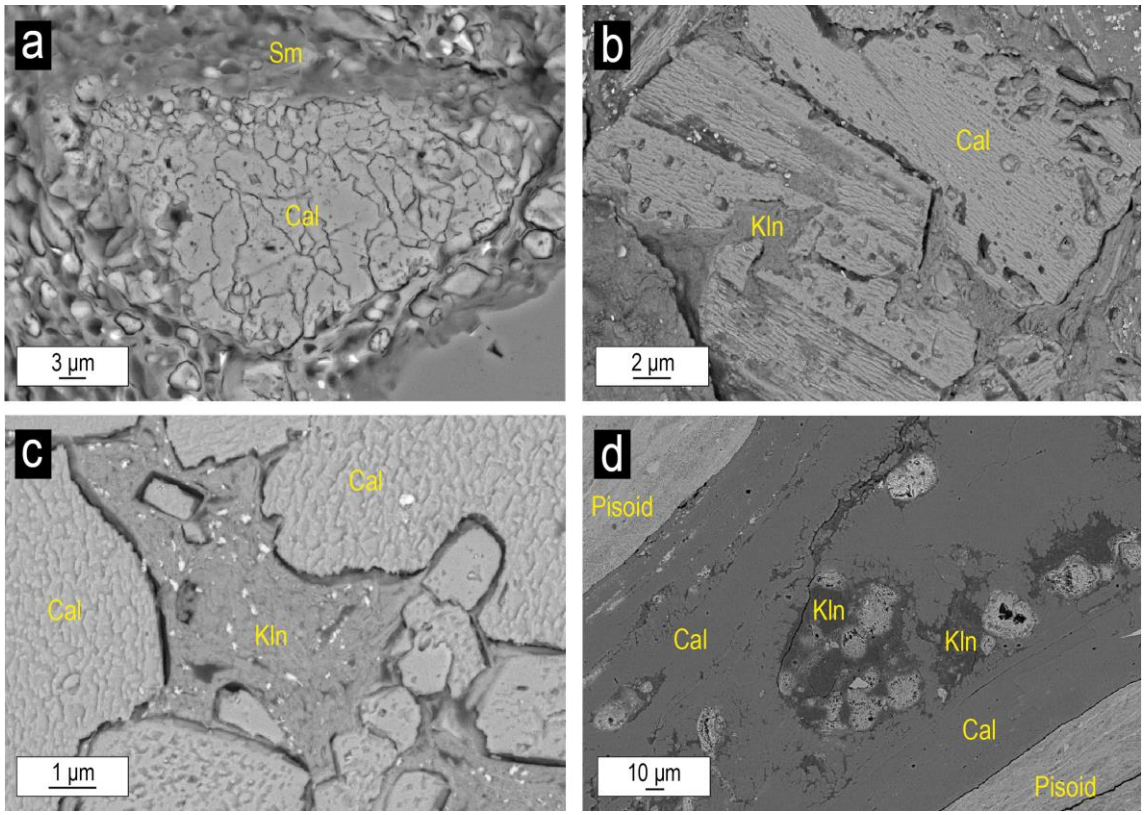

Fig. 3.12. FESEM images of carbonates in the study samples. **a)** Calcite intraclast in the matrix of the ochre clays/marls; **b)** reworked calcite fragment with evidence of dissolution and cemented by kaolinite in the ochre clays/marls; **c)** palustrine-lacustrine limestone where kaolinite is cementing calcite; **d)** sparitic calcite replacing the matrix of clays and clays/marls and the concentric layers of the cortex of pisoids. *Sm*=smectite, *Cal*=calcite, *Kln*=kaolinite.

4.4.2 EDS results

The results of the EDS analyses were used to calculate chemical formulas for the kaolinite, smectite and illite found in the matrix of the red clays, ochre clays/marls and violet clays/marls (Table 3.3).

Three compositional groups of kaolinite were established: 1) platy kaolinite, 2) booklets of kaolinite, and 3) booklets of kaolinite filling the cavities of pisoids. The formulas calculated for the first and the second groups show that these kaolinites present low proportions of Fe, whereas the third group does not contain Fe.

The calculated smectite compositions of the ochre clays/marls correspond to dioctahedral smectites, as deduced from the higher content of trivalent cations (Al and Fe) in the octahedral layer. Furthermore, the tetrahedral charge is higher than the octahedral charge, so they correspond to a beidellite-type smectite. The illite composition presents lower K and higher Al and Fe content than the theoretical.

Table 3.3. EDS analysis (Wt%) of phyllosilicates detected in clay and clay/marl samples (standard deviation in brackets).

	O	Na	Mg	Al	Si	K	Ca	Ti	Fe	Calculated composition
Platy kaolinite (n=37)	49.80 (3.16)	0.05 (0.15)	0.08 (0.16)	21.81 (1.40)	25.30 (1.28)	0.28 (0.29)	-	0.38 (0.77)	2.30 (1.56)	$Fe_{0.1}Al_{1.8}Si_2O_5(OH)_4$
Kaolinite Booklets in matrix (n=6)	56.68 (5.04)	-	-	19.81 (3.00)	21.82 (3.23)	0.03 (0.05)	-	0.17 (0.30)	1.48 (1.41)	$Fe_{0.3}Al_{1.7}Si_2O_5(OH)_4$
Kaolinite Booklets in pisoids cavities (n=3)	52.77 (2.47)	-	-	22.04 (1.41)	25.08 (1.54)	0.12 (0.20)	-	-	-	$Al_{1.9}Si_{2.1}O_5(OH)_4$
Illitic phases (n=4)	42.50 (7.60)	-	1.21 (0.26)	14.12 (2.44)	26.50 (5.09)	3.72 (1.39)	5.46 (5.00)	0.94 (1.53)	5.55 (2.23)	$(K_{0.5},H_3O)(Al_{1.2}Mg_{0.2}Fe_{0.4})(Si_{3.4}Al_{0.6})O_{10}(OH)_2,(H_2O))$
Smectite (n=17)	46.31 (12.52)	0.07 (0.29)	0.87 (0.58)	14.42 (3.90)	24.23 (6.55)	1.93 (1.36)	4.58 (4.14)	1.15 (2.83)	6.44 (6.12)	$(Ca_{0.1}K_{0.2})(Al_{1.5}Fe_{0.4}Ti_{0.1}Mg_{0.1})(Si_{3.1}AL_{0.9})O_{10}(OH)_2nH_2O$

5. DISCUSSION

5.1 The matrix of the clays and clays/marls

The XRD results of the clays and clays/marls of the LBS indicate that, according to the compositional classification of Allix et al. (2011), the lower red clays correspond to argillaceous mudstones and argillaceous marlstones, whereas the overlying ochre and violet clay/marl levels are formed by siliceous marlstones and calcareous mudstones. The sedimentary evolution in the LBS from continental clayey facies to palustrine-lacustrine carbonate facies described by Aurell et al. (2018) may account for the lithological variation found in the studied materials.

The combination of XRD and optical and electron microscopy shows that the red clays and ochre and violet clays/marls are formed by calcite, quartz and clay minerals, with minor quantities of orthoclase, hematite, goethite, anatase, rutile, ilmenite and diaspore. The lower red clays present the highest hematite, anatase, diaspore, goethite and kaolinite content and do not contain smectite or illite. The intermediate ochre clays/marls contain smectite and have higher illite content compared to the red clays. The upper violet clays/marls present the highest illite content compared to the red clays and the ochre clays/marls, and they also contain mixed-layers of I/S and C/S, but they do not contain smectite.

The textural study by means of electron microscopy provides key information for the interpretation of the origin of these clay minerals in clays and clays/marls: 1) In the case of the platy kaolinites and kaolinite booklets recorded, electron microscopy analyses suggest that they are authigenic. The platy kaolinites present pseudohexagonal morphologies that are incompatible with a detrital origin, since erosion and transport processes would have modified them. In the same way, the kaolinite booklets are also thought to have an *in-situ* origin because they are so delicate that they cannot resist any transport processes (Bauluz et al., 2014). The presence of Fe, albeit in low proportions, in the kaolinites (both platy and booklets) found in the matrix of the clays and clays/ marls may be substituting the Al in the octahedral sheet of kaolinite, as occurs in similar materials (Mendelovici et al., 1979). The low kaolinite crystallinity is probably due to the presence of Fe in the structure, as is common in weathering processes (Mestdagh et al., 1980; Cantinolle et al., 1984; Yuste et al., 2015). Alternatively, given that the electron beam of the microscope has a larger diameter than the kaolinite particles, the analyses could be contaminated with nanometric Fe oxides.

2) As far as smectite is concerned, which is only recorded in the ochre clays/marls, its flake-type morphology and its presence as cement in the matrix of these clays/marls also suggest an *in-situ* origin. The chemical composition corresponds to dioctahedral,

beidellite-type smectite. This type of smectite has previously been described in similar materials as a result of the weathering of dioctahedral micas (Singh and Gilkes, 1991). Therefore, both kaolinite and smectite were probably formed as a consequence of edaphic processes, which involved the dissolution of previous aluminum silicate phases (feldspars, micas) and the crystallization of new ones (kaolinite and smectite).

3) Regarding illite, which is abundant in the ochre and violet clays/marls, especially in the latter, its formation is normally associated with diagenetic environments (Bauluz et al., 2000). A detrital origin is described for illite in materials similar to those studied in the present work (Franceschelli et al., 2003). The illite-type phases found in the ochre and violet clays/marls are probably of detrital origin, given that the genesis conditions of kaolinite in soils are not compatible with illite genesis. The anhedral morphologies of these phases would corroborate their detrital origin (Bauluz et al., 2014).

Hematite and goethite are present not only in the matrix of the clays and clays/marls, but also in the pisoids found in the red clays and ochre clays/marls (see 5.2 below). This suggests that the oxides and oxyhydroxides found in the matrix have an edaphic origin. By contrast, the quartz fragments and orthoclase would be of detrital origin. The low quartz and orthoclase content and their anhedral morphologies suggest that they are relicts of the original rocks and were probably partially dissolved during weathering.

5.2 Ferruginous pisoids in red clays and ochre clays/marls

In soils, the formation of *in-situ* pisoids is related to dissolution and re-precipitation processes, which are controlled by several factors, such as climatic variations, the chemistry of the groundwater and the difference in mobility of the chemical components of the parent rock during chemical weathering (Valeton, 1972; Bhattacharyya and Kakimoto, 1982). According to Bárdossy (1982), the formation of these particles requires permanent groundwater saturation. The presence of scour-and-fill features like those described by Taylor et al. (2008) in some of the studied pisoids thus shows deformation in a semi-plastic state, indicating water saturation (Yuste et al., 2015).

The studied pisoids are hematite-goethite pisoids, also including clay minerals (kaolinite, as deduced by FESEM analysis). Previous investigations classified pisoids according to their hematite and kaolinite content (Szamatek et al., 1993; Sayed and Youssef, 1996). The pisoids studied here could thus be classified as hematitic-kaolinitic pisoids. In fact, the differences in the kaolinite and Fe oxide contents observed in the cortex of the studied pisoids allow the different concentric layers to be distinguished.

The presence in the pisoids and macropisoids of hematite, goethite and kaolinite,with textural features similar to those observed in the matrix, along with their concentric structure comprising a nucleus and a cortex, indicates that they were formed *in-situ* during the development of the soils. The sequences of goethite-hematite layers observed in macropisoids have previously been described in gossan development on metallic deposits (Velasco et al., 2013). According to these authors, the presence of this alternation of goethite and hematite layers reflects a change to less humid conditions.

The fact that the Fe oxides are cementing kaolinite in the pisoids suggests that these oxides form at a late stage in comparison with the kaolinite during the edaphic processes. On the other hand, the EDS results for the booklets of kaolinite filling the cavities of pisoids indicate that these booklets do not contain Fe and are larger in size compared with those found in the matrix of the clays and clays/marls, a fact that may be due to recrystallization during very early diagenesis.

5.3 The palustrine-lacustrine limestones

According to the classification by Allix et al. (2011), the palustrine-lacustrine limestones intercalated in red clays with pisoids correspond to calcareous mudstones. A rise in water level probably led to a palustrine-lacustrine environment where carbonate muds precipitated, resulting in the formation of the calcareous mudstones. The reworked calcite fragments cemented by kaolinite in the ochre and violet clays and clays/marls may come from these calcareous mudstones.

These calcareous mudstones also contain pisoids, most of them broken, and ferruginous ooids, which may be reworked from the underlying red clays. The possible decrease in the water level may have enhanced the overprint of edaphic processes in the palustrine-lacustrine limestone (e.g. limestone with micritic nodules/intraclasts), favouring the reworking and fracturation of some of the pisoids. Other authors have described reworking processes as suggesting different episodes in the development of soils (Mücke et al., 1999). These calcareous mudstones are also cemented by kaolinite, suggesting that they also underwent edaphic processes during the decrease in the water level.

5.4 Nodular limestones and diagenesis of clays and clays/marls

During the early diagenesis, the matrix of the clays and clays/marls was cemented by microsparite and sparite. In addition, diagenesis may have also generated the micritic nodules and sparitic-microsparitic intraclasts observed in the ochre and violet clays/marls. Sparitic cement also filled the gaps and replaced some fractured

pisoids found in red clays and ochre clays/marls. Thus, calcite was eliminated from the quantification results, since much of it results from the diagenesis.

In the AlC2, VE and EST sections, the beds of fibrous-radial calcite nodules also overlie a lowermost red clay level with pisoids. According to Rossi and Cañaveras (1999), many of the calcites included in freshwater cements forming during diagenesis are fibrous, so the fibrous-radial calcite nodules could have also been formed in the early diagenesis. Given the presence of pisoids and their location in the lower part of the LSB, these nodule-bearing beds would correspond to palustrine-lacustrine limestones. They would have been affected by intense early diagenetic processes during an initial unstable stage with frequent hiatuses/erosional gaps after the long, Tithonian–Hauterivian period of subaerial exposure represented by the karstified surface on top of the Jurassic limestones.

As indicated above, the morphology of the kaolinite and smectite from the matrix of the clays and clays/marls suggests an *in-situ* origin. These early diagenetic processes would therefore not have modified the clay mineralogy of the facies significantly.

5.5 Palaeoweathering events deduced from clay mineral assemblages

The mineralogical association in the studied clays and clays/marls, the red, ochre and violet colours, along with the presence of ferruginous pisoids in the red clays and ochre clays/marls, allow them to be classified as palaeosols. According to Schellmann (1981), lateritic palaeosols are formed by mineral assemblages of goethite, hematite, aluminum hydroxides, kaolinite and quartz. Several authors (e.g. Foos, 1991; Mücke et al., 1999; Giovannini et al., 2017; Faris et al., 2019) have reported these mineral phases as well as the presence of ferruginous pisoids in lateritic palaeosols. The mineral assemblages and the high content of ferruginous pisoids in the lower red clays thus allow them to be classified as lateritic palaeosols.

The combination of XRD and electron microscopy showed that kaolinite is the dominant clay mineral in these lateritic palaeosols. The presence of this mineral suggests a warm and humid climate, along with an intense chemical weathering (Chamley, 1989; Raucskik and Varga, 2008; Bauluz et al., 2014), which are characteristic conditions of tropical climates (Molina and Salas, 1993; Yuste et al., 2017).

The generation of red lateritic soils alternated (and was coeval) with the deposition of palustrine-lacustrine limestone with broken pisoids, reflecting a rapid rise (and probably subsequent falls) in water level, which could be related with variations in humidity, with local developments of palustrine-lacustrine areas. The afore-mentioned sequences of goethite-hematite layers in macropisoids might also be related to these conditions.

In the intermediate and upper ochre and violet clays/marls, the presence of smectite (beidellite; only present in ochre clays/marls), illite (highest content in violet clays/marls) and mixed-layers of I/S and C/S coincides with a decrease in and near-absence of kaolinite content. This trend can be interpreted in accordance with the weathering pattern proposed by Sheldon and Tabor (2009). These authors suggest trends in clay mineralogy that reflect weathering patterns changing from warm/humid to cold/dry conditions: kaolinite➔smectite➔vermiculite➔chlorite and mixed-layer phyllosilicates➔illite and mica. In our studied case, the vertical trend is: kaolinite (dominant in red clays)➔kaolinite, smectite and illite (intermediate ochre clays/marls)➔illite and mixed-layer I/S and C/S (violet clays/marls), suggesting a less intense chemical weathering due to a change from warm and humid to colder and drier conditions. The absence of pisoids in the violet clays/marls would support the idea of generally drier conditions, which would have prevented permanent groundwater saturation and therefore pisoid formation.

In the east of the Maestrazgo Basin, the Cantaperdius Formation (Salas, 1987), which is equivalent in age to the formation studied here (Barremian–Aptian), includes lacustrine and palustrine limestones and the development of soils and laterites like those described by Combes (1969). In addition, karst bauxite deposits, probably originating from lateritic materials laterally equivalent to the Cantaperdius Formation, have been reported in the nearby Morella subbasin (Molina and Salas, 1993; Yuste et al., 2015). Furthermore, Lower Cretaceous lateritic and bauxitic deposits have been described in the Cuenca Basin by Fregenal-Martínez et al. (2017). On the other hand, several authors have also reported the presence of laterites and bauxites in the Catalan Coastal Ranges and the Pyrenees (Combes, 1969; Ordóñez et al., 1990; Reinhardt et al., 2018; Seranne et al., 2019). According to Salas et al. (2004), the bauxites of the Catalan Coastal Ranges were probably formed from lower Barremian lateritic clays of the Cantaperdius Formation, whereas Seranne et al. (2019) dated the bauxite event of the Pyrenees to between early Albian and latest Albian. Nevertheless, the age of these deposits within the Barremian–Aptian interval cannot be precisely established. It is thus not possible to determine whether the early Barremian palaeoclimatic evolution (i.e., from humid to dry conditions) documented here was regional or local in extent.

A change from warm to cooler climatic conditions during the Barremian–Aptian has been described in Europe (Pucéat et al., 2003; Steuber et al., 2005; Dinis et al., 2020), but there is no general agreement as regards the trend in humidity during the Early Cretaceous. A humid climate is described in the northwestern part of Europe during the early Barremian (Wright et al., 2000). The temperature models show warm and humid

conditions for this period along the northern margin of the Tethys (Bodin et al., 2009; Price et al., 2011), as well as an increase in humidity during the mid-Barremian (= upper lower–lower upper Barremian) recorded at least at a European scale (Mutterlose et al., 2014). By contrast, an alternation of wet and dry seasons during the early Barremian (Haywood et al., 2004) and a trend to more arid and dry conditions towards the Albian–Cenomanian (Rodríguez-López et al., 2006) have also been reported.

The seasonal subtropical climate during the Lower Cretaceous in the Iberian Range described by Buscalioni and Fregenal-Martínez (2010) is supported by the presence of Barremian bauxitic and lateritic deposits (Molina and Salas, 1993; Bauluz et al., 2014; Yuste et al., 2015; Yuste et al., 2017). In addition, the Cretaceous ocean circulation models of Pucéat et al. (2005) and Hay (2008) substantiate the prevalence of wetter conditions in Iberia, which could be related to a warm and humid equatorial current in the Western Tethys (Dinis et al., 2020).

6. CONCLUSIONS

A combination of facies analysis and XRD and optical and electron microscopy studies has allowed us to characterize the mineralogical and textural changes found in the successive clay/carbonate levels found in the lower Blesa Formation (early Barremian, Oliete subbasin).

The lower part of the studied succession consists of red clay levels with abundant pisoids, recording the lowest calcite content but the highest content in hematite, anatase, diaspore, goethite and kaolinite. The intermediate ochre clay/marl levels contain smectite and illite and have few or no pisoids. The upper violet clay/marl levels contain illite and do not have pisoids.

The morphologies of the kaolinite crystals (platy and booklets) found in the lower red clay levels indicate that the kaolinite is authigenic. The smectite frequently recorded in the intermediate ochre clay/marl levels corresponds to a beidellite-type smectite, and the flake-type crystals forming the matrix of these levels also indicate an *in-situ* origin. The genesis of the illite-type phases is not compatible with the formation of kaolinite, so they might be of detrital origin.

Episodic rises in water level resulted in the formation of the palustrine-lacustrine limestone levels which are found interbedded within the clay-dominated succession. These levels may contain pisoids reworked from the underlying palaeosol levels and are cemented by kaolinite, indicating that they underwent edaphic processes during the episodic stages of decreased water level.

The mineralogical composition and structure of pisoids and macropisoids indicate an *in-situ* origin during lateritic soil formation. The decrease in the water level also favoured the reworking of the materials, involving the fracturing of some of these pisoids, which may have eventually formed the nucleus of pisoids formed in earlier stages of soil development.

During the early diagenesis, both the matrix of the clays and clays/marls was cemented and the cavities of the pisoids were filled by microsparite and sparite cements. This diagenesis did not affect the morphology of kaolinite and smectite.

The mineralogy of the red clay levels, along with the presence of ferruginous pisoids, indicates that they are lateritic palaeosols. Kaolinite is the dominant clay mineral in the lower red clay levels, indicating humid and warm climatic conditions and an intense chemical weathering. This is consistent with the palaeoclimate conditions described for the early Barremian in the NE Iberian. The decrease in the kaolinite and the oxide and oxyhydroxide contents from the bottom to the top of the stratigraphic profiles, along with the increase in the quartz content and the presence of smectite and illite, indicates a change to a less intense chemical weathering. These variations reflect a change from warm and humid to generally colder and drier conditions in the studied area across the early Barremian.

Palaeoclimatic data recorded in lower Cretaceous palaeosols from the NW Iberian Chain (NE Spain)

4

The facies and clay mineral study of clay/marl-rich levels from the Torrelapaja Formation (latest Hauterivian–early Barremian, NW Iberian Range, NE Spain) allowed to establish the palaeoclimatic and palaeoenvironmental conditions under they were generated. The muddy levels and pisoids contained therein of two logs were sampled and studied by X-ray diffraction and optical and electron microscopy. A similar mineralogical upwards trend is recorded in both logs, with a decrease in calcite coupled with an increase in quartz and orthoclase content and constant proportions in goethite, hematite, diaspore, anatase, rutile, ilmenite, and clay mineral content. The lower muddy levels have higher kaolinite content than the upper levels, where illitic phases are the dominant clay minerals. Smectite and intergrowths of illitic phases and kaolinite are also detected upwards. The kaolinite and smectite textures indicate an authigenic origin, whereas the illitic phases are former phases acting as a substrate for kaolinite crystallization. Pisoids mineralogy and texture show an *in-situ* origin, but some are fractured, indicating reworking processes. The mineral association found in the muddy levels is characteristic of oxisols formed under warm and humid conditions. The upward decrease in kaolinite content is coeval with an increase in the illitic phases and quartz content, related to siliciclastic input, but is also coeval with the presence of authigenic smectite. This indicates a decrease in chemical weathering, not fully registered due to the siliciclastic contribution, which was possibly associated with a change to colder, drier conditions during the latest Hauterivian–early Barremian in the studied area.

1 INTRODUCTION

The study of the soils that formed in the landscapes of the past (i.e., palaeosols) provides key data for palaeoclimatic and palaeoenvironmental reconstructions (Mack et al., 1993). The formation of soils takes place near the Earth's surface in the contact among lithosphere, atmosphere, hydrosphere, and biosphere (Tabor et al., 2017), and the weathering processes that generate them are subject to strong climatic control. For this reason, the study of the mineral phases formed during soil formation, such as clay minerals and oxides, is of great interest, since they directly provide information about the climate and environment (Chamley, 1989; Sheldon and Tabor, 2009; Do Campo et al., 2018; Varela et al., 2018; Laita et al., 2020).

In this way, the variations in the clay mineral assemblages have been used as palaeoclimatic and palaeoenvironmental proxies for palaeosols developed in continental sequences. Those of Mesozoic sequences have been described by several authors (e.g., Ehrmann et al., 2005; Raucskik and Varga, 2008; Föllmi, 2012; Do Campo et al., 2010; Bauluz et al., 2014; Do Campo et al., 2018; Laita et al., 2020 and references therein).

Under humid subtropical to tropical conditions, intense chemical weathering produces very effective hydrolysis, which gives rise to oxisols (commonly known as laterites), where kaolinite is the main clay mineral along with aluminium hydroxides and Fe oxyhydroxides (Chamley, 1989; Mack et al., 1993; Righi and Meunier, 1995; Velde, 1995; Do Campo et al., 2018). By contrast, under dry and cold climates, the production of clay minerals depends on physical weathering because of the absence of significant hydrolysis (Chamley, 1989). These conditions enhance the genesis of gleysols, where the clay mineral assemblages are essentially dominated by smectite and illite (Dhillon and Dhillon, 1991; Do Campo et al., 2018). Gleysols are formed under dysoxic or anoxic conditions that give rise to redoximorphic features and gleyed horizons generated by the influence of the shallow or fluctuating groundwater table, which inhibits drainage and creates low-oxygen conditions (Tabor et al., 2017).

In Western Europe, the presence of ferruginous palaeosols including kaolinite indicates warm and humid conditions during the late Hauterivian–early Barremian (Bárdossy, 1982; Wright et al., 2000; Föllmi, 2012). On the other hand, Haywood et al. (2004) have described an alternation of wet and dry seasons during the early Barremian in the west of Europe.

Within the Iberian Plate, a seasonal subtropical climate has been described during the Lower Cretaceous in the Iberian Range (NE Spain) (Buscalioni and Fregenal-Martínez, 2010; Bauluz et al., 2014). This climate is evidenced by the presence of kaolinite-rich clays, bauxites, and lateritic clays in several areas of the Iberian Plate

(Combes, 1990; Molina and Salas, 1993; Bauluz et al., 2014; Yuste et al., 2015, 2017; Laita et al., 2020; Yuste et al., 2020). By contrast, Laita et al. (2020) also pointed out a change from warm/humid to cold/dry conditions in Barremian continental successions from the NW Maestrazgo Basin (SE Iberian Range), which are age-equivalent with some of the palaeosols levels studied in this work.

Usually, clay-rich sediments, rocks, and palaeosols include authigenic clay minerals, but they may also contain diagenetic clays. This must be borne in mind when using clay mineral assemblages as palaeoclimatic and palaeoenvironmental indicators, since diagenetic processes may transform clay minerals and invalidate their use as palaeoclimatic proxies (Dera et al., 2009; Bauluz et al., 2014). To evaluate the origin of the clays and rule out a possible diagenetic imprint, it is necessary to carry out thorough microtextural studies.

Considering all the above mentioned, this study applies a combination of facies analysis and the study of the clay mineralogy of clay/marl-rich outcrops of uppermost Hauterivian–lower Barremian continental successions located in the Torrelapaja subbasin (NE Spain) to evaluate their usefulness as a palaeoclimate indicator. The main aims of this research are: (1) to determine whether the clay minerals are authigenic, as a consequence of the edaphic process, detrital (inherited from the source area), or diagenetic; and (2) to examine the vertical and lateral variations in the clay mineralogy and their relationships with the palaeoenvironmental conditions, or other controlling factors, to deduce the palaeoclimate during the latest Hauterivian–early Barremian in this area of the Iberian Range (NE Spain).

2 GEOLOGICAL SETTING

2.1 Stratigraphic context

The progressive opening of the Atlantic Ocean and the westward propagation of the Tethys Ocean during the Late Jurassic–Early Cretaceous generated a rifting process in the Iberian Basin located in the eastern part of the Iberian Plate (e.g., Salas et al., 2001). The resulting extensional fault activity gave rise to the compartmentalization of the Basin into a set of subsident basins, subbasins and troughs (Aurell, Bádenas, et al., 2019a; Aurell, Fregenal-Martínez, et al., 2019b; Liesa et al., 2019). One of these subsiding basins was the Cameros Basin, a wide Late Jurassic–Early Cretaceous sedimentary domain located in the northwestern part of this rifting system, in the northwestern Iberian Range (Fig. 4.1a) (e.g., Casas-Sainz, 1993; Gómez-Fernández and Meléndez, 1994; Mas et al., 2004; Clemente, 2010; Mas et al., 2019). The high subsidence rates recorded in this basin during the Late Jurassic-Early Cretaceous rifting episode allowed the accumulation of

more than 8000 m of continental and coastal sediments in its depocentral areas (Casas-Sainz et al., 2009).

The uppermost Hauterivian–lower Barremian succession studied here accumulated in the so-called Torrelapaja subbasin, located at the southeastern edge of the Cameros Basin (Fig. 4.1b). In this area, the Upper Jurassic–Lower Cretaceous synrift sedimentary record encompasses a 100–500 m-thick, terrigenous, calcareous succession that is divided into three synrift sequences (SS-1, SS-2, and SS-3 in Fig. 4.1c; Aurell et al., 2021). SS-1 (middle Tithonian–middle Berriasian) is composed of continental deposits, including the terrigenous alluvial deposits of the Bijuesca Formation and the lacustrine-palustrine carbonates of the Ciria Formation. SS-2 (uppermost Hauterivian–lower Barremian) includes the continental mixed (terrigenous-carbonate) Torrelapaja Formation. SS-3 (middle–upper Albian) corresponds to the Escucha Formation and includes terrigenous-carbonate continental to coastal successions (Aurell et al., 2021).

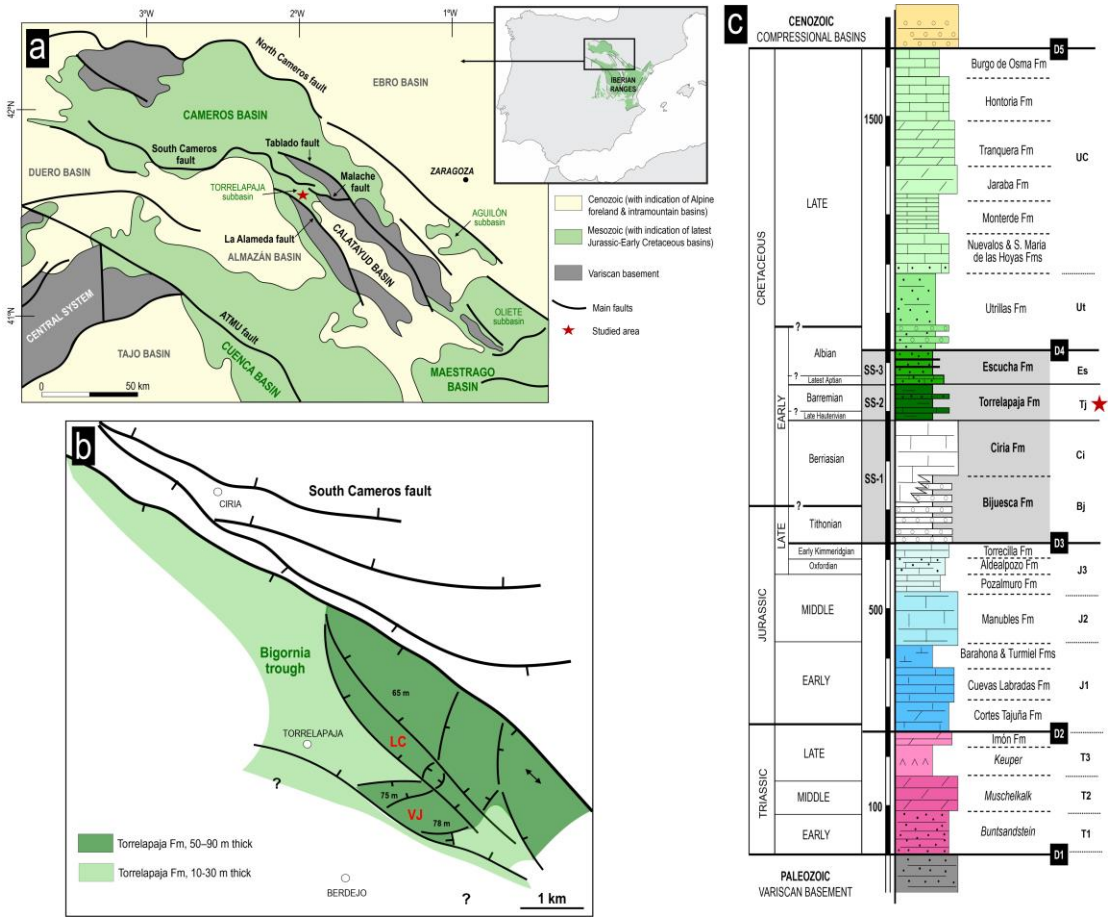

Fig. 4.1. a) Geological location of the studied Torrelapaja subbasin at the SE edge of the Cameros Basin (slightly modified from Aurell et al., 2021); **b)** reconstruction of the sedimentation area during synrift sequence 2, showing the location of the studied logs (slightly modified from Aurell et al., 2021); **c)** summary of the Mesozoic sedimentary units indicating the distribution of the Lower Cretaceous synrift sequences in grey. The red star indicates the studied unit (slightly modified from Aurell et al., 2021)

The continental Torrelapaja Fm (SS-2), studied in this work, is an up-to-80 m-thick succession of muddy facies, limestones, sandstones, and conglomerates that accumulated preferentially in the so-called Bigornia Trough of the Torrelapaja subbasin (Fig. 4.1 and 4.2). The latest Hauterivian–early Barremian age of this unit was dated based on the presence of charophytes (Martín-Closas, 1989; Aurell et al., 2021). The boundary with the underlying Ciria Formation is a major angular unconformity, which is associated with a stratigraphic gap that encompasses the late Berriasian, the Valanginian and most of the Hauterivian. An irregular karstic surface is observed on top of the lacustrine limestones of the Ciria Formation. This occasionally presents multiepisodic filling, allowing the preservation of a rich assemblage of vertebrate remains (Aurell et al., 2021).

2.2 Sedimentological context

A facies analysis of the continental Torrelapaja Fm in the Bigornia Trough was performed by Aurell et al. (2021), based on the data collected in three logs (the LC, VT and VJ logs in Fig. 4.2a). The deposition of the muddy facies, limestones, sandstones, and conglomerates of this unit took place in distal alluvial fans and shallow lakes. The vertical and lateral distribution of facies allowed three sedimentary stages of evolution to be differentiated (Fig. 4.2a). The argillaceous Stage 1 corresponds to the sedimentary filling of the palaeokarstic surface on top of the underlying Ciria Fm (SS-1/SS-2 boundary) and is dominated by ochre to violet mudstones and ochre to violet mudstones/calcareous mudstones of argillaceous composition (Fig. 4.2b). The carbonate-dominated Stage 2 is characterized by the expansion of palustrine-lacustrine facies, localized alluvial clastic input (sandstones), and the deposition of carbonate-richer distal plain muddy facies (marlstone/calcareous mudstones; Fig. 4.2b). In the siliciclastic-dominated Stage 3, there is a significant increase in siliciclastic and a reduction in lacustrine-palustrine areas. Middle-distal alluvial fan channels (conglomerates with quartzite and limestone clasts, sandstones, and ochre to violet siliceous marlstones) developed southwards as a result of the increasing tectonic activity of this margin (Fig. 4.2a); by contrast, the northern area was dominated by an alluvial-fluvial plain with ochre to violet mudstones of siliceous composition and ephemeral braided streams (conglomerates with quartzite pebbles).

Of particular interest for the present study are the muddy facies recorded mainly in distal alluvial plains (Fig. 4.2b). The ochre to violet mudstones and ochre to violet marlstones/calcareous mudstones that accumulated in the distal alluvial plains have features indicating soil development (levels with Fe pisoids and root traces/hydromorphic horizons) and are similar to those found in lateritic palaeosols in

age-equivalent units from the southern Maestrazgo Basin (Laita et al., 2020). The palustrine to shallow lacustrine grey marlstones/calcareous mudstones also contain Fe pisoids, which could be reworked from nearby distal alluvial plain areas (Aurell et al., 2021).

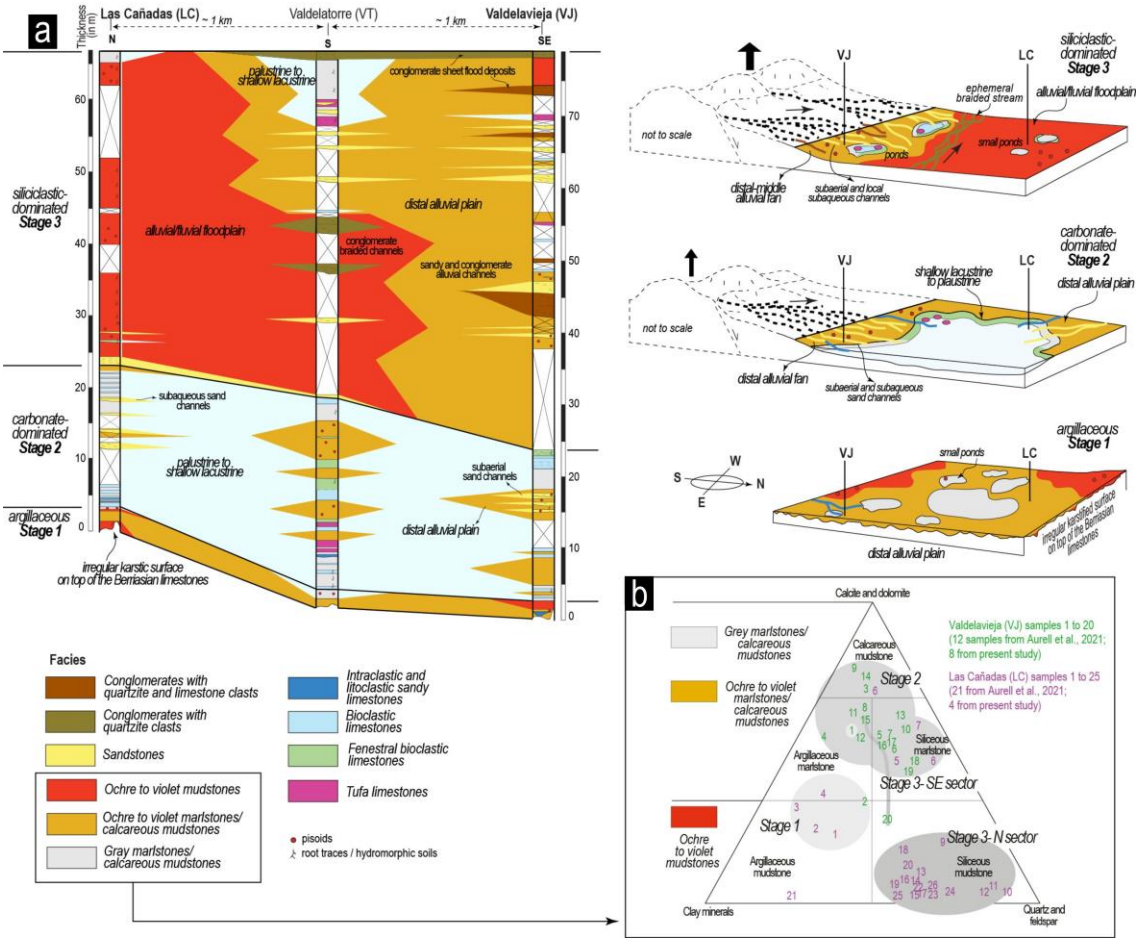

Fig. 4.2. a) Facies correlation of the Torrelapaja Fm (SS-2) in the Bigornia Trough and sedimentary models of the three stages differentiated (adapted from Aurell et al., 2021). The detailed facies distribution recognized by Aurell et al. (2021) in the Las Cañadas and Valdelavieja logs studied here is included in Fig. 4.5; **b)** mineralogical composition of muddy facies following the classification of Allix et al. (2011).

3 SAMPLES AND METHODS

The Las Cañadas (LC) and Valdelavieja (VJ) outcrops of the Torrelapaja Fm, previously studied by Aurell et al. (2021) from a stratigraphic and sedimentological point of view, were selected for the sampling of the different muddy facies (Fig. 4.2b). They include ochre to violet mudstones, ochre to violet marlstones/calcareous mudstones, and grey marlstones/calcareous mudstones (hereinafter referred to as mudstones to calcareous mudstones), and some of them contain Fe pisoids (Fig. 4.3). On the whole, the VJ log represents deposition in a more proximal position of the distal

alluvial plain compared to the LC log (Fig. 4.2a). A total of 49 samples (42 mudstone to calcareous mudstone samples and 7 Fe pisoids) were taken from throughout the two sections in order to analyse their texture and mineralogical composition (Table 4.1).

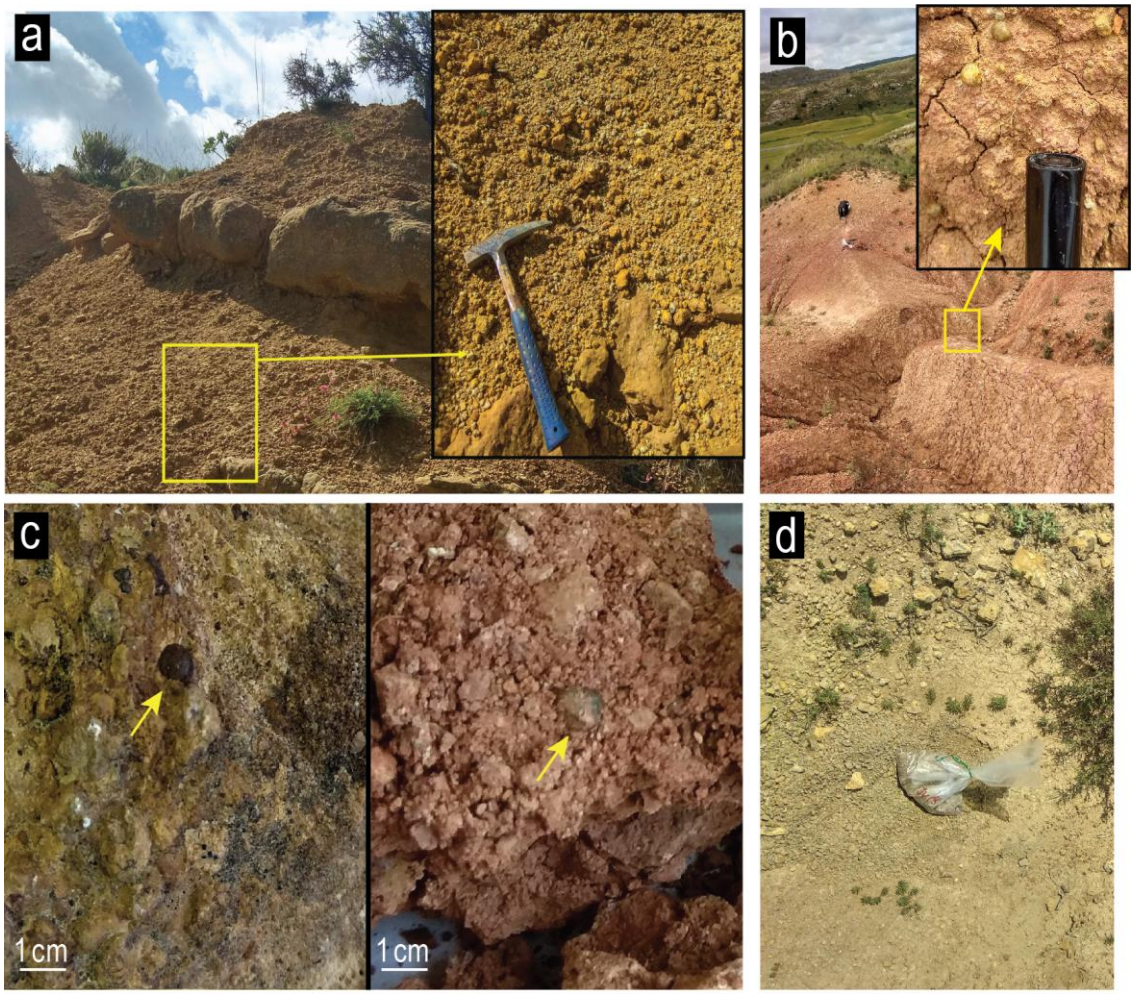

Fig. 4.3. a) Close view of the VJ log showing ochre to violet mudstones interbedded with sandstones levels; **b)** close view of the LC log showing the ochre to violet mudstones; **c)** hand samples from the VJ (left) and LC (right) logs including Fe pisoids; **d)** close view of the VJ log showing the grey marlstones/calcareous mudstones.

3.1 X-ray diffraction study

The 49 samples were studied by X-ray diffraction (XRD) to determine their mineralogical composition. The <2 μm fractions were extracted by centrifugation and analysed in air-dried and ethylene–glycol-treated oriented aggregates to determine the clay minerals present in the samples.

To obtain the diffraction patterns, a Philips 1710 diffractometer was used at the University of Zaragoza (Zaragoza, Spain), with 40 kV voltage, 30 mA current, CuKα radiation, an automatic slit, and a graphite monochromator. The XRD patterns were acquired from 3 to 60 °C 2θ for the whole rock samples and from 3 to 30 °C for the <2

μm fractions. In both cases, the goniometer velocity was 0.1º 2θ/s and the integration time was 0.45 s. The recording was made with XPowderX software (Martin, 2017).

The relative proportions of the minerals were calculated using Reference Intensity Ratio (RIR) values from the literature (Schultz, 1964; Biscaye, 1965; Smith and Johnson, 2000). These RIR values were calculated in accordance with Hillier (2003). The kaolinite crystallinity (KC) was calculated measuring the full width at half maximum of the 001 reflection corresponding to 7 Å in the air-dried oriented aggregates. KC values are inversely related to kaolinite crystallinity, that is, the lower the KC value, the higher the kaolinite crystallinity.

3.2 Optical and electron microscopy study

To gain a precise mineralogical and textural characterization of the samples, seven thin sections of the mudstones to calcareous mudstones and Fe pisoids were selected for microscopy studies. Firstly, the thin sections were studied by transmitted and reflected light microscopy to identify both transparent and opaque minerals and to characterize their texture (Table 4.1). The seven thin sections and four rock fragments were then analysed using a Carl Zeiss Merlin field emission scanning electron microscope (FESEM) with an Oxford energy-dispersive X-ray (EDS) detector at the University of Zaragoza (Zaragoza, Spain) (Table 4.1).

The thin sections had previously been carbon-coated. Compositional images were obtained using two detectors: an angular selective backscattered electron detector (AsB) and an energy selective backscattered electron detector (EsB). To obtain chemical information, semi-quantitative analyses were performed by energy-dispersive X-ray spectroscopy (EDS), with a detection limit of 0.1%. The accelerating voltage for the AsB and the EDS was 15 kV with a beam current of 600 pA, whereas for the EsB, the accelerating voltage was 4 kV with a beam current of 1000 pA. Morphological images of the rock fragments were obtained using a secondary electron (SE) detector (in-lens) with an accelerating voltage of 5 kV and a beam current of 100 pA. In this case, the accelerating voltage was 5 kV with a beam current of 800 pA.

Table 4.1. Summary of sample analyses at the laboratory (n=number of samples/analyses)

Field samples (**n=49**)	**X-ray diffraction** (Mineralogical composition)		**Optical and electron microscopy** (Textural and chemical analysis)	
	whole rock (**n=49**)	<2 μm fraction of clays and clays/marls (**n=42**)	Optical microscopy (**n=7**)	Electron microscopy-FESEM/EDS (**n=11**)
Ochre to violet clays/marls **(n=36)**	**36**	**36**	**5**	**9**
Grey marls **(n=6)**	**6**	**6**	**-**	**-**
Ferruginous pisoids **(n=7)**	**7**	**-**	**2**	**2**
	-Relative proportions of the mineral phases	-Clay minerals identification -Kaolinite crystallinity	-Textures -Identification of opaque and transparent minerals	-Micro- and nanotextures -Chemical composition of the phases
	Derived data			

4 RESULTS

4.1 Whole rock data

4.1.1 XRD data

The mudstones to calcareous mudstone of the LC and VJ logs are mainly formed by quartz, calcite, and clay minerals together with orthoclase, goethite, hematite, diaspore, anatase, rutile and ilmenite (Fig. 4.4). The XRD patterns of the whole rock show the same differences from bottom to top in both logs, with an increase in the intensity of quartz peaks and a decrease in those of calcite (Fig. 4.4a and c).

In the <2 μm fraction, abundant kaolinite and illitic phases are identified in the XRD patterns (Fig. 4.4b and d). Characteristic reflections of kaolinite are observed at 7.14, 4.18, 3.84, 3.57 Å, and dickite and nacrite have not been detected. The term "illitic phases" includes both illite and micas (quantified together) as well as accessory random mixed-layer illite/smectite (I/S), which were identified in some of the <2 μm fraction XRD patterns (but not quantified). These XRD patterns show a decrease in the intensity of kaolinite peaks to the top and that the illitic phases are detected from middle to top in both logs (Fig. 4.4b and d).

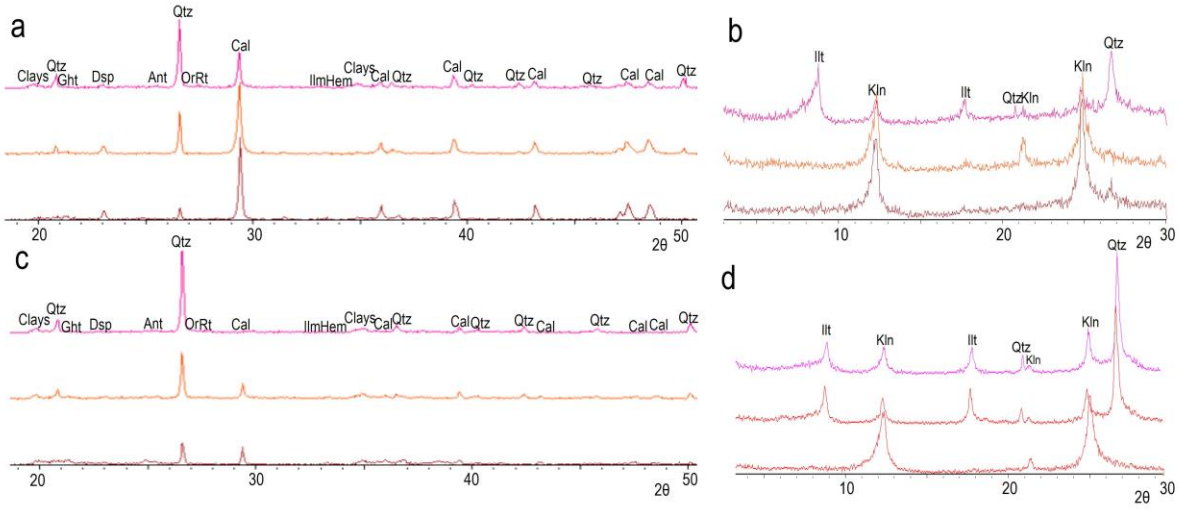

Fig. 4.4. XRD patterns obtained from the whole rock and <2 μm fractions of samples in the VJ (**a** and **b**) and LC (**c** and **d**) logs. *Clays*=clay minerals, *Qtz*=quartz, *Cal*=calcite, *Dsp*=diaspore, *Ght*=goethite, *Ant*=anatase, *Or*=orthoclase, *Rt*=rutile, *Ilm*=ilmenite, *Hem*=hematite, *Kln*=kaolinite, *Ilt*=illitic phases.

The whole rock mineralogical composition varies both vertically and laterally (Fig. 4.5a). On the whole, calcite is more abundant in the proximal VJ log (28–70%), whereas quartz + orthoclase predominate in the distal LC log (8–88%). In general, the calcite content decreases and quartz + orthoclase are more abundant towards the top of the logs. Clay minerals and goethite, hematite, diaspore, anatase, rutile, and ilmenite remain quite constant from the bottom to the top of the stratigraphic profiles. However, in detail there are slight vertical trends related to sedimentary stages 1 to 3. In the argillaceous Stage 1, the main lateral difference is the higher relative abundance of calcite in the proximal VJ log, and of clay minerals in the distal LC log. As regards the carbonate-dominated Stage 2, despite the presence of covered intervals (not sampled) in LC, a quite similar mineralogy dominated by calcite is recorded in both sections. The main lateral differences are recorded in the siliciclastic Stage 3, the proximal VJ log being dominated by calcite (with an upward decreasing trend), whereas in the distal LC log calcite is almost absent, especially at the top of the log, and quartz + orthoclase and clay minerals are more abundant compared to in VJ.

As regards the <2 μm fraction, kaolinite is the main clay mineral in the lower mudstone to calcareous mudstone levels (>50%), but its content decreases upwards coeval with an increase in the content of illitic phases. More specifically, samples of the argillaceous Stage 1 are only formed by kaolinite in the proximal VJ log but also have illitic phases in the distal LC log. In the carbonate-dominated Stage 2, kaolinite is again

the main clay in the proximal VJ log, whereas in the distal LC log illitic phases predominate. This predominance of illitic phases is observed in both sections in the siliciclastic-dominated Stage 3, with a particularly notable upward increase in the proximal VJ log.

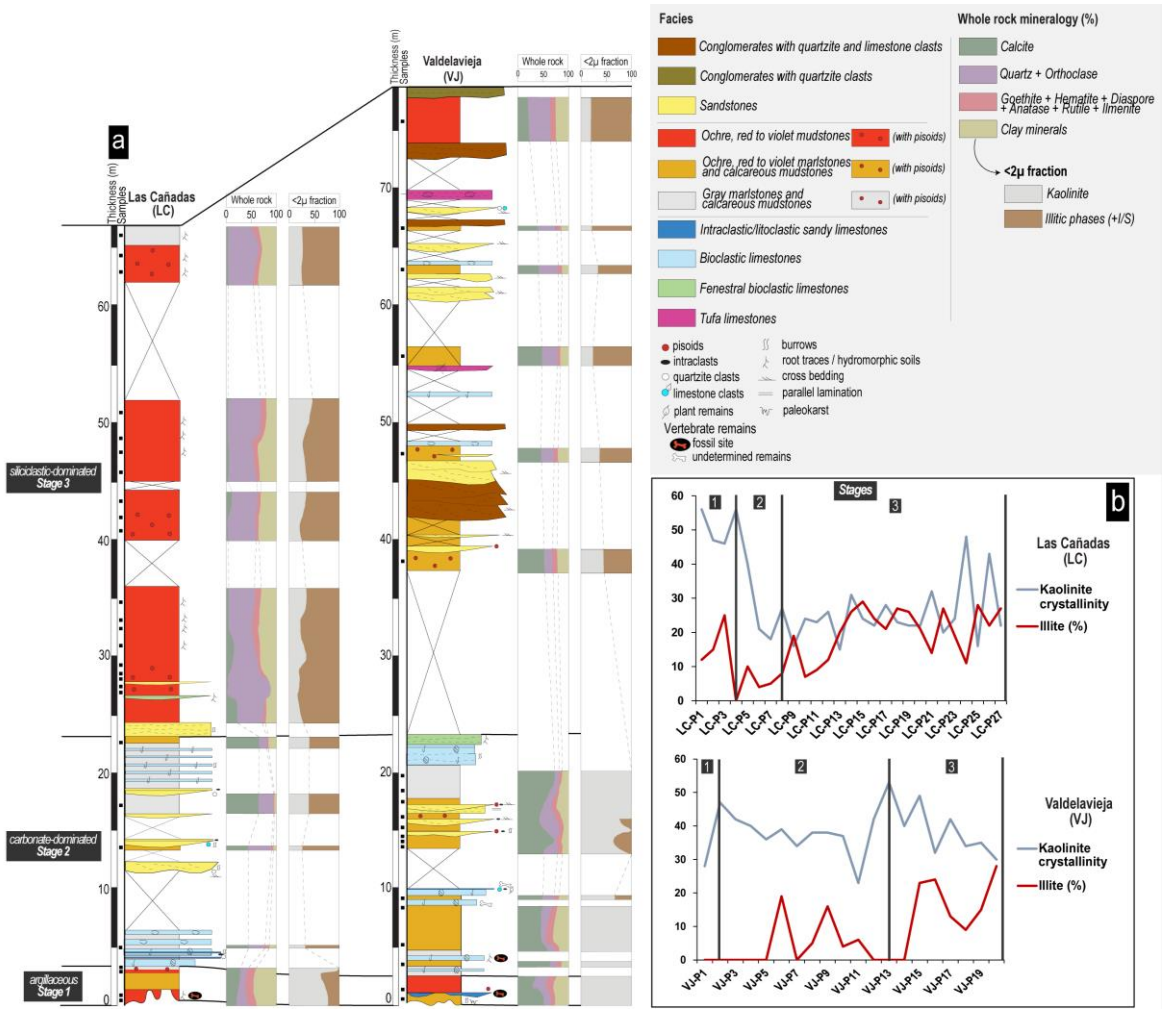

Fig. 4.5. a) Variations in mineral content of the mudstones to calcareous mudstones in the LC and VJ logs; **b)** evolution of kaolinite crystallinity vs. content of illitic phases from bottom to top of the logs. The kaolinite crystallinity value was multiplied by 100 for comparison with the content of illitic phases. Lower values indicate higher kaolinite crystallinity, and vice versa.

Kaolinite crystallinity is shown in Fig. 4.5b and in Table 4.2. In the argillaceous Stage 1, in the distal LC log (with its higher relative proportion of clay minerals including a predominance of kaolinite over illitic phases), kaolinite is less crystalline than in the proximal VJ log, where kaolinite is the only clay mineral and there is a higher relative abundance of calcite. In the carbonate-dominated Stage 2, with calcite predominating in both sections, kaolinite is slightly less crystalline and predominates in the proximal VJ log, whereas in the distal LC log, where illite predominates, an increase in kaolinite crystallinity can be observed upwards. In the siliciclastic Stage 3, in the proximal VJ log,

kaolinite crystallinity shows an increasing trend coupled with an increase in illitic phases and a decrease in calcite. By contrast, in the distal LC log, dominated by quartz + orthoclase and clay minerals (illitic phases), the kaolinite crystallinity is higher compared to the previous Stages 1 and 2, but decreases in some samples towards the top of the log, where the content of illitic phases is somewhat lower. Although there is not a general trend in kaolinite crystallinity, it should be noted that during Stage 3, especially in the distal LC log, kaolinite is more crystalline when the proportions of illitic phases are higher.

Table 4.2. Kaolinite crystallinity values of the samples of mudstones to calcareous mudstones measured in airdried (AD) samples.

Valdelavieja (VJ)			Las Cañadas (LC)		
Sample number	**Muddy facies**	**KC Air-dried (001)**	**Sample number**	**Muddy facies**	**KC Air-dried (001)**
1	OVMC	0.28	1	OVM	0.56
2	OVM	0.47	2	OVM	0.47
3	GMC	0.42	3	OVM	0.46
4	OVMC	0.40	4	GMC	0.56
5	OVMC	0.36	5	GMC	0.40
6	OVMC	0.39	6	OVMC	0.21
7	OVMC	0.34	7	GMC	0.18
8	OVMC	0.38	8	GMC	0.16
9	OVMC	0.38	9	OVM	0.16
10	OVMC	0.37	10	OVM	0.24
11	OVMC	0.23	11	OVM	0.23
12	OVMC	0.42	12	OVM	0.26
13	GMC	0.53	13	OVM	0.15
14	GMC	0.40	14	OVM	0.31
15	OVMC	0.49	15	OVM	0.24
16	OVMC	0.32	16	OVM	0.22
17	OVMC	0.42	17	OVM	0.28
18	OVMC	0.34	18	OVM	0.23
19	OVMC	0.35	19	OVM	0.22
20	OVM	0.30	20	OVM	0.22
			21	OVM	0.32
			22	OVM	0.20
			23	OVM	0.24
			24	OVM	0.48
			25	OVM	0.16
			26	OVM	0.43
			27	GMC	0.22

Classification of muddy facies from Aurell et al. (2021)
OVM=ochre to violet mudstones, *OVMC*=ochre to violet marlstones/calcareous mudstones, *GMC*=grey marlstones/calcareous mudstones.

4.1.2 Optical and electron microscopy data

The optical microscopy images show that the mudstones to calcareous mudstones are formed by a fine-grained matrix composed of clay minerals and oxides that cannot be identified at optical microscope resolution (Fig. 4.6a and b). Abundant quartz clasts (40–200 μm) are recognised (Fig. 4.6a). Microsparitic carbonate nodules (100 μm to 1 mm in size; Fig. 4.6b), as well as microsparitic calcite filling pores in the matrix, are also present.

Compositional (EsB and AsB) and secondary electron (SE) images of the lower mudstone to calcareous mudstone levels show that kaolinite appears in the matrix both as subhedral to euhedral nanometric plates, commonly showing pseudohexagonal outlines with random orientation (Fig. 4.6c and d), and as booklets 1–10 μm in length (Fig. 4.6e and f).

In samples where illitic phases predominate (towards the upper mudstone to calcareous mudstone levels), smectite flakes (not detected by XRD) are also observed (Fig. 4.7a). The illitic phases are heterometric (1–10 μm) and present wavy and anhedral morphologies and frequently separated sheets (Fig. 4.7a–c). Intergrowths of illitic phases and kaolinite are also observed (Fig. 4.7c), like those described in similar materials (Bauluz et al., 2014; Do Campo et al., 2018).

According to the optical microscopy study, the carbonate both in the nodules and filling pores in the matrix is sparitic and/or microsparitic, and the EDS analyses indicate calcite compositions (Fig. 4.7d and e). Occasionally, some of the carbonate nodules are cemented by kaolinite (Fig. 4.7e). Fibrous calcite crystals cementing the matrix are also present (Fig. 4.7f).

EDS average analyses of the kaolinite, illitic phases, and smectite, as well as the average chemical formulae calculated, are included in Table 4.3. According to these analyses, the kaolinite composition is close to the theoretical one but presents low proportions of Fe (≤ 0.1 a.p.f.u.). The illitic phases compositions are within the range commonly reported in the bibliography. The smectite compositions correspond to dioctahedral smectite, given the higher content of trivalent cations (Al and Fe) in the octahedral layer, and are consistent with a montmorillonite-type smectite.

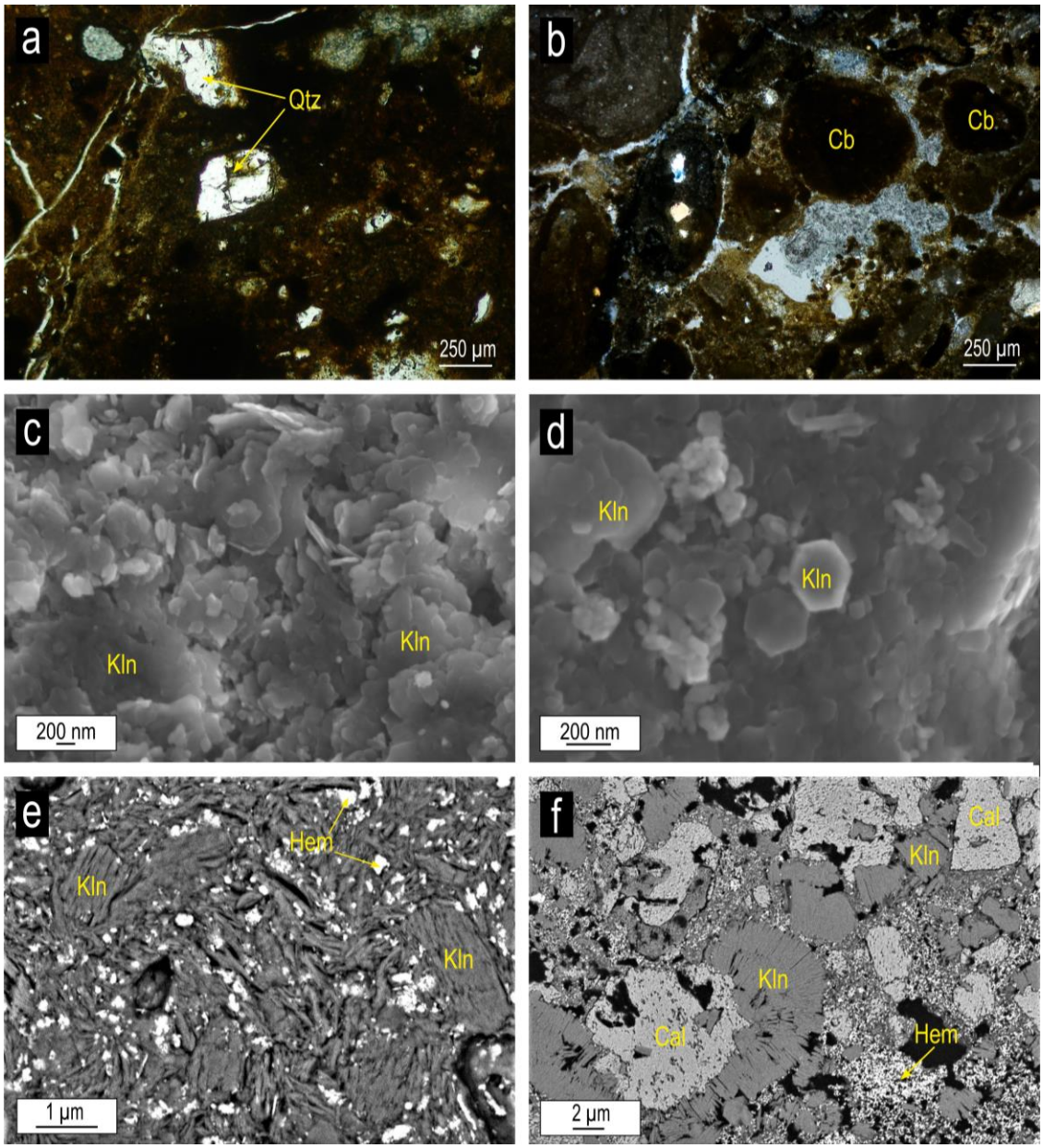

Fig. 4.6. Transmitted light optical microscopy images (**a** and **b**) and SEM images (**c–f**) of the lower mudstone to calcareous mudstone levels. **a)** Quartz clasts in the matrix of the mudstones to calcareous mudstones from the LC log; **b)** microsparitic carbonate nodules in the mudstones to calcareous mudstones from the VJ log; **c)** and **d)** SE images showing platy kaolinite aggregates with random orientation and pseudohexagonal outlines; **e)** 1–2 µm-sized kaolinite booklets and hematite crystals; **f)** kaolinite booklets reaching up to 10 µm in length and growing on microsparitic calcite nodules. *Qtz*=quartz, *Cb*=carbonate, *Kln*=kaolinite, *Hem*=hematite, *Cal*=calcite.

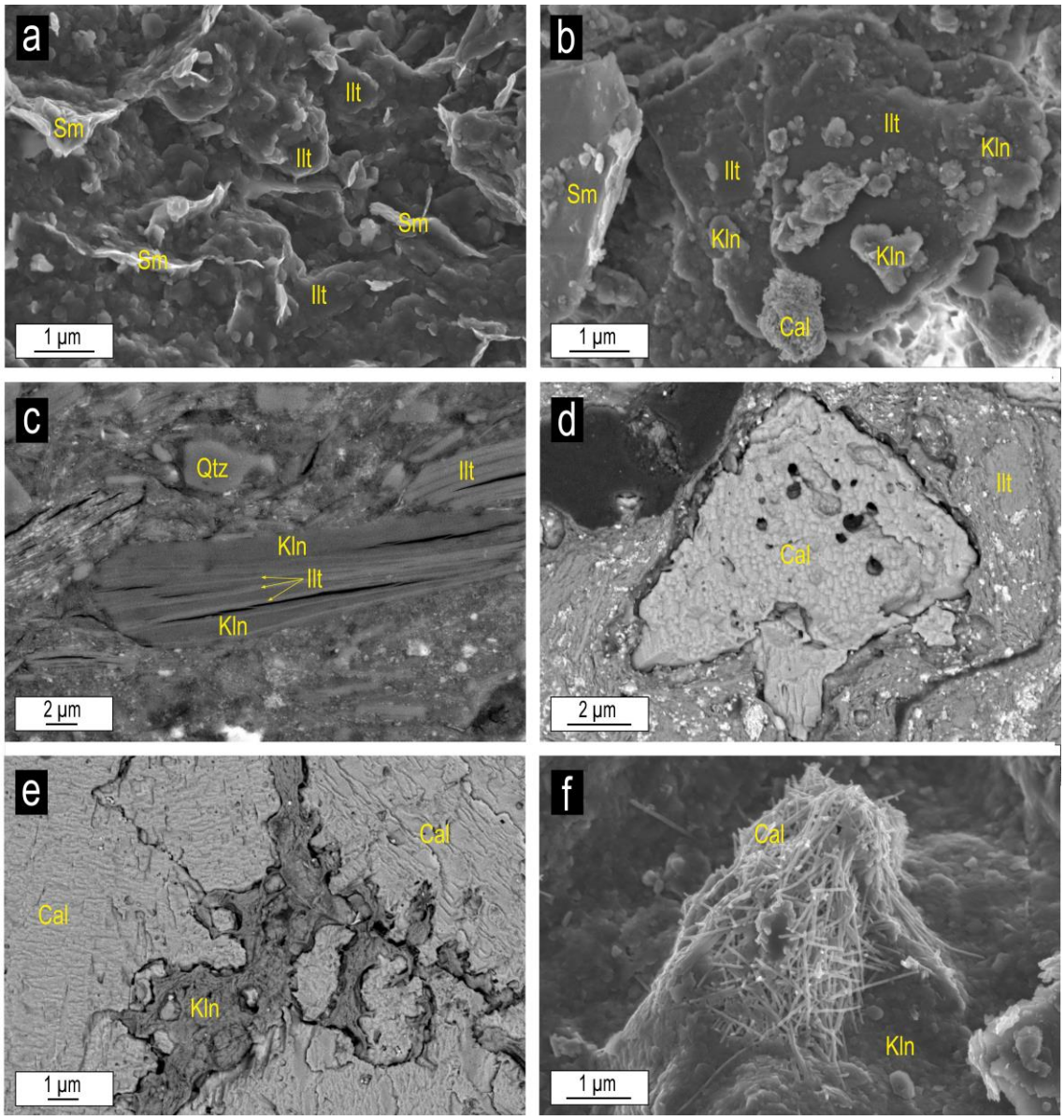

Fig. 4.7. FESEM images of the matrix of the middle and upper mudstones to calcareous mudstones (**a–c**) and the carbonates observed in the mudstones to calcareous mudstones (**d–f**). **a)** SE image of smectite flakes and anhedral illitic phases; **b)** SE image of anhedral illitic phases and subhedral kaolinite; **c)** BSE images showing intergrowths of illitic phases and kaolinite; **d)** microsparitic calcite filling a matrix pore; **e)** kaolinite cementing calcite in a microsparitic nodule; **f)** fibrous calcite crystals cementing the matrix of the mudstone to calcareous mudstone. *Sm*=smectite, *Kln*=kaolinite, *Ilt*=illitic phases, *Qtz*=quartz, *Cal*=calcite.

Table 4.3. EDS analyses (Wt%) of clay minerals in the mudstones and calcareous mudstones (standard deviation in brackets).

	O	Na	Mg	Al	Si	K	Ti	Fe	Calculated formula
Kaolinite (n=28)	49.08 (2.83)	-	-	21.88 (1.20)	24.87 (1.46)	-	0.21 (0.31)	3.95 (3.56)	$Fe_{0.1}Al_{1.9}Si_2O_5(OH)_4$
Illitic phases (n=33)	45.72 (2.12)	0.16 (0.26)	0.68 (0.36)	16.75 (3.20)	26.21 (2.84)	8.23 (2.23)	0.08 (0.20)	2.18 (1.44)	$(K_{0.8},H_3O)(Al_{1.7}Mg_{0.1}Fe_{0.2})(Si_{3.4}Al_{0.6})O_{10}[(OH)_2,(H2O)]$
Smectite (n=20)	44.90 (3.20)	0.14 (0.21)	1.42 (2.95)	18.38 (2.92)	25.64 (5.13)	4.94 (1.34)	0.39 (0.98)	4.22 (3.36)	$(K_{0.5})(Al_{1.7}Fe_{0.3}Mg_{0.1})(Si_{3.3}Al_{0.7})O_{10}(OH)_2nH_2O$

4.2 Pisoids data

The Fe pisoids are embedded in the clay-rich matrix of the mudstone to calcareous mudstones. They are from 3 mm to 1 cm in diameter and show spherical to ellipsoidal morphologies and some of them are fractured. According to their size, following the classification given by Bárdossy (1982): macropisoids (>5 mm), pisoids (1–5 mm), ooids (100–1000 μm) and micro-ooids (<100 μm), the Fe pisoids are pisoids and macropisoids.

On the other hand, Reolid et al. (2008) also classified as ferruginous ooids and pisoids those grains formed by a nucleus enveloped by an iron oxide coating, which also fits with the Fe pisoids of this study. According to their morphological features and lamination, these pisoids and macropisoid would be included in the Type A ooids and pisoids defined by these authors, which are formed by a thin, regular lamination that forms concentric layers enclosing a nucleus. In Type A ooids and pisoids, the nucleus can be a fragment of an older ferruginous ooid or an indeterminate ferruginous lump. The nuclei of the Fe pisoids studied here are always formed by and indeterminate ferruginous lump, so following the classification given by Guerrak (1987) they can also be classified as simple pisoids.

4.2.1 XRD data

The XRD patterns of two macropisoids (one of each log) indicate that they contain quartz, clay minerals, hematite, goethite, together with orthoclase, diaspore, anatase, rutile, and ilmenite (Fig. 4.8a). Calcite was also detected in the XRD patterns (especially in those of the macropisoids from the LC log), but it is not represented because, as it will be explained below, part of this calcite was not formed coetaneously with the mudstones and calcareous mudstones and the Fe pisoids. The relative proportions of these phases indicate that the macropisoids from the two logs are mainly formed by quartz, clay minerals (kaolinite and illitic phases, as deduced from the FESEM results), hematite, goethite and minor amounts of orthoclase, diaspore, anatase, rutile and ilmenite (Fig. 4.8b).

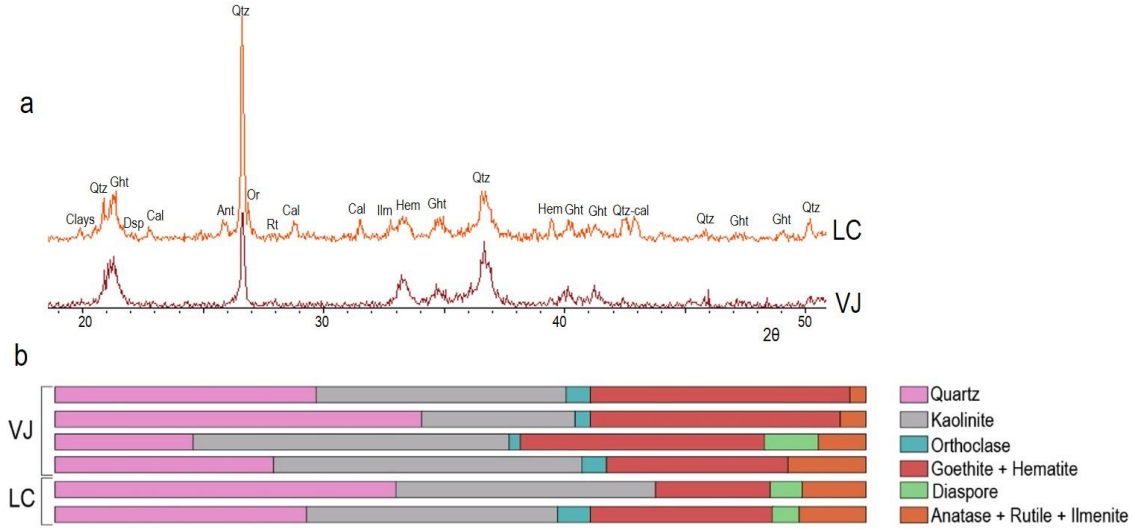

Fig. 4.8. a) XRD patterns of two macropisoids from the VJ and LC logs; **b)** relative proportions of mineral phases in several macropisoids from the LC and VJ logs. *Clays*=clay minerals, *Qtz*=quartz, *Cal*=calcite, *Dsp*=diaspore, *Ght*=goethite, *Ant*=anatase, *Or*=orthoclase, *Rt*=rutile, *Ilm*=ilmenite, *Hem*=hematite.

4.2.2 Optical and electron microscopy data

The pisoids and macropisoids are constituted by a nucleus and an outer cortex formed by several layers, both composed of a mixture of hematite, goethite, and clay minerals (Fig. 4.9a–c). In the case of the macropisoids, the outer cortex is 1–3 mm thick, and quartz clasts are frequently included among the layers (Fig. 4.9b and c). The nucleus is formed by an indeterminate ferruginous lump along with goethite and hematite. Both hematite and goethite show botryoidal textures, occasionally in alternating layers (10–30 μm) and some parts of the nucleus are replaced by carbonate at times (Fig. 4.9d). The electron microscopy images show that the layers constituting the cortex of the macropisoids are formed by different amounts of kaolinite mixed with hematite and goethite, allowing one layer to be differentiated from another based on its kaolinite content. Hematite frequently cements kaolinite in the macropisoids (Fig. 4.9e). In both the pisoids and macropisoids, there is kaolinite with platy shapes with random orientation and as booklets like those found in the matrix of the lower mudstone to calcareous mudstone levels (Fig. 4.9e). Intergrowths of illitic phases and kaolinite with the same morphologies as those found in the upper mudstone to calcareous mudstone levels are also observed (Fig. 4.9f). Microsparitic calcite and occasional barite fill cavities in the macropisoids (Fig. 4.9f and g).

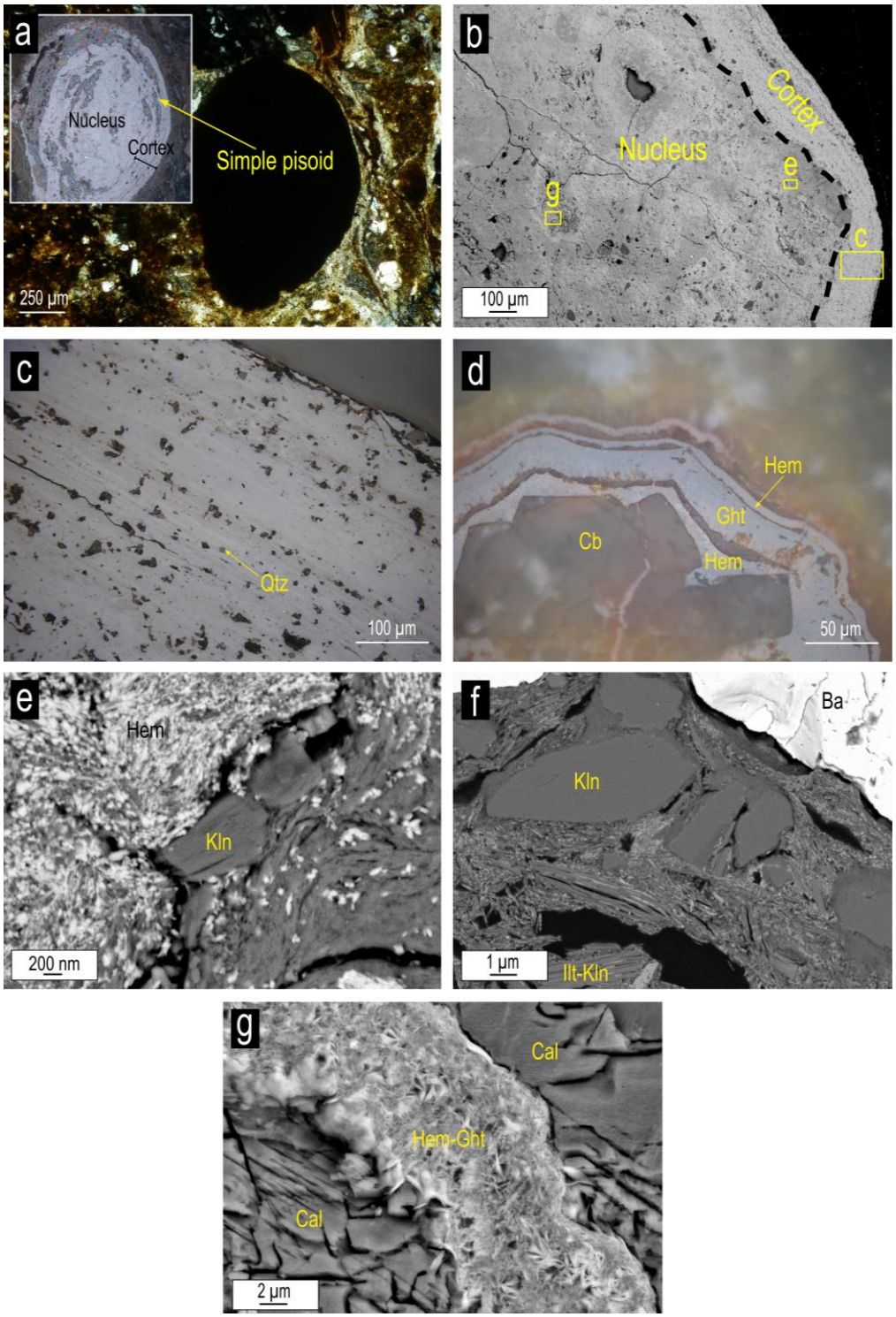

Fig. 4.9. Transmitted and reflected light optical microscopy and SEM images of pisoids and macropisoids. **a)** Simple pisoid from the LC log; **b)** nucleus and cortex of a macropisoid. The squares show the areas were the enlarged images c, e and g were taken; **c)** macropisoid cortex formed by several layers with quartz clasts included among the layers; **d)** hematite and goethite forming alternating layers in the nucleus of a macropisoids and microsparitic carbonate replacing partially the nucelus; **e)** booklets of platy kaolinite and hematite in the nucleus of a macropisoid; **f)** quartz clasts, barite filling cavities, and illitic phases/kaolinite intergrowths in the nucleus of a macropisoid; **g)** microsparitic calcite filling cavities of a macropisoid. *Qtz*=quartz, *Cb*=carbonate, *Hem*=hematite, *Ght*=goethite, *Kln*=kaolinite, *Ilt*=illitic phases, *Ba*=barite, *Cal*=calcite

5 DISCUSSION

5.1 Origin of the clay minerals, pisoids, and carbonates in the palaeosols

The mineralogy of the mudstone to calcareous mudstone levels consists of calcite, quartz (and orthoclase), clay minerals (kaolinite, illitic phases, smectite), Fe and Ti oxides, and Fe oxyhydroxides. The high content in clay minerals, along with the oxides and oxyhydroxides and the presence of Fe pisoids is a consequence of the development of palaeosols in the Torrelapaja Fm. The determined mineralogical association is common in oxisols, as categorised by the Soil Taxonomy Classification.

Compositional and morphological images show that the platy kaolinite is commonly euhedral to subhedral and displays pseudohexagonal outlines, indicating that it is probably authigenic. The presence of kaolinite booklets is not compatible with a detrital origin since they are too delicate to withstand erosion or transport processes, thus suggesting that they formed *in-situ* during the edaphic process (Bauluz et al., 2014; Do Campo et al., 2018; Laita et al., 2020). The lower and variable relative crystallinity of kaolinite in Stages 1 and 2 could be attributed to the presence of Fe in the kaolinite structure (as detected in EDS analyses, although in low proportions), since substitutions of Al by Fe in the octahedral sheet of kaolinite has been described in similar materials (Laita et al., 2020; Mendelovici et al., 1979) and is something common in weathering processes (Mestdagh et al., 1980; Cantinolle et al., 1984; Yuste et al., 2015). On the other hand, the kaolinite presents somewhat higher crystallinity towards the top of the studied logs, coeval with the increase in illitic phases in Stage 3 and the presence of intergrowths of illitic phases and kaolinite, in which the illitic phases act as a substrate for the kaolinite crystallization. This may enhance more effective crystallization of kaolinite.

Smectite is detected by electron microscopy but not by XRD, probably because its content lies below the detection limit of XRD. The flake-type morphologies observed in the smectite by electron microscopy suggest an *in-situ* origin, and the EDS analysis indicates that it corresponds to dioctahedral montmorillonite-type smectite. This kind of smectite has previously been reported in palaeosols as a product of the weathering of feldspars and micas (Fesharaki et al., 2007). Kaolinite and smectite would have thus been formed during the edaphic process by the dissolution of previous aluminium silicates (e.g., feldspars and illitic phases).

Authigenic illite is described in brackish and freshwater clays, lacustrine marls and gleysols during the Eocene–Oligocene, due to illitization of smectite and mixed-layer I/S during pedogenic processes (Huggett and Cuadros, 2005, 2010; Huggett et al., 2001). However, this process is not observed in the uppermost Hauterivian–lower Barremian palaeosols studied here, which can be classified as oxisols. The origin of illitic

phases in palaeosols is not compatible with the genesis of kaolinite (Bauluz et al., 2000). Detrital illite can degrade to interstratified illite–smectite under humid conditions (Chamley, 1989). Smectitization of illite induced by pedogensis has also been described in palaeosols (Schaetzl and Thompson, 2015; Meenakshi et al., 2020). The fact that the illitic phases studied here act as a substrate for kaolinite crystallization indicates that they are former phases (Bauluz et al., 2014). Thus, these illitic phases may have a detrital origin and intervene in the genesis of kaolinite and smectite during the edaphic process. In addition, their anhedral morphologies are consistent with a detrital origin (Bauluz et al., 2014; Laita et al., 2020).

The calcite nodules observed in some of the mudstone to calcareous mudstone levels are cemented by kaolinite, pointing to a previous genesis for the nodules. Other investigations (Mücke et al., 1999; Laita et al., 2020) suggest that soil development usually occurs in various episodes involving changes in the water level and reworking processes. In the present study, the calcite nodules may come from the underlying limestone levels generated during the rising of the water level. A subsequent lowering of the water level would allow the calcite nodules to be cemented by kaolinite. This would also be the factor responsible for the reworking and fracturing of some of the macropisoids.

As other authors suggest (Rossi and Cañaveras, 1999), the fibrous calcite crystals cementing the matrix of the mudstone to calcareous mudstone levels would have formed during diagenesis. This diagenesis would also allow the filling of the matrix pores and macropisoids cavities and the replacements of some parts of their nuclei by microsparitic calcite. The barite observed within the cavities of macropisoids may also have a diagenetic origin; it has been described cementing palaeosols in other areas (Michel et al., 2016). The calcite and barite cements thus postdate the kaolinite and smectite. These cements must have therefore formed during early diagenesis, which would not have altered the palaeoclimatic signal registered in the clay minerals formed *in-situ*.

Saber et al. (2018) classified ferriferous pisoids formed by *in-situ* growth in lateritic weathering profiles according to their mineralogical composition as: (1) pure kaolinitic pisoids, (2) kaolinitic-hematitic or hematitic-kaolinitic pisoids, and (3) hematitic pisoids. The second group includes those pisoids whose inner nucleus is composed of kaolinite and/or hematite surrounded by an outer cortex formed by kaolinite and hematite laminae. This latter subgroup is consistent with the pisoids and macropisoids studied here, since according to the XRD and electron microscopy results, they are mainly formed by hematite, goethite, kaolinite, and occasional quartz and illitic phases. FESEM images indicate that the kaolinite in the macropisoids displays platy

morphologies and also occurs as booklets, similar to the kaolinite found in the matrix constituting the lower mudstone to calcareous mudstone levels. Likewise, the illitic phases and the intergrowths of illitic phases and kaolinite in the macropisoids are similar to those observed in the matrix of the upper mudstone to calcareous mudstone levels.

According to Bárdossy (1982), the formation of Fe pisoids and macropisoids in soils is usually associated with conditions of permanent groundwater saturation. These conditions are congruent with the genesis of Type A ferruginous ooids and pisoids described by Reolid et al. (2008). The growth of the concentric layers that form the cortex of the pisoids and macropisoids also indicates physical and chemical changes in the environmental conditions, giving place to the precipitation of several mineral phases, such as kaolinite and Fe and Ti oxides, and Fe oxyhydroxides, in different quantitates (Yuste et al., 2020).

These data, along with the concentric structure and morphology of the Fe pisoids studied here indicate that they would have an *in-situ* origin and were thus formed during the edaphic process. However, the fractures observed in the macropisoids filled with calcite and barite also suggest that they underwent some reworking. On the other hand, the presence of hematite cementing kaolinite in the macropisoids indicates that the genesis of Fe oxides took place during the edaphic process but after the formation of kaolinite, as described in similar materials in the Iberian Range (Laita et al., 2020).

5.2 Clay mineral trends and climate vs. tectonic controls

5.2.1 Clay minerals and sediment supply

The clay minerals show vertical and lateral trends related to the three sedimentary stages defined by Aurell et al. (2021), which can shed some light on the factors (climate, tectonics) controlling the genesis of the mineralogical assemblages and the development of the palaeosols.

Stage 1 is dominated by distal alluvial plain muddy facies of argillaceous composition (Fig. 4.2), with a somewhat lower quartz content and higher clay mineral content in the distal LC log (kaolinite being the main clay mineral) but higher calcite content in the proximal VJ log. This lateral trend could be associated with local factors (e.g., differential supply) but the reduced sediment thickness of this stage and lack of significant sedimentological differences between the logs precludes a more definitive interpretation (Figs. 4.2 and 4.5). Stage 2 is characterised by an increase in the water level, allowing the expansion of palustrine-lacustrine areas, but also a coeval increase in the terrigenous sediment supply (Aurell et al., 2021; Fig. 4.2). The mineralogical composition of distal alluvial plain and palustrine muddy facies is very homogeneous, as they are dominated by calcite in the distal LC and proximal VJ logs. In addition, kaolinite

predominates over illitic phases in the proximal VJ log, as in Stage 1. These data reflect the fact that there is no significant control of the increasing terrigenous supply in the soil development during this stage. Stage 3 is characterised by an increase in terrigenous-clastic supply due to an increase in tectonic activity in southern areas (VJ log; Fig. 4.2) (Aurell et al., 2021). The change in the sedimentological conditions during this stage, with a greater contribution of terrigenous sediment, leads to higher amounts of quartz and illitic phases (Fig. 4.5). Nevertheless, calcite, with a decreasing tendency, is present in the proximal VJ log, where a greater terrigenous supply is recorded. As explained below, the higher crystallinity of kaolinite towards the top of the logs may be a consequence of the higher quantities of illitic phases. These illitic phases form intergrowths in which they act as a substrate for the growth of the kaolinite, enhancing a more effective crystallization for the kaolinite. Additionally, the increase in quartz content towards the top of the profiles, may generate a possible increase in the porosity of the upper mudstone to calcareous mudstone levels, which could allow the kaolinite to be more crystalline and also favour the genesis of calcite cements during diagenesis as it would lead to better conditions for fluid circulation.

5.2.2 Clay minerals and palaeoclimate

As commented in a previous section, the mineralogical association determined in the mudstone to calcareous mudstone levels of this research is common in oxisols, as categorised by the Soil Taxonomy Classification. Oxisol development occurs under humid tropical climates (Do Campo et al., 2018).

Several authors have reported mineral assemblages comprising goethite, hematite, aluminium hydroxides, kaolinite, and quartz, as well as the presence of Fe pisoids in lateritic palaeosols (e.g., Bauluz et al., 2014; Giovannini et al., 2017; Yuste et al., 2017; Nkalih Mefire et al., 2018; Nouazi Momo et al., 2019).

On the other hand, the genesis of the palaeosols in the Torrelapaja Fm was also coeval with a rise and possibly a subsequent fall in the water level, as evidenced by the presence of kaolinite cementing calcite nodules and of reworked features in the pisoids.

The general climate described for the Hauterivian–Aptian period in Western Europe includes a trend from seasonal to warm climates and then to cooler conditions. During the Hauterivian, a seasonal climate prevailed (Godet et al., 2008; Föllmi, 2012), evidenced by the presence of illite and smectite in marine sedimentary successions (Mutterlose and Ruffell, 1999). From the latest Hauterivian to early Barremian, the increase in kaolinite in the palaeosols is consistent with a trend towards warmer conditions (Bárdossy, 1982; Wright et al., 2000; Godet et al., 2008; Föllmi, 2012), which prevailed during the mid and late Barremian (Scotese et al., 2021). On the other hand,

during this period, Moiroud et al. (2012) also reported marl–limestone alternations, with limestones enriched in I/S mixed-layers and kaolinite and illite-rich marls. According to these authors, the presence of kaolinite and illite in the marls is a consequence of continental runoff under humid tropical conditions, whereas the I/S contained in the limestones were formed under seasonally semi-arid conditions. Thus, this is reflecting a distortion in the climatic signal obtained from the clay minerals assemblages formed in continental or marine domains. A later change from warm to cooler conditions is recorded during the early Aptian (Steuber et al., 2005; Godet et al., 2006; Dinis et al., 2020).

As pointed out by Laita et al. (2020), the trend in humidity during the Early Cretaceous of Western Europe is not so clear. Clay mineral assemblages from French and Swiss sections show a change from dry to more humid conditions during the Hauterivian (Godet et al., 2008). In the Tethys area, arid and humid regimes are recorded during the late Hauterivian (Föllmi, 2012), and temperature models show warm and humid conditions for the early Barremian (Bodin et al., 2009; Price et al., 2011; Föllmi, 2012). However, alternate wet and dry seasons during the early Barremian have also been reported (Haywood et al., 2004). Finally, an increase in humid conditions is described during the mid-Barremian in Europe (Mutterlose et al., 2014), whereas $\delta^{18}O$ records show a trend towards cooler and more arid conditions towards the late Barremian of the Tethys (Föllmi, 2012).

In northwestern Spain, a seasonal subtropical climate is described during the Early Cretaceous (Buscalioni and Fregenal-Martínez, 2010). In addition, the presence of Barremian kaolinite-rich bauxites and laterites in the Iberian Range (NE Spain) is also consistent with warm and humid conditions (Bauluz et al., 2014; Yuste et al., 2015, 2017; Laita et al., 2020).

In the western part of the Cameros Basin, stacked sheet flood deposits and sandy channels, along with conglomerates, mottled mudstones, and pedogenic carbonates included in the Piedrahita de Muñó Formation (Barremian–Aptian), suggest a semi-arid climate with seasonal rainfall (Platt, 1989).

In the uppermost Hauterivian–lower Barremian Torrelapaja Fm of the Torrelapaja subbasin (southeastern Cameros Basin), XRD and electron microscopy results show a higher content of kaolinite formed *in-situ* in the lower mudstone to calcareous mudstone levels, suggesting an intense chemical weathering characteristic of a warm and humid climate (Raucskik and Varga, 2008; Bauluz et al., 2014; Won et al., 2018; Nouazi Momo et al., 2019). As regards the pisoids and macropisoids, these would

have been formed in environments of permanent groundwater saturation, which would have occurred in different episodes during the three sedimentary stages.

The decrease in kaolinite towards the top of the stratigraphic profiles correlates with the increase in the content of detrital quartz and illitic phases, which is related to a greater terrigenous-clastic supply during Stage 3. This could have partially inhibited soil formation. On the other hand, this trend is also coeval with the presence of authigenic smectite, thus reflecting a decrease in chemical weathering perhaps associated with a change to colder and drier conditions during the late Hauterivian–early Barremian in this part of the Cameros Basin. In addition, the above-mentioned alternating goethite-hematite sequences in the macropisoids are also associated with less humid conditions (Velasco et al., 2013; Laita et al., 2020).

In the east of the Maestrazgo Basin (SE Iberian Range), the presence of laterites in the Cantaperdius Formation (Barremian–Aptian) has been reported (Salas, 1987; Combes, 1990). In the nearby Morella subbasin, karst bauxite deposits, which probably developed from lateritic materials laterally equivalent to the Cantaperdius Fm, have also been described (Molina and Salas, 1993; Yuste et al., 2015). Moreover, in the Oliete subbasin (NW Maestrazgo Basin), Laita et al. (2020) described a decrease in kaolinite and an increase in smectite and illite content in lateritic palaeosols present in the lower part of the Blesa Formation (early Barremian), which reflected a change from warm/humid to cold/dry conditions. The lateritic palaeosols described in the lower Blesa Fm are regarded as age-equivalent with the palaeosols from Stages 1 and 2 of the uppermost Hauterivian–lower Barremian Torrelapaja Fm (Aurell et al., 2021). The same tendency in the climatic conditions can be deduced in this part of the Cameros Basin, but the record is not as good as in the Oliete subbasin due to the high siliciclastic contribution during Stage 3, associated with an increase in tectonic activity. All these data reflect warm and humid conditions during the early Barremian in these two Iberian subbasins over 100 km apart, followed by a change to drier, colder conditions, at least in the Oliete subbasin (Maestrazgo Basin, SE Iberian Range; Laita et al., 2020), which could also have taken place in the Torrelapaja subbasin (Cameros Basin, NW Iberian Range).

6. CONCLUSIONS

A combination of facies analysis and a study of the clay mineralogy of clay/marl-rich outcrops has allowed us to characterize the mineralogical and textural changes found in the mudstones to calcareous mudstones of the Torrelapaja Formation (uppermost Hauterivian–lower Barremian).

Kaolinite is the main clay mineral in the lower levels. Its euhedral morphologies and the presence of aggregates forming booklets indicate an authigenic origin for this mineral. The growth of the kaolinite to form intergrowths with illitic phases indicates that the illitic phases are former phases and act as a substrate for the kaolinite crystallization. This may favour the higher crystallinity of kaolinite in the upper levels, whereas the lower Fe proportions in the kaolinite in the lower levels could be the reason for its lower crystallinity. The smectite (montmorillonite-type composition) detected in the upper levels and its flake-type morphologies are consistent with an authigenic origin. The mineralogy and structure of the pisoids and macropisoids also reflect an *in-situ* origin during the edaphic process, but some of them are fractured, indicating reworking processes.

The matrix of the mudstones to calcareous mudstones and the cavities of the pisoids were later cemented by microsparitic calcite (and barite in some macropisoids) during early diagenesis. This diagenesis did not alter the palaeoclimatic signal registered in the kaolinite and smectite formed *in-situ*.

The mineralogical association in the mudstones and calcareous mudstones is characteristic of oxisols (laterites), which developed under humid tropical climates.

The higher content of kaolinite formed *in-situ* in the lower levels suggests intense chemical weathering as a consequence of a warm and humid climate, which is consistent with the palaeoclimatic conditions reported during the latest Hauterivian–early Barremian in the NE of the Iberian Plate.

The decrease in the kaolinite content, along with the increase in quartz and illitic phases, in the upper levels is related with an increase in siliciclastic input during Stage 3, which may have inhibited soil genesis. However, this trend in kaolinite content, along with the presence of authigenic smectite, also reflects a decrease in chemical weathering, perhaps associated with a change to colder and drier conditions, maybe concealed by the siliciclastic contribution, during the latest Hauterivian–early Barremian in this part of the Cameros Basin (NW Iberian Range).

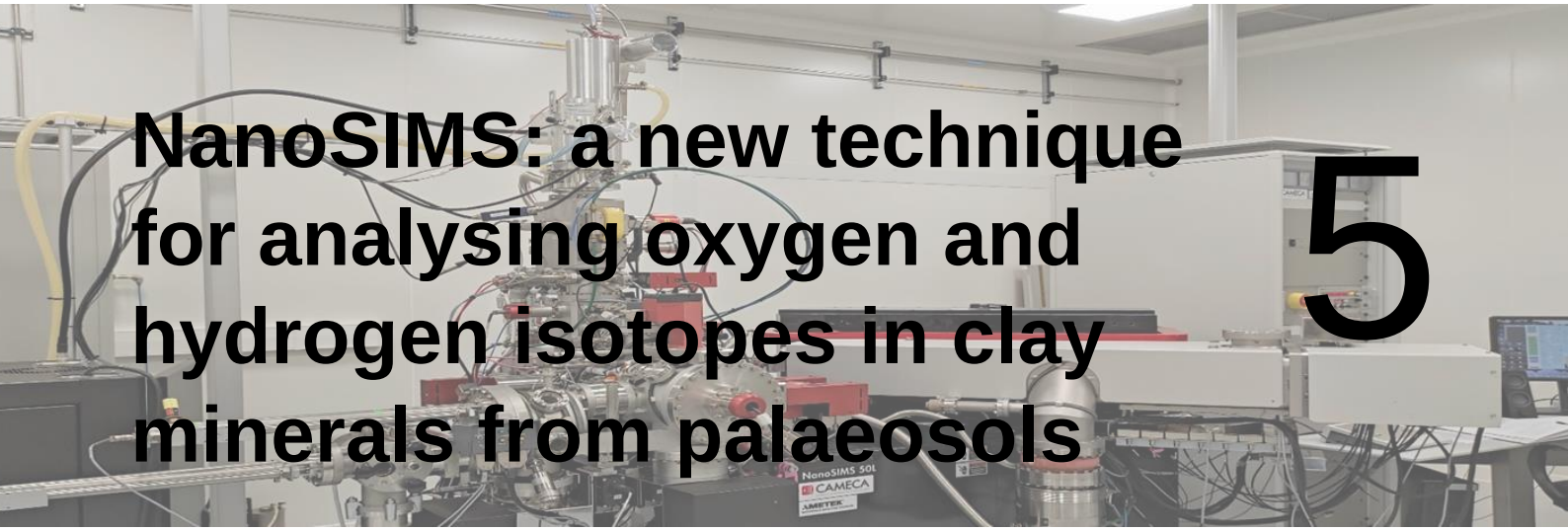

NanoSIMS: a new technique for analysing oxygen and hydrogen isotopes in clay minerals from palaeosols

5

Isotopic geochemistry has been used to characterize clay minerals and infer their origin. Usually, sediments, rocks and palaeosols contain not only authigenic clay minerals, but also detrital and/or diagenetic ones. Together with the usually small size (micro- or nanometric) of the clay minerals in these materials, this can generate difficulties during isotopic analyses by conventional spectroscopies. To avoid this problem, we used nanoscale secondary ion mass spectrometry (NanoSIMS) to analyse authigenic clay minerals included in palaeosol levels in early Barremian continental profiles located in NE Spain. The bottom levels of the profiles are rich in kaolinite, whereas the top levels contain smectite. The isotopic compositions of pure powder standards of kaolinite and smectite were previously measured to obtain reference values for calibrating the instrumental mass fractionation. Two common preparation techniques for geological samples were tested (thin sections and thick polished sections), revealing that thin sections are more suitable for NanoSIMS analysis due to their lower resin content. The high spatial resolution and accuracy of the instrument allowed the elemental mapping of the samples, permitting the localization of the minerals of interest and the measurement of isotopic ratios at selected points (1 x 1 μm^2) within the samples. The high sensitivity of the NanoSIMS allowed a decrease to be distinguished in the $^{18}O/^{16}O$ and D/H ratios from the kaolinite in the bottom levels to the smectite in the top levels, reflecting a change in the climatic conditions. The $\delta^{18}O$ and δD values obtained for kaolinite ($\delta^{18}O_{SMOW}$=18‰; δD_{SMOW}=-83‰ and $\delta^{18}O_{SMOW}$=14‰; δD_{SMOW}=-97‰) and smectite ($\delta^{18}O_{SMOW}$=13‰; δD_{SMOW}=-167‰ and $\delta^{18}O_{SMOW}$=11‰; δD_{SMOW}=-180‰), respectively, are consistent with the crystallization of the clays in weathering conditions. The temperature obtained for kaolinite formation is 21–22 ºC, whereas for smectite it is 16–17 ºC. Given suitable calibration using pure isotopic standards and adequate sample preparation, NanoSIMS can thus have a great applicability in palaeoclimatic studies involving the isotopic composition of nanometre-sized clay minerals.

1. INTRODUCTION

NanoSIMS (nanoscale secondary ion mass spectrometry) is a dynamic SIMS technique that allows the mapping of different chemical elements at nanometre scale, with high sensitivity as well as high spatial resolution (Mosenfelder et al., 2011; Blanc et al., 2012; Subirana et al., 2021).

The high spatial resolution of NanoSIMS is achieved by focusing the primary ion beam perpendicular to the sample surface, which makes high spatial resolution possible in combination with high-sensitivity chemical and isotopic images (Subirana et al., 2021). The primary ion bean of NanoSIMS can be positive (Cs+) or negative (O-), in order to generate respectively either negative or positive secondary ions from the sample surface and obtain the corresponding elemental images. The positive Cs^+ ion beam can achieve 50 nm resolution images of electronegative elements such as oxygen, silicon, carbon and hydrogen. On the other hand, the rf (radio frequency) plasma O^- ion beam allows high lateral resolution imaging below 40 nm of electropositive elements, such as most metals (Malherbe et al., 2016; Agüi-Gonzalez et al., 2019; Subirana et al., 2021). In addition, the NanoSIMS instrument is equipped with a charged-coupled device (CCD) camera, which allows optical imaging and thus the preselection of regions of the sample of interest for subsequent SIMS analysis (Chew et al., 2014; Ender et al., 2019).

These characteristics make NanoSIMS suitable for investigating heterogeneous materials, since it allows the mapping and carrying out of stable isotopic analyses of nanometric phases. In this way, NanoSIMS has been applied to several geological materials to achieve sub-micron scale imaging and *in-situ* isotope ratio analysis. For example, Wacey et al. (2008) described a biological origin of ambient inclusion tails (AIT) through elemental images of C, N, P, S, Co, Fe, Ni and Zn, together with $^{13}C/^{12}C$ isotope ratios analysis. Hu et al. (2014) measured D/H ratios in water contents of melt inclusions and apatite in a Martian meteorite. Other examples of NanoSIMS applications in the Geosciences are reported in Kilburn and Wacey (2015), (e.g., $^{56}Fe^{16}O^-$ and $^{12}C^{14}N^-$ maps in iron oxides concretions or variations in 24Mg-/44Ca ratios in foraminifera).

There are also investigations that use the NanoSIMS for elemental mapping of certain elements (e.g., C, N, Ca, Fe, Mn, Al, O, Cu) in soil samples (Mueller et al., 2012; Vogel et al., 2013; Rennert et al., 2014; Boiteau et al., 2020; Inagaki et al., 2020; Li et al., 2020 Vidal et al., 2020). Some of these studies report 40 x 40 μm^2 maps of the ions $^{16}O^-$, $^{12}C^-$, $^{13}C^-$, $^{12}C^{14}N^-$, $^{27}Al^{16}O$, $^{56}Fe^{16}O$ in the clay mineral fraction of the soils (Vogel et al., 2013; Inagaki et al., 2020).

As yet, however, there have been no investigations into the usefulness of NanoSIMS in measuring separately the isotopic composition of the different nanometre-

sized clay minerals that frequently constitute the matrix of the soils that formed in the landscapes of the past (i.e., palaeosols), which provide key data for palaeoclimatic reconstructions.

Measurement of the $^{18}O/^{16}O$ ratios of the structural oxygen in clay minerals is usually combined with D/H ratio analysis, since they both provide information about the genesis conditions of these minerals (Savin and Hsieh, 1998; Sheppard and Gilg, 1996; Sheldon and Tabor, 2009; Kuligiewicz et al., 2021).

Under warm and humid conditions (subtropical to tropical), very effective hydrolysis is produced by intense chemical weathering, giving rise to the genesis of oxisols. In oxisols (commonly known as laterites), the main clay mineral is kaolinite, along with aluminium and iron oxides, oxyhydroxides and hydroxides (e.g., Mack et al., 1993; Do Campo et al., 2018; Laita et al., 2020; Laita et al., 2021). In contrast, under drier and colder conditions there is an absence of significant hydrolysis, enhancing the genesis of smectite and illite (Dhillon and Dhillon, 1991; Do Campo et al., 2018; Laita et al., 2021).

During lateritic weathering, kaolinite, and iron oxides/oxyhydroxides are formed in isotopic equilibrium with the meteoric water (Bird et al., 1992; Girard et al., 2000; Girard et al., 2002). However, the presence of other silicates, such as detrital quartz or micas, in palaeosols may create problems in isotopic investigations since they are not in isotopic equilibrium with the minerals formed during weathering (Kuligiewicz et al., 2021).

Mineralogical studies that report $\delta^{18}O$ and δD values of clay minerals with paleoclimatic interpretation purposes used powder samples and applied isotope ratio mass spectrometers (IRMS) or mass spectrometers in a dual-inlet configuration (e.g., Fernández-Caliani et al., 2010; Mix and Chamberlain, 2014; Clauer et al., 2015).

For this kind of studies, the bulk powder samples are centrifugated to obtain fine fractions (0.5-2 μm) to isolate the clay minerals. However, even in these fractions there can be a great variety of clay mineral assemblages of different genesis. In other studies, the mineral of interest is separated from the rest of the phases by applying specific chemical treatments to the sample (e.g., Delgado y Reyes, 1996; Giral-Kacmarcík et al., 1998; Gilg et al., 2003; Gilg et al., 2004).

Although these sample treatments can reduce the problem of analysing the isotopic signal of mixed phases, there is no reliable way to ensure that the clay mineral of interest is isolated for the analysis. This fact, along with the small particle size of the clay minerals (from micrometric to nanometric), leads to difficulties during isotopic analysis of these minerals by conventional spectroscopies (Tabor et al., 2002; Kuligiewicz et al., 2021). These difficulties have been reported in other geological materials (e.g.,

chondrites), where the mixture of organic matter and hydrous silicates hinders the individual determination of D/H ratios (Piani et al., 2012 Piani et al., 2015).

The use of NanoSIMS for the isotopic study of clay minerals included in palaeosols during weathering could solve this problem, since the high spatial resolution of the technique allows isotopic analysis of the small-sized authigenic clay minerals in polished palaeosols samples separately, without interference from other silicates.

In this research, therefore, we carried out $^{18}O/^{16}O$ and D/H isotopic analysis of the authigenic clay minerals (kaolinite and smectite) included in Lower Cretaceous (early Barremian) lateritic palaeosols from NE Spain with two aims: 1) to evaluate the usefulness of NanoSIMS in this kind of research, since there is to date no published research in this topic, and 2) to obtain first results that help to deduce the climatic conditions under which these materials were generated.

2. PALAEOSOL SAMPLES DESCRIPTION

The samples are from palaeosol levels included in early Barremian (Early Cretaceous ~129–128 million years) continental profiles from the Iberian Range (NE Spain). Laita et al. (2020) characterised these materials through a combined facies and clay mineral study by X-ray diffraction (XRD), optical and field emission scanning electron microscopy (FESEM) and energy-dispersive X-ray (EDS) analyses. The facies analyses of these continental successions revealed that the palaeosols levels developed *in-situ* by the chemical weathering of lacustrine marlstones. According to the XRD patterns and the EDS analyses the palaeosol levels are mainly formed by clay minerals (kaolinite, smectite and illitic phases), together with Fe and Ti oxides and oxyhydroxides (goethite, hematite, anatase, rutile, ilmenite, and diaspore), quartz and calcite nodules (Fig. 5.1a–c) (Laita et al., 2020).

The textural data reported by Laita et al. (2020) indicate that kaolinite and smectite are authigenic and crystallized during the soil development. FESEM images showing kaolinite books and smectite with flake-type morphologies forming the matrix of the palaeosols together with the Fe and Ti oxides and oxyhydroxides discard a detrital origin of these minerals (Fig. 5.2a–c). On the other hand, the anhedral morphologies of the illitic phases (Fig. 5.2d), along with the fact that the genesis of illite is not compatible with that of the kaolinite in these environments, suggest a detrital origin for the illitic phases (Bauluz et al., 2014; Laita et al., 2020). The mineral assemblage that forms the palaeosols, along with the presence of the ferruginous pisoids allowed Laita et al. (2020) to classify them as laterites.

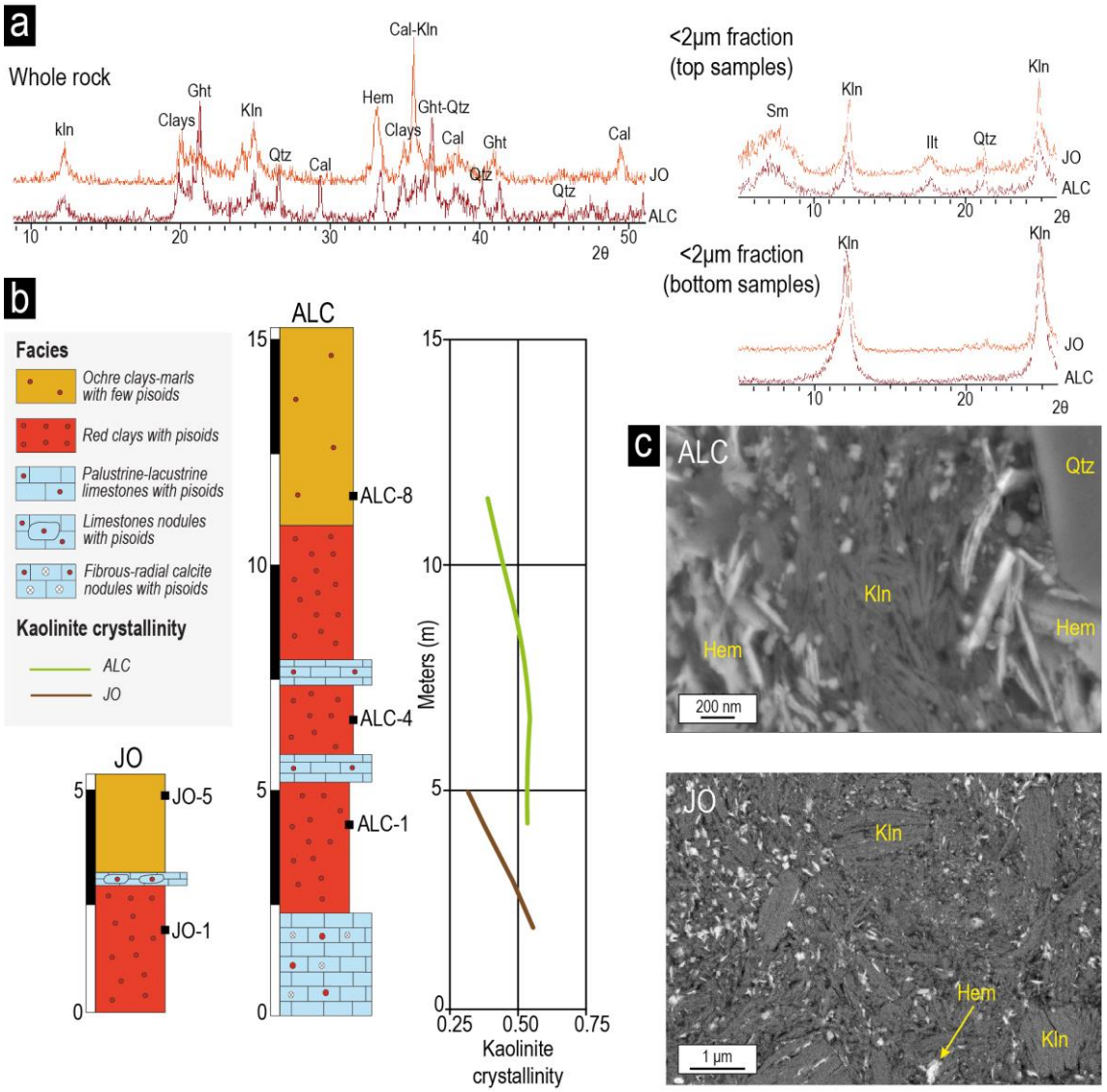

Fig. 5.1. a) XRD patters of the whole rock and <2 μm fractions of palaeosols samples from the ALC and JO profiles; **b)** location of the samples under study in the Lower Barremian ALC (ALC-1, ALC-4 and ALC-8) and JO (JO-1 and JO-5) stratigraphic logs and kaolinite crystallinity values measured in these samples, with an average value of 0.5 and 0.4 for kaolinites from the ALC and JO samples, respectively; **c)** backscattered electron images from the matrix of palaeosols samples from both profiles showing kaolinite plates and booklets. *Clays*=clay minerals, *Ght*=goethite, *Qtz*=quartz, *Cal*=calcite, *Hem*=hematite, *Kln*=kaolinite, *Sm*=smectite, *Ilt*=illitic phases. (Modified from Laita et al., 2020)

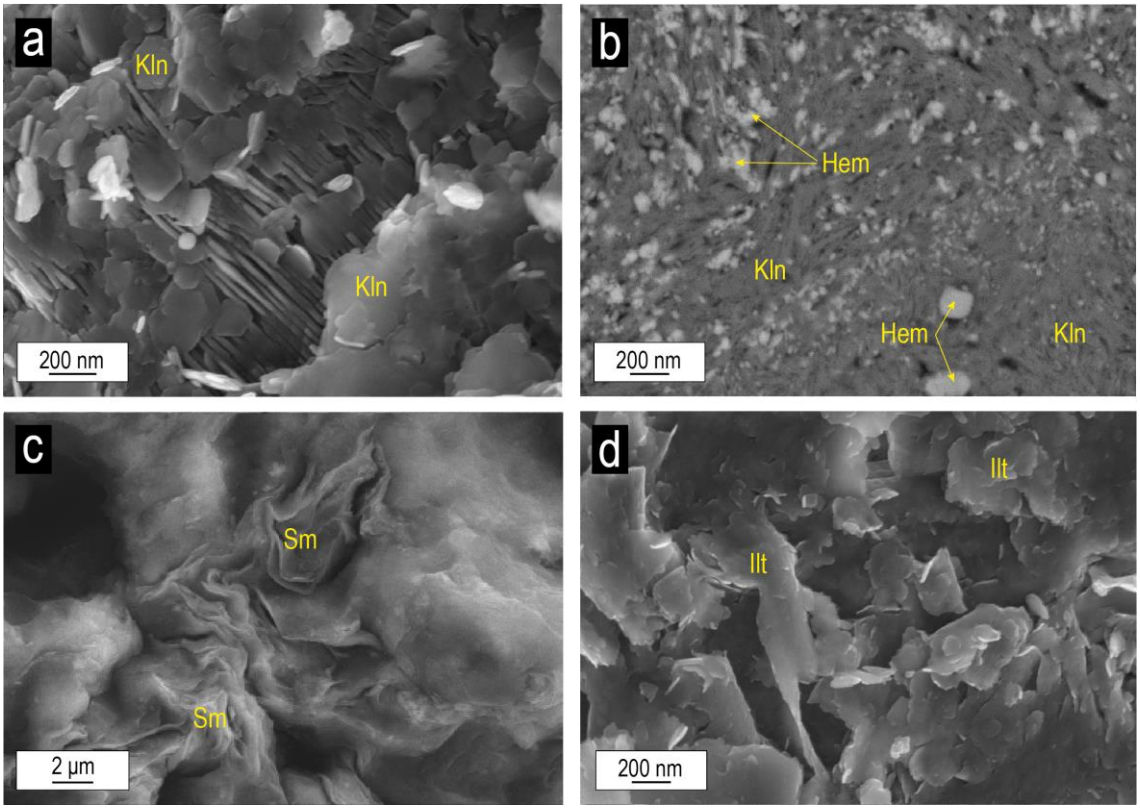

Fig. 5.2. Backscattered and secondary electron images of the matrix of palaeosol samples from the ALC and JO profiles showing: **a)** and **b)** kaolinite book-type aggregates and platy kaolinites displaying pseudohexagonal outlines; **c)** smectite with flake-type morphologies; **d)** anhedral illitic phases. *Kln*=kaolinite, *Hem*=hematite, *Sm*=smectite, *Ilt*=illitic phases. (Modified from Laita et al., 2020).

Laita et al. (2020) described a decrease in the authigenic kaolinite content towards the top of the profiles that coincided with an increase in authigenic smectite and detrital illitic phases content, which reflected a decrease in the chemical weathering intensity related with a change from warm/humid to colder/drier conditions.

Due the aforementioned reasons, samples from two profiles of those described by Laita et al. (2020) (ALC and JO) were selected for the NanoSIMS study. Samples were chosen due to their high content in authigenic kaolinite and smectite, whose isotopic composition can yield information about the palaeoenvironment and palaeotemperature in which they were generated. Three samples correspond to lower, middle and upper palaeosol levels from the ALC profile (samples ALC-1, ALC-4 and ALC-8, respectively), and two other samples correspond to lower and upper palaeosol levels from the JO profile (samples JO-1 and JO-5, respectively), which are laterally equivalent to those of the ALC profile (Fig. 5.1b). The samples from the lower and middle palaeosol levels (ALC-1, ALC-4, and JO-1) are rich in authigenic kaolinite, whereas the samples from the upper levels (ALC-8 and JO-5) contain authigenic smectite (Fig. 5.1a and c).

3. EXPERIMENTAL SECTION

3.1 Standard reference analysis

The isotopic compositions of pure powder standards of kaolinite and smectite were measured at the Nucleus Laboratory of the University of Salamanca (Spain) to obtain reference values. A mass spectrometer (SIRA II) operating in dual-inlet mode was used for the $^{18}O/^{16}O$ and D/H analysis of oxygen and hydrogen. The oxygen and hydrogen isotope compositions of the standards were reported in δ notation relative to SMOW (standard mean ocean water) (Table 5.1). Following the equation given by Hoefs (1997):

$$\delta_{in}‰ = [(R_{(Sample)} - R_{(Standard)})/R_{(Standard)}] \times 1000$$

where "R" represents the measured isotope ratio, and knowing the $\delta^{18}O_{SMOW}$ and δD_{SMOW} values of the kaolinite and smectite standards reported by the reference laboratory, the $^{18}O/^{16}O$ and D/H ratios of the standards can be calculated as follows:

$$^{18}O/^{16}O_s = [(\delta^{18}O_s \times {}^{18}O/^{16}O_{SMOW}) /1000] + {}^{18}O/^{16}O_{SMOW}$$

$$D/H_s = [(\delta D_s \times D/H_{SMOW})/1000] + D/H_{SMOW}$$

where *s* is the powder standard (kaolinite or smectite) and the SMOW is the standard mean ocean water: $^{18}O/^{16}O_{SMOW} = 1.99 \times 10^{-3}$ and $D/H_{SMOW} = 1.58 \times 10^{-4}$ (Craig, 1961).

Table 5.1. $\delta^{18}O$ and δD relative to SMOW for the standards reported by the reference laboratory and calculated oxygen and hydrogen ratios.

	Referenced standards data			
	$^{18}O/^{16}O$ Ratio	**$\delta^{18}O_{SMOW}$ (‰)**	**D/H Ratio**	**δD_{SMOW} (‰)**
Kaolinite	2.03E-03	19.8	1.48E-04	-62.4
Smectite	2.03E-03	18.9	1.45E-04	-79.4

3.2 NanoSIMS analysis of the standards

The oxygen and hydrogen isotopes of the kaolinite and smectite standards were then measured by a CAMECA NanoSIMS 50L at the IPREM (CNRS-UPPA, Pau, France), equipped with a Cs^+ ion source and seven parallel electron multiplier detectors.

The standards were dispersed on a carbon tape and coated with 5 nm of gold using a Cressington 108 Auto Sputter Coater (Cressington, Watford, UK). Two areas of 30 x 30 μm^2 were pre-sputtered with Cs^+ ions in order to optimize the secondary ion yield. In each area, several spots of 1 x 1 μm^2 were analysed, firstly applying a magnetic field allowing the separation of the $^{18}O/^{16}O$ isotopes, and subsequently with a magnetic field adequate for the separation of the D/H isotopes (the distance in mass between O and H prevents the positioning of the electron multiplier detectors in a configuration allowing all isotopes to be measured simultaneously, so two different calibrations were used).

Each spot analysed was rastered by the Cs^+ beam with 32 x 32 pixels and a measuring time of 132 μs/pixel, with a Cs^+ current of 2.0-5.0 pA. Each spot was measured 270 times, organized in 10 blocks of 27 measurements each, resulting in 1 minute of measurement per spot. The average was calculated and corrected for the electron multiplier yield and dead time and for the background collected during the analysis, to obtain the resulting isotopic ratio. The aging of the detectors was also adjusted at the start of each analysis session. The use of an entrance slit allowed the optimization of mass resolution to 6000–8000 in order to resolve possible isotopic interferences. The isotopic ratios obtained by NanoSIMS for the kaolinite and smectite standards can be found in Table 5.2.

The ratios obtained for the kaolinite and smectite standards, in comparison with the ratios determined at the reference laboratory, were used for calibrating the instrumental mass fractionation (IMF) in the O and H isotope compositions of the samples by applying the formulae $\alpha_{IMF}=(^{18}O/^{16}O_m)/(^{18}O/^{16}O_r)$, and $\alpha_{IMF}=(D/H_m)/(D/H_r)$, where *m* is the ratio measured by NanoSIMS and *r* is the ratio reported by the reference laboratory. The instrumental mass fractionation was calibrated with the standards in each session of analysis (Table 5.2).

Table 5.2. $^{18}O/^{16}O$ and D/H ratios obtained for the kaolinite and smectite standards during the different NanoSIMS analytical sessions and the α_{IMF} obtained for each ratio. *Kln*=kaolinite, *Sm*=smectite, *SD*=standard deviation.

Session 1 (Kln)				Session 2 (Kln)				Session 3 (kln)		Session 4 (Sm)				Session 5 (Sm)		Session 6 (Kln)				Session 7 (Sm)			
$^{18}O/^{16}O$	α_{IMF}	D/H	α_{IMF}	$^{18}O/^{16}O$	α_{IMF}	D/H	α_{IMF}	$^{18}O/^{16}O$	α_{IMF}	$^{18}O/^{16}O$	α_{IMF}	D/H	α_{IMF}	D/H	α_{IMF}	$^{18}O/^{16}O$	α_{IMF}	D/H	α_{IMF}	$^{18}O/^{16}O$	α_{IMF}	D/H	α_{IMF}
1.92E-03	0.95	1.67E-04	1.13	2.01E-03	0.99	1.47E-04	0.99	1.98E-03	0.98	1.92E-03	0.95	1.33E-04	0.90	1.51E-04	1.02	2.06E-03	1.01	0.00	0.81	1.97E-03	0.97	1.34E-04	0.92
1.98E-03	0.97	1.83E-04	1.24	1.98E-03	0.98	1.43E-04	0.96	1.97E-03	0.97	2.00E-03	0.98	1.11E-04	0.75	1.53E-04	1.03	1.98E-03	0.97	0.00	0.82	2.04E-03	1.01	1.33E-04	0.92
1.91E-03	0.94	1.71E-04	1.15	1.98E-03	0.97	1.45E-04	0.98	1.92E-03	0.95	1.97E-03	0.97	1.20E-04	0.81	1.35E-04	0.91	1.97E-03	0.97	0.00	0.84	2.03E-03	1.00	1.22E-04	0.84
1.95E-03	0.96	1.90E-04	1.28	2.22E-03	1.09	1.42E-04	0.96	1.94E-03	0.95	2.01E-03	0.99	1.12E-04	0.76	1.37E-04	0.92	2.01E-03	0.99	0.00	0.86	2.05E-03	1.01	1.25E-04	0.86
1.97E-03	0.97	1.86E-04	1.26	1.90E-03	0.93	1.48E-04	1.00	2.05E-03	1.01	2.05E-03	1.01	1.39E-04	0.94	1.47E-04	0.99	2.03E-03	1.00	0.00	0.86	2.06E-03	1.02	1.56E-04	1.07
1.96E-03	0.97	1.99E-04	1.34	2.06E-03	1.01	1.43E-04	0.96	2.02E-03	0.99	2.06E-03	1.02	1.60E-04	1.08	1.32E-04	0.89	2.02E-03	0.99	0.00	0.85	2.07E-03	1.02	1.25E-04	0.86
1.96E-03	0.96	1.92E-04	1.30	1.98E-03	0.97	1.46E-04	0.98	2.01E-03	0.99	2.05E-03	1.01	1.27E-04	0.86	-	-	2.02E-03	0.99	0.00	0.80	2.07E-03	1.02	1.28E-04	0.88
1.91E-03	0.94	1.52E-04	1.03	2.16E-03	1.06	1.43E-04	0.97	1.99E-03	0.98	2.09E-03	1.03	1.31E-04	0.89	-	-	1.99E-03	0.98	0.00	0.77	2.08E-03	1.02	1.23E-04	0.84
1.95E-03	0.96	1.86E-04	1.26	2.11E-03	1.04	-	-	1.93E-03	0.95	2.05E-03	1.01	9.46E-05	0.64	-	-	2.00E-03	0.98	0.00	0.79	1.98E-03	0.98	1.23E-04	0.85
1.96E-03	0.97	1.50E-04	1.01	1.89E-03	0.93	-	-	1.99E-03	0.98	2.09E-03	1.03	1.27E-04	0.86	-	-	2.05E-03	1.01	0.00	0.85	-	-	1.22E-04	0.84
1.91E-03	0.94	1.72E-04	1.16	2.04E-03	1.00	-	-	2.04E-03	1.00	2.09E-03	1.03	1.30E-04	0.88	-	-	2.05E-03	1.01	0.00	0.78	-	-	1.24E-04	0.85
1.94E-03	0.95	1.34E-04	0.91	1.83E-03	0.90	-	-	1.93E-03	0.95	2.09E-03	1.03	1.14E-04	0.77	-	-	-	-	0.00	0.81	-	-	1.32E-04	0.91
2.00E-03	0.98	1.39E-04	0.94	2.00E-03	0.98	-	-	1.93E-03	0.95	2.02E-03	0.99	1.24E-04	0.84	-	-	-	-	0.00	0.82	-	-	1.37E-04	0.94
2.04E-03	1.00	1.06E-04	0.71	1.99E-03	0.98	-	-	2.03E-03	1.00	1.98E-03	0.97	1.50E-04	1.01	-	-	-	-	-	-	-	-	1.41E-04	0.97
1.98E-03	0.97	1.35E-04	0.91	2.09E-03	1.03	-	-	1.94E-03	0.95	1.96E-03	0.96	1.76E-04	1.19	-	-	-	-	-	-	-	-	1.28E-04	0.88
2.03E-03	1.00	1.36E-04	0.92	2.04E-03	1.00	-	-	1.91E-03	0.94	1.95E-03	0.96	1.99E-04	1.34	-	-	-	-	-	-	-	-	1.23E-04	0.85
2.00E-03	0.98	1.30E-04	0.88	2.03E-03	1.00	-	-	-	-	1.94E-03	0.95	1.57E-04	1.06	-	-	-	-	-	-	-	-	-	-
2.02E-03	0.99	1.27E-04	0.86	2.04E-03	1.00	-	-	-	-	1.94E-03	0.96	1.40E-04	0.94	-	-	-	-	-	-	-	-	-	-
2.04E-03	1.00	1.50E-04	1.01	1.91E-03	0.94	-	-	-	-	1.94E-03	0.96	2.18E-04	1.47	-	-	-	-	-	-	-	-	-	-
2.00E-03	0.98	1.43E-04	0.97	2.05E-03	1.01	-	-	-	-	1.90E-03	0.94	1.45E-04	0.98	-	-	-	-	-	-	-	-	-	-
2.02E-03	0.99	1.38E-04	0.93	1.97E-03	0.97	-	-	-	-	1.91E-03	0.94	1.70E-04	1.15	-	-	-	-	-	-	-	-	-	-
2.02E-03	0.99	1.50E-04	1.02	1.98E-03	0.97	-	-	-	-	1.94E-03	0.96	2.18E-04	1.47	-	-	-	-	-	-	-	-	-	-
2.00E-03	0.98	1.35E-04	0.91	1.97E-03	0.97	-	-	-	-	1.93E-03	0.95	1.74E-04	1.18	-	-	-	-	-	-	-	-	-	-
-	-	1.41E-04	0.95	2.06E-03	1.01	-	-	-	-	-	-	-	-	-	-	-	-	-	-	-	-	-	-
1.98E-03	**0.97**	**1.55E-04**	**1.04**	**2.01E-03**	**0.99**	**1.44E-04**	**0.98**	**1.97E-03**	**0.97**	**2.00E-03**	**0.98**	**1.46E-04**	**0.99**	**1.42E-04**	**0.96**	**2.02E-03**	**0.99**	**1.21E-04**	**0.82**	**2.04E-03**	**1.00**	**1.30E-04**	**0.89**
±4.18E-05	**±0.02**	**±2.49E-05**	**±0.17**	**±8.38E-05**	**±0.04**	**±2.52E-06**	**±0.02**	**±4.64E-05**	**±0.02**	**±6.40E-05**	**±0.03**	**±3.34E-05**	**±0.23**	**±9.09E-06**	**±0.06**	**±3.01E-05**	**±0.01**	**±4.52E-06**	**±0.03**	**±3.83E-05**	**±0.02**	**±9.13E-06**	**±0.06**

3.3 Preparation of palaeosols for analysis

The samples were prepared for analysis by NanoSIMS in order to evaluate the potential of this technique for analysing areas rich in these minerals and determining their isotopic composition.

Thin sections were prepared from the five samples and studied using a Carl Zeiss Merlin field emission scanning electron microscope (FESEM) equipped with an Oxford energy-dispersive X-ray (EDS) detector at the University of Zaragoza (Zaragoza, Spain). The purpose of the FESEM imaging was to find areas in each sample enriched in the clay minerals suitable for isotopic analysis. Additionally, thick polished sections of samples ALC-1 and ALC-4 embedded in epoxy resin were also prepared in order to evaluate which method of sample preparation (thin section or thick polished section) was better for carrying out the isotopic analysis of clay minerals by NanoSIMS.

The common geological thin sections (27 x 45 mm, 30 μm thick) are larger than the NanoSIMS sample holder (Ø=25.4 mm), so they were cut smaller, and a custom metal sample holder was designed and manufactured in-house at the SIAME laboratory of the University of Pau and the Pays de l'Adour (France) so the thin sections would fit in the NanoSIMS sample holder and thus be positioned for analysis perpendicular to the primary ion beam.

The interlayer and absorbed water in clay minerals can exchange with the atmospheric water vapour within a few hours (Savin and Hsieh, 1998), and surface contamination can lead to a high background in the hydrogen measures (Hu et al., 2014). These factors could result in lower measured δD values (Bauer and Vennemann., 2014).

To minimize these problems, both the thin sections and the thick polished sections were heated at 150 ºC for at least 2h to remove the absorbed atmospheric water. Afterwards, they were coated with 5 nm of gold using a Cressington 108 Auto Sputter Coater (Cressington, Watford, UK) and rapidly placed inside the NanoSIMS under vacuum in order to prevent the reabsorption of water. Additionally, they were kept in the vacuum chamber of the equipment overnight before the oxygen analyses and for a week before the hydrogen analyses to ensure the removal of remaining gases and water that could be trapped within the sample. The resulting pressure in the analysis chamber was $4x10^{-11}$ mbar, which is the same pressure that is achieved without any sample in the chamber.

3.4 NanoSIMS imaging

Elemental images of the ions $^{12}C^-$, $^{16}O^-$, $^{18}O^-$, $^{28}Si^-$, $^{27}Al^{16}O^-$ and $^{56}Fe^{16}O^-$ were measured in preselected areas from thin sections. The cluster ions $^{27}Al^{16}O^-$ and $^{56}Fe^{16}O^-$ were used to enhance the secondary ion yield obtained for Al and Fe, in the form of negative secondary ions (an opposite polarity to the positive primary ion beam is required by the coaxial optics). Mass calibration was performed using the kaolinite and smectite standards.

Areas of 40 x 40 μm^2 were pre-sputtered with Cs^+ ions and analysed using a 2.0 pA primary ion current. They were measured with 256 x 256 pixels with a dwell time of 5 ms/pixel. Two planes were consecutively analysed and stacked to obtain the final image using the software WinImage (CAMECA).

The visualisation of the different elements facilitated the identification of pure zones of kaolinite and smectite for the following isotopic analyses, and the exclusion of iron oxides and oxyhydroxides and other silicates. The size of the primary ion beam was calculated by the knife-edge method (16–84% criterion) (Malherbe et al., 2016) in order to determine the spatial resolution achieved by this method. By this criterion, the probe size was 70 nm, which allowed the separation of the different nanoscale mineral components present on the selected area.

3.5 NanoSIMS isotopic analysis

After the image acquisition, isotopic measurements were taken at different selected points containing kaolinite or smectite within those areas. The same instrumental conditions as those used for the measurement of the standards were used; an entrance slit was also used to optimize the mass resolution to 6000–8000, and the aging of the detectors was likewise adjusted at the start of each analysis session. Two different magnetic fields were used to collect, firstly, the $^{18}O/^{16}O$ isotopic ratio and, subsequently, the D/H ratio in the same spots. The same analysis conditions were used for O and H measurements. However, slightly different conditions were used for the analysis of thin sections and thick polished sections.

In thin sections, oxygen and hydrogen analyses were carried out in kaolinites of the samples ALC-1, ALC-4 and JO-1 and smectites of the samples ALC-8 and JO-5. Spots of 1 x 1 μm^2 were analysed with 32 x 32 pixels and a dwell time of 132 μs/pixel and a 2.0 pA Cs^+ current, in 10 blocks of 27 measurements (1 min analysis time). The use of a small current as well as short measuring times were necessary due to the thinness of the sample, which was otherwise rapidly consumed.

In thick polished sections, oxygen analyses were carried out in kaolinites from samples ALC-1 and ALC-4, and hydrogen analyses in kaolinites from ALC-1. In a similar

manner to thin sections, spots of 1 x 1 μm² were measured with 32 x 32 pixels, in 10 blocks of 27 measurements. However, the use of thicker samples permitted the use of higher measuring times and beam current without consuming the sample, which resulted in a higher signal for the measured isotopes and thus better statistics. A measuring time of 244 μs/pixel was used (which corresponds to 1.5 min analysis time), with a Cs^+ current of 5.0 pA. This higher current and dwell time also helped compensate for the lower secondary ion yield caused by the deterioration of the pressure in the analysis chamber due to the degassing of the epoxy resin.

In all cases, the resulting isotopic ratio was corrected for the electron multiplier yield and dead time as well as the background collected during the analysis.

4. RESULTS AND DISCUSSION

4.1 NanoSIMS imaging

The optical imaging of the CCD camera of the NanoSIMS allowed to locate the preselected regions by FESEM in the thin sections. Then elemental images were obtained for the ions $^{16}O^-$, $^{18}O^-$, $^{28}Si^-$, $^{27}Al^{16}O^-$, $^{56}Fe^{16}O^-$ and $^{12}C^-$ in these regions by analysing areas of 40 x 40 μm² (Fig. 5.3). The submicron resolution of NanoSIMS reveals that the clay minerals can be differentiated from the oxides and oxyhydroxides in the samples by their higher content in Si and Al ($^{28}Si^-$, $^{27}Al^{16}O^-$ maps in Fig. 5.3a and b). The absence of K allowed to discard the presence of illitic phases. In addition, although the areas previously selected in the samples by FESEM were only enriched in kaolinite or smectite, the presence of Na also enabled the differentiation of smectite from kaolinite.

In some samples, the high image resolution also allows the outlines of kaolinite crystals to be identified (Fig. 5.3a).

The topography of the surface plays an important role in the reproducibility and accuracy of the NanoSIMS measurements (Höschen et al., 2013; Thomen et al., 2014). When a rough, uneven sample surface is present, the impact of the primary ion beam in certain analysis zones may not be perpendicular, which results in different secondary ion yields depending on the angle of the beam and leads to artefacts in the image. Accordingly, the quality of the image is directly related with the polishing of the sample (Höschen et al., 2015).

Unfortunately, palaeosol samples can occasionally be poorly consolidated, leading to problems with the polishing of sections, since the surface of the sample can undergo plucking and deformation (Camuti and McGuire, 1999). For this reason, two different commonly used preparation methods were tested, thin sections and thick polished sections.

However, thick polished sections have a high content of epoxy resin. The resin can capture atmospheric air and water during the embedding process, resulting in a degassing of the sample in the high vacuum of the analysis chamber. In this case, degassing led to deterioration of the high vacuum, in turn leading to lower secondary ion yields for the ions and thus lower-resolution elemental images. As pointed out above, this effect was partially compensated by using longer dwell times and higher Cs^+ currents, but still the results obtained in thick polished sections were worse than in thin sections. For this reason, the study focused in greater detail on the thin sections, where the low epoxy content (just a cover) produced more favourable vacuum conditions in the analysis chamber for elemental imaging and oxygen and hydrogen isotopic analyses.

The palaeosol samples used in this study showed varying degrees of consolidation. For example, sample JO-1 was better consolidated, so a good polishing could be achieved in the thin section. This is reflected in the NanoSIMS images obtained from this sample, where the resolution is high and kaolinite crystals can be clearly differentiated from the iron oxides and oxyhydroxides by their higher content in Si and Al ($^{28}Si^-$ and $^{27}Al^{16}O^-$ maps in Fig. 5.3a).

In comparison, sample ALC-4 was poorly consolidated, and part of it was removed during the polishing of the thin section, giving rise to a more irregular surface, which clearly affects the quality of the elemental images (Fig. 5.3b). The areas with little or no signal correspond to cracks or areas where sections of the sample were lost during polishing, as well as to areas that are deeper due to the irregular surface.

However, although these differences in polishing make it more difficult to identify the outlines of kaolinite crystals, certain areas with higher Si and Al and lower Fe content are differentiated ($^{28}Si^-$, $^{27}Al^{16}O^-$ and $^{56}Fe^{16}O^-$ maps in Fig. 5.3b), making it possible to carry out the isotopic analysis of kaolinite in sample ALC-4.

On the other hand, the intensely coloured areas in the $^{12}C^-$ maps are probably dominated by resin (Fig. 5.3a), but some of the calcite nodules can also be differentiated (Fig. 5.3b). The pre-sputtering of the sample surface of the sections increases the secondary ion yield by caesium implantation in the surface and can also remove the surface resin, but the pre-sputtering should be careful in the thin section to prevent excessive consumption of the sample before analysis.

Elemental images can be overlaid to see the relationship between the elements and define areas for subsequent isotopic analyses (Fig. 5.4). In the case of the palaeosol samples, $^{28}Si^-$ and $^{27}Al^{16}O^-$ maps show a perfect overlay in the areas rich in clay minerals, which are clearly differentiated from iron oxides ($^{56}Fe^{16}O^-$ maps). Fig. 5.4 shows the overlaid $^{28}Si^-$, $^{27}Al^{16}O^-$ and $^{56}Fe^{16}O^-$ maps of 35 x 35 μm^2 in the thin sections of JO-1 and

ALC-4, where the isotopic ratios of kaolinite were measured in 1 x 1 μm² areas (white squares in Fig. 5.4).

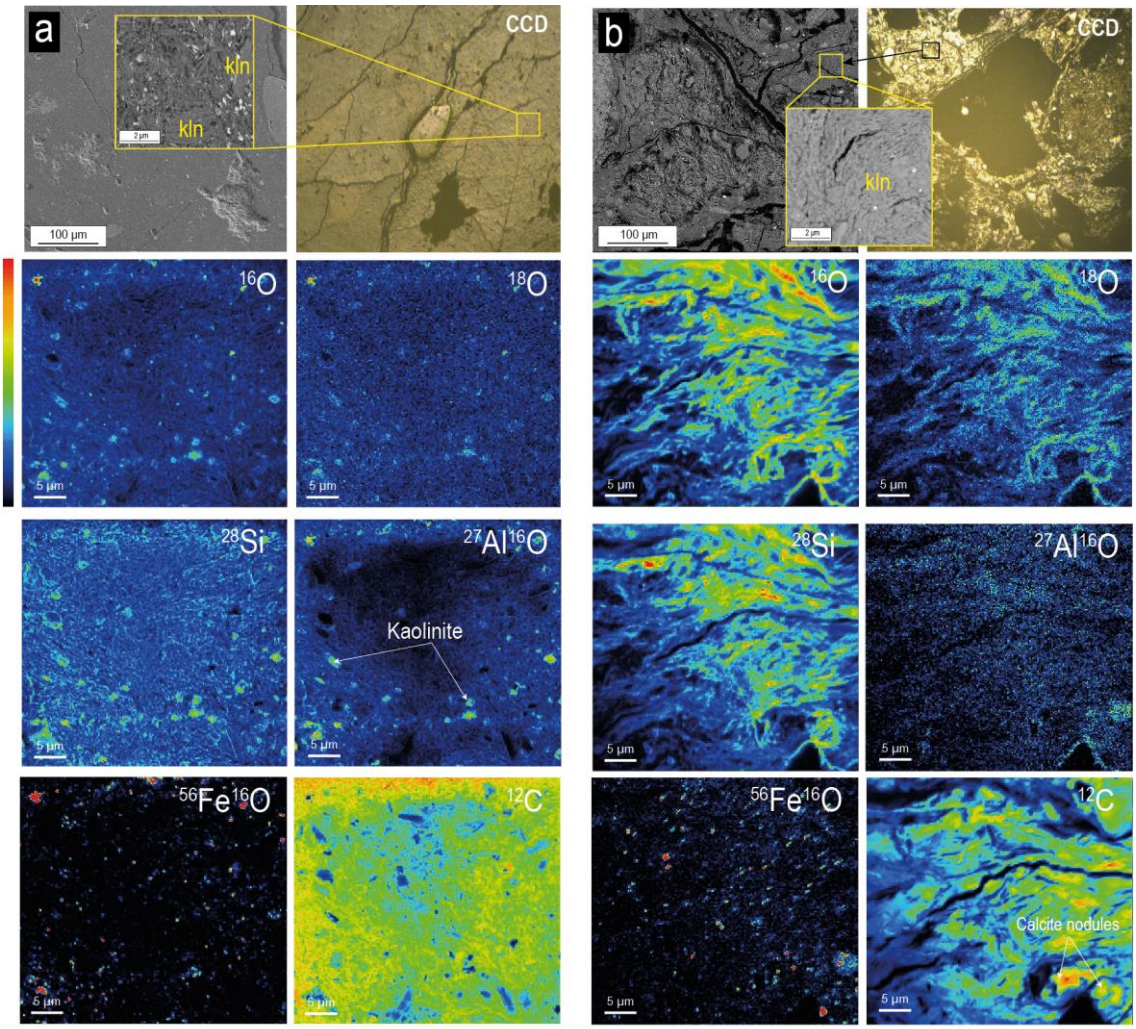

Fig. 5.3. 40 x 40 μm² elemental maps obtained for the ions $^{16}O^-$, $^{18}O^-$, $^{28}Si^-$, $^{27}Al^{16}O^-$, $^{56}Fe^{16}O^-$ and $^{12}C^-$ in the thin sections of samples JO-1 **(a)** and ALC-4 **(b)**. Images of the selected areas by FESEM and the same region observed in the CCD camera of the NanoSIMS are included to show the location of the maps in the sample. The images display kaolinite-rich areas ($^{16}O^-$, $^{18}O^-$, $^{28}Si^-$, $^{27}Al^{16}O^-$), iron-oxide-rich areas ($^{56}Fe^{16}O^-$) and areas with higher $^{12}C^-$ content, probably related to the resin or carbonates.

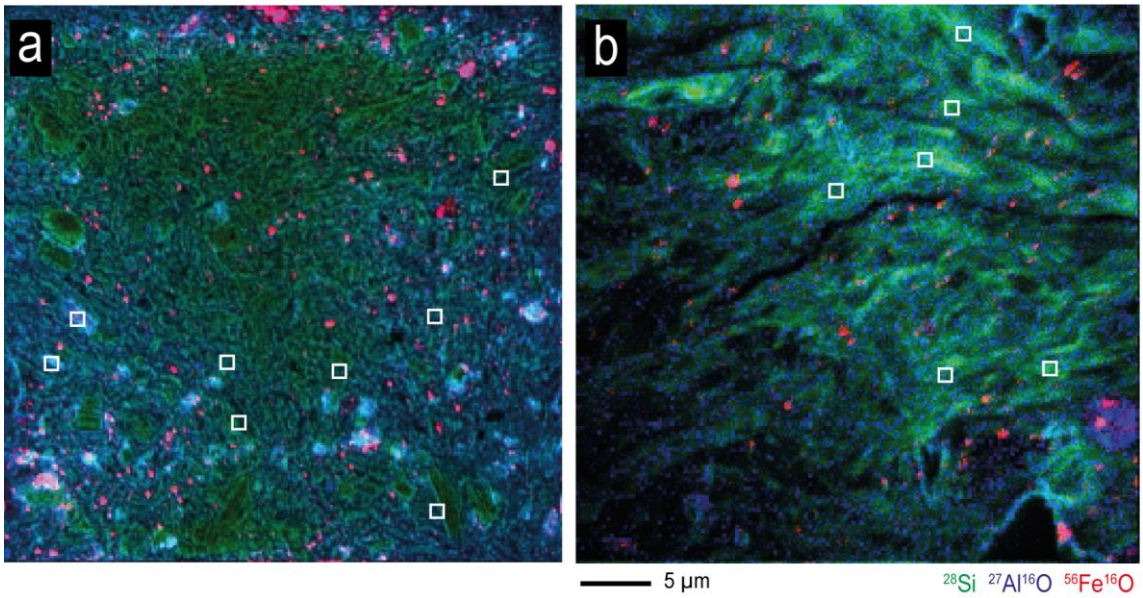

Fig. 5.4. Colour overlay of mapping of $^{28}Si^-$ (green), $^{27}Al^{16}O^-$ (blue) and $^{56}Fe^{16}O^-$ (red) in thin sections: **a)** colour overlay in sample JO-1, showing kaolinite outlines due to the good polishing; **b)** colour overlay in sample ALC-4, where kaolinite-rich areas (green and blue) can be differentiated from those with iron (red), but the bad polishing does not allow the kaolinite outlines to be distinguished. The white squares represent the 1 x 1 μm^2 points of the isotopic analyses.

4.2 NanoSIMS isotopical analysis

4.2.1 Oxygen and hydrogen ratios in the clay minerals

The average $\delta^{18}O$ and δD values relative to SMOW obtained for the clay minerals in the thin sections from the ALC and JO profiles are represented in Fig. 5.5. The detailed isotope values for the kaolinite and smectite obtained in the thin sections and the thick polished sections can be found in Table 5.3.

Kaolinite from sample ALC-1 (bottom) displays average $\delta^{18}O$ and δD values of 18‰ (± 15‰) and -82‰ (± 36‰) respectively, which are higher than those for the kaolinite from sample ALC-4 (middle): $\delta^{18}O$ = 14‰ (± 4‰) and δD = -97‰ (± 37‰). The smectite from sample ALC-8 (top) shows lower ratios than the kaolinites from the lower levels, with average $\delta^{18}O$ and δD values of 11‰ (± 6‰) and -180‰ (± 40‰), respectively (Fig. 5.5a). Regarding the JO profile, the kaolinite from sample JO-1 (bottom) shows $\delta^{18}O$ and δD values of 81‰ (± 10‰) and 24‰ (± 42‰) respectively, which are higher than those for the smectite from sample JO-5 (top): $\delta^{18}O_{SMOW}$ = 13 ‰ (± 14‰) and δD_{SMOW} = -167‰ (± 87‰) (Fig. 5.5b). Comparing the two profiles, the kaolinite from the JO profile presents higher $\delta^{18}O$ and δD values than the kaolinite from the ALC profile (samples ALC-1 and ALC-4). The smectite presents somewhat higher $\delta^{18}O$ and δD values in the JO profile (sample JO-1) than in the ALC profile (sample ALC-8), but this difference is much lower than that observed between the kaolinites from the two profiles. In any case,

there is a clear decrease in the oxygen and hydrogen isotope values of the clay minerals from bottom to top in both profiles (Table 5.3 and Fig. 5.5).

The $^{18}O/^{16}O$ of kaolinite was also measured in the thick polished sections of samples ALC-1 and ALC-4, and the D/H ratio was also obtained in sample ALC-1. As in the thin sections, a decrease in the average $\delta^{18}O$ value of kaolinite from sample ALC-1, (34‰ (± 4‰)), to sample ALC-4 (-17‰ (± 4‰)), is observed in the thick polished sections. However, the $\delta^{18}O$ and δD values achieved by NanoSIMS for the thick polished sections are different from those obtained for the same samples in the thin sections. In sample ALC-1, the $\delta^{18}O$ of the kaolinite is higher in the thick polished section (34‰ (± 4‰)) than in the thin section (18‰ (± 15‰)). In sample ALC-4, by contrast, the $\delta^{18}O$ of the kaolinite is lower in the thick polished section (-17‰ (± 4‰)) than in the thin section (14‰ (± 4‰)). In addition, the δD value of the kaolinite in sample ALC-1, like the $\delta^{18}O$ value, is higher in the thick polished section (-64‰ (± 43‰)) than in the thin section (-82‰ (± 36‰)).

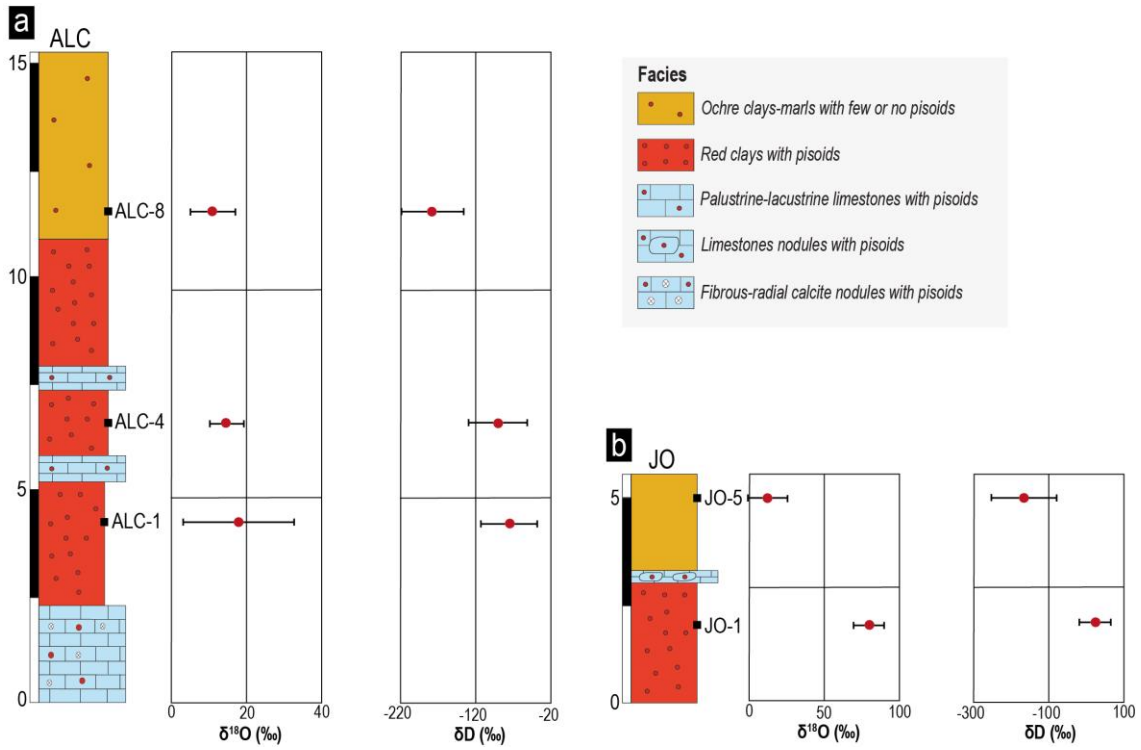

Fig. 5.5. Stratigraphic logs of the ALC **(a)** and JO **(b)** Lower Barremian continental profiles including the palaeosol levels (modified from Laita et al., 2020). The $\delta^{18}O$ and δD average values (with the standard deviations) obtained in each palaeosol sample are represented, showing a decrease from bottom to top in both profiles.

Table 5.3. $^{18}O/^{16}O$ and D/H and $\delta^{18}O$ and δD values obtained for the kaolinite and smectite in the palaeosol samples. *SD*=standard deviation.

Sample	$^{18}O/^{16}O$	D/H	$\delta^{18}O$(‰)	δD(‰)	Sample	$^{18}O/^{16}O$	D/H	$\delta^{18}O$(‰)	δD(‰)	Sample	$^{18}O/^{16}O$	D/H	$\delta^{18}O$(‰)	δD(‰)	Sample	$^{18}O/^{16}O$	$\delta^{18}O$(‰)
ALC-1 Kaolinite (Thin section) Analytical session: 1	2.05E-03	1.38E-04	29	-129	ALC-1 Kaolinite (Thick polished section) Analytical session: 2	2.07E-03	1.47E-04	37	-72	ALC-4 Kaolinite (Thin section) Analytical session: 3	2.01E-03	1.45E-04	8	-81	ALC-1 Kaolinite (Thick polished section) Analytical session: 3	1.96E-03	-16
	2.07E-03	1.47E-04	38	-73		2.06E-03	1.55E-04	33	-17		2.03E-03	1.31E-04	19	-169		1.96E-03	-16
	2.06E-03	1.44E-04	36	-91		2.05E-03	1.56E-04	27	-13		2.03E-03	1.43E-04	18	-97		1.95E-03	-23
	2.07E-03	1.43E-04	36	-93		2.05E-03	1.53E-04	29	-34		2.02E-03	1.45E-04	16	-80		1.96E-03	-17
	2.06E-03	1.40E-04	35	-113		2.07E-03	1.44E-04	36	-88		2.02E-03	1.49E-04	16	-57		1.97E-03	-10
	2.02E-03	1.37E-04	11	-132		2.07E-03	1.40E-04	39	-116		2.01E-03	1.47E-04	11	-71		1.95E-03	-22
	2.03E-03	1.47E-04	19	-69		2.06E-03	1.41E-04	31	-107		-	1.46E-04	-	-79		1.96E-03	-19
	2.01E-03	1.52E-04	8	-39		2.06E-03	-	36	-		-	1.34E-04	-	-153		1.96E-03	-14
	2.00E-03	1.49E-04	1	-57		2.07E-03	-	36	-		-	1.49E-04	-	-57		1.96E-03	-17
	2.00E-03	1.53E-04	1	-29		-	-	-	-		-	1.43E-04	-	-93		1.96E-03	-15
	2.03E-03	-	20	-		-	-	-	-		-	1.38E-04	-	-126		1.96E-03	-15
	2.01E-03	-	6	-		-	-	-	-		-	-	-	-		-	-
	2.00E-03	-	1	-		-	-	-	-		-	-	-	-		-	-
	2.01E-03	-	6	-		-	-	-	-		-	-	-	-		-	-
Average	**2.03E-03**	**1.45E-04**	**18**	**-82**		**2.06E-03**	**1.48E-04**	**34**	**-64**		**2.02E-03**	**1.43E-04**	**14**	**-97**		**1.96E-03**	**-17**
SD	**(±2.91E-05)**	**(±5.64E-06)**	**(±15)**	**(±36)**		**(±8.45E-06)**	**(±6.75E-06)**	**(±4)**	**(±43)**		**(±8.95E-06)**	**(±5.86E-06)**	**(±4)**	**(±37)**		**(±7.59E-06)**	**(±4)**

Sample	$^{18}O/^{16}O$	D/H	$\delta^{18}O$(‰)	δD(‰)	Sample	$^{18}O/^{16}O$	D/H	$\delta^{18}O$(‰)	δD(‰)	Sample	$^{18}O/^{16}O$	D/H	$\delta^{18}O$(‰)	δD(‰)
ALC-8 Smectite (Thin section) Analytical session: 4 and 5	2.00E-03	1.32E-04	3	-164	JO-1 Kaolinite (Thin section) Analytical session: 3 and 6	2.17E-03	1.65E-04	87	45	JO-5 Smectite (Thin section) Analytical session: 4 and 7	2.03E-03	1.35E-04	17	-145.7
	2.00E-03	1.20E-04	4	-240		2.14E-03	1.61E-04	72	16		2.00E-03	1.28E-04	5	-187.0
	2.01E-03	1.29E-04	10	-183		2.13E-03	1.71E-04	70	81		2.06E-03	1.33E-04	32	-156.6
	2.02E-03	1.28E-04	11	-187		2.17E-03	1.71E-04	86	82		2.06E-03	1.39E-04	32	-118.2
	2.03E-03	1.38E-04	18	-126		2.13E-03	1.68E-04	69	65		2.04E-03	1.35E-04	23	-144.5
	2.03E-03	1.27E-04	17	-193		2.15E-03	1.57E-04	78	-7		1.98E-03	1.34E-04	-5	-151.9
	2.03E-03	1.39E-04	18	-121		2.16E-03	1.60E-04	84	12		2.03E-03	1.38E-04	17	-123.7
	2.01E-03	1.23E-04	8	-224		2.19E-03	1.70E-04	99	78		2.04E-03	1.23E-04	23	-220.1
	2.00E-03	1.30E-04	5	-180		-	1.55E-04	-	-22		2.04E-03	1.35E-04	24	-146.8
	-	-	-	-		-	1.55E-04	-	-18		1.99E-03	1.23E-04	-4	-224.1
	-	-	-	-		-	1.65E-04	-	43		2.00E-03	1.23E-04	1	-218.8
	-	-	-	-		-	1.52E-04	-	-37		1.99E-03	-	1	-
	-	-	-	-		-	1.58E-04	-	-2		1.99E-03	-	-3	-
	-	-	-	-		-	1.68E-04	-	61		-	-	-	-
	-	-	-	-		-	1.65E-04	-	47		-	-	-	-
	-	-	-	-		-	1.58E-04	-	-1		-	-	-	-
	-	-	-	-		-	1.52E-04	-	-41		-	-	-	-
Average	**2.01E-03**	**1.30E-04**	**11**	**-180**		**2.15E-03**	**1.62E-04**	**81**	**24**		**2.02E-03**	**1.32E-04**	**13**	**-167**
SD	**(±1.20E-05)**	**(±6.67E-06)**	**(±6)**	**(±40)**		**(±3.42E-05)**	**(±6.65E-06)**	**(±10)**	**(±42)**		**(±2.79E-05)**	**(±6.14E-06)**	**(±14)**	**(±87)**

The obtained standard deviations for the hydrogen analysis in sample ALC-1 are similar in thin section and the thick polished section (36‰ and 43‰, respectively).

As previously mentioned, both analysis conditions consisted in spots of 1 x 1 μm^2 scanned with 32 x 32 pixels, during 270 measurements. However, a higher Cs^+ current was used in thick polished sections than in thin sections, 5.0 pA versus 2.0 pA Cs^+, and higher integration times in thick polished sections (1.5 min with a dwell time of 244 μs/pixel versus 1 min with 132 μs/pixel). These higher integration times could be the reason for the lower standard deviations obtained in the oxygen analyses from the thick polished sections (4 ‰) compared to those from the thin sections (4–18‰).

Nevertheless, despite the lower standard deviations obtained in the thick polished sections analyses, the differences in the $\delta^{18}O_{SMOW}$ and δD_{SMOW} compared with the thin sections could be related to their high content in epoxy resin. As pointed out above, the high content of epoxy resin in the thick polished sections can result in a degassing of the sample, affecting the high vacuum (Aboura and Moore, 2021) and thus leading to lower secondary ion yields and resulting in poor-quality elemental mapping. Furthermore, the resin can also produce interference in the H and O ratios (Stadermann et al., 2005). Due to the poor-quality imaging, therefore, the ratios measured in the thick polished section may be altered not only by the resin but also by other mineral phases present in the samples (e.g., Fe oxides, quartz or carbonates).

4.2.2 Palaeoclimatic deductions from the isotopic results

The decrease observed in the $\delta^{18}O_{SMOW}$ and δD_{SMOW} values from kaolinite to smectite in the studied palaeosols is indicative of an enrichment in the light isotopes ^{16}O and ^{1}H towards the top of the profiles, which could reflect a change in the palaeoclimatic conditions.

The kaolinite from sample JO-1 presented higher $\delta^{18}O_{SMOW}$ and δD_{SMOW} compared to those of the kaolinites from the ALC profile and the standards. This may indicate that this kaolinite underwent some process after its genesis during soil formation (e.g., diagenesis), altering its original isotopic signature. This is also supported by the mineralogical data reported by Laita et al. (2020), since this kaolinite displays larger crystals sizes than that of the ALC profile (see Fig. 5.1) and the average full width at half maximum (FWHM) value of the 001 reflections is lower (JO kaolinite=0.4; ALC kaolinite=0.5), indicating that is more crystalline. The characteristics of this kaolinite are compatible with a recrystallization process. For this reason, the $\delta^{18}O_{SMOW}$ and δD_{SMOW} values of this kaolinite are not used for the palaeoclimatic deductions. However, all these data show that the oxygen and hydrogen isotopic analysis by NanoSIMS allows

authigenic kaolinites (formed during soil development) to be discriminated from those recrystallized during diagenesis.

On the other hand, as the isotope values obtained by NanoSIMS in the thin sections are more consistent than those from the thick polished sections, the average $\delta^{18}O$ and δD values from thin sections relative to SMOW for kaolinites (samples ALC-1 and ALC-4) and smectites (samples ALC-8 and JO-5) are plotted on a $\delta^{18}O$-δD diagram (Fig. 5.6).

The $\delta^{18}O_{SMOW}$ and δD_{SMOW} values of kaolinite and smectite are within the range commonly reported for these minerals (Delgado and Reyes, 1996; Savin and Hsieh, 1998; Gilg et al., 2003; Fernández-Caliani et al., 2010; Mix and Chamberlain, 2014; Clauer et al., 2015; He et al., 2019).

The kaolinite isotopic compositions depict two points on the kaolinite line calculated at 20 ºC (Sheppard and Gilg, 1996) (Fig. 5.6a), whereas the smectite isotopic compositions are included between the smectite lines at 30 and 0 ºC reported by Mix and Chamberlain (2014) (Fig. 5.6b).

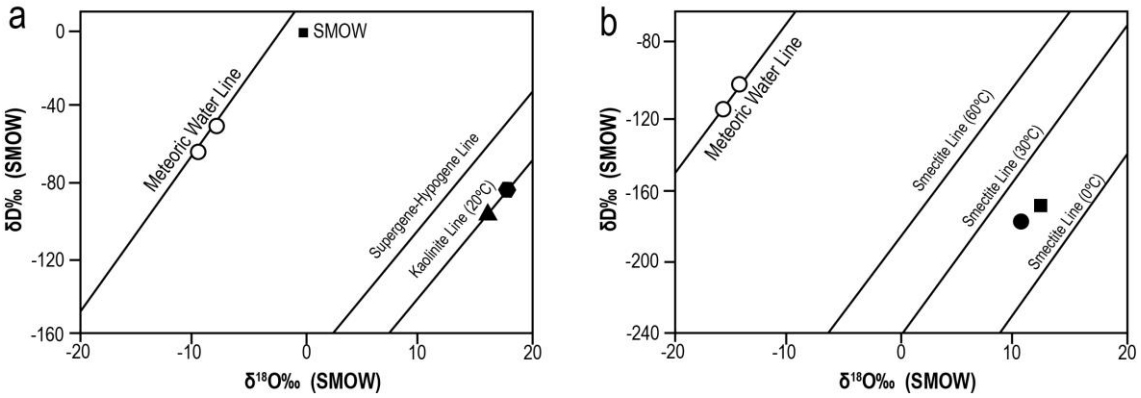

Fig. 5.6. a) Average $\delta^{18}O_{SMOW}$ and δD_{SMOW} values of kaolinite included in the bottom (black hexagon) (standard deviation: $\delta^{18}O$=±15‰ and δD=± 36‰) and middle levels (black triangle) (standard deviation: $\delta^{18}O$=±4‰ and δD=± 37‰) of the ALC profile. The supergene-hypogene line (Sheppard et al., 1969), the kaolinite weathering line at 20 ºC (Sheppard and Gilg, 1996), the meteoric water line (Craig, 1961), and the isotopic composition of modern ocean water (SMOW) are given as references. The open circles correspond to the oxygen and hydrogen isotopic composition of the water with which kaolinite formed in equilibrium at 21-22 ºC (same standard deviation that the kaolinite analyses); **b)** Average $\delta^{18}O_{SMOW}$ and δD_{SMOW} values of smectite included in the top level of the ALC profile (black circle) (standard deviation: $\delta^{18}O$=± 6‰ and δD=±40‰) and the top level of the JO profile (black square) (standard deviation: $\delta^{18}O$=± 14‰ and δD=± δD=±87‰). The smectite lines at 0 ºC, 30 ºC, 60 ºC (Mix and Chamberlain, 2014) and the meteoric water line (Craig, 1961) are given as references. The open circles correspond to the oxygen and hydrogen isotopic composition of the water with which smectite formed in equilibrium at 16–17 ºC (same standard deviation that the smectite analyses).

Previous investigations have indicated that Mesozoic kaolinites that formed in different environments preserved their original $^{18}O/^{16}O$ and D/H ratios (Savin and Epstein, 1970; Lawrence and Taylor, 1971; Sheppard, 1977).

As the kaolinite and smectite from the studied palaeosols have an authigenic origin (Laita et al., 2020), they may have formed in equilibrium with the environment, and their isotopic composition would thus depend on that of the meteoric water from which they crystallized (Savin and Epstein, 1970; Delgado and Reyes, 1996; Sheppard and Gilg, 1996).

The isotopic composition of kaolinite and smectite can thus give useful information about their origin during palaeosol formation, since equilibrium isotopic fractionation factors are a function of temperature (Delgado and Reyes, 1996; Fernández-Caliani et al., 2010).

The isotopic composition and temperature of the meteoric water from which the kaolinite and smectite crystallized can thus be estimated by combining the following equations:

[1] The meteoric-water equation $\delta D = 8\ \delta^{18}O + 10$ (Craig, 1961)

[2] The equations relating the isotopic fractionation of oxygen to temperature in the kaolinite-water or smectite-water system:

[2.1] $10^3 \ln \alpha_{k\text{-}w} = 2.76 \times 10^6 T^{-2} - 6.75$ for kaolinite (Sheppard and Gilg, 1996)

[2.2] $10^3 \ln \alpha_{sm\text{-}w} = 2.55 \times 10^6 T^{-2} - 4.05$ for smectite (Sheppard and Gilg, 1996)

[3] The equations relating the isotopic fractionation of hydrogen to temperature in the kaolinite-water or smectite-water system:

[3.1] $1000 \ln \alpha_{k\text{-}w} = -2.2 \times 10^6 T^{-2} - 7.7$ for kaolinite (Sheppard and Gilg, 1996)

[3.2] $1000 \ln \alpha_{sm\text{-}w} = -7.5 \times 10^6 T^{-2} + 27.37$ for smectite (Capuano, 1992)

Applying these equations, the crystallization temperatures deduced are 21–22 ºC for the kaolinites of samples ALC-1 and ALC-4, whereas the crystallization temperatures for the smectite in samples JO-5 and ALC-8 are 16–17 ºC.

The $\delta^{18}O$ and δD values inferred for the waters are $\delta^{18}O_{SMOW}$ = -8‰ and δD_{SMOW} = -49‰ for the kaolinite from sample ALC-1 and $\delta^{18}O_{SMOW}$ = -9‰ and δD_{SMOW} = -63‰ for the kaolinite from sample ALC-4. The $\delta^{18}O$ and δD values for the water of smectites are $\delta^{18}O_{SMOW}$ = -15‰ and δD_{SMOW} = -118‰ and $\delta^{18}O_{SMOW}$ = -13‰ and δD_{SMOW} = -106‰ for the smectites in samples ALC-8 and JO-5, respectively. All the calculated $\delta^{18}O$ and δD values for the waters plot on the meteoric water line (see Fig. 5.6). The standard deviations of these values are in the same range as those of the $\delta^{18}O$ and δD values for kaolinite and smectite (see the 4.2.1 section).

Lower $^{18}O/^{16}O$ ratios in kaolinites suggest colder intervals in the past (Giral-Kacmarcík et al., 1998), and the $\delta^{18}O$ and δD values of meteoric water decrease with the decrease in temperature, which should be reflected in the authigenic clays formed from this water (Savin and Hsieh, 1998).

Laita et al. (2020) described a decrease in the authigenic kaolinite and oxides and oxyhydroxides content, along with an increase in the authigenic smectite and detrital quartz and illite, from the bottom to the top of the lateritic profiles studied here. These changes reflect less intense chemical weathering towards the top of the profiles, perhaps associated with a change from warm and humid to generally colder and drier conditions.

The $\delta^{18}O$ and δD values obtained by NanoSIMS for kaolinite and smectite in the studied palaeosol samples agree with the change in climatic conditions from the bottom to the top of the lateritic profiles deduced by Laita et al. (2020) using mineralogical tools. The temperature calculated for the meteoric water also support this hypothesis, showing a decrease in temperature from 21–22 to 16–17 ºC during the early Barremian in the studied area.

4.3 Application of NanoSIMS in isotopic analyses of clay minerals

NanoSIMS reported an average $^{18}O/^{16}O$ ratio value for the kaolinite standard of $1.99x10^{-3}$ ($\pm 5.05x10^{-5}$) in the different analytical sessions and an average D/H value of $1.40x10^{-3}$ ($\pm 1.07x10^{-5}$). In the same way, the average $^{18}O/^{16}O$ ratio obtained by NanoSIMS for the smectite standard is $2.02\ x10^{-3}$($\pm 1.81x10^{-5}$) and the average D/H ratio reported for this mineral is $1.40x10^{-3}$ ($\pm 1.72x10^{-5}$). These values are close to those of the reference laboratory ($^{18}O/^{16}O=2.3x10^{-3}$ for kaolinite and smectite; $D/H=1.48x10^{-4}$ for kaolinite and $1.45x10^{-4}$ for smectite).

The $\delta^{18}O_{SMOW}$ and δD_{SMOW} obtained by NanoSIMS for kaolinite and smectite in the thin sections are within the range of values reported for these minerals in the literature. Although the standard deviations are in the range of 4–15‰ for $\delta^{18}O$ and 36–87‰ for δD.

The uncertainty (expressed as standard deviation) of the hydrogen measures of this study is in the range reported by other authors in previous studies (e.g., Piani et al., 2015; Lévy et al., 2019) for hydrogen analysis of samples containing hydrous silicates (50–97‰).

Lower uncertainties have been previously reported in the $\delta^{18}O$ values of carbonates (2.3‰) and melilites included in chondrites (3‰) analysed by NanoSIMS (Ito and Messenger, 2008; Bojanowski et al., 2015), but the spots used for these analyses are larger ($5 \times 5\ \mu m^2$) than the used in this study for the nanometre-sized clay minerals ($1 \times 1\ \mu m^2$). Also, the thickness of the sample played an important role in the measures, since

in the thin sections (30 μm thick) the dwell time had to be shorter than in the thick polished sections to not consume the sample and this could affect the precision of the analyses. A future study with thicker polished samples and lower epoxy resin content could be of interest to test if lower uncertainties can be achieved.

The results obtained from this study reflects, therefore, the potential of NanoSIMS for the acquisition of light isotope data (oxygen and hydrogen) in authigenic nanometer-sized clay minerals from palaeosols samples.

5 CONCLUSIONS

This study shows that, with suitable calibration using pure isotopic standards and appropriate sample preparation, NanoSIMS can represent a breakthrough in the isotopic study of nanometre-sized clay minerals.

The high spatial resolution and accuracy of NanoSIMS allowed the elemental mapping and analysis of the oxygen and hydrogen isotopic compositions of nanometre-sized clay minerals from early Barremian polymineralic palaeosol samples within a complex matrix, where conventional analytical techniques would have only provided average isotopic ratios of a mixture of several mineral phases.

The capacity of NanoSIMS to generate an elemental image of the sample surface permitted the precise localization of the minerals of interest. By the same token, the high spatial resolution enabled the measurement of the isotopic ratios in selected positions within the samples, excluding undesired mineral phases. The high sensitivity of the instrument made it possible to obtain isotopic ratios with a sufficient precision to distinguish changes in the $^{18}O/^{16}O$ and D/H isotopic composition between different depths in a palaeosol profile.

Additionally, two common sample preparation techniques in the geological sciences were tested. We showed that in the case of palaeosol samples, thin sections are better suited for NanoSIMS analysis than thick polished sections due to their lower resin content, even though a special in-house fabricated holder is required to introduce the thin sections into the NanoSIMS analysis chamber. However, the thickness of the thin section must be considered, since very thin samples can be consumed quickly and do not permit long dwell times, which can give place to greater uncertainty in the analyses.

The first results show that oxygen and hydrogen isotopic values obtained by NanoSIMS allow populations of clay minerals formed under different conditions to be discriminated, since in this study authigenic and diagenetic kaolinites are differentiated.

There is a decrease in the average $\delta^{18}O_{SMOW}$ and δD_{SMOW} values of the authigenic kaolinite and smectite towards the top of the palaeosol profiles, reflecting a change in the climatic conditions.

These values indicate formation in a weathering environment at Earth-surface temperatures and the inferred temperature formation for the clay minerals shows a decrease from the kaolinite of the bottom lateritic levels (21–22 ºC) to the smectite of the top lateritic levels (16–17 ºC) in the studied area during the early Barremian.

This work thus contributes to demonstrating the applicability of NanoSIMS in palaeoclimatic studies involving nanometre-sized clay minerals, opening up a novel path within this research field.

6 The effect of mixing Al-rich and Al–K-rich clays on the refractory potential of fired products

The present work analyses a set of cylinders manufactured by pressing and fired from 1000 ºC to 1270 ºC, which are composed of pure Al-rich rocks (bauxite) and mixtures of bauxite with Al–K-rich clays. The aim of the study is to determine the mineral and textural transformations that take place in the mixtures with firing and their influence on the physical properties of the final products in order to evaluate their refractory potential by comparing them with various fired commercial bauxites. To this end, raw and fired samples were analysed by X-ray diffraction, X-ray fluorescence, and optical and field emission scanning electron microscopy, and significant physical properties (e.g. density, linear shrinkage, porosity, colour, water absorption, thermal conductivity and point load resistance) were determined in the fired cylinders. The raw bauxite was mainly formed by boehmite, kaolinite and hematite whereas the illite- and kaolinite-rich clay was formed by quartz, illite and kaolinite. Kaolinite, illite and boehmite are not detected at 1000 ºC and, from this temperature upwards, mullite, corundum, γ-Al_2O_3, hercynite, ilmenite, cristobalite and vitreous phase are formed. Changes in physical properties with rising temperature are associated with the mineralogical changes. The increases in density and linear shrinkage are related to the formation of vitreous phase and the crystallization of mullite, and correlate with the decrease in porosity, water absorption and thermal conductivity. The changes in the colour of the samples are related to the hematite content at each temperature, whereas the point load resistance is greater with higher corundum content. Both the firing temperature and the clay content play an important role in the refractory potential of the mixtures, since samples mixed with illite- and kaolinite-rich clay present similar properties at lower temperatures to those of the fired commercial bauxites.

1 INTRODUCTION

Bauxites (Al-rich rocks) and illite- and kaolinite-rich clays (Al- and K- rich clays) are the most important raw materials in manufacturing refractory ceramics. For this reason, knowledge of the mineralogical and textural transformations that occur during the firing process, as well as their influence on the physical properties of the final products, is a matter of great interest in characterizing these materials and inferring their refractory potential (Altun, 2001; Laita and Bauluz, 2018; Gavshina et al., 2019; Jordán et al., 2020).

The mineral transformations that take place when aluminium- and clay-rich materials are fired at high temperature are influenced by the mineralogical composition of the raw materials, their granulometry, the firing temperature and the atmosphere conditions of the oven (Maggetti, 1989; Ghassemi Kakroudi et al., 2008). To understand how the calcination process occurs, it is thus necessary to analyse the mineral reactions, textural variations and compositional changes of the initial phases with the increase in temperature at both micron- and nano-scale (Laita and Bauluz, 2018; Jordán et al., 2020; Bauluz et al., 2004).

In the literature, there are numerous studies that report mineralogical and textural changes in illite- and kaolinite-rich clays (Jordán et al., 1999; Pardo et al., 2011; Jordán et al., 2020), pyrophyllite-rich clays or carbonate-rich clays (Bauluz et al., 2004; Laita and Bauluz, 2018) during firing processes.

Some of these studies have also reported modifications in physical properties with firing (Ghassemi Kakroudi et al., 2008; Boussen et al., 2016; Semiz and Çelik, 2020). However, there are no investigations that have described in detail the mineral and textural transformations with firing in bauxite materials and their relationship with the physical properties. This is what the present study does.

Mullite and corundum are frequent phases in ceramic products, and their formation influences the porosity of ceramics (Yang et al., 2012; Jordán et al., 2020). The crystallization of new phases with firing is therefore of great interest. However, little attention has been paid to how mixtures of bauxite with Al–K-rich clays can affect the mineralogy and physical properties of the final products. The study of these mixtures fired at different temperatures allows their refractory potential to be characterized and is thus of great interest for engineering and industrial applications.

With the aim of analysing the refractory potential of the mixtures, this research shows that the mixture of illite- and kaolinite-rich clays with bauxite raw materials can affect the mineralogical transformations that occur with firing and thus their physical properties and refractory potential.

The research has two aims: 1) to determine in detail and using high- resolution techniques the mineralogical and textural transformations that take place in the mixtures during the firing processes at different temperatures, and 2) to evaluate their influence on the physical properties (density, linear shrinkage, porosity, colour, water absorption, thermal conductivity and point load resistance) of the final products and, with these data, to deduce the refractory potential of the obtained products by comparing them with various fired commercial bauxites.

2 GEOLOGICAL SETTING

In the southern Pyrenean mountains (NE Spain), there are several karst bauxite deposits, which were opencast-mined during the 1990s. One of the most important bauxite sites in this area is the Sierra de Boada, where the bauxite used in this study was obtained (Fig. 6.1). Here, 15–20 m of bauxite levels are found overlying Middle Jurassic (Dogger) dolostones and covered by Upper Cretaceous (Cenomanian) sandstones. The Middle Jurassic dolostones are affected by a palaeokarstic surface, above which the bauxites are arranged. By contrast, the surface contact with the Upper Cretaceous sandstones at the top shows a flat geometry. The bauxites are of a clayey aspect, predominantly red and violet colours, and contain millimetric spherical ferruginous pisoids (Molina et al., 1994).

On the other hand, in the Iberian Range (NE Spain) there are illite- and kaolinite-rich clay deposits belonging to the Lower Cretaceous Escucha Formation (Fig. 6.1) (Aguilar et al., 1971). This formation has been traditionally divided into three members: lower, middle and upper (Cervera et al., 1976). The lower member of the Escucha Formation is formed by abundant claystones with a high kaolinite content, which are currently mined by the ceramic and refractory industries (Díaz Rodríguez and Torrecillas, 2002; Bauluz et al., 2008; Jordán et al., 2020).

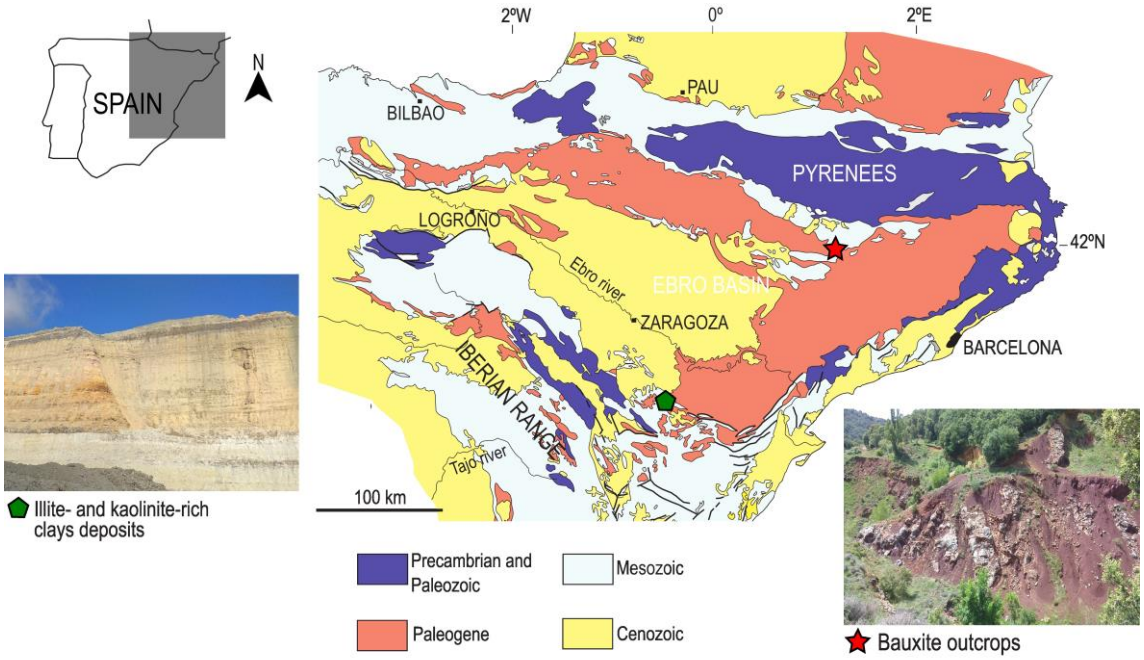

Fig. 6.1. Simplified geological map of the NE Iberian Peninsula indicating the location where the bauxite and the illite- and kaolinite-rich clays were obtained.

3 MATERIALS AND METHODS

3.1 Samples and firing process

The bauxite and the illite- and kaolinite-rich clay were milled under 100 μm. Pure bauxite (labelled as BX100) and mixtures of bauxite with the illite- and kaolinite-rich clay in 75/25 and 50/50 proportions (labelled as BX75 and BX50, respectively) were used to manufacture the cylinders (5 cm in diameter and 0.8 cm high) by pressing. The cylinders of the raw samples thus obtained were then fired in a Tecno-piro PR4T oven. The firing temperatures were 1000 ºC, 1100 ºC, 1200 ºC and 1270 ºC under oxidizing conditions, increasing the temperature in steps of 200 ºC/h and maintaining the maximum temperature for 2 h. Cylinders made from the raw and the fired samples are shown in Fig. 6.2.

To deduce the refractory potential of the manufactured cylinders, three fired commercial bauxites were used to compare their mineralogical and physical properties with those of the cylinders.

3.2 X-ray fluorescence and X-ray diffraction

X-ray fluorescence analysis was carried out for the three raw samples (BX50, BX75 and BX100) and for the illite- and kaolinite-rich clay at Actlabs laboratories (Ontario, Canada) to obtain their chemical composition. Samples were fused in platine crucibles using an automated crucible fluxer, automatically poured into platine moulds

for casting, and analysed on a Panalytical Axios Advanced wavelength dispersive XRF spectrometer. The detection limit of the technique was 0.01% for SiO_2, Al_2O_3, Fe_2O_3, MgO, CaO, Na_2O, K_2O, TiO_2, P_2O_5, and Cr_2O_3, 0.005% for Co_3O_4 and CuO, 0.003% for NiO and V_2O_5, and 0.001% for MnO.

Mineralogical analyses of both the raw and the fired samples as well as the three fired commercial bauxites were performed by X-ray diffraction (XRD). XRD patterns were obtained from the 3 to 60º 2θ interval using a Philips 1710 diffractometer at the University of Zaragoza (Zaragoza, Spain) with 40 kV voltage, 30 mA current, CuKα radiation, automatic slit and graphite monochromator. The goniometer velocity was 0.03º 2θ/s and the integration time was 1s. The recording was performed with XpowderX software (Martín, 2017).

After determining the mineral phases present in the samples, the relative proportions of these phases were ascertained using Reference Intensity Ratio (RIR) values from the literature (Schultz, 1964; Biscaye, 1965; Hill, 1984; Smith and Johnson, 2000; Laita and Bauluz, 2018). To determine the formation of the vitreous phase in the samples during firing, the amorphous/crystals relationship was obtained using XpowderX software.

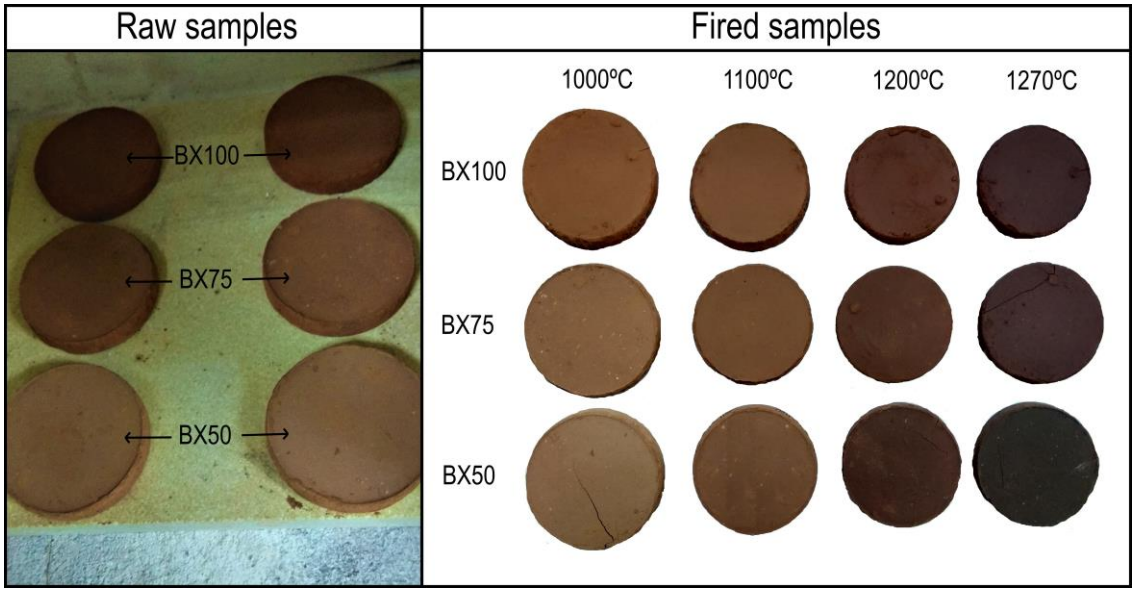

Fig. 6.2. Raw and fired cylinders obtained from pure bauxite (sample BX100) and mixtures of bauxite with the illite- and kaolinite-rich clay in 75/25 (sample BX75) and 50/50 proportions (sample BX50).

3.3 Optical and electron microscopy studies

Given that the XRD results showed similar mineralogical changes in samples fired at 1000 ºC and 1100 ºC, thin sections of all the samples fired at 1000 ºC, 1200 ºC and

1270 ºC were studied by transmitted and reflected light microscopy in order to identify the mineral phases and characterize their texture.

The same thin sections were analysed using a Carl Zeiss Merlin field emission scanning electron microscope (FESEM) with an Oxford energy- dispersive X-ray (EDS) detector at the University of Zaragoza (Zaragoza, Spain). The thin sections had been previously coated with carbon. Compositional images of the samples were obtained using two types of backscattered electron detectors: angular selective backscattered (AsB) and energy selective backscattered (EsB). The accelerating voltage was 15 kV for AsB and 4 kV for EsB, and the beam current was 400 pA for AsB and 2.0 nA for EsB. Semi-quantitative analyses were also performed by the energy-dispersive X-ray detector (EDS), which has a detection limit of 0.1%. The accelerating voltage and the beam current for this detector were the same as those used for the AsB detector.

3.4 Physical properties

3.4.1 Density and linear shrinkage (LS)

The density was measured for both the raw samples and those fired at the different temperatures. The apparent density of the fired commercial bauxites was provided by the company.

The linear shrinkage of the fired samples was determined according to the following formula:

$$LS(\%) = (D_1 - D_2/D_1) \times 100$$

where D_1 is the diameter of the raw sample and D_2 is the diameter of the fired sample.

3.4.2 Colour

To determine the precise colour of the samples, an X·Rite portable spectrophotometer, model Ci6X, was used, which yields colour values in the Munsell system and in the CIE L*a*b* scale. The spectrophotometer was used to measure colour values in the raw and fired samples, as well as in the fired commercial bauxites.

3.4.3 Porosity

The porosimetric analysis was carried out in the Thermal Analysis and Porous Solids Unit of the University of Alicante (Spain). An Ultrapyc 1200e Helium Pycnometer was used to obtain the pore size and distribution in the fired samples, as well as their total porosity. The apparent porosity of the fired commercial bauxites was provided by the company.

3.4.4 Water absorption (WA)

Water absorption values were obtained for samples fired at the different temperatures according to the following formula:

$$WA(\%) = [(A - B)/B] \times 100\%$$

where *A* is the weight of the wet cylinder after 3 h in a vacuum and *B* is the weight of the dry cylinder. The absorption capacity values of the fired commercial bauxites were provided by the company.

3.4.5 Thermal conductivity (k)

Samples mixed with the illite- and kaolinite-rich clay fired at 1200 ºC seems to have similar physical properties to those of the fired commercial bauxites. For this reason, samples BX50, BX75 and BX100 fired at 1200 ºC were selected to measure their thermal conductivity. Thermal conductivity values were obtained at room temperature by using a C-THERM Thermal Conductivity Analyzer, with an accuracy of ±5%. Ten measurements were made for each sample using Wakefield grease as the contact material. The setup of the equipment was previously checked using a standard sample (Pyroceram) suggested by the company.

3.4.6 Point load test (PLT)

The Point Load Test (PLT) allowed the Point Load Resistance Index $I_{s(50)}$ to be determined in samples fired at 1200 and 1270 ºC. Samples fired at 1000 and 1100 ºC were not resistant enough to carry out the test. A point load measuring equipment was used to obtain the point load value of each sample (I_s) in kg/cm^2. Several measures per sample (between 6 and 12 depending on sample availability) were carried out. To obtain the $I_{s(50)}$ index, a correction factor was necessary, according to the expression:

$$I_{s(50)} = F \cdot I_s$$

F being the correction factor that was obtained using the following formula:

$$F = (D_e/50)^{0.45}$$

where D_e is the equivalent diameter of the regular prisms, which can be calculated by means of the expression:

$$D_e^2 = 4A/\pi$$

where *A* is the minimum cross-sectional area containing the two load application points.

4 RESULTS

4.1 XRF and XRD results

The XRF results (Fig. 6.3) show that the illite- and kaolinite-rich clay presents higher proportions of SiO_2 (57.76%) and K_2O (3.47%) but lower proportions of Al_2O_3 (24.34%) and Fe_2O_3 (3.36%) than samples BX100, BX75 and BX50. Of these three samples, sample BX100 presents the highest Al_2O_3 and Fe_2O_3 contents and the lowest SiO_2 and K_2O contents.

The loss of ignition (LOI) produced in all the samples is related to the loss of the OH groups of the phyllosilicates and the hydroxides. As will be seen below, raw sample BX100 has the highest total boehmite + clay minerals content, which may be the cause of its higher LOI percentage (11.62%).

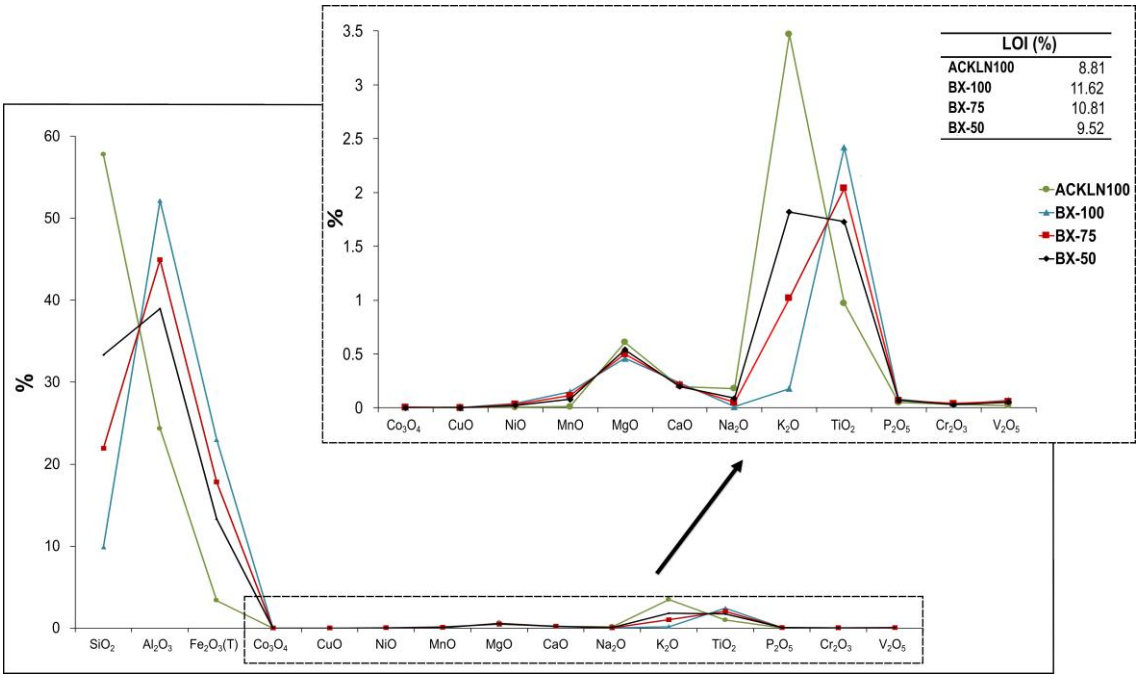

Fig. 6.3. XRF results showing the contents of major and several minor elements in the illite- and kaolinite-rich clay (ACKLN100) and the raw cylinders (BX100, BX75 and BX50).

The XRD patterns and the relative proportions of the different phases obtained from the raw and the fired samples are represented in Fig. 6.4.

The pure bauxite (sample BX100) is mainly formed by boehmite (62%), kaolinite (25%), hematite (9%) and minor proportions of anatase, goethite and rutile (<5%). Sample BX75 is formed by boehmite (43%), illite-kaolinite (35%), quartz (12%) hematite (6%) and minor proportions of anatase and rutile (<5%). Sample BX50 is composed of illite-kaolinite (46%), boehmite (27%), quartz (20%) and minor proportions of hematite, anatase and rutile (<5%). By contrast, the illite- and kaolinite-rich clay is mainly formed

by illite (39%), quartz (32%) and kaolinite (23%), with minor proportions of orthoclase and albite (<5%).

The kaolinite, illite, boehmite, anatase and goethite present in the raw samples are not detected from 1000 ºC upwards, indicating that they are the least stable phases during the firing process. By contrast, quartz, hematite and rutile are still detected at 1270 ºC, showing that these are more stable phases, which withstand higher temperatures. However, the quartz content in samples BX75 and BX50 decreases with temperature, indicating that it is partially destabilizing. The hematite content increases in all the samples at 1000 ºC (15–29%) compared to the raw samples (<5%–9%) but then decreases with increasing temperature, also indicating that it is partially destabilizing.

At 1000 ºC, ilmenite, cristobalite, γ-alumina, corundum (α-alumina), hercynite (Fe and Al spinel) and mullite are formed. It was not possible to obtain a RIR value for the γ-alumina, so it was not semi-quantified. At this temperature, the XRD results also show the presence of amorphous phase, indicating the occurrence of fusion processes.

Ilmenite (<5–10%) and cristobalite (<5%), which formed at 1000 ºC in all the samples, are later destabilized, as their content decreases with temperature.

Corundum is detected from 1000 ºC upwards; its content is higher at 1100 ºC in all the samples and then it decreases with temperature, especially in samples BX75 and BX50. At 1270 ºC the corundum content is higher in the BX100 sample (43%) than in BX75 and BX50 (12 and 7%, respectively).

Finally, the mullite content increases with temperature in all the samples. By contrast with corundum, its content is higher in samples BX75 and BX50 (79 and 77% respectively) than in sample BX100 (44%) at the highest temperature.

The relative proportions obtained from the fired commercial bauxites indicate that they are mainly composed of corundum (70–84%) and mullite (14–27%), and some of them occasionally present low contents of hematite, rutile, ilmenite and hercynite (<5%).

The amorphous/crystals relationship obtained by XpowderX software is represented in Table 6.1. According to these data, an amorphous phase is generated in the three samples from 1000 ºC upwards, its content seeming to rise with temperature up to 1200 ºC in samples BX75 and BX50. In addition, the amorphous phase content in the three samples is higher than that detected in the fired commercial bauxites.

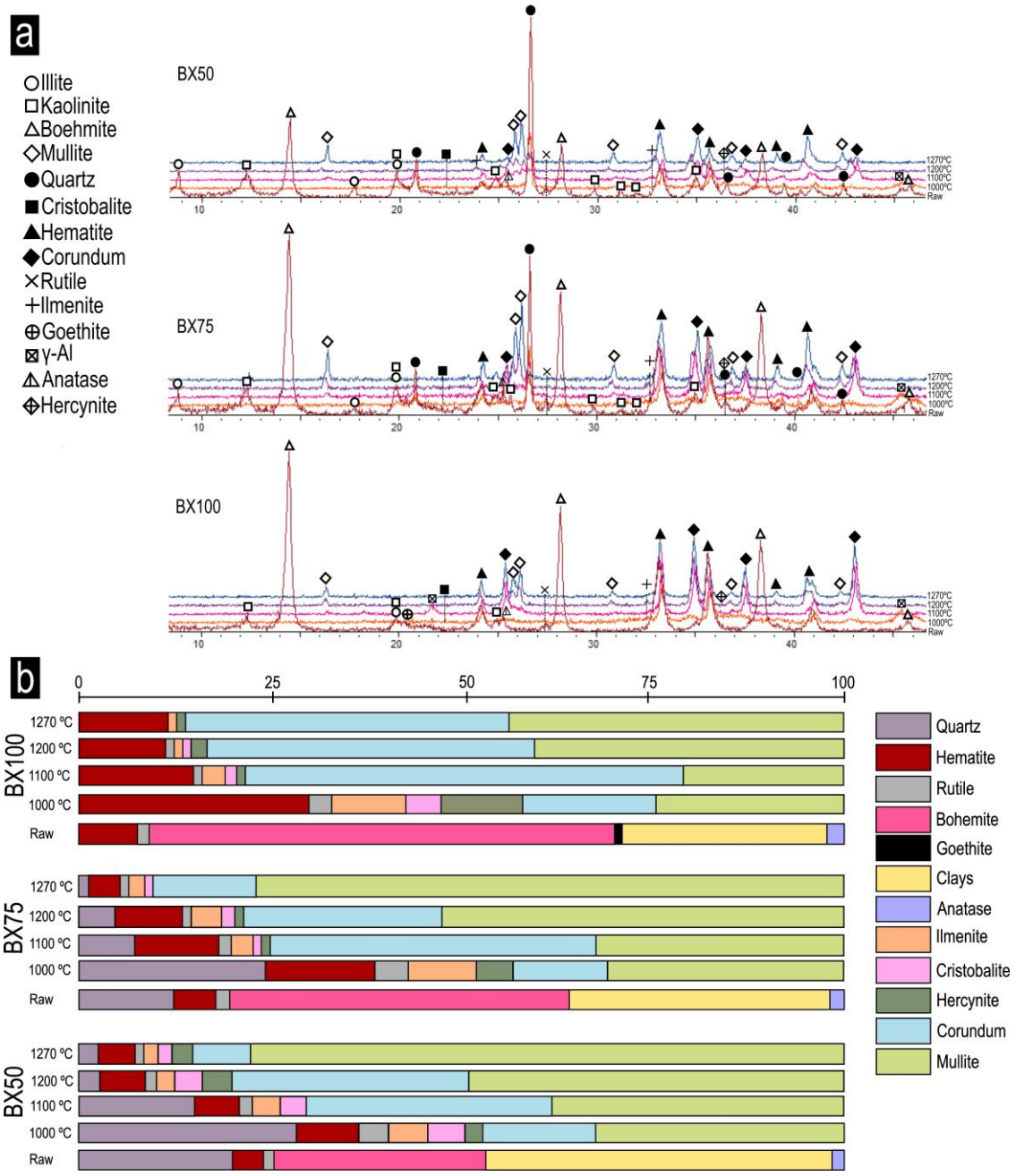

Fig. 6.4. a) XRD patterns of raw and fired samples; **b)** diagrams with the relative proportions of the mineral phases present in the analysed samples.

Table 6.1. Amorphous/crystals relationship obtained by XpowderX software for the three samples at the different temperatures and for the commercial bauxites.

Sample	Tº (ºC)	Amorphous/Crystals relationship
BX100	1000	0.146
	1100	0.088
	1200	0.091
	1270	0.106
BX75	1000	0.139
	1100	0.153
	1200	0.148
	1270	0.097
BX50	1000	0.089
	1100	0.110
	1200	0.225
	1270	0.120
Commercial bauxites		0.038
		0.044
		0.040

4.2 Optical and electron microscopy results

4.2.1 Optical and backscattered electron (BSE) images

At optical microscopy resolution, at 1000 ºC samples BX50 and BX75 show a fine-grained matrix, in which morphologies of the original phyllosilicates are still distinguished along with oxides and quartz fragments (10–80 μm) (Fig. 6.5a), whereas in sample BX100 only small hematite aggregates (<50 μm) are observed. With the increase in temperature, the texture of the three samples becomes very homogeneous. Scarce quartz fragments are still distinguished, which are smaller (10–50 μm) than at lower temperatures, along with hematite aggregates and replacement textures involving hematite and another unidentified opaque mineral (Fig. 6.5b).

BSE images show remarkable textural and mineralogical changes with the increase in firing temperature. At 1000 ºC rock fragments are still identified in samples BX100, BX75 and BX50. Iron and titanium oxides are recognized in some of these rock fragments, where they mainly occur in disseminated form, whereas other rock fragments are more homogeneous and contain almost no oxides. The rock fragments with abundant oxides seem to come from the original bauxite, whereas the most homogeneous ones seem to come from the illite- and kaolinite- rich clay (Fig. 6.5c). Some of the oxides have compositional zonation, with rutile and ilmenite or ilmenite and hematite compositions (Fig. 6.5d and e), and iron and titanium oxides forming aggregates (10–30 μm) are also recognized (Fig. 6.5e). At this temperature, in samples BX75 and BX50, quartz fragments (1–20 μm) are observed that are not yet destabilized, and corundum crystals are present in the three samples, with acicular morphologies,

nanometric lengths (50–400 nm) and random orientation (Fig. 6.5f). Kaolinite-type morphologies are differentiated in the three samples (Fig. 6.5d–f) and in almost all cases their sheets are separated. These morphologies could correspond at least in part to metakaolinites, since kaolinite was not detected by XRD at this temperature.

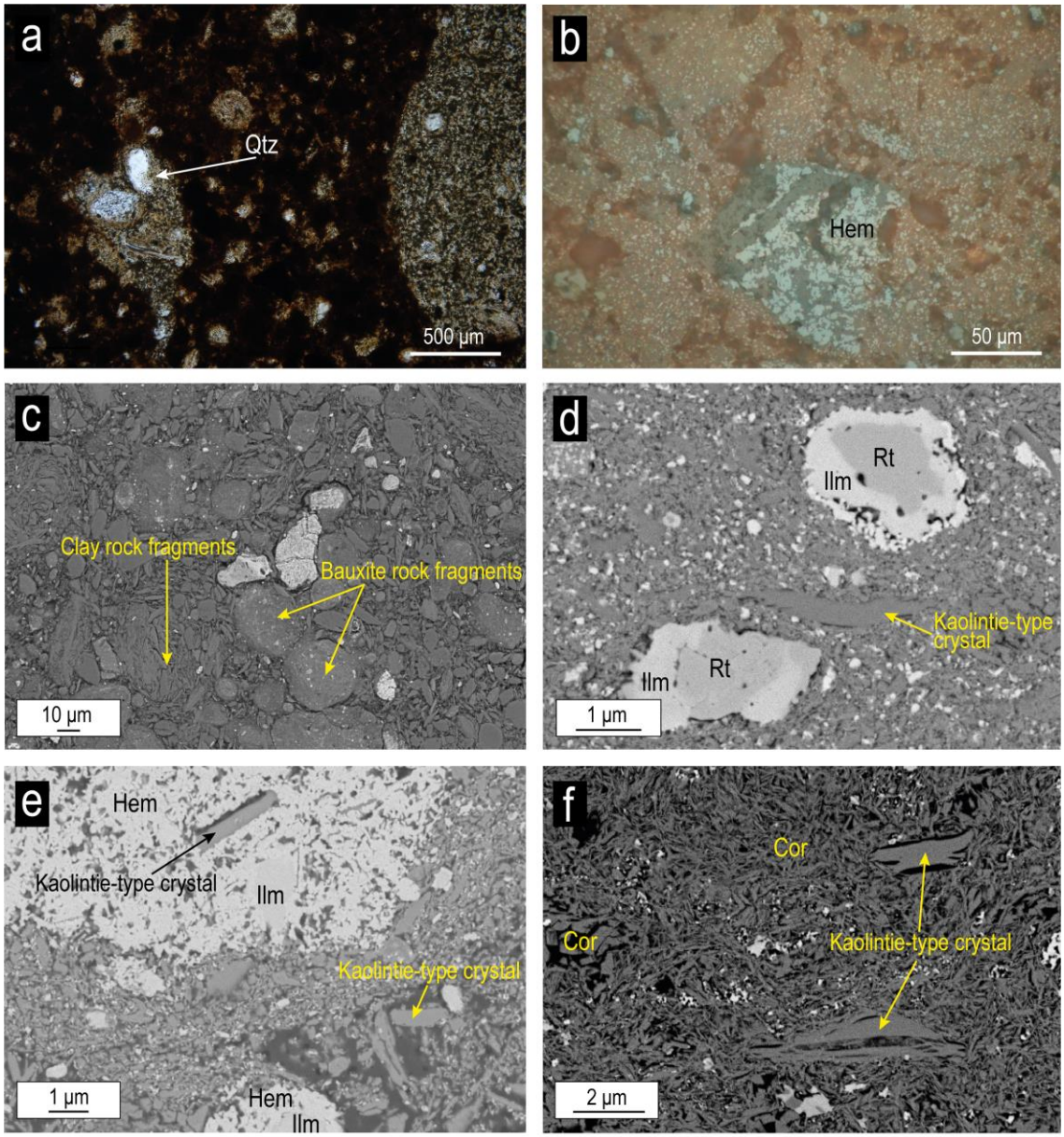

Fig. 6.5. a) Transmitted light optical microscope images showing the matrix formed by quartz fragments and oxides in sample BX50 at 1000 ºC; **b)** reflected light optical microscope images showing hematite replacement textures in sample BX100 at 1270 ºC. **(c–f)** FESEM images of samples fired at 1000 ºC showing: **c)** bauxite and clay rock fragments along with iron oxide aggregates in sample BX50; **d)** crystals with compositional zonation involving rutile and ilmenite compositions, and kaolinite-type crystals in sample BX100; **e)** oxide aggregate composed mainly of hematite and kaolinite-type crystals in sample BX75; **f)** acicular corundum crystals and kaolinite-type crystals with separated sheets in sample BX100. *Qtz*=quartz, *Rt*=rutile, *Ilm*=ilmenite, *Hem*=hematite, *Cor*=corundum.

At 1200 ºC the texture of the samples is much more homogeneous, possibly due to the vitrification process. Some of the rock fragments are still recognized, especially in sample BX100, indicating that bauxite may be the component most resistant to firing. In this sample, all the iron and titanium oxides are disseminated or form aggregates. By contrast, in samples BX75 and BX50 the rock fragments are not so easily distinguishable, and oxides are concentrated in certain areas, as well as forming aggregates. Instead of rock fragments, texturally and compositionally different areas can be discerned: homogeneous areas without oxides and more heterogeneous areas with iron and titanium oxides, both disseminated and aggregated (Fig. 6.6a). These different areas could correspond with the previous bauxite and illite- and kaolinite-rich clay fragments observed at 1000 ºC. Sample BX100 (Fig. 6.6b) does not contain rock fragments of the illite- and kaolinite-rich clay, but the XRD results showed that the raw sample contained kaolinite. Thus, the homogeneous areas in BX100 may come from the destabilization of the initial kaolinite during firing. In general, the homogeneous areas are formed by acicular and prismatic nanometre-sized mullite crystals (100–600 nm), with random orientation and immersed in vitreous phase (Fig. 6.6a–c) along with quartz fragments, which present reaction edges, indicating that they have begun to destabilize (Fig. 6.6c). The heterogeneous areas in all the samples, where the oxides are concentrated, also contain abundant acicular corundum crystals, with random orientation and sizes larger than those found at 1000 ºC (200 nm–2 μm). These corundum crystals can be found replacing hematite (Fig. 6.6a, b and d).

Finally, at 1270 ºC the texture of the three samples is very homogeneous (Fig. 6.7a). Iron and titanium oxides are less frequent and occur in the same form as at 1200 ºC. Quartz fragments only remain in sample BX50 although they are scarcer than at lower temperatures and show reaction edges. Mullite crystals are also found immersed in vitreous phase but with larger sizes (100 nm–2 μm) (Fig. 6.7b and d). The corundum has acicular and prismatic morphologies with larger sizes (200 nm–4 μm) and is immersed in a probably vitreous phase, occasionally replacing hematite (Fig. 6.7c and d).

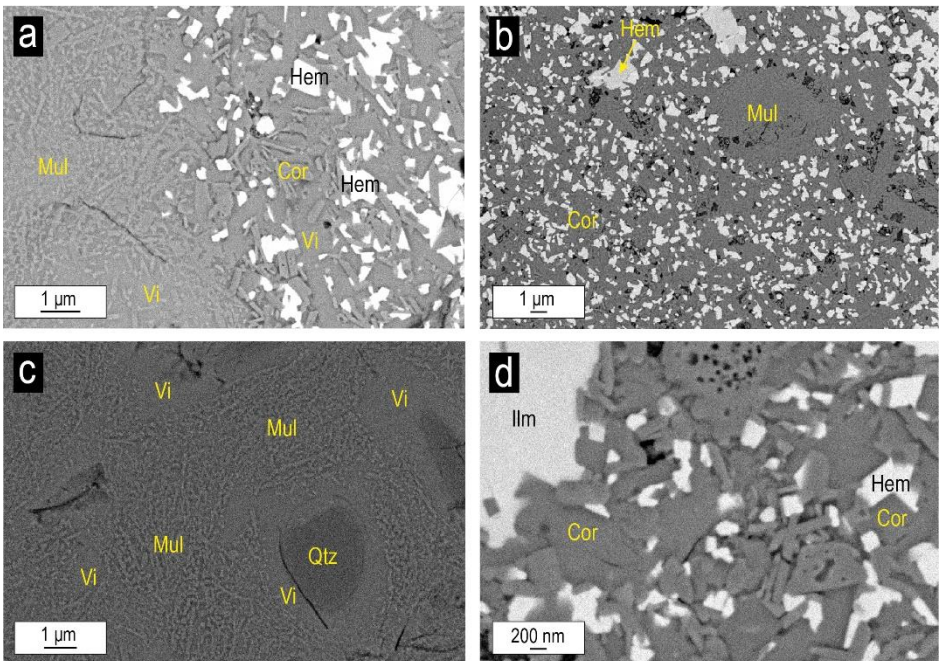

Fig. 6.6. FESEM images of samples fired at 1200 ºC showing: **a)** a homogeneous area with acicular mullite crystals and vitreous phase and a heterogeneous area with hematite and corundum crystals in sample BX75; **b)** the same zones in sample BX100, in which the corundum content is higher and the mullite content is lower than in the other samples; **c)** quartz fragments with reaction edges, acicular mullite crystals and vitreous phase in sample BX50; **d)** corundum replacing hematite in sample BX50. *Mul*=mullite, *Hem*=hematite, *Cor*=corundum, *Vi*=vitreous phase, *Qtz*=quartz, *Ilm*=ilmenite.

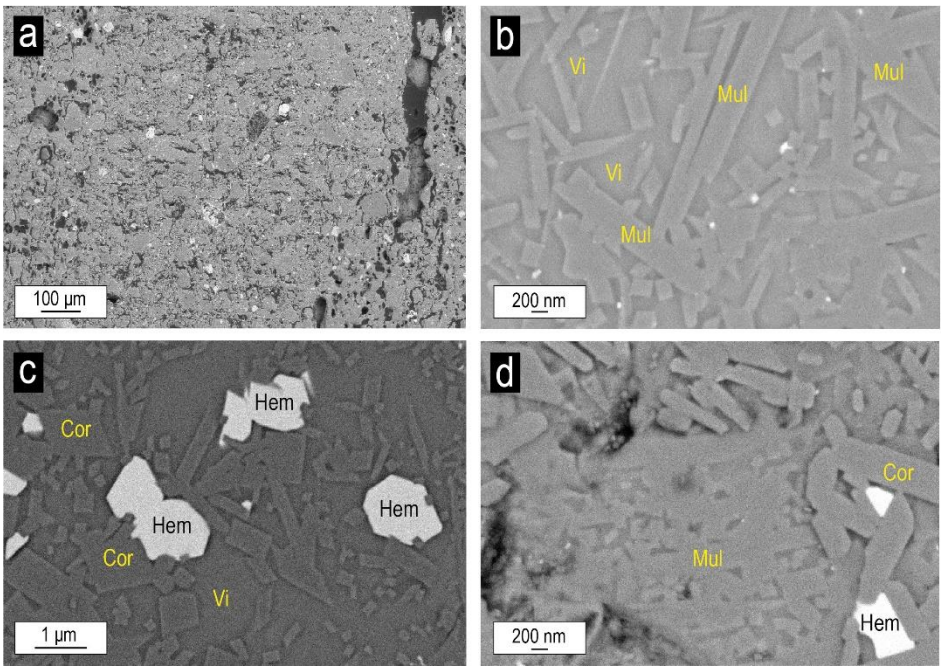

Fig. 6.7. FESEM images of samples fired at 1270 ºC showing: **a)** the general texture of sample BX75; **b)** acicular and prismatic mullite crystals immersed in vitreous phase and with larger sizes than at lower temperatures in sample BX75; **c)** acicular and prismatic corundum crystals with larger sizes than at lower temperatures, occasionally still replacing hematite crystals and immersed in vitreous phase in sample BX50; **d)** corundum and mullite crystals immersed in vitreous phase in sample BX100. *Vi*=vitreous phase, *Mul*=mullite, *Cor*=corundum, *Hem*=hematite.

4.2.2 Chemical analysis

EDS analyses indicate that hematite, corundum and ilmenite show compositional differences from sample to sample and even at sample scale. Al vs. Fe (wt%) plots at the different temperatures for the three samples show a trend among hematite, hercynite and corundum compositions (Fig. 6.8a–c). The Al vs. Fe plots show the presence of three compositional populations: 1) Fe-rich compositions that indicate hematite, 2) Al-rich compositions that are regarded as corundum, and 3) intermediate compositions between hematite and corundum.

Although hercynite was not clearly differentiated by FESEM analyses, it was detected by XRD in all the samples at the different temperatures, and some of the intermediate compositions included between hematite and corundum are close to theoretical hercynite (31.05% Al, 32.13% Fe, 36.82% O).

Ti vs. Fe (wt%) plots at the different temperatures for the three samples also show a trend among hematite, ilmenite and rutile compositions (Fig. 6.8d–f). In this case, compositions with Fe contents higher than 79% and Ti contents lower than 9% were considered hematite. Those compositions with Ti contents of 32–66% and Fe contents of 33–67% were considered ilmenite, whereas compositions with Ti contents higher than 75% and Fe contents lower than 25% were considered rutile.

Of all these phases, corundum and ilmenite are the two generated due to the firing process, as they were not detected by XRD in the raw samples. On average, the corundum composition at the different temperatures is close to theoretical corundum (52.093% Al and 47.07% O); it has an Al content of 44.07%, but it also contains Fe (6.72%), Si (3.82%) and minor proportions of Ti (0.43%) and K (0.15%). Ilmenite presents lower Ti and Fe contents (20.35 and 28.35% respectively) than theoretical ilmenite (31.56% Ti, 36.81% Fe and 31.63% O).

The Al vs. Si plot (Fig. 6.8g) shows mullite analyses from all the samples at the different temperatures. According to these results, the mullite presents a heterogeneous compositional range with compositions between kaolinite (or metakaolinite) and mullite. Those analyses at 1000 ºC close to the theoretical kaolinite composition correspond with the kaolinite-type morphologies observed in the backscattered electron images. Although mullite presents a heterogeneous compositional range, its Al/Si ratio increases from 1.49 at 1200 ºC to 1.76 at 1270 ºC.

Finally, the vitreous mass observed in all the studied samples in which mullite and corundum crystals are immersed probably corresponds with the amorphous phase deduced from XRD. It presents a heterogeneous composition mainly formed by Si and

Al (28.20 and 15.90%, respectively), along with Fe and K (3.56 and 3.20%, respectively) and minor proportions of Ti (0.64%), Mg (0.44%), Ca (0.16%) and Na (0.13%).

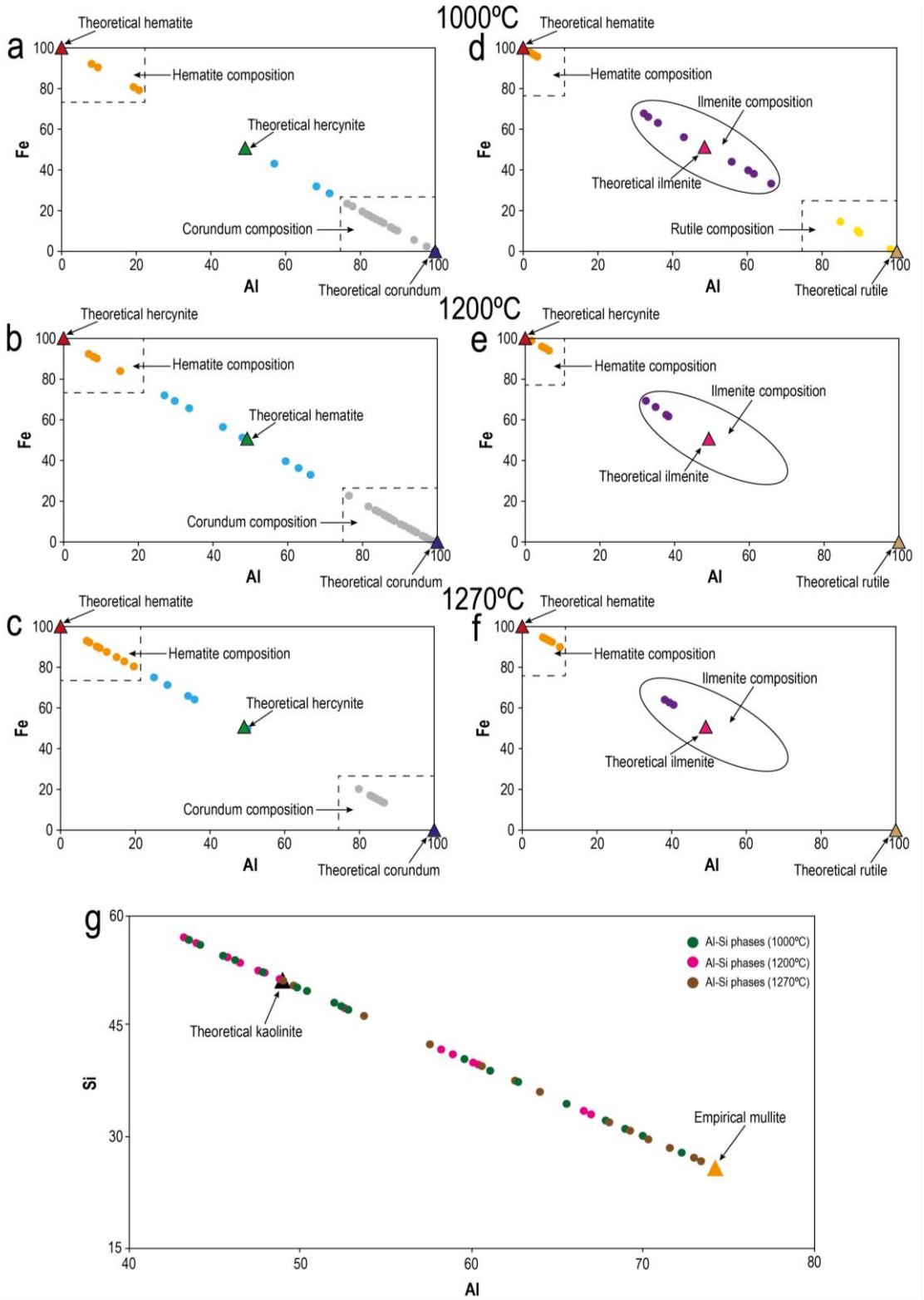

Fig. 6.8. a–c) Al vs. Fe plots showing the hematite-hercynite-corundum trend in all the samples at 1000, 1200 and 1270 ºC respectively; **d–f)** Ti vs. Fe plots showing ilmenite, rutile and hematite compositions in all the samples at 1000, 1200 and 1270 ºC; **g)** Al and Si-rich compositions obtained from the mullite crystals in the three samples at the different temperatures.

4.3 Physical properties

4.3.1 Density and linear shrinkage

The density of the cylinders is 1.73 g/cm^3, 1.74 g/cm^3 and 1.71 g/cm^3 for samples BX100, BX75 and BX50, respectively. The changes in the density values of the three samples are represented in Fig. 6.9a, which shows that the density values of the raw samples remain almost constant up to 1000 ºC. At 1100 ºC and 1200 ºC the density increases in all the samples, reaching values of 2.83 g/cm^3, 2.73 g/cm^3 and 2.55 g/cm^3 for samples BX100, BX75 and BX50, respectively. Finally, at 1270 ºC the density of samples BX75 and BX50 decreases to 2.55 g/cm^3 and 2.43 g/ cm^3, respectively, whereas the density of sample BX100 increases to 3.43 g/cm^3. The density values reached by sample BX75 fired at 1200 ºC and by sample BX100 fired at 1200 ºC and 1270 ºC are the closest to the density values given for the fired commercial bauxites (2.8–3.25 g/cm^3).

A similar trend is observed in the linear shrinkage values (Fig. 6.9b). At 1000 ºC the linear shrinkage value is 4.39% for sample BX100, 3.99% for sample BX75, and 2.97% for sample BX50. A notable increase in the linear shrinkage is observed in the three samples at 1100 ºC and 1200 ºC with values of 12.43% and 18.55% for sample BX100, 11.86% and 16.74% for sample BX75, and 9.97% and 14.95% for sample BX50. Finally, at 1270 ºC the linear shrinkage values undergo a slight decrease in samples BX75 and BX50 (15.07% and 14.32%, respectively), whereas the value increases in sample BX100 (22.56%).

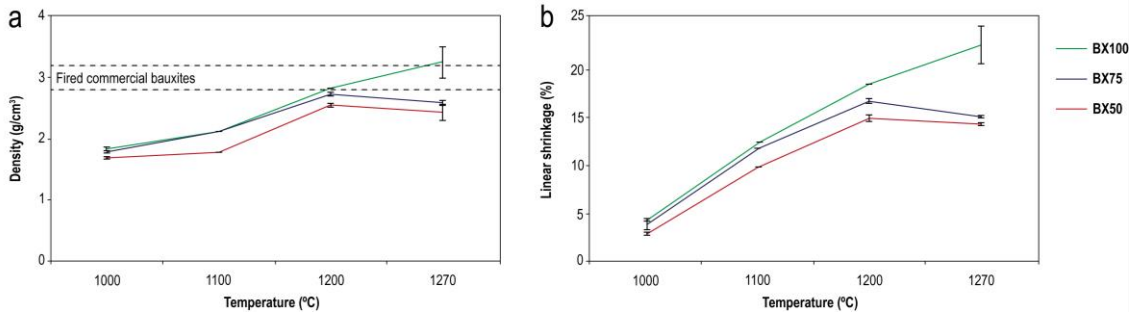

Fig. 6.9. Density vs. temperature **(a)** and linear shrinkage vs. temperature **(b)** graphs representing the changes in these properties in the fired samples.

4.3.2 Colour

According to the Munsell System (Fig. 6.10a), the BX100 and BX75 raw samples present a reddish brown colour, which changes to bright reddish brown at 1000 and 1100 ºC and to dull reddish brown from 1200 ºC. BX50 undergoes more colour changes with temperature. The raw sample is a dull reddish brown colour, which changes to orange at 1000 ºC, then to bright reddish brown at 1100 ºC, dull reddish brown at 1200 ºC, and finally to greyish brown at 1270 ºC.

The CIE L*a*b* scale (Fig. 6.10b) shows that there is a trend towards orange colours from the raw samples to those fired at 1000 ºC. From 1100 ºC, the a* and b* values then decrease progressively, which coincides with the change towards darker colours, also shown by the Munsell System. The hue values calculated for the samples show that all the raw samples and those fired at up to 1100 ºC present values between 34.22º and 37.03º, which coincide with pink hues, whereas those fired at 1200 ºC and 1270 ºC present hues close to red (40.36º and 46.94º), according to the hue scale displayed in Fig. 6.10c.

Comparing these colour values with those of the fired commercial bauxites, the Munsell notation for the fired commercial bauxites (2.1Y5.1/0.7, 1.6Y4.8/0.8 and 5.7Y4.1/0.2) indicates that the latter are of yellowish grey and grey colours, which are darker in colour than the fired cylinders. Likewise, the a* and b* coordinates presented by the fired commercial bauxites show lower values than the samples fired at 1270 ºC, and their hue values are somewhat higher (63.89–75.86º), indicating hues between red and orange.

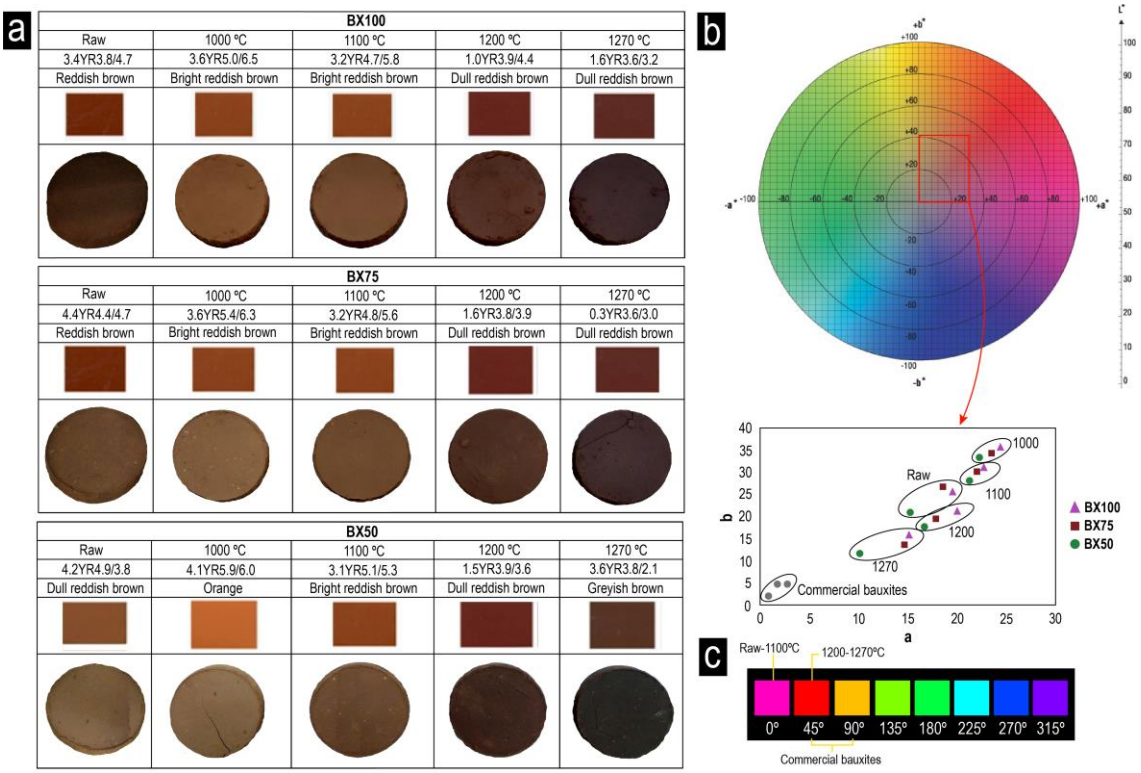

Fig. 6.10. Colours of the raw and fired samples represented in **a)** the Munsell System; **b)** the CIE L*a*b* scale; **c)** the hue scale.

4.3.3 Porosity

The distribution curves for porosity vary with the increase in firing temperature in all the samples (Fig. 6.11). At 1000 ºC the intrusion percentage is highest in sample BX50 (4.19%) and it occurs in pores whose radius reaches greater sizes (1 μm) than in samples BX75 and BX100. At this temperature, sample BX100 presents the lowest intrusion percentage (1.23–1.46%), with pores with a radius between 2×10^{-2} and 3×10^{-1} μm.

At 1100 and 1200 ºC the intrusion percentage increases in all the samples, this increase being higher in samples BX50 and BX75, which present a maximum intrusion of 5.62–11.31% and 4.79–7.78%, respectively. By contrast, sample BX100 has a maximum intrusion of 2.51%, occurring in pores with a radius of 4×10^{-2} – 4×10^{-1} μm, somewhat smaller than those where the maximum intrusion occurs in samples BX75 and BX50.

Finally, at 1270 ºC the maximum intrusion decreases in sample BX50 (4.29%) but it occurs in pores with a greater radius than at lower temperatures (3.5×10^{2} and 5.6×10^{2} μm). By contrast, the maximum intrusion increases in samples BX75 (9.13%) and BX100 (11.38%). In the case of sample BX75 it occurs in pores with a radius of 1×10^{-1}–1 μm, whereas in sample BX100 it occurs in pores with a similar radius to those in sample BX50 at this temperature (1×10^{2} – 5×10^{2} μm).

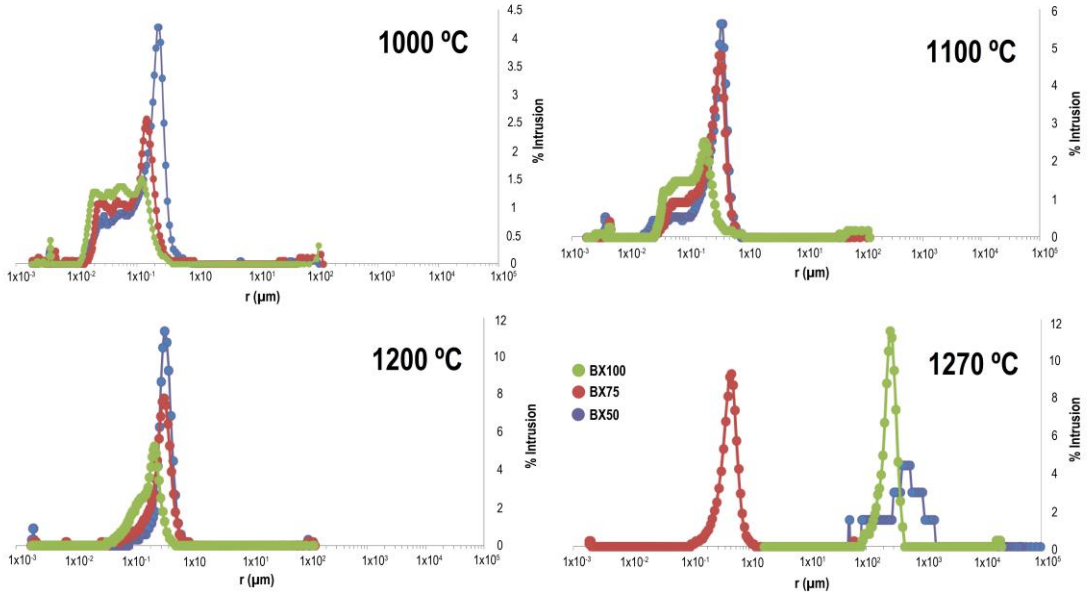

Fig. 6.11. Distribution curves for porosity obtained from the porosimetric analysis of the fired samples.

The mean, mode and total porosity of the fired samples are presented in Table 6.2. The average pore size (mean) decreases in all the samples with the increase in temperature. The mode values also decrease with temperature in samples BX75 and BX100 but increase in sample BX50. The total porosity decreases progressively with temperature in all the samples, although there is a slight increase in sample BX75 at 1270 ºC.

The apparent porosity values given for the fired commercial bauxites are between 7 and 14.5%, which are consistent with the values for all the fired samples at 1200 ºC and even at 1270 ºC in the case of sample BX100.

Table 6.2. Mean, mode and total porosity values obtained from the porosimetric analysis of the fired samples.

		Mean (μm)	Mode (μm)	Total porosity (%)
BX50	**1000**	$6.67x10^{-2}$	1.39	34.55
	1100	$4.46x10^{-2}$	1.96	25.69
	1200	$1.61x10^{-2}$	2.07	9.01
	1270	$3.05x10^{-3}$	3.21	0.19
BX75	**1000**	$1.34x10^{-1}$	2.28	34.67
	1100	$7.07x10^{-2}$	2.13	23.92
	1200	$2.31x10^{-2}$	$3.98x10^{-1}$	14.45
	1270	$3.34x10^{-2}$	$1.79x10^{-2}$	18.13
BX100	**1000**	$7.09x10^{-2}$	2.63	40.41
	1100	$4.38x10^{-2}$	$8.63x10^{-1}$	29.16
	1200	$1.78x10^{-2}$	$6.40x10^{-2}$	17.08
	1270	$9.70x10^{-3}$	$4.01x10^{-2}$	9.73

4.3.4 Water absorption, thermal conductivity, and point load test

The water absorption values show that in general the absorption capacity of samples BX100 and BX50 decreases with temperature, whereas that of sample BX75 decreases up to 1100 ºC and then slightly increases (Fig. 6.12a). This coincides with the decrease in porosity with temperature in all the samples and also with the subsequent slight increase in porosity of sample BX75 at 1270 ºC. The fired commercial bauxites have absorption capacity values between 2 and 4.5%, i.e. very close to those of sample BX75 at 1200–1270 ºC. In addition, the water absorption values of samples BX100 and BX50 fired at 1100–1200 ºC are also fairly close to the fired commercial bauxite values.

The average values for thermal conductivity (k) obtained for the samples fired at 1200 ºC are represented in Fig. 6.12b. This shows that samples BX75 and BX100 have a similar k value (2.46 and 2.40 W/m.K, respectively), which is greater than that of sample BX50 (1.94 W/m.K).

The results for the point load test (Fig. 6.12c) show that sample BX100 presents the highest resistance when it is fired at the highest temperature (1270 ºC). By contrast, sample BX50 presents higher resistance, even higher than that shown by sample BX100, at 1200 ºC than at 1270 ºC, whereas there is no significant change in the resistance values for sample BX75 between these temperatures.

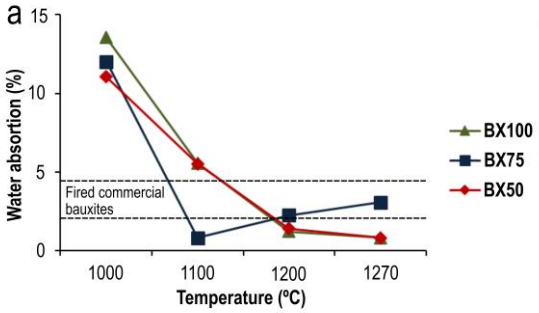

b

Thermal Conductivity (W/m.K)	
BX100	2.40 (±0.02)
BX75	2.46 (±0.02)
BX50	1.94 (±0.01)

c

	Is(50) (Mpa)	
BX100	1200	0.89 (±0.15)
	1270	1.32 (±0.19)
BX75	1200	1.12 (±0.16)
	1270	1.14 (±0.16)
BX50	1200	1.36 (±0.15)
	1270	1.20 (±0.14)

Fig. 6.12. a) Water absorption variations in the samples fired at the different temperatures; **b)** mean values of thermal conductivity of samples fired at 1200 ◦C (standard deviation in brackets); **c)** point load index ($I_{s(50)}$) obtained for samples fired at 1200 and 1270 ◦C (standard deviation in brackets).

5 DISCUSSION

5.1 Mineral and textural changes during the firing process

5.1.1 Destabilization of the initial phases

As pointed out in the Result sections, the raw samples initially contained boehmite, illite and/or kaolinite, hematite, rutile and anatase. Sample BX100 also had goethite, and BX75 and BX50 contained quartz.

Most of these initial phases were destabilized and melted during the firing process. Clay minerals were not detected at 1000 ºC, indicating that these minerals are the least stable phases. Previous studies (Laita and Bauluz, 2018) have reported the absence of kaolinite above 800 ºC in aluminium-rich ceramic materials, and the presence of illite up to 1000 ºC, but with clear signs of dehydroxylation processes from 450 ºC. The low stability of kaolinite in ceramic materials has also been reported by other authors (Cheng et al., 2000; Meng et al., 2016), who describe the presence between 500 and 1000 ºC of amorphous metakaolinite, which would be the precursor of mullite. The kaolinite-type morphologies observed in the fired samples at 1000 ºC (Fig. 6.5d–f) could correspond, at least in part, to metakaolinite, given the closeness of their composition to the theoretical kaolinite. Nevertheless, taking into account the presence of mullite as deduced from XRD and the lack of FESEM evidence for discrete mullite crystals, they could also correspond to mullite and would thus represent the pseudomorphic transformation from kaolinite to mullite, since there is no evidence of fusion processes affecting the kaolinite-type morphologies at this temperature.

In the case of illite, thermogravimetric analysis also reported dehydroxylation occurring at 500–550 ºC (Drits and McCarty, 2007).

Like the clay minerals, boehmite was not present at 1000 ºC due to a dehydration process that transforms boehmite (γ-AlOOH) into γ-Al_2O_3 at 490–510 ºC (Panias and Krestou, 2007; Jbara et al., 2017; Dong et al., 2020). Furthermore, neither the small amounts of anatase detected in all the raw samples nor the goethite detected in sample BX100 were present at 1000 ºC. This can be explained by the fact that goethite dehydrated into hematite at 500–600 ºC (Jang et al., 2014; Sun et al., 2020) and that anatase transforms into rutile at 500–550 ºC (Low et al., 2012). In addition, the presence of small amounts of amorphous or poor crystalline iron oxides (not detected by XRD in the raw samples) that would destabilize with temperature, along with the dehydration of goethite into hematite in sample BX100, may be the cause of the increase in the hematite content at 1000 ºC in all the samples.

The quartz content also increased at this temperature in samples BX75 and BX50. This may be a consequence of kaolinite and illite destabilization, which gives rise to an amorphous SiO_2 phase at 925–1050 ºC (Ondro et al., 2019).

5.1.2 Crystallization and composition of new phases

The morphology of synthetic γ-alumina has been described as irregular or thin flakes (Samain et al., 2014; Salahudeen et al., 2015), so the acicular and prismatic crystals observed at 1000 ºC by FESEM probably correspond to corundum.

These corundum crystals are of random orientation and of sizes that increase with temperature, reaching up to 4 μm at 1270 ºC, and they are immersed in a probably vitreous matrix as well as replacing hematite. Previous studies have described how hematite or magnetite can be replaced by spinel in igneous materials and natural clinkers (Treiman, 1984; Sandiford et al., 1987; Laita et al., 2019). In this way, the low hercynite proportions detected in the XRD patterns could be replacing hematite, with the hematite content thus decreasing with temperature.

The transformation of pseudo-spinel to γ-Al_2O_3 has also been described in the literature (Segal et al., 2018), so the detected hercynite could contribute to the alumina formation.

As commented above, boehmite dehydrates, also giving rise to γ-Al_2O_3, at 490–510 ºC (Panias and Krestou, 2007; Jbara et al., 2017; Dong et al., 2020). γ-Al_2O_3 is one of the seven transition phases of alumina (χ-Al_2O_3, κ-Al_2O_3, γ-Al_2O_3, θ-Al_2O_3, δ-Al_2O_3, η-Al_2O_3, ϱ-Al_2O_3). The corundum structure is called α-Al_2O_3 and is the last and most stable alumina phase, formed by increasing the temperature up to 1200 ºC (Cava et al., 2006; Jbara et al., 2017). Accordingly, the γ-Al_2O_3 peaks detected in the XRD patterns of the

three samples fired at 1000 ºC may be the remains of the transition phases of the alumina from the destabilization of boehmite and hercynite giving rise to corundum formation.

On the other hand, hematite (α-Fe_2O_3) and corundum (α-Al_2O_3) are isostructural phases and can form a solid solution at 1000–1300 ºC (Feenstra et al., 2005). This could also explain the compositions intermediate between these two phases in the studied ceramics.

FESEM analysis also showed a compositional trend among hematite, ilmenite and rutile compositions. During firing, part of the Ti from anatase and the Fe from hematite could lead to ilmenite crystallization. Ilmenite and hematite can form a solid solution above 650 ºC (Lindsley, 1991), which would explain the compositional zonation between hematite and ilmenite found in some grains/crystals. This solid solution results in separated hematite-rich and ilmenite-rich phases with cooling (Tan et al., 2015). Rutile, ilmenite and spinel intergrowths have also previously been described in igneous rocks (Markl et al., 2005) in a similar way to the compositional zonation between rutile and ilmenite observed in the studied samples.

The kaolinite-type morphologies observed at 1000 ºC present their sheets separately due to the dehydroxylation processes, indicating that kaolinite was probably destabilized into metakaolinite. This metakaolinite would be the precursor of mullite through a solid-state process, giving rise to the pseudomorphic formation of mullite at 1000 ºC, as commented in section 5.1.1. Later, the fusion process increases, which is evidenced by the presence of a vitreous phase, allowing the formation of discrete mullite crystals, which are clearly distinguished at 1200º and 1270 ºC in the FESEM images. At these temperatures, mullite is present as acicular and prismatic crystals of random orientation, whose sizes increase with temperature, reaching up to 2 μm in length at 1270 ºC. The mullite composition is not stoichiometric but follows a trend between kaolinite and empirical mullite compositions, and it shows a higher Al/ Si ratio at 1270 ºC. The Al diffusion was probably higher at 1270 ºC than at 1000 ºC (Laita and Bauluz, 2018), and thus there is an increase in the Al content of mullite crystals with the increase in temperature. The increase in crystal size and the changes in the composition with temperature are indicative of a decrease in the number of crystalline defects in the mullite structure (Laita and Bauluz, 2018).

5.1.3 The firing process and the vitreous phase formation

The vitrification process is responsible for the homogenization in the overall texture of all the samples with increasing temperature. At 1000 ºC the rock fragments from the bauxite and the illite- and kaolinite- rich clay are still recognized, but they are no longer so distinguishable at 1200–1270 ºC. The bauxite rock fragments seem to be

more stable with temperature, since they are better recognizable at these temperatures in sample BX100; this may be due to its higher corundum content, as materials with high alumina content can withstand temperatures greater than 1300 ºC and thermal shocks (Medvedovski, 2001).

The presence of the vitreous phase is deduced in the three samples from the XRD and FESEM results from 1000 ºC upwards. The FESEM analyses showed that this vitreous phase presents compositional variations depending on the sample and the area analysed, but in general it has an Al- and Si-rich composition and also contains Fe and minor proportions of Ti, Mg, Ca and Na. The Al and Si come from illite, kaolinite, boehmite and quartz, which were the main components of the raw samples and could also contribute Mg, Ca and Na, whereas the Fe and Ti come from hematite and from anatase and rutile, respectively.

The fact that the newly generated phases such as corundum or mullite are immersed in the vitreous phase demonstrates that the initial phases destabilized with the increase in temperature, giving rise to this vitreous phase from which the new phases crystallized from 1100 ºC on.

On the other hand, these new phases are non-stoichiometric, which may be due to the dynamics of the firing process resulting in incomplete mineral reactions (Laita and Bauluz, 2018). According to these authors, the aluminium diffusion is probably lower at 1000 ºC than at 1270 ºC, which is supported by the compositional trend of mullite towards a higher Al/Si ratio at 1270 ºC and by the high amounts of corundum crystallized in all the samples.

5.2 Changes in physical properties during the firing process

5.2.1 Changes in physical properties and their relation to the mineral transformations

The increase in density with temperature in all the samples may be associated with the formation of the vitreous phase that gives rise to mullite crystallization, as has been described in kaolinite-rich clay materials (Andrews et al., 2012). By contrast, the increase in linear shrinkage may be associated with the dehydroxylation of the phyllosilicates and hydroxides during the firing process. On the other hand, the slight decrease in these two properties detected at 1270 ºC in samples BX75 and BX50 could be due to the formation of internal fractures during firing, which may not be observable to the naked eye.

The red colours of the fired clays can be attributed to the presence of Fe_2O_3 (Semiz and Çelik, 2020), as well as to its crystal size and distribution. The colour change from brown to reddish colours at 1000 ºC may be related with the increase in hematite content

at this temperature. Similarly, the decrease in hematite content at 1200º and 1270º would cause the colour change from reddish to grey colours. The CIE L*a*b* scale reflects a decrease in the a* and b* values with the increase in temperature, which is more marked in samples BX75 and BX50. Decreases in a* and b* values with rising temperature have also been described in clayey materials in the literature (Murad and Wagner, 1988), so the decrease in these values in samples BX75 and BX50 may be associated with their higher clay content and lower hematite content.

The continuous pore filling by mullite and vitreous phase is also the consequence of the decrease in the total porosity of the samples, which decreased progressively with the increase in temperature in the studied samples, especially at 1200 ºC, when the vitreous phase and mullite content is higher in all the samples. A decrease in porosity with temperature due to the formation of vitreous phase has also been reported in similar materials (Loutou et al., 2018; Gavshina et al., 2019).

The increase in the density and linear shrinkage correlates with the decreases in water absorption, which has also been described in clayey materials (Semiz and Çelik, 2020). The decrease in water absorption is also related with the decrease in total porosity (Loutou et al., 2018) and/or in pore size and connectivity. Higher pore connectivity, along with the possible internal fractures produced during firing as commented above, would explain the slight increase in porosity and water absorption in sample BX75 at 1200–1270 ºC. The maximum helium intrusion in this sample at 1270 ºC occurred in pores with a smaller radius than in samples BX100 and BX50, but these pores may have been more connected, leading to a small increase in porosity and water absorption capacity.

The thermal conductivity values obtained for the samples fired at 1200 ºC are higher when the total porosity and density are higher and the pore mode values are lower. Sample BX50 presents the lowest k value, which coincides with a higher pore mode, but a lower total porosity caused by a higher vitreous phase content. Conversely, samples BX100 and BX75 have higher k values, which correlate with a lower pore mode, but a higher total porosity caused by a lower vitreous phase content.

Finally, the point load test indicated that sample BX50 has higher resistance at 1200 ºC than at 1270 ºC, whereas the opposite was the case for sample BX100. This may be related with the mullite and corundum content, since at 1270 ºC sample BX100 has a higher corundum content, whereas sample BX50 presents a higher mullite content.

5.2.2 Refractory potential of the studied materials

The fired commercial bauxites were mainly formed by corundum (67–80%) and mullite (13–26%). The most similar composition to this among the studied ceramics is

that of sample BX100 fired at 1100 ºC (57% corundum and 21% mullite), whereas samples BX75 and BX50 are poor in corundum and rich in mullite from 1000 ºC upwards.

By contrast, some of the physical properties of samples BX75 and BX50 are closer to those of the fired commercial bauxites than those of sample BX100. In addition, the firing temperature is also an important factor, as commented above, since it causes changes in all the measured physical properties.

Sample BX100 fired at 1270 ºC presents a density (3.43 g/cm^3) similar to those of the fired commercial bauxites (2.8–3.23 g/cm^3), whereas BX75 and BX50 present a slightly lower density at this temperature (2.55 g/cm^3 and 2.43 g/cm^3, respectively), which, as suggested above, may be caused by the presence of internal fractures. The porosity of samples BX75 and BX50 fired at 1200 ºC (9.01 and 14.45% respectively) and that of sample BX100 (9.73%) fired at 1270 ºC are those that fit best with the porosity of the fired commercial bauxites (7–14.5%). This indicates that the mixture of the bauxite with the illite- and kaolinite-rich clay also produces a decrease in porosity at lower temperatures.

The water absorption values of sample BX75 fired at 1200–1270 ºC (2.25–3.09%) are similar to those of the fired commercial bauxites, whereas samples BX100 and BX50 fired at 1100–1200 ºC present water absorption values outside those limits, though close to them. Regarding the colour, samples BX50 and BX75 presented lower a* and b* values with increasing temperature, and they are closest to the a* and b* values of fired commercial bauxite when fired at 1270 ºC. This could indicate that, due to the mixture of the bauxite with the illite- and kaolinite-rich clay, the hematite content is lower, and thus samples are darker.

The thermal conductivity of the samples is related with their porosity and vitreous phase content. To be a suitable refractory material, thermal conductivity should be as low as possible. According to our results, a sample mixed 50% with illite- and kaolinite-rich clay presents better values of thermal conductivity (1.94 W/m.K) than the pure bauxite (2.40 W/m.K) at the same firing temperature. Finally, the higher resistance observed in samples BX50 and BX75 at 1200 ºC in the point load test may be related with a higher mullite and vitreous phase content at this temperature in these samples. The presence of illite and kaolinite gives rise to an increase in resistance due to the higher K content (as was also reported by the XRF results), which reduces the melting point and results in earlier vitrification and/or more effective formation of vitreous phase. By contrast, the higher resistance of sample BX100 at 1270 ºC may be associated with its corundum content, which is higher at this temperature.

Therefore, pure bauxite fired at 1270 ºC shows characteristics closely resembling those of the fired commercial bauxites regarding mineralogical composition, porosity

and density, and it shows high resistance. However, mixtures of bauxite with illite- and kaolinite-rich clays fired at lower temperatures show features not so far from the ranges exhibited by the fired commercial bauxites, but they are richer in mullite and vitreous phase, which lead to higher resistance and (in the case of sample BX50) lower thermal conductivity of the fired products.

6 CONCLUSIONS

The study of mixtures of bauxite with illite- and kaolinite-rich clays fired between 1000 and 1270 ºC shows mineralogical and textural changes during firing that clearly affect the physical properties of the materials.

At 1000 ºC, the formation of mullite seems to occur as a pseudomorphic, solid-state process after amorphous metakaolinite has originated through kaolinite dehydroxylation. At higher temperatures, the ongoing destabilization of the initial phases gives rise to a Si- and Al-rich vitreous phase from which cristobalite, ilmenite, hercynite, mullite and corundum crystallize. The vitrification process causes the textural homogenization of the samples with increasing temperature and the short duration of the firing process allows the coexistence of some of the initial phases with those generated during the firing.

Mullite and corundum are the most abundant phases at a high temperature, the mullite content being higher in those samples mixed with the illite- and kaolinite-rich clay. Both phases are immersed in the vitreous phase and their crystal thickness increases with temperature up to 2–4 μm. The analysed mullite presents a heterogeneous composition, but its Al content increases with temperature.

The formation of vitreous phase and mullite and the process of dehydroxylation, gives rise to an increase in the density and linear shrinkage that correlates with a decrease in total porosity, water absorption and thermal conductivity. The changes in the colour are related to the hematite content, whereas the resistance of the samples is associated with their vitreous phase and corundum content.

Both the firing temperature and the clay content influence the refractory potential of the mixtures, since samples mixed with illite- and kaolinite-rich clay present similar properties at lower temperatures to those of the fired commercial bauxites. This study shows that when mixing bauxite with Al–K-bearing clays, it is not necessary to reach such high firing temperatures to achieve refractory properties like those of fired commercial materials.

7 High-temperature mineral phases in natural clinkers: a natural analogy to refractory materials

The aim of this study is to analyse natural clinkers (= calcined clays by coal combustion) from a lower Cretaceous coal outcrop in Ariño (Teruel, NE Spain) in order to describe mineral and textural transformations produced during the spontaneous combustion of coal. To achieve this aim, samples were analysed using X-ray diffraction and optical and electron microscopy. Spontaneous combustion resulted in the melting of the surrounding clays, with the generation of an Al–Si-rich vitreous phase. Subsequently, high-temperature phases crystallized from this vitreous phase. These new minerals are interesting due to their similarity with those formed during ceramic processes, used in the manufacture of stoneware and ceramic tiles, as well as in refractory ceramics, and with natural events such as metamorphic and igneous processes. The studied natural clinkers are composed of vitreous phase mullite, hematite, hercynite, cristobalite, quartz, pyroxenes, cordierite, gypsum, pyrite, and calcium oxides. A trend from hematite to hercynite composition indicates compositional variations at sample scale, which evidence d-spacing differences in hercynite and may be related to the Al and Fe content in hercynite depending on its texture. The mullite shows higher Si/Al ratio (1.21) than the theoretical composition (0.35), indicating that this mullite is more Si-rich. Three pyroxene-type compositions (diopside-type, ferrosilite-type, and a Ca–Al-rich pyroxene) were found. Both the mullite and the pyroxenes are non-stoichiometric.

1 INTRODUCTION

Spontaneous coal combustion is a frequent phenomenon that can take place in coal deposits when high quantities of these materials are stored for large periods (Smith and Glasser, 2005; Querol et al., 2011). Several researchers have described this process (Misra and Singh, 1994; Querol et al., 2008; Quintero et al., 2009; Ribeiro et al., 2010; Misz-Kennan and Fabiańska, 2010; Zhao et al., 2013; Xu et al., 2017). Spontaneous combustion occurs in coal seams, stockpiles, and coal wastes when the rate of heat generation from the oxidation of organic matter exceeds the rate of heat dissipation (Misra and Singh, 1994). However, other factors could also favour or hinder spontaneous combustion (Querol et al., 2008). According to these authors, heat from the oxidation of inorganic coal-bearing phases, such as pyrite, could be the key factor in attaining the necessary heat for the self-ignition of coal. Furthermore, several parameters influence the process of spontaneous heating and combustion in coal. These parameters relate to mining (panel dimension, ratio of coal, extraction, etc.), the geological parameters (faults, joints, etc.), and the coal chemical composition (Sinha and Singh, 2005).

When the spontaneous combustion of coal takes places, new mineral phases are generated from those present in the previous coal and surrounding materials, i.e., clays, producing natural clinkers. The occurrence of natural clinkers associated with coal deposits has frequently been described in some areas (Foit et al., 1987; Cosca et al., 1989; Sokol et al., 1998; Henao et al., 2010; Ciesielczuk et al., 2014; Ribeiro et al., 2016; Baboolal et al., 2018).

The province of Teruel (NE, Spain) has historically been an important coal mining area, and there are still abundant coal deposits that can generate spontaneous combustion. Previous researchers have described the occurrence of natural clinkers in this area and identified by means of X-ray diffraction a new mineral association generated by this spontaneous combustion (Alastuey et al., 1993; Besteiro et al., 1996). However, there are no recent studies using high-resolution techniques in this area.

Accordingly, the aim of the present research is to study natural clinker samples from the locality of Ariño (Teruel, Spain) in order to describe the mineral and textural transformations that take place during the spontaneous firing of the coal, emphasizing in the mineral chemistry of the high-temperature phases in order to understand the calcination process. To this end, X-ray diffraction (XRD) and optical and field-emission scanning electron microscopy (FESEM) were used.

The calcination process can be compared to ceramic processes since the new mineral phases generated are very similar (Alastuey et al., 1993; Besteiro et al., 1996; Laita and Bauluz, 2018). Mineral phases such as mullite or pyroxenes have previously

been described in ceramic materials in the literature (Dondi et al., 1998; Bauluz et al., 2004; Laita and Bauluz, 2018). These materials could thus be used in the manufacture of stoneware and ceramic floor, as well as in refractory ceramics. Some of these new phases are also reported in natural processes such as metamorphism (Cosca and Peacor, 1987; Sandiford et al., 1987; Sokol et al., 1998) and igneous processes (Treiman, 1985; Brotzu et al., 1997; Markl, 2005). For this reason, determining the chemical and textural characteristics of all the new phases may shed light on the characteristics of the spontaneous combustion of coal as well as on the differences between this natural process and other natural or ceramic processes.

2 GEOLOGICAL SETTING

The samples analysed in this study were taken from a coal mining area in the Iberian Range, NE Spain, in a natural outcrop near the coal mine of Santa Maria, close to the locality of Ariño (Teruel) (N 41º01053.28" W 0º34050.24", elevation 539 m).

The studied materials belong to the lower-middle Albian (Lower Cretaceous) sedimentary deposits of the Escucha Formation (Pardo, 1979), which consists of three members: lower, middle, and upper. The lower member consists of marls at the bottom and carbonaceous clays with lignite beds towards the top. Carbonaceous clays with lignite remains and sandstones form the middle member, and the upper member is formed by limestones and sandstones (Cervera et al., 1976).

This formation constitutes a depositional sequence that represents a freshwater swamp with brackish swamp plain areas. This environment allowed the accumulation and preservation of coal deposits, which can be found in the lower and middle members of the formation (Pardo, 1979; Salas, 1987; Querol, 1988).

Near Ariño, the Escucha Formation is 200 m thick and contains abundant dark claystones and siltstones with minor sandstones (Bauluz et al., 2008). Previous researchers have described several stratiform natural clinker levels in a nearby area, which are similar to that studied in this research. The natural clinkers are included in the coal seams (Alastuey et al., 1993).

The natural clinkers analysed in this study present a scoriaceous appearance, with light and versicolor tones; they include clay and carbonaceous levels. The arrangement of the natural clinkers is stratiform and they are located from above and under the original position of the coal levels whose spontaneous combustion produced the calcination.

3 MATERIALS AND METHODS

3.1 Description of the samples

Precursor clays show plastic behaviour and contain abundant organic matter, kaolinite, and illite, and minor proportions of quartz, K feldspar, siderite, pyrite, and Ti and Fe oxides (Bauluz et al., 2008). They can be classified as ball clays and are mined nowadays.

Four representative samples of natural clinkers were studied on the basis of their different macroscopic characteristics and labelled as ESC-1, ESC-2, ESC-3, and ESC-4. All the samples are versicolor, with a vitreous appearance and high porosity. The size of the pores varies from 1 to 5 mm and they have irregular morphologies.

Although they are heterogeneous in colour, samples ESC-1 and ESC-4 are mainly red with black areas (which are more abundant in sample ESC-4), and samples ESC-2 and ESC-3 are mainly black with some yellow areas (Fig. 7.1).

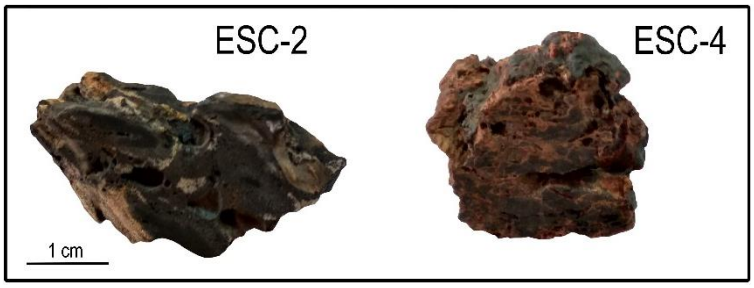

Fig 7.1. Images of a black natural clinker sample with yellow areas (ESC-2) and another red with black areas (ESC-4).

3.2 X-ray diffraction

Mineralogical analyses of the samples were performed by X-ray diffraction (XRD). Sample ESC-2 was divided into two subsamples: ESC-2B, corresponding to the black zones, and ESC-2BY, which includes black and yellow areas. Similarly, ESC-3 was divided into ESC-3B, predominantly black, and ESC-3YB, including black and yellow zones. As a result, six XRD patterns were obtained: two XRD patterns correspond to whole samples ESC-1 and ESC-4, and the other four patterns to samples ESC-2 and ESC-3.

To obtain the diffraction patterns, a RIGAKU D-Max/2500 diffractometer (Rigaku, Tokyo, Japan) was used with 40 kV voltage, 80 mA current, CuKα, and a graphite monochromator. XRD patterns were obtained from the 3–80º 2θ interval with a goniometer velocity of 0.03º 2θ/s and an integration time of 0.5 s.

Once the XRD patterns were obtained, $d_{(400)}$ values of hercynite and $d_{(104)}$ values of hematite were determined using the quartz of the sample as an internal standard. The

objective was to infer whether there was any relation between these parameters and the chemical composition of the phases. Hematite- and/or hercynite-rich samples (ESC-2B, ESC-2BY, ESC-3B, and ESC-3BY) were selected for this measure.

In order to quantify the different minerals, samples were homogenously mixed with 10 wt% corundum and analysed by XRD, following the RIR_{cor} method (Hillier, 2003). The amount (X) of each component (i) in a mixed sample with corundum can be obtained with the formula $X_i=[X_{cor}/RIR_{cor}][I_{(hkl)i}/I_{(113)cor}]$, where X_{cor} is the percentage of corundum mixed with the test sample, RIR_{cor} is the Reference Intensity Ratio of each phase with respect to corundum, $I_{(hkl)}$ is the absolute intensity of the strongest reflection of each mineral phase, and $I_{(113)cor}$ is the intensity of the (113) peak (2.08 Å) of corundum.

RIR_{cor} values of cristobalite (2.66) and gypsum (0.28) were calculated following the procedure described by Hillier (2003). The RIR_{cor} of hematite (1.587), mullite (0.5660), quartz (4.4045), cordierite (0.91), and hercynite (3.03) were taken from the literature (Hill, 1984; Schwartz et al., 1994; Laita and Bauluz, 2018). The reflections (hkl) used for the quantification of each mineral were 2.69 Å for hematite, 3.38 Å for mullite, 3.34 Å for quartz, 4.05 Å for cristobalite, 8.56 Å for cordierite, 2.45 Å for hercynite, and 7.64 Å for gypsum.

3.3 Optical and electron microscopy studies

Thin sections of the natural clinkers were studied by transmitted and reflected light microscopy to identify mineral phases and characterize their texture. The same thin sections were analysed by a Carl Zeiss Merlin field-emission scanning electron microscope (FESEM) with an Oxford energy-dispersive X-ray (EDS) detector at the University of Zaragoza (Zaragoza, Spain). The thin sections had previously been carbon-coated.

Compositional images of the samples were obtained using two types of backscattered electron detectors: angular selective (AsB) and energy selective (EsB). To obtain chemical information, semiquantitative analyses were acquired by an energy-dispersive X-ray (EDS) detector, with a detection limit of 0.1%. The accelerating voltage for AsB and EDS was 15 kV with a beam current of 400 pA; for EsB, the accelerating voltage was 4 kV with a beam current of 2.0 nA. Mineral formulas were obtained for the analysed minerals in order to compare them with the theoretical compositions.

4 RESULTS

4.1 X-ray diffraction (XRD): qualitative analysis and mineral quantification

Samples ESC-1 and ESC-4 contain mullite, cristobalite, hematite, quartz, pyroxenes, and cordierite (Fig. 7.2). The detected pyroxene reflections are common to several clynopyroxenes, so it is not possible to distinguish the type of pyroxene present in the natural clinkers on the basis of the XRD patterns. The coincidence of the characteristic peaks of tridymite with those of cristobalite and quartz does not allow its presence to be deduced, but it cannot be ruled out either.

Subsamples ESC-2B, ESC-2BY, ESC-3B, and ESC-3BY contain mullite, cristobalite, hematite, hercynite, quartz, and pyroxenes as detected in ESC-1 and ESC-4. Cordierite was identified in subsamples ESC-2B and ESC-3B and gypsum was identified in XRD patterns in ESC-2B, ESC-2BY, and ESC-3BY.

The hercynite $d_{(400)}$ values show differences from sample to sample. Two different $d_{(400)}$ peaks are observed in subsample ESC-2B (Fig. 7.2), corresponding to $d_{(400)}$ values of 8.208 Å and 8.196 Å, and we infer that these values pertain to two different reflections corresponding to the (400) planes. In subsample ESC-3B the $d_{(400)}$ value for hercynite is 8.168 Å. The hematite $d_{(104)}$ values are similar in all the subsamples, with values of 2.693 Å, 2.695 Å, 2.693 Å, and 2.693 Å for subsamples ESC-2B, ESC-2BY, ESC-3B, and ESC-3BY, respectively.

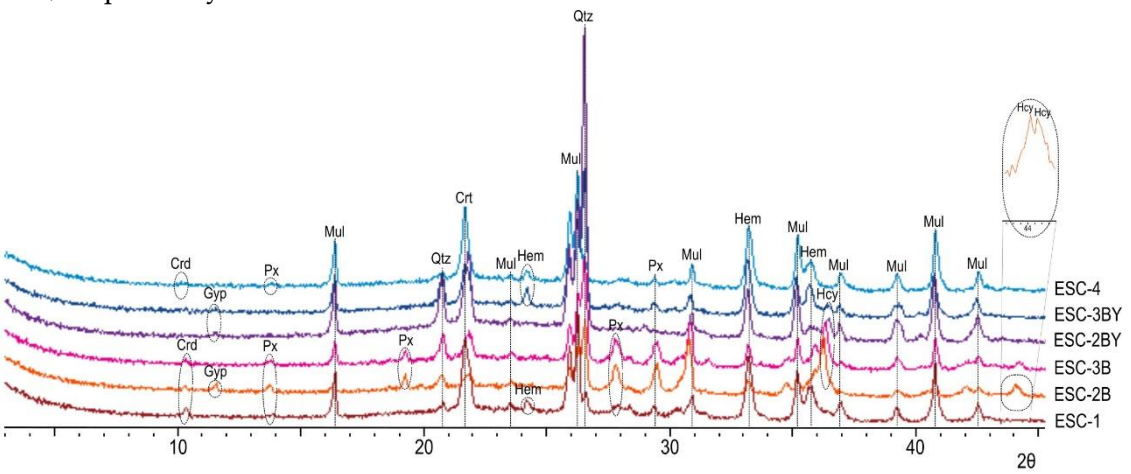

Fig 7.2. Mineral phases identified by XRD in the studied samples. *Qtz*=quartz, *Hem*=hematite, *Mul*=mullite, *Crt*=cristobalite, *Hcy*=hercynite, *Px*=pyroxene, *Crd*=cordierite, *Gyp*=gypsum.

According to quantitative XRD analyses (Table 7.1), mullite is the most abundant mineral, ranging from 16.3% to 38% of the total. The hercynite content is higher (>4%) in samples ESC-2B and ESC-3B and the hematite content is higher (~10%) in samples ESC-3BY and ESC-4. ESC-2BY and ESC-3BY present the highest quartz content (~7%). The

rest of the quantified phases (cristobalite, cordierite, and gypsum) are present in similar proportions in the samples where they are present.

The section labelled as "others" was obtained by summing up of all components to 100%. This section has the highest content in almost every sample (33.4% to 60.6%) and represents the amorphous phase. In addition, this section includes a small amount of pyroxenes (not quantified because it was not possible to identify the type of pyroxene).

Table 7.1. Mineral quantification of analysed natural clinkers.

Sample	Mineral Phase (%)							
	Quartz	**Hematite**	**Mullite**	**Cristobalite**	**Hercynite**	**Cordierite**	**Gypsum**	**Others**
ESC-1	1.3	7.5	27.9	2.8	-	2.2	-	58.3
ESC-2B	3.2	4.1	16.3	1.9	5	1.3	7.6	60.6
ESC-2BY	6.9	5.2	33.5	4.5	1.3	-	3.3	45.3
ESC-3B	4.6	3.7	27.8	2.6	4.3	2.5	-	54.5
ESC-3BY	6.9	10	38	4.4	1.4	-	5.9	33.4
ESC-4	1.7	9.5	35.4	5.5	-	1	-	46. 9

4.2 Optical microscopy

The natural clinkers show similar textures at the scale of the optical microscope. In general, the samples present a vitreous appearance and high and heterometric porosity with pore sizes from less than 1 μm to 5 mm. This porosity is probably a consequence of the dehydroxylation of phyllosilicates and the carbonate and organic matter destabilization.

The natural clinkers are formed by both transparent and opaque minerals immersed in a fine-grained matrix below the optical resolution of the microscope. These three components are distributed heterogeneously in the samples. In general, opaque minerals are more abundant than transparent phases at this scale of observation. Opaque minerals are concentrated in the black areas and transparent minerals in the red and yellow ones.

Under reflected light, spinel (hercynite, according to the XRD results) and hematite were identified. The relative abundance of these minerals varies from sample to sample and even at sample scale. As indicated above, and in agreement with the XRD data, hercynite, and hematite were concentrated in the black areas and were immersed in a continuous grey matrix that could not be identified by this technique. Hercynite is found as exsolution lamellae in hematite crystals (Fig. 7.3a) or forming replacement textures with hematite (Fig. 7.3b).

Under transmitted light, the only transparent minerals that are observed are quartz and degraded carbonate-type grains immersed in a fine-grained matrix with particle sizes below optical microscope resolution. Quartz is found as anhedral to subhedral clasts, with common angular grain boundaries, whereas carbonates occur as highly altered irregular rock fragments (Fig. 7.3c and d).

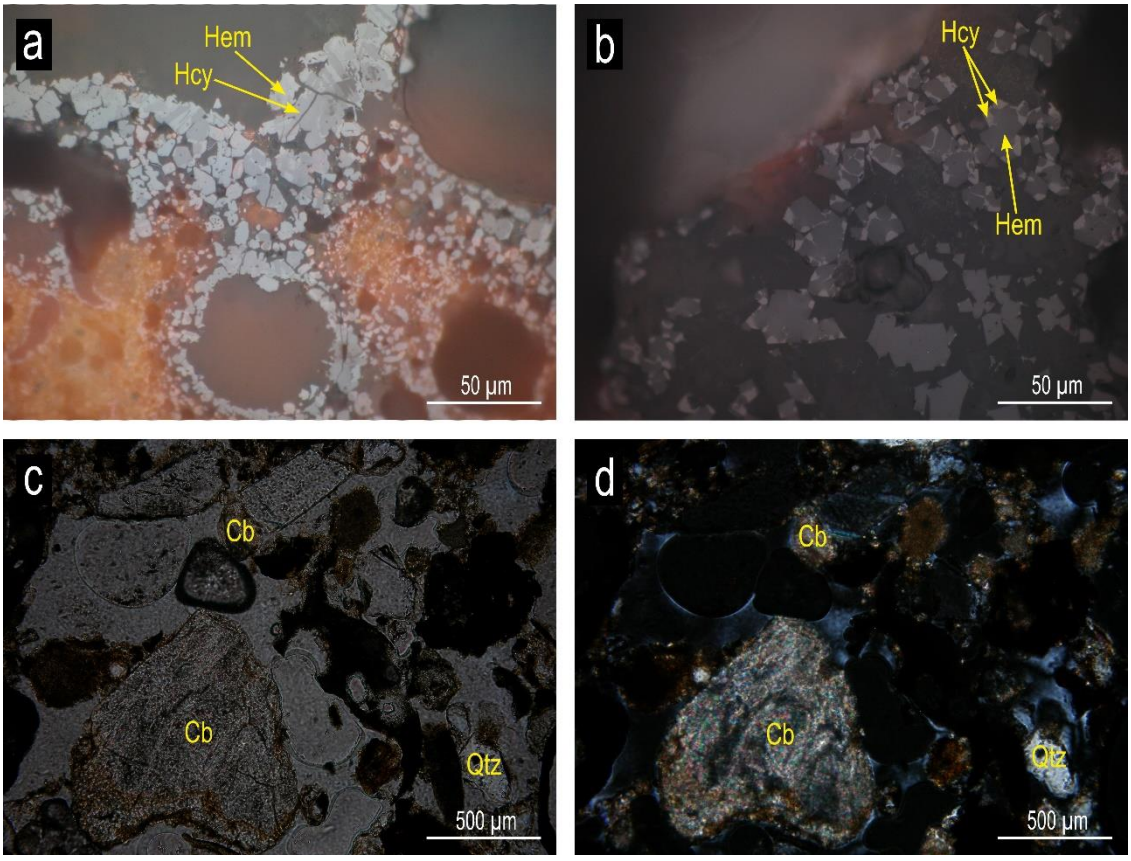

Fig 7.3. Reflected light optical microscopy images of hercynite and hematite in parallel nicols (**a** and **b**) and transmitted light optical microscopy images in parallel **(c)** and crossed nicols **(d)**. *Hem*=hematite, *Hcy*=hercynite, *Cb*=carbonates, *Qtz*=quartz.

4.3 Field-emission scanning electron microscopy (FESEM)

Backscattered electron images (EsB) and chemical analyses (EDS) of the natural clinkers show that they are texturally and compositionally heterogeneous. Electron images made it possible to observe the different minerals already identified by XRD, such as mullite, hematite, silica phases, pyroxenes, cordierite, and hercynite. Furthermore, pyrite and calcium oxides were detected by FESEM although they were not identified by XRD.

4.3.1 Major phases in the natural clinkers

The major phases present in the studied samples according to the XRD results are mullite, hematite, hercynite, pyroxenes, cordierite, quartz, and cristobalite. All these phases are embedded in an Al + Si-rich vitreous groundmass.

The mullite shows lenticular, acicular, and prismatic morphologies with random orientation. Its size is in general less than 1 μm in length, but in some areas it can reach up to 2 μm in length (Fig. 7.4a).

Hematite is present in all the samples and forms crystalline aggregates with different crystal morphologies and sizes. On the one hand, it occurs as anhedral crystals 1–20 μm in diameter, sometimes arranged in a mosaic-like texture (Fig. 7.4b). On the other hand, it appears as dendritic and arborescent aggregates (Fig. 7.4c), and it is also present as hexagonal plates smaller than 1 μm.

Hercynite is observed on the one hand as micron-sized euhedral to subeuhedral grains (Figure 4d), and in some cases as skeletal crystals showing polygonal sections, most of them hexagonal (Fig. 7.4e). On the other hand, hercynite lamellae, 1–2 μm wide and 1–6 μm long, are observed within hematite crystals suggesting the development of exsolution processes (Fig. 7.5a and b). The textural relationship between hercynite and hematite is correlated with EDS analyses of these phases, which are explained in the next section. Furthermore, replacement textures are observed between hematite and hercynite, where hercynite is replacing hematite (Fig. 7.5c). In some cases, hercynite is replacing hematite from the nucleus (Fig. 7.5e). In addition, hercynite lamellae are identified within cordierite crystals (Fig 7.5d); as in the case of hematite, this suggests exsolution processes between these two phases.

According to their chemical composition, three different groups of pyroxenes were distinguished: calcium- and aluminium-rich, calcium- and magnesium-rich, and iron-rich pyroxenes. Besides the differences in chemical composition, these show different textural features. Ca- and Al-rich pyroxenes are closely associated with hematite, hercynite and other pyroxenes, and appear randomly distributed in the matrix as micron-sized acicular crystals with no preferred orientation (Fig. 7.4f).

Ca- and Mg-rich pyroxenes appear as rounded crystals smaller than 1 μm, and are randomly distributed throughout the matrix (Fig 7.4g). They are texturally associated with the Ca- and Al-rich pyroxenes.

Fe-rich pyroxenes appear as rounded crystals smaller than 1 μm, as well as lenticular crystals with sizes greater than 10 μm. Occasionally, rounded crystals of Fe-rich pyroxene are in close relationship with pyrite, appearing in the outer limits of mosaic-like pyrite aggregates (Fig. 7.4h), suggesting that these pyroxenes could be replacing pyrite crystals.

A silica phase is observed as a groundmass filling the spaces among the crystals (Fig. 7.5e). From the XRD data it can be inferred that this phase corresponds to cristobalite. Furthermore, quartz fragments larger than 2 μm and showing reaction

edges (Fig. 7.5f) were recognized. These quartz fragments were probably already present in the previous clay.

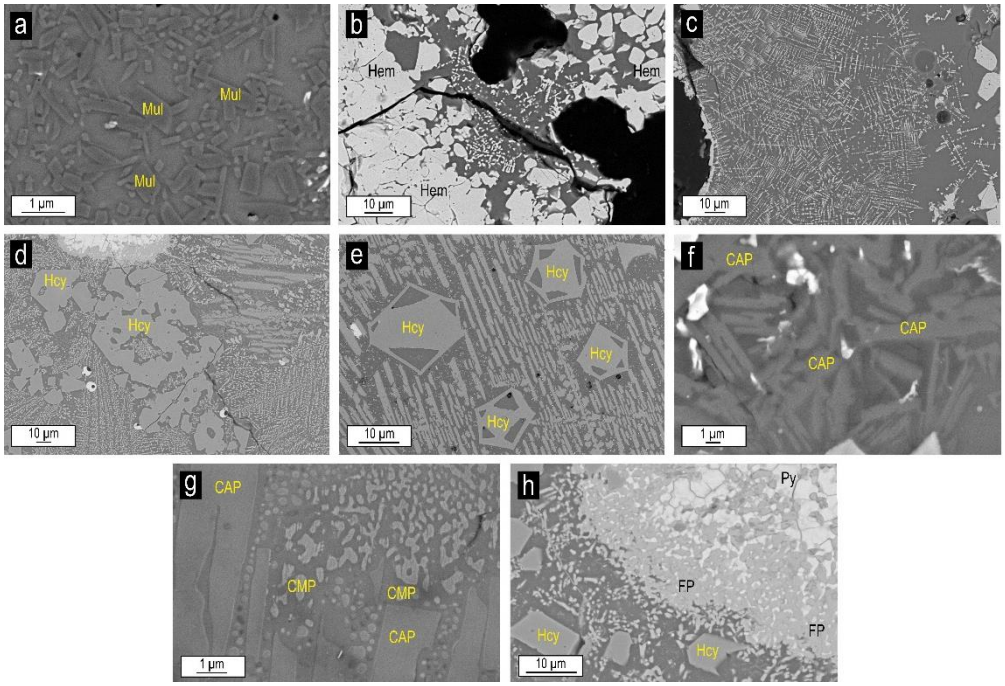

Fig 7.4. Backscattered electron images (BSE) images of **a)** micron-sized mullite crystals with random orientation; **b)** prismatic and subeuhedral hematite crystals; **c)** dendritic hematite crystals; **d)** subeuhedral hercynite crystals; **e)** hercynite crystals with polygonal sections; **f)** acicular Ca-Al-rich pyroxene crystals; **g)** Ca–Mg-rich pyroxene crystals, with rounded morphologies associated with Ca–Al-rich pyroxenes; and **h)** Fe-rich pyroxenes surrounding pyrite crystals. *Mul*=mullite, *Hem*=hematite, *Hcy*=hercynite, *CAP*=Ca–Al-rich pyroxene, *CMP*=Ca–Mg-rich pyroxene and *FP*=Fe-rich pyroxene.

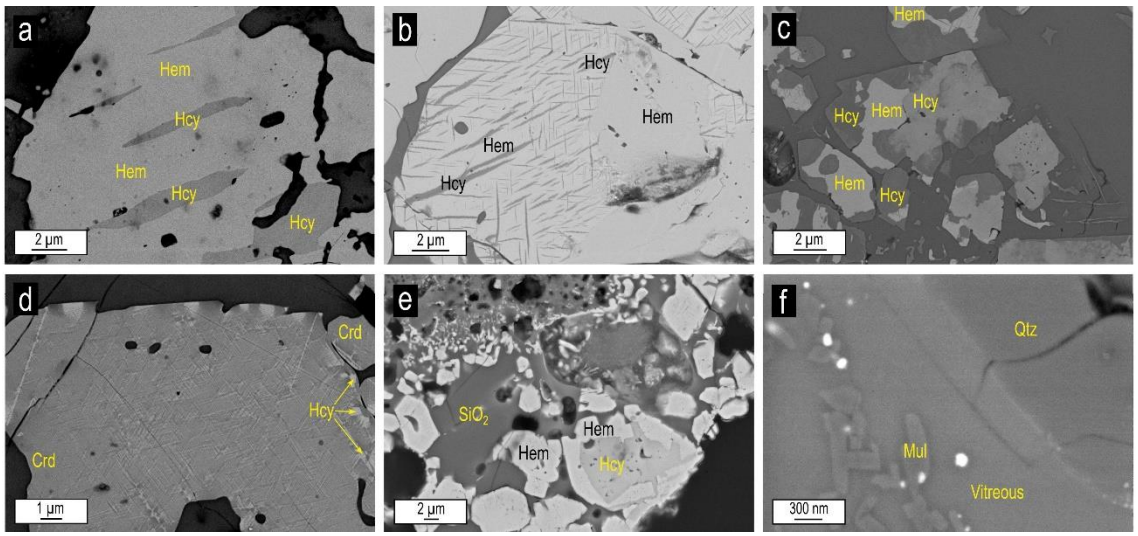

Fig 7.5. BSE images of **a)** and **b)** hercynite lamellae in hematite crystals; **c)** replacement texture between hematite and hercynite; **d)** hercynite lamellae in cordierite crystal; **e)** hercynite nucleus in hematite crystal and silica phase filling the spaces among the crystals; **f)** quartz fragment with reaction edge. *Hem*=hematite, *Hcy*=hercynite, *Crd*=cordierite, *SiO_2*=silica phases, *Mul*=mullite, *Qtz*=quartz, *Vitreous*=vitreous phase.

4.3.2 Minor phases in the natural clinkers

FESEM images revealed minor phases such as calcium oxides and pyrite that were not detected by XRD. Calcium oxides appear as microcrystalline aggregates with sizes of ~50 μm (Fig. 7.6a), which may come from carbonates in the precursor clay that have been destabilized with the spontaneous combustion.

Pyrite appears as anhedral crystals smaller than 1 μm, immersed in a grey matrix, probably vitreous (Fig. 7.6b), and associated with mullite, pyroxenes, and quartz fragments. Pyrite and quartz were present in the original rock and probably remained stable with the increase in temperature.

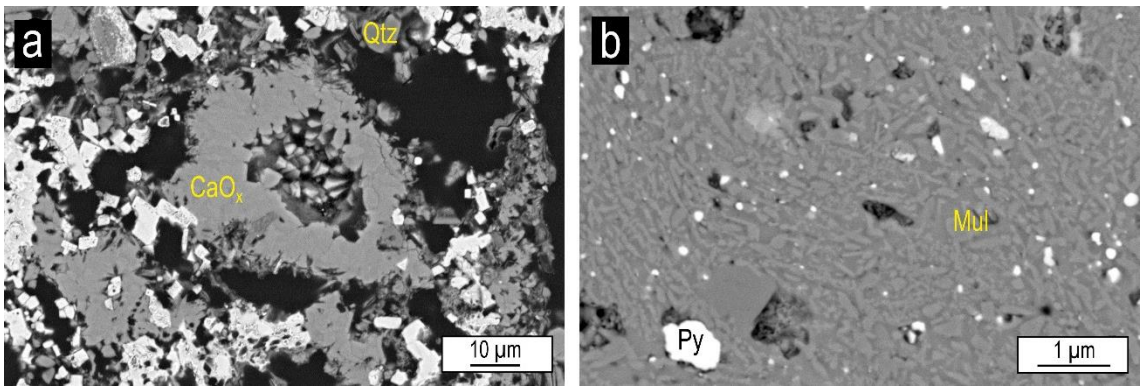

Fig 7.6. BSE images of **a)** microcrystalline aggregates of calcium oxides; **b)** anhedral pyrite crystals. *CaOx*=calcium oxides, *Qtz*=quartz, *Mul*=mullite, *Py*=pyrite.

4.3.3 Chemical analyses

EDS analyses of the major phases are shown in Table 7.2. As the analyses indicate, mullite has an Al–Si composition with minor proportions of Fe and Ti. Theoretical mullite has a Si/Al ratio of 0.35, whereas our analyses show an average Si/Al ratio of 1.21 and an average Si/(Al + Fe + Ti) ratio of 1.13, indicating that the analysed mullite is richer in Si than expected.

Hematite and hercynite show compositional differences from sample to sample and even at sample scale. Fig. 7.7 shows the Al vs. Fe contents (wt%) in these phases, indicating a trend from hematite to hercynite compositions. Taking into account all the analyses obtained from these phases, those with Fe contents higher than 56% and Al contents lower than 5% were considered to be hematite. Conversely, those analyses with Fe contents lower than 40% and Al contents higher than 18% were considered to be hercynite. The rest of the analyses, which are not included within these limits, were considered to be intermediate compositions. On average, the hematite composition is close to the theoretical one (69.9% Fe and 30% O), with a 59.6% content in Fe, but it also contains minor proportions of Al (2.3%). As regards the hercynite composition, the Al

(27%) and Fe (26.1%) contents are lower than the theoretical ones (31.05% Al, 32.13% Fe, and 36.82% O).

Table 7.2. Chemical composition (wt%) of all the mineral phases detected in the studied samples and average structural formula calculated. *n*=number of analyses; standard deviation in brackets.

Analysed Phases	wt% O	Na	Mg	Al	Si	K	Ca	Ti	Fe	Calculated Average Formula
Hematite (n=14)	37.7 (1.7)	-	-	2.3 (1.5)	-	-	-	-	59.6 (1.8)	$Al_{0.1}Fe_{1.9}O_3$
Hercynite (n=21)	44.6 (3.8)	-	1.8 (1.8)	27 (7.6)	-	-	-	0.4 (0.2)	26.1 (7.0)	$Mg_{0.1}Fe_{0.8}Al_{1.7}O_4$
Mullite (n=23)	51.3 (9.1)	-	-	21.4 (5.5)	25.9 (4.9)	-	-	0.3 (0.1)	1.1 (0.9)	$Fe_{0.1}Al_{2.3}Si_{2.9}O_{9.75}$
"Ceramic Pyroxenes" (n=9)	53.7 (0.9)	0.4 (0.2)	0.1 (0.2)	12.6 (1.3)	22.8 (2.2)	0.4 (0.3)	8.5 (1.5)	0.1 (0.1)	1.5 (0.9)	$Ca_{0.5}Fe_{0.1}Al_1(Al_{0.1}Si_{1.9})O6$
Cordierite (n=3)	45.6 (2.2)	-	1.4 (0.0)	16 (0.1)	5.4 (3.8)	-	-	0.8 (0.1)	30.9 (5.8)	$(Mg_{0.5}Fe_{1.6})(Fe_{1.4}Ti_{0.1})(Si_{2.6}Al_{2.4})Al_{2.8}O$
Silica phases (n=4)	50.7 (10.1)	-	-	1.4 (1.3)	48 (10.6)	-	-	-	-	$Al_{0.1}Si_{0.9}O_2$
Fe-pyroxenes (n = 3)	45.6 (0.2)	-	1.1 (0.3)	4.1 (0.1)	18.8 (0.4)	-	0.7 (0.1)	0.3 (0.1)	29.4 (0.6)	$Al_{0.1}Mg_{0.1}Fe_{1.3}(Al_{0.3}Si_{1.7})O_6$
Ca–Mg pyroxenes (n = 4)	54.1 (0.3)	-	2 (0.6)	5.2 (1.0)	27.4 (1.0)	-	6.9 (0.6)	0.1 0	4.3 (0.6)	$(Al_{0.4}Mg_{0.2}Fe_{0.2}Ca_{0.4})Si_{2.3}O_6$
Vitreous phase (n = 25)	48.8 (9.6)	0.2 (0.2)	1.1 (1.6)	11.6 (7.3)	30.9 (6.5)	2.4 (1.3)	1.4 (1.6)	0.2 (0.2)	2.9 (2.7)	-

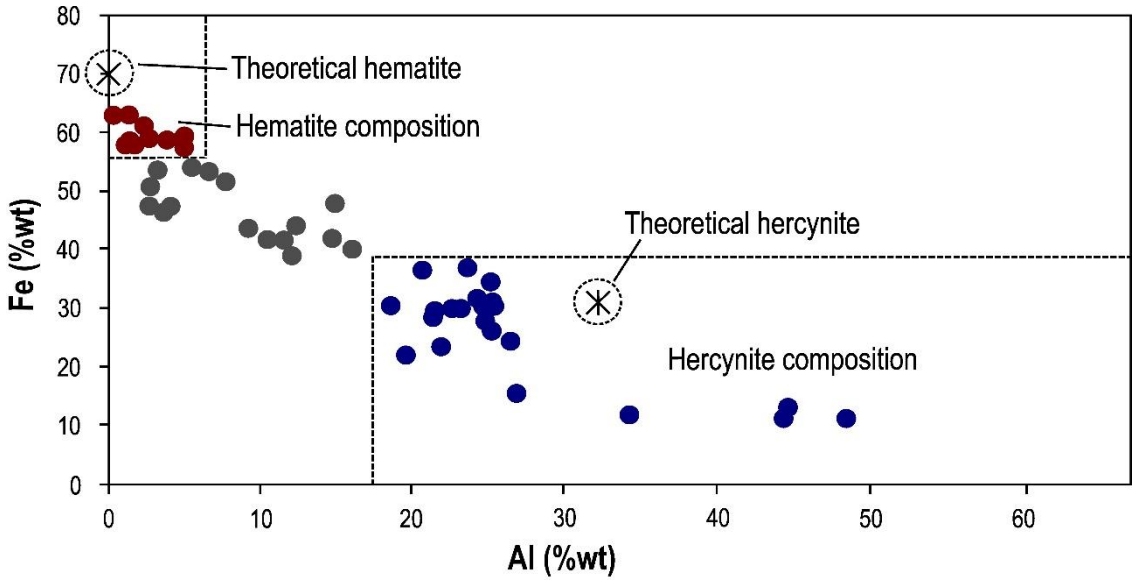

Fig 7.7. Al vs. Fe (wt%) graph showing hematite and hercynite composition.

Regarding pyroxenes, as mentioned above, three different compositional types were observed. The Ca- and Al-rich pyroxenes show low Fe, Na, K, Mg, and Ti contents. Their average structural formula is $Ca_{0.5}Fe_{0.1}Al_1(Al_{0.1}Si_{1.9})O_6$, and thus their composition may be described as intermediate between the fassaite compositions, reported by several authors (Dondi et al., 1998; Bauluz et al., 2004), diopside, and esseneite (Cosca and Peacor, 1987) (Fig. 7.8). Previous researchers have used the term "ceramic pyroxene" to refer to pyroxenes with an intermediate composition between fassaite and diopside (Dondi et al., 1998; Bauluz et al., 2004). Thus, in this study Ca- and Al-rich pyroxenes are called "ceramic pyroxenes".

The compositions of the Ca- and Mg-rich and Fe-rich pyroxenes are plotted in Fig. 7.9, showing that these groups have clearly different compositions. These compositions are close to diopside and ferrosilite compositions, respectively.

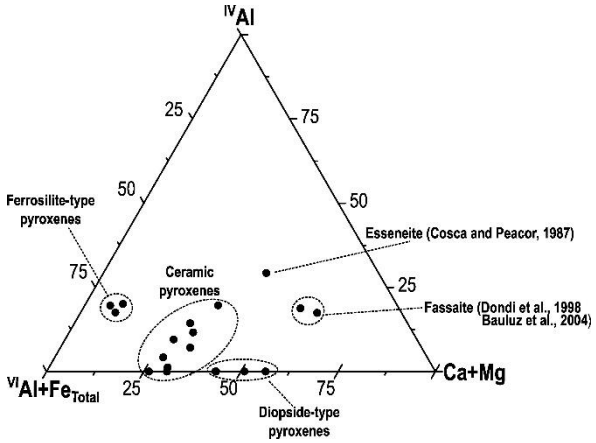

Fig 7.8. Plot of the EDS pyroxene compositions normalized on the basis of 6 oxygens in a ^{IV}Al–$^{VI}Al+Fe_{total}$–Ca+Mg diagram. Esseneite and fassaite compositions from the literature (Cosca and Peacor, 1987; Dondi et al., 1998; Bauluz et al., 2004) have also been plotted as reference.

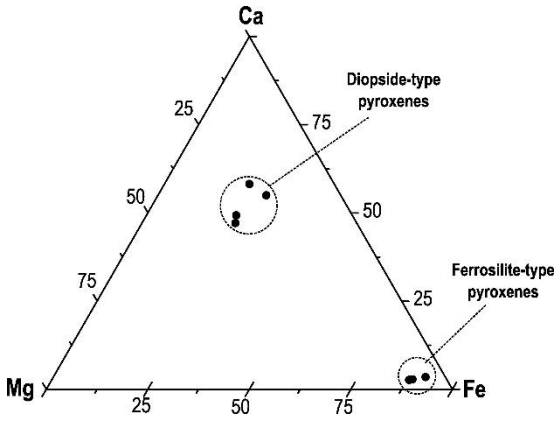

Fig 7.9. Plot of the EDS Ca–Mg-rich and Fe-rich pyroxene compositions normalized on the basis of 6 oxygens in a Ca–Mg–Fe diagram. The diagram shows the compositional differences between diopside- and ferrosilite-type pyroxenes.

The analysed diopside-type pyroxenes present lower Ca (6.9%) and Mg (2%) contents than the theoretical diopside (18.51% Ca, 11.22% Mg, 25.94% Si, and 44.33% O), and they also contain Fe, Al, and minor proportions of Ti. The average structural formula of these phases is $(Al_{0.4}Mg_{0.2}Fe_{0.2}Ca_{0.4})Si_{2.3}O_6$. Similarly, a comparison of the Fe-rich pyroxene with ferrosilite shows it to have lower Si (18.8%) and Mg (1.1%) contents and higher Fe (29.4%) content than the theoretical composition (10.46% Mg, 24.04% Fe, 24.18% Si, and 41.32% O), with an average structural formula $Al_{0.1}Mg_{0.1}Fe_{1.3}(Al_{0.3}Si_{1.7})O_6$. It also contains Al and minor proportions of Ca and Ti.

The analysed cordierite presents high Fe (30.9%) and Al (16%) contents and low Si, Mg, and Ti contents. Compared with the theoretical composition (8.31% Mg, 18.45% Al, 24.01% Si, and 49.23% O), the analysed cordierite is Mg- and Si- poor and Fe-rich.

Finally, the groundmass of all the studied samples presents a heterogeneous Al- and Si-rich composition, with minor Fe, K, Mg, Ca, Ti, and Na contents. It can be deduced that it corresponds to the vitreous phase detected by XRD.

5 DISCUSSION

5.1 Destabilization of the initial phases

The natural clinkers initially contained organic matter, abundant kaolinite and illite and minor proportions of quartz, K feldspar, siderite, pyrite, and Ti and Fe oxides (Bauluz et al., 2008). Most of these phases were destabilized and melted during the spontaneous combustion of coal.

The calcium oxides observed by FESEM may come from small amounts of carbonates present in the precursor clays that have been destabilized, as suggested by optical microscopy observations of degraded carbonate fragments. Carbonate destabilization can generate not only these calcium oxides, but also other Ca-rich phases such as pyroxenes (Bauluz et al., 2004).

Organic matter is eliminated between 200 and 800 ºC, although this depends on its content in the precursor material (Johnson et al., 1988). In addition, kaolinite, illite, and K feldspar are not detected in the studied natural clinkers, indicating that they have been destabilized, as described by other authors (Aras et al., 2002; Laita and Bauluz, 2018), and that they are therefore less stable phases than quartz or pyrite. Kaolinite is not stable at temperatures above 200 ºC in natural environments (Merriman and Peacor, 1998). Similarly, metamorphic rocks such as those from greenschist facies do not contain illite, which indicates that it is not stable above 350 ºC. With regard to K feldspars, it is possible that they were destabilized during the spontaneous combustion due to their low content in the precursor clays.

The oxidation of pyrite and siderite results in hematite and magnetite (Ram et al., 1995; Kapička et al., 1999) the former of which was identified in the study samples. In addition, when pyrite is oxidized, aqueous, acidic, and sulphate-rich solutions are produced (Floyd et al., 2003). These solutions, along with the presence of calcite, produce sulphate minerals such as gypsum. Accordingly, SO_4^{2-} released from pyrite oxidation, along with Ca from carbonates, allows gypsum precipitation (Ritsema et al., 1993), as it is identified by XRD in some of the studied samples.

Finally, quartz is also observed, indicating that it is the most stable phase during combustion, although it shows reaction edges, which suggest that it is partially destabilized due to the high-temperatures.

5.2 Crystallization of new phases

5.2.1 Hematite, hercynite and cordierite

Hematite, magnetite, hercynite, and cordierite are frequently described in natural clinkers (Cosca et al., 1989; Alastuey et al., 1993; Henao et al., 2010; Ribeiro et al., 2016; Baboolal et al., 2018). In the studied natural clinkers hematite, hercynite and cordierite were observed. Their textures are clearly related to neoformation associated with the combustion process.

Exsolution textures were observed between hematite and hercynite, as well as between cordierite and hercynite. These textures occur frequently as a consequence of cooling from a melted mass, in this case resulting from the spontaneous combustion process. With cooling, lamellae are separated within the host crystals due to differences in cation sizes, since at high-temperatures crystal structures can accommodate cations of different size more easily. However, at lower temperatures, the range of possible substitutions of different-sized cations is much less.

The existence of both magnetite exsolution lamellae in hercynite and hercynite exsolution lamellae in magnetite has been previously described (Cosca et al., 1989; Estrada et al., 2009). Solid solutions between both phases are also described in natural clinkers (Estrada et al., 2009; Henao et al., 2010). These textures are also formed in igneous and metamorphic rocks (Smith, 1965; Mücke, 2003; Markl, 2005). Furthermore, previous investigations have described titaniferous spinel intergrowths with hematite in igneous and metamorphic rocks and the possibility of a Zn-rich spinel formation that went into solution in cordierite in metamorphic rocks (Stoddar, 1979; Mücke, 2003).

Magnetite was not detected by XRD in this study. This may be due to the fact that part of a primary magnetite may be pseudomorphed by hematite in a martitization process (Estrada et al., 2009). In this case, it is possible that remnant traces of the original magnetite may persist in the studied samples, which may not have been detected due to the low concentration. Another possibility is that hematite was formed during the spontaneous combustion instead of magnetite.

The existence of hercynite lamellae in magnetite crystals and vice versa suggests that both phases can occur as discrete phases at peak temperatures with substantial mutual solid solution (Sandiford et al., 1987). However, the fact that the hercynite in the studied natural clinkers never contains exsolution lamellae supports the hypothesis that it has been exsolved from another phase. This phase could be a primary magnetite

subsequently transformed into hematite, or it could be a hematite that crystallized during the spontaneous combustion instead of magnetite.

Fig. 7.10 shows the Fe vs. Al content of hercynite crystals in different textural arrangements. Hercynite has a higher Al content and lower Fe content when it is found as scattered crystals or is involved in replacement textures with hematite (24.2% Al and 27.8% Fe). By contrast, the Al content is lower and the Fe content is higher when it forms exsolution lamellae within hematite (5.9% Al and 48.1% Fe) or cordierite (11.4% Al and 40.8% Fe).

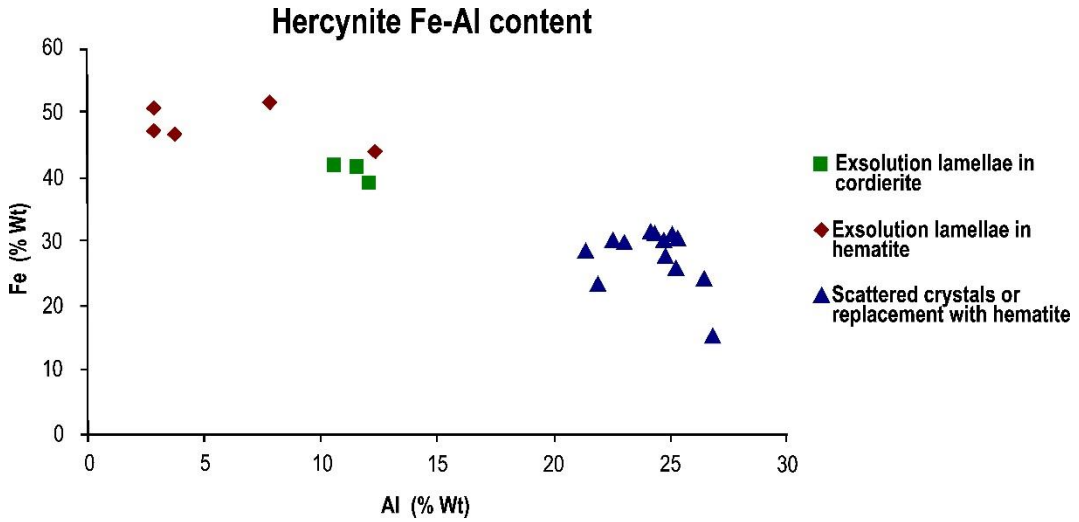

Fig 7.10. Fe vs. Al (wt %) content in hercynite crystals from samples ESC-2 and ESC-3. The proportion of the two elements depends on the way the crystals are arranged: exsolution lamellae in cordierite or hematite, or replacement textures with hematite or scattered crystals.

The replacement textures between hercynite and hematite imply that one mineral has been formed from another, so they are not coeval phases. A similar process where spinel is formed by replacement of magnetite, which reacts with the vitreous phase, is described in the literature (Treiman, 1985). This reaction could have occurred in the same way in the studied natural clinkers, with the later oxidation or martitization of magnetite to hematite.

Exsolution lamellae of hercynite within both hematite and cordierite were observed in sample ESC-2, whereas in sample ESC-3 such exsolution lamellae were only observed within hematite.

This may be related to the above-mentioned differences in the $d_{(400)}$ values of hercynite observed in the XRD patterns of these two samples (8.208, 8.196 for ESC-2 and 8.168 Å for ESC-3). Thus, a close relationship between the textural arrangement of hercynite and the compositional and structural variations of this mineral can be deduced. In other words, the hercynite composition is different when it appears as

exsolved lamellae within hematite or cordierite, and it shows structural differences depending on the mineral from which the exsolution process occurred.

The hematite $d_{(104)}$ values are similar among samples ESC-2 and ESC-3, indicating that much of the detected hematite has a close composition to the theoretical one. This supports the hypothesis that the hematite may proceed from magnetite. If the hematite were crystallized from the vitreous phase, a higher Al content would be expected.

In hercynite exsolution lamellae within hematite, the cation size difference between Al and Fe favours the exsolution, although Fe-rich phases, Al-rich phases, and intermediate phases were able to form. In contrast, in hercynite exsolution lamellae within cordierite, the structural and compositional differences between the two phases preclude the existence of intermediate compositions.

The intermediate compositions between hematite and hercynite (Fig. 7.7) may be due to the existence of nanometric exsolution textures, and thus EDS analyses may come from those areas where both phases are present. Alternatively, these intermediate analyses may also be reflecting the existence of minority solidus solutions that do not modify the $d_{(104)}$ values of hematite.

Finally, the idiomorphic skeletal textures that hercynite sometimes shows (Fig. 4.7e) suggest its crystallization in two stages. A possible hypothesis that would explain this situation is the formation of a first-stage hercynite from the vitreous phase that was subsequently destabilized, giving rise to convex morphologies. After that, a euhedral hercynite could have crystallized in a second stage, surrounding the first crystals and including part of the vitreous phase.

5.2.2 Mullite and pyroxenes

Mullite is present as 1–2 μm-long lenticular, acicular, and prismatic crystals with random orientation. Previous, electron microprobe analyses of mullite formed by the spontaneous combustion of coal reported Al-rich mullite with a composition close to the theoretical formula (38 wt% Al, 13.18 wt% Si, and 48.82 wt% O) (Sokol et al., 1998).

However, chemical analyses of mullite in this study showed a Si/Al ratio of 1.21, which is higher than the theoretical ratio (0.35), indicating that this mullite is Si-rich. Analysis of mullite from aluminium-rich clays during ceramic firing also shows a non-stoichiometric Si-rich composition (Laita and Bauluz, 2018). These authors explained that this is probably a consequence of the temperature and the length of time of the ceramic process. Similarly, the non-stoichiometric composition of mullite in the natural clinkers could be explained by the temperature reached and the duration of the spontaneous combustion in the studied area, which would not have provided ideal conditions for mullite crystals to reach the theoretical composition.

EDS analysis showed three pyroxene-type compositions: "ceramic pyroxenes", diopside-type, and ferrosilite-type.

The "ceramic pyroxenes" were observed as micron-sized acicular crystals texturally associated with the other pyroxenes. Previous researchers have defined an uncommon C2/c pyroxene called esseneite as a product of pyrometamorphism associated with naturally combusted coal seams, which is similar to some pyroxenes from our analysis (Cosca and Peacor, 1987). Other investigations have described pyroxenes formed during ceramic processes whose compositions are close to a pyroxene known as fassaite (Dondi et al., 1998; Bauluz et al., 2004). Even though the chemical compositions of the "ceramic pyroxenes" presented in this research do not match completely with those of fassaite or esseneite, they have intermediate compositions between these pyroxenes and diopside (Fig. 7.8).

Diopside has previously been reported in natural clinkers (Foit, 1987; Querol et al., 2011) as well as in igneous and metamorphic rocks and skarns (Berg, 1991; Ridolfi et al., 2016). In ceramics, it is described as a metastable calcium and/or magnesium phase formed by the reaction of calcite, quartz and aluminium clays (Trindade et al., 2009). The calculated formula for diopside-type in the analysed natural clinkers ($(Al_{0.4}Mg_{0.2}Fe_{0.2}Ca_{0.4})Si_{2.3}O_6$) shows a lower Ca and Mg content and a higher Si content than the theoretical formula ($CaMgSi_2O_6$).

Ferrosilite has been described in igneous rocks (D'Souza et al., 2006; Ridolfi et al., 2016). The melting of igneous crustal components at high-temperatures and very low, near-constant oxygen fugacity allows ferrosilite to crystallize (D'Souza et al., 2006). Ferrosilite-type pyroxene in the studied natural clinkers ($(Al_{0.4}Mg_{0.1}Fe_{1.3})Si_{1.7}O_6$) shows higher Fe and lower Mg contents than the theoretical ferrosilite ($(FeMg)SiO_3$).

As with the mullite composition, the fact that the analysed pyroxenes do not coincide with the theoretical ones could have to do with the firing dynamics associated with the spontaneous combustion of coal.

5.3 The spontaneous combustion of coal and the formation of the vitreous phase

An Al- and Si-rich vitreous phase is formed by the destabilization of the initial phases due to the increase in temperature, and it represents approximately 50% of the samples. The Al and Si come from quartz, kaolinite, and illite. Furthermore, this vitreous phase also contains minor proportions of K (from K feldspar and illite), Fe (from siderite, pyrite, and illite), Ca (from carbonates), and Mg (from illite). Previous researchers have described the appearance of a vitreous phase from 800 ºC due to the spontaneous

combustion of coal and resulting from the destabilization of clay minerals and other phases present in the initial rocks (Ram et al., 1995).

The new mineralogy and texture found in the studied samples are similar to that of fired aluminium-rich ceramics where the vitreous phase starts to form from 1000 ºC and, consequently, mineral phases also crystallize from that temperature (Laita and Bauluz, 2018). Furthermore, previous investigations indicate that the temperature reached in the studied area was probably higher than 1050 ºC and the calcination periods were longer than 100 h (Alastuey et al., 1993).

These differences in temperatures indicated in the literature for the formation of the vitreous phase and subsequent mineral transformations may be due to the fact that these firing processes are heterogeneous and their duration and intensity can vary within the stratum where the natural clinkers are found. In the case of spontaneous combustion, besides temperature and length of time, there are several parameters that influence the process of spontaneous heating and combustion in coal, such as factors relating to mining, geological parameters, and the chemical contents of coal (Sinha and Singh, 2005). These parameters affect the composition of the new mineral phases and explain the presence of non-stoichiometric phases such as mullite and pyroxenes.

The higher percentages of vitreous phase and mullite, together with the greater size of the mullite (1–2 μm in length), compared to those at 1000 ºC in ceramics (nanometer mullite) (Laita and Bauluz, 2018), allow to deduce that, in our case, the temperature reached was higher than 1000 ºC. Furthermore, Mössbauer spectroscopy and CCSEM measurements of the transformation products formed from pyrite included in coal in the drop tube furnace test at gas temperatures from 1038 ºC to 1454 ºC have shown magnetite to be the dominant oxide formed (Huffman et al., 1990).

In the studied samples, hematite may have resulted from magnetite martitization. Magnetite thus crystallized due to the spontaneous combustion and, in this case, the temperature reached could have been between 1000 and 1454 ºC.

6 CONCLUSIONS

Spontaneous combustion of coal generates textural and compositional changes in the precursor kaolinite-rich clays. These changes include the destabilization of original phases, giving rise to the genesis of an Al–Si-rich vitreous phase, and the subsequent crystallization of new mineral phases. These phases are similar to those formed in a ceramic process as well as in metamorphic and igneous environments.

The trend from hematite to hercynite composition indicates variations at sample scale, which are reflected in XRD patterns evidenced in crystallochemical parameters in hercynite. This suggests structural variations that can be related to the Al and Fe content in hercynite depending on its texture: exsolution lamellae within hematite (5.9% Al and 48.1% Fe), exsolution lamellae within cordierite (11.4% Al and 40.8% Fe), and replacement textures with hematite, as well as scattered hercynite crystals (24.2% Al and 27.8% Fe).

The analysed mullite is Si-rich (Si/Al=1.21) and non-stoichiometric compared with the theoretical mullite.

The study shows the crystallization of three different types of pyroxenes: diopside-type, ferrosilite-type, and a Ca–Al-rich pyroxene ("ceramic pyroxene") with an intermediate composition between that of diopside, fassaite, and esseneite. Compared with the theoretical compositions, the analysed pyroxenes are non-stoichiometric.

The presence of non-stoichiometric phases could be explained by the short duration of the spontaneous combustion, which would not favour the formation of phases reaching the theoretical composition.

The higher percentages of vitreous phase and the larger size of mullite crystals compared with those of the ceramic process support the idea that the temperature would have reached more than 1000 ºC.

Finally, the combination of XRD and electron microscopy has enabled a detailed characterization of the texture of the natural clinkers and the newly formed phase composition. The study of these new phases allows them to be compared with those formed during natural and ceramic processes and thus deepens our understanding of high-temperature crystallization processes.

Discusión general

8

In this chapter, the main contributions of this PhD thesis are discussed. The combined facies, clay mineralogy, and oxygen and hydrogen isotope analyses of the clay minerals of the continental successions including palaeosol levels recorded in the Blesa Formation (early Barremian, Oliete subbasin, SE Iberian Chain) and the Torrelapaja Formation (late Hauterivian–early Barremian, Torrelapaja subbasin, NW Iberian Chain) contribute to improving the Lower Cretaceous palaeoclimatic record of the NE of Spain. The usefulness of NanoSIMS as an analytic tool for isotopic analysis is demonstrated in this thesis, as the first results obtained allowed Lower Cretaceous palaeoclimatic and palaeotemperature conditions to be inferred, corroborating the change in the climatic conditions deduced from the clay mineralogy data.

The study of mineral and textural transformation in natural clinkers and refractory cylinders composed of mixtures of bauxite and illite- and kaolinite-rich clays allowed the characterization of the high-temperature mineral phases formed during firing. Given the similarity between the new mineral phases generated in the two materials, the ceramic and spontaneous coal combustion processes lend themselves to comparison, shedding new light on high-temperature crystallization processes. The analysis of the physical properties of the refractory cylinders during firing enabled to establish the relationship between the different mineral transformations that take place with the temperature, depending on the composition of the raw material and the changes in the physical properties of the fired products, as well as to deducing their refractory potential.

1 GÉNESIS DE LOS PALEOSUELOS DEL SE Y NW DE LA CORDILLERA IBERICA

1.1 Distribución y cambios de facies en los paleosuelos

Los paleosuelos de la Fm. Blesa y la Fm. Torrelapaja descritos en los capítulos 3 y 4 de esta tesis doctoral presentan litologías que van desde lutitas/margas arcillosas y silíceas hasta lutitas/margas calcáreas (Aurell et al., 2021), lo que indica que su desarrollo tuvo lugar a partir de la meteorización química de rocas lutítico-margosas. Esta variedad litológica se debe a diversos factores climáticos, tectónicos y sedimentarios (Aurell et al., 2018; Aurell et al., 2021).

Las variaciones litológicas que se observan en los afloramientos de la Fm. Blesa, con lutitas y margas arcillosas en la base y margas silíceas y lutitas calcáreas hacia las partes intermedias y el techo de los perfiles, se correlaciona con la evolución sedimentaria desde facies continentales arcillosas (en las que se desarrollaron los paleosuelos) hacia facies carbonatadas palustres-lacustres descrita por Aurell et al (2018) para la sección estratigráfica inferior de la Fm. Blesa (LBS) en la subcuenca de Oliete (SE de la Cordillera Ibérica) (Fig. 8.1a).

Sin embargo, el cambio de facies en los afloramientos de la Fm. Torrelapaja tiene lugar no solo en la vertical, sino también de manera lateral (Aurell et al., 2021), con un predominio de margas arcillosas y silíceas y lutitas calcáreas en el afloramiento de Valdelavieja y lutitas silíceas en el afloramiento de Las Cañadas (Fig. 8.1b). Esto se debe a que el depósito de los distintos materiales de la Fm. Torrelapaja, dentro de la subcuenca de Torrelapaja (NE de la Cordillera Ibérica), se produjo en tres estadios sedimentarios diferentes, siendo los dos primeros de predominancia arcillosa y carbonatada (Aurell et al., 2021) (Fig. 8.1c). Esto dio lugar tanto a la formación de las lutitas y margas (sobre las que se desarrollaron los paleosuelos), como de las calizas, areniscas y conglomerados que se observan en los afloramientos de Valdelavieja y Las Cañadas. Posteriormente, durante el tercer estadio sedimentario, se produjo el asentamiento de un sistema aluvial-fluvial dando lugar a un aumento del aporte de terrígenos por un incremento de la actividad tectónica en las zonas en las que se localiza el afloramiento de Valdelavieja (ver capítulo 4), dando lugar a una mayor presencia de niveles de areniscas y conglomerados en este afloramiento (Fig. 8.1c).

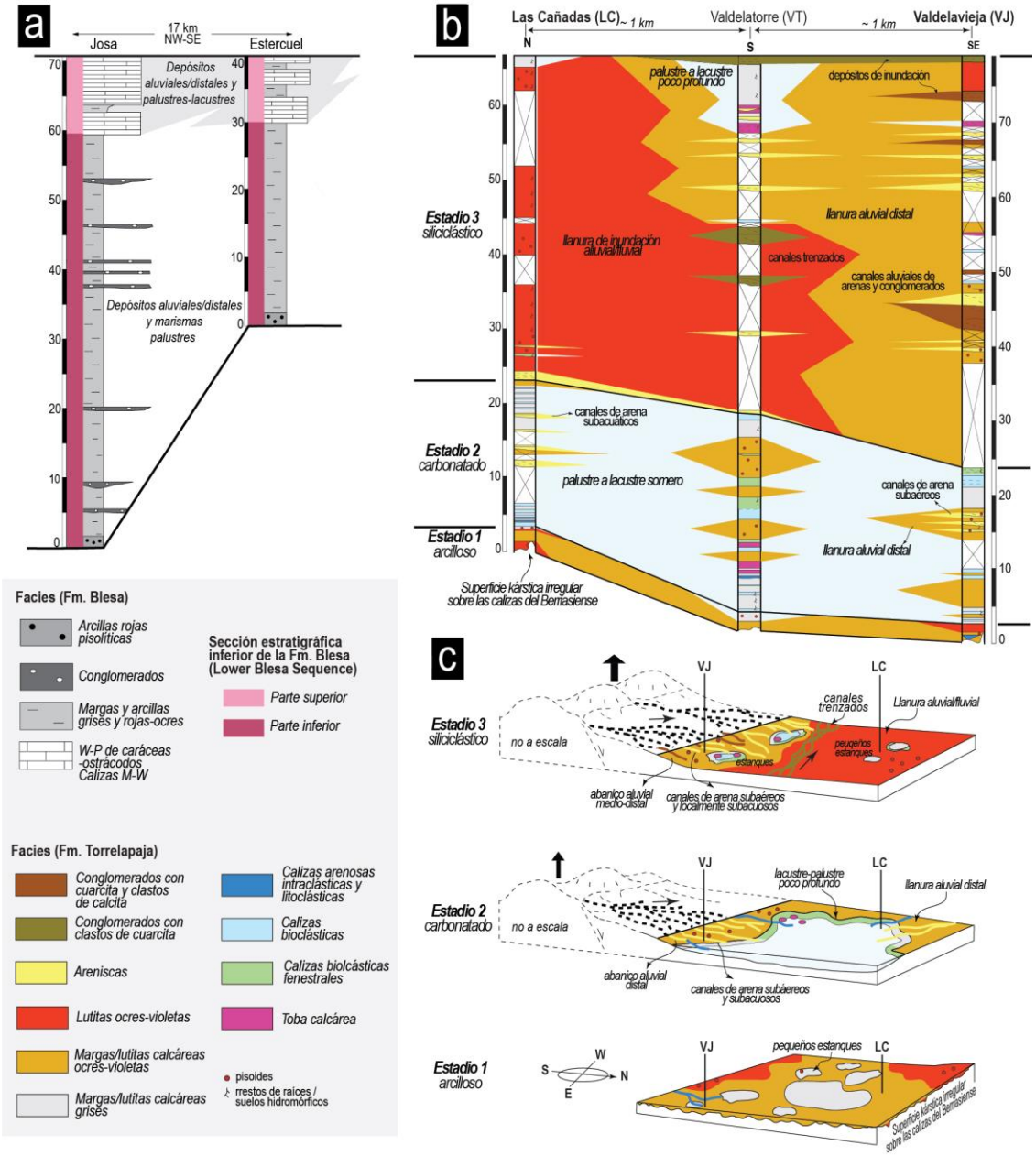

Fig. 8.1. **a)** Secciones estratigráficas representativas de la parte inferior de la Fm. Blesa (modificado de Aurell et al., 2018); **b)** correlación de facies de la Fm. Torrelapaja (modificado de Laita et al., 2022); **c)** modelo sedimentario de los estadios sedimentarios diferenciados en la Fm. Torrelapaja (adaptado de Aurell et al., 2021).

1.2 Minerales autigénicos y detríticos en la matriz de los paleosuelos

Las morfologías platiformes con contornos hexagonales (Fig. 8.2a y b) y los agregados tipo "book" (Fig. 8.2c) de la caolinita que se encuentra junto a hematites, goethita, anatasa, rutilo, ilmenita y diásporo formando la matriz de los paleosuelos de los niveles inferiores de las Fms. Blesa y Torrelapaja, sugieren un origen autigénico para este mineral, ya que son formas y texturas muy delicadas para soportar procesos de erosión o transporte (Bauluz et al., 2014; Do Campo et al., 2018; Yuste et al., 2020).

Además, han sido comúnmente descritas como productos de la meteorización química durante la formación de suelos (ej. Chamely, 1986; Mack et al., 1993; Righi y Meunier, 1995; Raucskik y Varga, 2008; Bauluz et al., 2014; Do Campo et al., 2018). Por otro lado, los análisis EDS realizados en el microscopio electrónico muestran que las caolinitas analizadas en ambas formaciones presentan pequeñas proporciones de Fe (2–4%) que podría estar sustituyendo al Al en la capa octaédrica (Mendelovici et al., 1979; Cantinolle et al., 1984; Mestdagh et al., 1980; Yuste et al., 2015).

La esmectita de los niveles de paleosuelos intermedios de las Fms. Blesa y Torrelapaja presenta morfologías onduladas e irregulares tipo "flake" (Fig. 8.2d) y se encuentra, junto con la caolinita, formando la matriz de los paleosuelos, lo que sugiere que también es autigénica. Los análisis EDS indican que el catión octaédrico dominante en estas esmectitas es el Al, por lo que se corresponden con esmectitas dioctaédricas. En el caso de las esmectitas analizadas en la Fm. Blesa se trataría de beidellitas, mientras que las de los paleosuelos de Fm. Torrelapaja se clasificarían como montmorillonitas. Ambos tipos de esmectita pueden formarse en suelos como producto de la meteorización química de feldespatos, plagioclasas y micas (ej. Singh y Gilkes, 1991; Fesharaki et al., 2007).

La caolinita y la esmectita se formaron, por tanto, durante el proceso edáfico debido a la disolución de los aluminosilicatos presentes en las rocas lutítico-margosas. Este proceso no es compatible con la génesis de illita, que normalmente se asocia con ambientes diagenéticos o hidrotermales en los que las temperaturas son más elevadas. En dichos ambientes se produciría la desestabilización de la esmectita y la caolinita a partir de los 70 y 120 ºC, respectivamente (Curtis, 1985; Bauluz et al., 2000; Lanson et al., 2002; Brosse et al., 2003). Además, la génesis de esmectita, así como de interestratificados I/S a partir de la degradación de la illita por la pérdida del K y otros elementos ha sido también descrita durante procesos de meteorización química en materiales similares a los paleosuelos aquí estudiados (ej. Galán et al., 2006; Jeong et al., 2011; Schaetzl y Thompson, 2015; Meenakshi et al., 2020).

Las fases illíticas presentes en los paleosuelos de las Fms. Blesa y Torrelapaja actúan como substrato para el crecimiento de la caolinita (Fig. 8.2e y f), lo que indica que son fases que se formaron previamente. Por tanto, las fases illíticas tendrían probablemente un origen detrítico, pudiendo desestabilizarse durante el proceso de meteorización química, dando lugar a la formación de caolinita, esmectita e interestratificados I/S en los paleosuelos de ambas formaciones. Del mismo modo, los interestratificados C/S detectados de manera ocasional en algunos niveles en la Fm. Blesa pudieron formarse a partir de una clorita primaria, que estaría en bajas proporciones al

no haberse detectado previamente por difracción de rayos X y que, al igual que la illita, tendría un origen probablemente detrítico.

Los óxidos y oxihidróxidos de hierro (hematites y goethita) forman parte, no solo de la matriz de los paleosuelos junto a las arcillas (Fig. 8.2c), sino también de los pisoides encontrados en ambas formaciones, lo que sugiere un origen edáfico para estos minerales (ej. Sayed y Youssed, 1996; Yuste et al., 2020). Por otra parte, el cuarzo y el feldespato potásico, con morfologías anhedrales, serían fases detríticas que representarían restos de la disolución parcial de las rocas lutítico-margosas originales.

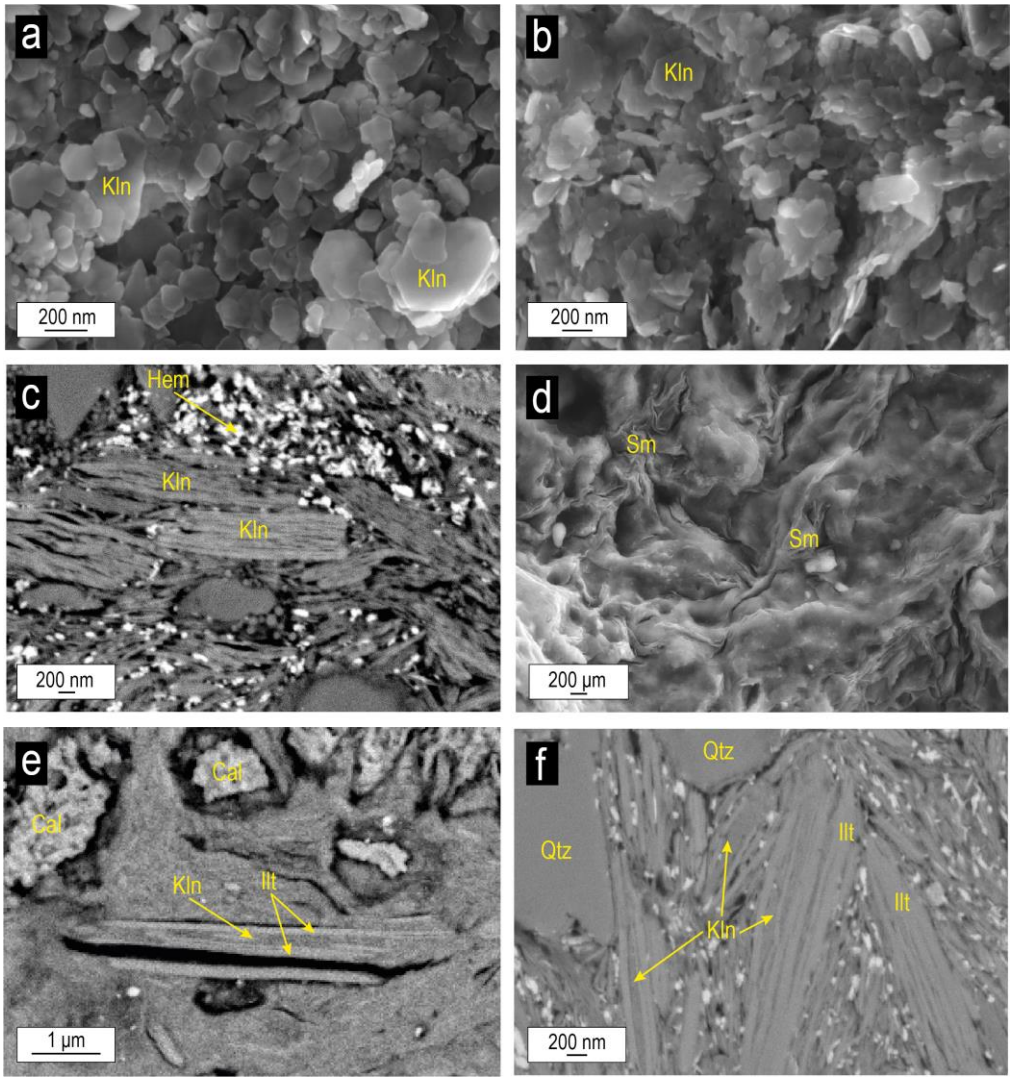

Fig. 8.2. Imágenes FESEM de la matriz de los paleosuelos de las Fms. Blesa y Torrelapaja: **a)** y **b)** Imágenes de electrones secundarios de caolinitas con morfologías platiformes y contornos pseudohexagonales en la matriz de los paleosuelos de ambas formaciones; **c)** imagen de electrones retrodispersados de agregados tipo "book" de caolinita en la matriz de los paleosuelos de la Fm. Torrelapaja; **d)** imagen de electrones secundarios de esmectita con morfologías tipo "flake" en la matriz de los paleosuelos de la Fm. Blesa; **e)** y **f)** imágenes de electrones retrodispersados de intercrecimientos de caolinita y fases illíticas en la matriz de los paleosuelos de ambas formaciones. *Kln*=caolinita, *Sm*=esmectita, *Ilt*=fases illíticas, *Cal*=calcita, *Qtz*=cuarzo.

1.3 Origen de los carbonatos y los pisoides ferruginosos

La presencia de niveles de calizas palustres-lacustres intercalados entre los niveles de paleosuelos de la Fm. Blesa y la Fm. Torrelapaja junto con el hecho de que los paleosuelos se hayan formado a partir de niveles lutítico-margosos, indicaría que la génesis de estos paleosuelos fue coetánea con ascensos y descensos episódicos del nivel del agua. La presencia de nódulos carbonatados en los paleosuelos tanto de la Fm. Blesa como de la Fm. Torrelapaja también respaldaría esta hipótesis, ya que los descensos episódicos del nivel del agua generarían el retrabajamiento de los materiales, dando lugar a la presencia de estos nódulos, que procederían de los niveles palustres-lacustres inferiores. Además, los niveles de carbonatos palustres-lacustres de los afloramientos de la Fm. Blesa contienen también pisoides ferruginosos y tanto estos niveles de carbonatos, como los nódulos carbonatados que se encuentran en los paleosuelos de las dos formaciones, están frecuentemente cementados por la misma caolinita que forma la matriz de los paleosuelos, lo que indica que los niveles carbonatados también fueron sometidos a procesos edáficos durante episodios de descenso del nivel del agua.

Los pisoides y macropisoides presentes en los paleosuelos de las Fms. Blesa y Torrelapaja están compuestos principalmente por hematites, goethita y caolinita, encontrándose estas mismas fases de manera dominante en la matriz de los paleosuelos. Cabe destacar que, en el caso de la Fm. Torrelapaja, los pisoides de los niveles intermedios y superiores contienen también fases illíticas y se observan los mismos intercrecimientos de caolinita y fases illíticas que se encontraban en la matriz de estos niveles de paleosuelos. Esta mineralogía, junto con la estructura concéntrica que presentan los pisoides, formada por un núcleo y una corteza, que es típica de la génesis de suelos (ej. Bárdossy, 1982; Taylor et al., 2008; Yuste et al., 2020), indicaría que estos pisoides se formaron *in-situ* durante el desarrollo de los paleosuelos. Tanto en los macropisoides de la Fm. Blesa como en los de la Fm. Torrelapaja se reconocen, además, secuencias alternantes de capas de goethita y hematites que previamente han sido descritas en depósitos metálicos de tipo gossan como consecuencia de cambios en las condiciones de humedad (Velasco et al., 2013).

Los procesos de retrabajamiento que tuvieron lugar en momentos de descenso del nivel del agua causarían la rotura de muchos de estos pisoides y macropisoides, permitiendo que algunos fragmentos actuasen posteriormente como núcleo de nuevos pisoides en subsecuentes episodios del desarrollo de los paleosuelos, como se observa en la Fm. Blesa.

Por otro lado, tanto en la Fm. Blesa como en la Fm. Torrelapaja se observa la presencia de carbonato esparítico y microesparítico reemplazando parte de los pisoides

y rellenando grietas. Este carbonato también se encuentra cementando en ocasiones la matriz de los paleosuelos y precipitaría gracias a la circulación de fluidos carbonatados durante la diagénesis, que también sería la responsable de la formación de los nódulos de calcita fibroso-radial y los intraclastos esparíticos y microesparíticos encontrados en algunos paleosuelos.

Sin embargo, esta diagénesis debió ser una diagénesis temprana, que no habría afectado a la caolinita y la esmectita presentes en los paleosuelos, ya que como se ha comentado anteriormente, su morfología y disposición, formando la matriz junto a los óxidos y oxihidróxidos, sugiere un origen edáfico y, además, no parece haber evidencias de procesos de recristalización o reemplazamiento posteriores en estos minerales.

2 APORTACIONES AL REGISTRO PALEOCLIMÁTICO DEL NE DE LA PENÍNSULA IBÉRICA

2.1. Deducciones paleoclimáticas en base a los minerales de la arcilla presentes en los paleosuelos

La evolución del clima en Europa durante el Cretácico Inferior ha sido ampliamente discutida en base a diversos indicadores paleoclimáticos y paleoambientales (minerales de la arcilla, curvas isotópicas, restos fósiles, etc.).

Durante el Hauteriviense predominó un clima templado y estacionalmente árido (Mutterlose y Ruffell, 1999; Godet et al., 2008), mientras que en el tránsito Hauteriviense superior–Barremiense inferior se produjo un cambio hacia unas condiciones más cálidas y húmedas que prevalecieron a lo largo de todo el Barremiense (Combes, 1969; Bárdossy, 1982; Deconinck y Bernoulli, 1991; Salas et al., 2004; Wright et al., 2000; Godet et al., 2008; Bodin et al., 2009; Buscalioni y Fregenal-Martínez, 2010; Mendes et al., 2010; Price et al., 2011; Föllmi, 2012; Bauluz et al., 2014; Mutterlose et al., 2014; Yuste et al., 2015; Yuste et al., 2017; Yuste et al., 2020). Posteriormente, en el tránsito Barremiense superior–Aptiense se describe un cambio hacia unas condiciones más frías y secas que se mantuvieron durante el Aptiense inferior (Ruffell y Batten, 1999; Steuber et al., 2005; Godet et al., 2006; Corentin et al., 2020) (Fig. 8.3).

Si bien la tendencia del clima durante el Hauterviense–Aptiense parece clara, con climas templados y estacionalmente áridos que cambiaron a unas condiciones más cálidas y húmedas y posteriormente más frías y secas, otros estudios muestran tendencias diferentes respecto a las condiciones de humedad y aridez para el periodo Hauterviense superior–Aptiense inferior (Fig. 8.3).

Godet et al (2008) describen un cambio desde condiciones áridas hacia otras más húmedas durante el Hauterviense superior, mientras que en otros estudios se proponen unas condiciones áridas o alternancias de condiciones húmedas y áridas para el tránsito Hauteriviense superior–Barremiense inferior (Mutterlose y Ruffell, 1999; Dinis et al., 2020).

Durante el Barremiense, la presencia de bauxitas y paleosuelos con caolinita evidencia unas condiciones húmedas (Bárdossy, 1982; Wright et al., 2000; Godet et al., 2008), aunque algunos autores sugieren unas condiciones húmedas, pero estacionalmente áridas o semiáridas durante este periodo (Haywood et al., 2004; Moiroud et al., 2012). Además, de acuerdo con algunos estudios, durante el Barremiense superior el clima fue más árido (Godet et al., 2006; Föllmi, 2012) y dicho clima se mantuvo durante el Aptiense (Corentin et al., 2020), mientras que otros autores apuntan hacia unas condiciones más húmedas durante el Aptiense inferior (Dinis et al., 2020).

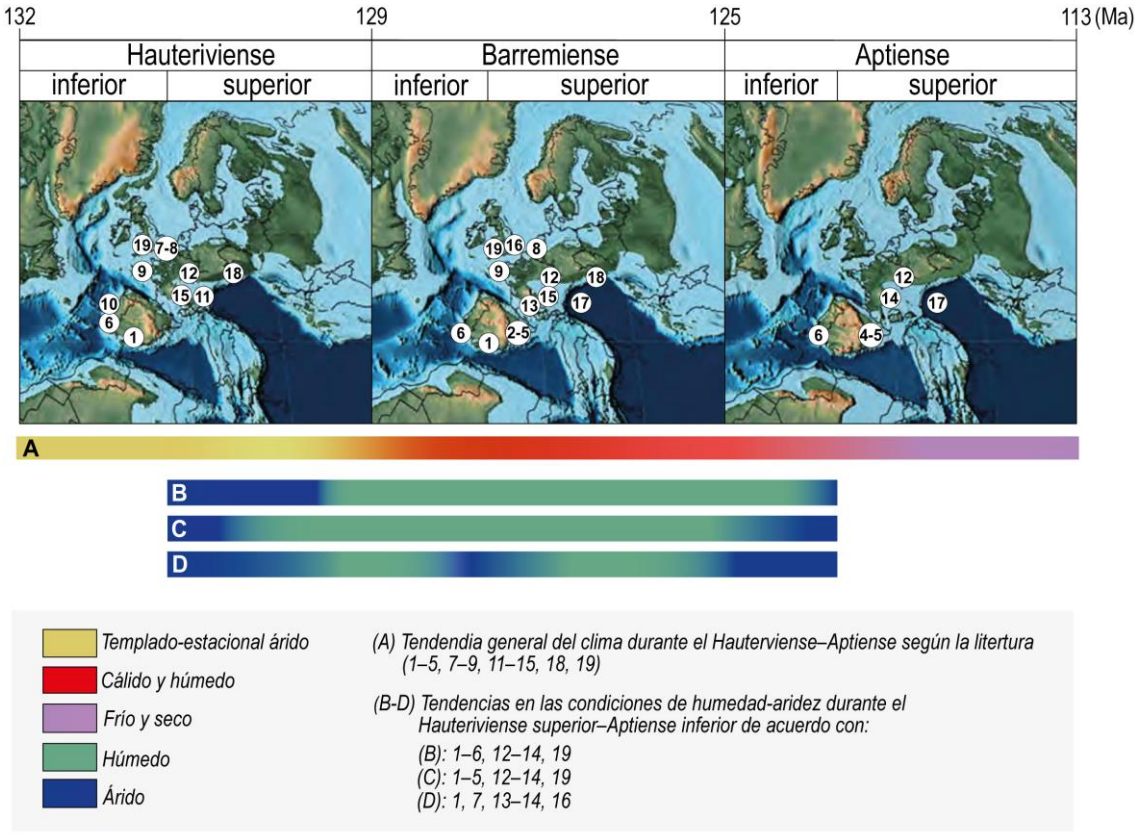

Fig. 8.3. Evolución general del clima y distintos modelos de tendencias de periodos húmedos y áridos para el oeste de Europa durante el periodo Hauteriviense–Aptiense basados en registros de la literatura: **1)** Moiroud et al., 2012; **2)** Bauluz et al., 2014; **3)** Yuste et al., 2015; **4)** Yuste et al., 2020; **5)** Salas et al., 2004; **6)** Dinis et al., 2020; **7)** Mutterlose y Ruffell, 1999; **8)** Mutterlose et al., 2014; **9)** Ruffell y Batten, 1990; **10)** Mendes et al., 2010; **11)** Deconinck y Bernoulli, 1991; **12)** Godet et al., 2008; **13)** Godet et al., 2006; **14)** Corentin et al., 2020; **15)** Bodin et al., 2009: **16)** Haywood et al., 2004; **17)** Steuber et al., 2005; **18)** Price et al., 2011; **19)** Wrigth et al., 2000.

La composición mineralógica de los paleosuelos de las Fms. Blesa y Torrelapaja, con asociaciones de minerales autigénicos formadas por minerales de la arcilla (caolinita y esmectita) y óxidos y oxihidróxidos de Fe, Ti y Al (goethita, hematites, anatasa, rutilo, ilmenita y diásporo), junto con la presencia de pisoides ferruginosos, permite clasificarlos como oxisoles, de acuerdo con la Clasificación Taxonómica de Suelos.

Los cambios mineralógicos observados desde la base hasta el techo de las series estratigráficas son muy similares en ambas formaciones, con un aumento en el contenido en cuarzo y feldespato potásico hacia el techo de las series, que coincide con una disminución en el contenido en óxidos y oxihidróxidos.

La disminución en el contenido de óxidos y oxihidróxidos hacia el techo de las series es mucho más evidente en los afloramientos de la Fm. Blesa y coincide con el cambio en el color de los niveles de paleosuelos (de rojos a ocres y violáceos). El color de los suelos refleja la cantidad relativa de hematites y goethita, con colores rojos donde

estos minerales son más abundantes (Foos, 1991; Yuste et al., 1995), como es el caso de los niveles inferiores de la Fm. Blesa. El menor contenido en hematites y goethita, junto con el mayor contenido en fases illíticas hacia el techo de las series de la Fm. Blesa estaría marcando ese cambio hacia colores ocres y violáceos.

La caolinita es el mineral de la arcilla dominante en los niveles de paleosuelos inferiores de todas las series estratigráficas, con un contenido del 50% o superior en muchas de las muestras de paleosuelos de dichos niveles, como se observa en todos los afloramientos de la Fm. Blesa y en el afloramiento de Las Cañadas, en la Fm. Torrelapaja (ver capítulos 3 y 4). La génesis de este mineral sugiere unas condiciones de intensa meteorización química, en relación con unas condiciones climáticas cálidas y húmedas que coinciden con las descritas durante el Hauteriviense superior–Barremiense en la Península Ibérica (ej. Pucéat et al., 2005; Hay, 2008; Buscalioni y Fregenal-Martínez, 2010; Mendes et al., 2010; Dinis et al., 2020; Bauluz et al., 2014; Yuste et al., 2015; Yuste et al., 2020).

Sin embargo, hacia el techo de todas las series se produce un cambio en el contenido y tipo de mineral de la arcilla presente, detectándose también esmectita (beidellita en la Fm. Blesa y montmorillonita en la Fm. Torrelapaja), fases illíticas (cuyo contenido aumenta notablemente) e interestratificados I/S y C/S.

Estos cambios en la vertical siguen siempre un mismo patrón caolinita → caolinita, esmectita y fases illíticas → caolinita, fases illíticas e interestratificados I/S y C/S, que puede interpretarse de acuerdo con el patrón de meteorización establecido por Sheldon y Tabor (2009) (caolinita → esmectita → vermiculita → clorita → interestratificados), que sugiere una menor intensidad de la meteorización química en relación con unas condiciones climáticas más frías y secas.

Por otro lado, si bien esta tendencia en la vertical se observa tanto en la Fm. Blesa como en la Fm. Torrelapaja, el registro en esta última no está tan bien conservado como en la Fm. Blesa. Esto puede ser debido al aporte de terrígenos que tuvo lugar durante el tercer estadio sedimentario descrito por Aurell et al. (2021), asociado a un aumento de la actividad tectónica en la subcuenca de Torrelapaja, que pudo inhibir en parte el desarrollo del suelo. A pesar de ello, la presencia de esmectita autigénica en esta formación estaría reflejando también esas condiciones de menor intensidad de meteorización química.

Todos estos datos indican, por tanto, un cambio desde condiciones climáticas cálidas y húmedas a otras más frías y secas durante el Barremiense inferior en las subcuencas de Oliete y Torrelapaja, al SE y NW de la Cordillera Ibérica respectivamente.

2.2. Deducciones paleoclimáticas a partir de los análisis isotópicos de oxígeno e hidrógeno en minerales de la arcilla mediante NanoSIMS

El estudio mediante NanoSIMS de los isótopos de oxígeno e hidrógeno en la caolinita y la esmectita presentes en los paleosuelos de dos afloramientos de la Fm. Blesa (Alacón y Josa) ha permitido establecer diferencias entre la señal isotópica de ambos minerales, pese a su tamaño nanométrico, sin obtener análisis mezclados con otras fases minerales de los paleosuelos (ej. cuarzos o fases illíticas detríticas).

Además, durante las sesiones analíticas se demostró que la preparación de muestra más adecuada para el estudio de paleosuelos mediante esta técnica es la lámina delgado-pulida en comparación con las probetas pulidas, en las que la gran cantidad de resina epoxi causa la desgasificación de la muestra, lo que afecta al alto vacío de la cámara del NanoSIMS y da lugar a mapas composicionales de baja calidad, así como a interferencias en las medidas isotópicas (Stadermann et al., 2005; Aboura y Moore, 2021).

El descenso en el contenido en caolinita hacia los niveles intermedios y superiores de las series, en los que se detecta la esmectita, coincide con un claro descenso en los valores de $\delta^{18}O$ y δD hacia el techo de las series, lo que estaría indicando un enriquecimiento en los isótopos ligeros y reflejando un cambio en las condiciones climáticas.

Cabe destacar que, si bien la caolinita y la esmectita presentes en todos los afloramientos estudiados mostraban texturas características de haberse generado durante el proceso edáfico, los valores de $^{18}O/^{16}O$ y D/H de las caolinitas analizadas en el perfil de Josa, son notablemente superiores a los de las caolinitas analizadas en el nivel equivalente en el afloramiento de Alacón, así como a los valores que se utilizaron como estándares de referencia.

Esto parece indicar que esta caolinita en particular podría haberse visto afectada por una diagénesis temprana después de su formación durante la génesis del suelo, alterando su señal isotópica e invalidando su uso como indicador paleoclimático. Este hecho queda evidenciado también a través de los datos mineralógicos, ya que, si se compara esta caolinita con la del perfil de Alacón, se observa que en ocasiones presenta mayores tamaños, mayor cristalinidad y ambos parámetros son además más homogéneos. Estas características son compatibles con procesos de recristalización (Fig. 8.4).

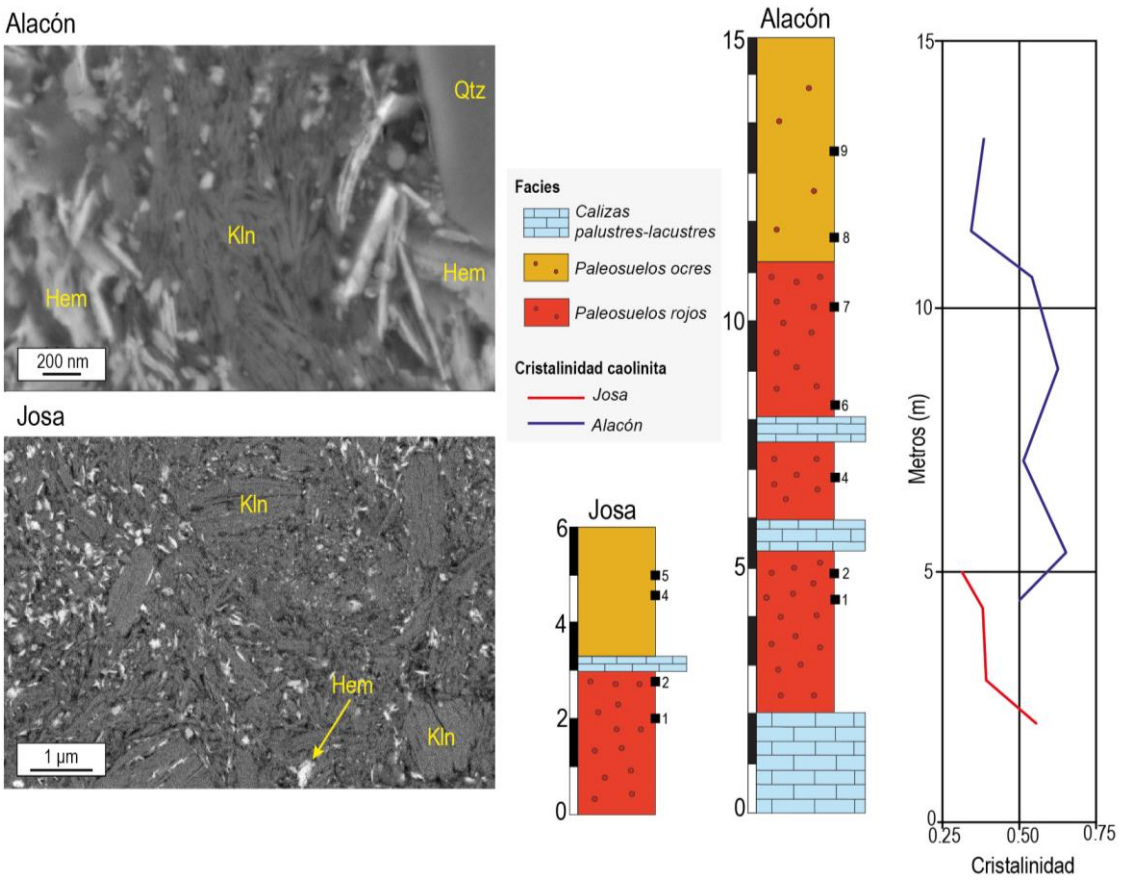

Fig. 8.4. Imágenes de FESEM de electrones retrodispersados mostrando caolinitas de tamaño nanométrico en la matriz de los paleosuelos del afloramiento de Alacón, frente a los tamaños micrométricos de la caolinita del afloramiento de Josa. La gráfica representa los cambios en la cristalinidad de base a techo de ambas series donde se observa que las caolinitas del afloramiento de Josa son, en general, más cristalinas en comparación con las de Alacón. *Qtz*=cuarzo, *Kln*=caolinita, *Hem*=hematites.

Los valores de $\delta^{18}O_{SMOW}$ y δD_{SMOW} obtenidos para la caolinita del nivel de paleosuelos inferior ($\delta^{18}O_{SMOW}$=18‰; δD_{SMOW}=-83‰) y medio ($\delta^{18}O_{SMOW}$=14‰; δD_{SMOW}=-97‰) y para la esmectita del nivel superior ($\delta^{18}O_{SMOW}$=11‰; δD_{SMOW}=-180‰) del perfil de Alacón, así como para la esmectita del nivel de paleosuelos superior del perfil de Josa ($\delta^{18}O_{SMOW}$=13‰; δD_{SMOW}=-167‰) están dentro del rango de valores registrado para estos minerales cuando se forman por procesos de meteorización química, lo que confirma su génesis durante el proceso edáfico (Savin y Hsieh, 1998; Gilg et al., 2003; Fernández-Caliani et al. 2010; Mix y Chamberlain, 2014; Clauer et al., 2015; He et al., 2019).

Por tanto, la caolinita y la esmectita de los paleosuelos de la Fm. Blesa conservan la señal isotópica original del agua meteórica a partir de la que se formaron (ej. Savin y Epstein 1970, Lawrence y Taylor 1971, Sheppard, 1977; Delgado y Reyes, 1996; Sheppard y Gilg, 1996), pudiendo entonces utilizarse como indicadores de paleotemperatura, ya

que los factores de fraccionamiento isotópico de equilibrio de estos minerales son función de la temperatura (Delgado y Reyes, 1996; Fernández-Caliani et al., 2010).

De este modo, combinando la ecuación del agua meteórica (Craig, 1961) con las ecuaciones que relacionan el fraccionamiento isotópico del oxígeno y el hidrógeno en el sistema caolinita-agua (Sheppard y Gilg, 1996) y esmectita-agua (Sheppard y Gilg, 1996; Capuano, 1992), se puede determinar la composición isotópica y la temperatura del agua meteórica a partir de la cual se formaron la caolinita y la esmectita, siguiendo el modelo de Delgado y Reyes (1996).

Los valores de $\delta^{18}O_{SMOW}$ y δD_{SMOW} obtenidos para el agua se proyectan en la Línea del Agua Meteórica (ver capítulo 5). Estos valores son más altos en las caolinitas de los niveles inferiores (Alacón: $\delta^{18}O_{SMOW}$ = -8‰ y δD_{SMOW} = -49‰ y $\delta^{18}O_{SMOW}$ = -9‰ y δD_{SMOW} = -63‰) que en las esmectitas de los niveles superiores (Alacón: $\delta^{18}O_{SMOW}$ = -15‰ y δD_{SMOW} = -118‰ y Josa: $\delta^{18}O_{SMOW}$ = -13‰ y δD_{SMOW} = -106‰) lo que estaría indicando un cambio hacia un clima más frío (Savin y Hsieh, 1998; Giral-Kacmarcík et al., 1998).

Además, la temperatura de cristalización obtenida para la caolinita es de 21–22 ºC mientras que para la esmectita es de 16–17 ºC, apoyando la hipótesis del cambio de un clima cálido y húmedo hacia otro más frío y seco como reflejaban los datos mineralógicos para el Barremiense inferior en los sectores NW y SE de la Cordillera Ibérica.

Estos resultados isotópicos también demuestran que, con una preparación de muestras adecuada, el NanoSIMS puede ser una técnica muy útil en los estudios paleoclimáticos que involucren minerales de la arcilla de pequeño tamaño (micrométrico o nanométrico) en paleosuelos.

3 TRANSFORMACIONES MINERALES Y TEXTURALES DURANTE LA COCCIÓN DE MATERIALES ARCILLOSOS

Los resultados del estudio mineralógico de las probetas refractarias y los clinkers naturales incluidos en los capítulos 6 y 7 de esta tesis doctoral permiten hacer una comparación entre las arcillas cocidas durante el proceso cerámico y las calcinadas de manera natural por procesos de autocombustión de carbón.

Las probetas refractarias se fabricaron a partir de diversas mezclas de bauxita con arcilla illítico-caoliníferа (BX100=100%bauxita, BX75=75%bauxita+25%arcilla y BX50=50%bauxita+50%arcilla). La bauxita contiene principalmente bohemita, caolinita y hematites, junto con proporciones menores de anatasa, goethita y rutilo, mientras que la arcilla illítico-caoliníferа se compone principalmente de illita, cuarzo, caolinita y proporciones menores de ortosa y albita.

Esta arcilla illítico-caoliníferа procede de niveles arcillosos de la Formación Escucha (Cretácico Inferior) donde se encuentran también niveles de carbón que sufrieron procesos de autocombustión, calcinando de manera natural las arcillas y dando como resultado clinkers naturales. Estudios previos muestran que, además de las fases indicadas anteriormente, la arcilla illítico-caoliníferа de la Formación Escucha también contiene ocasionalmente siderita, pirita y jarosita (Bauluz et al., 2008).

3.1 Desestabilización de las fases iniciales

En ambientes naturales, la caolinita no es estable a partir de los 200 ºC y la illita se desestabiliza a partir de los 350 ºC (Merriman y Peacor, 1998). Por ello, cabe esperar que no se detecten estos minerales en materiales calcinados a altas temperaturas. Sin embargo, estudios previos muestran la presencia de fases tipo illita en materiales cerámicos cocidos a 1000 ºC, aunque con evidencias de haber sufrido procesos de deshidroxilación a partir de los 450 ºC (Guggenheim et al., 1987; Drits y McCarty, 2007; Laita y Bauluz, 2018;).

En las probetas refractarias y los clinkers naturales estudiados, no se detecta por difracción de rayos X la presencia de caolinita ni de illita, si bien en todas las probetas cocidas a 1000 ºC sí que se identifican morfologías de tipo caolinita que se corresponderían con metacaolinita. Esta metacaolinita ya no se detecta en las probetas cocidas a 1200 ºC, lo que indica que se ha desestabilizado con el aumento de la temperatura.

Aunque el contenido en cuarzo disminuye con la temperatura en las probetas refractarias, esta fase se sigue diferenciando hasta los 1270 ºC y también se detecta en los clinkers naturales. Sin embargo, en ambos tipos de materiales se observa que los cristales de cuarzo presentan bordes de reacción, lo que indica que se ha desestabilizado

parcialmente. Por otro lado, a pesar de que durante la cocción de arcillas illíticas no suele formarse cristobalita debido a la acción fundente del K de la interlámina de la illita (Aras, 2002; Wattanasiriwech et al., 2009), la presencia de caolinita en la bauxita (25%) y de cuarzo y caolinita en la arcilla illítico-caoliníferа (32% y 23%, respectivamente) puede haber aportado la sílice necesaria para la formación de cristobalita en las probetas refractarias y en los clinkers naturales.

El contenido en hematites de los clinkers naturales y de las probetas refractarias cocidas a 1000 ºC es superior al que presentaban la bauxita y la arcilla illítico-caoliníferа. Esta hematites puede proceder, en ambos casos, de la recristalización de óxidos de hierro amorfos o poco cristalinos que estarían presentes en bajas proporciones en las muestras de partida. Por otro lado, la oxidación de la pirita y la siderita presentes en la arcilla illítico-caoliníferа y la deshidratación de la goethita presente en la bauxita, también pueden dar lugar a la formación de hematites (Ram et al., 1995; Kapička et al., 1999; Jang et al., 2014; Sun et al., 2020).

3.2 Formación de nuevas fases

El aumento de temperatura que se produce tanto por el proceso de cocción como por el de autocombustión del carbón, da lugar a la desestabilización de las fases minerales presentes en la bauxita y la arcilla illítico-caoliníferа, permitiendo la formación de fase vítrea. Este proceso de vitrificación es el responsable de la textura homogénea que presentan las probetas refractarias y los clinkers naturales (Fig. 8.5a y b).

La fase vítrea formada en las probetas refractarias y los clinkers naturales estudiados tiene una composición aluminosilicatada con menores proporciones de Fe, Ti, Mg, Ca, Na y K. Todos estos elementos proceden de la desestabilización de los minerales presentes en las materias primas de partida. Con el incremento de la temperatura, se forman nuevas fases minerales y las imágenes de microscopía electrónica reflejan que tanto en las probetas refractarias como en los clinkers naturales estas fases se encuentran inmersas en la fase vítrea, lo que indica que han cristalizado a partir de ella (Fig. 8.5c y d).

Uno de los minerales que se forma en las probetas refractarias a partir de 1000 ºC, y que no se ha detectado en los clinkers naturales, es la ilmenita. La formación de este mineral se debe a que la bauxita contiene óxidos de Ti (anatasa y rutilo) que no están presentes en la arcilla illítico-caoliníferа. La desestabilización de la anatasa durante la cocción aportaría el Ti necesario para, junto con el Fe de la hematites, dar lugar a la cristalización de la ilmenita. La presencia de hematites, anatasa y rutilo en la bauxita natural y la formación de ilmenita durante la cocción de las probetas refractarias dan

como resultado las soluciones sólidas entre ilmenita y hematites o entre rutilo e ilmenita que se observan en estos materiales (ver capítulo 6).

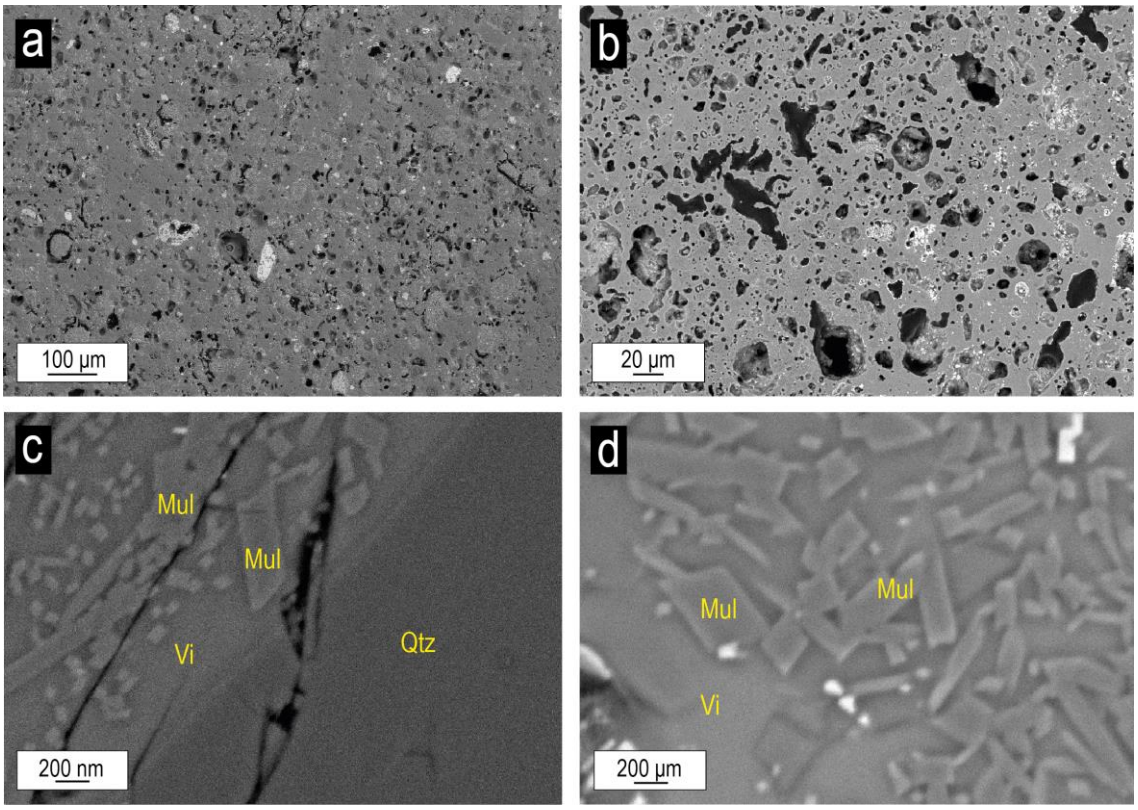

Fig. 8.5. Imágenes FESEM de electrones retrodispersados de las probetas refractarias y los clinkers naturales: **a)** y **b)** imágenes de la textura homogénea de las probetas refractarias y los clinkers naturales, respectivamente, debido al proceso de vitrificación; **c)** imagen de una probeta refractaria en la que se observan cristales aciculares de mullita inmersos en fase vítrea junto a un cristal de cuarzo que presenta borde de reacción y microfracturas; **d)** imagen de un clinker natural en la que se observan cristales aciculares de mullita inmersos en fase vítrea. *Mul*=mullita, *Qtz*=cuarzo, *Vi*=fase vítrea.

Por otro lado, en las probetas refractarias se observan composiciones que varían desde hematites a corindón, mientras que en los clinkers naturales esta tendencia se observa entre hematites y hercinita.

En los clinkers naturales se diferencian tres poblaciones composicionales (Fig. 8.6): 1) composiciones ricas en Fe correspondientes a la hematites 2) composiciones intermedias que podrían deberse a soluciones sólidas entre hematites y hercinita, como las que se han descrito en materiales similares entre magnetita y hercinita (Cosca et al., 1989) y 3) composiciones ricas en Al y Fe que se corresponden con hercinita.

En las probetas refractarias también se observan tres poblaciones composicionales (Fig. 8.6), coincidiendo la primera de ellas con las fases ricas en Fe, correspondientes a la hematites. Las composiciones intermedias en este caso son ricas en Al y Fe y pueden corresponderse con hercinita, dado que algunas se aproximan a la

composición teórica y, si bien este mineral no se identificaba claramente en microscopía electrónica, los resultados de difracción de rayos X confirman su presencia en todas las probetas. Por otro lado, aquellas composiciones intermedias que se alejan de la composición de la hercinita teórica pueden deberse a la existencia de soluciones sólidas entre hematites y corindón que suelen producirse entre los 1000 y los 1300 ºC (Feenstra et al., 2005). Por último, la tercera población composicional que se diferencia en las probetas refractarias presenta composiciones ricas en Al, que se corresponderían con corindón y que no se detectan en los clinkers naturales.

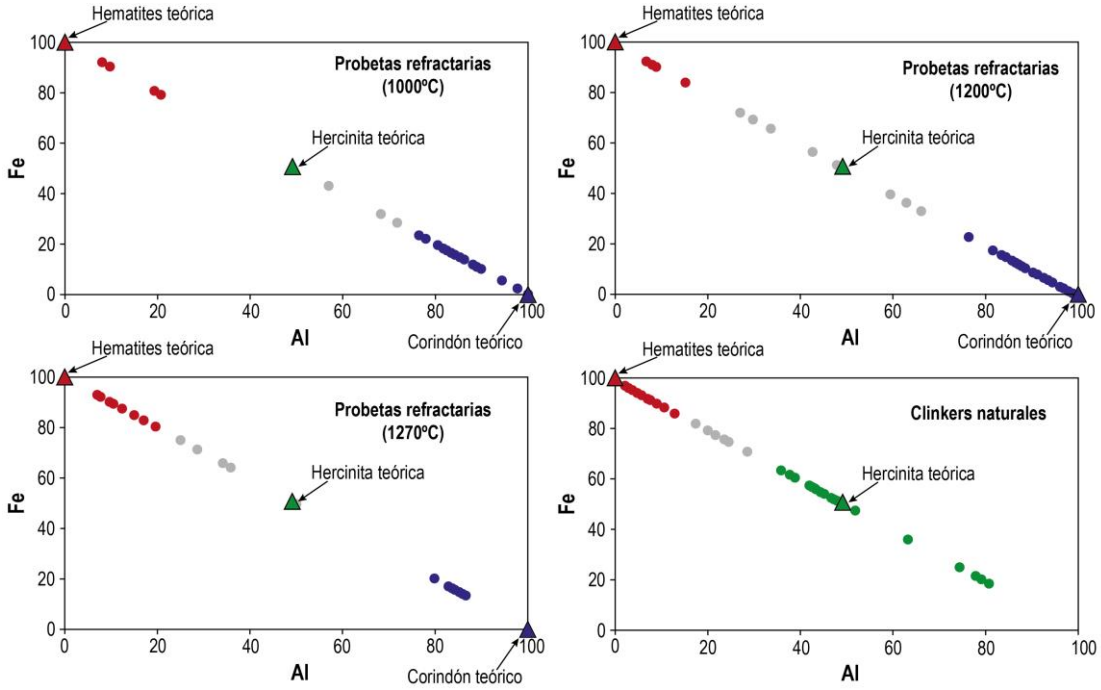

Fig. 8.6. Gráficos Al vs. Fe mostrando la tendencia composicional hematites-hercinita-corindón en las probetas refractarias a 1000, 1200 y 1270 ºC, así como la tendencia composicional hematites-hercinita en los clinkers naturales. Los análisis representados en color rojo se corresponden con hematites, los verdes con hercinita y los azules con corindón. Los análisis en gris representan las composiciones intermedias.

En las probetas refractarias, la hercinita se forma a 1000 ºC y posteriormente se desestabiliza con el aumento de la temperatura, llegando incluso a no detectarse a 1270 ºC (Fig.8.6), tal y como se describe en otros materiales cerámicos (Jordán et al., 2020) en los que el contenido en hercinita es superior a menores temperaturas de cocción (995 ºC).

Estudios previos han descrito el reemplazamiento de hematites por espinelas en rocas ígneas y en clinkers naturales (Treiman, 1984; Sandiford et al., 1987). En este sentido, la hercinita detectada en las probetas refractarias y en los clinkers naturales se formaría a partir de la hematites, hecho que queda también demostrado por las texturas de reemplazamiento de hematites por hercinita que se observan en los clinkers naturales

(ver Fig. 7.5 en capítulo 7). Sin embargo, al aumentar la temperatura, la hercinita de las probetas refractarias se transforma en γ-Al_2O_3 (Segal et al., 2018), contribuyendo, junto con otros minerales presentes en la bauxita natural (ej. bohemita) a la formación de corindón.

La hematites, la hercinita y la cordierita son fases que se forman comúnmente en los clinkers naturales (ej. Cosca et al., 1989; Alastuey et al., 1993; Henao et al., 2010; Ribeiro et al., 2016; Baboolal et al., 2018). En los clinkers naturales estudiados se observan lamelas de exsolución de hercinita dentro de cristales de hematites y de cordierita (ver Fig. 7.5 en capítulo 7), lo que sugiere que se produjo un enfriamiento tras el proceso de calcinación antes de alcanzar la temperatura necesaria para que tuviese lugar la transformación de hercinita en γ-Al_2O_3.

La mullita es otra de las fases que se detecta tanto en las probetas refractarias como en los clinkers naturales, siendo uno de los minerales dominantes en ambos materiales, en los que se presenta con morfologías aciculares y prismáticas y tamaños que alcanzan hasta las 2 μm. La desestabilización de la caolinita presente tanto en la bauxita como en la arcilla illítico-caolinífera da lugar a la formación de la mullita, pudiendo observase, como se ha comentado anteriormente, la metacaolinita en las probetas refractarias cocidas a 1000 ºC. Esta metacaolinita es la precursora de la mullita y se ha descrito en materiales similares entre los 500 y los 1000 ºC (Chen et al., 2000; Meng et al., 2016).

La mullita formada en las probetas refractarias y los clinkers naturales no es estequiométrica. En el caso de los clinkers naturales, este mineral presenta un ratio Al/Si de 0.82, que si se compara con el de la mullita empírica (Al/Si=2.88), indica que esta mullita es bastante más rica en Si. La mullita analizada en todas las probetas refractarias también presenta ratios Al/Si inferiores a los de la mullita empírica, si bien estos valores son superiores a los de los clinkers naturales debido al mayor contenido en Al_2O_3 de las probetas. El ratio Al/Si de la mullita de las probetas refractarias aumentan desde 1.36 en las probetas cocidas a 1000 ºC hasta 1.76 en las probetas cocidas a 1270 ºC, lo que indica que la difusión del aluminio aumenta con la temperatura, como se ha descrito en otros materiales cerámicos y sintéticos (Usov et al., 1999; Laita y Bauluz, 2018).

Por último, en los clinkers naturales se identifican tres tipos de piroxenos que no se han detectado en las probetas refractarias: 1) Piroxenos de Ca y Al, denominados "piroxenos cerámicos" siguiendo la nomenclatura utilizada por otros autores (Dondi et al., 1998; Bauluz et al., 2004), 2) piroxenos ricos en Ca y Mg y 3) piroxenos ricos en Fe.

La génesis de distintos tipos de piroxenos como diópsido, ferrosilita, esseneita o fassaita ha sido descrita previamente en materiales cerámicos, clinkers naturales y rocas

ígneas y metamórficas (ej. Cosca y Peacor, 1987; Foit et al., 1987; Dondi et al., 1998; Bauluz et al., 2004; D'Souza et al., 2006; Trindade et al., 2009; Querol et al., 2011; Ridolfi et al., 2016). A pesar de que la composición química de los piroxenos detectados en los clinkers naturales estudiados no es del todo estequiométrica, los "piroxenos cerámicos" presentan una composición entre la fassaita, la esseneita y el diópsido, mientras que los piroxenos ricos en Ca y Mg y los piroxenos ricos en Fe tienen composiciones próximas a las del diópsido y la ferrosilita, respectivamente.

La presencia de carbonatos (ej. siderita) en la arcilla illítico-caoliníferа pudo dar lugar a la formación de los piroxenos durante el proceso de autocombustión, tal y como se ha descrito en materiales cerámicos carbonatados, en los que los piroxenos se forman como producto de reacciones en estado sólido entre los carbonatos y los minerales de la arcilla (Dondi et al., 1998; Bauluz et al., 2004; Trindade et al., 2009).

El hecho de que la bauxita original no contenga carbonatos y que la arcilla illítico-caoliníferа haya sido mezclada con dicha bauxita para la fabricación de las probetas ha podido resultar en la ausencia del contenido en carbonato necesario para la formación de estos piroxenos en las probetas refractarias.

3.3 El proceso cerámico y la autocombustión de carbón

Las transformaciones minerales que tienen lugar en materiales arcillosos sometidos a procesos de cocción de alta temperatura están influenciadas por diversos factores como la composición mineralógica del material arcilloso de partida o la temperatura de cocción. Como se ha visto en el apartado anterior, estos factores han influido claramente en la formación de una determinada fase mineral u otra en las probetas refractarias y los clinkers naturales estudiados.

Por otro lado, las transformaciones minerales que se producen durante los procesos cerámicos estarán también influenciadas por la velocidad del proceso y las condiciones atmosféricas del horno (Maggetti, 1982), mientras que en los procesos de autocombustión de carbón también puede influir otros factores como la composición del carbón, las condiciones de la combustión, la historia térmica del material o factores geológicos o mineros (Cosca et al., 1989; Coates y Heffern, 1999; Sinha y Singh, 2005; Henao et al., 2010).

Las fases minerales formadas tanto en las probetas refractarias como en los clinkers naturales estudiados son similares a las descritas en muchos procesos ígneos y metamórficos (ej. Treiman et al., 1985; Cosca y Peacor, 1987; Sandiford et al., 1987; Markl et al., 2005; Sokol et al., 1998;). Sin embargo, la duración del proceso cerámico y de autocombustión de carbón es mucho más corta y el incremento de temperatura se produce de manera mucho más rápida, lo que da lugar a reacciones minerales

incompletas y a que no se alcance un equilibrio químico, formándose fases no estequiométricas como la mullita o los piroxenos descritos anteriormente.

Estudios previos indican que la temperatura alcanzada durante la combustión de carbón en el área donde se localizan los clinkers naturales estudiados fue superior a 1050 ºC, con periodos de calcinación superiores a 100 h (Alastuey et al., 1993).

Por otro lado, la transformación de magnetita primaria en hematites por procesos de martitización se ha descrito también en clinkers naturales que fueron calcinados a temperaturas de 1200–1400 ºC (Estrada et al., 2009). Si bien en los clinkers naturales estudiados no se ha detectado magnetita, este proceso de martitización podría haberse producido de igual modo, dando lugar a la hematites. Si ese hubiese sido el caso, el proceso de autocombustión podría haber alcanzado rangos de temperaturas entre 1000 ºC y 1400 ºC.

Algunas de las fases minerales presentes en los clinkers naturales son similares a las detectadas en las probetas refractarias, especialmente en aquellas cocidas entre 1000 y 1200 ºC en las que se ha empezado a formar mullita y se detecta un mayor contenido en hercinita. Esto refuerza la hipótesis de que la temperatura de autocombustión del carbón fue superior a los 1000–1050 ºC.

Sin embargo, la composición de la mullita de los clinkers naturales presenta un ratio Al/Si (0.82) más bajo que la empírica (2.88), que si se compara además con el de la mullita de las probetas refractarias, se observa que tiene un valor más próximo al de la mullita formada a 1000 ºC (Al/Si=1.36) que al de la formada a 1270 ºC (Al/Si=1.76). Si bien el menor ratio Al/Si de la mullita presente en los clinkers naturales puede deberse al menor contenido en Al_2O_3 de la arcilla illítico-caoliníferа de partida, estudios previos en materiales cerámicos indican, como ya se ha comentado anteriormente, que el contenido en hercinita es mayor a menor temperatura de cocción (Jordán et al., 2020). Esto podría estar indicando, por tanto, que la temperatura alcanzada durante el proceso de autocombustión del carbón fue superior a los 1000 ºC, pero que, probablemente, no llegó a superar los 1200 ºC.

4 CAMBIOS EN LAS PROPIEDADES FÍSICAS Y POTENCIAL REFRACTARIO DE LAS MEZCLAS DE BAUXITA Y ARCILLA ILLÍTICO-CAOLINÍFERA

4.1 Influencia del contenido en bauxita y arcilla illítico-caolinífera en la mineralogía y propiedades físicas de las probetas

Las transformaciones minerales y los cambios en las propiedades físicas que se observan en las probetas fabricadas a partir de mezclas de bauxita y arcilla illítico-caolinífera muestran algunas diferencias en función de la proporción de bauxita y arcilla utilizada en cada mezcla.

Una de las fases minerales dominantes en la bauxita de partida es la bohemita, que con el incremento de la temperatura se deshidrata, dando lugar a la formación de γ-Al_2O_3 (Panias y Krestou, 2007; Jbara et al., 2017; Dong et al., 2020), transformándose posteriormente esta γ-Al_2O_3 en α-Al_2O_3 (corindón). Por tanto, las mezclas con mayor contenido en bauxita (75–100%) son aquellas en las que se forma mayor cantidad de corindón durante el proceso de cocción. Por el contrario, el mayor contenido en arcilla illítico-caolinífera da lugar a un mayor contenido en Si y K y, por tanto, a un menor punto de fusión (Bhattacharjee et al., 2000), lo que permite la formación de mayor proporción de fase vítrea y posterior cristalización de mullita a partir de ella durante el proceso cerámico.

En general, la génesis de fase vítrea y mullita que tiene lugar en todas las probetas se correlaciona con un aumento en la densidad de las mismas conforme aumenta la temperatura. Además, durante el proceso de cocción tiene lugar la deshidroxilación de los filosilicatos presentes en la bauxita y arcilla de partida (Andrews et al., 2013; Laita y Bauluz, 2018), lo que puede estar relacionado con el aumento observado en la contracción lineal de todas las probetas con la temperatura. Por otro lado, en algunas cerámicas de mullita/corindón, el incremento en la contracción lineal se debe también a una mayor interconexión de los cristales de mullita con el incremento de la temperatura (Yang et al., 2012).

Sin embargo, pese a que el aumento en la densidad y contracción lineal se produce en todas las probetas, en aquellas que contienen arcilla illítico-caolinífera, el valor de ambas propiedades disminuye a 1270 ºC, siendo este descenso mayor en la muestra con más arcilla (BX50).

Un proceso similar se ha descrito en materiales cerámicos formados por mezclas de talco, caolinita y bauxita, en los que los valores de densidad y de resistencia a la flexión aumentan hasta los 1300 ºC y posteriormente disminuyen debido a la presencia de fracturas (Njoya et al., 2016).

Durante el enfriamiento tras el proceso de cocción, la tensión resultante de la dilatación térmica de las distintas fases presentes en la muestra da lugar a la formación de microfracturas (Bauluz et al., 2004; Štubňa et al., 2018). Este tipo de microfracturas se han descrito en partículas de cuarzo durante el enfriamiento de cerámicas cocidas a 1200-1250 ºC (ej. Chmelík et al., 2011; Knapek et al., 2016).

La bauxita utilizada en las mezclas no contiene cuarzo, mientras que la arcilla illítico-caoliníferа presenta un 32%, detectándose todavía este mineral durante el proceso de cocción hasta los 1270 ºC en las probetas mezcladas con esta arcilla. Por tanto, el descenso en la densidad y contracción lineal observado en estas muestras a 1270 ºC puede ser debido a la presencia de fracturas internas (ver Fig. 8.5c). Estas fracturas también podrían tener relación con la mayor o menor resistencia de las probetas, ya que a 1270 ºC la probeta con mayor contenido en arcilla (BX50) es la que presenta una menor resistencia a la carga puntual, mientras que las que tienen un 75–100% de bauxita (BX75 y BX100) tienen una resistencia mayor debido a su mayor contenido en corindón.

Durante la cocción también se produce una disminución del tamaño de los poros de las probetas que, además, se rellenan por fase vítrea y mullita, dando lugar a un descenso en la porosidad y la absorción de agua en todas las probetas. El mayor contenido en fase vítrea y mullita de la probeta BX50 hace que tenga una menor porosidad total a 1200–1270 ºC, ya que un mayor desarrollo de la vitrificación da lugar a valores de porosidad y absorción de agua más bajos (Bauluz et al., 2003).

Los cambios en el color desde colores marrones en las probetas crudas a rojizos en las muestras cocidas a 1000 ºC y posteriormente grises en las cocidas a 1200–1270 ºC estarían relacionados con el aumento y posterior descenso en el contenido en hematites observado en todas las probetas, ya que los colores rojos de los materiales cerámicos se suelen atribuir al contenido en Fe_2O_3 (Semiz y Çelik, 2020). Sin embargo, la escala CIE L*a*b* muestra un mayor descenso en los valores a* y b* en las probetas que contienen arcilla, por lo que el cambio hacia colores más oscuros observado se debe, no solo a la disminución en el contenido en hematites, sino también al contenido en arcilla de la muestra.

4.2 El potencial refractario de materiales formados por mezclas de bauxita y arcilla illítico-caolinífera

Los materiales refractarios se caracterizan en general por tener una alta densidad y una baja porosidad y conductividad térmica.

Algunas arcillas carbonatadas que se utilizan actualmente en la industria de fabricación de ladrillos presentan una densidad en torno a 2 g/cm^3 a temperaturas de cocción de 1000 ºC. La porosidad de estos materiales a dicha temperatura es, además, bastante elevada (~28%), debido a la descomposición del carbonato (Bauluz et al., 2003).

En cerámicas refractarias de mullita/corindón fabricadas a partir de andalucita se han registrado valores de densidad en torno a 2.5 g/cm^3, así como una porosidad de entre el 14% y el 25% a temperaturas de cocción de 1540 ºC (Xu et al., 2017). Otros estudios previos muestran también que las cerámicas refractarias de cordierita fabricadas a partir de mezclas de talco, caolinita y bauxita cocidas a 1200 ºC presentan valores de densidad en torno a 2.2 g/cm^3, así como alrededor de un 48% de porosidad total (Njoya et al., 2016).

Por otro lado, ciertas bauxitas calcinadas que se comercializan actualmente (algunas de ellas calcinadas a más de 1650 ºC) presentan valores de densidad más elevados (2.8–3.25 g/cm^3) y de porosidad más bajos (2–4.5%) que los de las arcillas carbonatadas y las cerámicas refractarias citadas anteriormente.

Si se comparan todos estos materiales con las probetas refractarias estudiadas (Fig. 8.7), se observa que la muestra formada por un 100% de bauxita (BX100) cocida a 1270 ºC es la que presenta una densidad similar a la de las bauxitas calcinadas comerciales. Sin embargo, a 1200 ºC todas las probetas estudiadas son más densas que las cerámicas refractarias fabricadas a partir de talco, caolinita y bauxita (Fig. 8.6a) y tampoco son necesarias temperaturas de cocción de 1540 ºC para alcanzar los valores de densidad de las cerámicas refractarias de mullita/corindón fabricadas a partir de andalucita.

Los valores de porosidad de las probetas mezcladas con la arcilla (BX75 y BX50) cocidas a 1200 ºC son los que más se aproximan a los de las bauxitas calcinadas comerciales. Estos valores son, además, más bajos que los que presentan las cerámicas refractarias anteriormente citadas a 1200 ºC y 1540 ºC (Fig. 8.6b).

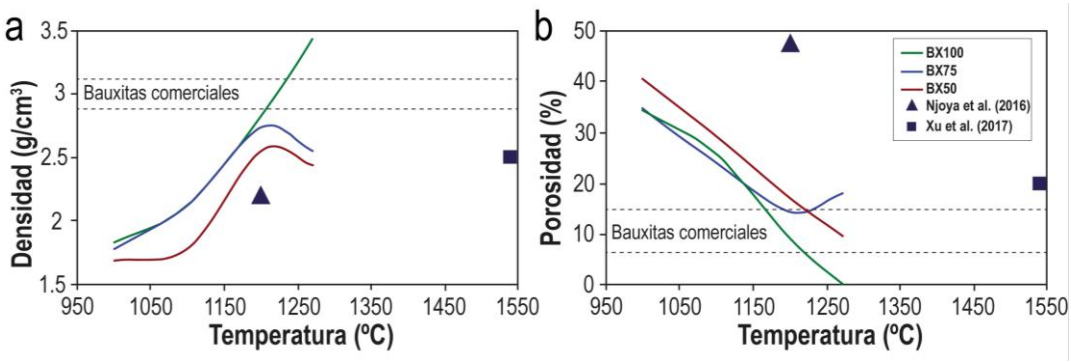

Fig. 8.7. Gráficos de densidad vs. temperatura **(a)** y de porosidad vs. temperatura **(b)** mostrando los cambios en estas propiedades en las distintas mezclas a distintas temperaturas de cocción. Se incluye como comparativa el rango de valores de densidad y porosidad de las bauxitas calcinadas comerciales, así como los valores de ambas propiedades en las cerámicas refractarias de mullita/corindón (Xu et al., 2017) y de cordierita (Njoya et al., 2016).

Por último, respecto a la conductividad térmica, la probeta con mayor contenido en arcilla (BX50) es la que presenta el valor más bajo a 1200 ºC, lo que se correlaciona con su menor porosidad y mayor densidad a esta temperatura de cocción.

Todos estos datos indican, por tanto, que la mezcla de bauxita con arcilla illítico-caolinífera permite obtener valores de porosidad y conductividad térmica más bajos y valores de densidad más altos a menor temperatura de cocción que la que se utiliza en la fabricación de algunas cerámicas refractarias y de bauxitas calcinadas comerciales.

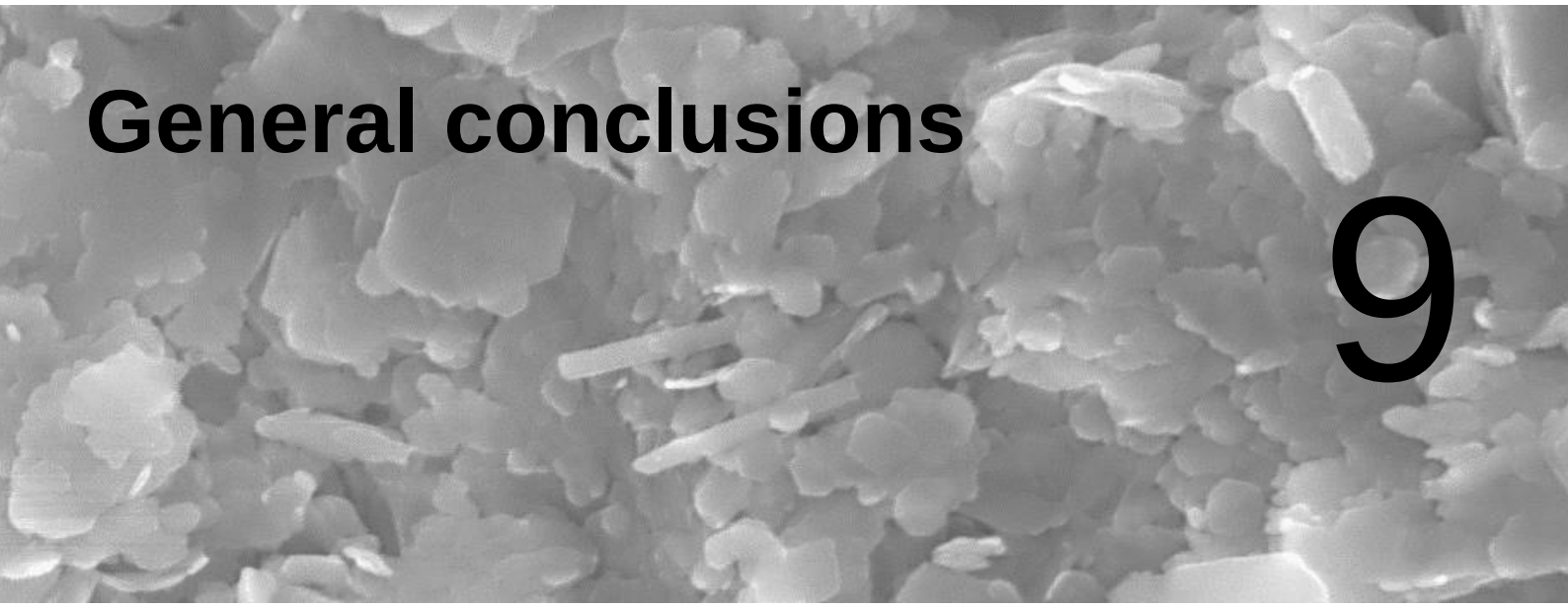

General conclusions

9

The main conclusions of this thesis are summarized in this chapter. They are organized according to the two main research lines followed in the thesis, pertaining both to the interest of clay minerals as palaeoclimatic indicators and their usefulness as raw materials in the ceramic and refractory industry.

The study of aluminium-rich clays from a geological and industrial point of view carried out in this PhD thesis has permitted a multidisciplinary characterization of these clays. These materials constitute an important mineral resource with both scientific and economic applications.

The following conclusions are drawn from the combination of field work, facies analysis, and mineralogical and geochemical studies of the upper Hauterivian–lower Barremian palaeosols included in the Blesa and Torrelapaja Fms. (SE and NW of the Iberian Chain, respectively):

1. The palaeosols can be classified as oxisols and contain both authigenic kaolinite, smectite, hematite, goethite, anatase, rutile, ilmenite and diaspore, and detrital quartz and illitic phases, along with frequent pisoids and macropisoids.
2. The pisoids and macropisoids originated *in-situ* during soil development, although they recorded reworking processes related to decreases in water level following episodic rises which resulted in the formation of palustrine-lacustrine limestone levels.
3. The higher content of authigenic kaolinite in the lower palaeosol levels indicates intense chemical weathering related to warm and humid climatic conditions, which is consistent with the palaeoclimate described for the lower Barremian in NE Iberia. The later decrease in kaolinite and Fe and Ti oxide and oxyhydroxide content towards the top of all the profiles, along with the increase in detrital quartz and illitic phases content and the presence of authigenic smectite, point to a decrease in the intensity of chemical weathering.
4. Calcite cements were generated during the early diagenesis, which did not produce the destabilization of kaolinite and smectite. However, some kaolinite from the Blesa Fm. recrystallized during this early diagenesis, as can be deduced from its higher crystallinity and $\delta^{18}O$ and δD values.
5. The high spatial resolution and accuracy of NanoSIMS allows the isotopic composition of nanometre-sized clay minerals included in polymineralic samples (e.g., palaeosols) to be determined, as well as populations of clay minerals formed under different conditions (edaphic and diagenetic) to be discriminated.
6. The $\delta^{18}O$ and δD values of kaolinite and smectite from the Blesa Fm. obtained by NanoSIMS are consistent with formation in a weathering environment (except the aforementioned recrystallized kaolinite).
7. The isotopic results show a decrease in the temperature of the clay mineral formation from the kaolinite of the bottom palaeosol levels (21–22 ºC) to the smectite

of the top palaeosols levels (16–17 ºC) in the SE of the Iberian Chain during the early Barremian.

8. All these data suggest a clear change from warm/humid to colder/dryer conditions during the lower Barremian of the Oliete subbasin (SE Iberian Chain), which could have also taken place in the Torrelapaja subbasin (NW Iberian Chain).

The following conclusions are drawn from the analyses of mixtures of bauxite and illite- and kaolinite-rich clays fired at 1000–1270 ºC and from the mineralogical study of natural clinkers:

1. With firing, the mineralogy is simplified, and the texture of the samples is homogenized. Mineralogical and textural changes during the ceramic and coal combustion processes include the destabilization of most of the initial phases and the genesis of an Al- and Si-rich vitreous phase from which new mineral phases such as mullite, corundum, cristobalite, hercynite and ceramic pyroxenes crystallized.
2. In the refractory cylinders, corundum is formed by the destabilization of the boehmite present in the raw bauxite whereas ceramic pyroxenes crystallize in the natural clinkers from the siderite included the illite- and kaolinite-rich clay. The corundum content increases with temperature in the refractory cylinders and is higher in those cylinders that contain bauxite.
3. The new mineral phases formed in both materials are not stoichiometric, due to the short duration of the ceramic and coal combustion processes, which also caused incomplete mineralogical reactions resulting in the coexistence of initial phases with those generated during firing.
4. Mullite and hercynite are formed in both the refractory cylinders and the natural clinkers. Their composition in the natural clinkers is similar to that of the refractory cylinders fired at 1000–1200 ºC, suggesting that the coal combustion took place at least at 1000 ºC but probably did not reach 1200 ºC.
5. The genesis of the vitreous phase and mullite, along with the dehydroxylation processes that take place during firing, generate an increase in the density and lineal contraction of the refractory cylinders that correlates with a decrease in the total porosity, water absorption and thermal conductivity. The changes in the colour are related to the hematite and clay content at each temperature and the point load resistance of the cylinders is associated with their corundum content.
6. Both the firing temperature and the clay content influence the refractory potential of the cylinders. The mixture of bauxite with illite- and kaolinite-rich clay makes it possible to obtain suitable refractory materials at lower temperatures (1200 ºC) than those usually reached by commercial refractory ceramics (up to 1540 ºC).

REFERENCES

A

Aboura, Y. and Moore, K.L., 2021. NanoSIMS analysis of hydrogen and deuterium in metallic alloys: Artefacts and best practice. Applied Surface Science 557, 149739.

Agüi-Gonzalez, P., Jähne, S., Phan, N.T.N., 2019. SIMS imaging in neurobiology and cell biology. Journal of Analytical Atomic Spectrometry 34, 1355–1368.

Aguilar, M.J., Ramírez del Pozo, J., Riba, O., 1971. Algunas precisiones sobre la sedimentación y paleontología del Cretácico inferior en la zona de Utrillas-Villarroya de los Pinares. Estudios Geológicos 27, 497–512.

Alastuey, A., Bastida, J., Fernández Turiel, J. L., Querol, X., Signes, M., 1993. Mineralogía de las arcillas calcinadas de la base de la Fm. Escucha en el área de Foz-Calanda. Cuadernos de Geología Ibérica 17, 171–184.

Allix, P., Burnham, A., Fowler, T., Herron, M., Kleinberg, R., Symington, B., 2011. Coaxing oil from Shale. Oilfield Review 22(4), 4–15.

Altun, I.A., 2001. Effect of temperature on the mechanical properties of self-flowing low cement refractory concrete. Cement and Concrete Research 31(8), 1233–1237.

Andrews, A., Adam, J., Gawu, S. K. Y., 2013. Development of fireclay aluminosilicate refractory from lithomargic clay deposits. Ceramics International, 39(1), 779–783.

Aras, A., 2002. The change of phase composition in kaolinita- and illite-rich clay-based ceramic bodies. Applied Clay Science 24, 257–269.

Aurell, M., Bádenas, B., Canudo, J.I., Castanera, D., García-Penas, A., Gasca, J.M., Martín-Closas, C., Moliner, L., Moreno-Azanza, M., Rosales, I., Santas, L., Sequero, C., Val, J., 2019a. Kimmeridgian–Berriasian stratigraphy and sedimentary evolution of the central Iberian Rift System (NE Spain). Cretaceous Research 102, 1–19.

Aurell, M., Bádenas, B., Castanera, D., Gasca, J.M., Canudo, J.I., Laita, E., Liesa, C. L., 2021. Latest Jurassic–Early Cretaceous synrift sedimentation of Torrelapaja Subbasin (Cameros Basin): implications for Northeast Iberia palaeogeography. Cretaceous Research 128, 104997.

Aurell, M., Fregenal-Martínez, M., Bádenas, B., Muñoz-García, M.B., Élez, J., Meléndez, N., de Santisteban, C., 2019b. Middle Jurassic–Early Cretaceous tectono-sedimentary evolution of the southwestern Iberian Basin (central Spain): Major palaeogeographical changes in the geotectonic framework of the Western Tethys. Earth-Science Reviews 199, 102983.

Aurell, M., Soria, A.R., Bádenas, B., Liesa, C.L., Canudo, J.I., Gasca, J.M., Moreno-Azanza, M., Medrano-Aguado, E., Mélendez, A., 2018. Barremian synrift sedimentation in the Oliete subbasin (Iberian Basin, Spain): palaeogeographical evolution and distribution of vertebrate remains. Journal of Iberian Geology 44, 285–308.

B

Baboolal, A.A., Knight, J., Wilson, B., 2018. Petrography and mineralogy of pyrometamorphic combustion metamorphic rocks associated with spontaneous oxidation of lignite seams of the Erin Formation, Trinidad. Journal of South American Earth Sciences, 82, 181–192.

Bailey S.W., 1980. Summary of recommendations of AIPEA nomenclature committee. Clays and Clay Minerals, 28, 73–78.

Bárdossy, G., 1982. Karst Bauxites. Elsevier, pp. 441.

Bartolomé, J.F., 1997. El Caolín: composición, estructura, génesis y aplicaciones. Boletín de la sociedad española de cerámica y vidrio 36(1), 7-20.

Barton, C.D., Karathanasis, A.D., 2002. Clay Minerals. En: Lal, R. (Ed), Encyclopedia of Soil Science. Marcel Dekker, pp. 187–192.

Bauer, K.K., Vennemann, T.W., 2014. Analytical methods for the measurement of hydrogen isotope composition and water content in clay minerals by TC/EA. Chemical Geology 363, 229–240.

Bauluz, B., Mayayo, M. J., Fernández-Nieto, C., Cultrone, G., Gonzalez Lopez, J. M., 2003. Assessment of technological properties of calcareous and non-calcareous clays used for the brick-making industry of Zaragoza (Spain). Applied Clay Science, 24(1–2), 121–126.

Bauluz, B., Mayayo, M.J., Fernández-Nieto, C., González López, J.M., 2000. Geochemistry of Precambrian and Paleozoic siliciclastic rocks from the Iberian Range (NE Spain): implications for source-area weathering, sorting, provenance, and tectonic setting. Chemical Geology 168, 135–150.

Bauluz, B., Mayayo, M.J., Laita, E., Yuste, A., 2021. Micro- and nanotexture and genesis of ball clays in the lower cretaceous (Se iberian range, ne spain). Minerals, 11(12).

Bauluz, B., Mayayo, M.J., Yuste, A., Fernandez-Nieto, C., Gonzalez Lopez, J.M., 2004. TEM study of mineral transformations in fired carbonated clays: relevance to brick making. Clay Minerals 39(3), 333–344.

Bauluz, B., Mayayo, M.J., Yuste, A., González López, J.M., 2008. Genesis of kaolinite from Albian sedimentary deposits of the Iberian Range (NE Spain): analysis by XRD, SEM and TEM. Clay Minerals 43(3), 459–475.

Bauluz, B., Yuste, A., Mayayo, M.J., Canudo, J.I., 2014. Early kaolinization of detrital Weald facies in the Galve Sub-basin (Central Iberian Chain, north-east Spain) and its relationship to palaeoclimate. Cretaceous Research 50, 214–227.

Berg, R., 1991. Tungsten skarn mineralizations in a regional metamorphic terrain in northern Norway: a possible metamorphic ore deposit. Mineralium Deposita 26, 281–289.

Besteiro, J., Bastida, J., Amigó, J.M., Lores, M.T., Lopez Buendia, A., Serrano, F.J., 1996. Sobre análisis microestructural por DRX y condiciones de formación de mullitas

naturales de la cuenca de Oliete (Teruel). Boletín de la Sociedad Española de Mineralogía 19, 119–129.

Bhattacharjee, S., Singh, S.K., Galgali, R.K., 2000. Preparation of zirconia toughened mullite by thermal plasma. Materials Letters 43, 77–80.

Bhattacharyya, D.P., Kakimoto, P.L., 1982. Origin of ferriferous ooids: a SEM study of ironstone ooids and bauxite pisoids. Journal of Sedimentary Petrology 52(3), 849–857.

Bird, M.I., Longstafee, F.J., Fyfe, W.S., Bildgen, P., 1992. Oxygen-isotope systematics in a multiphase weathering system in Haiti. Geochimica et Cosmochimica Acta 56, 2831–2838.

Biscaye, P.E., 1965. Mineralogy and sedimentation of recent deep-sea clay in the Atlantic Ocean and adjacent seas and oceans. Geological Society of American Bulletin 76, 803–832.

Blanc, W., Gullermier, C., Dussardier, B., 2012. Composition of nanoparticles in optical fibers by Secondary Ion Mass Spectrometry. Optical Materials Express 2, 1504–1510.

Bodin, S., Fiet, N., Godet, A., Matera, V., Westermann, S., Clément, A., Janssen, N.M.M., Stille, P., Föllmi, K.B., 2009. Early Cretaceous (late Berriasian to early Aptian) palaeoceanographic change along the northwestern Tethyan margin (Vocontian Trough, southeastern France): δ13C, δ18O and Sr-isotope belemnite and whole-rock records. Cretaceous Research 30, 1247–1262.

Boiteau, R. M., Kukkadapu, R., Cliff, J. B., Smallwood, C.R., Kovarik, L., Wirth, M.G., Engelhard, M.H., Varga, T., Dohnalkova, A., Perea, D.E., Wietsma, T., Moran, J. J. and Hofmockel, K.S., 2020. Calcareous organic matter coatings sequester siderophores in alkaline soils. Science of the Total Environment. 724, 138250.

Bojanowski, M.J., Bagiński, B., Guillermier, C., Franchi, I. A., 2015. Carbon and oxygen isotope analysis of hydrate-associated Oligocene authigenic carbonates using NanoSIMS and IRMS. Chemical Geology 416, 51–64.

Boussen, S., Sghaier, D., Chaabani, F., Jamoussi, B., Bennour, A., 2016. Characteristics and industrial application of the Lower Cretaceous clay deposits (Bouhedma Formation), Southeast Tunisia: Potential use for the manufacturing of ceramic tiles and bricks. Applied Clay Science 123, 210–221.

Brindley, G.W., Pedro, G., 1976. Meeting of the Nomenclature Committee of AIPEA. AIPEA Newsletter 12, 5–6.

Brosse, E., Margueron, T., Cassou, C., Sanjuan, B., Canham, A., Girad, J.P., Lacharpahne, J.C., Sommer, F., 2003. The formation and stability of kaolinite in Brent sandstone reservoirs: a modelling approach. International Association of Sedimentologists Special Publications 34, 383–408.

Brotzu, P., Gomes, C.B., Melluso, L., Morbidelli, L., Norra, V., Ruberti, E., 1997. Petrogenesis of coexisting SiO_2-undersaturated to SiO_2-oversaturated felsic

igneous rocks: The alkaline complex of Itatiaia, southeastern Brazil. Lithos 40, 133–156.

Buscalioni, A.D., Fregenal-Martínez, M.A., 2010. A holistic approach to the palaeoecology of Las Hoyas Konservat-Lagerstätte (La Huérguina Formation, Lower Cretaceous, Iberian Ranges, Spain). Journal of Iberian Geology 36 (2), 297–326.

Buurman, E., Meijer, E.L., van Wijck, J.H., 1988. Weathering of chlorite and vermiculite in ultramafic rocks of Cabo Ortegal, northwestern Spain. Clays and Clays Minerals 36, 263–269.

C

Camuti, K. S., McGuire, P. T., 1999. Preparation of polished thin sections from poorly consolidated regolith and sediment materials. Sedimentary Geology 128, 171–178.

Canérot, J., Cugny, P., Pardo, G., Salas, R., Villena, J. 1982. Ibérica Central-Maestrazgo. In: García, A (Ed.), El Cretácico de España. Madrid: Univ. Complutense de Madrid, 273–344.

Cantinolle, P., Didier, P., Meunier, J.D., Parron, C., Guendon, J.L., Bocquier, G., Nahon, D., 1984. Kaolinites ferrifères et oxyhydroxydes de fer et d'alumine dans les bauxites des Canonettes (S.E. de la France). Clay Minerals 19, 125–135.

Canudo, J.I., Gasca, J.M., Aurell, M., Badiola, A., Blain, H.A., Cruzado-Caballero, P., Gómez-Fernández, D., Moreno-Azanza, M., Parrilla, J., Rabal-Garcés, R., Ruiz-Omeñaca, J.I., 2010. La Cantalera: an exceptional window onto the vertebrate biodiversity of the Hauterivian-Barremian transition in the Iberian Peninsula. Journal of Iberian Geology 36(2), 205–224.

Capuano R.M., 1992. The temperature dependence of hydrogen isotope fractionation between clay minerals and water: Evidence from a geopressured system. Geochimica et Cosmochimica Acta 56, 2547-2554.

Casas, A.M., 1993. Oblique tectonic inversion and basement thrusting in the Cameros Massif (Northern Spain). Geodinamica Acta 6, 202–216.

Casas, A.M., Villalaín, J.J., Soto, R., Gil-Imaz, A., del Río, P., Fernández, G., 2009. Multidisciplinary approach to an extensional syncline model for the Mesozoic Cameros Basin (N Spain). Tectonophysics 470, 3–20.

Cava, S., Tebcherani, S.M., Pianaro, S.A., Paskocimas, C.A., Longo, E., Varela, J.A., 2006. Structural and spectroscopic analysis of γ-Al_2O_3 to α-Al_2O_3-$CoAl_2O_3$ phase transition. Materials Chemistry and Physics 97, 102–108.

Cervera A., Pardo G., Villena J., 1976. Algunas precisiones litoestratigráficas sobre la Formación 'Lignitos de Escucha'. Tecniterrae 3,25–33.

Chamley, H., 1989. Clay Sedimentology. Springer-Verlag, Berlin. Heidelberg New York, p. 622.

Chang, L.L.Y., 2002 Industrial mineralogy: materials, processes, and uses. Prentice Hall, Upper Saddle River, pp. 472.

Chanvry, E., Marchand, E., Lopez, M., Séranne, M., Le Saout, G., Vinches, M., 2020. Tectonic and climate control on allochthonous bauxite deposition. Example from the mid-Cretaceous Villeveyrac basin, southern France. Sedimentary Geology, 407, 105727.

Chen, C.Y., Lan, G.S., Tuan, W.H., 2000. Microstructural evolution of mullite during the sintering of kaolin powder compacts. Ceramics International 26(7), 715–720.

Chew, Y.V., Holmes, A.J., Cliff, J.B., 2014. Visualization of Metabolic Properties of Bacterial Cells Using Nanoscale Secondary Ion Mass Spectrometry (NanoSIMS). En: Paulsen, I.T., Holmes, A.J. (Eds), Environmental Microbiology Methods and Protocols. Humana Press, Totowa, pp. 133–146.

Chmelík, F., Trník, A., Štubňa, I., Pešička, J., 2011. Creation of microcracks in porcelain during firing. Journal of European Ceramic society 31, 2205–2209.

Christidis, G.E., 2013. Assessment of Industrial Clays. In *Developments in Clay Science*, Elsevier, pp. 425–449.

Ciesielczuk, Misz-Kennan, M., Hower, J.C., Fabiańska, M.J., 2014. Mineralogy and geochemistry of coal wastes from the Starzykowiec coal-waste dump (Upper Silesia, Poland). International Journal of Coal Geology 127, 42–55.

Clauer, N., Fallick, A.E., Galán, E., Aparicio, P., Miras, A., Fernández-Caliani, J.C., Aubert, A., 2015. Stable isotope constraints on the origin of kaolin deposits from Variscan granitoids of Galicia (NW Spain). Chemical Geology 417, 90–101.

Clemente, P., 2010. Review of the Upper Jurassic-Lower Cretaceous Stratigraphy in Western Cameros basin, Northern Spain. Revista de la Sociedad Geológica de España 23 (3-4), 101–143.

Coates, D., Heffern, E., 1999. Origin and geomorphology of clinker in the Powder River Basin, Wyoming and Montana: Wyoming Geological Association 50th Annual Field Conference Guidebook, pp. 211–229.

Coelho, C.V.S., Rosolen, V., Bueno, G.T., Mesquita, A., Moreira, C.A., Furlan, L.M., Govone, S., 2019. The formation of high-alumina clays in a pedosedimentary sequence of Marilia Formation (Western Minas Gerais, Brazil). Journal of South American Earth Sciences 95, 102263.

Combes, P.J., 1969. Recherches sur la genèse des bauxites dans le nord-est de l'Espagne le Languedoc et l'Ariége (France). Ph.D. Thesis, Montpellier, France, 375 p.

Combes, P.J., 1990. Typologie, cadre géodynamique et genèse des bauxites françaises. Geodinamica Acta 4:2, 91–109.

Corentin, P., Deconinck, J.F., Pellenard, P., Amédro, F., Bruneau, L., Chenot, E., Matrion, B., Huret, E., Landrein, P., 2020. Environmental and climatic controls of the clay mineralogy of Albian deposits in the Paris and Vocontian basins (France). Cretaceous Research 108, 104342.

Cosca, M.A., Peacor, D.R., 1987. Chemistry and structure of esseneite ($CaFe^{3+}AlSiO_6$) a new pyroxene produced by pyrometamorphism. American Mineralogist 72 (1-2), 148–156

Cosca, M.A., Essene, E.J., Geissman, J.W., Simmons, W. B., Coates, D. A., 1989. Pyrometamorphic rocks associated with naturally burned coal beds, Powder River Basin, Wyoming. American Mineralogist 74, 85–100.

Craig, H., 1961. Standard for Reporting Concentrations of Deuterium and Oxygen-18 in Natural Waters. Science 133, 1833–1834.

Curtis, C.D., 1985. Clay mineral precipitation and transformation during burial diagenesis. Philosophical Transactions of the Royal Society of London 315, 91–105.

D

Deconinck, J.F., Bernoulli, D., 1991. Clay mineral assemblages of Mesozoic pelagic and flysch sediments of the Lombardian Basin (Southern Alps): implications for palaeotectonics, palaeoclimate and diagenesis. Geologische Rundschau 80, 1–17.

Delgado, A., Reyes, E., 1996. Oxygen and hydrogen isotope compositions in clay minerals: A potential single-mineral geothermometer. Geochimica et Cosmochimica Acta, 60(21), 4285–4289.

Dera, G., Pellenard, P., Neige, P., Deconinck, J.F., Pucéat, E., Dommerguer, J.L., 2009. Distribution of clay minerals in Early Jurassic Peritethyan seas: Palaeoclimatic significance inferred from multiproxy comparisons. Palaeogeography, Palaeoclimatology, Palaeoecology 271(1–2), 39–51.

Dhillon, S.K., Dhillon, K.S., 1991. Characterisation of potassium in Red (Alfisols), Black (Vertisols) and Alluvial (Inceptisols and Entisols)) soils of India using electro-ultrafiltration. Geoderma 50, 185–196.

Díaz Rodríguez, L.A., Torrecillas, R., 2002. Arcillas cerámicas: Una revisión de sus distintos tipos, significados y aplicaciones. Boletin de La Sociedad Espanola de Cerámica y Vidrio 41(5), 459–470.

Dinis, P.A., Carvalho, J., Callapez, P.M., Mendes, M.M., Santos, V.F., Fernandes, P., 2020. Composition of Lower Cretaceous mudstones of the Algarve Basin and implications for Iberian paleoclimates. Cretaceous Research 110, 104404.

Do Campo, M., Bauluz, B., del Papa, C., White, T., Yuste, A., Mayayo, M.J., 2018. Evidence of cyclic climatic changes recorded in clay mineral assemblages from a continental Paleocene-Eocene sequence, northwestern Argentina. Sedimentary Geology 368, 44–57.

Do Campo, M., Bauluz, B., Papa del, C., Payrola, P., Yuste, A., Mayayo, M. J., 2021. Terrestrial record of cyclic early Eocene warm-humid events in clay mineral assemblages from the Salta basin, northwestern Argentina. Sedimentary Geology, 425, 106004.

Do Campo, M., del Papa, C., Nieto, F., Hongn, F., Petrinovic, I., 2010. Integrated analysis for constraining palaeoclimatic and volcanic influences on clay-mineral assemblages in orogenic basins (Palaeogene Andean foreland, Northwestern Argentina). Sedimentary Geology 228, 98–112.

Dondi, M., Ercolani, G., Fabbri, B., Marsigli, M., 1998. An approach to the chemistry of pyroxenes formed during the firing of Ca-rich silicate ceramics. Clay minerals 33, 443–452.

Dong, Y., Feng, X., Feng, X., Ding, Y., Liu, X., Meng, G., 2008. Preparation of low-cost mullite ceramics from natural bauxite and industrial waste fly ash. Journal of Alloys and Compounds, 460(1–2), 599–606.

Dong Y., Zhang, M., Xie, C., 2020. Effect of reaction conditions on agglomeration of aluminium hydroxide in the recovery of waste aluminium-catalyst. Separation and Purification Technology 248, 116978.

Doval Montoya, M., García Romero, E., Luque del Villar, F. J., Martín-Vivaldi Caballero, J.L., Rodas González, M., 1991. Arcillas industriales: yacimientos y aplicaciones. En: Lunar, R., Oyarzun, R. (Eds), Yacimientos minerales. Técnicas de estudio-Tipos-Evolución metalogénica-Exploración. Centro de estudios Ramón Areces. Madrid, pp. 581–608.

Drits, V., McCarty, D., 2007. The nature of structure-bonded H2O in illite and leucophyllite from dehydration and dehydroxylation experiments. Clays and Clays Minerals 55(1), 45–48

D'Souza, Mervin; D`Souza, M., Prasad, A V Keshava; Ravindra, R., 2006. Mineral analysis and geochemistry of Muehlig-Hofmannfjella granitoids, Central Drooning Maud Land, East Antarctica. En: Fütterer, D. K., Damaske, D., Kleinschmidt, G., Miller, H., Tessensohn, F. (Eds), Antarctica: Contributions to Global Earth Sciences, 1st ed. Spingrer: Verlag, Berlin Heidelberg, Germany, pp. 45–54.

E

Ehrmann, W., Setti, M., Marinoni, L., 2005. Clay minerals in Cenozoic sediments off Cape Roberts (McMurdo Sound, Antarctica) reveal palaeoclimatic history. Palaeogeography, Palaeoclimatology, Palaeoecology 229, 187–211.

Ender, E., Subirana, M.A., Raab, A., Krupp, E.M., Schaumlöffel, D., Feldmann, J., 2019. Why is NanoSIMS elemental imaging of arsenic in seaweed (Laminaria digitata) important for understanding of arsenic biochemistry in addition to speciation information? Journal of Analytical Atomic Spectrometry 34, 2295–2302.

Estrada, S., Piepjohn, K., Frey, M. J., Reinhardt, L., Andruleit, H., Von Gosen, W., 2009. Pliocene coal-seam fires on southern Ellesmere Island, Canadian Arctic. Neues Jahrbuch Für Geologie Und Paläontologie - Abhandlungen, 251(1), 33–52.

F

Faris, N., Ram, R., Tardio, J., Bhargava, S., Pownceby, M.I., 2019. Characterisation of a ferruginous rare earth beating lateritic ore and implications for rare earth mineral processing. Minerals Engineering 134, 23–36.

Feenstra, A., Sämann, S., Wunder, B., 2005. An Experimental Study of Fe-Al Solubility in the System Corundum-Hematite up to 40 kbar and 1300ºC. Journal of Petrology 46(9), 1881–1832

Fernández-Caliani, J.C., Galán, E., Aparicio, P., Miras, A., Márquez, M.G., 2010. Origin and geochemical evolution of the Nuevo Montecastelo kaolin deposit (Galicia, NW Spain). Applied Clay Science 49, 91–97.

Fesharaki, O., García-Romero, E., Cuevas-González, J., López-Martínez, N., 2007. Clay mineral genesis and chemical evolution in the Miocene sediments of Somosaguas, Madrid Basin, Spain. Clay Minerals 42, 187–201.

Floyd, M., Czerewko, M.A., Cripps, J.C., Spears, D.A., 2003. Pyrite oxidation in Lower Lias Clay at concrete highway structures affected by thaumasite, Gloucestershire, UK. Cement and Concrete Composites 25, 1015–1024.

Foit, F.F., Hooper, R.L., Rosenberg, P.E., 1987. An unusual pyroxene, melilite, and iron oxide mineral assemblage in a coal-fire buchite from Buffalo, Wyoming. American Mineralogist 72, 137–147.

Föllmi, K.B., 2012. Early Cretaceous life, climate and anoxia. Cretaceous Research 35, 230–257.

Foos, A.M., 1991. Aluminous lateritic soils, Eleuthera, Bahamas: a modern analog to carbonate paleosols. Journal of Sedimentary Petrology 61(3), 340–348.

Franceschelli, M., Puxeddu, M., Gattiglio, M., 2003. Geochemistry and origin of chloritoid schist from the Alpi Apuane, Italy: evidence of a prevailing lateritic signature. European Journal of Mineralogy 15, 575–588.

Fregenal-Martínez, M. A., Meléndez, N., Muñoz-García, B., Elez, J., de la Horra, R., 2017. The stratigraphic record of the Late Jurassic-Early Cretaceous rifting in the Alto Tajo-Serranía de Cuenca region (Iberian Ranges, Spain): Genetic and structural evidences for a revision and a new lithostratigraphic proposal. Revista de la Sociedad Geológica de España 30, 113–142.

G

Galán, E., 2003. Mineralogía aplicada. Síntesis, S.A. Madrid, pp. 432.

Galán, E., 2006. Genesis of clay minerals. En: Bergaya, F., Theng, B.K.G., Lagaly, G. (Eds), Developments in Clay Science, Vol. 1. Elsevier, pp. 1129–1162.

Gavshina, O.V., Doroganov, V.A., Doroganov, E.A., Onishchuk, V.I., Trepalina, Y.N., 2019. High-Alumina Mixes Based on Molded Bauxite Suspensions. Refractories and Industrial Ceramics 60(4), 350–354.

Ghassemi Kakroudi, M., Yeugo-Fogaing, E., Gault, C., Huger, M., Chotard, T., 2008. Effect of thermal treatment on damage chemical behaviour of refractory castables: Comparison between bauxite and andalusite aggregates. Journal of European Ceramic Society 28, 2471–2478.

Gilg, H. A., Weber, B., Kasbohm, J., Frei, R., 2003. Isotope geochemistry and origin of illite-smectite and kaolinite from the Seilitz and Kemmlitz kaolin deposits, Saxony, Germany. Clay Minerals, 38(1), 95–112.

Gilg, H.A., Girard, J.P., Sheppard, S.M.F., 2004. Conventional and Less Conventional Techniques for Hydrogen and Oxygen Isotope Analysis of Clays, Associated Minerals and Pore Waters in Sediments and Soils. En: Groot, P.A. (Ed), Handbook of Stable Isotope Analytical Techniques, Volume 1. Elsevier, pp. 38–61.

Giovannini, A.L., Bastos Neto, A.C., Porto, C.G., Pereira, V.P., Takehara, L., Barbanson, L., Bastos, P.H.S., 2017. Mineralogy and geochemistry of laterites from the Morro dos Seis Lagos Nb (Ti, REE) deposit (Amazonas, Brazil). Ore Geology Reviews 88, 461–480.

Giral-Kacmarcík, S., Savin, S.M., Nahon, D.B., Girard, J.P., Lucas, Y., Abel, L.J. 1998. Oxygen isotope geochemistry of kaolinite in laterite-forming processes, Manaus, Amazonas, Brazil. Geochimica et Cosmochimica Acta 62(11), 1865–1879.

Girard J.P., Freyssinet P., Chazot G., 2000. Unraveling climatic changes from intra-profile variation in oxygen and hydrogen isotopic composition of goethite and kaolinite in laterites: an integrated study from Yaou, French Guiana. Geochimica et Cosmochimica Acta 64, 409–426.

Girard, J.P., Freyssinet P., Morillon A.C., 2002. Oxygen isotope study of Cayenne duricrust paleosurfaces: implications for past climate and laterization processes over French Guiana. Chemical Geology 30, 329–343.

Godet, A., Bodin, S., Adatte, T., Föllmi, K.B., 2008. Platform-induced clay-mineral fractionation along a northern Tethyan basin-platform transect: implications for the interpretation of Early Cretaceous climate change (Late Hauterivian-Early Aptian). Cretaceous Research 29(5–6), 830–847.

Godet, A., Bodin, S., Föllmi, K.B., Vermeulen, J., Gardin, S., Fiet, N., Adatte T., Berner, Z., Stüben, D., Van de Schootbrugge, B., 2006. Evolution of the marine stable carbon-isotope record during the early Cretaceous: A focus on the late Hauterivian and Barremian in the Tethyan realm. Earth and Planetary Science Letters 242, 254–271.

Gómez-Fernández, J.C. and Meléndez, N., 1994. Estratigrafía de la Cuenca de los Cameros (Cordillera Ibérica Noroccidental, N de España) durante el tránsito Jurásico-Cretácico. Revista de la Sociedad Geológica de España 7, 121-139.

González-García, F., Romero-Acosta, V., García-Ramos, G., González Rodríguez, M., 1990. Firing transformations of mixtures of clays containing illite, kaolinite and

calcium carbonate used by ornamental tile industries. Applied Clay Science 5, 361–375.

Grim, R.E., 1968. Clay Mineralogy. International Series in the Earth and Planetary Sciences. McGraw-Hill Book Company, New York, pp. 596.

Guerrak, S., 1987. Metallogenesis of cratonic oolitic ironstone deposits in the Bled el Mass, Azzel Mani, Ahnet and Mouydir basins, Central Sahara. Geologische Rundschau 76, 903–922.

Guggenheim, S., Chang, Y., Koster van Groos, A.F., 1987. Muscovite dehydroxylation: high-temperature studies. American Mineralogist 72, 537–550.

Guggenheim, S., Martin, R.T., 1995. Definition of clay and clay minerals: joint report of the AIPEA and CMS nomenclature committees. Clay Minerals 30, 257–259.

Güven, N., 1988. Smectites. In: Bailey, S.W. (Ed.), Hydrous Pyllosilicates. Mineralogical Society of America, Reviews in Mineralogy 19, 497–559.

H

Harvey et al., 2003 (el tocho rojo de Pepa)

Hay, W.W., 2008. Evolving ideas about the Cretaceous climate and ocean circulation. Cretaceous Research 29, 725–753.

Haywood, A.M., Valdes, P.J., Markwick, P.J., 2004. Cretaceous (Wealden) climates: a modelling prospective. Cretaceous Research 25, 303–331.

He, S., Longstaffe, F.J., Zhou, Z., 2019. Stable isotopes of clay minerals from autoclave tests of oil sands: Implications for clay formation during steaming of Alberta Clearwater oil sands. Applied Geochemistry 104, 202–209.

Henao, J.A., Carreño, A.M., Quintero, J.A., Candela, S.A., Ríos, C.A., Ramos, M.A., Pinilla, J.A., 2010. Petrography and application of the rietveld method to the quantitative analysis of phases of natural Clinker generated by coal spontaneous combustion. Earth Sciences Research Journal 14 (1), 17–30.

Hill, R.J., 1984. X-ray powder diffraction profile refinement of synthetic hercynite. American Mineralogist 69(9-10), 937–942.

Hillier, S., 1995. Erosion, Sedimentation and Sedimentary Origin of Clays. En: Velde, B. (Ed), Origin and Mineralogy of Clays. Clays and the Environment. Springer-Verlag, Berlin. Heidelberg New York, pp. 162–219.

Hillier, S., 2003. Quantitative analysis of clay and other minerals in sandstones by X-ray powder diffraction (XRPD). International Association of Sedimentologists. Spec. Publ. 34, 213–251.

Hoefs, J., 1997. Stable isotope geochemistry. Springer, Berlin, pp. 201.

Höschen, C., Höschen, T., Mueller, C.W., Lugmeier, J., Elgeti, S., Rennert, T., Kögel-Knabner, I., 2015. Novel sample preparation technique to improve spectromicroscopic analyses of micrometer-sized particles. Environmental Science & Technology 49, 9874 − 9880.

Höschen, C., Mueller, C.W., Heister, K., Lugmeier, J., Kögel-Knabner, I., 2013. Application of NanoSIMS on Organo-Mineral Structures. NEA-RWM-CLAYCLUB--2013-1). Nuclear Energy Agency of the OECD (NEA).

Hu, S., Lin, Y., Zhang, J., Hao, J., Feng, L., Xu, L., Yang, W., Yang, J., 2014. NanoSIMS analyses of apatite and melt inclusions in the GRV 020090 Martian meteorite: Hydrogen isotope evidence for recent past underground hydrothermal activity on Mars. Geochimica et Cosmochimica Acta 140, 321–333.

Huffman, G.P., Huggins, F.E., Shah, N., 1990. Behavior of basic elements during coal combustion. Progress in Energy and Combustion Science 16, 243–251.

Huggett, J. M., Cuadros, J., 2005. Low-temperature illitization of smectite in the late Eocene and early Oligocene of the Isle of Wight (Hampshire basin), UK. American Mineralogist 90(7), 1192–1202.

Huggett, J. M., Cuadros, J., 2010. Glauconite formation in lacustrine/palaeosol sediments, Isle of Wight (Hampshire Basin), UK. Clay Minerals, 45(1), 35–49.

Huggett, J. M., Gale, A. S., Clauer, N., 2001. The nature and origin of non-marine 10 Å clay from the Late Eocene and Early Oligocene of the Isle of Wight (Hampshire Basin), UK. Clay minerals 36(3), 447–464.

I

Iglesias, I., Acosta, B., Yu, R., Ruiz, G., Aineto, M., Acosta, A., 2011. Estudio de caracterización mecáica de probetas ceráicas a partir de una adaptació del ensayo brasileño. Materiales de Construccion 61(303), 417–429.

Inagaki, T.M., Possinger, A.R., Grant, K.E., Schweizer, S.A., Mueller, C.W., Derry, L. A., Lehmann, J., Kögel-Knabner, I., 2020. Subsoil organo-mineral associations under contrasting climate conditions. Geochimica et Cosmochimica Acta. 270, 244–263.

Ito, M., Messenger, S., 2008. Isotopic imaging of refractory inclusions in meteorites with the NanoSIMS 50L. Applied Surface Science 255, 1446–1450.

Inoue A., 1995. Formation of Clay Minerals in Hydrothermal Environments. En: Velde, B. (Ed), Origin and Mineralogy of Clays. Clays and the Environment. Springer-Verlag, Berlin. Heidelberg New York, pp. 268–329.

J

Jang, K., Nunna, V.R.M., Hapugoda, S., Nguyen, A., Bruckard, W.J., 2014. Chemical and mineral transformations of a low grade goethite ore by dehydroxilation, reduction roasting and magnetic separation. Minerals Engineering 60, 14–22.

Jbara, A.S., Othaman, Z., Ati, A.A., Saeed, M.A., 2017. Characterization of γ-Al2O3 nanopowders synthesized by Co-precipitation method. Materials Chemistry and Physics 188, 24–29.

Jeong, G.Y., Hillier, S., Kemp, R.A., 2011. Changes in mineralogy of loess–paleosol sections across the Chinese Loess Plateau. Quaternary Research 75, 245–255.

Johnson, J.S., Clark, J., Miller-Antonio, S., Robins, D., Schiffer, M.B., Skibo, J.M., 1988. Effects of Firing Temperature on the Fate of Naturally Occurring Organic Matter in Clays. Journal of Archaeological Science 15, 403–414.

Jordán, M. M., Boix, A., Sanfeliu, T., De La Fuente, C., 1999. Firing transformations of cretaceous clays used in the manufacturing of ceramic tiles. Applied Clay Science 14(4), 225–234.

Jordán, M.M., Meseguer, S., Pardo, F., Montero, M.A., 2020. High-temperature new Minerals Formation after firing clay materials associated to mined coal in Teruel (Spain). Applied Sciences 10(9), 3114.

Jordan, T., Schlunegger, F., Cardozo, N., 2001. Unsteady and spatially variable evolution of the Neogene Andean Bermejo Foreland Basin, Argentina. Journal of South American Earth Sciences 14, 775–798.

K

Kakroudi, M. G., Yeugo-Fogaing, E., Gault, C., Huger, M., Chotard, T., 2008. Effect of thermal treatment on damage mechanical behaviour of refractory castables: Comparison between bauxite and andalusite aggregates. Journal of the European Ceramic Society, 28(13), 2471–2478.

Kakroudi, M.G., Yeugo-Fogaing, E., Gault, C., Huger, M., Chotard, T., 2008. Effect of thermal treatment on damage mechanical behaviour of refractory castables: Comparison between bauxite and andalusite aggregates. Journal of the European Ceramic Society 28(13), 2471–2478.

Kapička, A., Petrovsky, E., Ustjak, S., Macháčková, K., 1999. Proxy mapping of fly-ash pollution of soils around a coal-burning power plant: a case study in the Czech Republic. Journal of Geochemical Exploration 66, 291–297.

Kilburn, M.R. and Wacey, D., 2015. Nanoscale Secondary Ion Mass Spectrometry (NanoSIMS) as an Analytical Tool in the Geosciences. En: Grice, K. (Ed), Principles and Practice of Analytical Techniques in Geosciences. Royal Society of Chemistry, pp. 1–34.

Kim, K., Moon, B., Kim, D., Park, K., Seok, C. S., Kim, T., Yi, J., Choi, I. H., 2021. Influence of corundum content on integrity of porcelain after long-term exposure to thermo-mechanical fatigue environments. Ceramics International 47(20), 28479–28486.

Knapek, M., Húlan, T., Minárik, Dobroň, P., Štubňa, I., Stráská, J., Chmelík, F., 2016. Study of microcracking in illite-based ceramics during firing, Journal of European Ceramic Society 36, 221–226.

Kuligiewicz, A., Środoń, J., Liivamägi, S., 2021. Oxygen isotopic compositions of end-members in a multicomponent mixture: Ediacaran weathering material from the East European Craton. Geochimica et Cosmochimica Acta 306, 245–262.

L

Laita, E., Bauluz, B., 2018. Mineral and textural transformations in aluminium-rich clays during ceramic firing. Applied Clay Science 152, 284–294.

Laita, E., Bauluz, B., Yuste, A., 2019. High-temperature mineral phases generated in natural clinkers by spontaneous combustion of coal. Minerals 9(4), 213

Laita, E., Bauluz, B., Aurell, M., Bádenas, B., Canudo, J.I., Yuste, A., 2020. A change from warm/humid to cold/dry climate conditions recorded in lower Barremian clay-dominated continental successions from the SE Iberian Chain (NE Spain). Sedimentary Geology 403, 105673

Laita, E., Bauluz, B., Aurell, M., Bádenas, B., Yuste, A., 2022. Weathering events recorded in uppermost Hauterivian–lower Barremian clay-dominated continental successions from the NW Iberian Range: climatic vs. tectonic controls. Journal of Iberian Geology 48, 45–63.

Lanson, B., Beaufort, D., Berger, G., Bauer, A., Cassagnabère, A., Meunier, A., 2002. Authigenic kaolin and illitic minerals during burial diagenesis of sandstones: a review. Clay Minerals 37, 1–22.

Lawrence, J.R., Taylor, H.P., 1972. Hydrogen and oxygen isotope systematics in weathering profiles. Geochimica et Cosmochimica Acta 36, 1377–1393.

Lee, W. E., Souza, G. P., McConville, C. J., Tarvornpanich, T., Iqbal, Y., 2008. Mullite formation in clays and clay-derived vitreous ceramics. Journal of the European Ceramic Society 28(2), 465–471.

Lévy, D., Aléon, J., Aléon-toppani, A., Troadec, D., Duhamel, R., Gonzalez-cano, A., Bureau, H., Khodja, H., 2019. NanoSIMS imaging of D/H ratios on FIB sections. Analytical Chemistry 91, 13763–13771.

Li, Q., Hu, X., Hao, J., Chen, W., Cai, P., and Huang, Q., 2020. Characterization of Cu distribution in clay-sized soil aggregates by NanoSIMS and micro-XRF. Chemosphere. 249, 1–7.

Liesa, C.L., Soria, A.R., Casas, A., Aurell, M., Meléndez, N., Bádenas, B., Fregenal-Martínez, M., Navarrete, R., Peropadre, C., Rodríguez-López, J.P., 2019. The South Iberian, Central-Iberian and Maestrazgo basins. En: Quesada, C., Oliveira, J.T. (Eds.), The Geology of Iberia: A Geodynamic Approach. Volume 5: Active Processes: Seismicity, Active Faulting and Relief. Springer, pp. 214–228.

Lindsley, D.H., 1991. Experimental studies of oxide minerals. Reviews in Mineralogy and Geochemistry 25, 69–106.

Loutou, M., Hakkou, R., Argane, R., Mansori, M., Grase, L., Svinka, R., Mezinskis, G., 2018. Clayey Quarry Sludges: Thermal Transformation, Microstructure and Technological Properties. Waste Biomass Valorization 9, 1805–1815.

Low, J.M., Curtain, B., Philipps, M., Liu, Z.Q., Ionescu, M., 2012. High temperature diffraction study of in-situ crystallization of nanostructured TiO2 photocatalysts. Journal of the Australian Ceramic Society Volume 48 (2), 198–204.

M

Mack, G., Calvin, W., Curtis, H., 1993. Classification of paleosols. Geological Society of America Bulletin 105, 129–136.

Maggetti, M., 1982. Phase analysis and its significance for technology and origin. In: Olin, J.S. (Ed.), Archaeological Ceramics. Smithsonian Institution Press, pp. 121–133.

Malherbe, J., Penen, F., Isaure, M.P., Frank, J., Hause, G., Dobritzsch, D., Gontier, E., Horréard, F., Hillion, F., Schaumlöffel, D., 2016. A New Radio Frequency Plasma Oxygen Primary Ion Source on Nano Secondary Ion Mass Spectrometry for Improved Lateral Resolution and Detection of Electropositive Elements at Single Cell Level. Analitical Chemistry 88, 7130–7136.

Mameli, P., Mongelli, G., Sinisi, R., Oggiano, G., 2020. Weathering Products of a Dismantled Variscan Basement. Minero-Chemical Proxies to Insight on Cretaceous Palaeogeography and Late Neogene Palaeoclimate of Sardinia (Italy). Frontiers in Earth Science 8, 290.

Manning, D.A.C., 1995. Introduction to industrial minerals. Chapman and Hall, London, pp. 276.

Markl. G., 2005. Mullite-corundum-spinel-cordierite-plagioclase xenoliths in the Skaergaard Marginal Border Group: multi-stage interaction between metasediments and basaltic magma. Contributions to Mineralogy and Petrology 149, 196–215.

Martin, J.D., 2017. A software package for powder x-ray diffraction analysis. Qualitative, quantitative and microtexture. pp. 121.

Martín-Closas, C., 1989: Els caròfits del Cretaci Inferior de les conques periferiques del Bloc de l'Ebre. Tesis Doctoral. Universidad de Barcelona.

Mas, R., Benito, M.I., Arribas, J., Omodeo-Salé, S., Suarez-Gonzalez, P., Quijada, I.E., Guimerà, J., González-Acebrón, L., Arribas, M.E., 2019. The Cameros Basin. En: Quesada, C., Oliveira, J.T. (Eds.), The Geology of Iberia: A Geodynamic Approach. Volume 5: Active Processes: Seismicity, Active Faulting and Relief Springer, pp. 190–205.

Mas, R., García, A., Salas, R., Meléndez, A., Alonso, A., Aurell, M., Bádenas, B., Benito, M. I., Carenas, B., García-Hidalgo, J. F., Gil, J., Segura, M., 2004. Segunda Fase de rifting: Jurásico Superior-Cretácico Inferior. En: Vera, J.A. (Ed.), Geología de España. Sociedad Geológica de España-Instituto Geológico y Minero, pp. 503–510.

McCuistion y Wilsom, 2003 (el tocho gordo rojo de pepa)

Medvedovski, E., 2001. Wear-resistant engineering ceramics. Wear, 249(9), 821–828.

Meenakshi, Shrivastava, J.P, Chandra, R., 2020. Pedogenically degenerated illite and chlorite lattices aid to palaeoclimatic reconstruction for chronologically constrained (8–130 ka) loess-palaeosols of Dilpur Formation, Kashmir, India. Geoscience Frontiers 11(4), 1353–1367.

Mendelovici, E., Yariv, S.H., Villalba, R., 1979. Iron-bearing kaolinite in venezuelan laterites: I. Infrared spectroscopy and chemical dissolution evidence. Clay Minerals 14, 323–331.

Mendes, M.M., Dinis, J.G., Gomez, B., País, J., 2010. Reassessment of the cheirolepidiaceous conifer Frenelopsis teixeirae Alvin et Pais from the Early Cretaceous (Hauterivian) of Portugal and palaeoenvironmental considerations. Review of Palaeobotany and Palynology 161, 30–42.

Meng, Y., Gong, G., Wei, D., Xie, Y., 2016. In situ high temperature X-ray diffraction study on high strength aluminous porcelain insulator with the Al2O3-SiO2-K2O-Na2O system. Applied Clay Science 132–133, 760–767.

Merriman, R.J., Peacor, D.R., 1999. Very-low grade metapelites: mineralogy, microfabrics and measuring reaction progress. En: Frey, M., Robinson, D. (Eds.), Low-Grade Metamorphims. Blackwell Science, Oxford, pp. 10–60.

Mestdagh, M.M., Vielvoye, L., Herbillon, A.J., 1980. Iron in kaolinite: II. The relationships between kaolinite and iron content. Clay Minerals 15, 1–13.

Michel, L.A., Tabor, N. J., Montañez, I.P., 2016. Paleosol diagenesis and its deep-time paleoenvironmental implications Pennsylvanian-permian Lodève basin, France. Journal of Sedimentary Research 86, 813–829.

Misra, B.K. and Singh, B.D., 1994. Susceptibility to spontaneous combustion of Indian coals and lignites: an organic petrographic autopsy. International Journal of Coal Geology 25 (3-4), 265–286.

Misz-Kennan, M., Fabiańska, M., 2010. Thermal transformation of organic matter in coal waste from Rymer Cones (Upper Silesian Coal Basin, Poland). International Journal of Coal Geolology 81, 343-358

Mix, H., Chamberlain, C.P., 2014. Stable isotope records of hydrologic change and paleotemperature from smectite in Cenozoic western North America. Geochimica et Cosmochimica Acta 141, 532–546.

Moiroud, M., Martinez, M., Deconinck, J. F., Monna, F., Pellenard, P., Riquier, L., Company, M., 2012. High-resolution clay mineralogy as a proxy for orbital tuning: Example of the Hauterivian–Barremian transition in the Betic Cordillera (SE Spain). Sedimentary geology 282, 336–346.

Molina, J.M., 1991. A review of karst bauxites and related paleokarst in Spain, Acta Geologica Hungarica 34, 179–194.

Molina, J.M., Ruiz-Ortiz, P.A., Vera, J.A., Calonge, A., 1994. Bauxitas kársticas de la sierra de Boada (Sierras Marginales surpirenaicas, Alós de Balaguer, Lleida). Geogaceta 16, 148–150.

Molina, J.M., Salas, R., 1993. Bauxitas kársticas del Cretácico inferior en Fuentespalda (provincia de Teruel): estratigrafía, origen y paleogeografía. Cuadernos de Geología Ibérica 17, 207–230.

Moreno-Azanza, M., Canudo, J.I., Gasca, J.M., 2014. Spheroolithid eggshells in the Lower Cretaceous of Europe. Implications for eggshell evolution in ornithischian dinosaurs. Cretaceous Research 51, 75–87.

Mosbrugger, V., Utescher, T., Dilcher, D. L., 2005. Cenozoic continental climatic evolution of Central Europe. Proceedings of the National Academy of Sciences of the United States of America, 102(42), 14964–14969.

Mosenfelder, J.K., Le Voyer, M., Rossman, G.R., Guan, Y., Bell, D.R., Asinow, P.D., Eiler, J.M., 2011. Analysis of hydrogen in olivine by SIMS: Evaluation of standards and protocol. American Mineralogist 96, 1725–1741.

Mücke, A., Badejoko, A., Akande, S.O., 1999. Petrographic-microchemical studies and origin of the Agbaja Phanerozoic Ironstone Formation, Nupe Basin, Nigeria: a product of a ferruginized ooidal kaolin precursor not identical to the Minette-type. Mineralium Deposita 34, 284–296.

Mücke, A., 2003. Magnetite, ilmenite and ulvite in rocks and ore deposits: petrography, microprobe analyses and genetic implications. Mineralogy and Petrology 77, 215–234.

Mueller, C.W., Kölbl, A., Hoeschen, C., Hillion, F., Heister, K., Herrmann, A.M., Kögel-Knabner, I., 2012. Submicron scale imaging of soil organic matter dynamics using NanoSIMS–From single particles to intact aggregates. Organic Geochemistry 42, 1476–1488.

Murad, E., Wagner, U., 1988. Clays and clay minerals: the firing process. Hyperfine Interactions 117, 337–356.

Murakami, T., Isobe, H., Sato, T., Ohnuki, T., 1996. Weathering of chlorite in a quartz-chlorite schist. Mineralogical and chemical changes. Clays and Clay Minerals 44, 244–256.

Murray, H.H., 1991. Overview - clay mineral applications. Applied Clay Science 5(5–6), 379–395.

Murray, H.H., 1999. Applied clay mineralogy today and tomorrow. Clay Minerals 34, 39–49.

Murray, H.H., 2006. Structure and Composition of the Clay Minerals and their Physical and Chemical Properties. En: Murray, H.H. (Ed), Developments in Clay Science, Volume 2, Applied Clay Mineralogy - Occurrences, Processing and Application of Kaolins, Bentonites, Palygorskite-Sepiolite, and Common Clays. Elsevier, pp. 7–31.

Mutterlose, J., Bodin, S., Fähnrich, L., 2014. Strontium-isotope stratigraphy of the Early Cretaceous (Valanginian-Barremian): Implications for Boreal–Tethys correlation and paleoclimate. Cretaceous Research 50, 252–263.

Mutterlose, J., Ruffell, A., 1999. Milankovitch-scale palaeoclimate changes in pale–dark beddingrhythms from the Early Cretaceous (Hauterivian and Barremian) of eastern England and northern Germany. Palaeogeography, Palaeoclimatology, Palaeoecology 154, 133–160.

N

Nkalih Mefire, A., Yongue Fouateu, R., Njoya, A., Mache, J.R., Pilate, P., Hatert, F., Fagel, N., 2018. Mineralogy and geochemical features of Foumban clay deposits (west Cameroon): genesis and potential applications. Clay Minerals 53, 431–445.

Njoya, D., Elimbi, A., Fouejio, D., Hajjaji, M., 2016. Effects of two mixtures of kaolin-talc-bauxite and firing temperatures on the characteristics of cordierite- based ceramics. Journal of Building Engineering 8, 99–106.

Nouazi Momo, M., Beauvais, A., Tematio, P., Ambrosi, J.P., Yemefack, M., Palmer Kfuban Yerima, B., Yongue-Fouateu, R., 2019. Lateritic weathering of trachyte, and bauxite formation in West Cameroon: Morphological and geochemical evolution. Journal of Geochemical Exploration 205, 106324.

O

Ondro, T., Al-Shantir, O., Csáki, Š., Lukác, F., Trník, A., 2019. Kinetic analysis of sinter-crystallization of mullite and cristobalite from kaolinite. Thermochimica Acta 678, 178312.

Ordóñez, S., Fort, R., Bustillo, M., 1990. Estudio de las tierras raras en las bauxitas kársticas del noreste de la península ibérica. Estudios Geológicos 46, 373–384.

Ordóñez, S., 1991. Bauxitas. En: Lunar, R., Oyarzun, R. (Eds), Yacimientos minerales. Técnicas de estudio-Tipos-Evolución metalogénica-Exploración. Centro de estudios Ramón Areces. Madrid, pp. 535–579.

P

Panias, D., Krestou, A., 2007. Effect of synthesis parameters on precipitation of nanocrystalline boehmite from aluminate solutions. Powder Technology, 175 163–173.

Pardo, F., Meseguer, S., Jordán, M.M., Sanfeliu, T., González, I., 2011. Firing transformations of Chilean clays for the manufacture of ceramic tile bodies. Applied Clay Science 51(1–2), 147–150.

Pardo, G., 1979. Estratigrafía y sedimentología de las formaciones detríticas del Cretácico inferior terminal del Bajo Aragón Turolense. Tesis Doctoral. Universidad de Zaragoza, España, pp. 473.

Piani, L., Remusat, L., Robert, F., 2012. Determination of the H Isotopic Composition of Individual Components in Fine-Scale Mixtures of Organic Matter and

Phyllosilicates with the Nanoscale Secondary Ion Mass Spectrometry. Analitical Chemistry 84, 10199–10206.

Piani, L., Robert, F., Remusat, L., 2015. Micron-scale D/H heterogeneity in chondrite matrices: A signature of the pristine solar system water? Earth and Planetary Science Letters 415, 154–164.

Platt, N.H., 1989. Sedimentology and tectonics of western Cameros Basin. Province of Burgos. Northern Spain. Ph.D. Thesis. University of Oxford.

Plunkert, P.A., 2005. Bauxite and Alumina. En: Annual Mineral Commodity Summaries. U.S. Geological Survey, pp.12.

Price, G.D., Fözy, I., Janssen, N.M.M., Pálfy, J., 2011. Late Valanginian-Barremian (Early Cretaceous) palaeotemperatures inferred from belemnite stable isotope and Mg/Ca ratios Bersek Quarry (Gerecse Mountains, Transdanubian Range, Hungary). Palaeogeography, Palaeoclimatology, Palaeoecology 305, 1–9.

Pucéat, E., Lecuyer, C., Reisber, L., 2005. Neodymium isotope evolution of NW Tethyan upper ocean waters throughout the Cretaceous. Earth and Planteary Science Letters 236, 705–720.

Pucéat. E., Lécuyer, C., Sheppard, S.M.F., Dromart, G., Reboulet, S., Grandjean, P., 2003. Thermal evolution of Cretaceous Tehtyan marine waters inferred from oxygen isotope composition of fish tooth enamels. Paleoceanography and Paleoclimatology 18 (2), 1–12.

Q

Querol, X., 1988. Estudio geológico de la Formación Escucha en la Cueca del Maestrazgo, Cordillera Ibérica oriental. Tesis Doctoral. Universidad de Barcelona, España, pp. 261.

Querol. X., Izquierdo, M., Monfort, E., Alvarez, E., Font, O., Moreno, T. Alastuey, A., Zhuang, X., Lu, W., Wang, Y., 2008. Environmental characterization of burnt coal gangue banks at Yangquan, Shanxi Province, China. International Journal of Coal Geology 75, 93-104.

Querol, X. Zhuang, X., Font, O., Izquierdo, M., Alstuey, A., Castro, I., van Drooge, B.L., Moreno, T., Grimalt, J.O., Elvira, J., Cabañas, M., Bartroli, R., Hower, J.C., Ayora, C., Plana, F., López-Soler, A., 2011. Influence of soil cover on reducing the environmental impact of spontaneous coal combustion in coal waste gobs: A review and new experimental data. International Journal of Coal Geology 85 2-22.

Quintero, J.A., Candela, S.A., Ríos, C.A., Montes, C., Uribe, C., 2009. Spontaneous combustion of the Upper Paleocene Cerrejón Formation coal and generation of Clinker in La Guajira Peninsula (Caribben Region of Colombia). International Journal of Coal Geology 80, 196-210.

R

Ram, L.C. Tripathi, P.S.M., Mishra, S.P., 1995. Mössbauer spectroscopic studies on the transformations of iron-bearing minerals during combustion of coals: Correlation with fouling and slagging. Fuel Processing Technology 42, 47–60.

Raucskik, B., Varga, A., 2008. Climato-environmental controls on clay mineralogy of the Hettangian-Bajocian successions of the Mecsek Mountains, Hungary: An evidence for extreme continental weathering during the early Toarcian oceanic anoxic event. Palaeogeography, Palaeoclimatology, Palaeoecology 265, 1–13.

Reinhardt, N., Proenza, J.A., Villanova-de-Benavent, C., Aiglsperger, T., Bover-Arnal, T., Torró, L., Salas, R., Dziggel, A., 2018. Geochemistry and Mineralogy of Rare Earth Elements (REE) in Bauxitic Ores of the Catalan Coastal Range, NE Spain. Minerals 8(12), 562.

Rennert, T., Händel, M., Höschen, C., Lugmeier, L. Steffens, M., Totsche, K.U., 2014. A NanoSIMS study on the distribution of soil organic matter, iron and manganese in a nodule from a Stagnosol. European Journal of Soil Science 65, 684–692.

Reolid, M., Abad, I., Martín-García, J. M., 2008. Palaeoenvironmental implications of ferruginous deposits related to a Middle–Upper Jurassic discontinuity (Prebetic Zone, Betic Cordillera, southern Spain). Sedimentary Geology 203(1-2), 1–16.

Ribeiro, J., Ferreira da Silva, E., Flores, D., 2010. Burning of coal waste piles from Douro Coalfield (Portugal): Petrological, geochemical and mineralogical characterization. International Journal of Coal Geology 81, 359–372.

Ribeiro, J., Suárez-Ruiz, I., Flores, D., 2016. Geochemistry of self-burning coal mining residues from El Bierzo Coalfield (NW Spain): Environmental implications. International Journal of Coal Geology 159, 155–168.

Ridolfi, F., Braga, R., Cesare, B., Renzulli, A., Perugini, D., Del Moro, S., 2016. Unravelling the complex interaction between mantle and cristal magmas encoded in the lavas of San Vincenzo (Tuscany, Italy). Part I: Petrography and Thermobarometry. Lithos 244, 218–232.

Righi, D., Meunier, A., 1995. Origin of Clays by Rick Weahtering and Soil Formation. En: Velde, B. (Ed), Origin and Mineralogy of Clays. Clays and the Environment. Springer-Verlag, Berlin. Heidelberg New York, pp. 43–161.

Ritsema, C.J., Groenenberg, J.E., 1993. Pyrite Oxidation, Carbonate Weathering, and Gypsum Formation in a Drained Potential Acid Sulfate Soil. Soil Science Society of America Journal 57, 968–976.

Rodríguez-López, J.P., de Boer, P.L., Meléndez, N., Soria, A.R., Pardo, G., 2006. Windblown desert sands in coeval shallow marine deposits: a key for the recognition of coastal ergs in the mid-Cretaceous Iberian Basin, Spain. Terra Nova 18, 314–320.

Rodríguez-López, J.P., Meléndez, N., Soria, A.R., Poppe L. de B., 2009. Reinterpretación estratigráfica y sedimentológica de las Formaciones Escucha y Utrillas de la Cordillera Ibérica. Revista de la Sociedad Geológica de España 22 (3–4), 163–217.

Rossi, C., Cañaveras, J.C., 1999. Pseudospherulitic fibrous calcite in paleo-groundwater, unconformity-related diagenetic carbonates (Paleocene of the Ager basin and Miocene of the Madrid basin, Spain). Journal of Sedimentary Research 69, 224–238.

Ruffell, A., Batten, B., 1990. The Barremian–Aptian arid phase in western Europe. Palaeogeography, Palaeoclimatology, Palaeoecology 80, 197–212.

Ruffell, A., McKinley, J. M., Worden, R. H., 2002. Comparison of clay mineral stratigraphy to other proxy palaeoclimate indicators in the Mesozoic of NW Europe. Philosophical Transactions of the Royal Society A: Mathematical, Physical and Engineering Sciences, 360(1793), 675–693.

S

Saber, E.S., Ali, M., El-Sheikh, A., 2018. Provenance studies of Kalabsha kaolin deposits, Egypt: a petrographical and geochemical approach. Arabian Journal of Geosciences 11, 339.

Salahudeen, N., Ahmed, A., Al-Muhtaseb, A.H., Dauda, M., Waziri, S.M., Jibril, B.Y., 2015. Synthesis of gamma alumina from Kankara kaolin using a novel technique. Applied Clay Science 105–106, 170–177.

Salas, R., 1987. El Malm y el Cretaci inferior entre el Massis de Garrafi la Serra d'Espada. Ph.D. Thesis, University of Barcelona, Spain, 345p.

Salas, R., Guimerà, J., Mas, R., Martín-Closas, C., Meléndez, A. y Alonso, A., 2001. Evolution of the Mesozoic central Iberian Rift System and its Cainozoic inversion (Iberian chain). Peri-Tethys Memoir 6, 145–185.

Salas, R., Vaquer, R., Travé, A., 2004. Bauxitas karsticas y arcillas lateríticas de la Cadena Ibérica oriental y la Cadena Costera Catalana: relaciones genéticas y áreas de procedencia. Geo-Temas 6(2), 123–126.

Samain, L., Jaworski, A., Edén, M., Ladd, D.M., Seo, D.K., Garcia-Carcia, F.J., Häussermann, U., 2014. Structural analysis of highly porous γ-Al2O3. Journal of Solid State Chemistry 217, 1–8.

Sandiford, M., Neall, F.B., Powell, R., 1987. Metamorphic evolution of aluminous granulites from Labwor Hills, Uganda. Contributions to Mineralogy and Petrology 95, 217–225.

Savin, S.M., Epstein, S., 1970. The oxygen and hydrogen isotope geochemistry of clay minerals. Geochimica et Cosmochimica Acta 34, 25–42.

Savin, S.M., Hsieh, J.C.C., 1998. The hydrogen and oxygen isotope geochemistry of pedogenic clay minerals: Principles and theoretical background. Geoderma, 82(1–3), 227–253.

Sayed, E., Youssef, A.A., 1996. Sedimentaological studies on the central Wadi Kalabsha kaolin deposits, Southwest of Aswan, Egypy. Journal of mineralogy, petrology and economic geology 91, 353–363.

Schaetzl, R., Thompson, M.L., 2015. Soils: Genesis and Geomorphology. Cambridge, pp. 779.

Schellmann, W., 1981. Considerations on the definition and classification of laterites. Proceedings of the International Seminar on Lateritisation Processes, Trivandrum, India. A.A. Balkema, Rotterdam, pp. 1–10.

Schellmann, W., 1994. Geochemical differentiation in laterite and bauxite formation. Catena 21, 131–143.

Schneider, H., Schreuer, J., Hildmann, B., 2008. Structure and properties of mullite e a review. Journal of the European Ceramic Society 28, 329–344.

Schultz L.G., 1964. Quantitative interpretation of mineralogical composition from X-ray and chemical data for the Pierre shale. USGS Professional Paper 391-C, 1–131.

Schwartz, K.B., Leong, D.B., McConville, R.L., 1994. Structural chemistry of synthetic cordierite: Evidence for solid solutions and disordered compositional domains in Bi-flux-grown Mg-cordierites. Physics and Chemistry of Minerals 20, 563–574.

Scotese, C., Song, H., Mills, B.J.W., Van der Meer, D.G., 2021. Phanerozoic paleotemperatures: The earth's changing climate during the last 540 million years. Earth-Science Reviews 215, 103503.

Segal, F.M., Correa, M.F., Bacani, R., Castanheira, B., Politi, M.J., Brochsztain, S., Triboni, E.R., 2018. A Novel Synthesis Route of Mesoporous γ-Alumina from Polyoxohydroxide Aluminum. Materials Research 21(1), e20170674.

Semiz, B., Çelik, S.B., 2020. Mineralogical and geochemical characteristics of Belevi clay deposits at Denizli, SW Turkey: industrial raw material potential. Arabian Journal of Geosciences 13(8), 1–12.

Seranne, M., Marchand, E., Bruguier, O., Husson, E., Vinches, M., 2019. New U-Pb zircon-dating constraints on the age and origin of allochthonous bauxite deposits of Languedoc (southern France): geodynamic consequences. Geophysical Research Abstracts. 21 EGU General Assembly 2019.

Sheldon, N.D., Tabor, N.J., 2009. Quantitative paleoenvironmental and paleoclimatic reconstruction using paleosols. Earth-Science Reviews 95(1–2), 1–52.

Sheppard, S.M.F., 1977. The Cornubian batholith, SW England: D/H and 18O/16O studies of kaolinite and other alteration minerals. Journal of the Geological Society 133, 573–591.

Sheppard, S.M.F., Gilg, H.A., 1996. Stable isotope geochemistry of clay minerals. Clay Minerals 31, 1–24.

Singh, B., Gilkes, R.J., 1991. A potassium-rich beidellite from a laterite pallid zone in western Australia. Clay Minerals 26, 233–244.

Sinha, A., Singh, V.K., 2005. Spontaneous Coal Seam Fires: A Global Phenomenon. En: Voigt, S., Rüter, H., Jiahong, L., Jayakumar, R., (Eds.), International Research for

Sustainable Control and Management. Vol 4: Spontaneous Coal Seam Fires: Mitigating a Global Disaster. Beijing, P.R. China, pp. 42–66.

Smith, D.K., Johnson, G.G. Jr., 2000. Digitized database quantification, DDBQ, analysis of complex mixtures using fully digitized patterns. Advances in X-ray Analysis 42, 276–286.

Smith, M.A. and Glasser, D., 2005. Spontaneous combustion of carbonaceous stockpiles. PartI. The relativeimportance of various intrinsiccoalproperties and properties of the reaction system. Fuel 84, 1151-1160.

Smith. D.G.W., 1965. The chemistry and mineralogy of some emery-like rocks from Sithean Sluaigh, Strachur, Argyllshire. The American Mineralogist 50, 1982–2022.

Sokol, E., Volkova, N., Lepezin, G., 1998. Mineralogy of pyrometamorphic rocks associated with naturally burned coal-bearing spoil-heaps of the Chelyabinsk coal basin, Russia. European Journal of Mineralogy 10, 1003–1014.

Stadermann, F.J., Croat, T.K., Bernatowicz, T.J., Amari, S., Messenger, S., Walker, R.M., Zinner, E., 2005. Supernova graphite in the NanoSIMS: Carbon, oxygen and titanium isotopic compositions of a spherule and its TiC sub-components. Geochimica et Cosmochimica Acta 69, 177–188.

Steuber, T., Rauch, M., Masse, J.P., Graaf, J., Malkoc, M., 2005. Low-latitude seasonality of Cretaceous temperatures in warm and cold episodes. Nature 437(27), 1341–1344.

Stoddar, E.F., 1979. Zinc-rich hercynite in high-grade metamorphic rocks: a product of the dehydration of staurolite. American Mineralogist 64, 736–741.

Štubňa, I., Húlan, T., Kaljuvee, T., Vozár, L., 2018. Investigation of dynamic mechanical properties of Estonian clay Arumetsa during firing. Applied Clay Science 153, 23–28.

Subirana, M.A., Paton, L., Hall, J., Brownlow, A., Krupp, E.M., Feldmann, J., Schaumlöffel, D., 2021. Development of Mercury Analysis by NanoSIMS for the Localization of Mercury−Selenium Particles in Whale Liver. Analitical Chemistry 93, 12733–12739.

Sun, Y., Zhu, X., Han, Y., Li, Y., Gao, P., 2020. Iron recovery from refractory limonite ore using suspension magnetization roasting: A pilot-scale study. Journal of Cleaner Production 261, 121221.

Szamatek, K., Barczuk, A., Youssed, E.A.A., 1993. Genesis and mineralogy of lateritic kaolin at Aswan area (Sw Egypt). Archiwum Mineralogicze (Warsaw) 2, 81–97.

T

Tabor, N. J., 2007. Permo-Pennsylvanian palaeotemperatures from Fe-Oxide and phyllosilicate δ18O values. Earth and Planetary Science Letters, 253(1–2), 159–171.

Tabor, N.J., Montanez, I.P., Southard, R.J. 2002. Paleoenvironmental reconstruction from chemical and isotopic compositions of Permo-Pennsylvanian pedogenic minerals. Geochimica et Cosmochimica Acta 66(17), 3093–3107.

Tabor, N.J., Myers, T.S., 2015. Palaeosols as Indicators of Paleoenvironment and Paleoclimate. Annual Review of Earth and Planetary Sciences 43, 33–61.

Tabor, N.J., Myers, T.S., Michel, L.A., 2017. Sedimentologist's Guide for Recognition, Description, and Classification of Paleosols. En: Zeigler, K.E., Parker, W.G. (EDS), Terrestrial Depositional Systems: Deciphering Complexities through Multiple Stratigraphic Methods. Elsevier, pp. 165–208.

Tan, W., Yan Wang, C., He, H., Xing, C., Liang, X., Dong, H., 2015. Magnetite-rutile symplectite derived from ilmenite-hematite solid solution in the Xinjie Fe-Ti oxide-bearing, mafic-ultramafic layered intrusion (SW China). American Mineralogist 100, 2348–2351.

Taylor, G., Eggleton, R.A., Foster, L.D., Tilley, D.B. Le Gleuher, M., Morgan, C.M. 2008. Nature of the Weipa Bauxite deposit, northern Australia. Australian Journal of Earth Science 55, 45–70.

Thiry, M., 2000. Palaeoclimatic interpretation of clay minerals in marine deposits: an outlook from the continental origin. Earth Science Reviews. 49, 201–221.

Thomen, A., Robert, F., Remusat, L., 2014. Determination of the nitrogen abundance in organic materials by NanoSIMS quantitative imaging. Journal of Analytical Atomic Spectrometry 29, 512–519.

Török, K. (2002). Multiple fluid migration events in the Sopron Gneisses during the Alpine high-pressure metamorphism, as recorded by bulk-rock and mineral chemistry and fluid inclusions. Neues Jahrbuch für Mineralogie-Abhandlungen, 1-36.

Treiman, A.H., 1985. Amphibole and hercynite spinel in Shergotty and Zagami: Magmatic water, depth of crystallization, and metasomatism. Meteoritics 20, 229–243.

Trindade, M.J., Dias, M.I., Coroado, J., Rocha, F., 2009. Mineralogical transformations of calcareous rich clays with firing: A comparative study between calcite and dolomite rich clays from Algarve, Portugal. Applied Clay Science 42(3–4), 345–355.

U

Usov, I.O., Suvorova, A.A., Sokolov, V.V., Kudryavtsev, Y.A., 1999. Transient enhanced diffusion of aluminum in SiC during high temperature ion implantation. Journal of Applied Physics 86, 6039–6042.

Utescher, T., Mosbrugger, V., Ashraf, A.R., 2000. Terrestrial climate evolution in northwest Germany over the last 25 million years. Palaios, 15(5), 430–449.

V

Valeton, J., 1972. Bauxites, Elsevier, Amsterdam, 226 pp.

Van Wees, J.D., Arche, A., Beijdorff, C.G., López-Gómez, J., 1998. Temporal and spatial variations in tectonic subsidence in the Iberian Basin (eastern Spain): inferences from automated forward modelling of high-resolution stratigraphy (Permian–Mesozoic). Tectonophysics 300, 285–310.

Varela, A.N., Raigemborn, M.S., Richiano, S., White, T., Poiré, D.G., Lizzoli, S., 2018. Late Cretaceous paleosols as paleoclimate proxies of high-latitude Southern Hemisphere: Mata Amarilla Formation, Patagonia, Argentina. Sedimentary Geology 363, 83–95.

Velasco, F., Herrero, J.M., Suárez, S., Yusta, I., Alvaro, A., Tornos, F., 2013. Supergene features and evolution of gossans capping massive sulphide deposits in the Iberian Pyrite Belt. Ore Geology Reviews 53, 181–203.

Velde, B., 1992. Introduction to Clay Minerals: Chemistry, origins uses and environmental significance. Springer, London, pp. 198.

Velde, B., 1995. Origin and Mineralogy of Clays. Clays and the Environment. Springer-Verlag, Berlin. Heidelberg New York, pp. 334.

Vidal, A., Lenhart, T., Dignac, M.F., Biron, P., Höschen, C., Barthod, J., Vedere, C., Vaury, V., Bariac, T., Rumpel, C., 2020. Promoting plant growth and carbon transfer to soil with organic amendments produced with mineral additives. Geoderma. 374, 114454.

Vogel, C., Mueller, C.W., Höschen, C., Buegger, F., Heister, K., Schulz, S., Schloter, M., Kögel-Knabner, I., 2014. Submicron structures provide preferential spots for carbon and nitrogen sequestration in soils. Nature Communications 5, 1–7.

W

Wacey, D., Kilburn, M.R., Mcloughlin, N., Parnell, J., Stoakes, C.A., Grovenor, C.R.M. and Brasier, M.D., 2008. Use of NanoSIMS in the search for early life on Earth: ambient inclusion trails in a c. 3400 Ma sandstone. Journal of the Geological Society 165, 43–53.

Wang, C., Adriaens, R., Hong, H., Elsen, J., Vandenberghe, N., Lourens, L.J., Gingerich, P.D., Abels, H.A., 2017. Clay mineralogical constraints on weathering in response to early Eocene hyperthermal events in the Bighorn Basin, Wyoming (Western Interior, USA). Bulletin of the Geological Society of America 129(7–8), 997–1011.

Wang, C., Feng, Z., Zhang, L., Huang, Y., Cao, K., Wang, P., Zhao, B., 2013. Cretaceous paleogeography and paleoclimate and the setting of SKI borehole sites in Songliao Basin, northeast China. Palaeogeography, Palaeoclimatology, Palaeoecology, 385, 17–30.

Wattanasiriwech, D., Saiton, A., Wattanasiriwech, S., 2009. Paving blocks from ceramic tile production waste. Journal of Cleaner Production 17(18), 1663–1668.

Weaver, C.E, 1989. Clays, muds and shales. Springer, pp. 818

White, A.F., Brantley, S.L., 2003. The effect of time on the weathering of silicate minerals: why do weathering rates differ in the laboratory and field?. Chemical Geology 202, 479–506.

Wilson, M.J., 1999. The origin and formation of clay minerals in soils: past, present and future perspectives. Clay minerals 34(1), 7-25.

Won, C., Hong, H., Cheng, F., Fang, Q., Wang, C., Zhao, L., Churchman, G.J., 2018. Clay mineralogy and its palaeoclimatic significance in the Luochuan loess-palaeosols over ~1.3 Ma, Shaanxi, northwestern China. Frontiers of Earth Science 12(1), 134–147.

Worden, R.H., Droop, G.T.R., Champness, P.E., 1992. The influence of crystallography and kinetics on phengite breakdown reactions in a low-pressure metamorphic aureole. Contributions to Mineralogy and Petrology 110, 329–345.

Wright, V.P., Taylor, K.G., Beck, V.H., 2000. The paleohydrology of Lower Cretaceous seasonal wetlands, Isle of Wight, Southern England. Journal of Sedimentary Research 70, 619-632.

X

Xu, Y.L.; Wang, L.Y.; Tian, N.; Zhang, J.P.; Yu, M.G.; Delichatsios, M.A., 2017. Spontaneous combustion coal parameters for the Crossing-Point Temperature (CPT) method in a Temperature-Programmed System (TPS). Fire Safety Journal 91, 147-157.

Y

Yang, F., Li, C., Lin, Y., Wang, C-A., 2012. Effects of sintering temperature on properties of porous mullite/corundum ceramics, Materials Letters 73, 36–39.

Yuste, A., Bauluz, B., Mayayo, M.J., 2015. Genesis and mineral transformations in Lower Cretaceous karst bauxites (NE Spain): Climatic influence and superimposed processes. Geological Journal 50(6), 839–857.

Yuste, A., Bauluz, B., Mayayo, M.J., 2017. Origin and geochemical evolution from ferrallitized Clays to karst bauxite: An example from the Lower Cretaceous of NE Spain. Ore Geology Reviews 84, 67–69.

Yuste, A., Camacho, I., Bauluz, B., Mayayo, M.J., Laita, E., 2020. Palaeoweathering events recorded on siliciclastic continental deposits (Albian, Lower Cretaceous) in NE Spain. Applied Clay Science 190, 105598.

Z

Zhao, X.; Wang, Q.; Xiao, H.; Mao, Z.; Chen, P.; Sun, J., 2013. Prediction of coal stockpile autoignition delay time using micro-calorimeter technique. Fuel Processing Technology 110, 86-93.

Zake-Tiluga, I., Svinka, R., Svinka, V., 2014. Highly porous corundum–mullite ceramics – Structure and properties. Ceramics International 40, 3071–3077.

Zawrah, M.F.M., Khalil, N.M., 2001. Effect of mullite formation on properties of refractory castables. Ceramics International 27, 689–694.

ANNEX I: Factor de impacto y áreas temáticas de las publicaciones

De acuerdo con el Reglamento de Tesis Doctorales de la Universidad de Zaragoza, en este anexo se indica el factor de impacto y área temática correspondiente de las revistas en las que se incluyen las publicaciones que se recogen en esta tesis (todas ellas indexadas en el JCR), así como la contribución de la estudiante de doctorado al tratarse de trabajos realizados en coautoría.

- **Laita, E.**, Bauluz, B., Yuste, A., 2019. High-Temperature Mineral Phases Generated in Natural Clinkers by Spontaneous Combustion of Coal. Minerals 9(4), 213. https://doi.org/10.3390/min9040213
  Minerals, Factor de Impacto (JCR) en 2019: 2,380
  Q2 en el área temática *Mineralogy*
  Q2 en el área temática *Mining & Mineral Processing*
  Contribución de la estudiante de doctorado: revisión bibliográfica; estudio de difracción de rayos X, microscopio óptico y microscopio electrónico de barrido; análisis, interpretación y discusión de los resultados; redacción del trabajo; elaboración de imágenes y revisiones durante el proceso de envío.
- **Laita, E.,** Bauluz, B., Aurell, M., Bádenas, B., Canudo, J. I., Yuste, A., 2020. A change from warm/humid to cold/dry climate conditions recorded in lower Barremian clay-dominated continental successions from the SE Iberian Chain (NE Spain). Sedimentary Geology 403, 105673. https://doi.org/10.1016/j.sedgeo.2020.105673
  Sedimentary Geology, Factor de Impacto (JCR) en 2020: 3,397
  Q1 en el área temática *Geology*
  Contribución de la estudiante de doctorado: revisión bibliográfica; trabajo de campo y toma de muestras; estudio de difracción de rayos X, microscopio óptico y microscopio electrónico de barrido; análisis, interpretación y discusión de los resultados; redacción del trabajo; elaboración de imágenes y revisiones durante el proceso de envío.
- **Laita, E.,** Bauluz, B., Mayayo, M. J., Yuste, A., 2021. Mineral and textural transformations in mixtures of Al-rich and Al–K-rich clays with firing: Refractory potential of the fired products. Ceramics International 47(10), 14527–14539. https://doi.org/10.1016/j.ceramint.2021.02.032
  Ceramics International, Factor de Impacto (JCR) en 2021: 5,532
  Q1 en el área temática *Materials Science, Ceramics*
  Contribución de la estudiante de doctorado: revisión bibliográfica; toma de muestras, elaboración de las mezclas y cocción de las probetas; estudio de difracción de rayos X, fluorescencia de rayo X, microscopio óptico y microscopio electrónico

de barrido; estudio de las propiedades físicas (densidad, contracción lineal, porosidad, color, absorción de agua, resistencia a la carga puntual y conductividad térmica); análisis, interpretación y discusión de los resultados; redacción del trabajo; elaboración de imágenes y revisiones durante el proceso de envío.

- **Laita, E.,** Bauluz, B., Aurell, M., Bádenas, B., Yuste, A., 2022. Weathering events recorded in uppermost Hauterivian–lower Barremian clay-dominated continental successions from the NW Iberian Range: climatic vs. tectonic controls. Journal of Iberian Geology 48, 45–63. https://doi.org/10.1007/s41513-021-00181-0
  Journal of Iberian Geology, Factor de Impacto (JCR) en 2021: 1,590
  Q2 en el área temática *Geology*
  Contribución de la estudiante de doctorado: revisión bibliográfica; trabajo de campo y toma de muestras; estudio de difracción de rayos X, microscopio óptico y microscopio electrónico de barrido; análisis, interpretación y discusión de los resultados; redacción del trabajo; elaboración de imágenes y revisiones durante el proceso de envío.

Otras publicaciones relacionadas con la tesis, no incluidas en el compendio, pero en las que también ha participado la estudiante de doctorado son las siguientes:

- **Laita, E.,** Bauluz, B., 2018. Mineral and textural transformations in aluminium-rich clays during ceramic firing. Applied Clay Science 152, 284–294.
  https://doi.org/10.1016/j.clay.2017.11.025
  Applied Clay Science, Factor de Impacto (JCR) en 2018: 3,890
  Q1 en el área temática *Mineralogy*
  Q2 en el área temática *Materials Science, Multidisciplinary*
  Q2 en el área temática *Chemistry, Physical*
  Contribución de la estudiante de doctorado: revisión bibliográfica; estudio de difracción de rayos X, microscopio óptico, microscopio electrónico de barrido y microscopio electrónico de transmisión; análisis, interpretación y discusión de los resultados; redacción del trabajo; elaboración de imágenes y revisiones durante el proceso de envío.
- Yuste, A., Camacho, I., Bauluz, B., Mayayo, M.J., **Laita, E.,** 2020. Palaeoweathering events recorded on siliciclastic continental deposits (Albian, Lower Cretaceous) in NE Spain. Applied Clay Science 190, 105598.
  https://doi.org/10.1016/j.clay.2020.105598
  Applied Clay Science, Factor de Impacto (JCR) en 2020: 5,467
  Q1 en el área temática Mineralogy

Q2 en el área temática Materials Science, Multidisciplinary

Q2 en el área temática Chemistry, Physical

Contribución de la estudiante de doctorado: revisión bibliográfica y redacción del trabajo

- Brlek, M., Gaynor, S. P., Mongelli, G., Bauluz, B., Sinisi, R., Brčić, V., Peytcheva, I., Mišur, I., Tapster, S., Trinajstić, N., **Laita, E.,** Yuste, A. Šuica, S., Grizelj, A., Kukoč, D., Schaltegger, U., 2021. Karst bauxite formation during Miocene Climatic Optimum (central Dalmatia, Croatia): mineralogical, compositional and geochronological perspectives. International Journal of Earth Sciences, 110(8), 2899–2922. https://doi.org/10.1007/s00531-021-02091-z

  International Journal of Earth Sciences, Factor de Impacto (JCR) en 2021: 2,698

  Q3 en el área temática *Geosciences, Multidisciplinary*

  Contribución de la estudiante de doctorado: estudio de microscopio electrónico de barrido, interpretación y discusión de los resultados; redacción del trabajo; elaboración de imágenes.

- Aurell, M., Bádenas, B., Castanera, D., Gasca, J. M., Canudo, J. I., **Laita, E.,** Liesa, C. L., 2021. Latest Jurassic–Early Cretaceous synrift evolution of the Torrelapaja Subbasin (Cameros Basin): implications for Northeast Iberia palaeogeography. Cretaceous Research 128, 104997 https://doi.org/10.1016/j.cretres.2021.104997

  Cretaceous Research, Factor de Impacto (JCR) en 2021: 2,432

  Q2 en el área temática *Geology*

  Q1 en el área temática *Paleontology*

- Bauluz, B., Mayayo, M. J., **Laita, E.,** Yuste, A., 2021. Micro- and nanotexture and genesis of ball clays in the lower cretaceous (SE Iberian Range, NE Spain). Minerals 11(12), 1339 https://doi.org/10.3390/min11121339

  Minerals, Factor de Impacto (JCR) en 2021: 2,818

  Q2 en el área temática *Mineralogy*

  Q2 en el área temática *Mining & Mineral Processing*

  Q2 en el área temática *Geochemistry & Geophysics*

  Contribución de la estudiante de doctorado: revisión bibliográfica y redacción del trabajo

ANNEX II

Sedimentary Geology 403 (2020) 105673

Contents lists available at ScienceDirect

Sedimentary Geology

journal homepage: www.elsevier.com/locate/sedgeo

A change from warm/humid to cold/dry climate conditions recorded in lower Barremian clay-dominated continental successions from the SE Iberian Chain (NE Spain)

Elisa Laita *, Blanca Bauluz, Marcos Aurell, Beatriz Bádenas, José Ignacio Canudo, Alfonso Yuste

IUCA-Department of Earth Sciences, Faculty of Sciences, Universidad de Zaragoza, Pedro Cerbuna 12, 50009 Zaragoza, Spain

ARTICLE INFO

Article history:
Received 18 February 2020
Received in revised form 14 April 2020
Accepted 15 April 2020
Available online 21 April 2020

Editor: Dr. Brian Jones

Keywords:
Palaeosols
Palaeoclimate
Pisoids
Kaolinite
Weathering

ABSTRACT

A combined facies and clay mineralogy analysis of the continental succession recorded in the lower part of the Blesa Formation (early Barremian, Oliete subbasin, NE Spain) allowed us to specify the palaeoclimatic and palaeoenvironmental conditions under which this sedimentary record originated. Six outcrops including clays, clays/marls and dm-thick interbedded palustrine-lacustrine limestone levels were logged and sampled for X-ray diffraction and optical and electron microscopy analysis. The lower levels consist of red clays with abundant ferruginous pisoids (1–5 mm in size) and macropisoids (>5 mm), whereas the intermediate and upper levels are ochre and violet clays/marls with few or no pisoids. The pisoids normally consist of a nucleus and a cortex made up of several layers. Some pisoids have a fragment of a previous pisoid acting as a nucleus, indicating local reworking processes. Both the nucleus and the cortex are formed by hematite, goethite, variable contents of kaolinite, and minor proportions of ilmenite. Their texture and mineralogy show an *in-situ* growth. Interbedded limestone beds within the clay- and clay/marl-dominated levels are formed by micrite, microsparite and sparite. These limestones are cemented by kaolinite and they also have pisoids, indicating the occurrence of edaphic processes. The red clays have the lowest calcite content and the highest hematite, anatase, diaspore, goethite and kaolinite content. By contrast, the ochre and violet clays/marls have higher illite content. Smectite is only detected in the ochre clays/marls. This mineral association is characteristic of lateritic palaeosols, formed under warm and humid conditions. Kaolinite and smectite textures indicate that they are authigenic, whereas illite may be of detrital origin. The upward decrease in kaolinite, hematite, anatase, diaspore and goethite content, along with the increase in quartz content and the presence of smectite and illite, reflect a change from warm and humid conditions to drier and colder conditions during the early Barremian in the studied area.

1. Introduction

The study of both facies and clay mineralogy in sedimentary successions is of great interest in allowing palaeoclimatic and palaeoenvironmental conditions to be inferred (Chamley, 1989; Velde, 1995; Thiry, 2000). In Mesozoic and Cenozoic sequences of continental materials, which include palaeosol developments, the variations in clay mineral assemblages have been widely used as palaeoclimatic and palaeoenvironmental proxies (*e.g.* Ehrmann et al., 2005; Raucskik and Varga, 2008; Do Campo et al., 2010; Bauluz et al., 2014; Do Campo et al., 2018 and references therein). Notably, palaeosols are formed in direct contact with the atmosphere, and thus clay minerals formed during their development can be correlated with climatic and palaeoenvironmental factors such as temperature, water availability during pedogenesis and vegetation cover, which control chemical weathering (Sheldon and Tabor, 2009; Varela et al., 2018).

Physical weathering processes predominate in dry and cold climates, and palaeosols that form under these conditions contain mineral assemblages dominated by illite and/or chlorite (Chamley, 1989). In contrast, intense hydrolysis processes take place under humid subtropical to tropical climates, giving rise to the formation of laterites, lateritic clays, and bauxites, where kaolinite is the main clay mineral (Chamley, 1989; Righi and Meunier, 1995). On the other hand, chemical weathering is less intense under warm climates with alternating humid and dry seasons, and in these cases smectite is formed (Buurman et al., 1988; Güven, 1988; Chamley, 1989; Murakami et al., 1996).

In NW Europe, a warm and humid climate was recorded during the early Barremian (Wright et al., 2000), which is also evidenced by the presence of ferruginous palaeosols and bauxites (Bárdossy, 1982). By contrast, an alternation of wet and dry seasons has been described during this period in the west of Europe (Haywood et al., 2004).

* Corresponding author at: IUCA-Department of Earth Sciences, Faculty of Sciences, Universidad de Zaragoza, Pedro Cerbuna 12, 50009 Zaragoza, Spain.
E-mail address: laita@unizar.es (E. Laita).

https://doi.org/10.1016/j.sedgeo.2020.105673
0037-0738/

In the Iberian Range (NE Spain), a seasonal subtropical climate has been described during the Lower Cretaceous (Buscalioni and Fregenal-Martínez, 2010). Previous researchers pointed out the presence of Barremian kaolinite-rich clays, bauxite deposits and lateritic clays in this area (Combes, 1969; Molina and Salas, 1993; Bauluz et al., 2014; Yuste et al., 2015; Yuste et al., 2017), which is also consistent with relatively warm and humid conditions.

The link of clay mineral assemblages with the palaeoclimate-palaeoenvironment is not always straightforward. Clay-rich rocks and palaeosols frequently include not only authigenic clay minerals, but also others that formed during diagenetic processes. These processes could transform the clay minerals initially formed and therefore alter the palaeoclimatic-palaeoenvironmental signal (Dera et al., 2009; Bauluz et al., 2014). For this reason, it is necessary to conduct textural studies to assess possible diagenetic modifications in clay minerals before using them as palaeoclimatic indicators.

In this work, the use of X-ray diffraction and optical and electron microscopy to undertake a sedimentological, mineralogical and textural characterization of clay-rich outcrops present in the early Barremian (Lower Cretaceous) continental successions of the Oliete subbasin (Maestrazgo Basin; NE Spain) allowed us: 1) to characterize sedimentary (*in-situ vs.* detrital) and diagenetic minerals; 2) to establish the variation in *in-situ* clay mineral assemblages and the palaeoenvironmental conditions under which they were formed; 3) to link the vertical trends of *in-situ* clay mineral assemblages with variations in the formation conditions, in particular temperature/humidity.

2. Geological setting

The opening of the Atlantic Ocean along with the westward spread of the Tethys Ocean during the Late Jurassic-Early Cretaceous generated rifting processes in the eastern part of the Iberian Plate. During this active rifting period, extensional fault activity resulted in the progressive structural compartmentalization of the wide marine carbonate platforms that had previously developed during the Jurassic. All this resulted in the generation of independent subsiding rift-related sedimentary basins and subbasins, such as the Maestrazgo Basin in the eastern part of the Iberian Plate (*e.g.*, Van Wees et al., 1998; Salas et al., 2001; Aurell et al., 2019).

The subbasin under study, the Oliete subbasin, is located in the northwestern marginal area of the Maestrazgo Basin (Fig. 1). The lower synrift sedimentary unit of the Oliete subbasin is the Blesa Formation, which reaches a thickness of up to 150 m (Canérot et al., 1982). This formation is divided into three genetic stratigraphic sequences: the lower Blesa (LBS), middle Blesa (MBS) and upper Blesa (UBS) sequences (Aurell et al., 2018). These authors describe the LBS as consisting of distal alluvial to palustrine marls/clays and palustrine-lacustrine limestones upwards and including clay-rich materials in its lowermost part; these are the materials studied in the present work. The MBS is formed by oyster-rich limestones and marls grading upwards and landwards to distal alluvial and palustrine-lacustrine marls/clays and limestones. Finally, the UBS contains distal alluvial red clays in its lowermost part and palustrine and lacustrine carbonates and marls/clays towards the top (Aurell et al., 2018). The Barremian age of the Blesa Formation is well-constrained by the presence of charophytes in the palustrine–lacustrine marly and limestone facies found in the LBS and UPS (Canudo et al., 2010; Moreno-Azanza et al., 2014).

The lower part of the LBS studied here contains red to ochre and violet-ochre marls/clays of very variable thickness (0–60 m thick) at subbasin scale and local intercalations of carbonate-rich beds with root traces, charophytes and vertebrate fossils (Aurell et al., 2018 and references therein). Of particular interest for this work is the presence of dominant red clays in the lowermost part of the LBS, including ferruginous pisoids, thus indicating soil development at the onset of the

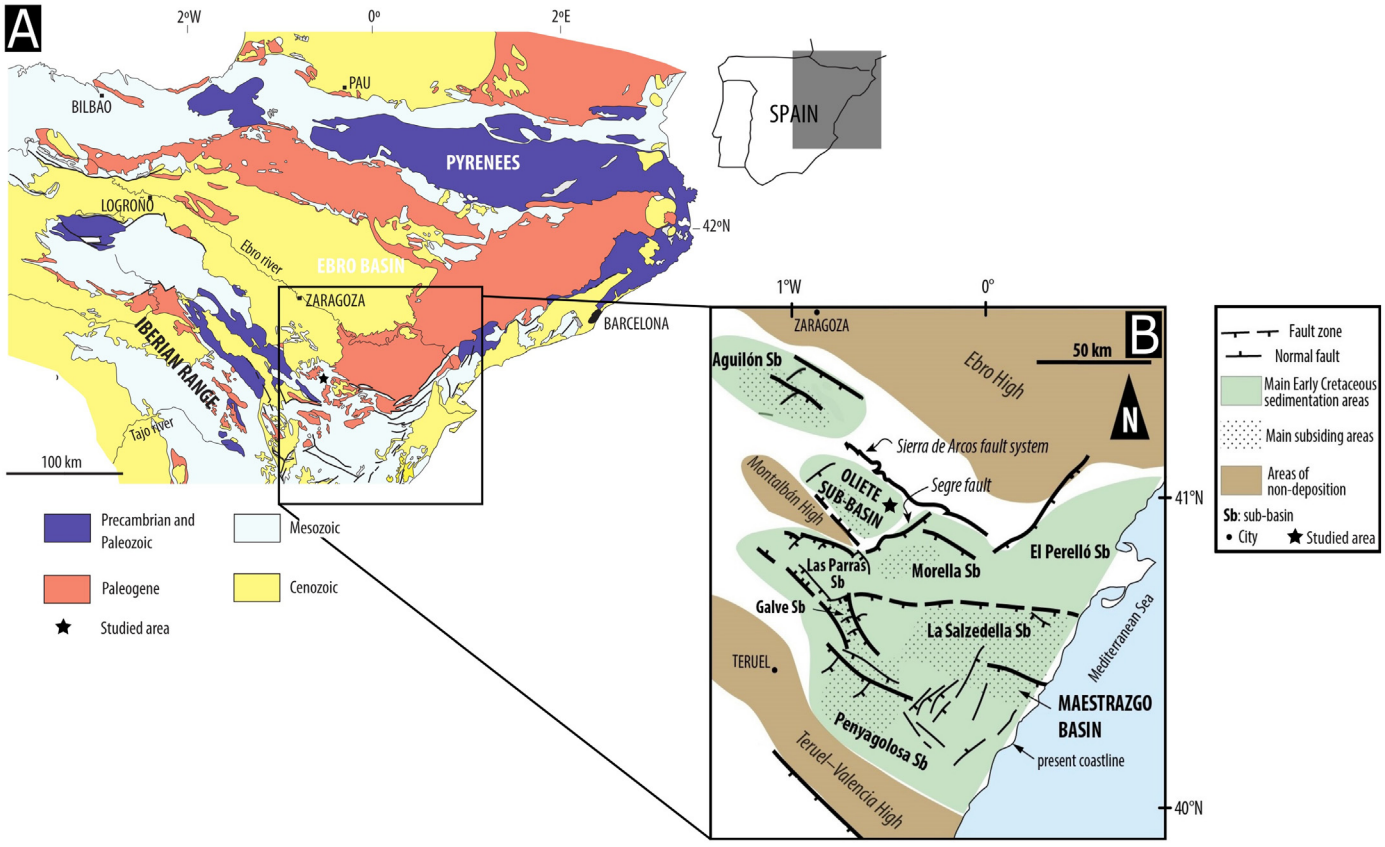

Fig. 1. (A) Simplified geological map of the NE Iberian Peninsula (B) Palaeogeographical reconstruction of the main Early Cretaceous sedimentation areas in NE Iberia, including the studied Oliete subbasin within the Maestrazgo Basin (from Aurell et al., 2018).

sedimentation of the Blesa Formation. The tectono-sedimentary evolution at this initial development stage of the Oliete subbasin has been documented in Aurell et al. (2018). According to these authors, there was a period of subaerial exposure and erosion after the Jurassic marine carbonate sedimentation, which encompassed most of the Tithonian–Hauterivian, and normal faulting involved the overall tilting of the Jurassic limestones, which resulted in higher uplift and erosion of the areas located to the SW. In these areas only the lowermost Jurassic units are preserved from erosion (see the Montalbán Anticline in Fig. 2A), whereas a more complete Upper Jurassic succession is preserved in the NE domains (see the Alacón area in Fig. 2A). The angular erosive unconformity (Fig. 2C–E) over the tilted Jurassic limestones is linked to a palaeokarst surface, which includes dissolution–precipitation meteoric features. The clay/marl-dominated succession of the lower part of the LBS studied here covers this palaeokarst (Fig. 2C, E). The main areas of clay-rich deposits with ferruginous pisoids within the Oliete subbasin are located in the northern (around Alacón) and southern regions (between the villages of Josa and Estercuel) (Fig. 2A). Further tectonic reactivation during the early Barremian gave rise to the development of an orthogonal system of NW–SE and NE–SW trending normal faults (Fig. 2B), which enabled the spreading of the distal alluvial and palustrine-shallow lacustrine sedimentation that characterizes most of the LBS (Aurell et al., 2018).

3. Methods

3.1. Logging and sampling

Six outcrops of the lower part of the LBS in the northern and southern areas of the Oliete subbasin were selected for logging and sampling (Fig. 2A). Logs ALC1, ALC2, ALC3 and VE are located to the north of the locality of Alacón, whereas logs JO and EST are found to the south of the towns of Josa and Estercuel, respectively.

The logged sections include different levels of red clays with pisoids, ochre or violet clays/marls with few or no pisoids, and a few intercalated palustrine-lacustrine limestone beds. Thickness, lithology, colour, texture and stratification were studied bed-by-bed, and a total of 47 samples of clays and clays/marls, palustrine-lacustrine limestones and ferruginous pisoids were taken for further analyses of texture and mineralogical composition in the laboratory (Table 1).

3.2. X-ray diffraction

The mineralogical composition of 47 samples was determined by X-ray diffraction (XRD). The <2 μm fractions of clay and clay/marl samples (n = 33) were also analysed (Table 1). These fractions were concentrated by centrifugation and analysed on both air-dried and ethylene-glycol-treated oriented aggregates, following the procedure described by Bauluz et al. (2014). The diffraction patterns were obtained using a Philips 1710 diffractometer at the University of Zaragoza (Zaragoza, Spain), with 40 kV voltage, 30 mA current, CuKα radiation, automatic slit, and a graphite monochromator. The XRD patterns were acquired from 3 to 60° 2θ and 3 to 30° 2θ for whole samples and < 2 μm fractions, respectively. The analyses were performed using the XPowderX software (Martin, 2017).

After determining the mineralogy of the samples, relative proportions of the mineral phases were acquired using Reference Intensity Ratio (RIR) values from Schultz (1964), Biscaye (1965) and Smith and Johnson Jr. (2000). The RIR values were calculated according to Hillier (2003). In addition, the full width at half maximum (FWHM) of the 001 reflections of kaolinite in both air-dried and ethylene-glycol-treated oriented aggregates was measured in order to determine kaolinite crystallinity.

3.3. Optical and electron microscopy

Twenty-one thin sections of clays and clays/marls, palustrine-lacustrine limestones and ferruginous pisoids (coated with a thin layer of epoxy resin) were studied by both transmitted and reflected light microscopy in order to identify transparent and opaque minerals as well as to characterize their texture (Table 1). The description of the ferruginous particles was made following the terms given by Bárdossy (1982): macropisoids (>5 mm), pisoids (1–5 mm), ooids (100 mm–1000 μm) and micro-ooids (<100 μm).

Seventeen thin sections were studied using a Carl Zeiss Merlin field emission scanning electron microscope (FESEM) equipped with an Oxford energy-dispersive X-ray (EDS) detector at the University of Zaragoza (Zaragoza, Spain) (Table 1). For this, the thin sections were previously carbon-coated. Compositional images of the samples were obtained using two types of backscattered electron detectors: angular selective (AsB) and energy selective (EsB). The accelerating voltage used for the former and for the EDS was 15 kV with a beam current of 400 pA. For the latter, the accelerating voltage was 4 kV with a beam current of 2.0 nA. In addition, morphological images were obtained from fragments of the rocks using a secondary electron detector (Inlens). In this case, the accelerating voltage was 5 kV with a beam current of 800 pA.

Semi-quantitative analyses were carried out using the EDS detector, which has a detection limit of 0.1%. From these analyses, clay mineral formulas were calculated in order to compare them with the theoretical compositions. The kaolinite formula was calculated on the basis of $O_5(OH)_4$, and the smectite and illite-type-phase formulas were calculated on the basis of $O_{10}(OH)_2$.

4. Results

4.1. Stratigraphy and facies distribution

4.1.1. Northern area

In the Alacón area (logs ALC1, ALC2, ALC3 and VE), the lower part of the LBS has a very variable thickness ranging from 3 to 23 m (Fig. 3A–C). Within individual logs there is a vertical distribution of facies from red clays with variable pisoid content to ochre clays/marls with few pisoids, and to violet clays/marls without pisoids. In addition, a dm- to m-thick fibrous-radial nodular calcite bed and limestone beds are also recognized in the lower part of the successions, intercalated in the red clays.

Log correlation indicates that the number and thickness of clayey and limestone levels vary among the outcrops studied around Alacón (Fig. 3A). The first deposits of the LBS overlying the palaeokarstified Jurassic limestones correspond to a lowermost, 3-m-thick red clay level with fibrous-radial calcite nodules (5–12 cm in diameter) and pisoids, which is only recorded in log ALC2. This level pinches out laterally due to the irregular topography of the underlying palaeokarstified Jurassic limestones. A lower nodular limestone level (0.5 to 2 m thick) with fibrous-radial calcite nodules (5–10 cm in diameter) and some ferruginous pisoids overlies the basal red clay level in ALC2 and the palaeokarstic surface in ALC1, ALC3 and VE.

Upwards, red clay levels with abundant pisoids and intercalated palustrine-lacustrine limestone beds are recognized (Fig. 3A-D). Log correlation indicates variation in the number and thickness of red clay levels. In particular, there are three red clay levels (~1.5 m thick) in logs ALC1 and VE (levels 1 to 3 in Fig. 3A), whereas there is only one level (up to 5 m thick) in log ALC3. The intercalated limestone beds are 0.6 to 2 m in thickness and contain ferruginous pisoids but no fibrous-radial calcite nodules.

Overlying the red clays with interbedded limestones, there is an ochre clay/marl level (4 to 5 m thick) that contains few ferruginous pisoids (level 4 in Fig. 3A), which in turn is overlain by a topmost 1.5 to 2 m-thick violet clay/marl level without pisoids (level 5 in Fig. 3A).

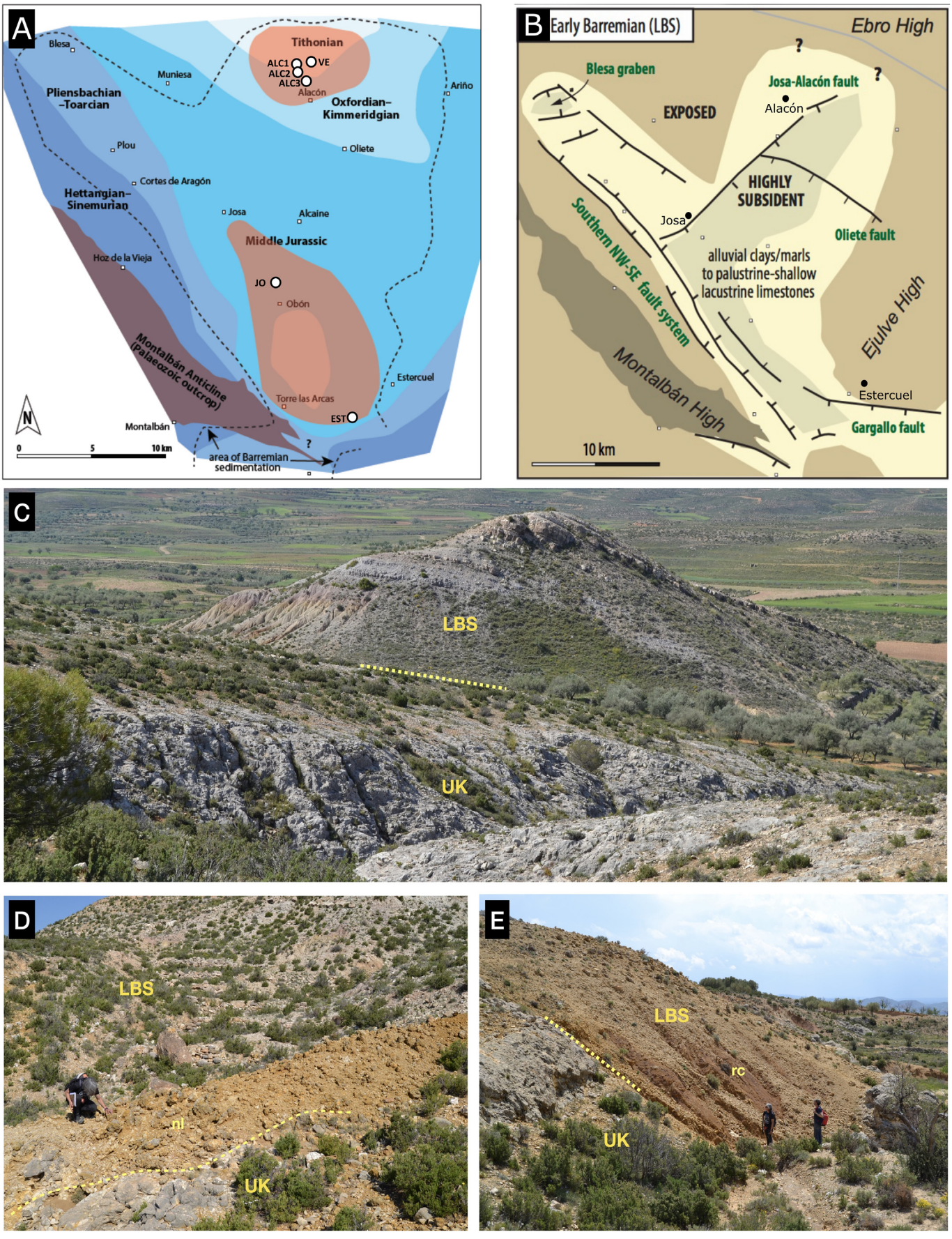
A
Blesa
Muniesa
Pliensbachian
–Toarcian
Tithonian
ALC1
ALC2
ALC3
VE
Alacón
Oxfordian–
Kimmeridgian
Ariño
Plou
Oliete
Cortes de Aragón
Hettangian–
Sinemurian
Josa
Alcaine
Middle Jurassic
Hoz de la Vieja
JO
Obón
Montalbán Anticline
(Palaeozoic outcrop)
Estercuel
Torre las Arcas
EST
N
Montalbán
0
5
10 km
area of Barremian
sedimentation
?
B
Early Barremian (LBS)
Ebro High
?
Blesa graben
Josa-Alacón fault
?
EXPOSED
Alacón
HIGHLY
SUBSIDENT
Josa
Oliete fault
Southern NW-SE fault system
alluvial clays/marls
to palustrine-shallow
lacustrine limestones
Ejulve High
Montalbán High
Estercuel
Gargallo fault
10 km
C
LBS
UK
D
LBS
nl
UK
E
LBS
rc
UK

Table 1
Summary of sample analyses at the laboratory (n = number of samples/analyses).

Field samples (n = 47)	X-ray diffraction (Mineralogical composition)		Optical and electron microscopy (Texture & mineral identification)	
	whole rock (n = 47)	<2 μm fraction of clays & clays/marls (n = 33)	Optical microscopy (n = 21)	Electron microscopy-FESEM/EDS (n = 17)
Red clays- 24	24	24	9	7
Ocher clays/marls- 7	7	7	2	2
Violet clays/marls- 2	2	2	1	1
Ferruginous pisoids- 6	6	–	5	3
Limestones- 8	8	–	4	4
	- Relative proportions of the mineral phases - Kaolinite crystallinity		-Textures -Identification of opaque and transparent minerals	-Micro- and nanotextures -Chemical composition of the phases
			Derived data	

4.1.2. Southern area

The overall thickness of the lower part of the LBS is variable in the southern outcrops logged near Josa (JO, 9 m thick; Fig. 4A) and Estercuel (EST, 36 m thick; Fig. 4B). Successive red clay levels (3 to 6 m thick) overlie the palaeokarstic surface that developed over the Jurassic limestones. These levels contain abundant ferruginous pisoids (with the exception of the last level of red clays of EST). Limestone beds intercalated in these red clays are very scarce. In the EST log, a 0.3-m-thick limestone bed with fibrous-radial calcite nodules and pisoids, similar to that observed in ALC2 and VE, is interbedded between the two red clay levels with abundant pisoids. In the JO log, on top of the red clay there is a 0.3-m-thick palustrine-lacustrine limestone bed with micrite intraclasts and pisoids, but without fibrous-radial calcite nodules.

The successions end with an ochre clay/marl level (2 m thick in JO, 10 m thick in EST) and a 10-m-thick violet clay/marl level in the EST log. Neither the ochre nor the violet levels contain ferruginous pisoids.

4.2. Optical microscopy results

The fine-grained matrix of red clays and ochre and violet clays/marls are formed by clay minerals and oxides that cannot be identified at the resolution of the optical microscope. Occasionally, quartz fragments (10–600 μm) and micron-sized oxides can be recognized (Fig. 5A). Carbonate is observed as micritic nodules (Fig. 5B) or as sparitic crystals cementing the matrix (Fig. 5C). Microsparite carbonate cement is also observed in some samples.

The ferruginous pisoids found in the red clays and ochre clays/marls encompass macropisoids, pisoids and ooids/micro-ooids, following the classification proposed by Bárdossy (1982).

Macropisoids are spherical to ellipsoidal and have a nucleus formed by pisoids (Fig. 6A), ooids and micro-ooids coated by goethite and hematite with botryoidal textures (Fig. 6B, C, D and E), sometimes forming a sequence of alternate layers (25 to 700 μm thick) of both phases (Fig. 6B, D and E). Occasionally, an up to 1–3 mm-thick outer cortex formed by several concentric layers is observed over the nucleus of some macropisoids (Fig. 6D). The concentric layers consist of goethite, as deduced by optical properties under reflected light. Occasional quartz fragments and small rutile crystals are included among the cortex layers.

The pisoids display spherical and occasionally ellipsoidal morphologies. Using the classification of Guerrak (1987), they can be categorized as simple or fragmented. Simple pisoids show a massive nucleus and a cortex with several concentric layers (Fig. 5D), both formed by a mixture of iron oxides and clay minerals with occasional quartz fragments and rutile crystals. Fragmented pisoids have a nucleus formed by a fragment of a pisoid and a cortex with concentric layers similar to that of the simple pisoids (Fig. 5D). Some pisoids (both simple and fragmented) are fractured and partly replaced by sparitic carbonate (Fig. 5C). Broken pisoids are also observed. In addition, scour-and-fill textures, similar to those described by Taylor et al. (2008), are found in the cortex in some pisoids (Fig. 5E).

Ooids and micro-ooids (*sensu* Bárdossy, 1982) are also observed in some clayey levels. The size ranges from 200 to 400 μm for the ooids and from 20 to 100 μm for the micro-ooids. Like the simple pisoids, they present spherical morphologies with a massive nucleus and a cortex with concentric layers and are formed by hematite and goethite (Fig. 5F).

The palustrine-lacustrine limestones are formed mainly by micrite, locally with microsparite and sparite crystals, and they also contain some micritic nodules and intraclasts (1–4 mm in size; Fig. 5H), spherical ferruginous pisoids (1–4 mm) and ferruginous ooids (200–400 μm). Fe-rich pisoids are simple, with a massive nucleus and concentric layers; most of them are fractured and others are partly replaced by micritic and sparitic carbonate (Fig. 5G). Some limestones also contain fossil remains such as disarticulated bivalve shells (Fig. 5H).

4.3. XRD results

XRD patterns of samples of the clays and clays/marls of the ALC1 and EST logs are shown in Fig. 7. The same mineral phases were detected in the samples taken in the rest of the outcrops. The XRD results show that the clays and clays/marls are formed mainly by calcite, quartz, and clay minerals, with minor quantities of orthoclase, hematite, goethite, anatase, rutile, ilmenite and diaspore. In the <2 μm fraction, abundant kaolinite with illite, smectite and mixed-layers of illite/smectite (I/S) and chlorite/smectite (C/S) are identified as clay minerals.

The red clays have the lowest calcite content but they present the highest hematite, anatase, diaspore, goethite and kaolinite content. By contrast, the ochre and violet clays/marls have higher illite content, and smectite is only detected in the ochre clays/marls.

Using the classification of Allix et al. (2011), the studied samples of clays and clays/marls show hybrid compositions including argillaceous mudstones, argillaceous marlstones, siliceous marlstones and

Fig. 2. (A) Palaeogeological map of the Oliete subbasin showing the age of the youngest marine units preserved below the unconformity between the Jurassic and the Barremian Blesa Formation (modified from Aurell et al., 2018). The areas where the lowermost Blesa Formation (*i.e.* lower Blesa Sequence: LBS) includes frequent clays with pisoids are indicated in orange. The six outcrops of the lower part of the LSB logged and sampled in the present work are located near the villages of Alacón, Josa and Estercuel (see white circles). (B) Palaeogeography of the Oliete subbasin during the sedimentation of the LBS (modified from Aurell et al., 2018). (C) Field view around the ALC2 log showing the upper Kimmeridgian (UK) shallow marine carbonates overlain by the clays and limestones of the LBS. (D) Close view near the ALC2 log showing the irregular palaeokarstic surface (yellow dashed line) that developed at the boundary between the UK and the LBS, and overlain by a nodular level (nl) formed by abundant fibrous-radial calcite nodules. (E) Field view of the lowermost part of the LBS at the ALC-3 log showing the red clays (rc) overlying the UK.

calcareous mudstones. These variations in lithology are a consequence of the variable proportions of carbonates and silicates. Specifically, the red clays correspond to argillaceous mudstones and argillaceous marlstones, whereas the ochre and violet clays/marls are formed by siliceous marlstones and calcareous mudstones. Palustrine-lacustrine limestones are classified as calcareous mudstones.

The relative proportions of mineral phases in the thickest outcrops (the ALC1, VE, JO and EST logs) are shown in Fig. 8. Calcite detected by XRD is not represented, because, as will be explained below, a large

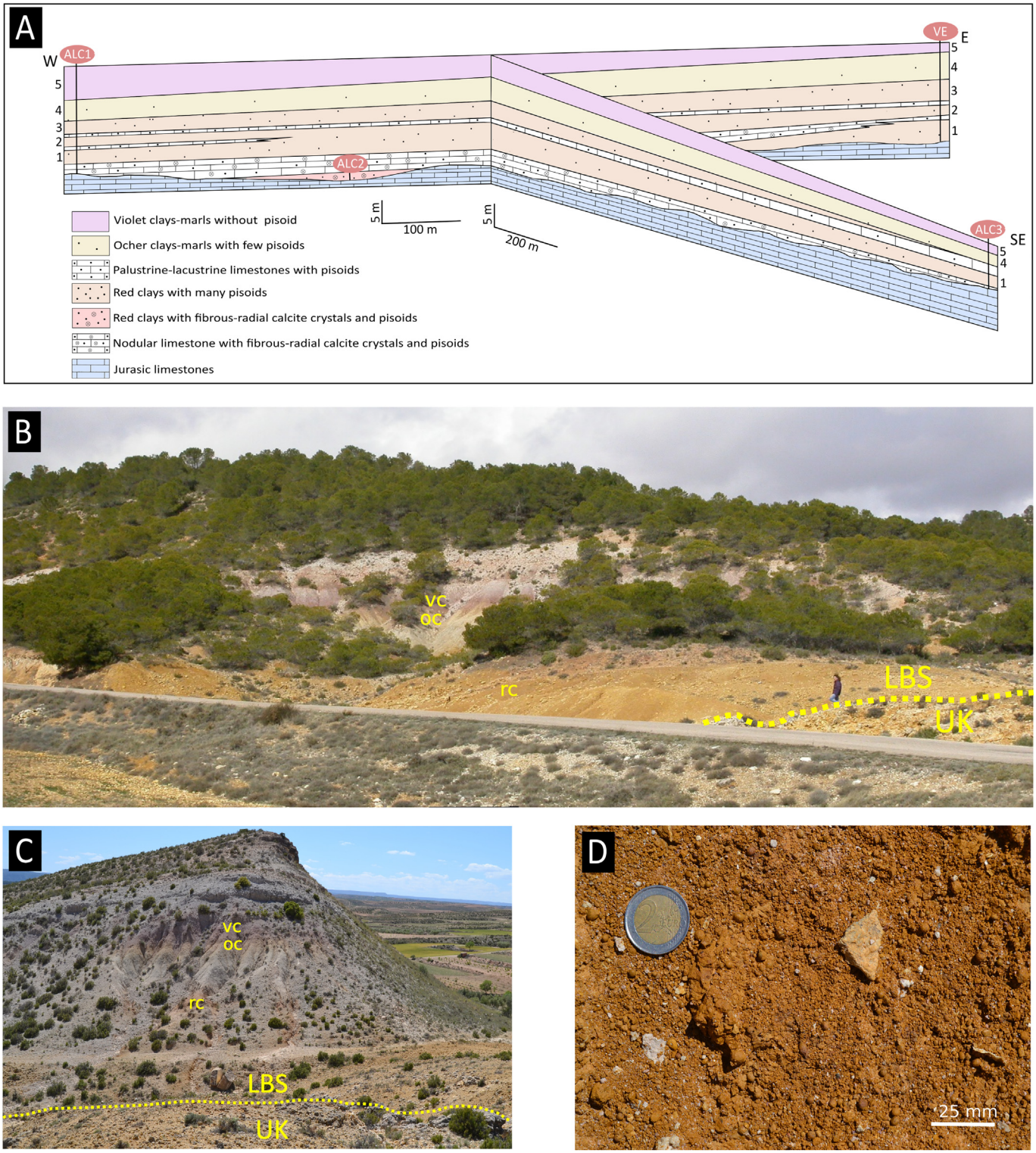

Fig. 3. (A) Stratigraphic correlation between the four stratigraphic logs from the Alacón area (their geographical coordinates are ALC1: N41°2′42.0" W0°42′47.6″; ALC2: N41°2′29.1" W0°42′42.4″; ALC3: N41°2′3.3" W0°42′10.9″; and VE: N41°02′46.5" W0°42′07″). The proposed correlation is based on the observation of lateral continuity at outcrop scale in continuous outcrops. (B, C) Field views around the VE and ALC1 logs, respectively, showing the upper Kimmeridgian (UK) shallow marine limestones, overlain successively by red clays (rc), ochre clays/marls (oc) and violet clays/marls (vc). (D) Detail of ferruginous pisoids and macropisoids (up to several mm in diameter) found in the red clays.

part of it did not form coetaneously with the clays and clays/marls. Proportions of mineral phases vary from base to top. Quartz content increases upwards whereas hematite, goethite, anatase, rutile, ilmenite and diaspore content decrease. Furthermore, kaolinite is the only clay mineral in the lower red clays reaching >50%. Its content decreases upwards coeval with an increase in the variety of clay minerals, where illite, smectite and mixed-layers of I/S and C/S are detected along with the kaolinite. This change almost coincides with the change from red clays to ochre clays/marls. Finally, in the violet clays/marls at the top, the dominant clay mineral is illite.

Table 2 shows kaolinite crystallinity values, which are in general >0.4 and thus indicate low crystallinity. Overall, comparison of the values measured in air-dried and ethylene-glycol-treated samples shows that there are no significant differences, except in some cases where the difference between the two values could be indicative of the presence of expandable components such as smectite.

As far as macropisoids are concerned, XRD patterns show that they contain quartz, calcite, clay minerals (kaolinite, as deduced from the FESEM study), hematite, goethite, ferrihydrite and ilmenite. The relative proportions of these minerals in four macropisoids from the first and second red clay levels in the ALC1 and VE logs are shown in Fig. 9 as an example. In particular, macropisoids are mainly formed by Fe oxyhydroxides (hematite, goethite and ferrihydrite), kaolinite, and occasionally lower proportions of ilmenite. Calcite was not included, for the same reason as in the case of the clays and clays/marls.

4.4. FESEM results

4.4.1. Backscattered and secondary electron images

Backscattered and secondary electron images of clay and clay/marl samples (Fig. 10) show that the matrix of red clays is formed by kaolinite, hematite, goethite, anatase/rutile and ilmenite. Quartz fragments and orthoclase with anhedral morphologies are occasionally observed.

Kaolinite appears mainly as subhedral to euhedral nanometric plates, commonly showing pseudohexagonal outlines (Fig. 10A and B) and less frequently forming booklets (Fig. 10C and D). In the

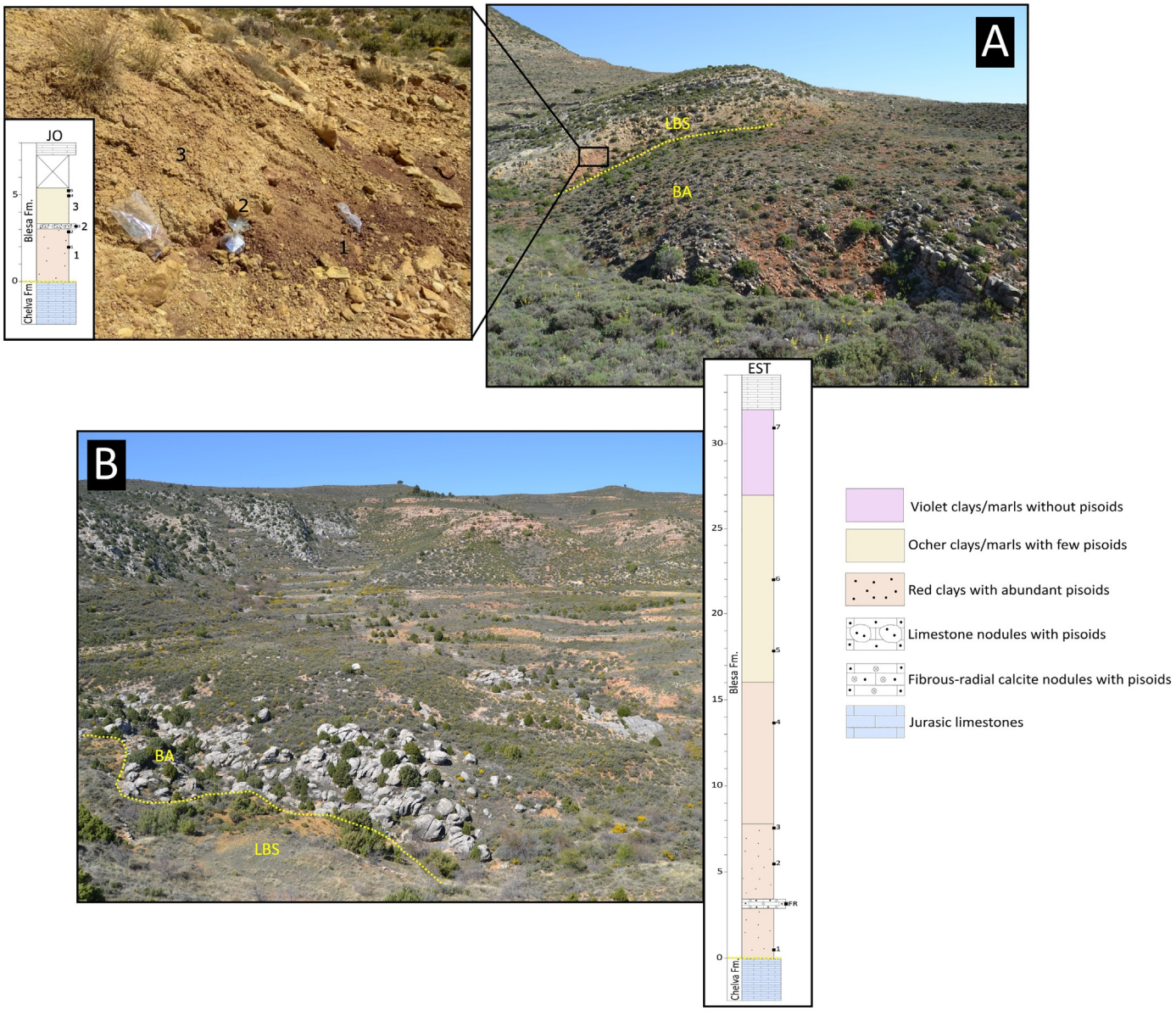

Fig. 4. (A) Field view of the Josa (JO) outcrop (at N40°55′20.64" W0°44′33.18″) showing the Bajocian-Bathonian (BA) shallow marine limestones, overlain by the red LBS succession. The stratigraphic log shows the red and ochre clays/marls found in this area. (B) Field view of the Estercuel (EST) outcrop (at N40°50′22.58" W0°39′36.53″) showing the lowermost red clays over the upper Bajocian-Bathonian limestones (BA). The stratigraphic log shows the red clays, and ochre and violet clay/marls dominant in this section.

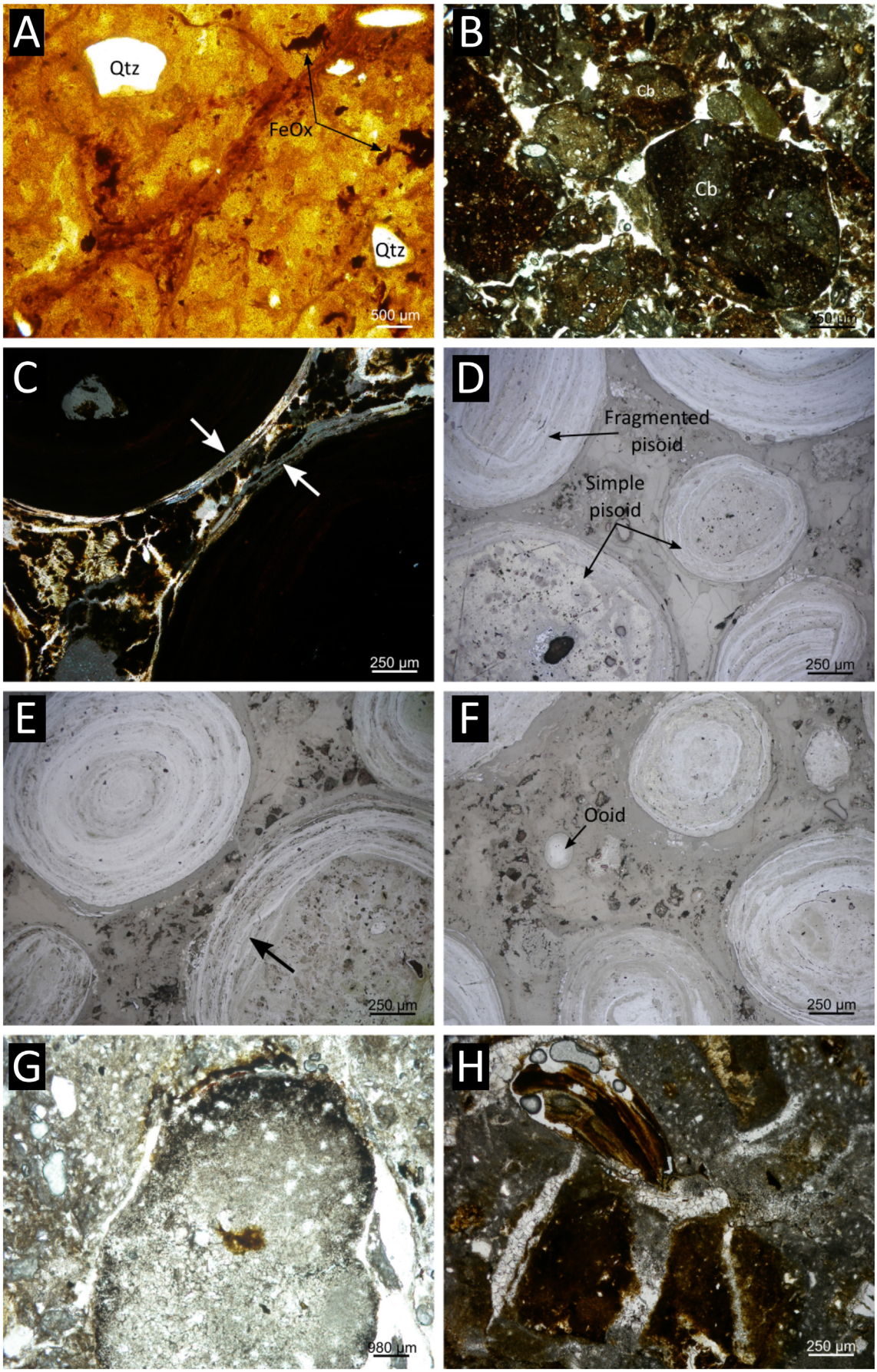
A
Qtz
FeOx
Qtz
500 µm
B
Cb
Cb
250 µm
C
250 µm
D
Fragmented pisoid
Simple pisoid
250 µm
E
250 µm
F
Ooid
250 µm
G
980 µm
H
250 µm

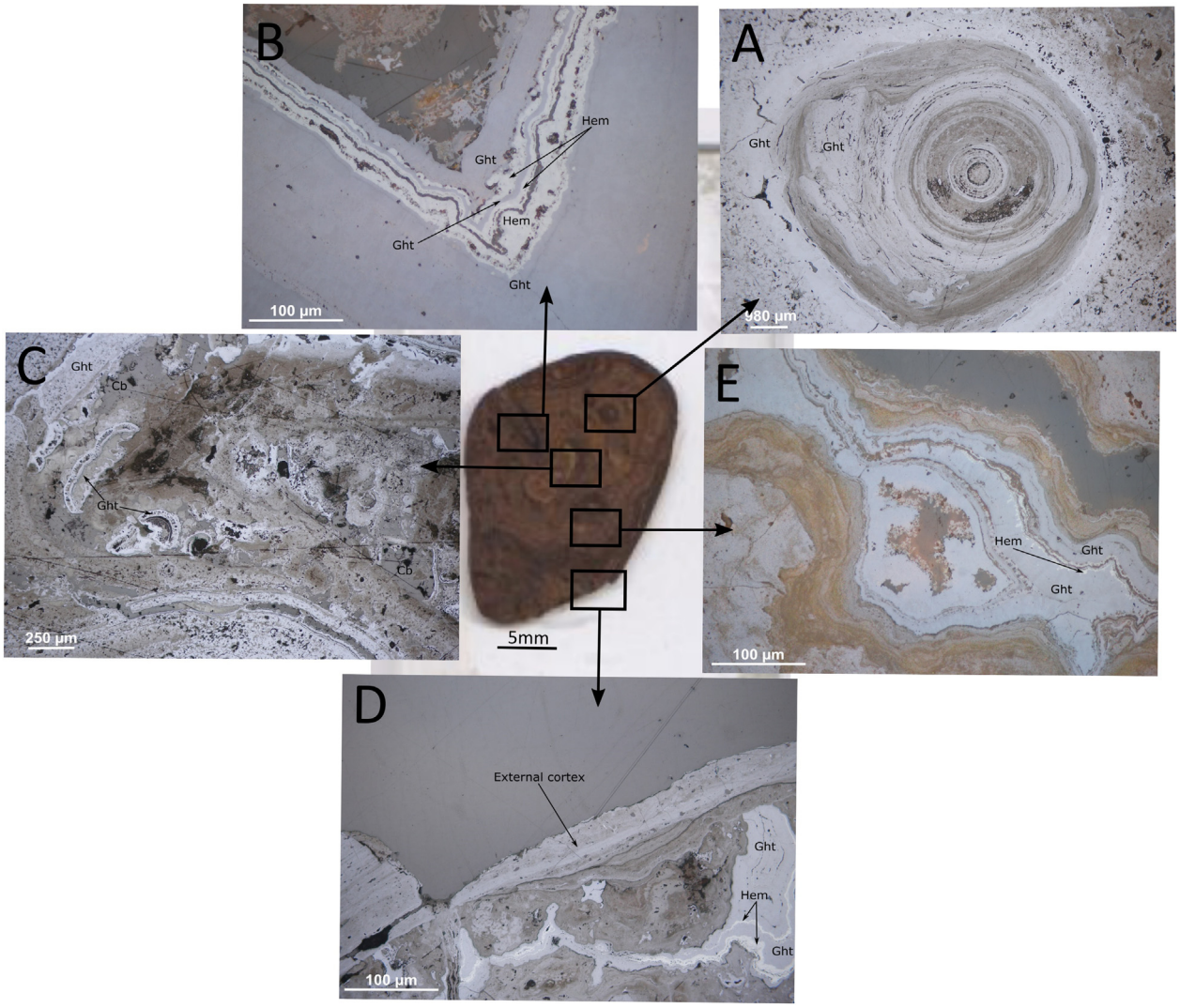

Fig. 6. Reflected light optical microscopy images of different parts of a macropisoid showing: (A) a pisoid in the nucleus of the macropisoid. (B, C, D and E), goethite and hematite with botryoidal textures and/or forming a sequence of alternate layers. (D) the external cortex formed by concentric layers. Hem = hematite, Ght = goethite, Cb = carbonate.

ochre and violet clays/marls, Fe and Ti oxides are less abundant or are even absent. In these cases, smectite (in the ochre samples) with flake morphologies and illite with wavy shapes (Fig. 10E and F) are observed.

Pisoids and macropisoids are mainly composed of hematite and goethite, with different proportions of kaolinite and minor proportions of ilmenite and calcite. Oxides in the nucleus are occasionally observed to be acicular whereas those in the cortex are anhedral (Fig. 11A). Kaolinite in the pisoids, in both the nucleus and the cortex, shows the same morphologies as those observed in the matrix, occurring with platy shapes and random orientation (Fig. 11B) or, alternatively, forming booklet aggregates (Fig. 11C). Booklets are also observed filling the internal cavities of the pisoids. These booklets are larger in size compared with those found in the matrix of the clays and the clays/marls and the nucleus of the pisoids. They reach up to 1 µm in diameter and >2 µm of longitudinal development in the direction of the c crystallographic axis (Fig. 11D). On the other hand, the concentric layers of the cortex show different proportions of kaolinite and Fe oxides, allowing one layer to be distinguished from another. Fe oxides also appear among the matrix of the clays and clays/marls (Figs. 11B and C).

Carbonate intraclasts found in the violet and ochre clays and clays/marls are formed by sparite and/or microsparite, whose EDS analyses show homogeneous calcite compositions (Fig. 12A). Partly dissolved, reworked calcite fragments cemented by kaolinite from the matrix are observed in the ochre and violet clays and clays/marls (Fig. 12B). The palustrine-lacustrine limestones are also locally cemented by kaolinite (Fig. 12C). On the other hand, the replacement of some fractured pisoids and partially of the clay matrix by sparitic calcite (Fig. 12D) is better observed with the FESEM images than by optical microscopy.

4.4.2. EDS results

The results of the EDS analyses were used to calculate chemical formulas for the kaolinite, smectite and illite found in the matrix of the red clays, ochre clays/marls and violet clays/marls (Table 3).

Three compositional groups of kaolinite were established: 1) platy kaolinite, 2) booklets of kaolinite, and 3) booklets of kaolinite filling

Fig. 5. Transmitted and reflected light optical microscopy images of the samples. (A) Clays and clays/marls including occasional quartz grains and Fe oxides. (B) Micritic carbonate nodules in violet clays/marls. (C) Sparitic carbonate cementing the matrix and replacing the external concentric layers of pisoids in the red clays (see arrows). (D) Simple and fragmented pisoids in the red clays. (E) Scour-and-fill texture in the cortex of a simple pisoid. (F) Ferruginous pisoids and ooids in the red clays (see arrow). (G) Pisoid partly replaced by carbonate in the ochre marls/clays. (H) Micritic intraclasts and disarticulated bivalve shell in a palustrine-lacustrine limestone sample. Qtz = quartz, Cb = carbonate.

the cavities of pisoids. The formulas calculated for the first and the second groups show that these kaolinites present low proportions of Fe, whereas the third group does not contain Fe.

The calculated smectite compositions of the ochre clays/marls correspond to dioctahedral smectites, as deduced from the higher content of trivalent cations (Al and Fe) in the octahedral layer. Furthermore, the tetrahedral charge is higher than the octahedral charge, so they correspond to a beidellite-type smectite. The illite composition presents lower K and higher Al and Fe content than the theoretical.

5. Discussion

5.1. The matrix of the clays and clays/marls

The XRD results of the clays and clays/marls of the LBS indicate that, according to the compositional classification of Allix et al. (2011), the lower red clays correspond to argillaceous mudstones and argillaceous marlstones, whereas the overlying ochre and violet clay/marl levels are formed by siliceous marlstones and calcareous mudstones. The sedimentary evolution in the LBS from continental clayey facies to palustrine-lacustrine carbonate facies described by Aurell et al. (2018) may account for the lithological variation found in the studied materials.

The combination of XRD and optical and electron microscopy shows that the red clays and ochre and violet clays/marls are formed by calcite, quartz and clay minerals, with minor quantities of orthoclase, hematite, goethite, anatase, rutile, ilmenite and diaspore. The lower red clays present the highest hematite, anatase, diaspore, goethite and kaolinite content and do not contain smectite or illite. The intermediate ochre clays/marls contain smectite and have higher illite content compared to the red clays. The upper violet clays/marls present the highest illite content compared to the red clays and the ochre clays/marls, and they also contain mixed-layers of I/S and C/S, but they do not contain smectite.

The textural study by means of electron microscopy provides key information for the interpretation of the origin of these clay minerals in clays and clays/marls: 1) In the case of the platy kaolinites and kaolinite booklets recorded, electron microscopy analyses suggest that they are authigenic. The platy kaolinites present pseudohexagonal morphologies that are incompatible with a detrital origin, since erosion and transport processes would have modified them. In the same way, the kaolinite booklets are also thought to have an *in-situ* origin because they are so delicate that they cannot resist any transport processes (Bauluz et al., 2014). The presence of Fe, albeit in low proportions, in the kaolinites (both platy and booklets) found in the matrix of the clays and clays/marls may be substituting the Al in the octahedral sheet of kaolinite, as occurs in similar materials (Mendelovici et al., 1979). The low kaolinite crystallinity is probably due to the presence of Fe in the structure, as is common in weathering processes (Mestdagh et al., 1980; Cantinolle et al., 1984; Yuste et al., 2015). Alternatively, given that the electron beam of the microscope has a larger diameter than the kaolinite particles, the analyses could be contaminated with nanometric Fe oxides.

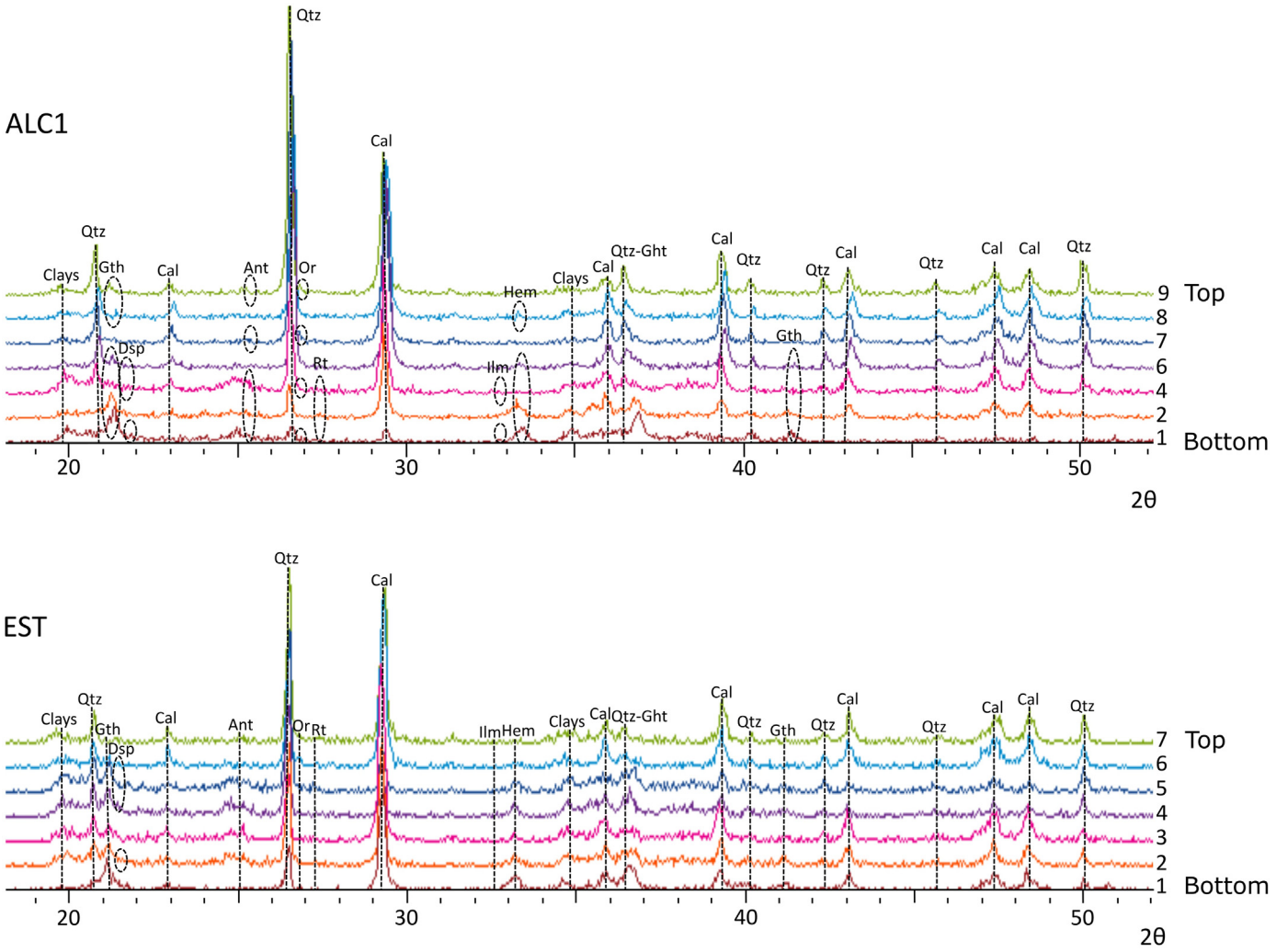

Fig. 7. XRD patterns obtained from clay and clay/marl samples in the ALC1 log (samples 1–9) and EST log (samples 1–7). Clays = clay minerals, Qtz = quartz, Cal = calcite, Ght = goethite, Dsp = diaspore, Ant = anatase, Or = orthoclase, Rt = rutile, Ilm = ilmenite, Hem = hematite.

2) As far as smectite is concerned, which is only recorded in the ochre clays/marls, its flake-type morphology and its presence as cement in the matrix of these clays/marls also suggest an *in-situ* origin. The chemical composition corresponds to dioctahedral, beidellite-type smectite. This type of smectite has previously been described in similar materials as a result of the weathering of dioctahedral micas (Singh and Gilkes, 1991). Therefore, both kaolinite and smectite were probably formed as a consequence of edaphic processes, which involved the dissolution of previous aluminum silicate phases (feldspars, micas) and the crystallization of new ones (kaolinite and smectite).

3) Regarding illite, which is abundant in the ochre and violet clays/marls, especially in the latter, its formation is normally associated with diagenetic environments (Bauluz et al., 2000). A detrital origin is described for illite in materials similar to those studied in the present work (Franceschelli et al., 2003). The illite-type phases found in the ochre and violet clays/marls are probably of detrital origin, given that the genesis conditions of kaolinite in soils are not compatible with illite genesis. The anhedral morphologies of these phases would corroborate their detrital origin (Bauluz et al., 2014).

Hematite and goethite are present not only in the matrix of the clays and clays/marls, but also in the pisoids found in the red clays and ochre clays/marls (see 5.2 below). This suggests that the oxides and oxyhydroxides found in the matrix have an edaphic origin. By contrast, the quartz fragments and orthoclase would be of detrital origin. The low quartz and orthoclase content and their anhedral morphologies suggest that they are relicts of the original rocks and were probably partially dissolved during weathering.

5.2. Ferruginous pisoids in red clays and ochre clays/marls

In soils, the formation of *in-situ* pisoids is related to dissolution and re-precipitation processes, which are controlled by several factors, such as climatic variations, the chemistry of the groundwater and the difference in mobility of the chemical components of the parent rock during chemical weathering (Valeton, 1972; Bhattacharyya and Kakimoto, 1982). According to Bárdossy (1982), the formation of these particles requires permanent groundwater saturation. The presence of scour-and-fill features like those described by Taylor et al. (2008) in some of the studied pisoids thus shows deformation in

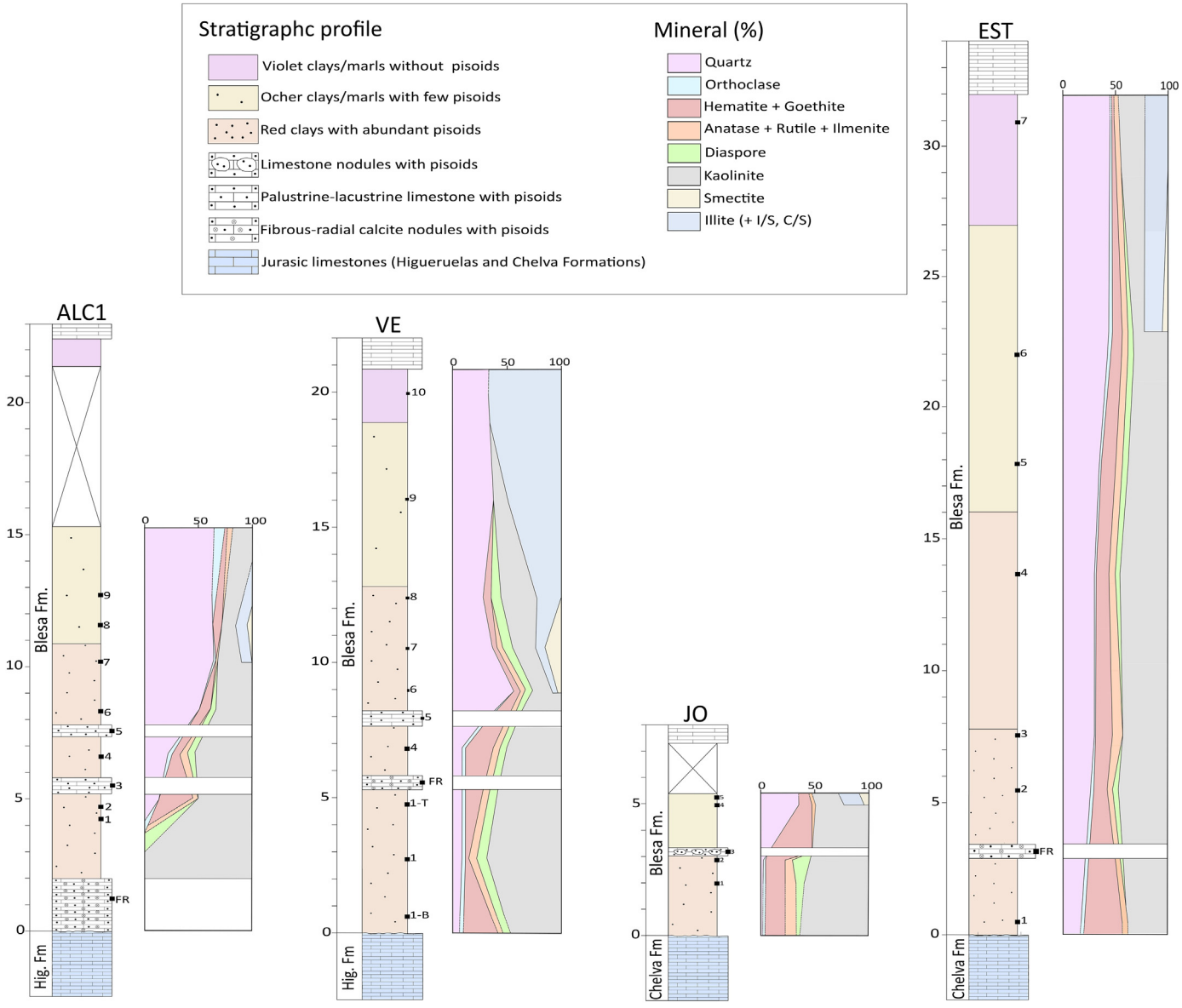

Fig. 8. Variations in mineral content of clays and clays/marls in the ALC1, VE, JO and EST logs. The Jurassic marine carbonate rocks are represented either by the latest Kimmeridgian Higueruelas Formation (Hig. Fm) or by the Bajocian-Bathonian Chelva Formation.

a semi-plastic state, indicating water saturation (Yuste et al., 2015).

The studied pisoids are hematite-goethite pisoids, also including clay minerals (kaolinite, as deduced by FESEM analysis). Previous investigations classified pisoids according to their hematite and kaolinite content (Szamatek et al., 1993; Sayed and Youssef, 1996). The pisoids studied here could thus be classified as hematitic-kaolinitic pisoids. In fact, the differences in the kaolinite and Fe oxide contents observed in the cortex of the studied pisoids allow the different concentric layers to be distinguished.

The presence in the pisoids and macropisoids of hematite, goethite and kaolinite, with textural features similar to those observed in the matrix, along with their concentric structure comprising a nucleus and a cortex, indicates that they were formed *in-situ* during the development of the soils. The sequences of goethite-hematite layers observed in macropisoids have previously been described in gossan development on metallic deposits (Velasco et al., 2013). According to these authors, the presence of this alternation of goethite and hematite layers reflects a change to less humid conditions.

The fact that the Fe oxides are cementing kaolinite in the pisoids suggests that these oxides form at a late stage in comparison with the kaolinite during the edaphic processes. On the other hand, the EDS results for the booklets of kaolinite filling the cavities of pisoids indicate that these booklets do not contain Fe and are larger in size compared with those found in the matrix of the clays and clays/marls, a fact that may be due to recrystallization during very early diagenesis.

5.3. The palustrine-lacustrine limestones

According to the classification by Allix et al. (2011), the palustrine-lacustrine limestones intercalated in red clays with pisoids correspond to calcareous mudstones. A rise in water level probably led to a palustrine-lacustrine environment where carbonate muds precipitated, resulting in the formation of the calcareous mudstones. The reworked calcite fragments cemented by kaolinite in the ochre and violet clays and clays/marls may come from these calcareous mudstones.

These calcareous mudstones also contain pisoids, most of them broken, and ferruginous ooids, which may be reworked from the underlying red clays. The possible decrease in the water level may have enhanced the overprint of edaphic processes in the palustrine-lacustrine limestone (*e.g.* limestone with micritic nodules/intraclasts), favouring the reworking and fracturation of some of the pisoids. Other authors have described reworking processes as suggesting different episodes in the development of soils (Mücke et al., 1999). These calcareous mudstones are also cemented by kaolinite, suggesting that they also underwent edaphic processes during the decrease in the water level.

5.4. Nodular limestones and diagenesis of clays and clays/marls

During the early diagenesis, the matrix of the clays and clays/marls was cemented by microsparite and sparite. In addition, diagenesis may have also generated the micritic nodules and sparitic-microsparitic intraclasts observed in the ochre and violet clays/marls. Sparitic cement also filled the gaps and replaced some fractured pisoids found in red clays and ochre clays/marls. Thus, calcite was eliminated from the quantification results, since much of it results from the diagenesis.

In the AlC2, VE and EST sections, the beds of fibrous-radial calcite nodules also overlie a lowermost red clay level with pisoids. According to Rossi and Cañaveras (1999), many of the calcites included in freshwater cements forming during diagenesis are fibrous, so the fibrous-radial calcite nodules could have also been formed in the early diagenesis. Given the presence of pisoids and their location in the lower part of the LSB, these nodule-bearing beds would correspond to palustrine-lacustrine limestones. They would have been affected by intense early diagenetic processes during an initial unstable stage with frequent hiatuses/erosional gaps after the long, Tithonian–Hauterivian period of subaerial exposure represented by the karstified surface on top of the Jurassic limestones.

As indicated above, the morphology of the kaolinite and smectite from the matrix of the clays and clays/marls suggests an *in-situ* origin. These early diagenetic processes would therefore not have modified the clay mineralogy of the facies significantly.

Table 2
Kaolinite crystallinity values of the samples of clays and clays/marls from the different outcrops measured in air-dried (AD) and ethylene-glycol-treated (EG) samples. Am = argillaceous mudstone; Amr = argillaceous marlstone; Smr = siliceous marlstone; Cm = Calcareous marlstone.

Alacón						Josa and Estercuel					
Log	Sample number	Sample description	Facies	KC		Log	Sample number	Sample description	Facies	KC	
				AD(001)	EG(001)					AD(001)	EG(001)
	1	Am	red clays	0.5	0.5		1	Am	red clays	0.5	0.4
	2	Amr	red clays	0.7	0.4	**JO**	2	Am	red clays	0.4	0.4
	4	Am	red clays	0.5	0.6		4	Amr	ocher clays/marls	0.4	0.4
ALC1	6	Smr	red clays	0.6	0.4		5	Amr	ocher clays/marls	0.3	0.4
	7	Smr	red clays	0.5	0.4	**EST**	1	Am	red clays	0.3	0.3
	8	Smr	ocher clays/marls	0.3	0.5		2	Amr	red clays	0.4	0.5
	9	Smr	ocher clays/marls	0.4	0.3		3	Amr	red clays	0.4	0.4
	2M	Am	red clays	0.6	0.5		4	Am	red clays	0.4	0.6
ALC2	2V	Am	red clays	0.5	0.6		5	Am	ocher clays/marls	0.5	0.6
	3	Am	red clays	0.6	0.6		6	Amr	ocher clays/marls	0.2	0.6
	1	Amr	red clays	0.5	0.5		7	Am	violet clays/marls	0.3	0.3
ALC3	2M	Am	red clays	0.6	0.6						
	2V	Am	red clays	0.6	0.6						
	1-B	Am	red clays	0.6	0.6						
	1	Am	red clays	0.6	0.7						
	1-T	Am	red clays	0.5	0.6						
VE	4	Am	red clays	0.4	0.4						
	6	Smr	red clays	0.5	0.5						
	7	Amr	red clays	0.5	0.5						
	8	Amr	red clays	0.5	0.4						
	9	Cm	ocher clays/marls	0.6	0.5						

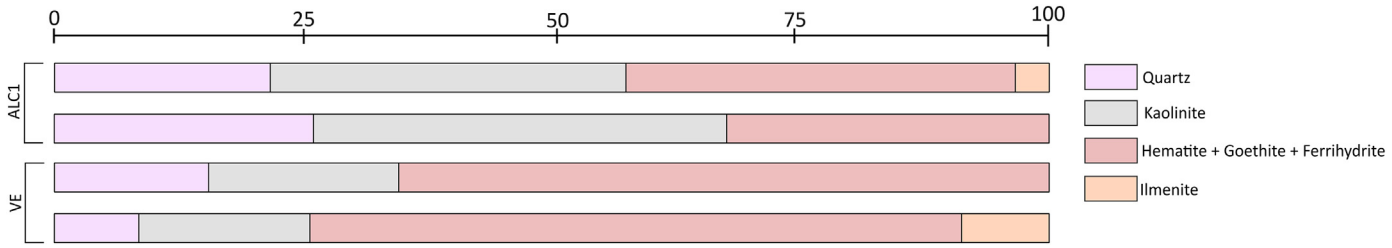

Fig. 9. Relative proportions of mineral phases in macropisoids from the first and second red clay levels of the ALC1 and VE logs.

5.5. Palaeoweathering events deduced from clay mineral assemblages

The mineralogical association in the studied clays and clays/marls, the red, ochre and violet colours, along with the presence of ferruginous pisoids in the red clays and ochre clays/marls, allow them to be classified as palaeosols. According to Schellmann (1981), lateritic palaeosols are formed by mineral assemblages of goethite, hematite, aluminum hydroxides, kaolinite and quartz. Several authors (*e.g.* Foos, 1991; Mücke et al., 1999; Giovannini et al., 2017; Faris et al., 2019) have reported these mineral phases as well as the presence of

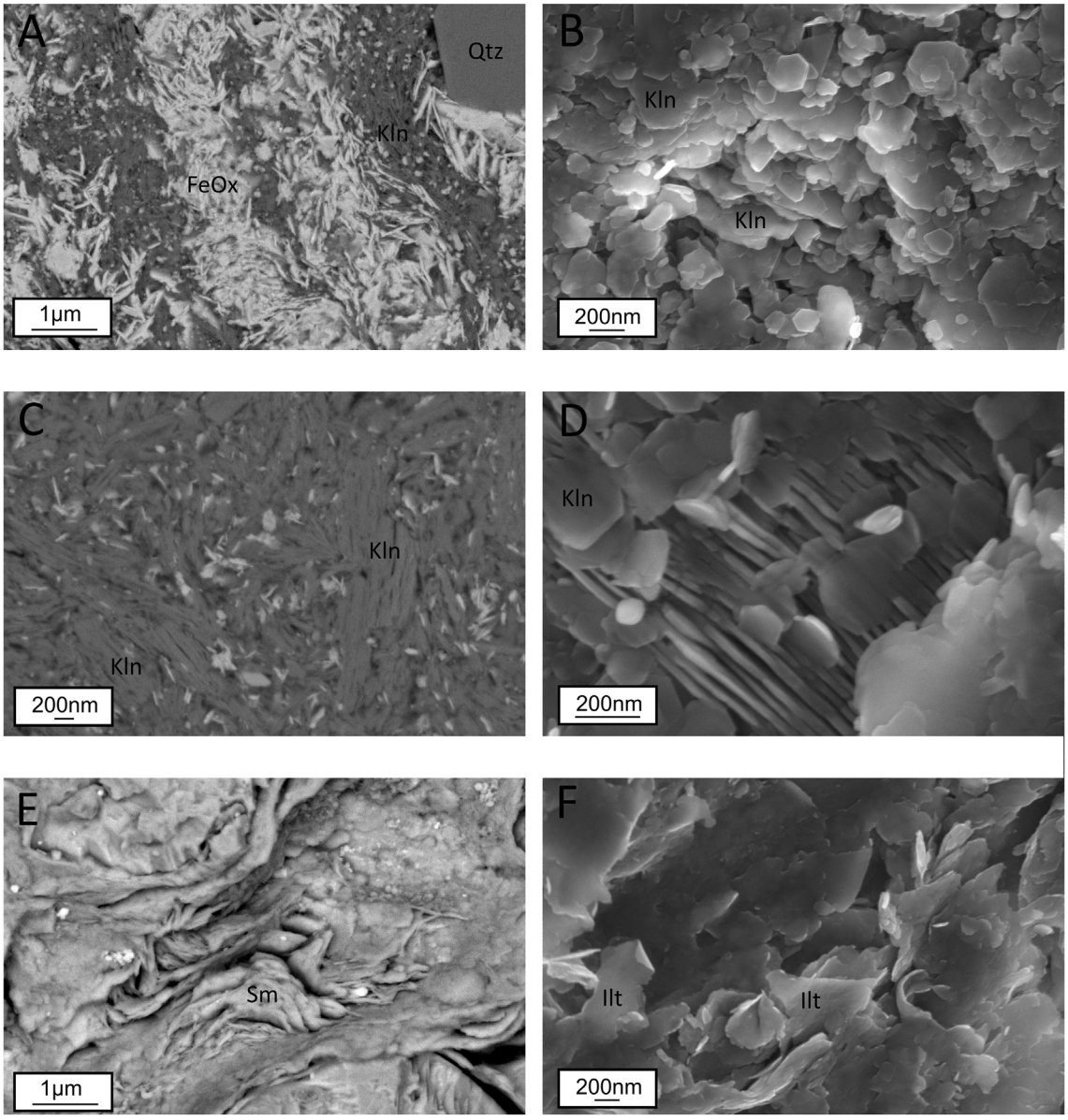

Fig. 10. FESEM images of samples of red clays, ochre clays/marls and violet clays/marls. (A) Matrix of the red clays. (B) Pseudohexagonal kaolinite crystals in red clays. (C) and (D) Kaolinite booklets in red clays. (E) Smectite with flake morphologies in ochre clays/marls. (F) Illite-type morphologies in violet clays/marls. Kln = kaolinite, FeOx = Fe oxides, Qtz = quartz, Sm = smectite and Ilt = illite.

ferruginous pisoids in lateritic palaeosols. The mineral assemblages and the high content of ferruginous pisoids in the lower red clays thus allow them to be classified as lateritic palaeosols.

The combination of XRD and electron microscopy showed that kaolinite is the dominant clay mineral in these lateritic palaeosols. The presence of this mineral suggests a warm and humid climate, along with an intense chemical weathering (Chamley, 1989; Raucskik and Varga, 2008; Bauluz et al., 2014), which are characteristic conditions of tropical climates (Molina and Salas, 1993; Yuste et al., 2017).

The generation of red lateritic soils alternated (and was coeval) with the deposition of palustrine-lacustrine limestone with broken pisoids, reflecting a rapid rise (and probably subsequent falls) in water level, which could be related with variations in humidity, with local developments of palustrine-lacustrine areas. The afore-mentioned sequences of goethite-hematite layers in macropisoids might also be related to these conditions.

In the intermediate and upper ochre and violet clays/marls, the presence of smectite (beidellite; only present in ochre clays/marls), illite (highest content in violet clays/marls) and mixed-layers of I/S and C/S coincides with a decrease in and near-absence of kaolinite content. This trend can be interpreted in accordance with the weathering pattern proposed by Sheldon and Tabor (2009). These authors suggest trends in clay mineralogy that reflect weathering patterns changing from warm/humid to cold/dry conditions: kaolinite➔smectite➔vermiculite➔chlorite and mixed-layer phyllosilicates➔ illite and mica. In our studied case, the vertical trend is: kaolinite (dominant in red clays) ➔ kaolinite, smectite and illite (intermediate ochre clays/marls) ➔ illite and mixed-layer I/S and C/S (violet clays/marls), suggesting a less intense chemical weathering due to a change from warm and humid to colder and drier conditions. The absence of pisoids in the violet clays/marls would support the idea of generally drier conditions, which would have prevented permanent groundwater saturation and therefore pisoid formation.

In the east of the Maestrazgo Basin, the Cantaperdius Formation (Salas, 1987), which is equivalent in age to the formation studied here (Barremian–Aptian), includes lacustrine and palustrine limestones and the development of soils and laterites like those described by Combes (1969). In addition, karst bauxite deposits, probably originating from lateritic materials laterally equivalent to the Cantaperdius Formation, have been reported in the nearby Morella subbasin (Molina and Salas, 1993; Yuste et al., 2015). Furthermore, Lower Cretaceous lateritic and bauxitic deposits have been described in the Cuenca Basin by Fregenal-Martínez et al. (2017). On the other hand, several authors have also reported the presence of laterites and bauxites in the Catalan Coastal Ranges and the Pyrenees (Combes, 1969; Ordóñez et al., 1990; Reinhardt et al., 2018; Seranne et al., 2019). According to Salas et al. (2004), the bauxites of the Catalan Coastal Ranges were probably formed from lower Barremian lateritic clays of the Cantaperdius Formation, whereas Seranne et al. (2019) dated the bauxite event of the Pyrenees to between early Albian and latest Albian. Nevertheless, the age of these deposits within the Barremian–Aptian interval cannot be precisely established. It is thus not possible to determine whether the early Barremian palaeoclimatic evolution (*i.e.*, from humid to dry conditions) documented here was regional or local in extent.

A change from warm to cooler climatic conditions during the Barremian–Aptian has been described in Europe (Pucéat et al., 2003; Steuber et al., 2005; Dinis et al., 2020), but there is no general agreement as regards the trend in humidity during the Early Cretaceous. A humid climate is described in the northwestern part of Europe during the early Barremian (Wright et al., 2000). The temperature models show warm and humid conditions for this period along the northern margin of the Tethys (Bodin et al., 2009; Price et al., 2011), as well as an increase in humidity during the mid-Barremian (= upper lower–lower upper Barremian) recorded at least at a European scale (Mutterlose et al., 2014). By contrast, an alternation of wet and dry seasons during the early Barremian (Haywood et al., 2004) and a trend to more arid and dry conditions towards the Albian–Cenomanian (Rodríguez-López et al., 2006) have also been reported.

The seasonal subtropical climate during the Lower Cretaceous in the Iberian Range described by Buscalioni and Fregenal-Martínez (2010) is supported by the presence of Barremian bauxitic and lateritic deposits (Molina and Salas, 1993; Bauluz et al., 2014; Yuste et al., 2015; Yuste et al., 2017). In addition, the Cretaceous ocean circulation models of Pucéat et al. (2005) and Hay (2008) substantiate the prevalence of wetter conditions in Iberia, which could be related to a warm and humid equatorial current in the Western Tethys (Dinis et al., 2020).

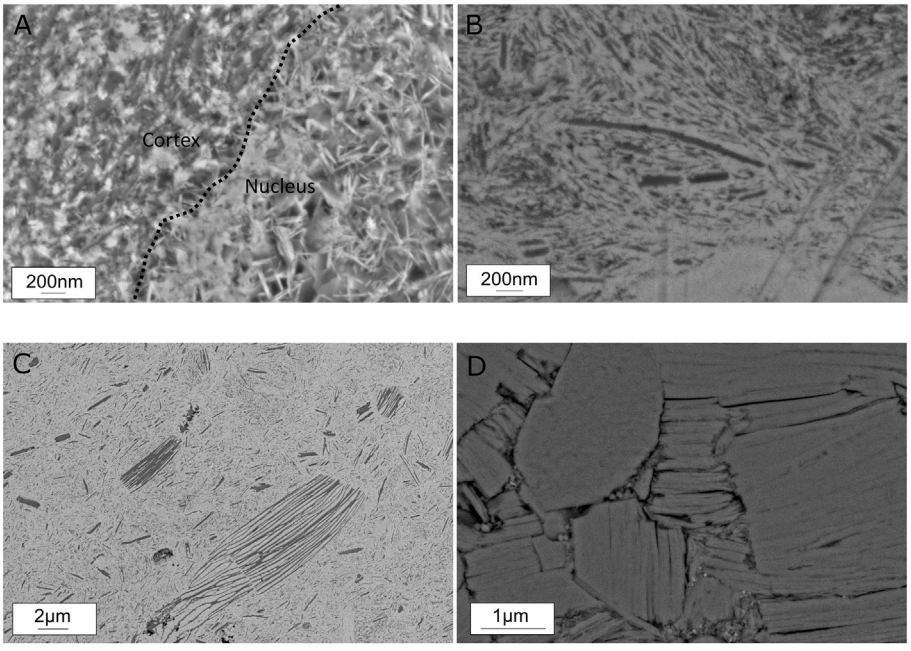

Fig. 11. FESEM images of ferruginous pisoids showing: (A) Nucleus and cortex contact with acicular (in the nucleus) and anhedral (in the cortex) oxide crystals. (B) Platy kaolinites in the nucleus of pisoids together with abundant Fe oxides. (C) Kaolinite booklets in the nucleus of pisoids. (D) Kaolinite booklets filling cavities observed within some pisoids.

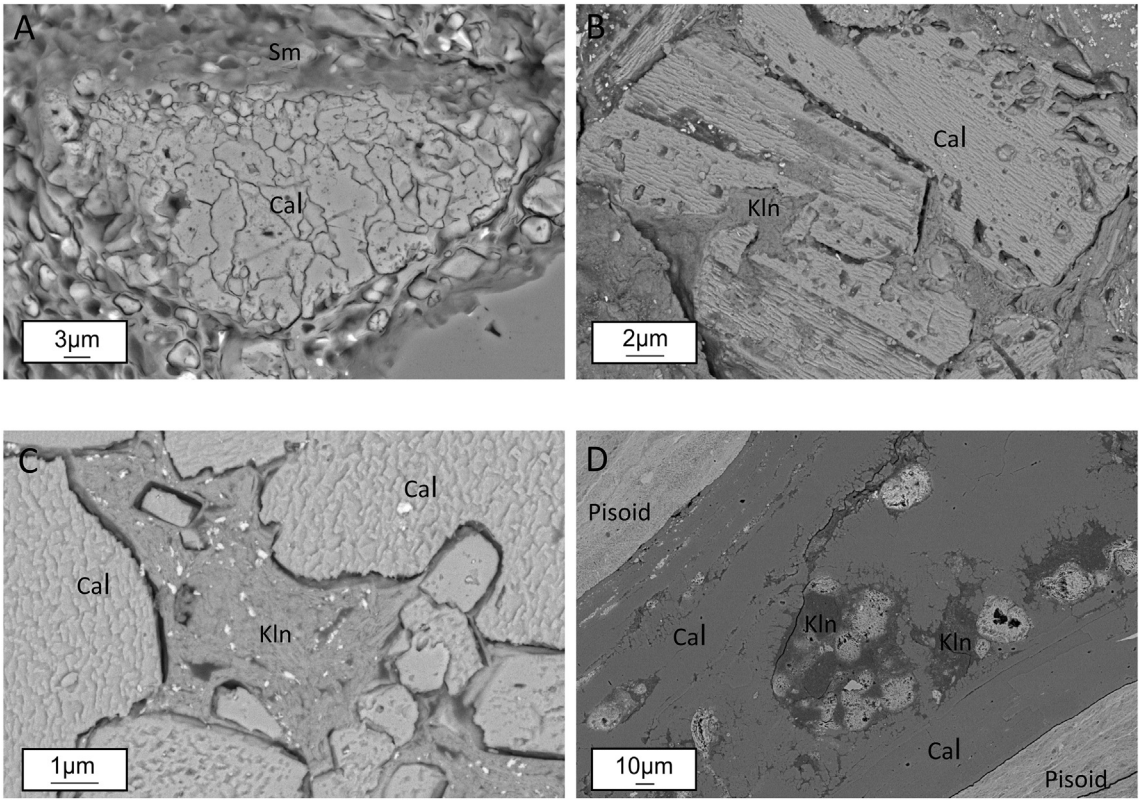

Fig. 12. FESEM images of carbonates in the study samples. (A) Calcite intraclast in the matrix of the ochre clays/marls. (B) Reworked calcite fragment with evidence of dissolution and cemented by kaolinite in the ochre clays/marls. (C) Palustrine-lacustrine limestone where kaolinite is cementing calcite. (D) Sparitic calcite replacing the matrix of clays and clays/marls and the concentric layers of the cortex of pisoids. Sm = smectite, Cal = calcite, Kln = kaolinite.

6. Conclusions

A combination of facies analysis and XRD and optical and electron microscopy studies has allowed us to characterize the mineralogical and textural changes found in the successive clay/carbonate levels found in the lower Blesa Formation (early Barremian, Oliete subbasin).

The lower part of the studied succession consists of red clay levels with abundant pisoids, recording the lowest calcite content but the highest content in hematite, anatase, diaspore, goethite and kaolinite. The intermediate ochre clay/marl levels contain smectite and illite and have few or no pisoids. The upper violet clay/marl levels contain illite and do not have pisoids.

The morphologies of the kaolinite crystals (platy and booklets) found in the lower red clay levels indicate that the kaolinite is authigenic. The smectite frequently recorded in the intermediate ochre clay/marl levels corresponds to a beidellite-type smectite, and the flake-type crystals forming the matrix of these levels also indicate an *in-situ* origin. The genesis of the illite-type phases is not compatible with the formation of kaolinite, so they might be of detrital origin.

Episodic rises in water level resulted in the formation of the palustrine-lacustrine limestone levels which are found interbedded within the clay-dominated succession. These levels may contain pisoids reworked from the underlying palaeosol levels and are cemented by kaolinite, indicating that they underwent edaphic processes during the episodic stages of decreased water level.

The mineralogical composition and structure of pisoids and macropisoids indicate an *in-situ* origin during lateritic soil formation. The decrease in the water level also favoured the reworking of the materials, involving the fracturing of some of these pisoids, which may have eventually formed the nucleus of pisoids formed in earlier stages of soil development.

During the early diagenesis, both the matrix of the clays and clays/marls was cemented and the cavities of the pisoids were filled by microsparite and sparite cements. This diagenesis did not affect the morphology of kaolinite and smectite.

The mineralogy of the red clay levels, along with the presence of ferruginous pisoids, indicates that they are lateritic palaeosols. Kaolinite is the dominant clay mineral in the lower red clay levels, indicating humid

Table 3
EDS analysis (Wt%) of phyllosilicates detected in clay and clay/marl samples (standard deviation in brackets).

	O	Na	Mg	Al	Si	K	Ca	Ti	Fe	Calculated composition
Platy kaolinite (n = 37)	49.80 (3.16)	0.05 (0.15)	0.08 (0.16)	21.81 (1.40)	25.30 (1.28)	0.28 (0.29)	–	0.38 (0.77)	2.30 (1.56)	$Fe_{0.1}Al_{1.8}Si_2O_5(OH)_4$
Kaolinite Booklets in matrix (n = 6)	56.68 (5.04)	–	–	19.81 (3.00)	21.82 (3.23)	0.03 (0.05)	–	0.17 (0.30)	1.48 (1.41)	$Fe_{0.3}Al_{1.7}Si_2O_5(OH)_4$
Kaolinite Booklets in pisoids cavities (n = 3)	52.77 (2.47)	–	–	22.04 (1.41)	25.08 (1.54)	0.12 (0.20)	–	–	–	$Al_{1.9}Si_{2.1}O_5(OH)_4$
Illitic phases (n = 4)	42.50 (7.60)	–	1.21 (0.26)	14.12 (2.44)	26.50 (5.09)	3.72 (1.39)	5.46 (5.00)	0.94 (1.53)	5.55 (2.23)	$(K_{0.5},H_3O)(Al_{1.2}Mg_{0.2}Fe_{0.4})(Si_{3.4}Al_{0.6})O_{10}(OH)_2,(H_2O))$
Smectite (n = 17)	46.31 (12.52)	0.07 (0.29)	0.87 (0.58)	14.42 (3.90)	24.23 (6.55)	1.93 (1.36)	4.58 (4.14)	1.15 (2.83)	6.44 (6.12)	$(Ca_{0.1}K_{0.2})(Al_{1.5}Fe_{0.4}Ti_{0.1}Mg_{0.1})(Si_{3.1}AL_{0.9})O_{10}(OH)_2nH_2O$

and warm climatic conditions and an intense chemical weathering. This is consistent with the palaeoclimate conditions described for the early Barremian in the NE Iberian. The decrease in the kaolinite and the oxide and oxyhydroxide contents from the bottom to the top of the stratigraphic profiles, along with the increase in the quartz content and the presence of smectite and illite, indicates a change to a less intense chemical weathering. These variations reflect a change from warm and humid to generally colder and drier conditions in the studied area across the early Barremian.

Declaration of competing interest

The authors declare that they have no known competing financial interests or personal relationships that could have appeared to influence the work reported in this paper

Acknowledgments

This work was supported by the European Regional Development Fund and the Government of Aragón [Aragosaurus Group: Geological Resources and Palaeoenvironments, grant number E18_20R] and the Spanish Ministry of Science, Innovation and Universities [grant number RTI2018-093419-B-I00]. The authors would like to acknowledge the use of the Servicio General de Apoyo a la Investigación-SAI, University of Zaragoza. They would also like to thank C. Gallego for her advice during the FESEM sessions. E. Laita received a grant by the Government of Aragon for the development of her PhD. The authors would also like to thank the reviewers Dr. T. Bover-Arnal and Dr. J. M. Molina, whose comments and suggestions helped to improve the manuscript.

References

Allix, P., Burnham, A., Fowler, T., Herron, M., Kleinberg, R., Symington, B., 2011. Coaxing oil from Shale. Oilfield Review 22 (4), 4–15.

Aurell, M., Soria, A.R., Bádenas, B., Liesa, C.L., Canudo, J.I., Gasca, J.M., Moreno-Azanza, M., Medrano-Aguado, E., Mélendez, A., 2018. Barremian synrift sedimentation in the Oliete subbasin (Iberian Basin, Spain): palaeogeographical evolution and distribution of vertebrate remains. J. Iber. Geol. 44, 285–308. https://doi.org/10.1007/s41513-018-0057-3.

Aurell, M., Fregenal-Martínez, M., Bádenas, B., Muñoz-García, M.B., Élez, J., Meléndez, N., de Santisteban, C., 2019. Middle Jurassic–Early Cretaceous tectono-sedimentary evolution of the southwestern Iberian Basin (central Spain): Major palaeogeographical changes in the geotectonic framework of the Western Tethys. Earth Sci. Rev. 199, 102983. https://doi.org/10.1016/j.earscirev.2019.102983.

Bárdossy, G., 1982. Karst Bauxites. Elsevier, p. 441.

Bauluz, B., Mayayo, M.J., Fernández-Nieto, C., González López, J.M., 2000. Geochemistry of Precambrian and Paleozoic siliciclastic rocks from the Iberian Range (NE Spain): implications for source-area weathering, sorting, provenance, and tectonic setting. Chem. Geol. 168, 135–150. https://doi.org/10.1016/S0009-2541(00)00192-3.

Bauluz, B., Yuste, A., Mayayo, M.J., Canudo, J.I., 2014. Early kaolinization of detrital Weald facies in the Galve Subbasin (Central Iberian Chain, north-east Spain) and its relationship to paleoclimate. Cretac. Res. 50, 214–227. https://doi.org/10.1016/j.cretres.2014.03.014.

Bhattacharyya, D.P., Kakimoto, P.L., 1982. Origin of ferriferous ooids: a SEM study of ironstone ooids and bauxite pisoids. J. Sediment. Petrol. 52 (3), 849–857.

Biscaye, P.E., 1965. Mineralogy and sedimentation of recent deep-sea clay in the Atlantic Ocean and adjacent seas and oceans. Geol. Soc. Am. Bull. 76, 803–832.

Bodin, S., Fiet, N., Godet, A., Matera, V., Westermann, S., Clément, A., Janssen, N.M.M., Stille, P., Föllmi, K.B., 2009. Early Cretaceous (late Berriasian to early Aptian) palaeoceanographic change along the northwestern Tethyan margin (Vocontian Trough, southeastern France): $\delta^{13}C$, $\delta^{18}O$ and Sr-isotope belemnite and whole-rock records. Cretac. Res. 30, 1247–1262. https://doi.org/10.1016/j.cretres.2009.06.006.

Buscalioni, A.D., Fregenal-Martínez, M.A., 2010. A holistic approach to the palaeoecology of Las Hoyas Konservat-Lagerstätte (La Huérguina Formation, Lower Cretaceous, Iberian Ranges, Spain). J. Iber. Geol. 36 (2), 297–326. https://doi.org/10.5209/rev_JIGE.2010.v36.n2.13.

Buurman, E., Meijer, E.L., van Wijck, J.H., 1988. Weathering of chlorite and vermiculite in ultramafic rocks of Cabo Ortegal, northwestern Spain. Clays Clay Miner. 36, 263–269.

Canérot, J., Cugny, P., Pardo, G., Salas, R., Villena, J., 1982. Ibérica Central-Maestrazgo. In: García, A. (Ed.), El Cretácico de España. Univ. Complutense de Madrid, Madrid, pp. 273–344.

Cantinolle, P., Didier, P., Meunier, J.D., Parron, C., Guendon, J.L., Bocquier, G., Nahon, D., 1984. Kaolinites ferrifères et oxyhydroxydes de fer et d'alumine dans les bauxites des Canonettes (S.E. de la France). Clay Miner. 19, 125–135.

Canudo, J.I., Gasca, J.M., Aurell, M., Badiola, A., Blain, H.A., Cruzado-Caballero, P., Gómez-Fernández, D., Moreno-Azanza, M., Parrilla, J., Rabal-Garcés, R., Ruiz-Omeñaca, J.I., 2010. La Cantalera: an exceptional window onto the vertebrate biodiversity of the Hauterivian-Barremian transition in the Iberian Peninsula. J. Iber. Geol. 36 (2), 205–224.

Chamley, H., 1989. Clay Sedimentology. Springer-Verlag, Berlin. Heidelberg New York, p. 623.

Combes, P.J., 1969. Recherches sur la genèse des bauxites dans le nord-est de l'Espagne le Languedoc et l'Ariége (France). Ph.D. Thesis, Montpellier, France. p. 375.

Dera, G., Pellenard, P., Neige, P., Deconinck, J.-F., 2009. Distribution of clay minerals in Early Jurassic Peritethyan seas: palaeoclimatic significance inferred from multiproxy comparisons. Palaeogeogr. Palaeoclimatol. Palaeoecol. 271, 39–51. https://doi.org/10.1016/j.palaeo.2008.09.010.

Dinis, P.A., Carvalho, J., Callapez, P.M., Mendes, M.M., Santos, V.F., Fernandes, P., 2020. Composition of Lower Cretaceous mudstones of the Algarve Basin and implications for Iberian paleoclimates. Cretac. Res. 110, 104404. https://doi.org/10.1016/j.cretres.2020.104404.

Do Campo, M., del Papa, C., Nieto, F., Hongn, F., Petrinovic, I., 2010. Integrated analysis for constraining palaeoclimatic and volcanic influences on clay-mineral assemblages in orogenic basins (Palaeogene Andean foreland, Northwestern Argentina). Sediment. Geol. 228, 98–112. https://doi.org/10.1016/j.sedgeo.2010.04.002.

Do Campo, M., Bauluz, B., del Papa, C., White, T., Yuste, A., Mayayo, M.J., 2018. Evidence of cyclic climatic changes recorded in clay mineral assemblages from a continental Paleocene-Eocene sequence, northwestern Argentina. Sediment. Geol. 368, 44–57. https://doi.org/10.1016/j.sedgeo.2018.03.007.

Ehrmann, W., Setti, M., Marinoni, L., 2005. Clay minerals in Cenozoic sediments off Cape Roberts (McMurdo Sound, Antarctica) reveal palaeoclimatic history. Palaeogeogr. Palaeoclimatol. Palaeoecol. 229, 187–211. https://doi.org/10.1016/j.palaeo.2005.06.022.

Faris, N., Ram, R., Tardio, J., Bhargava, S., Pownceby, M.I., 2019. Characterisation of a ferruginous rare earth beating lateritic ore and implications for rare earth mineral processing. Miner. Eng. 134, 23–36. https://doi.org/10.1016/j.mineng.2019.01.019.

Foos, A.M., 1991. Aluminous lateritic soils, Eleuthera, Bahamas: a modern analog to carbonate paleosols. J. Sediment. Petrol. 61 (3), 340–348.

Franceschelli, M., Puxeddu, M., Gattiglio, M., 2003. Geochemistry and origin of chloritoid schist from the Alpi Apuane, Italy: evidence of a prevailing lateritic signature. Eur. J. Mineral. 15, 575–588. https://doi.org/10.1127/0935-1221/2003/0015-0575.

Fregenal-Martínez, M.A., Meléndez, N., Muñoz-García, B., Elez, J., de la Horra, R., 2017. The stratigraphic record of the Late Jurassic-Early Cretaceous rifting in the Alto Tajo-Serranía de Cuenca region (Iberian Ranges, Spain): Genetic and structural evidences for a revision and a new lithostratigraphic proposal. Rev. Soc. Geol. Esp. 30, 113–142.

Giovannini, A.L., Bastos Neto, A.C., Porto, C.G., Pereira, V.P., Takehara, L., Barbanson, L., Bastos, P.H.S., 2017. Mineralogy and geochemistry of laterites from the Morro dos Seis Lagos Nb (Ti, REE) deposit (Amazonas, Brazil). Ore Geol. Rev. 88, 461–480. https://doi.org/10.1016/j.oregeorev.2017.05.008.

Guerrak, S., 1987. Metallogenesis of cratonic oolitic ironstone deposits in the Bled el Mass, Azzel Mani, Ahnet and Mouydir basins, Central Sahara. Geol. Rundsch. 76, 903–922. https://doi.org/10.1007/BF01821072.

Güven, N., 1988. Smectites. In: Bailey, S.W. (Ed.), Hydrous Pyllosilicates. Mineralogical Society of America, Reviews in Mineralogy 19, pp. 497–559.

Hay, W.W., 2008. Evolving ideas about the Cretaceous climate and ocean circulation. Cretac. Res. 29, 725–753. https://doi.org/10.1016/j.cretres.2008.05.025.

Haywood, A.M., Valdes, P.J., Markwick, P.J., 2004. Cretaceous (Wealden) climates: a modelling prospective. Cretac. Res. 25, 303–331. https://doi.org/10.1016/j.cretres.2004.01.005.

Hillier, S., 2003. Quantitative analysis of clay and other minerals in sandstones by X-ray powder diffraction (XRPD). International Association of Sedimentologists. Spec. Publ. 34, 213–251.

Martin, J.D., 2017. A software package for powder x-ray diffraction analysis. Qualitative, Quantitative and Microtexture 121.

Mendelovici, E., Yariv, S.H., Villalba, R., 1979. Iron-bearing kaolinite in venezuelan laterites: I. Infrared spectroscopy and chemical dissolution evidence. Clay Miner. 14, 323–331.

Mestdagh, M.M., Vielvoye, L., Herbillon, A.J., 1980. Iron in kaolinite: II. The relationships between kaolinite and iron content. Clay Miner. 15, 1–13. https://doi.org/10.1180/claymin.1980.015.1.01.

Molina, J.M., Salas, R., 1993. Bauxitas kársticas del Cretácico inferior en Fuentespalda (provincia de Teruel): estratigrafía, origen y paleogeografía. Cuad. Geol. Iber. 17, 207–230.

Moreno-Azanza, M., Canudo, J.I., Gasca, J.M., 2014. Spheroolithid eggshells in the Lower Cretaceous of Europe. Implications for eggshell evolution in ornithischian dinosaurs. Cretac. Res. 51, 75–87. https://doi.org/10.1016/j.cretres.2014.05.017.

Mücke, A., Badejoko, A., Akande, S.O., 1999. Petrographic-microchemical studies and origin of the Agbaja Phanerozoic Ironstone Formation, Nupe Basin, Nigeria: a product of a ferruginized ooidal kaolin precursor not identical to the Minette-type. Mineral. Deposita 34, 284–296.

Murakami, T., Isobe, H., Sato, T., Ohnuki, T., 1996. Weathering of chlorite in a quartz-chlorite schist. Mineralogical and chemical changes. Clay Clay Miner. 44, 244–256.

Mutterlose, J., Bodin, S., Fähnrich, L., 2014. Strontium-isotope stratigraphy of the Early Cretaceous (Valanginian-Barremian): Implications for Boreal–Tethys correlation and paleoclimate. Cretac. Res. 50, 252–263. https://doi.org/10.1016/j.cretres.2014.03.027.

Ordóñez, S., Fort, R., Bustillo, M., 1990. Estudio de las tierras raras en las bauxitas kársticas del noreste de la península ibérica. Estud. Geol. 46, 373–384.

Price, G.D., Főzy, I., Janssen, N.M.M., Pálfy, J., 2011. Late Valanginian-Barremian (Early Cretaceous) palaeotemperatures inferred from belemnite stable isotope and Mg/Ca ratios Bersek Quarry (Gerecse Mountains, Transdanubian Range, Hungary). Palaeogeogr. Palaeoclimatol. Palaeoecol. 305, 1–9. https://doi.org/10.1016/j.palaeo.2011.02.007.

Pucéat, E., Lécuyer, C., Sheppard, S.M.F., Dromart, G., Reboulet, S., Grandjean, P., 2003. Thermal evolution of Cretaceous Tehtyan marine waters inferred from oxygen iso-

tope composition of fish tooth enamels. Palaeogeogr. Palaeoclimatol. 18 (2), 1–12. https://doi.org/10.1029/2002PA000823.
Pucéat, E., Lecuyer, C., Reisber, L., 2005. Neodymium isotope evolution of NW Tethyan upper ocean waters throughout the Cretaceous. Earth Planet. Sci. Lett. 236, 705–720. https://doi.org/10.1016/j.epsl.2005.03.015.
Raucskik, B., Varga, A., 2008. Climato-environmental controls on clay mineralogy of the Hettangian-Bajocian successions of the Mecsek Mountains, Hungary: an evidence for extreme continental weathering during the early Toarcian oceanic anoxic event. Palaeogeogr. Palaeoclimatol. Palaeoecol. 265, 1–13. https://doi.org/10.1016/j.palaeo.2008.02.004.
Reinhardt, N., Proenza, J.A., Villanova-de-Benavent, C., Aiglsperger, T., Bover-Arnal, T., Torró, L., Salas, R., Dziggel, A., 2018. Geochemistry and mineralogy of rare earth elements (REE) in Bauxitic Ores of the Catalan Coastal Range, NE Spain. Minerals 8 (12), 562. https://doi.org/10.3390/min8120562.
Righi, D., Meunier, A., 1995. Origin of clays by rock weathering and soil formation. In: Velde, B. (Ed.), Origin and Mineralogy of Clays: Clays and the Environment. Springer-Verlag, Heidelberg , p. 43 161. https://doi.org/10.1007/978-3-662-12648-6_3.
Rodríguez-López, J.P., de Boer, P.L., Meléndez, N., Soria, A.R., Pardo, G., 2006. Windblown desert sands in coeval shallow marine deposits: a key for the recognition of coastal ergs in the mid-Cretaceous Iberian Basin, Spain. Terra Nova 18, 314–320. https://doi.org/10.1111/j.1365-3121.2006.00695.x.
Rossi, C., Cañaveras, J.C., 1999. Pseudospherulitic fibrous calcite in paleo-groundwater, unconformity-related diagenetic carbonates (Paleocene of the Ager basin and Miocene of the Madrid basin, Spain). J. Sediment. Res. 69, 224–238. https://doi.org/10.2110/jsr.69.224.
Salas, R., 1987. El Malm y el Cretaci Inferior Entre el Massis de Garrafi la Serra d'Espada. Ph.D. Thesis. University of Barcelona, Spain, p. 345.
Salas, R., Guimerà, J., Mas, R., Martín-Closas, C., Meléndez, A. y Alonso, A., 2001. Evolution of the Mesozoic central Iberian Rift System and its Cainozoic inversion (Iberian chain). Peri-Tethys Memoirs 6, 145–185.
Salas, R., Vaquer, R., Travé, A., 2004. Bauxitas kársticas y arcillas lateríticas barremienses de la Cadena Ibérica oriental y la Cadena Costero Catalana: Relaciones genéticas y áreas de procedencia. Geo-Temas 6, 123–126.
Sayed, E., Youssef, A.A., 1996. Sedimentaological studies on the central Wadi Kalabsha kaolin deposits, Southwest of Aswan, Egypy. J. Mineral. Petrol. Econ. Geol. 91, 353–363.
Schellmann, W., 1981. Considerations on the definition and classification of laterites. Proceedings of the International Seminar on Lateritisation Processes, Trivandrum, India. A.A. Balkema, Rotterdam, pp. 1–10.
Schultz, L.G., 1964. Quantitative interpretation of mineralogical composition from X-ray and chemical data for the Pierre shale. USGS Professional Paper 391-C, 1–131.
Seranne, M., Marchand, E., Bruguier, O., Husson, E., Vinches, M., 2019. New U-Pb zircon-dating constraints on the age and origin of allochthonous bauxite deposits of Languedoc (Southern France): geodynamic consequences. Geophys. Res. Abstr. 21 EGU General Assembly 2019.
Sheldon, N.D., Tabor, N.J., 2009. Quantitative paleoenvironmental and paleoclimatic reconstruction using paleosols. Earth Sci. Rev. 95, 1–52. https://doi.org/10.1016/j.earscirev.2009.03.004.
Singh, B., Gilkes, R.J., 1991. A potassium-rich beidellite from a laterite pallid zone in western Australia. Clay Miner. 26, 233–244.
Smith, D.K., Johnson Jr., G.G., 2000. Digitized database quantification, DDBQ, analysis of complex mixtures using fully digitized patterns. Adv. X-ray Anal. 42, 276–286.
Steuber, T., Rauch, M., Masse, J.P., Graaf, J., Malkoc, M., 2005. Low-latitude seasonality of cretaceous temperatures in warm and cold episodes. Nature 437 (27), 1341–1344. https://doi.org/10.1038/nature04096.
Szamatek, K., Barczuk, A., Youssed, E.A.A., 1993. Genesis and mineralogy of lateritic kaolin at Aswan area (Sw Egypt). Arch. Mineral. 2, 81–97.
Taylor, G., Eggleton, R.A., Foster, L.D., Tilley, D.B. Le Gleuher, M., Morgan, C.M., 2008. Nature of the Weipa Bauxite deposit, northern Australia. Aust. J. Earth Sci. 55, 45–70. https://doi.org/10.1080/08120090802438241.
Thiry, M., 2000. Palaeoclimatic interpretation of clay minerals in marine deposits: an outlook from the continental origin. Earth Sci. Rev. 49, 201–221. https://doi.org/10.1016/S0012-8252(99)00054-9.
Valeton, J., 1972. Bauxites. Elsevier, Amsterdam, p. 226.
Van Wees, J.D., Arche, A., Beijdorff, C.G., López-Gómez, J., 1998. Temporal and spatial variations in tectonic subsidence in the Iberian Basin (eastern Spain): inferences from automated forward modelling of high-resolution stratigraphy (Permian–Mesozoic). Tectonophysics 300, 285–310. https://doi.org/10.1016/S0040-1951(98)00244-3.
Varela, A.N., Raigemborn, M.S., Richiano, S., White, T., Poiré, A.G., Lizzoli, S., 2018. Late cretaceous paleosols as paleoclimate proxies of high-latitude Southern Hemisphere: Mata Amarilla Formation, Patagonia, Argentina. Sediment. Geol. 363, 83–95. https://doi.org/10.1016/j.sedgeo.2017.11.001.
Velasco, F., Herrero, J.M., Suárez, S., Yusta, I., Alvaro, A., Tornos, F., 2013. Supergene features and evolution of gossans capping massive sulphide deposits in the Iberian Pyrite Belt. Ore Geol. Rev. 53, 181–203. https://doi.org/10.1016/j.oregeorev.2013.01.008.
Velde, B., 1995. Origin and mineralogy of clays. Clays and the Environment. Springer-Verlag, Berlin. Heidelberg New York, p. 334.
Wright, V.P., Taylor, K.G., Beck, V.H., 2000. The paleohydrology of Lower Cretaceous seasonal wetlands, Isle of Wight, Southern England. J. Sediment. Res. 70, 619–632.
Yuste, A., Bauluz, B., Mayayo, M.J., 2015. Genesis and mineral transformations in Lower Cretaceous karst bauxites (NE Spain): climatic influence and superimposed processes. Geol. J. 50, 839–857. https://doi.org/10.1002/gj.2604.
Yuste, A., Bauluz, B., Mayayo, M.J., 2017. Origin and geochemical evolution from ferrallitized Clays to karst bauxite: an example from the Lower Cretaceous of NE Spain. Ore Geol. Rev. 84, 67–69. https://doi.org/10.1016/j.oregeorev.2016.12.025.

ANNEX III

Journal of Iberian Geology (2022) 48:45–63
https://doi.org/10.1007/s41513-021-00181-0

RESEARCH PAPER

Weathering events recorded in uppermost Hauterivian–lower Barremian clay-dominated continental successions from the NW Iberian Range: climatic vs. tectonic controls

Elisa Laita[1] · Blanca Bauluz[1] · Marcos Aurell[1] · Beatriz Bádenas[1] · Alfonso Yuste[1]

Received: 3 September 2021 / Accepted: 15 November 2021 / Published online: 1 December 2021

Abstract
The facies and clay mineral study of clay/marl-rich levels from the Torrelapaja Formation (latest Hauterivian–early Barremian, NW Iberian Range, NE Spain) allowed to establish the palaeoclimatic and palaeoenvironmental conditions under they were generated. The muddy levels and pisoids contained therein of two logs were sampled and studied by X-ray diffraction and optical and electron microscopy. A similar mineralogical upwards trend is recorded in both logs, with a decrease in calcite coupled with an increase in quartz and orthoclase content and constant proportions in goethite, hematite, diaspore, anatase, rutile, ilmenite, and clay mineral content. The lower muddy levels have higher kaolinite content than the upper levels, where illitic phases are the dominant clay minerals. Smectite and intergrowths of illitic phases and kaolinite are also detected upwards. The kaolinite and smectite textures indicate an authigenic origin, whereas the illitic phases are former phases acting as a substrate for kaolinite crystallization. Pisoids mineralogy and texture show an in-situ origin, but some are fractured, indicating reworking processes. The mineral association found in the muddy levels is characteristic of oxisols formed under warm and humid conditions. The upward decrease in kaolinite content is coeval with an increase in the illitic phases and quartz content, related to siliciclastic input, but is also coeval with the presence of authigenic smectite. This indicates a decrease in chemical weathering, not fully registered due to the siliciclastic contribution, which was possibly associated with a change to colder, drier conditions during the latest Hauterivian–early Barremian in the studied area.

Keywords Illitic phases · Kaolinite · Palaeoclimate · Palaeosols · Weathering

Eventos de meteorización registrados en sucesiones continentales arcillosas del Hauteriviense superior-Barremiense inferior del NW de la Cordillera Ibérica: control climático vs. tectónico

Resumen
El estudio de facies y minerales de la arcilla de nieles de arcillas/margas de la Formación Torrelapaja (Hauteriviense superior–Barremiense inferior, NW Cordillera Ibérica, NE España) ha permitido establecer el paleoclima y el paleoambiente bajo las que se formaron. Se muestrearon y estudiaron por difracción de rayos X y microscopía óptica y electrónica los niveles de arcillas/margas y los pisoides que contienen dos afloramientos. Se observa una tendencia mineralógica similar hacia el techo en ambos afloramientos, con un descenso en el contenido en calcita junto a un aumento del de cuarzo y ortoclasa y proporciones constantes de goethita, hematites, diásporo, anatasa, rutilo, ilmenita y minerales de la arcilla. Los niveles inferiores tienen mayor contenido en caolinita que los niveles superiores, en los que las fases illíticas son los minerales de la arcilla

✉ Elisa Laita
laita@unizar.es

[1] IUCA-Department of Earth Sciences, Faculty of Sciences, Universidad de Zaragoza, Pedro Cerbuna 12, 50009 Zaragoza, Spain

dominante. Hacia el techo se detectan esmectita e interestratificados de fases illíticas y caolinita. La textura de la caolinita y la esmectita indican un origen autigénico, mientras que las fases illíticas son fases previas que actúan como substrato para la cristalización de la caolinita. La mineralogía y textura de los pisoides indican un origen in-situ, pero algunos están fracturados, indicando procesos de retrabajamiento. La asociación mineral presente en los niveles inferiores es características de oxisoles, formados bajo condiciones climáticas cálidas y húmedas. El descenso del contenido en caolinita hacia techo es coetáneo con el aumento en el contenido en fases illíticas y cuarzo, relacionado con el aporte de detríticos, pero también es coetáneo con la presencia de esmectita autigénica. Esto indica una disminución en la meteorización química, no completamente registrada debido al aporte detrítico, que posiblemente se asocie con un cambio hacia condiciones más frías y secas durante el Hauteriviense superior–Barremiense inferior en el área estudiada.

Palabras clave Caolinita · Fases illíticas · Meteorización · Paleoclima · Paleosuelos

1 Introduction

The study of the soils that formed in the landscapes of the past (i.e., palaeosols) provides key data for palaeoclimatic and palaeoenvironmental reconstructions (Mack et al., 1993). The formation of soils takes place near the Earth's surface in the contact among lithosphere, atmosphere, hydrosphere, and biosphere (Tabor et al., 2017), and the weathering processes that generate them are subject to strong climatic control. For this reason, the study of the mineral phases formed during soil formation, such as clay minerals and oxides, is of great interest, since they directly provide information about the climate and environment (Chamley, 1989; Do Campo et al., 2018; Laita et al., 2020; Sheldon & Tabor, 2009; Varela et al., 2018).

In this way, the variations in the clay mineral assemblages have been used as palaeoclimatic and palaeoenvironmental proxies for palaeosols developed in continental sequences. Those of Mesozoic sequences have been described by several authors (e.g., Bauluz et al., 2014; Do Campo et al., 2010, 2018; Ehrmann et al., 2005; Föllmi, 2012; Laita et al., 2020; Raucskik & Varga, 2008 and references therein).

Under humid subtropical to tropical conditions, intense chemical weathering produces very effective hydrolysis, which gives rise to oxisols (commonly known as laterites), where kaolinite is the main clay mineral along with aluminium hydroxides and Fe oxyhydroxides (Chamley, 1989; Do Campo et al., 2018; Mack et al., 1993; Righi & Meunier, 1995; Velde, 1995). By contrast, under dry and cold climates, the production of clay minerals depends on physical weathering because of the absence of significant hydrolysis (Chamley, 1989). These conditions enhance the genesis of gleysols, where the clay mineral assemblages are essentially dominated by smectite and illite (Dhillon & Dhillon, 1991; Do Campo et al., 2018). Gleysols are formed under dysoxic or anoxic conditions that give rise to redoximorphic features and gleyed horizons generated by the influence of the shallow or fluctuating groundwater table, which inhibits drainage and creates low-oxygen conditions (Tabor et al., 2017).

In Western Europe, the presence of ferruginous palaeosols including kaolinite indicates warm and humid conditions during the late Hauterivian–early Barremian (Bárdossy, 1982; Föllmi, 2012; Wright et al., 2000). On the other hand, Haywood et. al. (2004) have described an alternation of wet and dry seasons during the early Barremian in the west of Europe.

Within the Iberian Plate, a seasonal subtropical climate has been described during the Lower Cretaceous in the Iberian Range (NE Spain) (Bauluz et al., 2014; Buscalioni & Fregenal-Martínez, 2010). This climate is evidenced by the presence of kaolinite-rich clays, bauxites, and lateritic clays in several areas of the Iberian Plate (Bauluz et al., 2014; Combes, 1990; Laita et al., 2020; Molina & Salas, 1993; Yuste et al., 2015, 2017, 2020). By contrast, Laita et. al. (2020) also pointed out a change from warm/humid to cold/dry conditions in Barremian continental successions from the NW Maestrazgo Basin (SE Iberian Range), which are age-equivalent with some of the palaeosols levels studied in this work.

Usually, clay-rich sediments, rocks, and palaeosols include authigenic clay minerals, but they may also contain diagenetic clays. This must be borne in mind when using clay mineral assemblages as palaeoclimatic and palaeoenvironmental indicators, since diagenetic processes may transform clay minerals and invalidate their use as palaeoclimatic proxies (Bauluz et al., 2014; Dera et al., 2009). To evaluate the origin of the clays and rule out a possible diagenetic imprint, it is necessary to carry out thorough microtextural studies.

Considering all the above mentioned, this study applies a combination of facies analysis and the study of the clay mineralogy of clay/marl-rich outcrops of uppermost Hauterivian–lower Barremian continental successions located in the Torrelapaja subbasin (NE Spain) to evaluate their usefulness as a palaeoclimate indicator. The main aims of this research are: (1) to determine whether the clay minerals are authigenic, as a consequence of the edaphic process, detrital (inherited from the source area), or diagenetic; and (2) to examine the vertical and lateral variations in the clay mineralogy and their relationships with the palaeoenvironmental conditions, or other controlling factors, to deduce the palaeoclimate during the latest Hauterivian–early Barremian in this area of the Iberian Range (NE Spain).

2 Geological setting

2.1 Stratigraphic context

The progressive opening of the Atlantic Ocean and the westward propagation of the Tethys Ocean during the Late Jurassic-Early Cretaceous generated a rifting process in the Iberian Basin located in the eastern part of the Iberian Plate (e.g., Salas et al., 2001). The resulting extensional fault activity gave rise to the compartmentalization of the Basin into a set of subsident basins, subbasins and troughs (Aurell, Bádenas, et al., 2019a; Aurell, Fregenal-Martínez, et al., 2019b; Liesa et al., 2019). One of these subsiding basins was the Cameros Basin, a wide Late Jurassic–Early Cretaceous sedimentary domain located in the northwestern part of this rifting system, in the northwestern Iberian Range (Fig. 1a) (e.g., Casas-Sainz, 1993; Clemente, 2010; Gómez-Fernández & Meléndez, 1994; Mas et al., 2004, 2019). The high subsidence rates recorded in this basin during the Late Jurassic-Early Cretaceous rifting episode allowed the accumulation of more than 8000 m of continental and coastal sediments in its depocentral areas (Casas-Sainz et al., 2009).

The uppermost Hauterivian–lower Barremian succession studied here accumulated in the so-called Torrelapaja subbasin, located at the southeastern edge of the Cameros Basin (Fig. 1b). In this area, the Upper Jurassic–Lower Cretaceous synrift sedimentary record encompasses a 100–500 m-thick, terrigenous, calcareous succession that is divided into three synrift sequences (SS-1, SS-2,

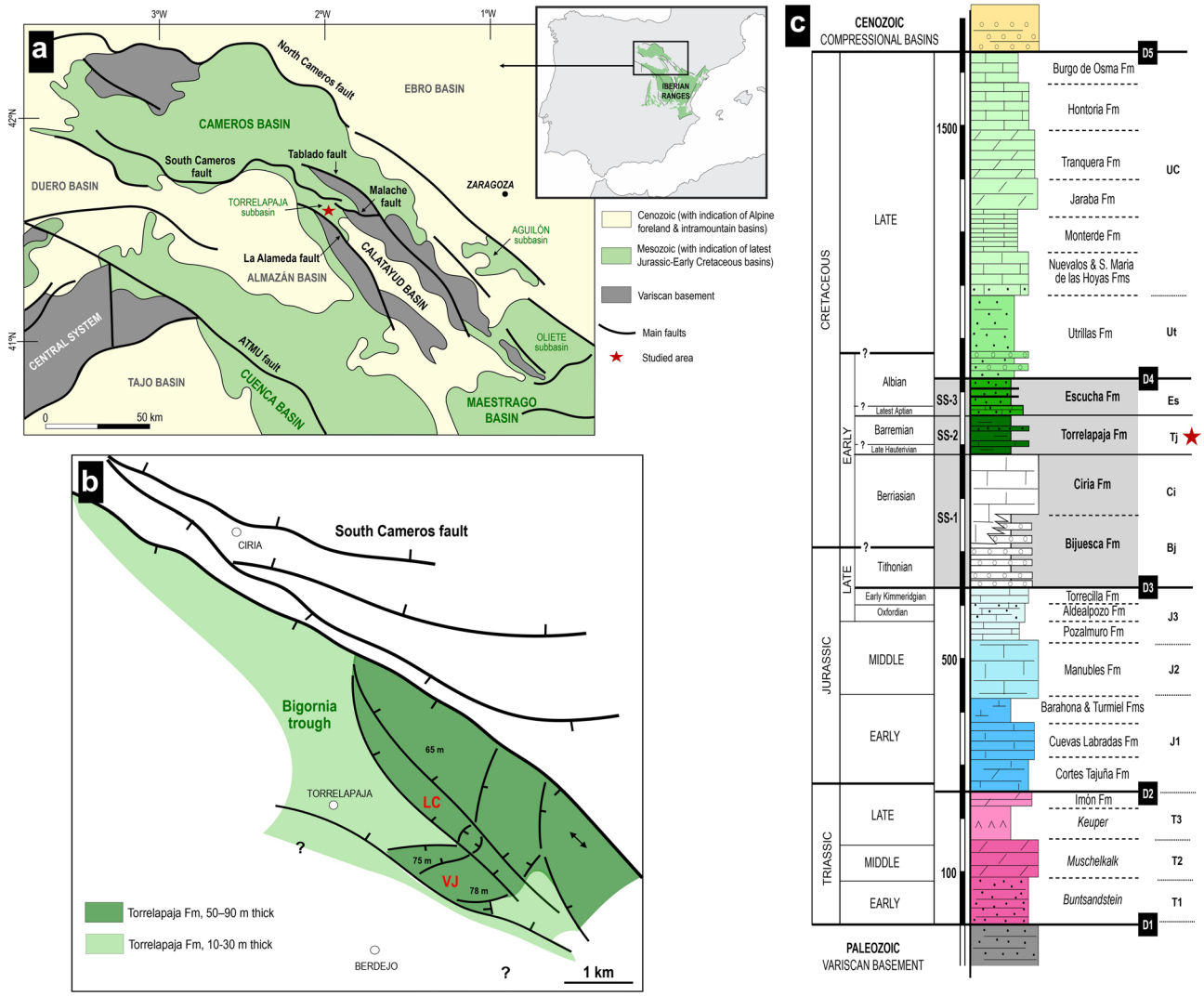

Fig. 1 **a** Geological location of the studied Torrelapaja subbasin at the SE edge of the Cameros Basin (slightly modified from Aurell et al., 2021); **b** Reconstruction of the sedimentation area during synrift sequence 2, showing the location of the studied logs (slightly modified from Aurell et al., 2021); **c** Summary of the Mesozoic sedimentary units indicating the distribution of the Lower Cretaceous synrift sequences in grey. The red star indicates the studied unit (slightly modified from Aurell et al., 2021)

and SS-3 in Fig. 1c; Aurell et al., 2021). SS-1 (middle Tithonian–middle Berriasian) is composed of continental deposits, including the terrigenous alluvial deposits of the Bijuesca Formation and the lacustrine-palustrine carbonates of the Ciria Formation. SS-2 (uppermost Hauterivian–lower Barremian) includes the continental mixed (terrigenous-carbonate) Torrelapaja Formation. SS-3 (middle–upper Albian) corresponds to the Escucha Formation and includes terrigenous-carbonate continental to coastal successions (Aurell et al., 2021).

The continental Torrelapaja Fm (SS-2), studied in this work, is an up-to-80 m-thick succession of muddy facies, limestones, sandstones, and conglomerates that accumulated preferentially in the so-called Bigornia Trough of the Torrelapaja subbasin (Fig. 1 and 2). The latest Hauterivian–early Barremian age of this unit was dated based on the presence of charophytes (Aurell et al., 2021; Martín-Closas, 1989). The boundary with the underlying Ciria Formation is a major angular unconformity, which is associated with a stratigraphic gap that encompasses the late Berriasian, the Valanginian and most of the Hauterivian. An irregular karstic surface is observed on top of the lacustrine limestones of the Ciria Formation. This occasionally presents multiepisodic filling, allowing the preservation of a rich assemblage of vertebrate remains (Aurell et al., 2021).

2.2 Sedimentological context

A facies analysis of the continental Torrelapaja Fm in the Bigornia Trough was performed by Aurell et. al. (2021),

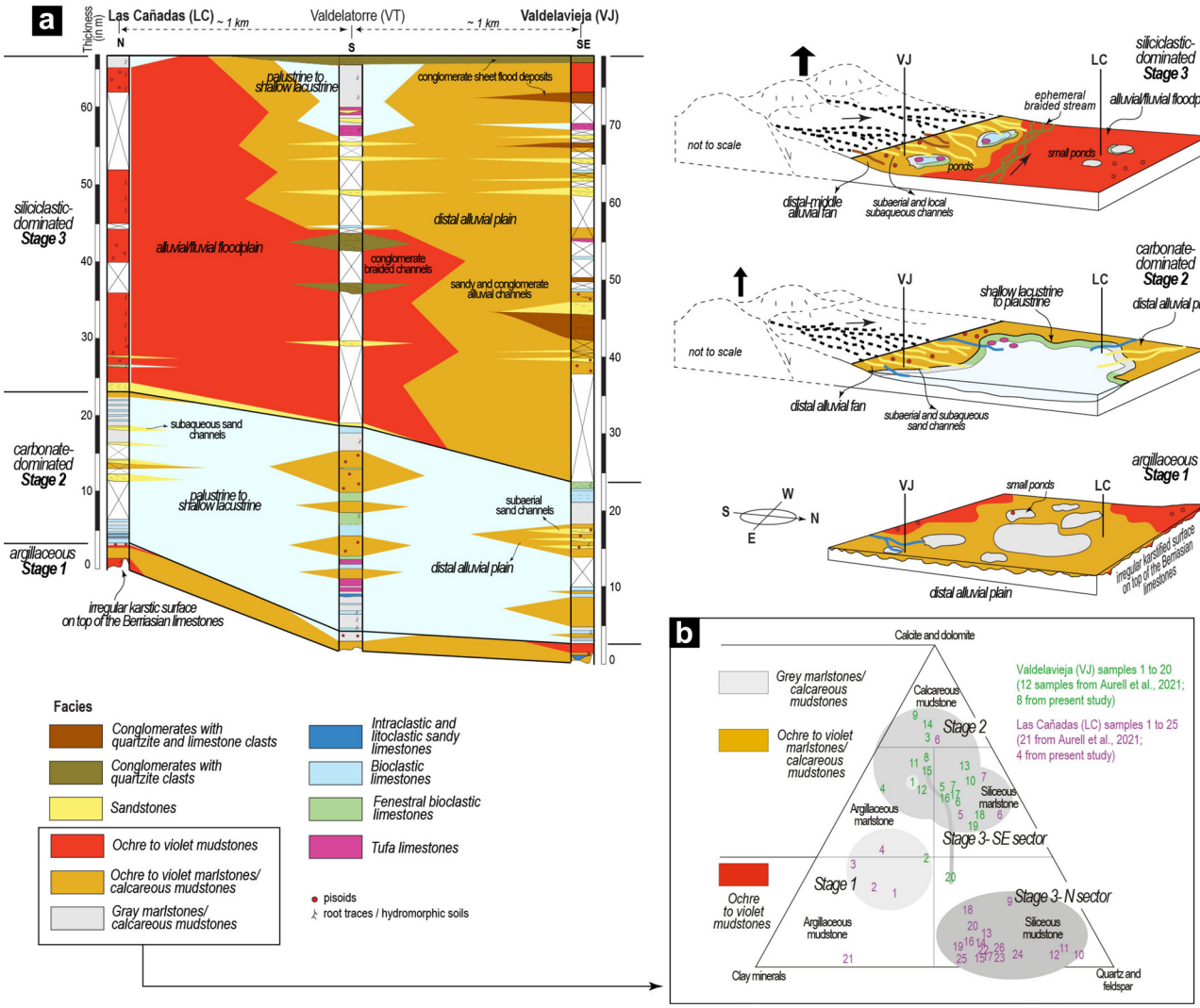

Fig. 2 **a** Facies correlation of the Torrelapaja Fm (SS-2) in the Bigornia Trough and sedimentary models of the three stages differentiated (adapted from Aurell et al., 2021). The detailed facies distribution recognized by Aurell et. al. (2021) in the Las Cañadas and Valdelavieja logs studied here is included in Fig. 5; **b** Mineralogical composition of muddy facies following the classification of Allix et. al. (2011)

based on the data collected in three logs (the LC, VT and VJ logs in Fig. 2a). The deposition of the muddy facies, limestones, sandstones, and conglomerates of this unit took place in distal alluvial fans and shallow lakes. The vertical and lateral distribution of facies allowed three sedimentary stages of evolution to be differentiated (Fig. 2a). The argillaceous Stage 1 corresponds to the sedimentary filling of the palaeokarstic surface on top of the underlying Ciria Fm (SS-1/SS-2 boundary) and is dominated by ochre to violet mudstones and ochre to violet mudstones/calcareous mudstones of argillaceous composition (Fig. 2b). The carbonate-dominated Stage 2 is characterized by the expansion of palustrine-lacustrine facies, localized alluvial clastic input (sandstones), and the deposition of carbonate-richer distal plain muddy facies (marlstone/calcareous mudstones; Fig. 2b). In the siliciclastic-dominated Stage 3, there is a significant increase in siliciclastic and a reduction in lacustrine-palustrine areas. Middle-distal alluvial fan channels (conglomerates with quartzite and limestone clasts, sandstones, and ochre to violet siliceous marlstones) developed southwards as a result of the increasing tectonic activity of this margin (Fig. 2a); by contrast, the northern area was dominated by an alluvial-fluvial plain with ochre to violet mudstones of siliceous composition and ephemeral braided streams (conglomerates with quartzite pebbles).

Of particular interest for the present study are the muddy facies recorded mainly in distal alluvial plains (Fig. 2b). The ochre to violet mudstones and ochre to violet marlstones/calcareous mudstones that accumulated in the distal alluvial plains have features indicating soil development (levels with Fe pisoids and root traces/hydromorphic horizons) and are similar to those found in lateritic palaeosols in age-equivalent units from the southern Maestrazgo Basin (Laita et al., 2020). The palustrine to shallow lacustrine grey marlstones/calcareous mudstones also contain Fe pisoids, which could be reworked from nearby distal alluvial plain areas (Aurell et al., 2021).

3 Samples and methods

The Las Cañadas (LC) and Valdelavieja (VJ) outcrops of the Torrelapaja Fm, previously studied by Aurell et. al. (2021) from a stratigraphic and sedimentological point of view, were selected for the sampling of the different muddy facies (Fig. 2b). They include ochre to violet mudstones, ochre to violet marlstones/calcareous mudstones, and grey marlstones/calcareous mudstones (hereinafter referred to as mudstones to calcareous mudstones), and some of them contain Fe pisoids (Fig. 3). On the whole, the VJ log represents deposition in a more proximal position of the distal alluvial plain compared to the LC log (Fig. 2a). A total of 49 samples (42 mudstone to calcareous mudstone samples and 7 Fe pisoids) were taken from throughout the two sections in order to analyse their texture and mineralogical composition (Table 1).

3.1 X-ray diffraction study

The 49 samples were studied by X-ray diffraction (XRD) to determine their mineralogical composition. The < 2 µm fractions were extracted by centrifugation and analysed in air-dried and ethylene–glycol-treated oriented aggregates to determine the clay minerals present in the samples.

To obtain the diffraction patterns, a Philips 1710 diffractometer was used at the University of Zaragoza (Zaragoza, Spain), with 40 kV voltage, 30 mA current, CuKα radiation, an automatic slit, and a graphite monochromator. The XRD patterns were acquired from 3 to 60 °C 2θ for the whole rock samples and from 3 to 30 °C for the < 2 µm fractions. In both cases, the goniometer velocity was 0.1º2θ/s and the integration time was 0.45 s. The recording was made with XPowderX software (Martin, 2017).

The relative proportions of the minerals were calculated using Reference Intensity Ratio (RIR) values from the literature (Biscaye, 1965; Schultz, 1964; Smith & Johnson, 2000). These RIR values were calculated in accordance with Hillier (2003). The kaolinite crystallinity (KC) was calculated measuring the full width at half maximum of the 001 reflection corresponding to 7 Å in the air-dried oriented aggregates. KC values are inversely related to kaolinite crystallinity, that is, the lower the KC value, the higher the kaolinite crystallinity.

3.2 Optical and electron microscopy study

To gain a precise mineralogical and textural characterization of the samples, seven thin sections of the mudstones to calcareous mudstones and Fe pisoids were selected for microscopy studies. Firstly, the thin sections were studied by transmitted and reflected light microscopy to identify both transparent and opaque minerals and to characterize their texture (Table 1). The seven thin sections and four rock fragments were then analysed using a Carl Zeiss Merlin field emission scanning electron microscope (FESEM) with an Oxford energy-dispersive X-ray (EDS) detector at the University of Zaragoza (Zaragoza, Spain) (Table 1). The thin sections had previously been carbon-coated. Compositional images were obtained using two detectors: an angular selective backscattered electron detector (AsB) and an energy selective backscattered electron detector (EsB). To obtain chemical information, semi-quantitative analyses were performed by energy-dispersive X-ray spectroscopy (EDS), with a detection limit of 0.1%. The accelerating voltage for the AsB and the EDS was 15 kV

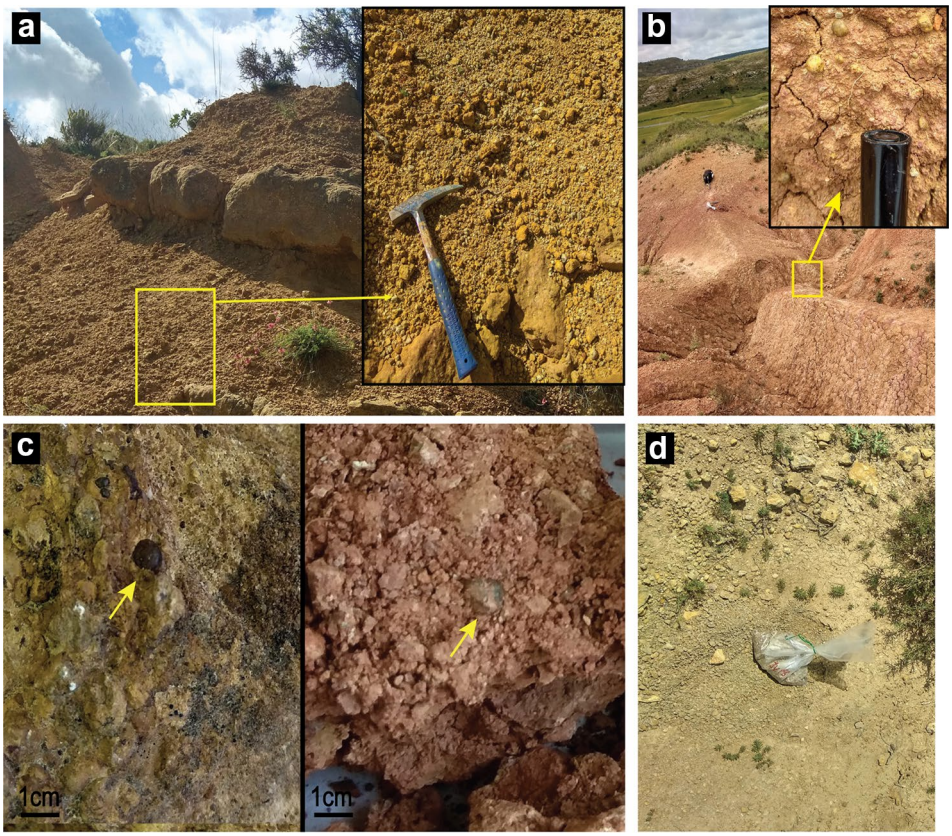

Fig. 3 **a** Close view of the VJ log showing ochre to violet mudstones interbedded with sandstones levels; **b** Close view of the LC log showing the ochre to violet mudstones; **c** Hand samples from the VJ (left) and LC (right) logs including Fe pisoids; **d** Close view of the VJ log showing the the grey marlstones/calcareous mudstones

with a beam current of 600 pA, whereas for the EsB, the accelerating voltage was 4 kV with a beam current of 1000 pA. Morphological images of the rock fragments were obtained using a secondary electron (SE) detector (in-lens) with an accelerating voltage of 5 kV and a beam current of 100 pA. In this case, the accelerating voltage was 5 kV with a beam current of 800 pA.

Table 1 Summary of sample analyses at the laboratory (n = number of samples/analyses)

Field samples (n = 49)	X-ray diffraction (Mineralogical composition)		Optical and electron microscopy (Textural and chemical analysis)	
	Whole rock (n = 49)	< 2 µm fraction of clays & clays/marls (n = 42)	Optical microscopy (n = 7)	Electron microscopy-FESEM/EDS (n = 11)
Ochre to violet clays/marls (n = 36)	36	36	5	9
Grey marls- (n = 6)	6	6	–	–
Ferruginous pisoids-7	7	–	2	2
	Relative proportions of the mineral phases	Clay minerals identification Kaolinite crystallinity	Textures Identification of opaque and transparent minerals	Micro- and nanotextures Chemical composition of the phases
	Derived data			

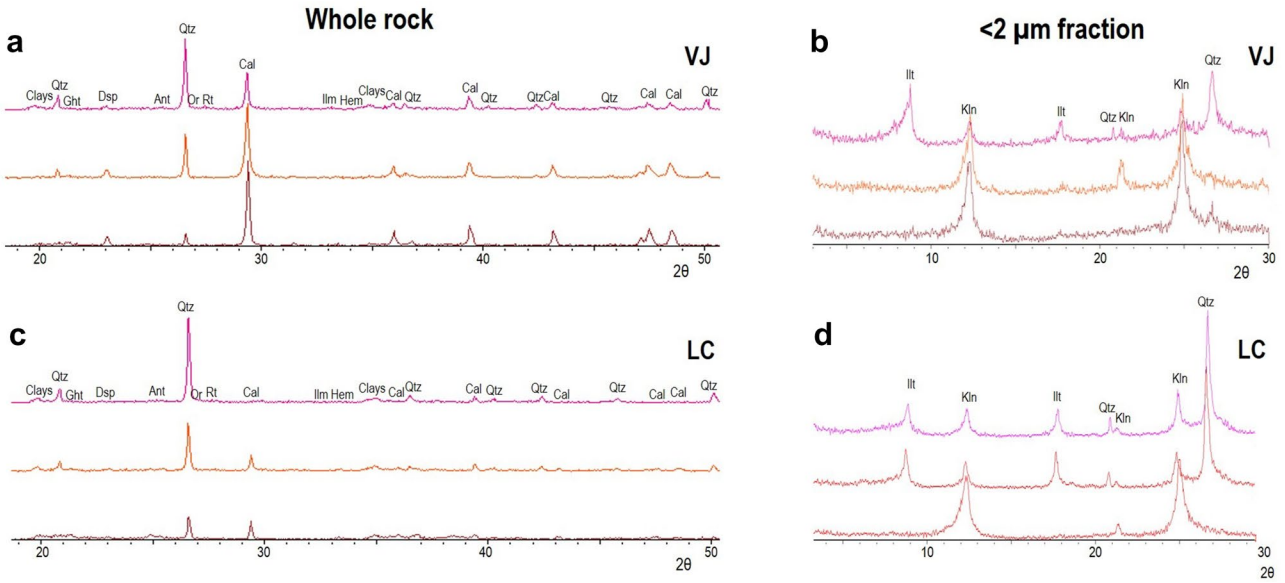

Fig. 4 XRD patterns obtained from the whole rock and < 2 µm fractions of samples in the VJ (**a** and **b**) and LC (**c** and **d**) logs. *Clays* = clay minerals, *Qtz* = quartz, *Cal* = calcite, *Dsp* = diaspore, *Ght* = goethite, *Ant*=anatase, *Or* = orthoclase, *Rt* = rutile, *Ilm* = ilmenite, *Hem* = hematite, *Kln* = kaolinite, *Ilt* = illitic phases

4 Results

4.1 Whole rock data

4.1.1 XRD data

The mudstones to calcareous mudstone of the LC and VJ logs are mainly formed by quartz, calcite, and clay minerals together with orthoclase, goethite, hematite, diaspore, anatase, rutile and ilmenite (Fig. 4). The XRD patterns of the whole rock show the same differences from bottom to top in both logs, with an increase in the intensity of quartz peaks and a decrease in those of calcite (Fig. 4a and c).

In the < 2 µm fraction, abundant kaolinite and illitic phases are identified in the XRD patterns (Fig. 4b and d). Characteristic reflections of kaolinite are observed at 7.14, 4.18, 3.84, 3.57 Å, and dickite and nacrite have not been detected. The term "illitic phases" includes both illite and micas (quantified together) as well as accessory random mixed-layer illite/smectite (I/S), which were identified in some of the < 2 µm fraction XRD patterns (but not quantified). These XRD patterns show a decrease in the intensity of kaolinite peaks to the top and that the illitic phases are detected from middle to top in both logs (Fig. 4b and d).

The whole rock mineralogical composition varies both vertically and laterally (Fig. 5a). On the whole, calcite is more abundant in the proximal VJ log (28–70%), whereas quartz + orthoclase predominate in the distal LC log (8–88%). In general, the calcite content decreases and quartz + orthoclase are more abundant towards the top of the logs. Clay minerals and goethite, hematite, diaspore, anatase, rutile, and ilmenite remain quite constant from the bottom to the top of the stratigraphic profiles. However, in detail there are slight vertical trends related to sedimentary stages 1 to 3. In the argillaceous Stage 1, the main lateral difference is the higher relative abundance of calcite in the proximal VJ log, and of clay minerals in the distal LC log. As regards the carbonate-dominated Stage 2, despite the presence of covered intervals (not sampled) in LC, a quite similar mineralogy dominated by calcite is recorded in both sections. The main lateral differences are recorded in the siliciclastic Stage 3, the proximal VJ log being dominated by calcite (with an upward decreasing trend), whereas in the distal LC log calcite is almost absent, especially at the top of the log, and quartz + orthoclase and clay minerals are more abundant compared to in VJ.

As regards the < 2 µm fraction, kaolinite is the main clay mineral in the lower mudstone to calcareous mudstone levels (> 50%), but its content decreases upwards coeval with an increase in the content of illitic phases. More specifically, samples of the argillaceous Stage 1 are only formed by kaolinite in the proximal VJ log but also have illitic phases in the distal LC log. In the carbonate-dominated Stage 2, kaolinite is again the main clay in the proximal VJ log, whereas in the distal LC log illitic phases predominate. This predominance of illitic phases is observed in both sections in the siliciclastic-dominated Stage 3, with a particularly notable upward increase in the proximal VJ log.

Kaolinite crystallinity is shown in Fig. 5b and in Table 2. In the argillaceous Stage 1, in the distal LC log (with its

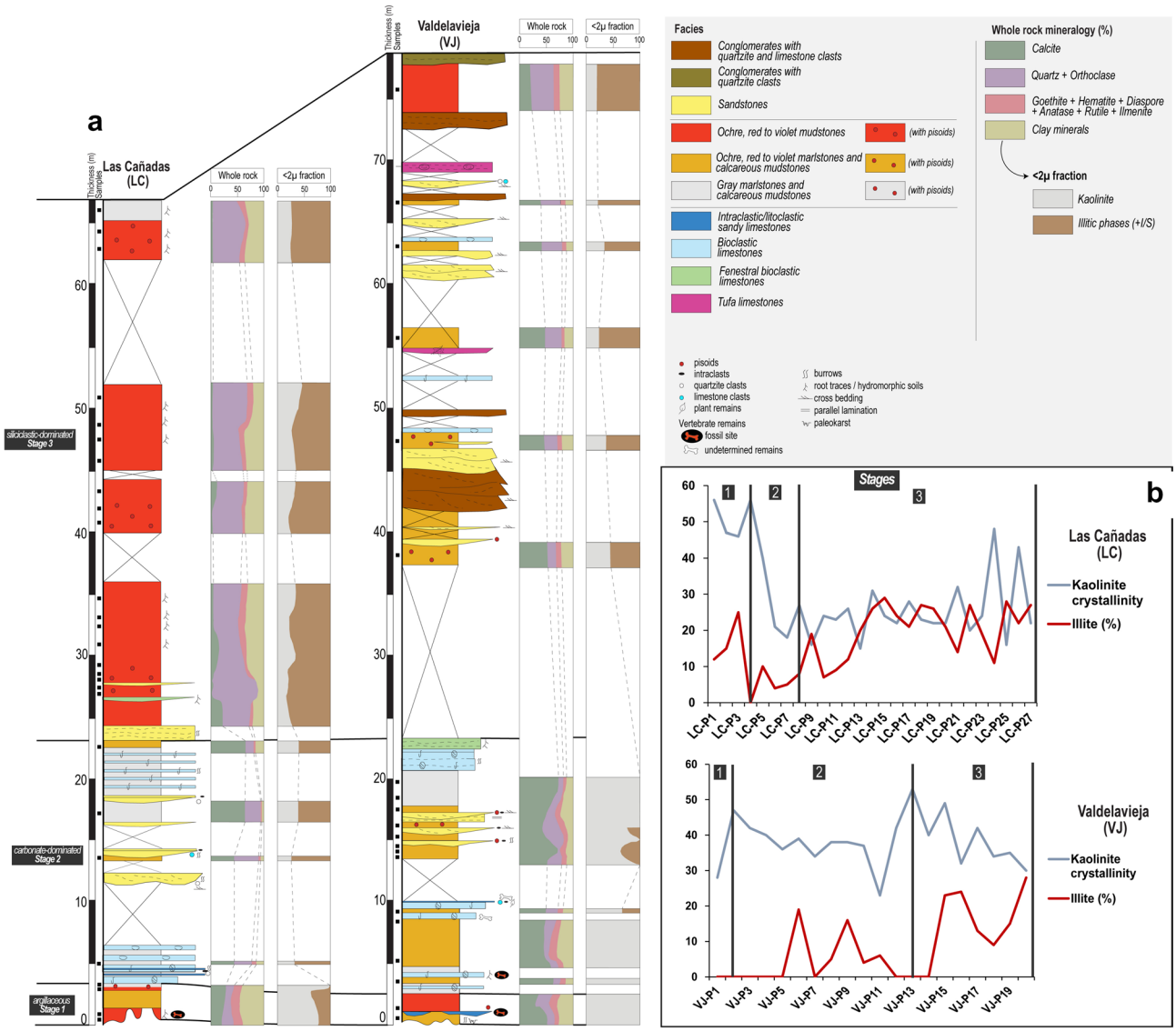

Fig. 5 **a** Variations in mineral content of the mudstones to calcareous mudstones in the LC and VJ logs; **b** Evolution of kaolinite crystallinity vs content of illitic phases from bottom to top of the logs. The kaolinite crystallinity value was multiplied by 100 for comparison with the content of illitic phases. Lower values indicate higher kaolinite crystallinity, and vice versa

higher relative proportion of clay minerals including a predominance of kaolinite over illitic phases), kaolinite is less crystalline than in the proximal VJ log, where kaolinite is the only clay mineral and there is a higher relative abundance of calcite. In the carbonate-dominated Stage 2, with calcite predominating in both sections, kaolinite is slightly less crystalline and predominates in the proximal VJ log, whereas in the distal LC log, where illite predominates, an increase in kaolinite crystallinity can be observed upwards. In the siliciclastic Stage 3, in the proximal VJ log, kaolinite crystallinity shows an increasing trend coupled with an increase in illitic phases and a decrease in calcite. By contrast, in the distal LC log, dominated by quartz + orthoclase and clay minerals (illitic phases), the kaolinite crystallinity is higher compared to the previous Stages 1 and 2, but decreases in some samples towards the top of the log, where the content of illitic phases is somewhat lower. Although there is not a general trend in kaolinite crystallinity, it should be noted that during Stage 3, especially in the distal LC log, kaolinite is more crystalline when the proportions of illitic phases are higher.

4.1.2 Optical and electron microscopy data

The optical microscopy images show that the mudstones to calcareous mudstones are formed by a fine-grained matrix composed of clay minerals and oxides that cannot be identified at optical microscope resolution (Fig. 6a–b). Abundant quartz clasts (40–200 μm) are recognised (Fig. 6a).

Table 2 Kaolinite crystallinity values of the samples of mudstones to calcareous mudstones measured in air-dried (AD) samples

Valdelavieja (VJ)			Las Cañadas (LC)		
Sample number	Muddy facies	KC Air-dried (001)	Sample number	Muddy facies	KC Air-dried (001)
1	OVMC	0.28	1	OVM	0.56
2	OVM	0.47	2	OVM	0.47
3	GMC	0.42	3	OVM	0.46
4	OVMC	0.40	4	GMC	0.56
5	OVMC	0.36	5	GMC	0.40
6	OVMC	0.39	6	OVMC	0.21
7	OVMC	0.34	7	GMC	0.18
8	OVMC	0.38	8	GMC	0.16
9	OVMC	0.38	9	OVM	0.16
10	OVMC	0.37	10	OVM	0.24
11	OVMC	0.23	11	OVM	0.23
12	OVMC	0.42	12	OVM	0.26
13	GMC	0.53	13	OVM	0.15
14	GMC	0.40	14	OVM	0.31
15	OVMC	0.49	15	OVM	0.24
16	OVMC	0.32	16	OVM	0.22
17	OVMC	0.42	17	OVM	0.28
18	OVMC	0.34	18	OVM	0.23
19	OVMC	0.35	19	OVM	0.22
20	OVM	0.30	20	OVM	0.22
			21	OVM	0.32
			22	OVM	0.20
			23	OVM	0.24
			24	OVM	0.48
			25	OVM	0.16
			26	OVM	0.43
			27	GMC	0.22

Classification of muddy facies from Aurell et. al. (2021)

OVM = ochre to violet mudstones, *OVMC* = ochre to violet marlstones/calcareous mudstones, *GMC*=grey marlstones/calcareous mudstones

Microsparitic carbonate nodules (100 µm to 1 mm in size; Fig. 6b), as well as microsparitic calcite filling pores in the matrix, are also present.

Compositional (EsB and AsB) and secondary electron (SE) images of the lower mudstone to calcareous mudstone levels show that kaolinite appears in the matrix both as subhedral to euhedral nanometric plates, commonly showing pseudohexagonal outlines with random orientation (Fig. 6c and d), and as booklets 1–10 µm in length (Fig. 6e–f).

In samples where illitic phases predominate (towards the upper mudstone to calcareous mudstone levels), smectite flakes (not detected by XRD) are also observed (Fig. 7a). The illitic phases are heterometric (1–10 µm) and present wavy and anhedral morphologies and frequently separated sheets (Fig. 7a–c). Intergrowths of illitic phases and kaolinite are also observed (Fig. 7c), like those described in similar materials (Bauluz et al., 2014; Do Campo et al., 2018).

According to the optical microscopy study, the carbonate both in the nodules and filling pores in the matrix is sparitic and/or microsparitic, and the EDS analyses indicate calcite compositions (Fig. 7d and e). Occasionally, some of the carbonate nodules are cemented by kaolinite (Fig. 7e). Fibrous calcite crystals cementing the matrix are also present (Fig. 7f).

EDS average analyses of the kaolinite, illitic phases, and smectite, as well as the average chemical formulae calculated, are included in Table 3. According to these analyses, the kaolinite composition is close to the theoretical one but presents low proportions of Fe ($\leq$0.1 a.p.f.u.). The illitic phases compositions are within the range commonly reported in the bibliography. The smectite compositions correspond to dioctahedral smectite, given the higher content of trivalent cations (Al and Fe) in the octahedral layer, and are consistent with a montmorillonite-type smectite.

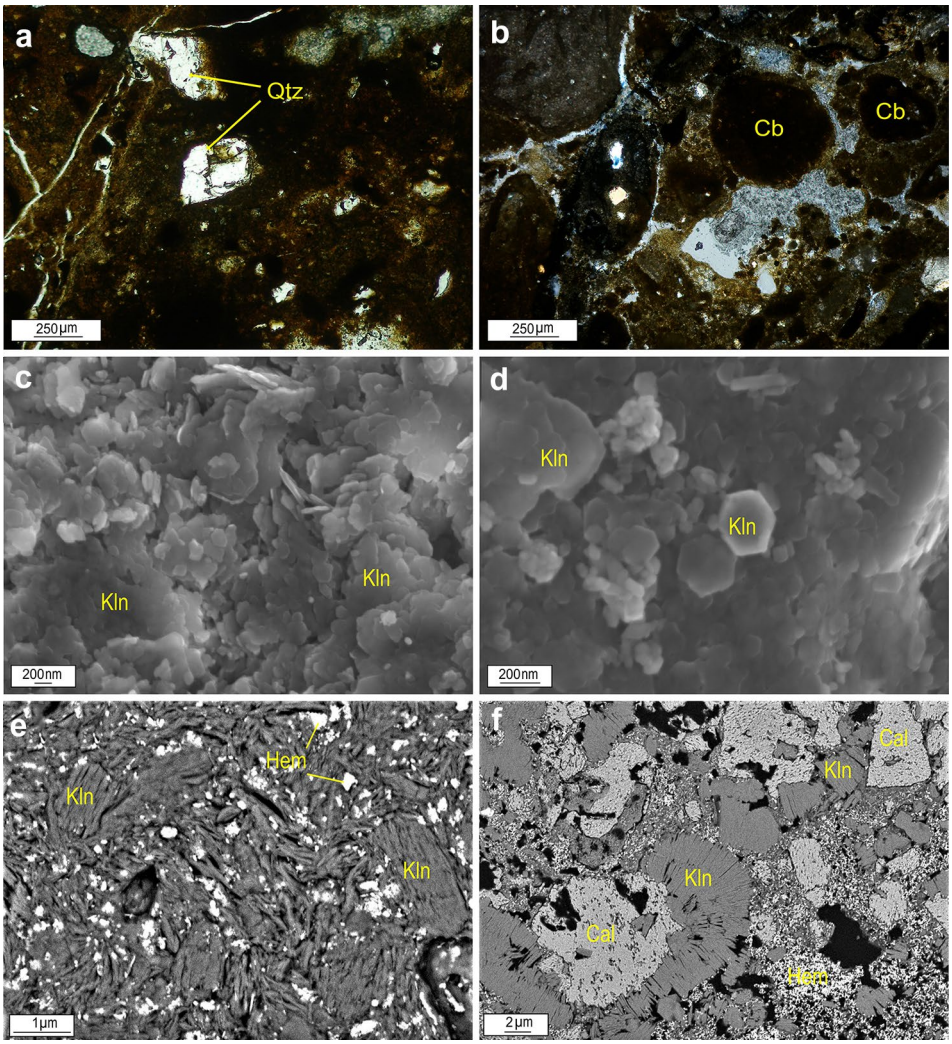

Fig. 6 Transmitted light optical microscopy images (**a** and **b**) and SEM images (**c**–**f**) of the lower mudstone to calcareous mudstone levels. **a** Quartz clasts in the matrix of the mudstones to calcareous mudstones from the LC log; **b** Microsparitic carbonate nodules in the mudstones to calcareous mudstones from the VJ log; **c** and **d** SE images showing platy kaolinite aggregates with random orientation and pseudohexagonal outlines; **e** 1–2 µm-sized kaolinite booklets and hematite crystals; **f** Kaolinite booklets reaching up to 10 µm in length and growing on microsparitic calcite nodules. *Qtz* = quartz, *Cb* = carbonate, *Kln* = kaolinite, *Hem* = hematite, *Cal* = calcite

4.2 Pisoid data

The Fe pisoids are embedded in the clay-rich matrix of the mudstone to calcareous mudstones. They are from 3 mm to 1 cm in diameter and show spherical to ellipsoidal morphologies and some of them are fractured. According to their size, following the classification given by Bárdossy (1982): macropisoids (> 5 mm), pisoids (1–5 mm), ooids (100–1000 µm) and micro-ooids (< 100 µm), the Fe pisoids are pisoids and macropisoids.

On the other hand, Reolid et. al. (2008) also classified as ferruginous ooids and pisoids those grains formed by a nucleus enveloped by an iron oxide coating, which also fits with the Fe pisoids of this study. According to their morphological features and lamination, these pisoids and macropisoid would be included in the Type A ooids and pisoids defined by these authors, which are formed by a thin, regular lamination that forms concentric layers enclosing a nucleus. In Type A ooids and pisoids, the nucleus can be a fragment of an older ferruginous ooid or an indeterminate ferruginous lump. The nuclei of the Fe pisoids studied here are always formed by and indeterminate ferruginous lump, so following the classification given by Guerrak (1987) they can also be classified as simple pisoids.

4.2.1 XRD data

The XRD patterns of two macropisoids (one of each log) indicate that they contain quartz, clay minerals, hematite, goethite, together with orthoclase, diaspore, anatase, rutile, and ilmenite (Fig. 8a). Calcite was also detected in the XRD patterns (especially in those of the macropisoids from the LC log), but it is not represented because, as it will be explained below, part of this calcite was not formed coetaneously with the mudstones and calcareous mudstones and the Fe pisoids. The relative proportions of these phases indicate that the macropisoids from the two logs are mainly formed by quartz, clay minerals (kaolinite and illitic phases, as deduced from the FESEM results), hematite, goethite and minor amounts of orthoclase, diaspore, anatase, rutile and ilmenite (Fig. 8b).

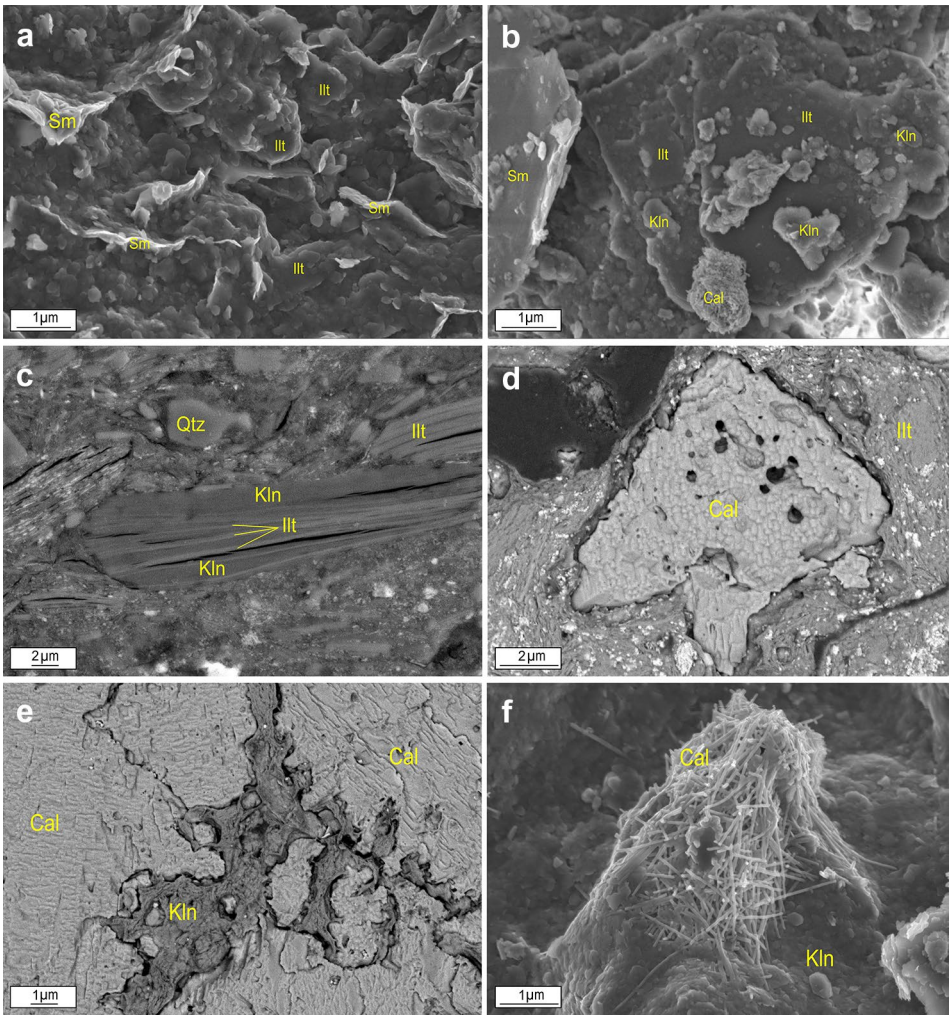

Fig. 7 FESEM images of the matrix of the middle and upper mudstones to calcareous mudstones (**a**–**c**) and the carbonates observed in the mudstones to calcareous mudstones (**d**–**f**). **a** SE image of smectite flakes and anhedral illitic phases; **b** SE image of anhedral illitic phases and subhedral kaolinite; **c** BSE images showing intergrowths of illitic phases and kaolinite; **d** Microsparitic calcite filling a matrix pore; **e** Kaolinite cementing calcite in a microsparitic nodule; **f** Fibrous calcite crystals cementing the matrix of the mudstone to calcareous mudstone. *Sm* = smectite, *Kln* = kaolinite, *Ilt* = illitic phases, *Qtz* = quartz, *Cal* = calcite

Table 3 EDS analyses (Wt%) of clay minerals in the mudstones and calcareous mudstones (standard deviation in brackets)

	O	Na	Mg	Al	Si	K	Ti	Fe	Calculated formula
Kaolinite ($n=28$)	49.08 (2.83)	–	–	21.88 (1.20)	24.87 (1.46)	–	0.21 (0.31)	3.95 (3.56)	$Fe_{0.1}Al_{1.9}Si_2O_5(OH)_4$
Illitic phases ($n=33$)	45.72 (2.12)	0.16 (0.26)	0.68 (0.36)	16.75 (3.20)	26.21 (2.84)	8.23 (2.23)	0.08 (0.20)	2.18 (1.44)	$(K_{0.8},H_3O)(Al_{1.7}Mg_{0.1}Fe_{0.2})(Si_{3.4}Al_{0.6})O_{10}[(OH)_2,(H2O)]$
Smectite ($n=20$)	44.90 (3.20)	0.14 (0.21)	1.42 (2.95)	18.38 (2.92)	25.64 (5.13)	4.94 (1.34)	0.39 (0.98)	4.22 (3.36)	$(K_{0.5})(Al_{1.7}Fe_{0.3}Mg_{0.1})(Si_{3.3}Al_{0.7})O_{10}(OH)_2nH_2O$

4.2.2 Optical and electron microscopy data

The pisoids and macropisoids are constituted by a nucleus and an outer cortex formed by several layers, both composed of a mixture of hematite, goethite, and clay minerals (Fig. 9a–c). In the case of the macropisoids, the outer cortex is 1–3 mm thick, and quartz clasts are frequently included among the layers (Fig. 9b and c). The nucleus is formed by an indeterminate ferruginous lump along with goethite and hematite. Both hematite and goethite show botryoidal textures, occasionally in alternating layers (10–30 µm) and some parts of the nucleus are replaced by carbonate at times (Fig. 9d). The electron microscopy images show that the

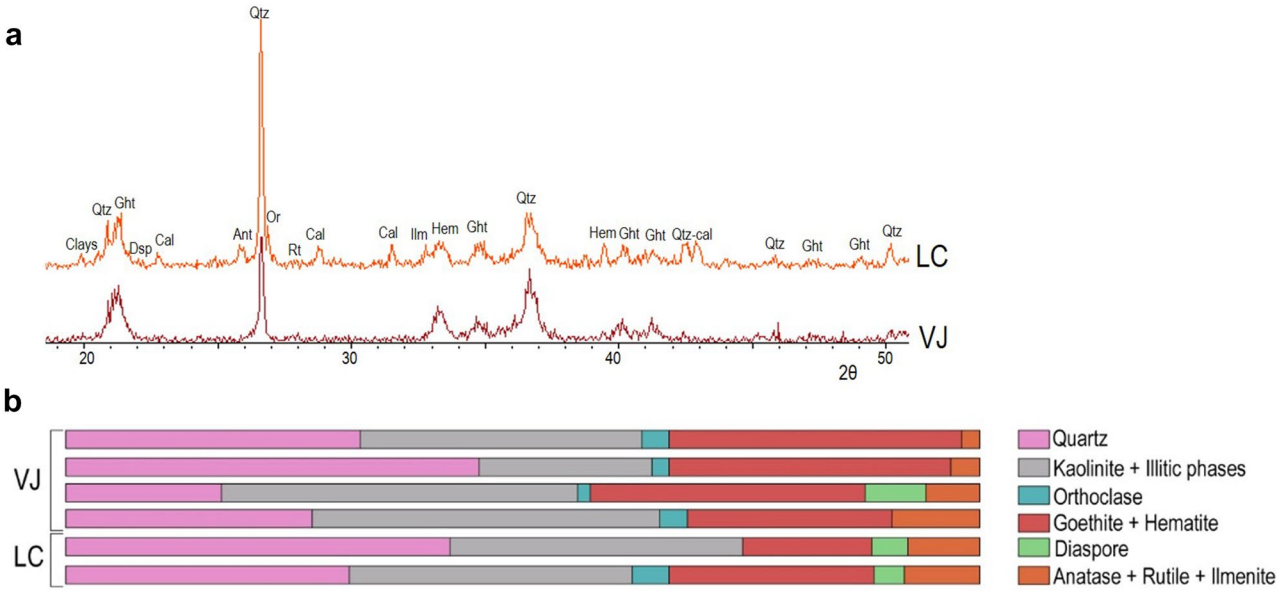

Fig. 8 **a** XRD patterns of two macropisoids from the VJ and LC logs; **b** relative proportions of mineral phases in several macropisoids from the LC and VJ logs

layers constituting the cortex of the macropisoids are formed by different amounts of kaolinite mixed with hematite and goethite, allowing one layer to be differentiated from another based on its kaolinite content. Hematite frequently cements kaolinite in the macropisoids (Fig. 9e). In both the pisoids and macropisoids, there is kaolinite with platy shapes with random orientation and as booklets like those found in the matrix of the lower mudstone to calcareous mudstone levels (Fig. 9e). Intergrowths of illitic phases and kaolinite with the same morphologies as those found in the upper mudstone to calcareous mudstone levels are also observed (Fig. 9f). Microsparitic calcite and occasional barite fill cavities in the macropisoids (Fig. 9f and g).

5 Discussion

5.1 Origin of the clay minerals, pisoids, and carbonates in the palaeosols

The mineralogy of the mudstone to calcareous mudstone levels consists of calcite, quartz (and orthoclase), clay minerals (kaolinite, illitic phases, smectite), Fe and Ti oxides, and Fe oxyhydroxides. The high content in clay minerals, along with the oxides and oxyhydroxides and the presence of Fe pisoids is a consequence of the development of palaeosols in the Torrelapaja Fm. The determined mineralogical association is common in oxisols, as categorised by the Soil Taxonomy Classification.

Compositional and morphological images show that the platy kaolinite is commonly euhedral to subhedral and displays pseudohexagonal outlines, indicating that it is probably authigenic. The presence of kaolinite booklets is not compatible with a detrital origin since they are too delicate to withstand erosion or transport processes, thus suggesting that they formed in-situ during the edaphic process (Bauluz et al., 2014; Do Campo et al., 2018; Laita et al., 2020). The lower and variable relative crystallinity of kaolinite in Stages 1 and 2 could be attributed to the presence of Fe in the kaolinite structure (as detected in EDS analyses, although in low proportions), since substitutions of Al by Fe in the octahedral sheet of kaolinite has been described in similar materials (Laita et al., 2020; Mendelovici et al., 1979) and is something common in weathering processes (Cantinolle et al., 1984; Mestdagh et al., 1980; Yuste et al., 2015). On the other hand, the kaolinite presents somewhat higher crystallinity towards the top of the studied logs, coeval with the increase in illitic phases in Stage 3 and the presence of intergrowths of illitic phases and kaolinite, in which the illitic phases act as a substrate for the kaolinite crystallization. This may enhance more effective crystallization of kaolinite.

Smectite is detected by electron microscopy but not by XRD, probably because its content lies below the detection limit of XRD. The flake-type morphologies observed in the smectite by electron microscopy suggest an in-situ origin, and the EDS analysis indicates that it corresponds to dioctahedral montmorillonite-type smectite. This kind of smectite has previously been reported in palaeosols as a product of the weathering of feldspars and micas (Fesharaki et al.,

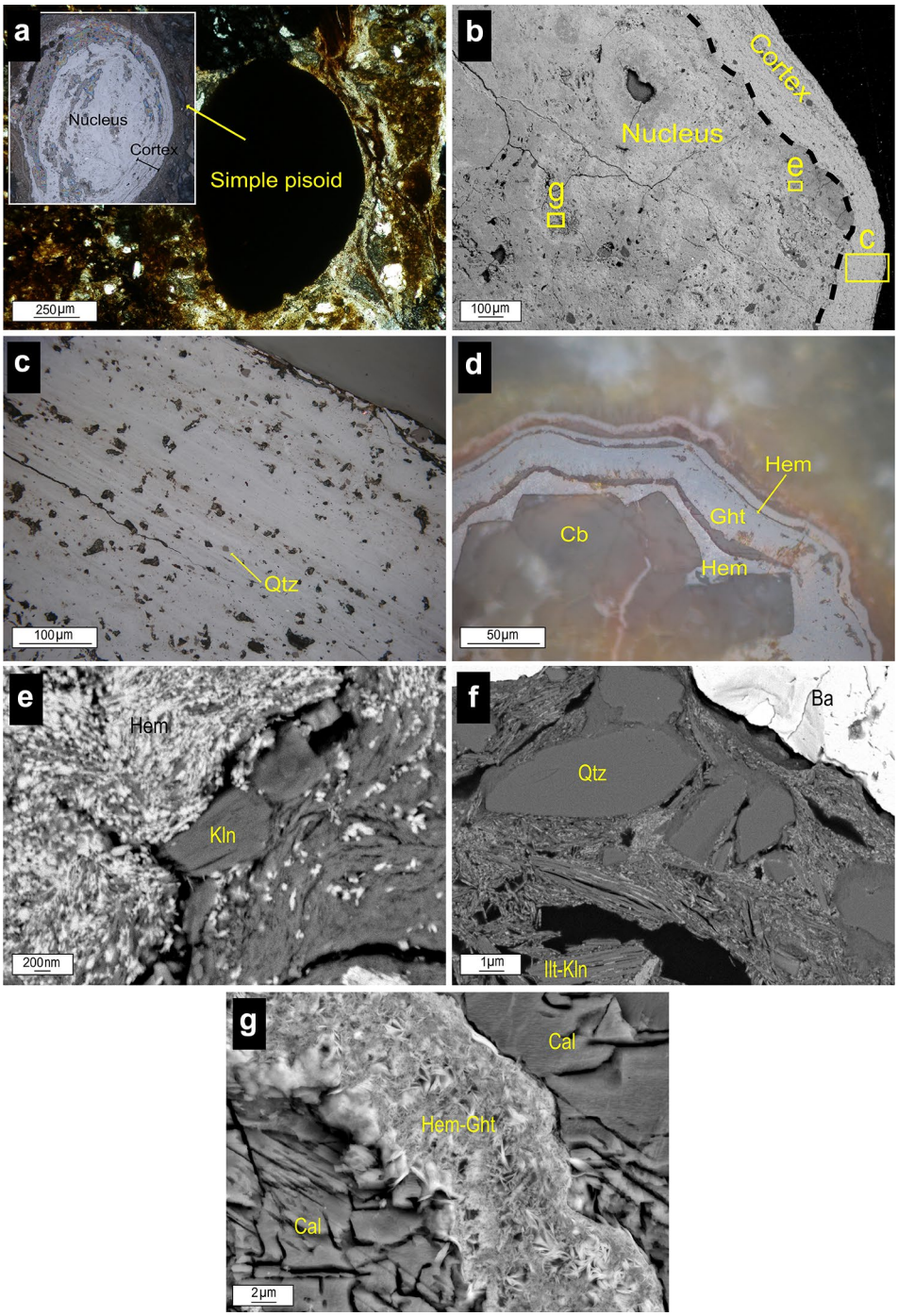

Fig. 9 Transmitted and reflected light optical microscopy and SEM images of pisoids and macropisoids. **a** Simple pisoid from the LC log; **b** Nucleus and cortex of a macropisoids. The squares show the areas were the enlarged images **c**, **e** and **g** were taken; **c** Macropisoid cortex formed by several layers with quartz clasts included among the layers; **d** Hematite and goethite forming alternating layers in the nucleus of a macropisoids and microsparitic carbonate replacing partially the nucelus; **e** Booklets of platy kaolinite and hematite in the nucleus of a macropisoid; **f** Quartz clasts, barite filling cavities, and illitic phases/kaolinite intergrowths in the nucleus of a macropisoid; **g** Microsparitic calcite filling cavities of a macropisoid. *Qtz* = quartz, *Cb* = carbonate, *Hem* = hematite, *Ght* = goethite, *Kln* = kaolinite, *Ilt* = illitic phases, *Ba* = barite, *Cal* = calcite

2007). Kaolinite and smectite would have thus been formed during the edaphic process by the dissolution of previous aluminium silicates (e.g., feldspars and illitic phases).

Authigenic illite is described in brackish and freshwater clays, lacustrine marls and gleysols during the Eocene–Oligocene, due to illitization of smectite and mixed-layer I/S during pedogenic processes (Huggett & Cuadros, 2005, 2010; Huggett et al., 2001). However this process is not observed in the uppermost Hauterivian–lower Barremian palaeosols studied here, which can be classified as oxisols. The origin of illitic phases in palaeosols is not compatible with the genesis of kaolinite (Bauluz et al., 2000). Detrital illite can degrade to interstratified illite–smectite under humid conditions (Chamley, 1989). Smectitization of illite induced by pedogensis has also been described in palaeosols (Meenakshi et al., 2020; Schaetzl & Thompson, 2015). The fact that the illitic phases studied here act as a substrate for kaolinite crystallization indicates that they are former phases

(Bauluz et al., 2014). Thus, these illitic phases may have a detrital origin and intervene in the genesis of kaolinite and smectite during the edaphic process. In addition, their anhedral morphologies are consistent with a detrital origin (Bauluz et al., 2014; Laita et al., 2020).

The calcite nodules observed in some of the mudstone to calcareous mudstone levels are cemented by kaolinite, pointing to a previous genesis for the nodules. Other investigations (Laita et al., 2020; Mücke et al., 1999) suggest that soil development usually occurs in various episodes involving changes in the water level and reworking processes. In the present study, the calcite nodules may come from the underlying limestone levels generated during the rising of the water level. A subsequent lowering of the water level would allow the calcite nodules to be cemented by kaolinite. This would also be the factor responsible for the reworking and fracturing of some of the macropisoids.

As other authors suggest (Rossi & Cañaveras, 1999), the fibrous calcite crystals cementing the matrix of the mudstone to calcareous mudstone levels would have formed during diagenesis. This diagenesis would also allow the filling of the matrix pores and macropisoids cavities and the replacements of some parts of their nuclei by microsparitic calcite. The barite observed within the cavities of macropisoids may also have a diagenetic origin; it has been described cementing palaeosols in other areas (Michel et al., 2016). The calcite and barite cements thus postdate the kaolinite and smectite. These cements must have therefore formed during early diagenesis, which would not have altered the palaeoclimatic signal registered in the clay minerals formed in-situ.

Saber et. al. (2018) classified ferriferous pisoids formed by in-situ growth in lateritic weathering profiles according to their mineralogical composition as: (1) pure kaolinitic pisoids, (2) kaolinitic-hematitic or hematitic-kaolinitic pisoids, and (3) hematitic pisoids. The second group includes those pisoids whose inner nucleus is composed of kaolinite and/or hematite surrounded by an outer cortex formed by kaolinite and hematite laminae. This latter subgroup is consistent with the pisoids and macropisoids studied here, since according to the XRD and electron microscopy results, they are mainly formed by hematite, goethite, kaolinite, and occasional quartz and illitic phases. FESEM images indicate that the kaolinite in the macropisoids displays platy morphologies and also occurs as booklets, similar to the kaolinite found in the matrix constituting the lower mudstone to calcareous mudstone levels. Likewise, the illitic phases and the intergrowths of illitic phases and kaolinite in the macropisoids are similar to those observed in the matrix of the upper mudstone to calcareous mudstone levels.

According to Bárdossy (1982), the formation of Fe pisoids and macropisoids in soils is usually associated with conditions of permanent groundwater saturation. These conditions are congruent with the genesis of Type A ferruginous ooids and pisoids described by Reolid et. al. (2008). The growth of the concentric layers that form the cortex of the pisoids and macropisoids also indicates physical and chemical changes in the environmental conditions, giving place to the precipitation of several mineral phases, such as kaolinite and Fe and Ti oxides, and Fe oxyhydroxides, in different quantitates (Yuste et al., 2020).

These data, along with the concentric structure and morphology of the Fe pisoids studied here indicate that they would have an in-situ origin and were thus formed during the edaphic process. However, the fractures observed in the macropisoids filled with calcite and barite also suggest that they underwent some reworking. On the other hand, the presence of hematite cementing kaolinite in the macropisoids indicates that the genesis of Fe oxides took place during the edaphic process but after the formation of kaolinite, as described in similar materials in the Iberian Range (Laita et al., 2020).

5.2 Clay mineral trends and climate vs. tectonic controls

5.2.1 Clay minerals and sediment supply

The clay minerals show vertical and lateral trends related to the three sedimentary stages defined by Aurell et. al. (2021), which can shed some light on the factors (climate, tectonics) controlling the genesis of the mineralogical assemblages and the development of the palaeosols.

Stage 1 is dominated by distal alluvial plain muddy facies of argillaceous composition (Fig. 2), with a somewhat lower quartz content and higher clay mineral content in the distal LC log (kaolinite being the main clay mineral) but higher calcite content in the proximal VJ log. This lateral trend could be associated with local factors (e.g., differential supply) but the reduced sediment thickness of this stage and lack of significant sedimentological differences between the logs precludes a more definitive interpretation (Figs. 2 and 5). Stage 2 is characterised by an increase in the water level, allowing the expansion of palustrine-lacustrine areas, but also a coeval increase in the terrigenous sediment supply (Aurell et al., 2021; Fig. 2). The mineralogical composition of distal alluvial plain and palustrine muddy facies is very homogeneous, as they are dominated by calcite in the distal LC and proximal VJ logs. In addition, kaolinite predominates over illitic phases in the proximal VJ log, as in Stage 1. These data reflect the fact that there is no significant control of the increasing terrigenous supply in the soil development during this stage. Stage 3 is characterised by an increase in terrigenous-clastic supply due to an increase in tectonic activity in southern areas (VJ log; Fig. 2) (Aurell et al., 2021). The change in the sedimentological conditions during this stage, with a greater contribution of terrigenous

sediment, leads to higher amounts of quartz and illitic phases (Fig. 5). Nevertheless, calcite, with a decreasing tendency, is present in the proximal VJ log, where a greater terrigenous supply is recorded. As explained below, the higher crystallinity of kaolinite towards the top of the logs may be a consequence of the higher quantities of illitic phases. These illitic phases form intergrowths in which they act as a substrate for the growth of the kaolinite, enhancing a more effective crystallization for the kaolinite. Additionally, the increase in quartz content towards the top of the profiles, may generate a possible increase in the porosity of the upper mudstone to calcareous mudstone levels, which could allow the kaolinite to be more crystalline and also favour the genesis of calcite cements during diagenesis as it would lead to better conditions for fluid circulation.

5.2.2 Clay minerals and palaeoclimate

As commented in a previous section, the mineralogical association determined in the mudstone to calcareous mudstone levels of this research is common in oxisols, as categorised by the Soil Taxonomy Classification. Oxisol development occurs under humid tropical climates (Do Campo et al., 2018).

Several authors have reported mineral assemblages comprising goethite, hematite, aluminium hydroxides, kaolinite, and quartz, as well as the presence of Fe pisoids in lateritic palaeosols (e.g., Bauluz et al., 2014; Giovannini et al., 2017; Nkalih Mefire et al., 2018; Nouazi Momo et al., 2019; Yuste et al., 2017).

On the other hand, the genesis of the palaeosols in the Torrelapaja Fm was also coeval with a rise and possibly a subsequent fall in the water level, as evidenced by the presence of kaolinite cementing calcite nodules and of reworked features in the pisoids.

The general climate described for the Hauterivian–Aptian period in Western Europe includes a trend from seasonal to warm climates and then to cooler conditions. During the Hauterivian, a seasonal climate prevailed (Föllmi, 2012; Godet et al., 2008), evidenced by the presence of illite and smectite in marine sedimentary successions (Mutterlose & Ruffell, 1999). From the latest Hauterivian to early Barremian, the increase in kaolinite in the palaeosols is consistent with a trend towards warmer conditions (Bárdossy, 1982; Föllmi, 2012; Godet et al., 2008; Wright et al., 2000), which prevailed during the mid and late Barremian (Scotese et al., 2021). On the other hand, during this period, Moiroud et. al. (2012) also reported marl–limestone alternations, with limestones enriched in I/S mixed-layers and kaolinite and illite-rich marls. According to these authors, the presence of kaolinite and illite in the marls is a consequence of continental runoff under humid tropical conditions, whereas the I/S contained in the limestones were formed under seasonally semi-arid conditions. Thus, this is reflecting a distortion in the climatic signal obtained from the clay minerals assemblages formed in continental or marine domains. A later change from warm to cooler conditions is recorded during the early Aptian (Dinis et al., 2020; Godet et al., 2006; Steuber et al., 2005).

As pointed out by Laita et. al. (2020), the trend in humidity during the Early Cretaceous of Western Europe is not so clear. Clay mineral assemblages from French and Swiss sections show a change from dry to more humid conditions during the Hauterivian (Godet et al., 2008). In the Tethys area, arid and humid regimes are recorded during the late Hauterivian (Föllmi, 2012), and temperature models show warm and humid conditions for the early Barremian (Bodin et al., 2009; Föllmi, 2012; Price et al., 2011). However, alternate wet and dry seasons during the early Barremian have also been reported (Haywood et al., 2004). Finally, an increase in humid conditions is described during the mid-Barremian in Europe (Mutterlose et al., 2014), whereas $\delta^{18}O$ records show a trend towards cooler and more arid conditions towards the late Barremian of the Tethys (Föllmi, 2012).

In northwestern Spain, a seasonal subtropical climate is described during the Early Cretaceous (Buscalioni & Fregenal-Martínez, 2010). In addition, the presence of Barremian kaolinite-rich bauxites and laterites in the Iberian Range (NE Spain) is also consistent with warm and humid conditions (Bauluz et al., 2014; Laita et al., 2020; Yuste et al., 2015, 2017).

In the western part of the Cameros Basin, stacked sheet flood deposits and sandy channels, along with conglomerates, mottled mudstones, and pedogenic carbonates included in the Piedrahita de Muñó Formation (Barremian–Aptian), suggest a semi-arid climate with seasonal rainfall (Platt, 1989).

In the uppermost Hauterivian–lower Barremian Torrelapaja Fm of the Torrelapaja subbasin (southeastern Cameros Basin), XRD and electron microscopy results show a higher content of kaolinite formed in-situ in the lower mudstone to calcareous mudstone levels, suggesting an intense chemical weathering characteristic of a warm and humid climate (Bauluz et al., 2014; Nouazi Momo et al., 2019; Raucskik & Varga, 2008; Won et al., 2018). As regards the pisoids and macropisoids, these would have been formed in environments of permanent groundwater saturation, which would have occurred in different episodes during the three sedimentary stages.

The decrease in kaolinite towards the top of the stratigraphic profiles correlates with the increase in the content of detrital quartz and illitic phases, which is related to a greater terrigenous-clastic supply during Stage 3. This could have partially inhibited soil formation. On the other hand, this trend is also coeval with the presence of authigenic smectite,

thus reflecting a decrease in chemical weathering perhaps associated with a change to colder and drier conditions during the late Hauterivian–early Barremian in this part of the Cameros Basin. In addition, the above-mentioned alternating goethite-hematite sequences in the macropisoids are also associated with less humid conditions (Laita et al., 2020; Velasco et al., 2013).

In the east of the Maestrazgo Basin (SE Iberian Range), the presence of laterites in the Cantaperdius Formation (Barremian–Aptian) has been reported (Combes, 1990; Salas, 1987). In the nearby Morella subbasin, karst bauxite deposits, which probably developed from lateritic materials laterally equivalent to the Cantaperdius Fm, have also been described (Molina & Salas, 1993; Yuste et al., 2015). Moreover, in the Oliete subbasin (NW Maestrazgo Basin), Laita et. al. (2020) described a decrease in kaolinite and an increase in smectite and illite content in lateritic palaeosols present in the lower part of the Blesa Formation (early Barremian), which reflected a change from warm/humid to cold/dry conditions. The lateritic palaeosols described in the lower Blesa Fm are regarded as age-equivalent with the palaeosols from Stages 1 and 2 of the uppermost Hauterivian–lower Barremian Torrelapaja Fm (Aurell et al., 2021). The same tendency in the climatic conditions can be deduced in this part of the Cameros Basin, but the record is not as good as in the Oliete subbasin due to the high siliciclastic contribution during Stage 3, associated with an increase in tectonic activity. All these data reflect warm and humid conditions during the early Barremian in these two Iberian subbasins over 100 km apart, followed by a change to drier, colder conditions, at least in the Oliete subbasin (Maestrazgo Basin, SE Iberian Range; Laita et al., 2020), which could also have taken place in the Torrelapaja subbasin (Cameros Basin, NW Iberian Range).

6 Conclusions

A combination of facies analysis and a study of the clay mineralogy of clay/marl-rich outcrops has allowed us to characterize the mineralogical and textural changes found in the mudstones to calcareous mudstones of the Torrelapaja Formation (uppermost Hauterivian–lower Barremian).

Kaolinite is the main clay mineral in the lower levels. Its euhedral morphologies and the presence of aggregates forming booklets indicate an authigenic origin for this mineral. The growth of the kaolinite to form intergrowths with illitic phases indicates that the illitic phases are former phases and act as a substrate for the kaolinite crystallization. This may favour the higher crystallinity of kaolinite in the upper levels, whereas the lower Fe proportions in the kaolinite in the lower levels could be the reason for its lower crystallinity. The smectite (montmorillonite-type composition) detected in the upper levels and its flake-type morphologies are consistent with an authigenic origin. The mineralogy and structure of the pisoids and macropisoids also reflect an in-situ origin during the edaphic process, but some of them are fractured, indicating reworking processes.

The matrix of the mudstones to calcareous mudstones and the cavities of the pisoids were later cemented by microsparitic calcite (and barite in some macropisoids) during early diagenesis. This diagenesis did not alter the palaeoclimatic signal registered in the kaolinite and smectite formed in-situ.

The mineralogical association in the mudstones and calcareous mudstones is characteristic of oxisols (laterites), which developed under humid tropical climates.

The higher content of kaolinite formed in-situ in the lower levels suggests intense chemical weathering as a consequence of a warm and humid climate, which is consistent with the palaeoclimatic conditions reported during the latest Hauterivian–early Barremian in the NE of the Iberian Plate.

The decrease in the kaolinite content, along with the increase in quartz and illitic phases, in the upper levels is related with an increase in siliciclastic input during Stage 3, which may have inhibited soil genesis. However, this trend in kaolinite content, along with the presence of authigenic smectite, also reflects a decrease in chemical weathering, perhaps associated with a change to colder and drier conditions, maybe concealed by the siliciclastic contribution, during the latest Hauterivian–early Barremian in this part of the Cameros Basin (NW Iberian Range).

Acknowledgements This study was supported by the European Regional Development Fund and the Government of Aragón [Aragosaurus Group: Geological Resources and Palaeoenvironments, Grant number E18_20R] and the Spanish Ministry of Science, Innovation and Universities [Grant numbers RTI2018-093419-B-I00 and CGL2017-85038-P]. The authors acknowledge the use of the Servicio General de Apoyo a la Investigación-SAI of the University of Zaragoza. They would also like to thank C. Gallego for her advice during the FESEM sessions. E. Laita received a grant from the Government of Aragon for the development of her PhD. Our appreciation also goes out to the reviewers Dr. JF Deconinck and an anonymous reviewer to help us to improve the manuscript.

Author contributions All authors contributed to the study conception and design.

Funding Open Access funding provided thanks to the CRUE-CSIC agreement with Springer Nature. This study was supported by the European Regional Development Fund and the Government of Aragón [Aragosaurus Group: Geological Resources and Palaeoenvironments, Grant number E18_20R] and the Spanish Ministry of Science, Innovation and Universities [Grant number RTI2018-093419-B-I00].

Availability of data and material All data, materials and software application support the authors claims and comply with field standards.

Code availability Not applicable.

Declarations

Conflict of interest The authors have no conflicts of interest to declare that are relevant to the content of this article.

Ethical approval We confirm that the manuscript is original and is not being submitted to other journal.

Consent to participate Not applicable.

Consent for publication Not applicable.

References

Allix, P., Burnham, A., Fowler, T., Herron, M., Kleinberg, R., & Symington, B. (2011). Coaxing oil from Shale. *Oilfield Review, 22*(4), 4–15.

Aurell, M., Bádenas, B., Canudo, J. I., Castanera, D., García-Penas, A., Gasca, J. M., Martín-Closas, C., Moliner, L., Moreno-Azanza, M., Rosales, I., Santas, L., Sequero, C., & Val, J. (2019). Kimmeridgian-Berriasian stratigraphy and sedimentary evolution of the central Iberian Rift System (NE Spain). *Cretaceous Research, 102*, 1–19. https://doi.org/10.1016/j.cretres.2019.05.011

Aurell, M., Fregenal-Martínez, M., Bádenas, B., Muñoz-García, M. B., Élez, J., Meléndez, N., & de Santisteban, C. (2019). Middle Jurassic-Early Cretaceous tectono-sedimentary evolution of the southwestern Iberian Basin (central Spain): Major palaeogeographical changes in the geotectonic framework of the Western Tethys. *Earth-Science Reviews Science, 199*, 102983. https://doi.org/10.1016/j.earscirev.2019.102983

Aurell, M., Bádenas, B., Castanera, D., Gasca, J. M., Canudo, J. I., Laita, E., & Liesa, C. L. (2021). Latest Jurassic-Early Cretaceous synrift sedimentation of Torrelapaja Subbasin (Cameros Basin): Implications for Northeast Iberia palaeogeography. *Cretaceous Research, 128*, 104997. https://doi.org/10.1016/j.cretres.2021.104997

Bárdossy, G. (1982). *Karst Bauxites*. Elsevier.

Bauluz, B., Mayayo, M. J., Fernández-Nieto, C., & González López, J. M. (2000). Geochemistry of Precambrian and Paleozoic siliciclastic rocks from the Iberian Range (NE Spain): implications for source-area weathering, sorting, provenance, and tectonic setting. *Chemical Geology, 168*, 135–150. https://doi.org/10.1016/S0009-2541(00)00192-3

Bauluz, B., Yuste, A., Mayayo, M. J., & Canudo, J. I. (2014). Early kaolinization of detritalWeald facies in the Galve Subbasin (Central Iberian Chain, north-east Spain) and its relationship to paleoclimate. *Cretaceous Research, 50*, 214–227. https://doi.org/10.1016/j.cretres.2014.03.014

Biscaye, P. E. (1965). Mineralogy and sedimentation of recent deep-sea clay in the Atlantic Ocean and adjacent seas and oceans. *Geological Society of American Bulletin, 76*, 803–832.

Bodin, S., Fiet, N., Godet, A., Matera, V., Westermann, S., Clément, A., Janssen, N. M. M., Stille, P., & Fölmi, K. B. (2009). Early Cretaceous (late Berriasian to early Aptian) palaeoceanographic change along the northwestern Tethyan margin (Vocontian Trough, southeastern France): δ13C, δ18O and Sr-isotope belemnite and whole-rock records. *Cretaceous Research, 30*, 1247–1262. https://doi.org/10.1016/j.cretres.2009.06.006

Buscalioni, A. D., & Fregenal-Martínez, M. A. (2010). A holistic approach to the palaeoecology of Las Hoyas Konservat-Lagerstätte (La Huérguina Formation, Lower Cretaceous, Iberian Ranges, Spain). *Journal of Iberian Geology, 36*(2), 297–326. https://doi.org/10.5209/rev_JIGE.2010.v36.n2.13

Cantinolle, P., Didier, P., Meunier, J. D., Parron, C., Guendon, J. L., Bocquier, G., & Nahon, D. (1984). Kaolinites ferrifères et oxyhydroxydes de fer et d'alumine dans les bauxites des Canonettes (S.E. de la France). *Clay Minerals, 19*, 125–135.

Casas, A. M. (1993). Oblique tectonic inversion and basement thrusting in the Cameros Massif (Northern Spain). *Geodinamica Acta, 6*, 202–216. https://doi.org/10.1080/09853111.1993.11105248

Casas, A. M., Villalaín, J. J., Soto, R., Gil-Imaz, A., del Río, P., & Fernández, G. (2009). Multidisciplinary approach to an extensional syncline model for the Mesozoic Cameros Basin (N Spain). *Tectonophysics, 470*, 3–20. https://doi.org/10.1016/j.tecto.2008.04.020

Chamley, H. (1989). *Clay sedimentology*. Springer.

Clemente, P. (2010). Review of the Upper Jurassic-Lower Cretaceous Stratigraphy in Western Cameros basin, Northern Spain. *Revista De La Sociedad Geológica De España, 23*(3–4), 101–143.

Combes, P. J. (1990). Typologie, cadre géodynamique et genèse des bauxites françaises. *Geodinamica Acta, 4*(2), 91–109. https://doi.org/10.1080/09853111.1990.11105202

Dera, G., Pellenard, P., Neige, P., & Deconinck, J.-F. (2009). Distribution of clay minerals in Early Jurassic Peritethyan seas: palaeoclimatic significance inferred from multiproxy comparisons. *Palaeogeography, Palaeoclimatology, Palaeoecology, 271*, 39–51. https://doi.org/10.1016/j.palaeo.2008.09.010

Dhillon, S. K., & Dhillon, K. S. (1991). Characterisation of potassium in Red (Alfisols), Black (Vertisols) and Alluvial (Inceptisols and Entisols)) soils of India using electro-ultrafiltration. *Geoderma, 50*, 185–196.

Dinis, P. A., Carvalho, J., Callapez, P. M., Mendes, M. M., Santos, V. F., & Fernandes, P. (2020). Composition of Lower Cretaceous mudstones of the Algarve Basin and implications for Iberian paleoclimates. *Cretaceous Research, 110*, 104404. https://doi.org/10.1016/j.cretres.2020.104404

Do Campo, M., del Papa, C., Nieto, F., Hongn, F., & Petrinovic, I. (2010). Integrated analysis for constraining palaeoclimatic and volcanic influences on clay-mineral assemblages in orogenic basins (Palaeogene Andean foreland, Northwestern Argentina). *Sedimentary Geology, 228*, 98–112. https://doi.org/10.1016/j.sedgeo.2010.04.002

Do Campo, M., Bauluz, B., del Papa, C., White, T., Yuste, A., & Mayayo, M. J. (2018). Evidence of cyclic climatic changes recorded in clay mineral assemblages from a continental Paleocene- Eocene sequence, northwestern Argentina. *Sedimentary Geology, 368*, 44–57. https://doi.org/10.1016/j.sedgeo.2018.03.007

Ehrmann, W., Setti, M., & Marinoni, L. (2005). Clay minerals in Cenozoic sediments off Cape Roberts (McMurdo Sound, Antarctica) reveal palaeoclimatic history. *Palaeogeography*

Palaeoclimatology Palaeoecology, 229, 187–211. https://doi.org/10.1016/j.palaeo.2005.06.022

Fesharaki, O., García-Romero, E., Cuevas-González, J., & López-Martínez, N. (2007). Clay mineral genesis and chemical evolution in the Miocene sediments of Somosaguas, Madrid Basin, Spain. *Clay Minerals, 42*, 187–201. https://doi.org/10.1180/claymin.2007.042.2.05

Föllmi, K. B. (2012). Early Cretaceous life, climate and anoxia. *Cretaceous Research, 35*, 230–257. https://doi.org/10.1016/j.cretres.2011.12.005

Giovannini, A. L., Bastos Neto, A. C., Porto, C. G., Pereira, V. P., Takehara, L., Barbanson, L., & Bastos, P. H. S. (2017). Mineralogy and geochemistry of laterites from the Morro dos Seis Lagos Nb (Ti, REE) deposit (Amazonas, Brazil). *Ore Geology Reviews, 88*, 461–480. https://doi.org/10.1016/j.oregeorev.2017.05.008

Godet, A., Bodin, S., Föllmi, K. B., Vermeulen, J., Gardin, S., Fiet, N., Adatte, T., Berner, Z., Stüben, D., & Van de Schootbrugge, B. (2006). Evolution of the marine stable carbon-isotope record during the early Cretaceous: a focus on the late Hauterivian and Barremian in the Tethyan realm. *Earth and Planetary Science Letters, 242*, 254–271. https://doi.org/10.1016/j.epsl.2005.12.011

Godet, A., Bodin, S., Adatte, T., & Föllmi, K. B. (2008). Platform-induced clay-mineral fractionation along a northern Tethyanbasin-platform transect: implications for the interpretation of EarlyCretaceous climate change (Late Hauterivian-Early Aptian). *Cretaceous Research, 29*, 830–847. https://doi.org/10.1016/j.cretres.2008.05.028

Gómez-Fernández, J. C., & Meléndez, N. (1994). Estratigrafía de la Cuenca de los Cameros (Cordillera Ibérica Noroccidental, N de España) durante el tránsito Jurásico-Cretácico. *Revista De La Sociedad Geológica De España, 7*, 121–139.

Guerrak, S. (1987). Metallogenesis of cratonic oolitic ironstone deposits in the Bled el Mass, Azzel Mani, Ahnet and Mouydir basins, Central Sahara. *Geologische Rundschau, 76*, 903–922. https://doi.org/10.1007/BF01821072

Haywood, A. M., Valdes, P. J., & Markwick, P. J. (2004). Cretaceous (Wealden) climates: a modelling prospective. *Cretaceous Research, 25*, 303–331. https://doi.org/10.1016/j.cretres.2004.01.005

Hillier, S. (2003). Quantitative analysis of clay and other minerals in sandstones by X-ray powder diffraction (XRPD). *International Association of Sedimentologists Special Publication, 34*, 213–251.

Huggett, J. M., & Cuadros, J. (2005). Low-temperature illitization of smectite in the late Eocene and early Oligocene of the Isle of Wight (Hampshire basin), UK. *American Mineralogist, 90*(7), 1192–1202. https://doi.org/10.2138/am.2005.1674

Huggett, J. M., & Cuadros, J. (2010). Glauconite formation in lacustrine/palaeosol sediments, Isle of Wight (Hampshire Basin), UK. *Clay Minerals, 45*(1), 35–49. https://doi.org/10.1180/claymin.2010.045.1.35

Huggett, J. M., Gale, A. S., & Clauer, N. (2001). The nature and origin of non-marine 10 Å clay from the Late Eocene and Early Oligocene of the Isle of Wight (Hampshire Basin), UK. *Clay Minerals, 36*(3), 447–464.

Laita, E., Bauluz, B., Aurell, M., Bádenas, B., Canudo, J. I., & Yuste, A. (2020). A change from warm/humid to cold/dry climate conditions recorded in lower Barremian clay-dominated continental successions from the SE Iberian Chain (NE Spain). *Sedimentary Geology, 403*, 105673. https://doi.org/10.1016/j.sedgeo.2020.105673

Liesa, C. L., Soria, A. R., Casas, A., Aurell, M., Meléndez, N., Bádenas, B., Fregenal-Martínez, M., Navarrete, R., Peropadre, C., & Rodríguez-López, J. P. (2019). The South Iberian, Central-Iberian and Maestrazgo basins. In C. Quesada & J. T. Oliveira (Eds.), *The geology of Iberia: a geodynamic approach. Volume 5: active processes: seismicity, active faulting and relief* (pp. 214–228). Springer.

Mack, G., Calvin, W., & Curtis, H. (1993). Classification of paleosols. *Geological Society of America Bulletin, 105*, 129–136.

Martin, J. D. (2017). A software package for powder x-ray diffraction analysis. *Qualitative, Quantitative and Microtexture, 121*, 143.

Martín-Closas, C. (1989). *Els caròfits del Cretaci Inferior de les conques periferiques del Bloc de l'Ebre.* Ph.D Thesis. University of Barcelona

Mas, R., García, A., Salas, R., Meléndez, A., Alonso, A., Aurell, M., Bádenas, B., Benito, M. I., Carenas, B., García-Hidalgo, J. F., Gil, J., & Segura, M. (2004). Segunda Fase de rifting: Jurásico Superior-Cretácico Inferior. In J. A. Vera (Ed.), *Geología de España* (pp. 503–510). Sociedad Geológica de España-Instituto Geológico y Minero.

Mas, R., Benito, M. I., Arribas, J., Omodeo-Salé, S., Suarez-Gonzalez, P., Quijada, I. E., Guimerà, J., González-Acebrón, L., & Arribas, M. E. (2019). The Cameros Basin. In C. Quesada & J. T. Oliveira (Eds.), *The geology of Iberia: a geodynamic approach. Volume 5: active processes: seismicity, active faulting and relief* (pp. 190–205). Springer.

Meenakshi, Shrivastava, J. P., & Chandra, R. (2020). Pedogenically degenerated illite and chlorite lattices aid to palaeoclimatic reconstruction for chronologically constrained (8–130 ka) loess-palaeosols of Dilpur Formation, Kashmir, India. *Geoscience Frontiers, 11*(4), 1353–1367. https://doi.org/10.1016/j.gsf.2019.11.007

Mendelovici, E., Yariv, S. H., & Villalba, R. (1979). Iron-bearing kaolinite in venezuelan laterites: I. Infrared spectroscopy and chemical dissolution evidence. *Clay Minerals, 14*, 323–331.

Mestdagh, M. M., Vielvoye, L., & Herbillon, A. J. (1980). Iron in kaolinite: II. The relationships between kaolinite and iron content. *Clay Minerals, 15*, 1–13. https://doi.org/10.1180/claymin.1980.015.1.01

Michel, L. A., Tabor, N. J., & Montañez, I. P. (2016). Paleosol diagenesis and its deep-time paleoenvironmental implications Pennsylvanian-permian Lodève basin, France. *Journal of Sedimentary Research, 86*, 813–829. https://doi.org/10.2110/jsr.2016.41

Moiroud, M., Martinez, M., Deconinck, J. F., Monna, F., Pellenard, P., Riquier, L., & Company, M. (2012). High-resolution clay mineralogy as a proxy for orbital tuning: example of the Hauterivian-Barremian transition in the Betic Cordillera (SE Spain). *Sedimentary Geology, 282*, 336–346. https://doi.org/10.1016/j.sedgeo.2012.10.004

Molina, J. M., & Salas, R. (1993). Bauxitas kársticas del Cretácico inferior en Fuentespalda (provincia de Teruel): estratigrafía, origen y paleogeografía. *Cuadernos De Geología Ibérica, 17*, 207–230.

Mücke, A., Badejoko, A., & Akande, S. O. (1999). Petrographic-microchemical studies and origin of the Agbaja Phanerozoic Ironstone Formation, Nupe Basin, Nigeria: a product of a ferruginized ooidal kaolin precursor not identical to the Minette-type. *Mineralium Deposita, 34*, 284–296.

Mutterlose, J., & Ruffell, A. (1999). Milankovitch-scale palaeoclimate changes in pale–dark beddingrhythms from the Early Cretaceous (Hauterivian and Barremian) of eastern England and northern Germany. *Palaeogeography, Palaeoclimatology, Palaeoecology, 154*, 133–160.

Mutterlose, J., Bodin, S., & Fähnrich, L. (2014). Strontium-isotope stratigraphy of the Early Cretaceous (Valanginian-Barremian): Implications for Boreal-Tethys correlation and paleoclimate. *Cretaceous Research, 50*, 252–263. https://doi.org/10.1016/j.cretres.2014.03.027

Nkalih Mefire, A., Yongue Fouateu, R., Njoya, A., Mache, J. R., Pilate, P., Hatert, F., & Fagel, N. (2018). Mineralogy and geochemical features of Foumban clay deposits (west Cameroon): genesis and

potential applications. *Clay Minerals, 53*, 431–445. https://doi.org/10.1180/clm.2018.31

Nouazi Momo, M., Beauvais, A., Tematio, P., Ambrosi, J. P., Yemefack, M., Palmer Kfuban Yerima, B., & Yongue-Fouateu, R. (2019). Lateritic weathering of trachyte, and bauxite formation in West Cameroon: Morphological and geochemical evolution. *Journal of Geochemical Exploration, 205*, 106324. https://doi.org/10.1016/j.gexplo.2019.06.006

Platt, N.H. (1989). *Sedimentology and tectonics of western Cameros Basin. Province of Burgos. Northern Spain.* Ph.D. Thesis. University of Oxford

Price, G. D., Főzy, I., Janssen, N. M. M., & Pálfy, J. (2011). Late Valanginian-Barremian (Early Cretaceous) palaeotemperatures inferred from belemnite stable isotope and Mg/Ca ratios from Bersek Quarry (Gerecse Mountains Transdanubian Range, Hungary). *Palaeogeography, Palaeoclimatology, Palaeoecology, 305*, 1–9. https://doi.org/10.1016/j.palaeo.2011.02.007

Raucskik, B., & Varga, A. (2008). Climato-environmental controls on clay mineralogy of the Hettangian-Bajocian successions of the Mecsek Mountains, Hungary: an evidence for extreme continental weathering during the early Toarcian oceanic anoxic event. *Palaeogeography, Palaeoclimatology, Palaeoecology, 265*, 1–13. https://doi.org/10.1016/j.palaeo.2008.02.004

Reolid, M., Abad, I., & Martín-García, J. M. (2008). Palaeoenvironmental implications of ferruginous deposits related to a Middle-Upper Jurassic discontinuity (Prebetic Zone, Betic Cordillera, southern Spain). *Sedimentary Geology, 203*(1–2), 1–16. https://doi.org/10.1016/j.sedgeo.2007.10.001

Righi, D., & Meunier, A. (1995). Origin of clays by rock weathering and soil formation. In B. Velde (Ed.), *Origin and mineralogy of clays: clays and the environment* (pp. 43–161). Springer. https://doi.org/10.1007/978-3-662-12648-6_3

Rossi, C., & Cañaveras, J. C. (1999). Pseudospherulitic fibrous calcite in paleo-groundwater, unconformity- related diagenetic carbonates (Paleocene of the Ager basin and Miocene of the Madrid basin, Spain). *Journal of Sedimentary Research, 69*, 224–238. https://doi.org/10.2110/jsr.69.224

Saber, E. S., Ali, M., & El-Sheikh, A. (2018). Provenance studies of Kalabsha kaolin deposits, Egypt: a petrographical and geochemical approach. *Arabian Journal of Geosciences, 11*(339), 9. https://doi.org/10.1007/s12517-018-3690-4

Salas, R., Guimerà, J., Mas, R., Martín-Closas, C., Meléndez, A., & Alonso, A. (2001). Evolution of the Mesozoic central Iberian Rift System and its Cainozoic inversion (Iberian chain). *Peri-Tethys Memoir, 6*, 145–185.

Salas, R. (1987). *El Malm i el Cretaci inferior entre el Massís de Garraf i la Serra de'espadà. Anàlisi de conca*. Ph.D. Thesis, University of Barcelona

Schaetzl, R., & Thompson, M. L. (2015). *Soils: genesis and geomorphology*. Cambridge University press.

Schultz, L. G. (1964). Quantitative interpretation of mineralogical composition from X-ray and chemical data for the Pierre shale. *USGS Professional Paper, 391–C*, 1–131.

Scotese, C., Song, H., Mills, B. J. W., & Van der Meer, D. G. (2021). Phanerozoic paleotemperatures: the earth's changing climate during the last 540 million years. *Earth-Science Reviews, 215*, 103503. https://doi.org/10.1016/j.earscirev.2021.103503

Sheldon, N. D., & Tabor, N. J. (2009). Quantitative paleoenvironmental and paleoclimatic reconstruction using paleosols. *Earth-Science Reviews, 95*, 1–52. https://doi.org/10.1016/j.earscirev.2009.03.004

Smith, D. K., & Johnson, G. G., Jr. (2000). Digitized database quantification, DDBQ, analysis of complex mixtures using fully digitized patterns. *Advances in X-Ray Analysis, 42*, 276–286.

Steuber, T., Rauch, M., Masse, J. P., Graaf, J., & Malkoč, M. (2005). Low-latitude seasonality of Cretaceous temperatures in warm and cold episodes. *Nature, 437*, 1341–1344. https://doi.org/10.1038/nature04096

Tabor, N. J., Myers, T. S., & Michel, L. A. (2017). Sedimentologist's guide for recognition, description and classification of paleosols. In K. E. Zeigler & W. G. Parker (Eds.), *Terrestrial depositional systems: deciphering complexities through multiple stratigraphic methods* (pp. 165–208). Elsevier. https://doi.org/10.1016/B978-0-12-803243-5.00004-2

Varela, A. N., Raigemborn, M. S., Richiano, S., White, T., Poiré, A. G., & Lizzoli, S. (2018). Late cretaceous paleosols as paleoclimate proxies of high-latitude Southern Hemisphere: mata amarilla formation, patagonia, argentina. *Sedimentary Geology, 363*, 83–95. https://doi.org/10.1016/j.sedgeo.2017.11.001

Velasco, F., Herrero, J. M., Suárez, S., Yusta, I., Alvaro, A., & Tornos, F. (2013). Supergene features and evolution of gossans capping massive sulphide deposits in the Iberian Pyrite Belt. *Ore Geology Reviews, 53*, 181–203. https://doi.org/10.1016/j.oregeorev.2013.01.008

Velde, B. (1995). *Origin and mineralogy of clays: clays and the environment*. Springer.

Won, C., Hong, H., Cheng, F., Fang, Q., Wang, C., Zhao, L., & Churchman, G. J. (2018). Clay mineralogy and its palaeoclimatic significance in the Luochuan loess-palaeosols over ~1.3 Ma, Shaanxi, northwestern China. *Frontiers of Earth Science, 12*(1), 134–147. https://doi.org/10.1007/s11707-017-0625-4

Wright, V. P., Taylor, K. G., & Beck, V. H. (2000). The paleohydrology of Lower Cretaceous seasonal wetlands, Isle of Wight, Southern England. *Journal of Sedimentary Research, 70*, 619–632. https://doi.org/10.1306/2DC4092C-0E47-11D7-8643000102C1865D

Yuste, A., Bauluz, B., & Mayayo, M. J. (2015). Genesis and mineral transformations in Lower Cretaceous karst bauxites (NE Spain): climatic influence and superimposed processes. *Geological Journal, 50*, 839–857. https://doi.org/10.1002/gj.2604

Yuste, A., Bauluz, B., & Mayayo, M. J. (2017). Origin and geochemical evolution from ferrallitized Clays to karst bauxite: an example from the Lower Cretaceous of NE Spain. *Ore Geology Reviews, 84*, 67–69. https://doi.org/10.1016/j.oregeorev.2016.12.025

Yuste, A., Camacho, I., Bauluz, B., Mayayo, M. J., & Laita, E. (2020). Palaeoweathering events recorded on siliciclastic continental deposits (Albian, Lower Cretaceous) in NE Spain. *Applied Clay Science, 190*, 105598. https://doi.org/10.1016/j.clay.2020.105598

ANNEX IV

Ceramics International 47 (2021) 14527–14539

Contents lists available at ScienceDirect

Ceramics International

journal homepage: www.elsevier.com/locate/ceramint

Mineral and textural transformations in mixtures of Al-rich and Al–K-rich clays with firing: Refractory potential of the fired products

Elisa Laita *, Blanca Bauluz, María José Mayayo, Alfonso Yuste

IUCA-Department of Earth Sciences, Faculty of Sciences, Universidad de Zaragoza, Pedro Cerbuna 12, 50009, Zaragoza, Spain

ARTICLE INFO

Keywords:
Bauxite
Illite- and kaolinite-rich clay
Mineral transformations
Mullite
Corundum

ABSTRACT

The present work analyses a set of cylinders manufactured by pressing and fired from 1000 °C to 1270 °C, which are composed of pure Al-rich rocks (bauxite) and mixtures of bauxite with Al–K-rich clays. The aim of the study is to determine the mineral and textural transformations that take place in the mixtures with firing and their influence on the physical properties of the final products in order to evaluate their refractory potential by comparing them with various fired commercial bauxites. To this end, raw and fired samples were analysed by X-ray diffraction, X-ray fluorescence, and optical and field emission scanning electron microscopy, and significant physical properties (e.g. density, linear shrinkage, porosity, colour, water absorption, thermal conductivity and point load resistance) were determined in the fired cylinders. The raw bauxite was mainly formed by boehmite, kaolinite and hematite whereas the illite- and kaolinite-rich clay was formed by quartz, illite and kaolinite. Kaolinite, illite and boehmite are not detected at 1000 °C and, from this temperature upwards, mullite, corundum, γ-Al_2O_3, hercynite, ilmenite, cristobalite and vitreous phase are formed. Changes in physical properties with rising temperature are associated with the mineralogical changes. The increases in density and linear shrinkage are related to the formation of vitreous phase and the crystallization of mullite, and correlate with the decrease in porosity, water absorption and thermal conductivity. The changes in the colour of the samples are related to the hematite content at each temperature, whereas the point load resistance is greater with higher corundum content. Both the firing temperature and the clay content play an important role in the refractory potential of the mixtures, since samples mixed with illite- and kaolinite-rich clay present similar properties at lower temperatures to those of the fired commercial bauxites.

1. Introduction

Bauxites (Al-rich rocks) and illite- and kaolinite-rich clays (Al- and K-rich clays) are the most important raw materials in manufacturing refractory ceramics. For this reason, knowledge of the mineralogical and textural transformations that occur during the firing process, as well as their influence on the physical properties of the final products, is a matter of great interest in characterizing these materials and inferring their refractory potential [1–4].

The mineral transformations that take place when aluminium- and clay-rich materials are fired at high temperature are influenced by the mineralogical composition of the raw materials, their granulometry, the firing temperature and the atmosphere conditions of the oven [5,6]. To understand how the calcination process occurs, it is thus necessary to analyse the mineral reactions, textural variations and compositional changes of the initial phases with the increase in temperature at both micron- and nano-scale [2,4,7].

In the literature, there are numerous studies that report mineralogical and textural changes in illite- and kaolinite-rich clays [4,8,9], pyrophyllite-rich clays or carbonate-rich clays [2,7] during firing processes.

Some of these studies have also reported modifications in physical properties with firing [6,10,11]. However, there are no investigations that have described in detail the mineral and textural transformations with firing in bauxite materials and their relationship with the physical properties. This is what the present study does.

Mullite and corundum are frequent phases in ceramic products, and their formation influences the porosity of ceramics [4,12]. The crystallization of new phases with firing is therefore of great interest. However, little attention has been paid to how mixtures of bauxite with Al–K-rich clays can affect the mineralogy and physical properties of the final products. The study of these mixtures fired at different temperatures

* Corresponding author. Department of Earth Sciences, Faculty of Sciences, Universidad de Zaragoza, Pedro Cerbuna 12, 50009, Zaragoza, Spain.
E-mail address: laita@unizar.es (E. Laita).

https://doi.org/10.1016/j.ceramint.2021.02.032
Received 23 October 2020; Received in revised form 2 January 2021; Accepted 4 February 2021
Available online 6 February 2021

allows their refractory potential to be characterized and is thus of great interest for engineering and industrial applications.

With the aim of analysing the refractory potential of the mixtures, this research shows that the mixture of illite- and kaolinite-rich clays with bauxite raw materials can affect the mineralogical transformations that occur with firing and thus their physical properties and refractory potential.

The research has two aims: 1) to determine in detail and using high-resolution techniques the mineralogical and textural transformations that take place in the mixtures during the firing processes at different temperatures, and 2) to evaluate their influence on the physical properties (density, linear shrinkage, porosity, colour, water absorption, thermal conductivity and point load resistance) of the final products and, with these data, to deduce the refractory potential of the obtained products by comparing them with various fired commercial bauxites.

2. Geological setting

In the southern Pyrenean mountains (NE Spain), there are several karst bauxite deposits, which were opencast-mined during the 1990s. One of the most important bauxite sites in this area is the Sierra de Boada, where the bauxite used in this study was obtained (Fig. 1). Here, 15–20 m of bauxite levels are found overlying Middle Jurassic (Dogger) dolostones and covered by Upper Cretaceous (Cenomanian) sandstones. The Middle Jurassic dolostones are affected by a palaeokarstic surface, above which the bauxites are arranged. By contrast, the surface contact with the Upper Cretaceous sandstones at the top shows a flat geometry. The bauxites are of a clayey aspect, predominantly red and violet colours, and contain millimetric spherical ferruginous pisoids [13].

On the other hand, in the Iberian Range (NE Spain) there are illite- and kaolinite-rich clay deposits belonging to the Lower Cretaceous Escucha Formation (Fig. 1) [14]. This formation has been traditionally divided into three members: lower, middle and upper [15]. The lower member of the Escucha Formation is formed by abundant claystones with a high kaolinite content, which are currently mined by the ceramic and refractory industries [4,16,17].

3. Materials and methods

3.1. Samples and firing process

The bauxite and the illite- and kaolinite-rich clay were milled under 100 μm. Pure bauxite (labelled as BX100) and mixtures of bauxite with the illite- and kaolinite-rich clay in 75/25 and 50/50 proportions (labelled as BX75 and BX50, respectively) were used to manufacture the cylinders (5 cm in diameter and 0.8 cm high) by pressing. The cylinders of the raw samples thus obtained were then fired in a Tecno-piro PR4T oven. The firing temperatures were 1000 °C, 1100 °C, 1200 °C and 1270 °C under oxidizing conditions, increasing the temperature in steps of 200 °C/h and maintaining the maximum temperature for 2 h. Cylinders made from the raw and the fired samples are shown in Fig. 2.

To deduce the refractory potential of the manufactured cylinders, three fired commercial bauxites were used to compare their mineralogical and physical properties with those of the cylinders.

3.2. X-ray fluorescence and X-ray diffraction

X-ray fluorescence analysis was carried out for the three raw samples (BX50, BX75 and BX100) and for the illite- and kaolinite-rich clay at

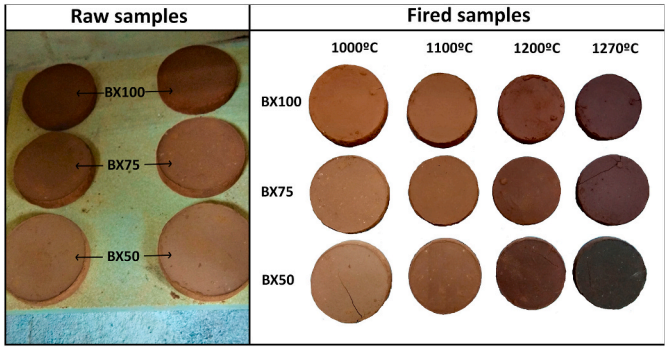

Fig. 2. Raw and fired cylinders obtained from pure bauxite (sample BX100) and mixtures of bauxite with the illite- and kaolinite-rich clay in 75/25 (sample BX75) and 50/50 proportions (sample BX50).

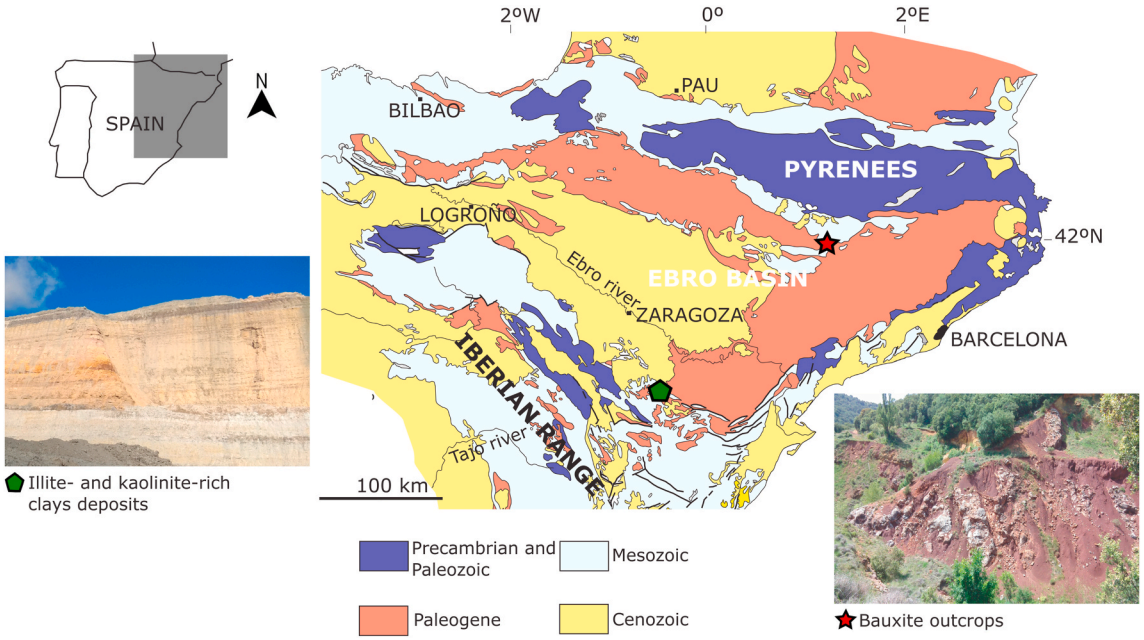

Fig. 1. Simplified geological map of the NE Iberian Peninsula indicating the location where the bauxite and the illite- and kaolinite-rich clays were obtained.

Actlabs laboratories (Ontario, Canada) to obtain their chemical composition. Samples were fused in platine crucibles using an automated crucible fluxer, automatically poured into platine moulds for casting, and analysed on a Panalytical Axios Advanced wavelength dispersive XRF spectrometer. The detection limit of the technique was 0.01% for SiO_2, Al_2O_3, Fe_2O_3, MgO, CaO, Na_2O, K_2O, TiO_2, P_2O_5, and Cr_2O_3, 0.005% for Co_3O_4 and CuO, 0.003% for NiO and V_2O_5, and 0.001% for MnO.

Mineralogical analyses of both the raw and the fired samples as well as the three fired commercial bauxites were performed by X-ray diffraction (XRD). XRD patterns were obtained from the 3 to 60° 2θ interval using a Philips 1710 diffractometer at the University of Zaragoza (Zaragoza, Spain) with 40 kV voltage, 30 mA current, CuKα radiation, automatic slit and graphite monochromator. The goniometer velocity was 0.03°2θ/s and the integration time was 1s. The recording was performed with XpowderX software [18].

After determining the mineral phases present in the samples, the relative proportions of these phases were ascertained using Reference Intensity Ratio (RIR) values from the literature [2,19–21]. To determine the formation of the vitreous phase in the samples during firing, the amorphous/crystals relationship was obtained using XpowderX software.

3.3. Optical and electron microscopy studies

Given that the XRD results showed similar mineralogical changes in samples fired at 1000 °C and 1100 °C, thin sections of all the samples fired at 1000 °C, 1200 °C and 1270 °C were studied by transmitted and reflected light microscopy in order to identify the mineral phases and characterize their texture.

The same thin sections were analysed using a Carl Zeiss Merlin field emission scanning electron microscope (FESEM) with an Oxford energy-dispersive X-ray (EDS) detector at the University of Zaragoza (Zaragoza, Spain). The thin sections had been previously coated with carbon. Compositional images of the samples were obtained using two types of backscattered electron detectors: angular selective backscattered (AsB) and energy selective backscattered (EsB). The accelerating voltage was 15 kV for AsB and 4 kV for EsB, and the beam current was 400 pA for AsB and 2.0 nA for EsB. Semi-quantitative analyses were also performed by the energy-dispersive X-ray detector (EDS), which has a detection limit of 0.1%. The accelerating voltage and the beam current for this detector were the same as those used for the AsB detector.

3.4. Physical properties

3.4.1. Density and linear shrinkage (LS)

The density was measured for both the raw samples and those fired at the different temperatures. The apparent density of the fired commercial bauxites was provided by the company.

The linear shrinkage of the fired samples was determined according to the following formula:

$$LS(\%) = \left(D_1 - D_2/D_1\right)x100$$

where D_1 is the diameter of the raw sample and D_2 is the diameter of the fired sample.

3.4.2. Colour

To determine the precise colour of the samples, an X·Rite portable spectrophotometer, model Ci6X, was used, which yields colour values in the Munsell system and in the CIE L*a*b* scale. The spectrophotometer was used to measure colour values in the raw and fired samples, as well as in the fired commercial bauxites.

3.4.3. Porosity

The porosimetric analysis was carried out in the Thermal Analysis and Porous Solids Unit of the University of Alicante (Spain). An Ultrapyc 1200e Helium Pycnometer was used to obtain the pore size and distribution in the fired samples, as well as their total porosity. The apparent porosity of the fired commercial bauxites was provided by the company.

3.4.4. Water absorption (WA)

Water absorption values were obtained for samples fired at the different temperatures according to the following formula:

$$WA(\%) = [(A - B)/B]x100\%$$

where A is the weight of the wet cylinder after 3 h in a vacuum and B is the weight of the dry cylinder. The absorption capacity values of the fired commercial bauxites were provided by the company.

3.4.5. Thermal conductivity (k)

Samples mixed with the illite- and kaolinite-rich clay fired at 1200 °C seems to have similar physical properties to those of the fired commercial bauxites. For this reason, samples BX50, BX75 and BX100 fired at 1200 °C were selected to measure their thermal conductivity. Thermal conductivity values were obtained at room temperature by using a C-THERM Thermal Conductivity Analyzer, with an accuracy of ±5%. Ten measurements were made for each sample using Wakefield grease as the contact material. The setup of the equipment was previously checked using a standard sample (Pyroceram) suggested by the company.

3.4.6. Point load test (PLT)

The Point Load Test (PLT) allowed the Point Load Resistance Index $I_{s(50)}$ to be determined in samples fired at 1200 and 1270 °C. Samples fired at 1000 and 1100 °C were not resistant enough to carry out the test. A point load measuring equipment was used to obtain the point load value of each sample (I_s) in kg/cm^2. Several measures per sample (between 6 and 12 depending on sample availability) were carried out. To obtain the $I_{s(50)}$ index, a correction factor was necessary, according to the expression:

$$I_{s(50)} = F \cdot I_s$$

F being the correction factor that was obtained using the following formula:

$$F = (D_e/50)^{0.45}$$

where D_e is the equivalent diameter of the regular prisms, which can be calculated by means of the expression:

$$D_e^2 = 4A/\pi$$

where A is the minimum cross-sectional area containing the two load application points.

4. Results

4.1. XRF and XRD results

The XRF results (Fig. 3) show that the illite- and kaolinite-rich clay presents higher proportions of SiO_2 (57.76%) and K_2O (3.47%) but lower proportions of Al_2O_3 (24.34%) and Fe_2O_3 (3.36%) than samples BX100, BX75 and BX50. Of these three samples, sample BX100 presents the highest Al_2O_3 and Fe_2O_3 contents and the lowest SiO_2 and K_2O contents.

The loss of ignition (LOI) produced in all the samples is related to the loss of the OH groups of the phyllosilicates and the hydroxides. As will be seen below, raw sample BX100 has the highest total boehmite + clay minerals content, which may be the cause of its higher LOI percentage (11.62%).

The XRD patterns and the relative proportions of the different phases obtained from the raw and the fired samples are represented in Fig. 4.

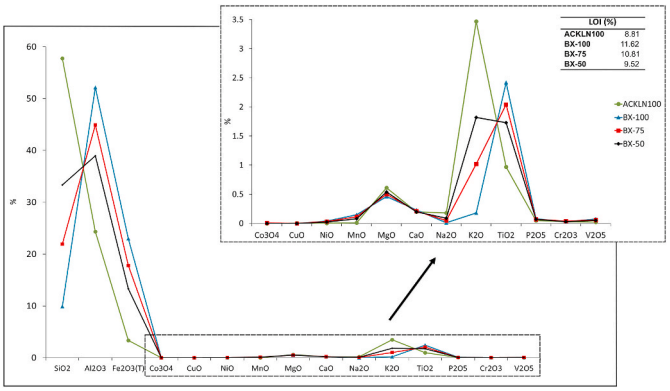

Fig. 3. XRF results showing the contents of major and several minor elements in the illite- and kaolinite-rich clay (ACKLN100) and the raw cylinders (BX100, BX75 and BX50).

The pure bauxite (sample BX100) is mainly formed by boehmite (62%), kaolinite (25%), hematite (9%) and minor proportions of anatase, goethite and rutile (<5%). Sample BX75 is formed by boehmite (43%), illite-kaolinite (35%), quartz (12%) hematite (6%) and minor proportions of anatase and rutile (<5%). Sample BX50 is composed of illite-kaolinite (46%), boehmite (27%), quartz (20%) and minor proportions of hematite, anatase and rutile (<5%). By contrast, the illite- and kaolinite-rich clay is mainly formed by illite (39%), quartz (32%) and kaolinite (23%), with minor proportions of orthoclase and albite (<5%).

The kaolinite, illite, boehmite, anatase and goethite present in the raw samples are not detected from 1000 °C upwards, indicating that they are the least stable phases during the firing process. By contrast, quartz, hematite and rutile are still detected at 1270 °C, showing that these are more stable phases, which withstand higher temperatures. However, the quartz content in samples BX75 and BX50 decreases with temperature, indicating that it is partially destabilizing. The hematite content increases in all the samples at 1000 °C (15–29%) compared to the raw samples (<5%–9%) but then decreases with increasing temperature, also indicating that it is partially destabilizing.

At 1000 °C, ilmenite, cristobalite, γ-alumina, corundum (α-alumina), hercynite (Fe and Al spinel) and mullite are formed. It was not possible to obtain a RIR value for the γ-alumina, so it was not semi-quantified. At this temperature, the XRD results also show the presence of amorphous phase, indicating the occurrence of fusion processes.

Ilmenite (<5–10%) and cristobalite (<5%), which formed at 1000 °C in all the samples, are later destabilized, as their content decreases with temperature.

Corundum is detected from 1000 °C upwards; its content is higher at 1100 °C in all the samples and then it decreases with temperature, especially in samples BX75 and BX50. At 1270 °C the corundum content is higher in the BX100 sample (43%) than in BX75 and BX50 (12 and 7%, respectively).

Finally, the mullite content increases with temperature in all the samples. By contrast with corundum, its content is higher in samples BX75 and BX50 (79 and 77% respectively) than in sample BX100 (44%) at the highest temperature.

The relative proportions obtained from the fired commercial bauxites indicate that they are mainly composed of corundum (70–84%) and mullite (14–27%), and some of them occasionally present low contents of hematite, rutile, ilmenite and hercynite (<5%).

The amorphous/crystals relationship obtained by XpowderX software is represented in Table 1. According to these data, an amorphous phase is generated in the three samples from 1000 °C upwards, its content seeming to rise with temperature up to 1200 °C in samples BX75 and BX50. In addition, the amorphous phase content in the three samples is higher than that detected in the fired commercial bauxites.

4.2. Optical and electron microscopy results

4.2.1. Optical and backscattered electron (BSE) images

At optical microscopy resolution, at 1000 °C samples BX50 and BX75 show a fine-grained matrix, in which morphologies of the original phyllosilicates are still distinguished along with oxides and quartz fragments (10–80 μm) (Fig. 5a), whereas in sample BX100 only small hematite aggregates (<50 μm) are observed. With the increase in temperature, the texture of the three samples becomes very homogeneous. Scarce quartz fragments are still distinguished, which are smaller (10–50 μm) than at lower temperatures, along with hematite aggregates and replacement textures involving hematite and another unidentified opaque mineral (Fig. 5b).

BSE images show remarkable textural and mineralogical changes with the increase in firing temperature. At 1000 °C rock fragments are still identified in samples BX100, BX75 and BX50. Iron and titanium oxides are recognized in some of these rock fragments, where they mainly occur in disseminated form, whereas other rock fragments are more homogeneous and contain almost no oxides. The rock fragments with abundant oxides seem to come from the original bauxite, whereas the most homogeneous ones seem to come from the illite- and kaolinite-rich clay (Fig. 5c). Some of the oxides have compositional zonation, with rutile and ilmenite or ilmenite and hematite compositions (Fig. 5d and e), and iron and titanium oxides forming aggregates (10–30 μm) are also recognized (Fig. 5e). At this temperature, in samples BX75 and BX50, quartz fragments (1–20 μm) are observed that are not yet destabilized, and corundum crystals are present in the three samples, with acicular morphologies, nanometric lengths (50–400 nm) and random orientation (Fig. 5f). Kaolinite-type morphologies are differentiated in the three samples (Fig. 5d and f) and in almost all cases their sheets are separated. These morphologies could correspond at least in part to metakaolinites, since kaolinite was not detected by XRD at this temperature.

At 1200 °C the texture of the samples is much more homogeneous, possibly due to the vitrification process. Some of the rock fragments are still recognized, especially in sample BX100, indicating that bauxite may be the component most resistant to firing. In this sample, all the iron and titanium oxides are disseminated or form aggregates. By contrast, in samples BX75 and BX50 the rock fragments are not so easily distinguishable, and oxides are concentrated in certain areas, as well as forming aggregates. Instead of rock fragments, texturally and compositionally different areas can be discerned: homogeneous areas without oxides and more heterogeneous areas with iron and titanium oxides, both disseminated and aggregated (Fig. 6a). These different areas could correspond with the previous bauxite and illite- and kaolinite-rich clay fragments observed at 1000 °C. Sample BX100 (Fig. 6b) does not contain rock fragments of the illite- and kaolinite-rich clay, but the XRD results showed that the raw sample contained kaolinite. Thus, the homogeneous areas in BX100 may come from the destabilization of the initial kaolinite during firing. In general, the homogeneous areas are formed by acicular and prismatic nanometre-sized mullite crystals (100–600 nm), with random orientation and immersed in vitreous phase (Fig. 6a, b and c) along with quartz fragments, which present reaction edges, indicating that they have begun to destabilize (Fig. 6c). The heterogeneous areas in all the samples, where the oxides are concentrated, also contain abundant acicular corundum crystals, with random orientation and sizes larger than those found at 1000 °C (200nm-2μm). These corundum crystals can be found replacing hematite (Fig. 6a, b and d).

Finally, at 1270 °C the texture of the three samples is very homogeneous (Fig. 7a). Iron and titanium oxides are less frequent and occur in the same form as at 1200 °C. Quartz fragments only remain in sample BX50 although they are scarcer than at lower temperatures and show reaction edges. Mullite crystals are also found immersed in vitreous phase but with larger sizes (100nm-2μm) (Fig. 7b and d). The corundum has acicular and prismatic morphologies with larger sizes (200nm-4μm) and is immersed in a probably vitreous phase, occasionally replacing hematite (Fig. 7c and d).

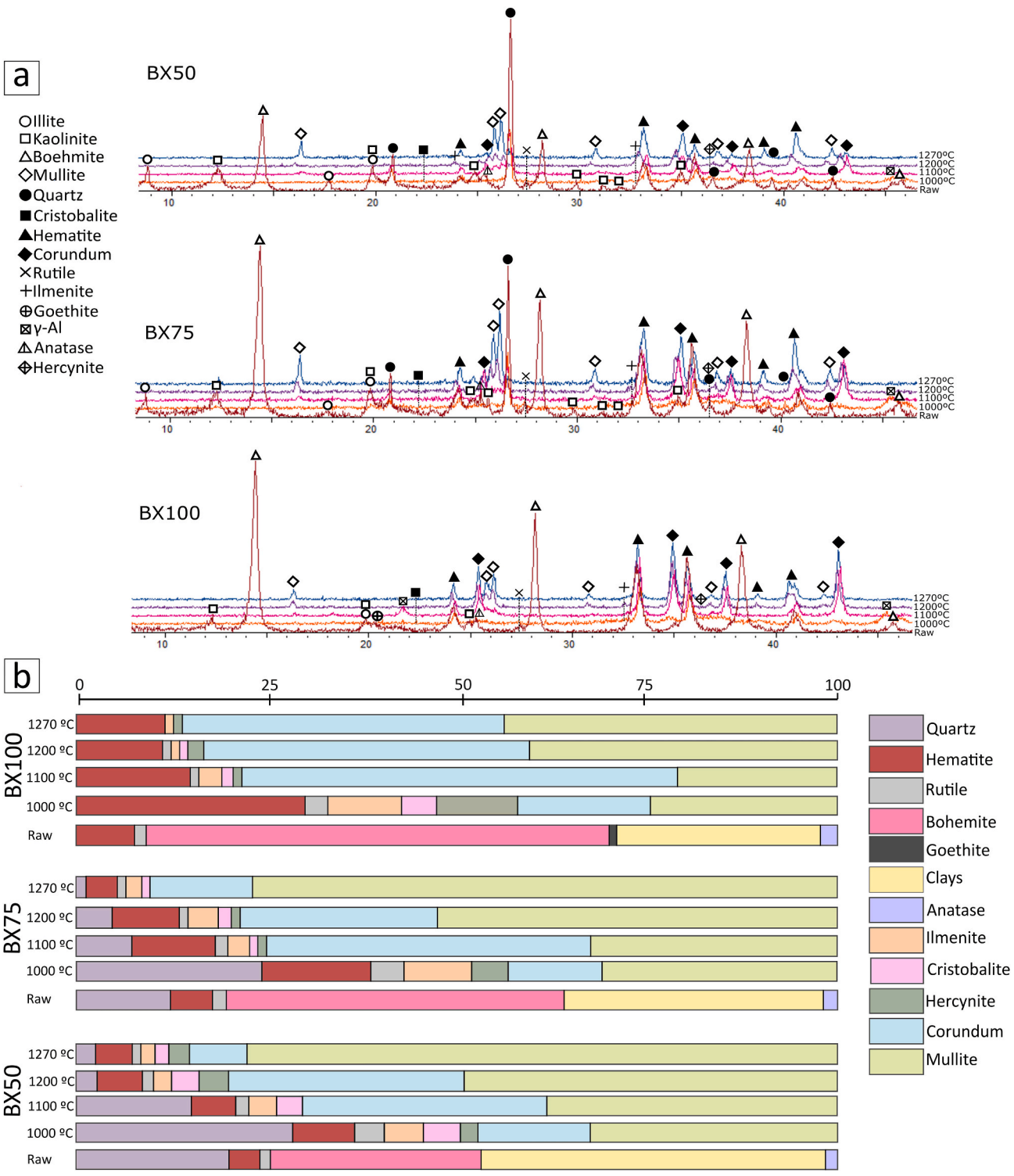

Fig. 4. (a) XRD patterns of raw and fired samples and (b) diagrams with the relative proportions of the mineral phases present in the analysed samples. Ilt = illite, Kln = kaolinite, Bhm = boehmite, Crt = cristobalite, An = anatase, Mul = mullite, Qtz = quartz, Rut = rutile, Ilm = ilmenite, Hem = hematite, Hcy = hercynite, Cor = corundum.

4.2.2. Chemical analysis

EDS analyses indicate that hematite, corundum and ilmenite show compositional differences from sample to sample and even at sample scale. Al vs. Fe (wt%) plots at the different temperatures for the three samples show a trend among hematite, hercynite and corundum compositions (Fig. 8a, b and c). The Al vs. Fe plots show the presence of three compositional populations: 1) Fe-rich compositions that indicate hematite, 2) Al-rich compositions that are regarded as corundum, and 3) intermediate compositions between hematite and corundum.

Although hercynite was not clearly differentiated by FESEM analyses, it was detected by XRD in all the samples at the different temperatures, and some of the intermediate compositions included between hematite and corundum are close to theoretical hercynite (31.05% Al, 32.13% Fe, 36.82% O).

Table 1
Amorphous/crystals relationship obtained by XpowderX software for the three samples at the different temperatures and for the commercial bauxites.

Sample	T°	Amorphous/Crystals relationship
BX100	1000	0.146
	1100	0.088
	1200	0.091
	1270	0.106
BX75	1000	0.139
	1100	0.153
	1200	0.148
	1270	0.097
BX50	1000	0.089
	1100	0.110
	1200	0.225
	1270	0.120
Commercial bauxites		0.038
		0.044
		0.040

Ti vs. Fe (wt%) plots at the different temperatures for the three samples also show a trend among hematite, ilmenite and rutile compositions (Fig. 8d, e and f). In this case, compositions with Fe contents higher than 79% and Ti contents lower than 9% were considered hematite. Those compositions with Ti contents of 32–66% and Fe contents of 33–67% were considered ilmenite, whereas compositions with Ti contents higher than 75% and Fe contents lower than 25% were considered rutile.

Of all these phases, corundum and ilmenite are the two generated due to the firing process, as they were not detected by XRD in the raw samples. On average, the corundum composition at the different temperatures is close to theoretical corundum (52.093% Al and 47.07% O); it has an Al content of 44.07%, but it also contains Fe (6.72%), Si (3.82%) and minor proportions of Ti (0.43%) and K (0.15%). Ilmenite presents lower Ti and Fe contents (20.35 and 28.35% respectively) than theoretical ilmenite (31.56% Ti, 36.81% Fe and 31.63% O).

The Al vs. Si plot (Fig. 8g) shows mullite analyses from all the samples at the different temperatures. According to these results, the mullite presents a heterogeneous compositional range with compositions between kaolinite (or metakaolinite) and mullite. Those analyses at 1000 °C close to the theoretical kaolinite composition correspond with the kaolinite-type morphologies observed in the backscattered electron images. Although mullite presents a heterogeneous compositional range, its Al/Si ratio increases from 1.49 at 1200 °C to 1.76 at 1270 °C.

Finally, the vitreous mass observed in all the studied samples in which mullite and corundum crystals are immersed probably corresponds with the amorphous phase deduced from XRD. It presents a heterogeneous composition mainly formed by Si and Al (28.20 and 15.90%, respectively), along with Fe and K (3.56 and 3.20%, respectively) and minor proportions of Ti (0.64%), Mg (0.44%), Ca (0.16%) and Na (0.13%).

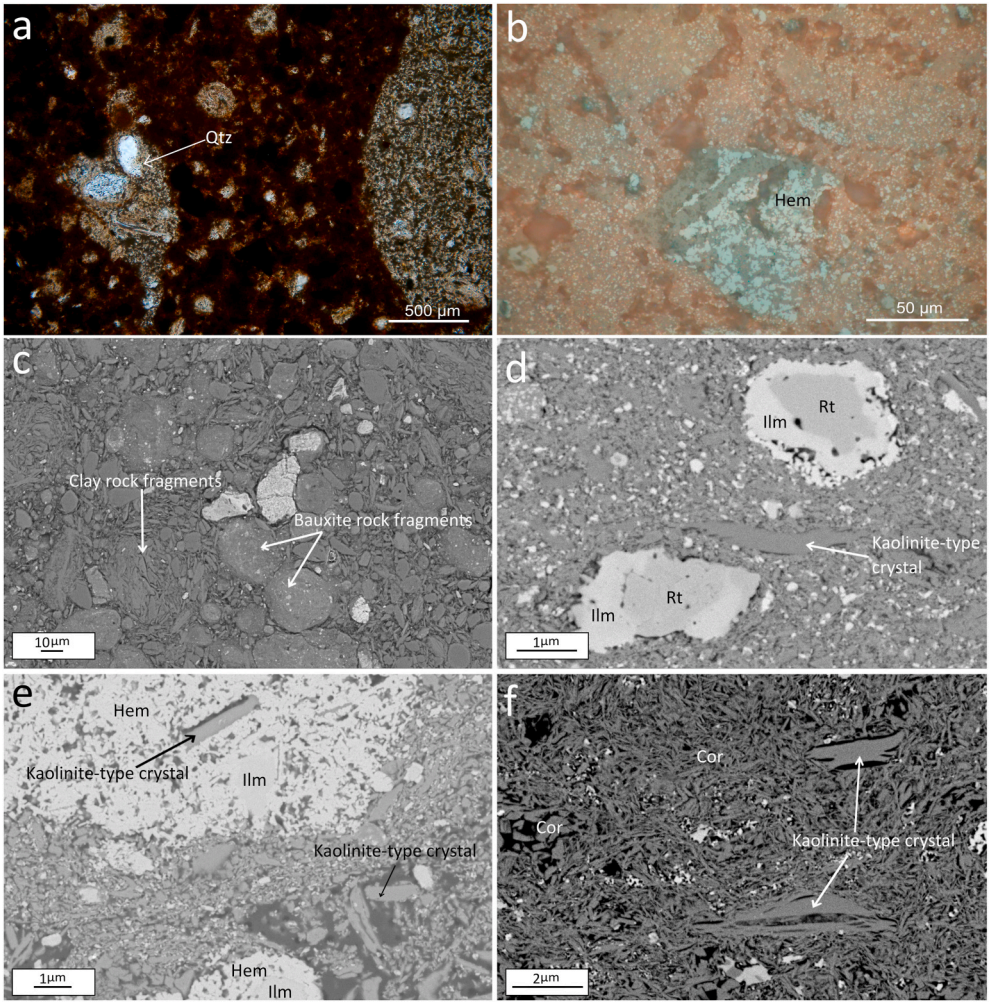

Fig. 5. (a) Transmitted light optical microscope images showing the matrix formed by quartz fragments and oxides in sample BX50 at 1000 °C. (b) Reflected light optical microscope images showing hematite replacement textures in sample BX100 at 1270 °C. (c–f) FESEM images of samples fired at 1000 °C showing: (c) Bauxite and clay rock fragments along with iron oxide aggregates in sample BX50. (d) Crystals with compositional zonation involving rutile and ilmenite compositions, and kaolinite-type crystals in sample BX100. (e) Oxide aggregate composed mainly of hematite and kaolinite-type crystals in sample BX75. (f) Acicular corundum crystals and kaolinite-type crystals with separated sheets in sample BX100. Qtz = quartz, Rt = rutile, Ilm = ilmenite, Hem = hematite, Cor = corundum.

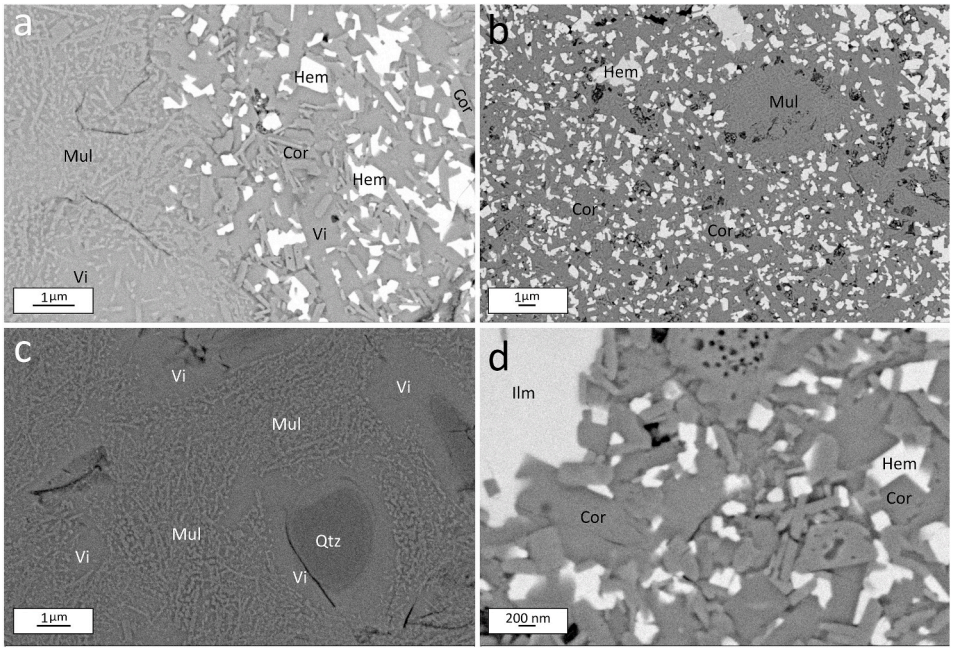

Fig. 6. FESEM images of samples fired at 1200 °C showing: (a) A homogeneous area with acicular mullite crystals and vitreous phase and a heterogeneous area with hematite and corundum crystals in sample BX75. (b) The same zones in sample BX100, in which the corundum content is higher and the mullite content is lower than in the other samples. (c) Quartz fragments with reaction edges, acicular mullite crystals and vitreous phase in sample BX50. (d) Corundum replacing hematite in sample BX50. Mul = mullite, Hem = hematite, Cor = corundum, Vi = vitreous phase, Qtz = quartz, Ilm = ilmenite.

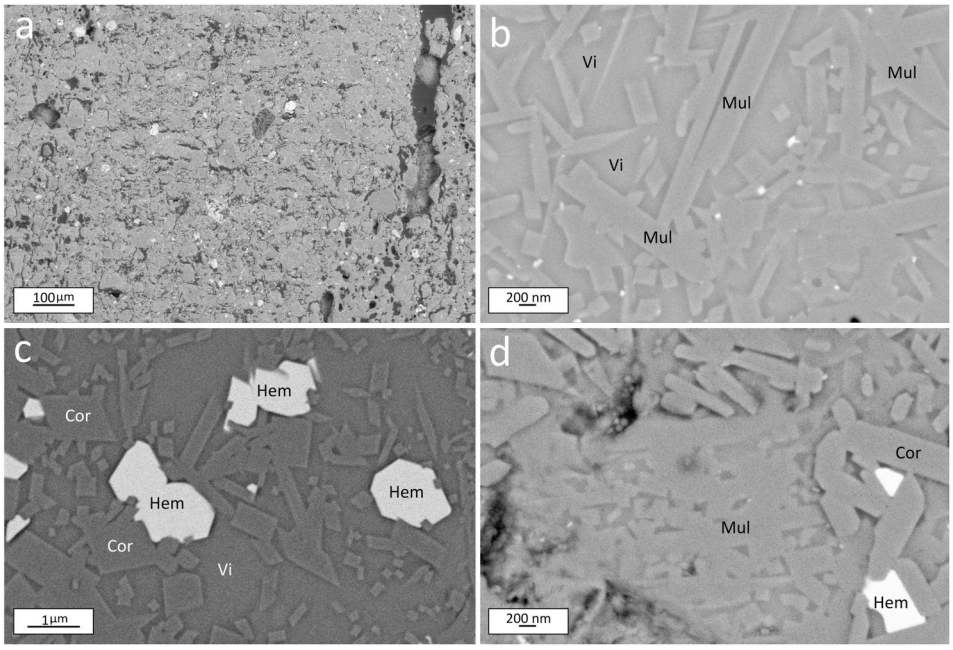

Fig. 7. FESEM images of samples fired at 1270 °C showing: (a) The general texture of sample BX75. (b) Acicular and prismatic mullite crystals immersed in vitreous phase and with larger sizes than at lower temperatures in sample BX75. (c) Acicular and prismatic corundum crystals with larger sizes than at lower temperatures, occasionally still replacing hematite crystals and immersed in vitreous phase in sample BX50. (d) Corundum and mullite crystals immersed in vitreous phase in sample BX100. Vi = vitreous phase, Mul = mullite, Cor = corundum, Hem = hematite.

4.3. Physical properties

4.3.1. Density and linear shrinkage

The density of the cylinders is 1.73 g/cm^3, 1.74 g/cm^3 and 1.71 g/cm^3 for samples BX100, BX75 and BX50, respectively. The changes in the density values of the three samples are represented in Fig. 9a, which shows that the density values of the raw samples remain almost constant up to 1000 °C. At 1100 °C and 1200 °C the density increases in all the samples, reaching values of 2.83 g/cm^3, 2.73 g/cm^3 and 2.55 g/cm^3 for samples BX100, BX75 and BX50, respectively. Finally, at 1270 °C the density of samples BX75 and BX50 decreases to 2.55 g/cm^3 and 2.43 g/cm^3, respectively, whereas the density of sample BX100 increases to 3.43 g/cm^3. The density values reached by sample BX75 fired at 1200 °C and by sample BX100 fired at 1200 °C and 1270 °C are the closest to the density values given for the fired commercial bauxites (2.8–3.25 g/cm^3).

A similar trend is observed in the linear shrinkage values (Fig. 9b). At 1000 °C the linear shrinkage value is 4.39% for sample BX100, 3.99% for sample BX75, and 2.97% for sample BX50. A notable increase in the linear shrinkage is observed in the three samples at 1100 °C and 1200 °C with values of 12.43% and 18.55% for sample BX100, 11.86% and 16.74% for sample BX75, and 9.97% and 14.95% for sample BX50. Finally, at 1270 °C the linear shrinkage values undergo a slight decrease in samples BX75 and BX50 (15.07% and 14.32%, respectively), whereas the value increases in sample BX100 (22.56%).

4.3.2. Colour

According to the Munsell System (Fig. 10a), the BX100 and BX75 raw samples present a reddish brown colour, which changes to bright

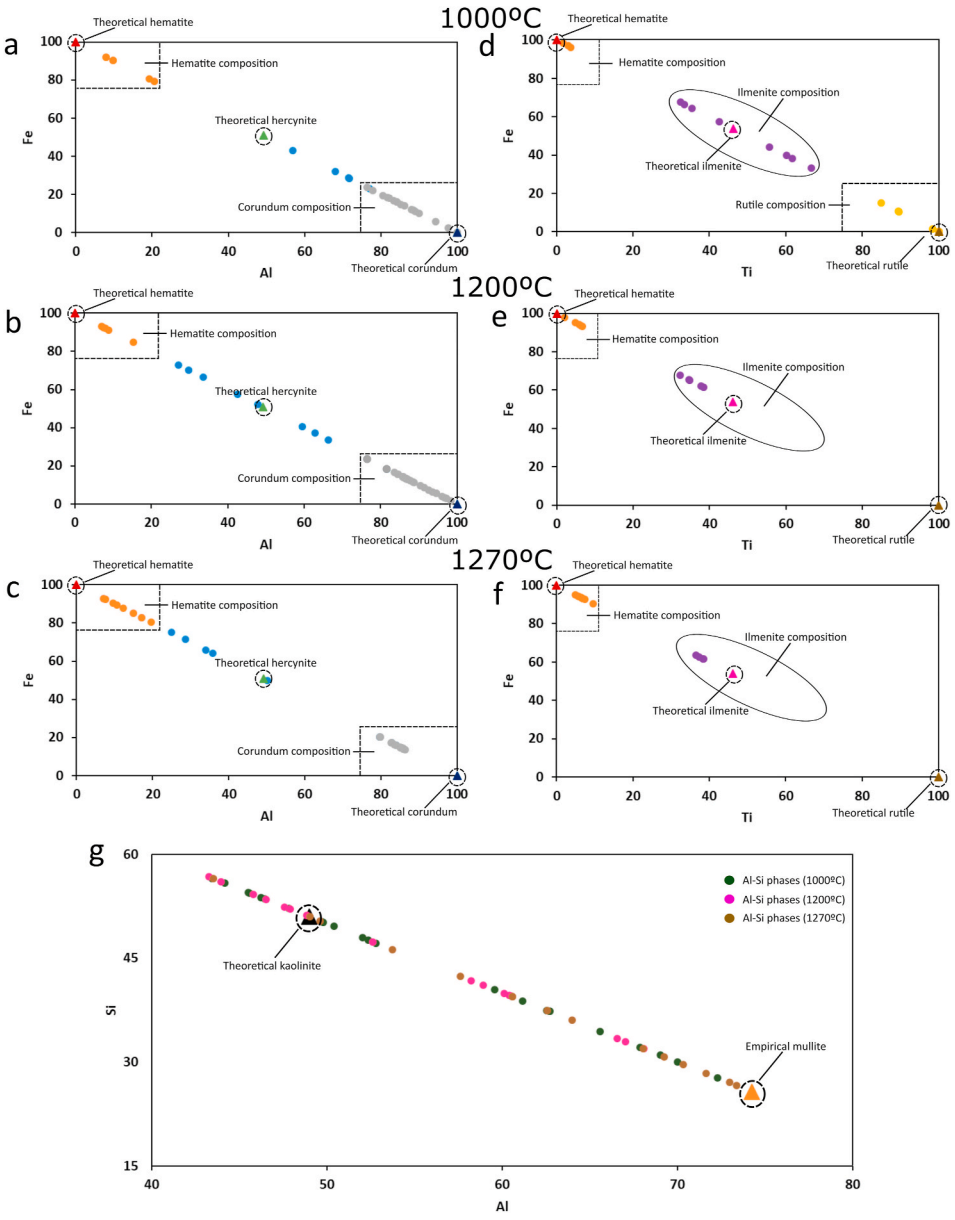

Fig. 8. (a, b, c) Al vs. Fe plots showing the hematite-hercynite-corundum trend in all the samples at 1000, 1200 and 1270 °C respectively. (d, e, f) Ti vs. Fe plots showing ilmenite, rutile and hematite compositions in all the samples at 1000, 1200 and 1270 °C. (g) Al and Si-rich compositions obtained from the mullite crystals in the three samples at the different temperatures.

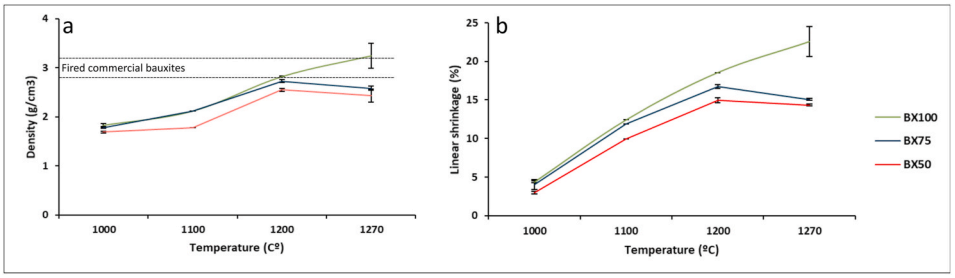

Fig. 9. Density vs temperature (a) and linear shrinkage vs temperature (b) graphs representing the changes in these properties in the fired samples.

reddish brown at 1000 and 1100 °C and to dull reddish brown from 1200 °C. BX50 undergoes more colour changes with temperature. The raw sample is a dull reddish brown colour, which changes to orange at 1000 °C, then to bright reddish brown at 1100 °C, dull reddish brown at 1200 °C, and finally to greyish brown at 1270 °C.

The CIE L*a*b* scale (Fig. 10b) shows that there is a trend towards orange colours from the raw samples to those fired at 1000 °C. From 1100 °C, the a* and b* values then decrease progressively, which

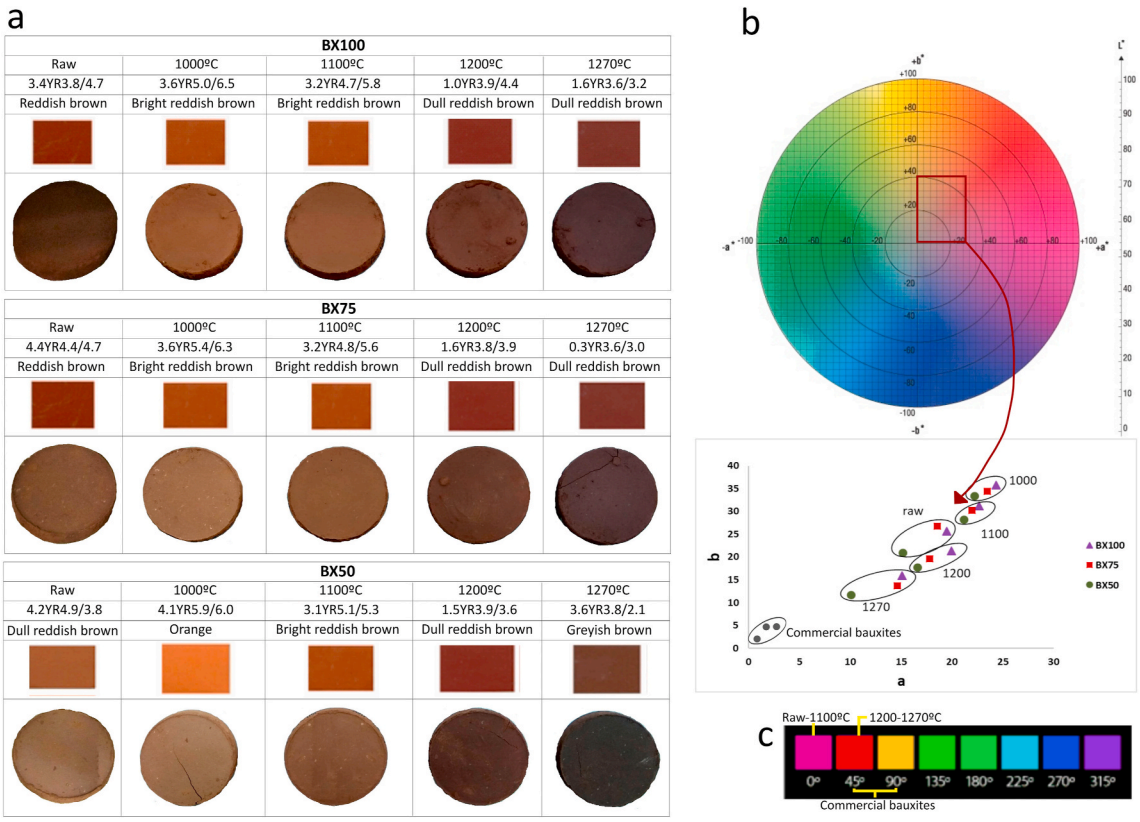

Fig. 10. Colours of the raw and fired samples represented in the Munsell System (a) and the CIE L*a*b* scale (b) and the hue scale (c). (For interpretation of the references to colour in this figure legend, the reader is referred to the Web version of this article.)

coincides with the change towards darker colours, also shown by the Munsell System. The hue values calculated for the samples show that all the raw samples and those fired at up to 1100 °C present values between 34.22° and 37.03°, which coincide with pink hues, whereas those fired at 1200 °C and 1270 °C present hues close to red (40.36° and 46.94°), according to the hue scale displayed in Fig. 10c.

Comparing these colour values with those of the fired commercial bauxites, the Munsell notation for the fired commercial bauxites (2.1Y5.1/0.7, 1.6Y4.8/0.8 and 5.7Y4.1/0.2) indicates that the latter are of yellowish grey and grey colours, which are darker in colour than the fired cylinders. Likewise, the a* and b* coordinates presented by the fired commercial bauxites show lower values than the samples fired at 1270 °C, and their hue values are somewhat higher (63.89–75.86°), indicating hues between red and orange.

4.3.3. Porosity

The distribution curves for porosity vary with the increase in firing temperature in all the samples (Fig. 11). At 1000 °C the intrusion percentage is highest in sample BX50 (4.19%) and it occurs in pores whose radius reaches greater sizes (1 μm) than in samples BX75 and BX100. At

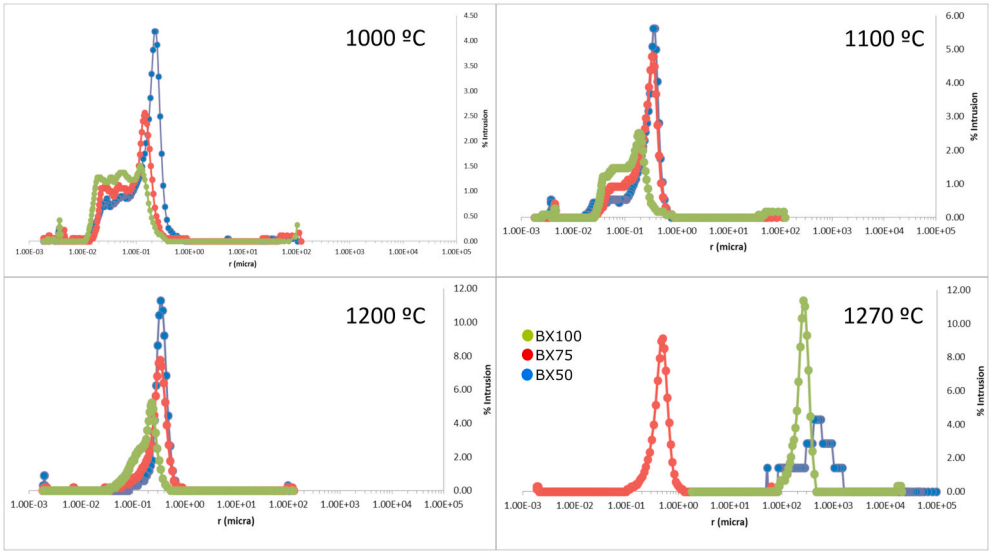

Fig. 11. Distribution curves for porosity obtained from the porosimetric analysis of the fired samples.

this temperature, sample BX100 presents the lowest intrusion percentage (1.23–1.46%), with pores with a radius between 2×10^{-2} and 3×10^{-1} μm.

At 1100 and 1200 °C the intrusion percentage increases in all the samples, this increase being higher in samples BX50 and BX75, which present a maximum intrusion of 5.62–11.31% and 4.79–7.78%, respectively. By contrast, sample BX100 has a maximum intrusion of 2.51%, occurring in pores with a radius of 4×10^{-2}-4x10^{-1} μm, somewhat smaller than those where the maximum intrusion occurs in samples BX75 and BX50.

Finally, at 1270 °C the maximum intrusion decreases in sample BX50 (4.29%) but it occurs in pores with a greater radius than at lower temperatures (3.5×10^{2} and 5.6×10^{2} μm). By contrast, the maximum intrusion increases in samples BX75 (9.13%) and BX100 (11.38%). In the case of sample BX75 it occurs in pores with a radius of 1×10^{-1}-1μm, whereas in sample BX100 it occurs in pores with a similar radius to those in sample BX50 at this temperature (1×10^{2}-5x10^{2} μm).

The mean, mode and total porosity of the fired samples are presented in Table 2. The average pore size (mean) decreases in all the samples with the increase in temperature. The mode values also decrease with temperature in samples BX75 and BX100 but increase in sample BX50. The total porosity decreases progressively with temperature in all the samples, although there is a slight increase in sample BX75 at 1270 °C.

The apparent porosity values given for the fired commercial bauxites are between 7 and 14.5%, which are consistent with the values for all the fired samples at 1200 °C and even at 1270 °C in the case of sample BX100.

4.3.4. Water absorption, thermal conductivity, and point load test

The water absorption values show that in general the absorption capacity of samples BX100 and BX50 decreases with temperature, whereas that of sample BX75 decreases up to 1100 °C and then slightly increases (Fig. 12a). This coincides with the decrease in porosity with temperature in all the samples and also with the subsequent slight increase in porosity of sample BX75 at 1270 °C. The fired commercial bauxites have absorption capacity values between 2 and 4.5%, i.e. very close to those of sample BX75 at 1200-1270 °C. In addition, the water absorption values of samples BX100 and BX50 fired at 1100-1200 °C are also fairly close to the fired commercial bauxite values.

The average values for thermal conductivity (k) obtained for the samples fired at 1200 °C are represented in Fig. 12b. This shows that samples BX75 and BX100 have a similar k value (2.46 and 2.40 W/m.K, respectively), which is greater than that of sample BX50 (1.94 W/m.K).

The results for the point load test (Fig. 12c) show that sample BX100 presents the highest resistance when it is fired at the highest temperature (1270 °C). By contrast, sample BX50 presents higher resistance, even higher than that shown by sample BX100, at 1200 °C than at 1270 °C, whereas there is no significant change in the resistance values for sample BX75 between these temperatures.

Table 2
Mean, mode and total porosity values obtained from the porosimetric analysis of the fired samples.

		Mean (μm)	Mode (μm)	Total porosity (%)
BX50	1000	6.67E-02	1.39E+00	34.55
	1100	4.46E-02	1.96E+00	25.69
	1200	1.61E-02	2.07 + 00	9.01
	1270	3.05E-03	3.21E+00	0.19
BX75	1000	1.34E-01	2.28E+00	34.67
	1100	7.07E-02	2.13E+00	23.92
	1200	2.31E-02	3.98E-01	14.45
	1270	3.34E-02	1.79E-02	18.13
BX100	1000	7.09E-02	2.63E+00	40.41
	1100	4.38E-02	8.63E-01	29.16
	1200	1.78E-02	6.40E-02	17.08
	1270	9.70E-03	4.01E-02	9.73

5. Discussion

5.1. Mineral and textural changes during the firing process

5.1.1. Destabilization of the initial phases

As pointed out in the Result sections, the raw samples initially contained boehmite, illite and/or kaolinite, hematite, rutile and anatase. Sample BX100 also had goethite, and BX75 and BX50 contained quartz.

Most of these initial phases were destabilized and melted during the firing process. Clay minerals were not detected at 1000 °C, indicating that these minerals are the least stable phases. Previous studies [2] have reported the absence of kaolinite above 800 °C in aluminium-rich ceramic materials, and the presence of illite up to 1000 °C, but with clear signs of dehydroxylation processes from 450 °C. The low stability of kaolinite in ceramic materials has also been reported by other authors [22,23], who describe the presence between 500 and 1000 °C of amorphous metakaolinite, which would be the precursor of mullite. The kaolinite-type morphologies observed in the fired samples at 1000 °C (Fig. 5d and f) could correspond, at least in part, to metakaolinite, given the closeness of their composition to the theoretical kaolinite. Nevertheless, taking into account the presence of mullite as deduced from XRD and the lack of FESEM evidence for discrete mullite crystals, they could also correspond to mullite and would thus represent the pseudomorphic transformation from kaolinite to mullite, since there is no evidence of fusion processes affecting the kaolinite-type morphologies at this temperature.

In the case of illite, thermogravimetric analysis also reported dehydroxylation occurring at 500-550 °C [24].

Like the clay minerals, boehmite was not present at 1000 °C due to a dehydration process that transforms boehmite (γ-AlOOH) into γ-Al_2O_3 at 490-510 °C [25–27]. Furthermore, neither the small amounts of anatase detected in all the raw samples nor the goethite detected in sample BX100 were present at 1000 °C. This can be explained by the fact that goethite dehydrated into hematite at 500-600 °C [28,29] and that anatase transforms into rutile at 500-550 °C [30]. In addition, the presence of small amounts of amorphous or poor crystalline iron oxides (not detected by XRD in the raw samples) that would destabilize with temperature, along with the dehydration of goethite into hematite in sample BX100, may be the cause of the increase in the hematite content at 1000 °C in all the samples.

The quartz content also increased at this temperature in samples BX75 and BX50. This may be a consequence of kaolinite and illite destabilization, which gives rise to an amorphous SiO_2 phase at 925-1050 °C [31].

5.1.2. Crystallization and composition of new phases

The morphology of synthetic γ-alumina has been described as irregular or thin flakes [32,33], so the acicular and prismatic crystals observed at 1000 °C by FESEM probably correspond to corundum.

These corundum crystals are of random orientation and of sizes that increase with temperature, reaching up to 4 μm at 1270 °C, and they are immersed in a probably vitreous matrix as well as replacing hematite. Previous studies have described how hematite or magnetite can be replaced by spinel in igneous materials and natural clinkers [34–36]. In this way, the low hercynite proportions detected in the XRD patterns could be replacing hematite, with the hematite content thus decreasing with temperature.

The transformation of pseudo-spinel to γ-Al_2O_3 has also been described in the literature [37], so the detected hercynite could contribute to the alumina formation.

As commented above, boehmite dehydrates, also giving rise to γ-Al_2O_3, at 490-510 °C [25–27]. γ-Al_2O_3 is one of the seven transition phases of alumina (χ-Al_2O_3, κ-Al_2O_3, γ-Al_2O_3, θ-Al_2O_3, δ-Al_2O_3, η-Al_2O_3, ρ-Al_2O_3). The corundum structure is called α-Al_2O_3 and is the last and most stable alumina phase, formed by increasing the temperature up to 1200 °C [26,38]. Accordingly, the γ-Al_2O_3 peaks detected in the XRD

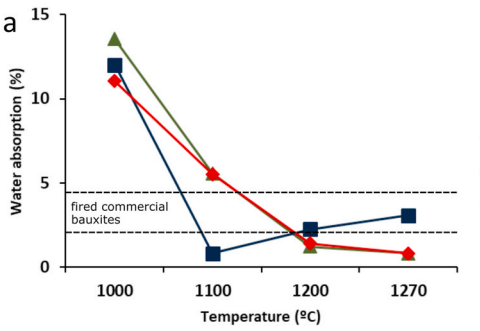

b

Thermal Conductivity (W/m.K)	
BX100	2.40 (±0.02)
BX75	2.46 (±0.02)
BX50	1.94 (±0.01)

c

	Is(50) (Mpa)	
BX100	1200	0.89(±0.15)
	1270	1.32(±0.19)
BX75	1200	1.12(±0.16)
	1270	1.14(±0.16)
BX50	1200	1.36(±0.15)
	1270	1.20(±0.14)

Fig. 12. (a) Water absorption variations in the samples fired at the different temperatures. (b) Mean values of thermal conductivity of samples fired at 1200 °C (standard deviation in brackets). (c) Point load index (Is(50)) obtained for samples fired at 1200 and 1270 °C (standard deviation in brackets).

patterns of the three samples fired at 1000 °C may be the remains of the transition phases of the alumina from the destabilization of boehmite and hercynite giving rise to corundum formation.

On the other hand, hematite (α-Fe_2O_3) and corundum (α -Al_2O_3) are isostructural phases and can form a solid solution at 1000-1300 °C [39]. This could also explain the compositions intermediate between these two phases in the studied ceramics.

FESEM analysis also showed a compositional trend among hematite, ilmenite and rutile compositions. During firing, part of the Ti from anatase and the Fe from hematite could lead to ilmenite crystallization. Ilmenite and hematite can form a solid solution above 650 °C [40], which would explain the compositional zonation between hematite and ilmenite found in some grains/crystals. This solid solution results in separated hematite-rich and ilmenite-rich phases with cooling [41]. Rutile, ilmenite and spinel intergrowths have also previously been described in igneous rocks [42] in a similar way to the compositional zonation between rutile and ilmenite observed in the studied samples.

The kaolinite-type morphologies observed at 1000 °C present their sheets separately due to the dehydroxylation processes, indicating that kaolinite was probably destabilized into metakaolinite. This metakaolinite would be the precursor of mullite through a *solid-state* process, giving rise to the pseudomorphic formation of mullite at 1000 °C, as commented in section 5.1.1. Later, the fusion process increases, which is evidenced by the presence of a vitreous phase, allowing the formation of discrete mullite crystals, which are clearly distinguished at 1200° and 1270 °C in the FESEM images. At these temperatures, mullite is present as acicular and prismatic crystals of random orientation, whose sizes increase with temperature, reaching up to 2 μm in length at 1270 °C. The mullite composition is not stoichiometric but follows a trend between kaolinite and empirical mullite compositions, and it shows a higher Al/Si ratio at 1270 °C. The Al diffusion was probably higher at 1270 °C than at 1000 °C [2], and thus there is an increase in the Al content of mullite crystals with the increase in temperature. The increase in crystal size and the changes in the composition with temperature are indicative of a decrease in the number of crystalline defects in the mullite structure [2].

5.1.3. *The firing process and the vitreous phase formation*

The vitrification process is responsible for the homogenization in the overall texture of all the samples with increasing temperature. At 1000 °C the rock fragments from the bauxite and the illite- and kaolinite-rich clay are still recognized, but they are no longer so distinguishable at 1200-1270 °C. The bauxite rock fragments seem to be more stable with temperature, since they are better recognizable at these temperatures in sample BX100; this may be due to its higher corundum content, as materials with high alumina content can withstand temperatures greater than 1300 °C and thermal shocks [43].

The presence of the vitreous phase is deduced in the three samples from the XRD and FESEM results from 1000 °C upwards. The FESEM analyses showed that this vitreous phase presents compositional variations depending on the sample and the area analysed, but in general it has an Al- and Si-rich composition and also contains Fe and minor proportions of Ti, Mg, Ca and Na. The Al and Si come from illite, kaolinite, boehmite and quartz, which were the main components of the raw samples and could also contribute Mg, Ca and Na, whereas the Fe and Ti come from hematite and from anatase and rutile, respectively.

The fact that the newly generated phases such as corundum or mullite are immersed in the vitreous phase demonstrates that the initial phases destabilized with the increase in temperature, giving rise to this vitreous phase from which the new phases crystallized from 1100 °C on.

On the other hand, these new phases are non-stoichiometric, which may be due to the dynamics of the firing process resulting in incomplete mineral reactions [2]. According to these authors, the aluminium diffusion is probably lower at 1000 °C than at 1270 °C, which is supported by the compositional trend of mullite towards a higher Al/Si ratio at 1270 °C and by the high amounts of corundum crystallized in all the samples.

5.2. *Changes in physical properties during the firing process*

5.2.1. *Changes in physical properties and their relation to the mineral transformations*

The increase in density with temperature in all the samples may be associated with the formation of the vitreous phase that gives rise to mullite crystallization, as has been described in kaolinite-rich clay materials [44]. By contrast, the increase in linear shrinkage may be associated with the dehydroxylation of the phyllosilicates and hydroxides during the firing process. On the other hand, the slight decrease in these two properties detected at 1270 °C in samples BX75 and BX50 could be due to the formation of internal fractures during firing, which may not be observable to the naked eye.

The red colours of the fired clays can be attributed to the presence of Fe_2O_3 [11], as well as to its crystal size and distribution. The colour change from brown to reddish colours at 1000 °C may be related with the increase in hematite content at this temperature. Similarly, the decrease in hematite content at 1200° and 1270° would cause the colour change from reddish to grey colours. The CIE L*a*b* scale reflects a decrease in the a* and b* values with the increase in temperature, which is more marked in samples BX75 and BX50. Decreases in a* and b* values with rising temperature have also been described in clayey materials in the literature [45], so the decrease in these values in samples BX75 and BX50 may be associated with their higher clay content and lower hematite content.

The continuous pore filling by mullite and vitreous phase is also the consequence of the decrease in the total porosity of the samples, which decreased progressively with the increase in temperature in the studied samples, especially at 1200 °C, when the vitreous phase and mullite content is higher in all the samples. A decrease in porosity with temperature due to the formation of vitreous phase has also been reported in

similar materials [3,46].

The increase in the density and linear shrinkage correlates with the decreases in water absorption, which has also been described in clayey materials [11]. The decrease in water absorption is also related with the decrease in total porosity [46] and/or in pore size and connectivity. Higher pore connectivity, along with the possible internal fractures produced during firing as commented above, would explain the slight increase in porosity and water absorption in sample BX75 at 1200-1270 °C. The maximum helium intrusion in this sample at 1270 °C occurred in pores with a smaller radius than in samples BX100 and BX50, but these pores may have been more connected, leading to a small increase in porosity and water absorption capacity.

The thermal conductivity values obtained for the samples fired at 1200 °C are higher when the total porosity and density are higher and the pore mode values are lower. Sample BX50 presents the lowest k value, which coincides with a higher pore mode, but a lower total porosity caused by a higher vitreous phase content. Conversely, samples BX100 and BX75 have higher k values, which correlate with a lower pore mode, but a higher total porosity caused by a lower vitreous phase content.

Finally, the point load test indicated that sample BX50 has higher resistance at 1200 °C than at 1270 °C, whereas the opposite was the case for sample BX100. This may be related with the mullite and corundum content, since at 1270 °C sample BX100 has a higher corundum content, whereas sample BX50 presents a higher mullite content.

5.2.2. *Refractory potential of the studied materials*

The fired commercial bauxites were mainly formed by corundum (67–80%) and mullite (13–26%). The most similar composition to this among the studied ceramics is that of sample BX100 fired at 1100 °C (57% corundum and 21% mullite), whereas samples BX75 and BX50 are poor in corundum and rich in mullite from 1000 °C upwards.

By contrast, some of the physical properties of samples BX75 and BX50 are closer to those of the fired commercial bauxites than those of sample BX100. In addition, the firing temperature is also an important factor, as commented above, since it causes changes in all the measured physical properties.

Sample BX100 fired at 1270 °C presents a density (3.43 g/cm^3) similar to those of the fired commercial bauxites (2.8–3.23 g/cm^3), whereas BX75 and BX50 present a slightly lower density at this temperature (2.55 g/cm^3 and 2.43 g/cm^3, respectively), which, as suggested above, may be caused by the presence of internal fractures. The porosity of samples BX75 and BX50 fired at 1200 °C (9.01 and 14.45% respectively) and that of sample BX100 (9.73%) fired at 1270 °C are those that fit best with the porosity of the fired commercial bauxites (7–14.5%). This indicates that the mixture of the bauxite with the illite- and kaolinite-rich clay also produces a decrease in porosity at lower temperatures.

The water absorption values of sample BX75 fired at 1200-1270 °C (2.25–3.09%) are similar to those of the fired commercial bauxites, whereas samples BX100 and BX50 fired at 1100-1200 °C present water absorption values outside those limits, though close to them. Regarding the colour, samples BX50 and BX75 presented lower a* and b* values with increasing temperature, and they are closest to the a* and b* values of fired commercial bauxite when fired at 1270 °C. This could indicate that, due to the mixture of the bauxite with the illite- and kaolinite-rich clay, the hematite content is lower, and thus samples are darker.

The thermal conductivity of the samples is related with their porosity and vitreous phase content. To be a suitable refractory material, thermal conductivity should be as low as possible. According to our results, a sample mixed 50% with illite- and kaolinite-rich clay presents better values of thermal conductivity (1.94 W/m.K) than the pure bauxite (2.40 W/m.K) at the same firing temperature. Finally, the higher resistance observed in samples BX50 and BX75 at 1200 °C in the point load test may be related with a higher mullite and vitreous phase content at this temperature in these samples. The presence of illite and kaolinite gives rise to an increase in resistance due to the higher K content (as was also reported by the XRF results), which reduces the melting point and results in earlier vitrification and/or more effective formation of vitreous phase. By contrast, the higher resistance of sample BX100 at 1270 °C may be associated with its corundum content, which is higher at this temperature.

Therefore, pure bauxite fired at 1270 °C shows characteristics closely resembling those of the fired commercial bauxites regarding mineralogical composition, porosity and density, and it shows high resistance. However, mixtures of bauxite with illite- and kaolinite-rich clays fired at lower temperatures show features not so far from the ranges exhibited by the fired commercial bauxites, but they are richer in mullite and vitreous phase, which lead to higher resistance and (in the case of sample BX50) lower thermal conductivity of the fired products.

6. Conclusions

The study of mixtures of bauxite with illite- and kaolinite-rich clays fired between 1000 and 1270 °C shows mineralogical and textural changes during firing that clearly affect the physical properties of the materials.

At 1000 °C, the formation of mullite seems to occur as a pseudomorphic, *solid-state* process after amorphous metakaolinite has originated through kaolinite dehydroxylation. At higher temperatures, the ongoing destabilization of the initial phases gives rise to a Si- and Al-rich vitreous phase from which cristobalite, ilmenite, hercynite, mullite and corundum crystallize. The vitrification process causes the textural homogenization of the samples with increasing temperature and the short duration of the firing process allows the coexistence of some of the initial phases with those generated during the firing.

Mullite and corundum are the most abundant phases at a high temperature, the mullite content being higher in those samples mixed with the illite- and kaolinite-rich clay. Both phases are immersed in the vitreous phase and their crystal thickness increases with temperature up to 2–4 μm. The analysed mullite presents a heterogeneous composition, but its Al content increases with temperature.

The formation of vitreous phase and mullite and the process of dehydroxylation, gives rise to an increase in the density and linear shrinkage that correlates with a decrease in total porosity, water absorption and thermal conductivity. The changes in the colour are related to the hematite content, whereas the resistance of the samples is associated with their vitreous phase and corundum content.

Both the firing temperature and the clay content influence the refractory potential of the mixtures, since samples mixed with illite- and kaolinite-rich clay present similar properties at lower temperatures to those of the fired commercial bauxites. This study shows that when mixing bauxite with Al–K-bearing clays, it is not necessary to reach such high firing temperatures to achieve refractory properties like those of fired commercial materials.

Declaration of competing interest

The authors declare that they have no known competing financial interests or personal relationships that could have appeared to influence the work reported in this paper.

Acknowledgments

This work was supported by the European Regional Development Fund and the Government of Aragon [Aragosaurus Group: Geological Resources and Palaeoenvironments, grant number E18_20R] and the Spanish Ministry of Science, Innovation and Universities [grant number RTI2018-093419-B-100]. The authors would like to acknowledge the use of the Servicio General de Apoyo a la Investigación-SAI, University of Zaragoza. They would also like to thank Cristina Gallego for her advice during the FESEM sessions and Miguel Castro for his help and

advice with the thermal conductivity measurements. Elisa Laita is also grateful for a Government of Aragón grant for the development of her Ph.D. The authors would also like to thank the reviewers, whose comments and suggestions helped to improve the manuscript.

References

[1] I.A. Altun, Effect of temperature on the mechanical properties of self-flowing low cement refractory concrete, Cement Concr. Res. 31 (2001) 1233–1237, https://doi.org/10.1016/S0008-8846(01)00533-6.

[2] E. Laita, B. Bauluz, Mineral and textural transformations in aluminium-rich clays during ceramic firing, Appl. Clay Sci. 152 (2018) 284–294, https://doi.org/10.1016/j.clay.2017.11.025.

[3] O.V. Gavshina, V.A. Doroganov, E.A. Doroganov, V.I. Onishehuk, Y.N. Trepalina, High-alumina mixes based on molded bauxite suspensions, Refract. Ind. Ceram. 60 (4) (2019) 350–354, https://doi.org/10.1007/s11148-019-00365-3.

[4] M.M. Jordán, S. Meseguer, F. Pardo, M.A. Montero, High-temperature mineral formation after firing clay materials associated with mined coal in teruel (Spain), Appl. Sci. 10 (2020) 3114, https://doi.org/10.3390/app10093114.

[5] M. Maggetti, Phase analysis and its significance for technology and origin, in: J. S. Olin (Ed.), Archaeological Ceramics Smithsonian, Institution Press, Boston, 1982, pp. 121–133.

[6] M. Ghassemi Kakroudi, E. Yeugo-Fogaing, C. Gault, M. Huger, T. Chotard, Effect of thermal treatment on damage chemical behaviour of refractory castables: comparison between bauxite and andalusite aggregates, J. Eur. Ceram. Soc. 28 (2008) 2471–2478, https://doi.org/10.1016/j.jeurceramsoc.2008.03.048.

[7] B. Bauluz, M.J. Mayayo, A. Yuste, C. Fernández-Nieto, J.M. González López, TEM study of mineral transformations in fired carbonated clays: relevance to brick making, Clay Miner. 39 (2004) 333–344, https://doi.org/10.1180/0009855043930138.

[8] M.M. Jordán, A. Boix, T. Sanfeliu, C. de la Fuente, Firing transformations of cretaceous clays used in the manufacturing of ceramic tiles, Appl. Clay Sci. 14 (1999) 225–234, https://doi.org/10.1016/S0169-1317(98)00052-0.

[9] F. Pardo, S. Meseguer, M.M. Jordán, T. Sanfeliu, I. González, Firing transformations of Chilean clays for the manufacture of ceramic tile bodies, Appl. Clay Sci. 51 (2011) 147–150, https://doi.org/10.1016/j.clay.2010.11.022.

[10] S. Boussen, D. Sghaier, F. Chaabani, B. Jamoussi, A. Bennour, Characteristics and industrial application of the Lower Cretaceous claydeposits (Bouhedma Formation), Southeast Tunisia: potential use for the manufacturing of ceramic tiles and bricks, Appl. Clay Sci. 123 (2016) 210–221, https://doi.org/10.1016/j.clay.2016.01.027.

[11] B. Semiz, S.B. Çelik, Mineralogical and geochemical characteristics of Belevi clay deposits at Denizli, SW Turkey: industrial raw material potential, Arab. J. Geosci. 13 (2020) 313, https://doi.org/10.1007/s12517-020-05292-z.

[12] F. Yang, C. Li, Y. Li, C.-A. Wang, Effects of sintering temperature on properties of porous mullite/corundum ceramics, Mater. Lett. 73 (2012) 36–39. https://10.1016/j.matlet.2011.12.087.

[13] J.M. Molina, P.A. Ruiz-Ortiz, J.A. Vera, A. Calonge, Bauxitas kársticas de la sierra de Boada (Sierras Marginales surpirenaicas, Alós de Balaguer, Lleida), Geogaceta 16 (1994) 148–150.

[14] M.J. Aguilar, J. Ramírez del Pozo, O. Riba, Algunas precisiones sobre la sedimentación y paleontología del Cretácico inferior en la zona de Utrillas-Villarroya de los Pinares, Estud. Geol. 27 (1971) 497–512.

[15] A. Cervera, G. Pardo, J. Villena, Algunas precisiones litoestratigráficas sobre la Formación 'Lignitos de Escucha', Tecniterrae 3 (1976) 25–33.

[16] L.A. Díaz Rodríguez, R. Torrecillas, Arcillas cerámicas: una revisión de sus distintos tipos, significados y aplicaciones, Bol. Soc. Esp. Ceram. V. 41 (5) (2002) 459–470.

[17] B. Bauluz, M.J. Mayayo, A. Yuste, J.M. González López, Genesis of kaolinite from Albian sedimentary deposits of the Iberian Range (NE Spain): analysis by XRD, SEM and TEM, Clay Miner. 43 (2008) 459–475, https://doi.org/10.1180/claymin.2008.043.3.10.

[18] J.D. Martin, A software package for powder x-ray diffraction analysis, Qualitative, Quantitative and Microtexture 121 (2017).

[19] L.G. Schultz, Quantitative interpretation of mineralogical composition from X-ray and chemical data for the Pierre shale, USGS Professional Paper 391-C (1964) 1–131.

[20] P.E. Biscaye, Mineralogy and sedimentation of recent deep-sea clay in the Atlantic Ocean and adjacent seas and oceans, Geol. Soc. Am. Bull. 76 (1965) 803–832.

[21] D.K. Smith, G.G. Johnson Jr., Digitized database quantification, DDBQ, analysis of complex mixtures using fully digitized patterns, Adv. X Ray Anal. 42 (2000) 276–286.

[22] C.Y. Chen, G.S. Lan, W.H. Tuan, Microstructural evolution of mullite during the sintering of kaolin powder compacts, Ceram. Int. 26 (7) (2000) 715–720, https://doi.org/10.1016/S0272-8842(00)00009-2.

[23] Y. Meng, G. Gong, D. Wei, Y. Xie, In situ high temperature X-ray diffraction study on high strength aluminous porcelain insulator with the Al_2O_3-SiO_2-K_2O-Na_2O system, Appl. Clay Sci. 132–133 (2016) 760–767, https://doi.org/10.1016/j.clay.2016.07.014.

[24] V. Drits, D. McCarty, The nature of structure-bonded H2O in illite and leucophyllite from dehydration and dehydroxylation experiments, Clay Clay Miner. 55 (1) (2007) 45–48, https://doi.org/10.1346/CCMN.2007.0550104.

[25] D. Panias, A. Krestou, Effect of synthesis parameters on precipitation of nanocrystalline boehmite from aluminate solutions, Powder Technol. 175 (2007) 163–173, https://doi.org/10.1016/j.powtec.2007.01.028.

[26] A.S. Jbara, Z. Othaman, A.A. Ati, M.A. Saeed, Characterization of γ-Al2O3 nanopowders synthesized by Co-precipitation method, Mater. Chem. Phys. 188 (2017) 24–29, https://doi.org/10.1016/j.matchemphys.2016.12.015.

[27] Y. Dong, M. Zhang, C. Xie, Effect of reaction conditions on agglomeration of aluminium hydroxide in the recovery of waste aluminium-catalyst, Separ. Purif. Technol. 248 (2020) 116978, https://doi.org/10.1016/j.seppur.2020.116978.

[28] K. Jang, V.R.M. Nunna, S. Hapugoda, A. Nguyen, W.J. Bruckard, Chemical and mineral transformations of a low grade goethite ore by dehydroxilation, reduction roasting and magnetic separation, Miner. Eng. 60 (2014) 14–22, https://doi.org/10.1016/j.mineng.2014.01.021.

[29] Y. Sun, X. Zhu, Y. Han, Y. Li, P. Gao, Iron recovery from refractory limonite ore using suspension magnetization roasting: a pilot-scale study, J. Clean. Prod. 261 (2020) 121221, https://doi.org/10.1016/j.jclepro.2020.121221.

[30] J.M. Low, B. Curtain, M. Philipps, Z.Q. Liu, M. Ionescu, High temperature diffraction study of in-situ crystallization of nanostructured TiO2 photocatalysts, J. Australas. Ceram. Soc. 48 (2) (2012) 198–204.

[31] T. Ondro, O. Al-Shantir, Š. Csáki, F. Lukác, A. Trník, Kinetic analysis of sinter-crystallization of mullite and cristobalite from kaolinite, Thermochim. Acta 678 (2019) 178312, https://doi.org/10.1016/j.tca.2019.178312.

[32] L. Samain, A. Jaworski, M. Edén, D.M. Ladd, D.K. Seo, F.J. Garcia-Garcia, U. Häussermann, Structural analysis of highly porous γ-Al_2O_3, J. Solid State Chem. 217 (2014) 1–8, https://doi.org/10.1016/j.jssc.2014.05.004.

[33] N. Salahudeen, A. Ahmed, A.H. Al-Muhtaseb, M. Dauda, S.M. Waziri, B.Y. Jibril, Synthesis of gamma alumina from Kankara kaolin using a novel technique, Appl. Clay Sci. 105–106 (2015) 170–177, https://doi.org/10.1016/j.clay.2014.11.041.

[34] A.H. Treiman, Amphibole and hecynite spinel in Shergotty and Zagami: magmatic water, depth of crystallization, and metasomatism, Meteoritics 20 (1984) 229–243, https://doi.org/10.1111/j.1945-5100.1985.tb00862.x.

[35] M. Sandiford, F.B. Neall, R. Powell, Metamorphic evolution of aluminous granulites from Labwor Hills, Uganda, Contrib. Mineral. Petrol. 95 (1987) 217–225, https://doi.org/10.1007/BF00381271.

[36] E. Laita, B. Bauluz, A. Yuste, High-temperature mineral phases generated in natural clinkers by spontaneous combustion of coal, Minerals 9 (4) (2019) 213, https://doi.org/10.3390/min9040213.

[37] F.M. Segal, M.F. Correa, R. Bacani, B. Castanheira, M.J. Politi, S. Brochsztain, E. R. Triboni, A novel synthesis route of mesoporous γ-alumina from polyoxohydroxide aluminum, Mater. Res. 21 (1) (2018), e20170674, https://doi.org/10.1590/1980-5373-MR-2017-0674.

[38] S. Cava, S.M. Tebcherani, S.A. Pianaro, C.A. Paskocimas, E. Longo, J.A. Varela, Structural and spectroscopic analysis of γ-Al_2O_3 to α-Al_2O_3-$CoAl_2O_3$ phase transition, Mater. Chem. Phys. 97 (2006) 102–108, https://doi.org/10.1016/j.matchemphys.2005.07.057.

[39] A. Feenstra, S. Sämann, B. Wunder, An experimental study of Fe-Al solubility in the system corundum-hematite up to 40 kbar and 1300°C, J. Petrol. 46 (9) (2005), https://doi.org/10.1093/petrology/egi038, 1881–1832.

[40] D.H. Lindsley, Experimental studies of oxide minerals, Rev. Mineral. Geochem. 25 (1991) 69–106.

[41] W. Tan, C. Yan Wang, H. He, C. Xing, X. Liang, H. Dong, Magnetite-rutile symplectite derived from ilmenite-hematite solid solution in the Xinjie Fe-Ti oxide-bearing, mafic-ultramafic layered intrusion (SW China), Am. Mineral. 100 (2015) 2348–2351, https://doi.org/10.2138/am-2015-5435.

[42] G. Markl, Mullite-corundum-spinel-cordierite-plagioclase xenoliths in the Skaergaard Marginal Border Group: multi-stage interaction between metasediments and basaltic magma, Contrib. Mineral. Petrol. 149 (2005) 196–215, https://doi.org/10.1007/s00410-004-0644-5.

[43] E. Medvedovski, Wear-resistant engineering ceramics, Wear 249 (2001) 821–828, https://doi.org/10.1016/S0043-1648(01)00820-1.

[44] A. Andrews, J. Adam, S.K.Y. Gawu, Development of fireclay aluminosilicate refractory from lithomargic clay deposits, Ceram. Int. 39 (1) (2012) 779–783, https://doi.org/10.1016/j.ceramint.2012.06.091.

[45] E. Murad, U. Wagner, Clays and clay minerals: the firing process, Hyperfine Interact. 117 (1988) 337–356.

[46] M. Loutou, R. Hakkou, R. Argane, M. Mansori, L. Grase, R. Svinka, G. Mezinskis, Clayey quarry sludges: thermal transformation, microstructure and technological properties, Waste. Biomass. Valor. 9 (2018) 1805–1815, https://doi.org/10.1007/s12649-017-9972-3.

ANNEX V

minerals

MDPI

Article

High-Temperature Mineral Phases Generated in Natural Clinkers by Spontaneous Combustion of Coal

Elisa Laita *, Blanca Bauluz and Alfonso Yuste

IUCA-Facultad de Ciencias, Universidad de Zaragoza, Pedro Cerbuna 12, 50009 Zaragoza, Spain; bauluz@unizar.es (B.B.); alfon@unizar.es (A.Y.)

* Correspondence: laita@unizar.es; Tel.: +34-627-675-602

Received: 4 March 2019; Accepted: 29 March 2019; Published: 1 April 2019

Abstract: The aim of this study is to analyze natural clinkers (= calcined clays by coal combustion) from a lower Cretaceous coal outcrop in Ariño (Teruel, NE Spain) in order to describe mineral and textural transformations produced during the spontaneous combustion of coal. To achieve this aim, samples were analyzed using X-ray diffraction and optical and electron microscopy. Spontaneous combustion resulted in the melting of the surrounding clays, with the generation of an Al–Si-rich vitreous phase. Subsequently, high-temperature phases crystallized from this vitreous phase. These new minerals are interesting due to their similarity with those formed during ceramic processes, used in the manufacture of stoneware and ceramic tiles, as well as in refractory ceramics, and with natural events such as metamorphic and igneous processes. The studied natural clinkers are composed of vitreous phase mullite, hematite, hercynite, cristobalite, quartz, pyroxenes, cordierite, gypsum, pyrite, and calcium oxides. A trend from hematite to hercynite composition indicates compositional variations at sample scale, which evidence d-spacing differences in hercynite and may be related to the Al and Fe content in hercynite depending on its texture. The mullite shows higher Si/Al ratio (1.21) than the theoretical composition (0.35), indicating that this mullite is more Si-rich. Three pyroxene-type compositions (diopside-type, ferrosilite-type, and a Ca–Al-rich pyroxene) were found. Both the mullite and the pyroxenes are nonstoichiometric.

Keywords: natural clinkers; coal spontaneous combustion; electron microscopy; high-temperature mineral transformations

1. Introduction

Spontaneous coal combustion is a frequent phenomenon that can take place in coal deposits when high quantities of these materials are stored for large periods [1,2]. Several researchers have described this process [3–9]. Spontaneous combustion occurs in coal seams, stockpiles, and coal wastes when the rate of heat generation from the oxidation of organic matter exceeds the rate of heat dissipation [3]. However, other factors could also favor or hinder spontaneous combustion [4]. According to these authors, heat from the oxidation of inorganic coal-bearing phases, such as pyrite, could be the key factor in attaining the necessary heat for the self-ignition of coal. Furthermore, several parameters influence the process of spontaneous heating and combustion in coal. These parameters relate to mining (panel dimension, ratio of coal, extraction, etc.), the geological parameters (faults, joints, etc.), and the coal chemical composition [10].

When the spontaneous combustion of coal takes places, new mineral phases are generated from those present in the previous coal and surrounding materials, i.e., clays, producing natural clinkers. The occurrence of natural clinkers associated with coal deposits has frequently been described in some areas [11–17].

The province of Teruel (NE, Spain) has historically been an important coal mining area, and there are still abundant coal deposits that can generate spontaneous combustion. Previous researchers have described the occurrence of natural clinkers in this area, and identified by means of X-ray diffraction a new mineral association generated by this spontaneous combustion [18,19]. However, there are no recent studies using high-resolution techniques in this area.

Accordingly, the aim of the present research is to study natural clinker samples from the locality of Ariño (Teruel, Spain) in order to describe the mineral and textural transformations that take place during the spontaneous firing of the coal, emphasizing in the mineral chemistry of the high-temperature phases in order to understand the calcination process. To this end, X-ray diffraction (XRD) and optical and field-emission scanning electron microscopy (FESEM) were used.

The calcination process can be compared to ceramic processes since the new mineral phases generated are very similar [18–20]. Mineral phases such as mullite or pyroxenes have previously been described in ceramic materials in the literature [20–22]. These materials could thus be used in the manufacture of stoneware and ceramic floor, as well as in refractory ceramics. Some of these new phases are also reported in natural processes such as metamorphism [14,23,24] and igneous processes [25–27]. For this reason, determining the chemical and textural characteristics of all the new phases may shed light on the characteristics of the spontaneous combustion of coal as well as on the differences between this natural process and other natural or ceramic processes.

2. Geological Setting

The samples analyzed in this study were taken from a coal mining area in the Iberian Range, NE Spain, in a natural outcrop near the coal mine of Santa Maria, close to the locality of Ariño (Teruel) (N 41°01′53.28″ W 0°34′50.24″, elevation 539 m).

The studied materials belong to the lower-middle Albian (Lower Cretaceous) sedimentary deposits of the Escucha Formation [28], which consists of three members: lower, middle, and upper. The lower member consists of marls at the bottom and carbonaceous clays with lignite beds towards the top. Carbonaceous clays with lignite remains and sandstones form the middle member, and the upper member is formed by limestones and sandstones [29].

This formation constitutes a depositional sequence that represents a freshwater swamp with brackish swamp plain areas. This environment allowed the accumulation and preservation of coal deposits, which can be found in the lower and middle members of the formation [28,30,31].

Near Ariño, the Escucha Formation is 200 m thick and contains abundant dark claystones and siltstones with minor sandstones [32]. Previous researchers have described several stratiform natural clinker levels in a nearby area, which are similar to that studied in this research. The natural clinkers are included in the coal seams [18].

The natural clinkers analyzed in this study present a scoriaceous appearance, with light and versicolor tones; they include clay and carbonaceous levels. The arrangement of the natural clinkers is stratiform and they are located from above and under the original position of the coal levels whose spontaneous combustion produced the calcination.

3. Materials and Methods

3.1. Description of the Samples

Precursor clays show plastic behavior and contain abundant organic matter, kaolinite, and illite, and minor proportions of quartz, K feldspar, siderite, pyrite, and Ti and Fe oxides [32]. They can be classified as ball clays and are mined nowadays.

Four representative samples of natural clinkers were studied on the basis of their different macroscopic characteristics and labeled as ESC-1, ESC-2, ESC-3, and ESC-4. All the samples are versicolor, with a vitreous appearance and high porosity. The size of the pores varies from 1 to 5 mm and they have irregular morphologies.

Although they are heterogeneous in color, samples ESC-1 and ESC-4 are mainly red with black areas (which are more abundant in sample ESC-4), and samples ESC-2 and ESC-3 are mainly black with some yellow areas (Figure 1).

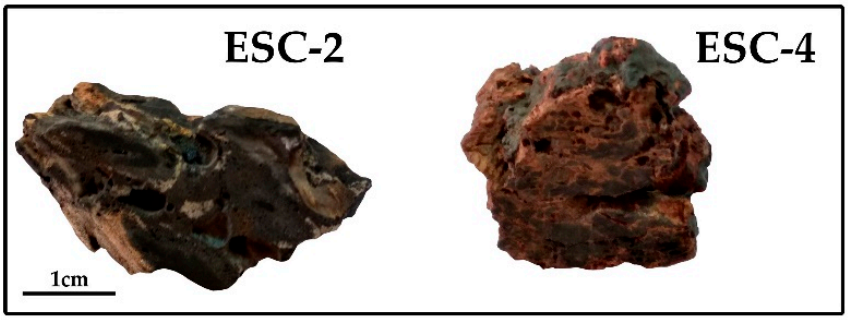

Figure 1. Images of a black natural clinker sample with yellow areas (ESC-2) and another red with black areas (ESC-4).

3.2. X-ray Diffraction

Mineralogical analyses of the samples were performed by X-ray diffraction (XRD). Sample ESC-2 was divided into two subsamples: ESC-2B, corresponding to the black zones, and ESC-2BY, which includes black and yellow areas. Similarly, ESC-3 was divided into ESC-3B, predominantly black, and ESC-3YB, including black and yellow zones. As a result, six XRD patterns were obtained: two XRD patterns correspond to whole samples ESC-1 and ESC-4, and the other four patterns to samples ESC-2 and ESC-3.

To obtain the diffraction patterns, a RIGAKU D-Max/2500 diffractometer (Rigaku, Tokyo, Japan) was used with 40 kV voltage, 80 mA current, CuKα, and a graphite monochromator. XRD patterns were obtained from the 3–80° 2θ interval with a goniometer velocity of 0.03° 2θ/s and an integration time of 0.5 s.

Once the XRD patterns were obtained, $d_{(400)}$ values of hercynite and $d_{(104)}$ values of hematite were determined using the quartz of the sample as an internal standard. The objective was to infer whether there was any relation between these parameters and the chemical composition of the phases. Hematite- and/or hercynite-rich samples (ESC-2B, ESC-2BY, ESC-3B, and ESC-3BY) were selected for this measure.

In order to quantify the different minerals, samples were homogenously mixed with 10 wt % corundum and analyzed by XRD, following the RIR_{cor} method [33]. The amount (X) of each component (i) in a mixed sample with corundum can be obtained with the formula $X_i = [X_{cor}/RIR_{cor}][I_{(hkl)i}/I_{(113)cor}]$, where X_{cor} is the percentage of corundum mixed with the test sample, RIR_{cor} is the Reference Intensity Ratio of each phase with respect to corundum, $I_{(hkl)}$ is the absolute intensity of the strongest reflection of each mineral phase, and $I_{(113)cor}$ is the intensity of the (113) peak (2.08 Å) of corundum.

RIR_{cor} values of cristobalite (2.66) and gypsum (0.28) were calculated following the procedure described by [33]. The RIR_{cor} of hematite (1.587), mullite (0.5660), quartz (4.4045), cordierite (0.91), and hercynite (3.03) were taken from the literature [20,34,35]. The reflections (*hkl*) used for the quantification of each mineral were 2.69 Å for hematite, 3.38 Å for mullite, 3.34 Å for quartz, 4.05 Å for cristobalite, 8.56 Å for cordierite, 2.45 Å for hercynite, and 7.64 Å for gypsum.

3.3. Optical and Electron Microscopy Studies

Thin sections of the natural clinkers were studied by transmitted and reflected light microscopy to identify mineral phases and characterize their texture. The same thin sections were analyzed by a Carl Zeiss Merlin field-emission scanning electron microscope (FESEM) with an Oxford energy-dispersive

X-ray (EDS) detector at the University of Zaragoza (Zaragoza, Spain). The thin sections had previously been carbon-coated.

Compositional images of the samples were obtained using two types of backscattered electron detectors: angular selective (AsB) and energy selective (EsB). To obtain chemical information, semiquantitative analyses were acquired by an energy-dispersive X-ray (EDS) detector, with a detection limit of 0.1%. The accelerating voltage for AsB and EDS was 15 kV with a beam current of 400 pA; for EsB, the accelerating voltage was 4 kV with a beam current of 2.0 nA. Mineral formulas were obtained for the analyzed minerals in order to compare them with the theoretical compositions.

4. Results

4.1. X-ray Diffraction (XRD): Qualitative Analysis and Mineral Quantification

Samples ESC-1 and ESC-4 contain mullite, cristobalite, hematite, quartz, pyroxenes, and cordierite (Figure 2). The detected pyroxene reflections are common to several clynopyroxenes, so it is not possible to distinguish the type of pyroxene present in the natural clinkers on the basis of the XRD patterns. The coincidence of the characteristic peaks of tridymite with those of cristobalite and quartz does not allow its presence to be deduced, but it cannot be ruled out either.

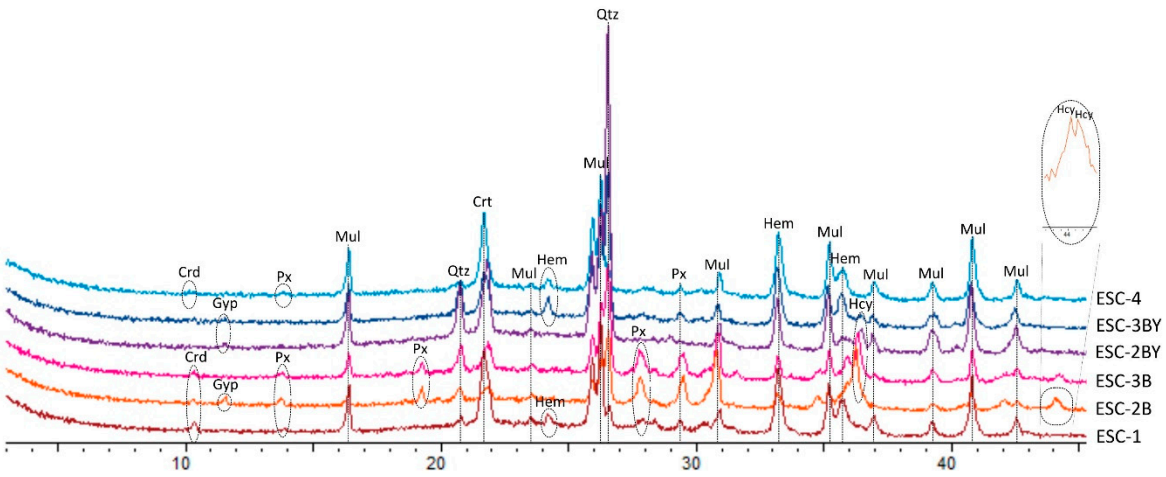

Figure 2. Mineral phases identified by XRD in the studied samples. Qtz = quartz, Hem = hematite, Mul = mullite, Crt = cristobalite, Hcy = hercynite, Px = pyroxene, Crd = cordierite, Gyp = gypsum.

Subsamples ESC-2B, ESC-2BY, ESC-3B, and ESC-3BY contain mullite, cristobalite, hematite, hercynite, quartz, and pyroxenes as detected in ESC-1 and ESC-4. Cordierite was identified in subsamples ESC-2B and ESC-3B and gypsum was identified in XRD patterns in ESC-2B, ESC-2BY, and ESC-3BY.

The hercynite $d_{(400)}$ values show differences from sample to sample. Two different $d_{(400)}$ peaks are observed in subsample ESC-2B (Figure 2), corresponding to $d_{(400)}$ values of 8.208 Å and 8.196 Å, and we infer that these values pertain to two different reflections corresponding to the (400) planes. In subsample ESC-3B the $d_{(400)}$ value for hercynite is 8.168 Å. The hematite $d_{(104)}$ values are similar in all the subsamples, with values of 2.693 Å, 2.695 Å, 2.693 Å, and 2.693 Å for subsamples ESC-2B, ESC-2BY, ESC-3B, and ESC-3BY, respectively.

According to quantitative XRD analyses (Table 1), mullite is the most abundant mineral, ranging from 16.3% to 38% of the total. The hercynite content is higher (>4%) in samples ESC-2B and ESC-3B and the hematite content is higher (~10%) in samples ESC-3BY and ESC-4. ESC-2BY and ESC-3BY present the highest quartz content (~7%). The rest of the quantified phases (cristobalite, cordierite, and gypsum) are present in similar proportions in the samples where they are present.

The section labeled as "others" was obtained by summing up of all components to 100%. This section has the highest content in almost every sample (33.4% to 60.6%) and represents the

amorphous phase. In addition, this section includes a small amount of pyroxenes (not quantified because it was not possible to identify the type of pyroxene).

Table 1. Mineral quantification of analyzed natural clinkers.

Sample	Mineral Phase (%)							
	Quartz	Hematite	Mullite	Cristobalite	Hercynite	Cordierite	Gypsum	Others
ESC-1	1.3	7.5	27.9	2.8	-	2.2	-	58.3
ESC-2B	3.2	4.1	16.3	1.9	5	1.3	7.6	60.6
ESC-2BY	6.9	5.2	33.5	4.5	1.3	-	3.3	45.3
ESC-3B	4.6	3.7	27.8	2.6	4.3	2.5	-	54.5
ESC-3BY	6.9	10	38	4.4	1.4	-	5.9	33.4
ESC-4	1.7	9.5	35.4	5.5	-	1	-	46. 9

4.2. Optical Microscopy

The natural clinkers show similar textures at the scale of the optical microscope. In general, the samples present a vitreous appearance and high and heterometric porosity with pore sizes from less than 1 μm to 5 mm. This porosity is probably a consequence of the dehydroxylation of phyllosilicates and the carbonate and organic matter destabilization.

The natural clinkers are formed by both transparent and opaque minerals immersed in a fine-grained matrix below the optical resolution of the microscope. These three components are distributed heterogeneously in the samples. In general, opaque minerals are more abundant than transparent phases at this scale of observation. Opaque minerals are concentrated in the black areas and transparent minerals in the red and yellow ones.

Under reflected light, spinel (hercynite, according to the XRD results) and hematite were identified. The relative abundance of these minerals varies from sample to sample and even at sample scale. As indicated above, and in agreement with the XRD data, hercynite, and hematite were concentrated in the black areas and were immersed in a continuous gray matrix that could not be identified by this technique. Hercynite is found as exsolution lamellae in hematite crystals (Figure 3a) or forming replacement textures with hematite (Figure 3b).

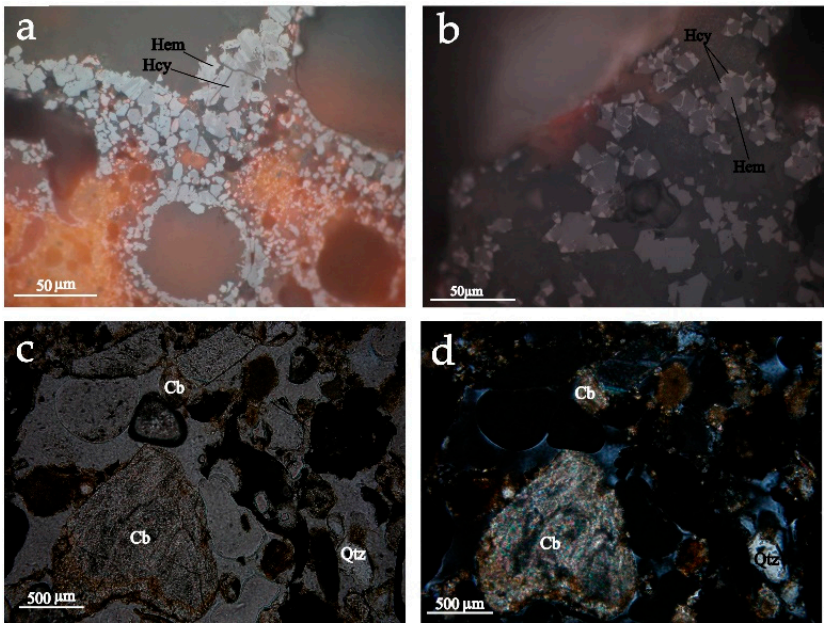

Figure 3. Reflected light optical microscopy images of hercynite and hematite in parallel nicols (**a**,**b**). Transmitted light optical microscopy images in parallel (**c**) and crossed nicols (**d**). Hem = hematite, Hcy = hercynite, Cb = carbonates, Qtz = quartz.

Under transmitted light, the only transparent minerals that are observed are quartz and degraded carbonate-type grains immersed in a fine-grained matrix with particle sizes below optical microscope resolution. Quartz is found as anhedral to subhedral clasts, with common angular grain boundaries, whereas carbonates occur as highly altered irregular rock fragments (Figure 3c,d).

4.3. Field-Emission Scanning Electron Microscopy (FESEM)

Backscattered electron images (BSE) and chemical analyses (EDS) of the natural clinkers show that they are texturally and compositionally heterogeneous. Electron images made it possible to observe the different minerals already identified by XRD, such as mullite, hematite, silica phases, pyroxenes, cordierite, and hercynite. Furthermore, pyrite and calcium oxides were detected by FESEM although they were not identified by XRD.

4.3.1. Major Phases in the Natural Clinkers

The major phases present in the studied samples according to the XRD results are mullite, hematite, hercynite, pyroxenes, cordierite, quartz, and cristobalite. All these phases are embedded in an Al + Si-rich vitreous groundmass.

The mullite shows lenticular, acicular, and prismatic morphologies with random orientation. Its size is in general less than 1 μm in length, but in some areas it can reach up to 2 μm in length (Figure 4a).

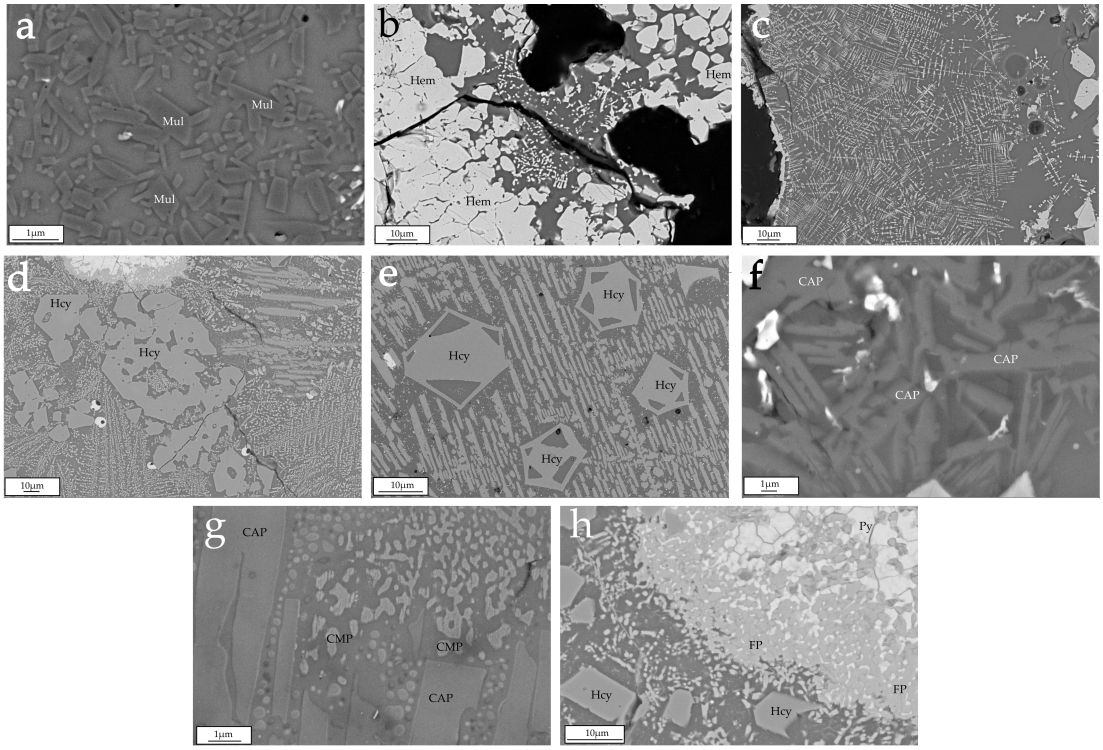

Figure 4. Backscattered electron images (BSE) images of (**a**) micron-sized mullite crystals with random orientation; (**b**) prismatic and subeuhedral hematite crystals; (**c**) dendritic hematite crystals; (**d**) subeuhedral hercynite crystals; (**e**) hercynite crystals with polygonal sections; (**f**) acicular Ca-Al-rich pyroxene crystals; (**g**) Ca–Mg-rich pyroxene crystals, with rounded morphologies associated with Ca–Al-rich pyroxenes; and (**h**) Fe-rich pyroxenes surrounding pyrite crystals. Mul = mullite, Hem = hematite, Hcy = hercynite, CAP = Ca–Al-rich pyroxene, CMP = Ca–Mg-rich pyroxene and FP = Fe-rich pyroxene.

Hematite is present in all the samples and forms crystalline aggregates with different crystal morphologies and sizes. On the one hand, it occurs as anhedral crystals 1–20 μm in diameter, sometimes

arranged in a mosaic-like texture (Figure 4b). On the other hand, it appears as dendritic and arborescent aggregates (Figure 4c), and it is also present as hexagonal plates smaller than 1 μm.

Hercynite is observed on the one hand as micron-sized euhedral to subeuhedral grains (Figure 4d), and in some cases as skeletal crystals showing polygonal sections, most of them hexagonal (Figure 4e). On the other hand, hercynite lamellae, 1–2 μm wide and 1–6 μm long, are observed within hematite crystals suggesting the development of exsolution processes (Figure 5a,b). The textural relationship between hercynite and hematite is correlated with EDS analyses of these phases, which are explained in the next section. Furthermore, replacement textures are observed between hematite and hercynite, where hercynite is replacing hematite (Figure 5c). In some cases, hercynite is replacing hematite from the nucleus (Figure 5e). In addition, hercynite lamellae are identified within cordierite crystals (Figure 5d); as in the case of hematite, this suggests exsolution processes between these two phases.

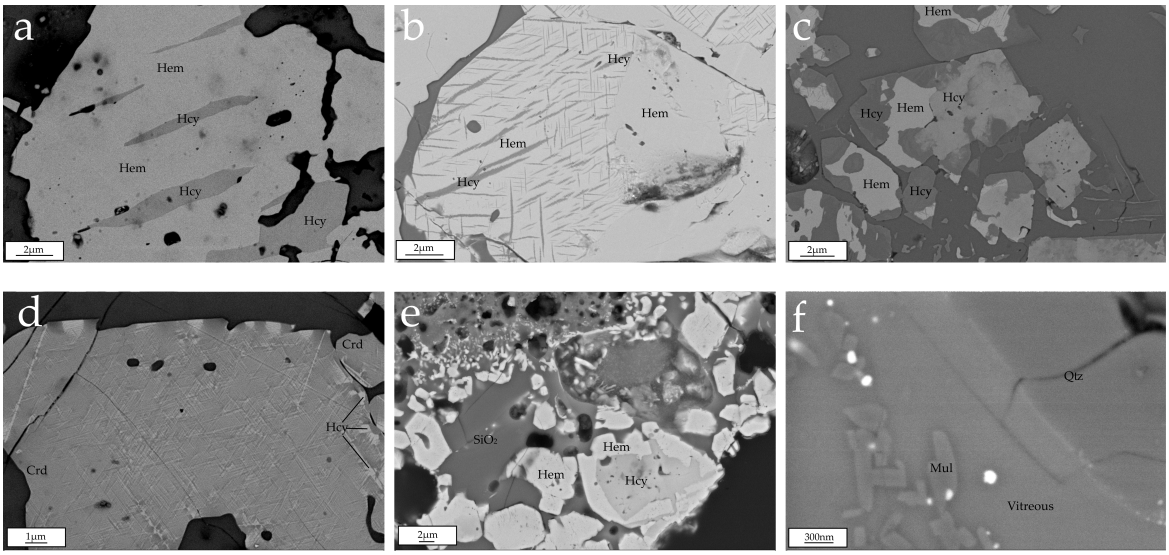

Figure 5. BSE images of (**a**,**b**) hercynite lamellae in hematite crystals, (**c**) replacement texture between hematite and hercynite, (**d**) hercynite lamellae in cordierite crystal, (**e**) hercynite nucleus in hematite crystal and silica phase filling the spaces among the crystals, and (**f**) quartz fragment with reaction edge. Hem = hematite, Hcy = hercynite, Crd = cordierite, SiO_2 = silica phases, Mul = mullite, Qtz = quartz, Vitreous = vitreous phase.

According to their chemical composition, three different groups of pyroxenes were distinguished: calcium- and aluminium-rich, calcium- and magnesium-rich, and iron-rich pyroxenes. Besides the differences in chemical composition, these show different textural features. Ca- and Al-rich pyroxenes are closely associated with hematite, hercynite and other pyroxenes, and appear randomly distributed in the matrix as micron-sized acicular crystals with no preferred orientation (Figure 4f).

Ca- and Mg-rich pyroxenes appear as rounded crystals smaller than 1 μm, and are randomly distributed throughout the matrix (Figure 4g). They are texturally associated with the Ca- and Al-rich pyroxenes.

Fe-rich pyroxenes appear as rounded crystals smaller than 1 μm, as well as lenticular crystals with sizes greater than 10 μm. Occasionally, rounded crystals of Fe-rich pyroxene are in close relationship with pyrite, appearing in the outer limits of mosaic-like pyrite aggregates (Figure 4h), suggesting that these pyroxenes could be replacing pyrite crystals.

A silica phase is observed as a groundmass filling the spaces among the crystals (Figure 5e). From the XRD data it can be inferred that this phase corresponds to cristobalite. Furthermore, quartz fragments larger than 2 μm and showing reaction edges (Figure 5f) were recognized. These quartz fragments were probably already present in the previous clay.

4.3.2. Minor Phases in the Natural Clinkers

FESEM images revealed minor phases such as calcium oxides and pyrite that were not detected by XRD. Calcium oxides appear as microcrystalline aggregates with sizes of ~50 μm (Figure 6a), which may come from carbonates in the precursor clay that have been destabilized with the spontaneous combustion.

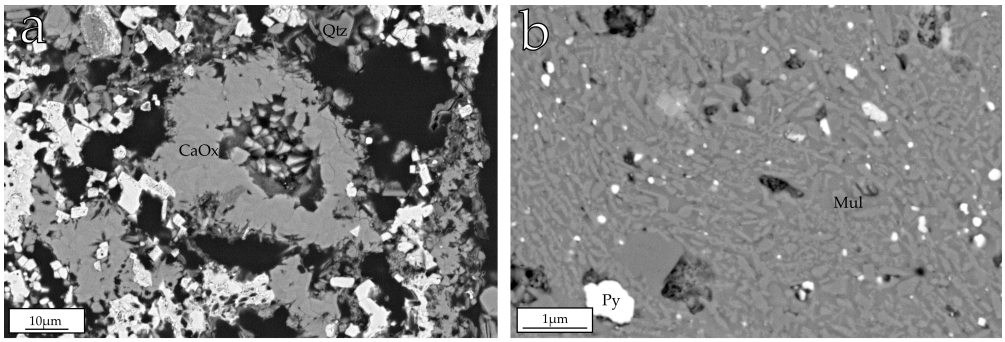

Figure 6. BSE images of (**a**) microcrystalline aggregates of calcium oxides and (**b**) anhedral pyrite crystals. CaOx = calcium oxides, Qtz = quartz, Mul = mullite, Py = pyrite.

Pyrite appears as anhedral crystals smaller than 1 μm, immersed in a gray matrix, probably vitreous (Figure 6b), and associated with mullite, pyroxenes, and quartz fragments. Pyrite and quartz were present in the original rock and probably remained stable with the increase in temperature.

4.3.3. Chemical Analyses

EDS analyses of the major phases are shown in Table 2. As the analyses indicate, mullite has an Al–Si composition with minor proportions of Fe and Ti. Theoretical mullite has a Si/Al ratio of 0.35, whereas our analyses show an average Si/Al ratio of 1.21 and an average Si/(Al + Fe + Ti) ratio of 1.13, indicating that the analyzed mullite is richer in Si than expected.

Table 2. Chemical composition (wt %) of all the mineral phases detected in the studied samples and average structural formula calculated. *n* = number of analysis; standard deviation in brackets.

Analyzed Phases	wt %									Calculated Average Formula
	O	Na	Mg	Al	Si	K	Ca	Ti	Fe	
Hematite	37.7	-	-	2.3	-	-	-	-	59.6	$Al_{0.1}Fe_{1.9}O_3$
(*n* = 14)	(1.7)	-	-	(1.5)	-	-	-	-	(1.8)	
Hercynite	44.6	-	1.8	27	-	-	-	0.4	26.1	$Mg_{0.1}Fe_{0.8}Al_{1.7}O_4$
(*n* = 21)	(3.8)	-	(1.8)	(7.6)	-	-	-	(0.2)	(7.0)	
Mullite (*n* = 23)	51.3	-	-	21.4	25.9	-	-	0.3	1.1	$Fe_{0.1}Al_{2.3}Si_{2.9}O_{9.75}$
	(9.1)	-	-	(5.5)	(4.9)	-	-	(0.1)	(0.9)	
"Ceramic pyroxenes"	53.7	0.4	0.1	12.6	22.8	0.4	8.5	0.1	1.5	$Ca_{0.5}Fe_{0.1}Al_1(Al_{0.1}Si_{1.9})O_6$
(*n* = 9)	(0.9)	(0.2)	(0.2)	(1.3)	(2.2)	(0.3)	(1.5)	(0.1)	(0.9)	
Cordierite	45.6	-	1.4	16	5.4	-	-	0.8	30.9	$(Mg_{0.5}Fe_{1.6})(Fe1.4Ti_{0.1})(Si_{2.6}Al_{2.4})Al_{2.8}O_{18}$
(*n* = 3)	(2.2)	-	(0.0)	(0.1)	(3.8)	-	-	(0.1)	(5.8)	
Silica phases	50.7	-	-	1.4	48	-	-	-	-	$Al_{0.1}Si_{0.9}O_2$
(*n* = 4)	(10.1)	-	-	(1.3)	(10.6)	-	-	-	-	
Fe-pyroxenes	45.6	-	1.1	4.1	18.8	-	0.7	0.3	29.4	$Al_{0.1}Mg_{0.1}Fe_{1.3}(Al_{0.3}Si_{1.7})O_6$
(*n* = 3)	(0.2)	-	(0.3)	(0.1)	(0.4)	-	(0.1)	(0.1)	(0.6)	
Ca–Mg pyroxenes	54.1	-	2	5.2	27.4	-	6.9	0.1	4.3	$(Al_{0.4}Mg_{0.2}Fe_{0.2}Ca_{0.4})Si_{2.3}O_6$
(*n* = 4)	(0.3)	-	(0.6)	(1.0)	(1.0)	-	(0.6)	0	(0.6)	
Vitreous phase	48.8	0.2	1.1	11.6	30.9	2.4	1.4	0.2	2.9	
(*n* = 25)	(9.6)	(0.2)	(1.6)	(7.3)	(6.5)	(1.3)	(1.6)	(0.2)	(2.7)	

Hematite and hercynite show compositional differences from sample to sample and even at sample scale. Figure 7 shows the Al vs. Fe contents (wt %) in these phases, indicating a trend from hematite to hercynite compositions. Taking into account all the analyses obtained from these phases,

those with Fe contents higher than 56% and Al contents lower than 5% were considered to be hematite. Conversely, those analyses with Fe contents lower than 40% and Al contents higher than 18% were considered to be hercynite. The rest of the analyses, which are not included within these limits, were considered to be intermediate compositions. On average, the hematite composition is close to the theoretical one (69.9% Fe and 30% O), with a 59.6% content in Fe, but it also contains minor proportions of Al (2.3%). As regards the hercynite composition, the Al (27%) and Fe (26.1%) contents are lower than the theoretical ones (31.05% Al, 32.13% Fe, and 36.82% O).

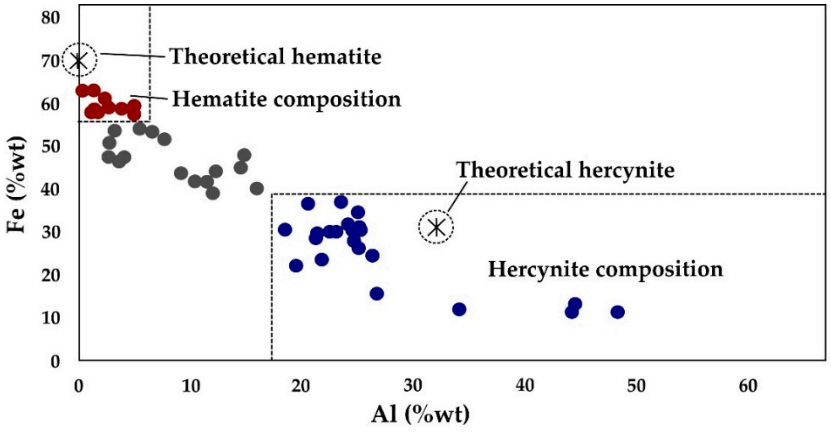

Figure 7. Al vs. Fe (wt %) graph showing hematite and hercynite composition.

Regarding pyroxenes, as mentioned above, three different compositional types were observed. The Ca- and Al-rich pyroxenes show low Fe, Na, K, Mg, and Ti contents. Their average structural formula is $Ca_{0.5}Fe_{0.1}Al_1(Al_{0.1}Si_{1.9})O_6$, and thus their composition may be described as intermediate between the fassaite compositions, reported by several authors [21,22], diopside, and esseneite [23] (Figure 8). Previous researchers have used the term "ceramic pyroxene" to refer to pyroxenes with an intermediate composition between fassaite and diopside [21,22]. Thus, in this study Ca- and Al-rich pyroxenes are called "ceramic pyroxenes".

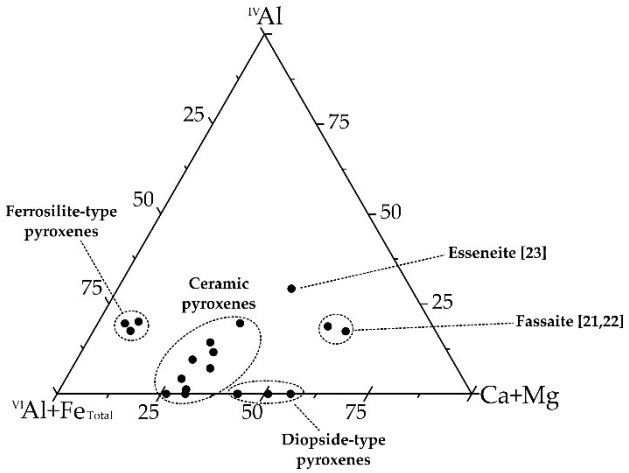

Figure 8. Plot of the EDS pyroxene compositions normalized on the basis of 6 oxygens in a $^{IV}Al - {}^{VI}Al + Fe_{total} - Ca + Mg$ diagram. Esseneite and fassaite compositions from the literature [21–23] have also been plotted as reference.

The compositions of the Ca- and Mg-rich and Fe-rich pyroxenes are plotted in Figure 9, showing that these groups have clearly different compositions. These compositions are close to diopside and ferrosilite compositions, respectively.

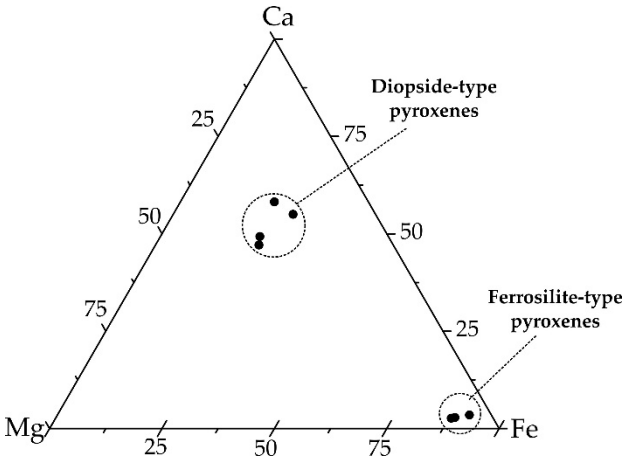

Figure 9. Plot of the EDS Ca–Mg-rich and Fe-rich pyroxene compositions normalized on the basis of 6 oxygens in a Ca–Mg–Fe diagram. The diagram shows the compositional differences between diopside- and ferrosilite-type pyroxenes.

The analyzed diopside-type pyroxenes present lower Ca (6.9%) and Mg (2%) contents than the theoretical diopside (18.51% Ca, 11.22% Mg, 25.94% Si, and 44.33% O), and they also contain Fe, Al, and minor proportions of Ti. The average structural formula of these phases is $(Al_{0.4}Mg_{0.2}Fe_{0.2}Ca_{0.4})Si_{2.3}O_6$. Similarly, a comparison of the Fe-rich pyroxene with ferrosilite shows it to have lower Si (18.8%) and Mg (1.1%) contents and higher Fe (29.4%) content than the theoretical composition (10.46% Mg, 24.04% Fe, 24.18% Si, and 41.32% O), with an average structural formula $Al_{0.1}Mg_{0.1}Fe_{1.3}(Al_{0.3}Si_{1.7})O_6$. It also contains Al and minor proportions of Ca and Ti.

The analyzed cordierite presents high Fe (30.9%) and Al (16%) contents and low Si, Mg, and Ti contents. Compared with the theoretical composition (8.31% Mg, 18.45% Al, 24.01% Si, and 49.23% O), the analyzed cordierite is Mg- and Si- poor and Fe-rich.

Finally, the groundmass of all the studied samples presents a heterogeneous Al- and Si-rich composition, with minor Fe, K, Mg, Ca, Ti, and Na contents. It can be deduced that it corresponds to the vitreous phase detected by XRD.

5. Discussion

5.1. Destabilization of the Initial Phases

The natural clinkers initially contained organic matter, abundant kaolinite and illite and minor proportions of quartz, K feldspar, siderite, pyrite, and Ti and Fe oxides [32]. Most of these phases were destabilized and melted during the spontaneous combustion of coal.

The calcium oxides observed by FESEM may come from small amounts of carbonates present in the precursor clays that have been destabilized, as suggested by optical microscopy observations of degraded carbonate fragments. Carbonate destabilization can generate not only these calcium oxides, but also other Ca-rich phases such as pyroxenes [22].

Organic matter is eliminated between 200 and 800 °C, although this depends on its content in the precursor material [36]. In addition, kaolinite, illite, and K feldspar are not detected in the studied natural clinkers, indicating that they have been destabilized, as described by other authors [20,37], and that they are therefore less stable phases than quartz or pyrite. Kaolinite is not stable at temperatures above 200 °C in natural environments [38]. Similarly, metamorphic rocks such as those from greenschist facies do not contain illite, which indicates that it is not stable above 350 °C. With regard to K feldspars, it is possible that they were destabilized during the spontaneous combustion due to their low content in the precursor clays.

The oxidation of pyrite and siderite results in hematite and magnetite [39,40], the former of which was identified in the study samples. In addition, when pyrite is oxidized, aqueous, acidic, and sulfate-rich solutions are produced [41]. These solutions, along with the presence of calcite, produce sulfate minerals such as gypsum. Accordingly, SO_4^{2-} released from pyrite oxidation, along with Ca from carbonates, allows gypsum precipitation [42], as it is identified by XRD in some of the studied samples.

Finally, quartz is also observed, indicating that it is the most stable phase during combustion, although it shows reaction edges, which suggest that it is partially destabilized due to the high-temperatures.

5.2. Crystallization of New Phases

5.2.1. Hematite, Hercynite and Cordierite

Hematite, magnetite, hercynite, and cordierite are frequently described in natural clinkers [11,13,16–18]. In the studied natural clinkers hematite, hercynite and cordierite were observed. Their textures are clearly related to neoformation associated with the combustion process.

Exsolution textures were observed between hematite and hercynite, as well as between cordierite and hercynite. These textures occur frequently as a consequence of cooling from a melted mass, in this case resulting from the spontaneous combustion process. With cooling, lamellae are separated within the host crystals due to differences in cation sizes, since at high-temperatures crystal structures can accommodate cations of different size more easily. However, at lower temperatures, the range of possible substitutions of different-sized cations is much less.

The existence both of magnetite exsolution lamellae in hercynite and of hercynite exsolution lamellae in magnetite has been previously described [11,43]. Solid solutions between both bases are also described in natural clinkers [13,43]. These textures are also formed in igneous and metamorphic rocks [26,44,45]. Furthermore, previous investigations have described titaniferous spinel intergrowths with hematite in igneous and metamorphic rocks and the possibility of a Zn-rich spinel formation that went into solution in cordierite in metamorphic rocks [44,46].

Magnetite was not detected by XRD in this study. This may be due to the fact that part of a primary magnetite may be pseudomorphed by hematite in a martitization process [43]. In this case, it is possible that remnant traces of the original magnetite may persist in the studied samples, which may not have been detected due to the low concentration. Another possibility is that hematite was formed during the spontaneous combustion instead of magnetite.

The existence of hercynite lamellae in magnetite crystals and vice versa suggests that both phases can occur as discrete phases at peak temperatures with substantial mutual solid solution [24]. However, the fact that the hercynite in the studied natural clinkers never contains exsolution lamellae supports the hypothesis that it has been exsolved from another phase. This phase could be a primary magnetite subsequently transformed into hematite, or it could be a hematite that crystallized during the spontaneous combustion instead of magnetite.

Figure 10 shows the Fe vs. Al content of hercynite crystals in different textural arrangements. Hercynite has a higher Al content and lower Fe content when it is found as scattered crystals or is involved in replacement textures with hematite (24.2% Al and 27.8% Fe). By contrast, the Al content is lower and the Fe content is higher when it forms exsolution lamellae within hematite (5.9% Al and 48.1% Fe) or cordierite (11.4% Al and 40.8% Fe).

The replacement textures between hercynite and hematite imply that one mineral has been formed from another, so they are not coeval phases. A similar process where spinel is formed by replacement of magnetite, which reacts with the vitreous phase, is described in the literature [27]. This reaction could have occurred in the same way in the studied natural clinkers, with the later oxidation or martitization of magnetite to hematite.

Exsolution lamellae of hercynite within both hematite and cordierite were observed in sample ESC-2, whereas in sample ESC-3 such exsolution lamellae were only observed within hematite.

This may be related to the above-mentioned differences in the $d_{(400)}$ values of hercynite observed in the XRD patterns of these two samples (8.208, 8.196 for ESC-2 and 8.168 Å for ESC-3). Thus, a close relationship between the textural arrangement of hercynite and the compositional and structural variations of this mineral can be deduced. In other words, the hercynite composition is different when it appears as exsolved lamellae within hematite or cordierite, and it shows structural differences depending on the mineral from which the exsolution process occurred.

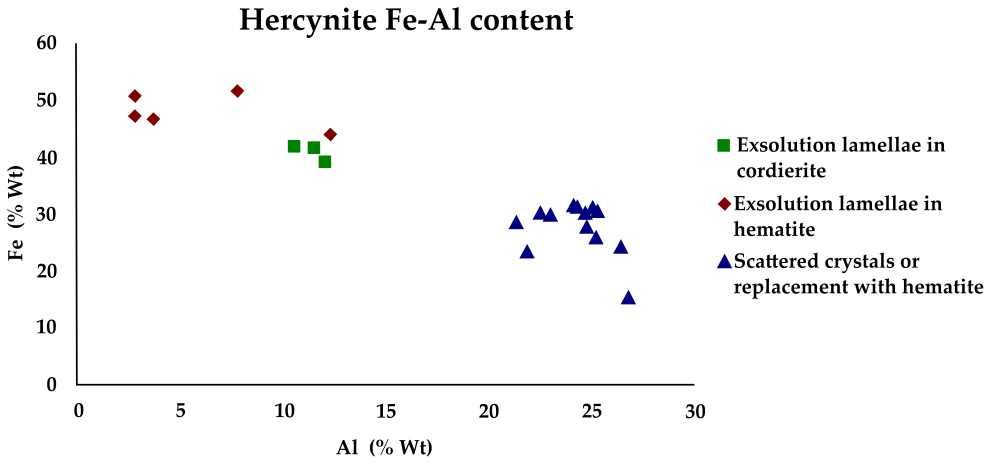

Figure 10. Fe vs. Al (wt %) content in hercynite crystals from samples ESC-2 and ESC-3. The proportion of the two elements depends on the way the crystals are arranged: exsolution lamellae in cordierite or hematite, or replacement textures with hematite or scattered crystals.

The hematite $d_{(104)}$ values are similar among samples ESC-2 and ESC-3, indicating that much of the detected hematite has a close composition to the theoretical one. This supports the hypothesis that the hematite may proceed from magnetite. If the hematite were crystallized from the vitreous phase, a higher Al content would be expected.

In hercynite exsolution lamellae within hematite, the cation size difference between Al and Fe favors the exsolution, although Fe-rich phases, Al-rich phases, and intermediate phases were able to form. In contrast, in hercynite exsolution lamellae within cordierite, the structural and compositional differences between the two phases preclude the existence of intermediate compositions.

The intermediate compositions between hematite and hercynite (Figure 7) may be due to the existence of nanometric exsolution textures, and thus EDS analyses may come from those areas where both phases are present. Alternatively, these intermediate analyses may also be reflecting the existence of minority solidus solutions that do not modify the $d_{(104)}$ values of hematite.

Finally, the idiomorphic skeletal textures that hercynite sometimes shows (Figure 4e) suggest its crystallization in two stages. A possible hypothesis that would explain this situation is the formation of a first-stage hercynite from the vitreous phase that was subsequently destabilized, giving rise to convex morphologies. After that, a euhedral hercynite could have crystallized in a second stage, surrounding the first crystals and including part of the vitreous phase.

5.2.2. Mullite and Pyroxenes

Mullite is present as 1–2 μm-long lenticular, acicular, and prismatic crystals with random orientation. Previous, electron microprobe analyses of mullite formed by the spontaneous combustion of coal reported Al-rich mullite with a composition close to the theoretical formula (38 wt % Al, 13.18 wt % Si, and 48.82 wt % O) [14].

However, chemical analyses of mullite in this study showed a Si/Al ratio of 1.21, which is higher than the theoretical ratio (0.35), indicating that this mullite is Si-rich. Analysis of mullite from aluminum-rich clays during ceramic firing also shows a nonstoichiometric Si-rich composition [20]. These authors explained that this is probably a consequence of the temperature and the length of time

of the ceramic process. Similarly, the nonstoichiometric composition of mullite in the natural clinkers could be explained by the temperature reached and the duration of the spontaneous combustion in the studied area, which would not have provided ideal conditions for mullite crystals to reach the theoretical composition.

EDS analysis showed three pyroxene-type compositions: "ceramic pyroxenes", diopside-type, and ferrosilite-type.

The "ceramic pyroxenes" were observed as micron-sized acicular crystals texturally associated with the other pyroxenes. Previous researchers have defined an uncommon C2/c pyroxene called esseneite as a product of pyrometamorphism associated with naturally combusted coal seams, which is similar to some pyroxenes from our analysis [23]. Other investigations have described pyroxenes formed during ceramic processes whose compositions are close to a pyroxene known as fassaite [21,22]. Even though the chemical compositions of the "ceramic pyroxenes" presented in this research do not match completely with those of fassaite or esseneite, they have intermediate compositions between these pyroxenes and diopside (Figure 8).

Diopside has previously been reported in natural clinkers [2,12] as well as in igneous and metamorphic rocks and skarns [47,48]. In ceramics, it is described as a metastable calcium and/or magnesium phase formed by the reaction of calcite, quartz and aluminum clays [49]. The calculated formula for diopside-type in the analyzed natural clinkers ($(Al_{0.4}Mg_{0.2}Fe_{0.2}Ca_{0.4})Si_{2.3}O_6$) shows a lower Ca and Mg content and a higher Si content than the theoretical formula ($CaMgSi_2O_6$).

Ferrosilite has been described in igneous rocks [47,50]. The melting of igneous crustal components at high-temperatures and very low, near-constant oxygen fugacity allow ferrosilite to crystallize [50]. Ferrosilite-type pyroxene in the studied natural clinkers ($(Al_{0.4}Mg_{0.1}Fe_{1.3})Si_{1.7}O_6$) shows higher Fe and lower Mg contents than the theoretical ferrosilite ($(FeMg)SiO_3$).

As with the mullite composition, the fact that the analyzed pyroxenes do not coincide with the theoretical ones could have to do with the firing dynamics associated with the spontaneous combustion of coal.

5.3. The Spontaneous Combustion of Coal and the Formation of the Vitreous Phase

An Al- and Si-rich vitreous phase is formed by the destabilization of the initial phases due to the increase in temperature, and it represents approximately 50% of the samples. The Al and Si come from quartz, kaolinite, and illite. Furthermore, this vitreous phase also contains minor proportions of K (from K feldspar and illite), Fe (from siderite, pyrite, and illite), Ca (from carbonates), and Mg (from illite). Previous researchers have described the appearance of a vitreous phase from 800 °C due to the spontaneous combustion of coal and resulting from the destabilization of clay minerals and other phases present in the initial rocks [39].

The new mineralogy and texture found in the studied samples are similar to that of fired aluminum-rich ceramics where the vitreous phase starts to form from 1000 °C and, consequently, mineral phases also crystallize from that temperature [20]. Furthermore, previous investigations indicate that the temperature reached in the studied area was probably higher than 1050 °C and the calcination periods were longer than 100 h [18].

These differences in temperatures indicated in the literature for the formation of the vitreous phase and subsequent mineral transformations may be due to the fact that these firing processes are heterogeneous and their duration and intensity can vary within the stratum where the natural clinkers are found. In the case of spontaneous combustion, besides temperature and length of time, there are several parameters that influence the process of spontaneous heating and combustion in coal, such as factors relating to mining, geological parameters, and the chemical contents of coal [10]. These parameters affect the composition of the new mineral phases and explain the presence of nonstoichiometric phases such as mullite and pyroxenes.

The higher percentages of vitreous phase and mullite, together with the greater size of the mullite (1–2 μm in length), compared to those at 1000 °C in ceramics (nanometer mullite) [20], allow to

deduce that, in our case, the temperature reached was higher than 1000 °C. Furthermore, Mössbauer spectroscopy and CCSEM measurements of the transformation products formed from pyrite included in coal in the drop tube furnace test at gas temperatures from 1038 °C to 1454 °C have shown magnetite to be the dominant oxide formed [51].

In the studied samples, hematite may have resulted from magnetite martitization. Magnetite thus crystallized due to the spontaneous combustion and, in this case, the temperature reached could have been between 1000 and 1454 °C.

6. Conclusions

Spontaneous combustion of coal generates textural and compositional changes in the precursor kaolinite-rich clays. These changes include the destabilization of original phases, giving rise to the genesis of an Al–Si-rich vitreous phase, and the subsequent crystallization of new mineral phases. These phases are similar to those formed in a ceramic process as well as in metamorphic and igneous environments.

The trend from hematite to hercynite composition indicate variations at sample scale, which are reflected in XRD patterns evidenced in crystallochemical parameters in hercynite. This suggests structural variations that can be related to the Al and Fe content in hercynite depending on its texture: exsolution lamellae within hematite (5.9% Al and 48.1% Fe), exsolution lamellae within cordierite (11.4% Al and 40.8% Fe), and replacement textures with hematite, as well as scattered hercynite crystals (24.2% Al and 27.8% Fe).

The analyzed mullite is Si-rich (Si/Al = 1.21) and nonstoichiometric compared with the theoretical mullite.

The study shows the crystallization of three different types of pyroxenes: diopside-type, ferrosilite-type, and a Ca–Al-rich pyroxene ("ceramic pyroxene") with an intermediate composition between that of diopside, fassaite, and esseneite. Compared with the theoretical compositions, the analyzed pyroxenes are nonstoichiometric.

The presence of nonstoichiometric phases could be explained by the short duration of the spontaneous combustion, which would not favor the formation of phases reaching the theoretical composition.

The higher percentages of vitreous phase and the larger size of mullite crystals compared with those of the ceramic process support the idea that the temperature would have reached more than 1000 °C.

Finally, the combination of XRD and electron microscopy has enabled a detailed characterization of the texture of the natural clinkers and the newly formed phase composition. The study of these new phases allows them to be compared with those formed during natural and ceramic processes and thus deepens our understanding of high-temperature crystallization processes.

Author Contributions: Conceptualization, E.L., B.B., and A.Y.; Formal Analysis, E.L.; Funding Acquisition, B.B.; Investigation, E.L., B.B., and A.Y.; Methodology, E.L. and B.B.; Project Administration, B.B.; Resources, B.B. and A.Y.; Supervision, B.B. and A.Y.; Validation, B.B. and A.Y.; Visualization, E.L.; Writing—Original Draft, E.L.; Writing—Review & Editing, E.L., B.B., and A.Y.

Funding: This research and the APC were funded by the European Regional Development Fund and the Government of Aragón (Grupo Aragosaurus: Recursos Geológicos y Paleoambientes), grant number CGL2017-85038-P.

Acknowledgments: The authors would like to acknowledge the use of the Servicio General de Apoyo a la Investigación-SAI, University of Zaragoza. They would also like to thank C. Gallego for her advice during the FESEM sessions. E.L. also thanks the Government of Aragón grant for the development her Ph.D.

Conflicts of Interest: The authors declare no conflicts of interest.

References

1. Smith, M.A.; Glasser, D. Spontaneous combustion of carbonaceous stockpiles. Part I. The relative importance of various intrinsic coal properties and properties of the reaction system. *Fuel* **2005**, *84*, 1151–1160. [CrossRef]
2. Querol, X.; Zhuang, X.; Font, O.; Izquierdo, M.; Alstuey, A.; Castro, I.; Van Drooge, B.L.; Moreno, T.; Grimalt, J.O.; Elvira, J.; et al. Influence of soil cover on reducing the environmental impact of spontaneous coal combustion in coal waste gobs: A review and new experimental data. *Int. J. Coal Geol.* **2011**, *85*, 2–22. [CrossRef]
3. Misra, B.K.; Singh, B.D. Susceptibility to spontaneous combustion of Indian coals and lignites: an organic petrographic autopsy. *Int. J. Coal Geol.* **1994**, *25*, 265–286. [CrossRef]
4. Querol, X.; Izquierdo, M.; Monfort, E.; Alvarez, E.; Font, O.; Moreno, T.; Alastuey, A.; Zhuang, X.; Lu, W.; Wang, Y. Environmental characterization of burnt coal gangue banks at Yangquan, Shanxi Province, China. *Int. J. Coal Geol.* **2008**, *75*, 93–104. [CrossRef]
5. Quintero, J.A.; Candela, S.A.; Ríos, C.A.; Montes, C.; Uribe, C. Spontaneous combustion of the Upper Paleocene Cerrejón Formation coal and generation of Clinker in La Guajira Peninsula (Caribbean Region of Colombia. *Int. J. Coal Geol.* **2009**, *80*, 196–210. [CrossRef]
6. Ribeiro, J.; Ferreira da Silva, E.; Flores, D. Burning of coal waste piles from Douro Coalfield (Portugal): Petrological, geochemical and mineralogical characterization. *Int. J. Coal Geol.* **2010**, *81*, 359–372. [CrossRef]
7. Misz-Kennan, M.; Fabiańska, M. Thermal transformation of organic matter in coal waste from Rymer Cones (Upper Silesian Coal Basin, Poland). *Int. J. Coal Geol.* **2010**, *81*, 343–358. [CrossRef]
8. Zhao, X.; Wang, Q.; Xiao, H.; Mao, Z.; Chen, P.; Sun, J. Prediction of coal stockpile autoignition delay time using micro-calorimeter technique. *Fuel Process. Technol.* **2013**, *110*, 86–93. [CrossRef]
9. Xu, Y.L.; Wang, L.Y.; Tian, N.; Zhang, J.P.; Yu, M.G.; Delichatsios, M.A. Spontaneous combustion coal parameters for the Crossing-Point Temperature (CPT) method in a Temperature-Programmed System (TPS). *Fire Saf. J.* **2017**, *91*, 147–157. [CrossRef]
10. Sinha, A.; Singh, V.K. Spontaneous Coal Seam Fires: A Global Phenomenon. In *Spontaneous Coal Seam Fires: Mitigating a Global Disaster*; Voigt, S., Rüter, H., Jiahong, L., Jayakumar, R., Eds.; ERSEC Ecological Book Series-4, Beijing, China, 29 November–1 December 2005; Tsinghua University Press: Beijing, China, 2005; pp. 41–66.
11. Cosca, M.A.; Essene, E.J.; Geissman, J.W.; Simmons, W.B.; Coates, D.A. Pyrometamorphic rocks associated with naturally burned coal beds, Powder River Basin, Wyoming. *Am. Mineral.* **1989**, *74*, 85–100.
12. Foit, F.F.; Hooper, R.L.; Rosenberg, P.E. An unusual pyroxene, melilite, and iron oxide mineral assemblage in a coal-fire buchite from Buffalo, Wyoming. *Am. Mineral.* **1987**, *72*, 137–147.
13. Henao, J.A.; Carreño, A.M.; Quintero, J.A.; Candela, S.A.; Ríos, C.A.; Ramos, M.A.; Pinilla, J.A. Petrography and application of the Rietveld method to the quantitative analysis of phases of natural Clinker generated by coal spontaneous combustion. *Earth Sci. Res. J.* **2010**, *14*, 17–30.
14. Sokol, E.; Volkova, N.; Lepezin, G. Mineralogy of pyrometamorphic rocks associated with naturally burned coal-bearing spoil-heaps of the Chelyabinsk coal basin, Russia. *Eur. J. Mineral.* **1998**, *10*, 1003–1014. [CrossRef]
15. Ciesielczuk, J.; Misz-Kennan, M.; Hower, J.C.; Fabiańska, M.J. Mineralogy and geochemistry of coal wastes from the Starzykowiec coal-waste dump (Upper Silesia, Poland). *Int. J. Coal. Geol.* **2014**, *127*, 42–55. [CrossRef]
16. Ribeiro, J.; Suárez-Ruiz, I.; Flores, D. Geochemistry of self-burning coal mining residues from El Bierzo Coalfield (NW Spain): Environmental implications. *Int. J. Coal. Geol.* **2016**, *159*, 155–168. [CrossRef]
17. Baboolal, A.A.; Knight, J.; Wilson, B. Petrography and mineralogy of pyrometamorphic combustion metamorphic rocks associated with spontaneous oxidation of lignite seams of the Erin Formation, Trinidad. *J. S. Am. Earth. Sci.* **2018**, *82*, 181–192. [CrossRef]
18. Alastuey, A.; Bastida, J.; Fernández-Turiel, J.L.; Querol, X.; Signes, M. Mineralogía de las arcillas calcinadas de la base de la Fm. Escucha en el área de Foz-Calanda. *Cuadernos de Geología Ibérica* **1993**, *17*, 171–184.
19. Besteiro, J.; Bastida, J.; Amigó, J.M.; Lores, M.T.; López Buendía, A.; Serrano, F.J. Sobre análisis microestructural por DRX y condiciones de formación de mullitas naturales de la cuenca de Oliete (Teruel). *Bol. Soc. Esp. Min.* **1996**, *19*, 119–129.
20. Laita, E.; Bauluz, B. Mineral and textural transformations in aluminium-rich clays during ceramic firing. *Appl. Clay Sci.* **2018**, *152*, 284–294. [CrossRef]

21. Dondi, M.; Ercolani, G.; Fabbri, B.; Marsigli, M. An approach to the chemistry of pyroxenes formed during the firing of Ca-rich silicate ceramics. *Clay Miner.* **1998**, *33*, 443–452. [CrossRef]
22. Bauluz, B.; Mayayo, M.J.; Yuste, A.; Fernandez-Nieto, C.; González López, J.M. Tem study of mineral transformations in fired carbonated clays: Relevance to brick making. *Clay Miner.* **2004**, *39*, 333–344. [CrossRef]
23. Cosca, M.A.; Peacor, D.R. Chemistry and structure of esseneite ($CaFe^{3+}AlSiO_6$) a new pyroxene produced by pyrometamorphism. *Am. Mineral.* **1987**, *72*, 148–156.
24. Sandiford, M.; Neall, F.B.; Powell, R. Metamorphic evolution of aluminous granulites from Labwor Hills, Uganda. *Contrib. Mineral. Petrol.* **1987**, *95*, 217–225. [CrossRef]
25. Brotzu, P.; Gomes, C.B.; Melluso, L.; Morbidelli, L.; Norra, V.; Ruberti, E. Petrogenesis of coexisting SiO_2-undersaturated to SiO_2-oversaturated felsic igneous rocks: The alkaline complex of Itatiaia, southeastern Brazil. *Lithos* **1997**, *40*, 133–156. [CrossRef]
26. Markl, G. Mullite-corundum-spinel-cordierite-plagioclase xenoliths in the Skaergaard Marginal Border Group: multi-stage interaction between metasediments and basaltic magma. *Contrib. Mineral. Petrol.* **2005**, *149*, 196–215. [CrossRef]
27. Treiman, A.H. Amphibole and hecynite spinel in Shergotty and Zagami: Magmatic water, depth of crystallization, and metasomatism. *Meteoritics.* **1985**, *20*, 229–243. [CrossRef]
28. Pardo, G. Estratigrafía y sedimentología de las formaciones detríticas del Cretácico inferior terminal del Bajo Aragón Turolense. Ph.D. Thesis, University of Zaragoza, Zaragoza, Spain, 1979. (In Spanish)
29. Cervera, A.; Pardo, G.; Villena, J. Algunas precisiones litoestratigráficas sobre la Formación "lignitos de Escucha". *Tecniterrae* **1976**, *3*, 25–33.
30. Querol, X. Estudio geológico de la Formación Escucha en la Cueca del Maestrazgo, Cordillera Ibérica oriental. Ph.D. Thesis, University of Barcelona, Barcelona, Spain, 1988. (In Spanish)
31. Salas, R. El Malm i el Cretaci inferior entre el Massis de Garraf i la Serra d'Espadà: Anàlisi de conca. Ph.D. Thesis, University of Barcelona, Barcelona, Spain, 1987. (In Catalan)
32. Bauluz, B.; Mayayo, M.J.; Yuste, A.; González López, J.M. Genesis of kaolinite from Albian sedimentary deposits of the Iberian Range (NE Spain): analysis by XRD, SEM and TEM. *Clay Miner.* **2008**, *43*, 459–475. [CrossRef]
33. Hillier, S. Quantitative analysis of clay and other minerals in sandstones by X-ray powder diffraction (XRPD). *Int. Assoc. Sedimentol. Spec. Publ.* **2003**, *34*, 213–251.
34. Schwartz, K.B.; Leong, D.B.; McConville, R.L. Structural chemistry of synthetic cordierite: Evidence for solid solutions and disordered compositional domains in Bi-flux-grown Mg-cordierites. *Phys. Chem. Miner.* **1994**, *20*, 563–574. [CrossRef]
35. Hill, R.J. X-ray powder diffraction profile refinement of synthetic hercynite. *Am. Mineral.* **1984**, *69*, 937–942.
36. Johnson, J.S.; Clark, J.; Miller-Antonio, S.; Robins, D.; Schiffer, M.B.; Skibo, J.M. Effects of Firing Temperature on the Fate of Naturally Occurring Organic Matter in Clays. *J. Archaeol. Sci.* **1988**, *15*, 403–414. [CrossRef]
37. Aras, A. The change of phase composition in kaolinita- and illite-rich clay-based ceramic bodies. *Appl. Clay Sci.* **2002**, *24*, 257–269. [CrossRef]
38. Merriman, R.J.; Peacor, D.R. Very-low grade metapelites: Mineralogy, microfabrics and measuring reaction progress. In *Low-Grade Metamorphism*, 1st ed.; Frey, M., Robinson, D., Eds.; Blackwell Science: Hoboken, NJ, USA, 1998; pp. 10–60. [CrossRef]
39. Ram, L.C.; Tripathi, P.S.M.; Mishra, S.P. Mössbauer spectroscopic studies on the transformations of iron-bearing minerals during combustion of coals: Correlation with fouling and slagging. *Fuel Process. Technol.* **1995**, *42*, 47–60. [CrossRef]
40. Kapička, A.; Petrovsky, E.; Ustjak, S.; Macháčková, K. Proxy mapping of fly-ash pollution of soils around a coal-burning power plant: A case study in the Czech Republic. *J. Geochem. Explor.* **1999**, *66*, 291–297. [CrossRef]
41. Floyd, M.; Czerewko, M.A.; Cripps, J.C.; Spears, D.A. Pyrite oxidation in Lower Lias Clay at concrete highway structures affected by thaumasite, Gloucestershire, UK. *Cem. Concr. Compos.* **2003**, *25*, 1015–1024. [CrossRef]
42. Ritsema, C.J.; Groenenberg, J.E. Pyrite Oxidation, Carbonate Weathering, and Gypsum Formation in a Drained Potential Acid Sulfate Soil. *Soil Sci. Soc. Am. J.* **1993**, *57*, 968–976. [CrossRef]

43. Estrada, S.; Piepjohn, K.; Frey, M.J.; Reinhardt, L.; Andruleit, H.; Von Gosen, W. Pliocene coal-seam fires on southern Ellesmere Island, Canadian Artic. *N. Jb. Geol. Paläont.* **2009**, *251*, 33–52. [CrossRef]
44. Müke, A. Magnetite, ilmenite and ulvite in rocks and ore deposits: petrography, microprobe analyses and genetic implications. In *Mineralogy and Petrology*, 1st ed.; Nasdala, L., Broekmans, M.A.T.M., Eds.; Spinger: Viena, Austria, 2003; Volume 77, pp. 215–234. [CrossRef]
45. Smith, D.G.W. The chemistry and mineralogy of some emery-like rocks from Sithean Sluaigh, Strachur, Argyllshire. *Am. Mineral.* **1965**, *50*, 1982–2022.
46. Stoddar, E.F. Zinc-rich hercynite in high-grade metamorphic rocks: A product of the dehydration of staurolite. *Am. Mineral.* **1979**, *64*, 736–741.
47. Ridolfi, F.; Braga, R.; Cesare, B.; Renzulli, A.; Perugini, D.; Del Moro, S. Unravelling the complex interaction between mantle and crustal magmas encoded in the lavas of San Vincenzo (Tuscany, Italy). Part I: Petrography and Thermobarometry. *Lithos.* **2016**, *244*, 218–232. [CrossRef]
48. Berg, R. Tungsten skarn mineralizations in a regional metamorphic terrain in northern Norway: A possible metamorphic ore deposit. *Miner. Deposita* **1991**, *26*, 281–289. [CrossRef]
49. Trindade, M.J.; Dias, M.I.; Coroado, J.; Rocha, F. Mineralogical transformations of calcareous rich clays with firing: A comparative study between calcite and dolomite rich clays from Algarve, Portugal. *Appl. Clay. Sci.* **2009**, *42*, 345–355. [CrossRef]
50. D'Souza, M.; Keshava Prasad, A.V.; Ravindra, R. Genesis of Ferropotassic A-Type Granitoids of Mühlig-Hofmannfjella, Central Dronning Maud Land, East Antarctica. In *Antarctica: Contributions to Global Earth Sciences*, 1st ed.; Fütterer, D.K., Damaske, D., Kleinschmidt, G., Miller, H., Tessensohn, F., Eds.; Springer: Berlin/Heidelberg Germany, 2006; pp. 45–54. [CrossRef]
51. Huffman, G.P.; Huggins, F.E.; Shah, N. Behavior of basic elements during coal combustion. *Prog. Energ. Combust.* **1990**, *16*, 243–251. [CrossRef]